SEDIMENT AND HYDRAULIC CHARACTERISTICS OF PALMER INLET, PRINCE EDWARD ISLAND, CANADA

BY

SHENMIN ZHANG, M.S.

A Thesis

Submitted to the School of Graduate Studies

in Partial Fulfilment of the Requirements

for the Degree

Doctor of Philosophy

McMaster University

April, 1991

This is not the end.

This is not even the beginning of the end.

But this is the end of the beginning.

—— Winston Churchill

PALMER INLET, PRINCE EDWARD ISLAND

DOCTOR OF PhILOSOPHY (1991) MCMASTER UNIVERSITY
(Geology) Hamilton, Ontario

TITLE: Sediment and Hydraulic Characteristics of Palmer Inlet, Prince Edward Island, Canada

AUTHOR: Shenmin Zhang, M.Sc. (East China Normal University)

SUPERVISOR: Professor Gerard V. Middleton

NUMBER OF PAGES: xxiii, 504, 138 Figures, 17 Tables

Abstract

In order to study the sediment and hydraulic characteristics of a small tidal inlet on the coast of the Gulf of St. Lawrence, field measurements were conducted at Palmer Inlet in 1984-1987. Data collected included continuous water level and velocity measurements at various sites, bed and suspension sediment samples, box- and tube-cores, direct and indirect (echo sounding) bedform observations, and general area mapping. Historic records and wind data were also available.

The first part of the thesis presents results of analyses of field data. Inlet morphology is described and its migratory behaviour analyzed by series of airphotos and maps. Surface sediment is divided into five depositional environments. Their characteristics, including grain size, bedforms and internal structures, are described based on the relative strength of tide and wave energy. Surface and subsurface data are then used to construct a three-dimensional stratigraphic model. Three sediment units were recognized, and discussed in terms of their relationship with the Holocene transgression. Generalized vertical sequences are compared with typical models, and their differences noted. Suspended sediments, megaripples and sediment transport data were also collected. Using these data, a number of existing theories and techniques are

tested. They include the Rouse equation, proposed stability fields of megaripples, and their description using a variance spectrum.

A series of numerical simulations was carried out in the second part of the thesis. Their purpose is to define the hydraulic mechanism that controls the bay tidal responses and related inlet currents. The effects of various factors were examined using idealized cases. The results show that in small tidal inlets, large intertidal sand bodies are the most important factor in distorting the tide and creating asymmetry. Overall, their presence imposes a force which retards the ebb more than the flood. The model, adjusted with measured data, is then applied to Palmer Inlet. Examples of model results are used to explain the observed tidal deformation. A stability analysis of the inlet was conducted using two existing methods, from which inlet evolution is inferred.

Acknowledgements

I would like to extend my sincere thanks to the members of my dissertation committee, G.V. Middleton, S.B. McCann and R.G. Walker. I thank them for their guidance and encouragement, which resulted in knowledge and a sense of appreciation that will always remain with me.

Special thanks go to my principal supervisor, Dr. Middleton, for his assistance through all these long and frustrated years, and for his sympathetic tolerance over all the bad aspects of working with a foreign student. Dr. McCann served as a major advisor in setting up this project, and remained supportive even when it was at the low points.

Many students at Department of Geology have helped at various stages. I thank them all. Steve Ash and Roggeband Adrian have each contributed significant skill, muscle and companionship in the field work. Steve Zymela introduced me to the computer world, and provided much-needed expertise in the final formatting of the thesis. Jack Whorwood did a great job of photographing the tube and box cores.

I would also like to thank the staff of the Department of Marine Geomorphology and Fishery and Ocean at the Bedford Institute of Oceanography. The names are too many to enumerate. People deserving special recognition are Kevin Robinson, Don Forbes and Donald Clattenburg. Nothing

could be said here to acknowledge adequately the time they shared generously with me.

This research was supported by the National Science and Engineering Research Council and by the Department of Energy, Mines and Resources of Canada, project number 181. Dr. Middleton serves as the principal investigator.

Table of Contents

List of Figures

List of Tables

Symbols and Definitions

Part I

b_o — Separation between wave orthogonals, m

C — grain size concentration, %

Ca — Grain size concentration at a reference level a, %

C_o — Wave celerity in deep water, m/s

E_o — Wave energy, kg-m/crest meter

g — Gravity constant, m/s^2

H_o — Deep water wave height, m

H_s — Wave height in the shallow water, m

H_{sb} — Significant wave height at break, m

k — K_rK_s

K_1 — Lunisolar declinational diurnal tide

K_o — The smallest wave number for the equilibrium subrange

K_r — Wave refraction coefficient

K_s — Wave shoaling coefficient

L_s — Wave length in the shallow water, m

L — Wave length, m

M_2 — Principal lunar semidiurnal tide

n, k = Number within spatial series (0, 1, 2, ..., N-1)

N — Total sample number

O_1 — Principal lunar diurnal tide

P_l — Longshore components of wave energy flux, kg-m/s/meter of beach front.

S_2 — Principal solar semidiurnal tide

M_m — Lunar monthly tide

$^{*}M_{sf}$ — Lunisolar fortnightly tide

U — Current velocity, m/s

U_{*} — Shear velocity, cm/s

U_{*avg} — Average shear velocity, cm/s

U_{*max} — Maximum shear velocity , cm/s

U_{em} — Maximum ebb current velocity, m/s

U_{fm} — Maximum flood current velocity, m/s

U_{1} — Current speed 1 m above the bed, m/s

U_{*cr} — Critical shear velocities for grain movement, cm/s

U_{1cr} — Critical velocity for sediment movement, cm/s

q_{s} — Sediment transport rate in g-cm-s units

W — Particle settling velocity, cm/s

X(t), Y(t) — Spatial series of bed profiles

Z_{o} — Roughness length

Δf — Frequency sample interval.

κ — von Karman's constant (0.4)

ϕ — Grain size unit, $-\log_{2}$(diameter in millimetre)

ρ_{w} — Seawater density, g/cm3

Θ — Angle between the wave orthogonal and the shorenormal, degree

α — Breaker angle between wave crest and shoreline, degree

* — For other tidal constituents, see Table 2-6 to 2-8

Part II

a_b — Amplitude of bay tides, m

a_o — Amplitude of sea tides, m

A — Bay surface area, m^2

A_b — Inlet cross-section area at the rear end, m^2

A_b' — A_b changes due to fluctuations of tides, m^2

A_c — Inlet gorge cross-section area, m^2

A_{co} — Inlet gorge cross-section area at mean sea level, m^2

A_{mr} — Bay surface area at mean water level, m^2

A_s — Inlet cross-section area at the entrance, m^2

A_s' — A_s changes due to fluctuations of tides, m^2

B — Channel width, m

C_k — Keulegan's (1967) correction coefficient for tidal prism calculation

D_I — Average depth of subsection I, m

D_s — Average depth of the shallow portion of channels, m

F — O'Brien and Clarks's impedance or total resistance factor, including friction entrance/exit loss

g — Gravitational acceleration, m/s^2

h_b — Bay water level, m

h — Sea water level, m

K — Keulegan's Coefficient of Repletion

K_{en} — Entrance loss coefficient

K_{ex} — Exit loss coefficient

K_1 — Mehta and Ozsoys' (1978) dimensionless damping coefficient

L_b — Length of the bay, km

P — Tidal prism, M^3/tidal cycle

Q — Inlet water discharge, M^3/s

Q_f — Fresh water discharge, M^3/s

Q_I — Discharge of subsection I, M^3/s

r^o — Superelevation of the bay tide

t — Time

T — Tidal period, hours

U_{eq} — Velocity when the inlet is in equilibrium state, m/s

U_m — Cross-section mean velocity, m/s

U_{mean} — Depth mean velocity, m/s

U_s — Average current velocity in the shallow portion, m/s

U_I — Average current velocity of the I^{th} section, m/s

U_{max} — Maximum cross-section mean velocity, m/s

W_c — Inlet width at the throat, m

W_I — Width of subsection I, m

x — Coordinate along the longitudinal axis of the inlet, m

α — Inlet channel slope, degree

β — Bay wall slope, degree

τ — Cross-section mean shear stress along x axis

τ_{max} — Maximum bottom stress, N/m^2

Part I

Morphology, Sediment and Hydraulics

— Observations and Analyses of Field Data

Chapter 1

Introduction

Tidal inlets on sandy barrier island coasts are tidally maintained channels, connecting a bay or lagoon with a larger body of water, usually a sea or ocean. Tidal inlets have been classified either by tidal range as microtidal (<2 m) and mesotidal (2-4 m) (Hayes, 1975), or by the antipathetic relationship between waves and tidal range as tide-dominated and wave-dominated (Hayes, 1979). Outlets of rivers at tidal coasts have also been called tidal inlets. In the context of the present study, they are considered as belonging to a different class of tidal environments - estuaries. Estuaries have large quantities of river-derived fresh water and fine sediments, and free communication with the sea which make them different from barrier-type inlets.

1.1 The problem

It has been recognized that microtidal barriers are subject to extensive modification of inlet processes. Microtidal inlets, because of shallow depth and high longshore drift, migrate faster than mesotidal inlets (Kumar and Sander, 1974; Hoyt and Henry, 1967). 30-50% of microtidal barriers have been found replaced by inlet

deposits as opposed to 10-20% of mesotidal barriers (Moslow and Tye, 1982). The great majority of studies of tidal inlets, however, has been conducted along mesotidal coasts, notably the Atlantic seaboard of the United States. Most of these studies are concerned about morphology and related processes (Hayes, 1979). Systematic study of sedimentary characters on the scale of those carried out in the Bay of Fundy (Dalrymple, 1977; Knight, 1977), and in the North Sea (Terwindt, 1981; de Mowbray and Visser, 1984) are rare. The lack of sediment data, particularly structure and sequence data, can be attributed, to a large extent, to the harsh working conditions particularly involved in coring or drilling programs (Moslow and Heron, 1978; Tye, 1984), and hampers the interpretation of similar environment in the stratigraphic record.

The coasts of the Southern Gulf of St. Lawrence, with more than 30 tidal inlets, offer a unique environment for field-based studies of microtidal inlets. While some of the most important coastal studies have been conducted in this area (Rosen, 1979; Davidson-Arnott and Greenwood, 1974; McCann, 1979; Armon, 1975; Owen, 1977), few are inlet related. These few studies were often conducted as a part of more general coastal studies with emphasis on such issues as the origin, history, sand body distribution (Armon, 1975, 1980; Armon and McCann, 1979) and stability of inlets (Keay, 1975). Detailed studies have been made in a large (Reinson,

1977; 1980) and a small inlet (Matsushita, 1986). In these studies, while fluid and sediment characters were monitored, actual data are far from sufficient for complete analysis of the hydraulic and sediment relationship. In addition, both inlets studied are navigational channels with considerable influence of human activities. The value of these studies as a descriptive framework for natural inlets in this region is thus affected.

1.2 Objectives

The basic scheme of this study is to provide a broad appraisal of interactions between water movement and the sediment surface in a small, natural tidal inlet on the Malpeque Barrier System, north coast of Prince Edward Island. The approaches adopted involved two separate but complementary parts: one was to conduct on-site observations of fluid and sediments, and the other was to perform numerical simulations using an existing inlet model (Seelig, 1977). The former strategy is to collect prototype data on fluid and sediment, and to provide a broad description and appraisal of sedimentary environments in an attempt to answer the following questions: (1) What is the basic characters of the tides and tidal flow in the inlet?; and (2) What are the substrate responses to these processes in terms of sediment texture, structures and resultant sequence? The numerical simulation is directed towards

better understanding of the above questions, and further to reveal the underlying factors which are responsible for observed process-response relationships. The intended feedback of a combined strategy is, hopefully, to lead to new insight into the nature of the processes, which are meaningful not only at this particular place, but on a more general level.

1.3 Outlines of the Thesis

In accordance with the two aims of the thesis, this paper is organized in two principal parts, each with its own introduction and conclusions. Part I is a synthesis of hydrodynamic and sedimentological data collected and interpreted over the field seasons of 1984, 1986 and 1987. Aside from the introductory Chapter 1, which includes literature review, it contains four other chapters. Chapter 2 sets the stage by describing the hydrodynamic setting of the area. It provides detailed description of processes such as winds, wave, tides and tidal currents. Chapter 3 deals with topography and morphology, and their historic development. Chapter 4 is a description of sedimentary environments in terms of sediment texture, bedforms, structures, and their stratigraphic sequence. The discussion of each environment is made in the light of relative strength between tide and wave energy. Chapter 5 is concerned with hydraulic interpretation of several types

of data, which were taken using the inlet as an experimental site. These include suspension sediments, megaripple geometries and sediment transport from bedform monitoring. A number of existing theories were tested using these data.

Part II commences with two preliminary chapters, introducing the major findings of previous work and the basic equations of the numerical model. Chapter 3 uses the Palmer Inlet for parametric studies, in which effects of various geometric and dynamic factors on tidal asymmetry are examined. Calibration of the inlet model is carried out in Chapter 4, using measured tidal as well as current data. The adjusted model is then applied in Chapter 5 to calculate, with the aid of an existing model of stability for a dual-inlet system (van de Kreeke, 1984), the present state of stability of the inlet.

1.4 Methods

Basic field work was carried out in June-August of 1984, 1986 and 1987. The first season was a reconnaissance in nature, including some basic mapping and bathymetric profiling. Field work of the later two seasons includes measurements of current speeds and tides, echo sounding, aerial photography, collection of grain size samples, bedform mapping and measurement, including digging of trenches, tube-and spade-box coring. Laboratory studies consist of opening tube-cores, making resin peels, grain

size analysis, digitization of echographs and analysis of aerial photographs. Tasks and instrumentation are outlined in Table 1-1, and will be further described where appropriate.

The sounding unit used for bathymetric and subtidal bedform observation is Raython Model DE-719B. This unit has a high sounding rate (9 soundings per second, or a sampling rate of 0.11 second per sample), and a narrow transducer-beam (8 degree at half power point), which gives a spatial resolution of 14 cm at 2 metre water depth. Operations were made at relatively calm weather to avoid disturbance by water motion. Buoys were implanted along the profiles to ensure that approximately the same track was followed for different runs. These buoys, which were recorded on the sounding chart by turning on a switch as the boat passed by them, were also used as scale-controllers as it was difficult to maintain constant boat speed on the route.

The majority of subtidal bedload sediment samples were obtained by a funnel-shaped sampler. Sediments were collected by dragging the sampler with a bag attached along the bottom. All samples were visually described, and subsampled on board to about 50 grams. In the lab, each sample was treated with hydrogen-peroxide and washed through 2 mm and 0.03 mm sieves to separate gravels, muds and sands. Grain size distributions of sand fractions were obtained by means of an automatically recording settling

Table 1-1 Tasks and instrumentation

Task	Instrumentation
Field work	
Tidal gaging	Ott-Boro pressure-type gages
Current gaging	RCM-4 Aanderaa automatic-recording meters Marsh-Mcbirney Model 201 direct-reading meter Endeco 110 remote reading current meters
Bathymetric survey	Raytheon DE-719B sounder Alidade Model 82500 and plane table
Suspended sediment measurements	Metal frame with plankton-net filters
Bedform measurements	Raytheon DE-719B sounder Brunton compass and tape measures diver
Grain size sampling	Shallow water sediment sampler
Internal structure	Spade-box corer and PVC tube corer
Laboratory work	
Grain size analysis	Settling-tube and Sedigraph
Air-photo analysis	Summa-sketch digitizer and PC computer
Bedform analysis	Summa-sketch digitizer and PC computer
Making resin peels	Cold Cure resin
Numerical modeling	VAX 6400

tube system using about 1 gram of sample.

Data on bedforms were obtained by echosounding and diving in subtidal areas, and by tape/Brunton measurement on intertidal flats. Echographs were acquired during different times of tidal cycles along tracks marked by buoys. Direct measurements of intertidal bedforms were restricted to low tides using a Brunton compass and a tape measure. Wave length was defined as the distance between two adjacent crests, and height is the vertical distance between the trough and the crest.

1.5 Microtidal versus Mesotidal Inlets — Previous Works

The literature on tidal inlets comes from different groups of researchers. This review focuses on the difference between micro- and meso-tidal inlets. Comprehensive reviews on tidal inlets have been given by Bruun (1978) and Boothroyd (1985). Some important works can be found in Cronin (1975), Leatherman (1979), Oertel and Leatherman (1985), and Greenwood and Davis (1984). Examples of excellent works on related topics are Klein (1970), Dalrymple (1977) and Knight (1977).

The literature records many antipathetically-related factors, which are responsible for basic differences between micro- and meso-tidal inlets (Table 1-2). The tidal range/wave height ratio determines the overall morphology of an inlet. Wave-dominated inlets are usually shallower with

Table 1-2 Antipathetic factors controlling large-scale features of tidal inlets. Q_{max} = Maximum inlet discharge in m^3/s. P = Tidal prism, m^3/ flood or ebb; M = longshore drift rate in m^3/yr. [1] - Bruun and Gerritsen (1959). [2] - FitzGerald (1982). [3] - Bruun (1978).

Antipathetic factors	Depositional process	Deposition response
Sea level/sediment supply	Relative sea level rise	Transgressive sediment sequence
	Relative sea level fall	Regressive sediment sequence
Tide range/wave height	Wave-dominated	Fewer inlets, shallow depth; open water lagoon; large flood deltas and small ebb deltas
	Tide-dominated	More inlets, deep channel; marsh-filled lagoon; large ebb deltas and small flood deltas
Tidal flow/longshore drift	Updrift deposition downdrift erosion	Lateral inlet migration; reworking of barrier deposits, filling of lagoon by flood delta attachment
$r = M/Q_{max}$ [1]	Bypassing through..	Transfer of sands from updrift to downdrift along
$r > 200\text{-}300$ [1]	Waves	ebb terminal lobe
$r = 50\text{-}150$ [2]	Waves & tidal currents	By swash bar landward migration or ebb delta breaching
$< 20\text{-}30$ [1]	Tidal currents	Through inlet main channel or by bar migration
$R = P/M$ [3]	Tidal flushing ability	Stability of inlet channel
$R > 100$	Good	Good
$R = 50 - 100$	Fairly good	Fair to poor
$R < 50$	Poor	Poor
Storm/fairweather	Strong storm action	Extensive overwash; inlet created or closed; ebb delta breaching and associated channel abandonment causing bar bypass; updrift migration of inlets
Flood/ebb currents	Time-velocity asymmetry flow-dominance	Zonation of bedforms; bedforms migrate in one dominant direction; reactivation surfaces; cross-bedding with bundle structure

larger flood tidal deltas and more overwash, and are backed by open water lagoons, while the opposite applies to the mesotidal inlets (Hayes, 1979; Hubbard et al., 1979; Nummedal and Penland, 1981). The volume of the tidal prism as opposed to the strength of longshore drift determines the tendency of wave forces to close or force an inlet to move laterally against tidal forces, which tend to keep it open and maintain its position. Wave-dominated inlets have small tidal prisms due to their relatively small tidal range, small bay size and usually distal locations in the bay. They tend to be less stable, migrating rapidly and/or closing periodically. The effects of storms are different from those of fairweather and between the two types of coasts. In microtidal coasts, storm effects are often in the form of excessive overwash or lateral migration. In mesotidal coasts, they are represented by sudden inlet abandonment and subsequent 'bar-passing' (Sexton and Hayes, 1982; Tye, 1984; FitzGerald, 1982). Storms can, depending on their intensity and approaching directions, either create (Pierce, 1969) or close an existing inlet (O'Brien, 1976; Bruun, 1978). Lynch-Blosse and Kumar (1976) reported that Brigantine Inlet, New Jersey, moved in the downdrift direction during storms, but in the updrift direction during periods of fairweather. In Wachapreague Inlet, Virginia large storms are felt throughout the inlet in cross section changes, while individual sections behave differently under

normal conditions (Byrne, et al., 1974). The relationship between sea level variation and sediment supply controls onshore-offshore movement, and thus the subsurface geometry of resultant inlet deposits (Uhlir, et al., 1988). With Holocene transgression and confined lateral migration due to undercutting of channels into the substrate (DeAlteris and Byrne, 1975; Imperato, et al., 1988), inlet sequences of tidal-dominated inlets are relatively narrow, plug-shaped, and oriented shore-normal (Tye, 1984; Heward, 1981). Preserved sequences of wave-dominated inlets are laterally-extensive, tabular-shaped and shore-parallel.

On a smaller scale, the interaction between water movement and sediments is controlled by the strength of, and in particular the difference between flood and ebb currents. Time-velocity asymmetry and related spatial segregation of ebb and flood currents are well-documented in mesotidal inlets (Lincoln and FitzGerald, 1988; Hayes, 1979). On the flood delta side, the incoming current concentrates in the central area, but is diverted, due to topographic shields (Finley, 1975; Hayes and Kana, 1976; Hubbard and Barwis, 1976), through the surrounding channels or breaches on ebb shields. A reverse pattern, attributed to the inertial effect, with outgoing flow occupying the central channel, is observed on the seaward side (Hayes and Kana, 1976; Nummedal and Penland, 1981; Hodge, 1982; FitzGerald, 1976). Spatial separation of flood and ebb flows results in close proximity

of sedimentary facies, in which both sediment and bedforms move dominantly in one direction with minor modification by the reverse flow. As a result, bedforms in inlets and estuaries are essentially comparable in types and behaviour with increasing velocity with their unidirectional counterparts (Middleton and Southard, 1984; Bocthroyd, 1985; Dalrymple, et al., 1978).

While most of bedform/structure-related work has been conducted in mesotidal inlets (Boothroyd and Hubbard, 1974, 1975; Finley, 1975; Hayes and Kana, 1976; Hubbard and Barwis, 1976), data on inlet stratigraphy come primarily from microtidal inlets (Kumar and Sander, 1974; Moslow and Heron, 1979; Moslow and Tye, 1985; Heron et al., 1984; Boothroyd et al., 1985; Israel et al., 1987; Berelson and Heron, 1985; Hennessy and Zarillo, 1987; Reddering, 1983). Inlet-filled sequence in both mesotidal inlets (Hayes and Kana, 1976; Penland, et al., 1988; Hubbard, et al., 1979; Hubbard and Barwis, 1976; Boothroyd, 1985) and microtidal inlets (Kumar and Sander, 1974; Moslow and Heron, 1978; Reddering, 1983) has been found similar to the classic point bar sequence of a meandering river. Such a sequence is characterized by a coarse lag with an erosive base overlain by cross-stratified sands deposited in both deep and shallow channels. The difference is that the unit above the channel deposits consists of channel-margin linear bar deposits made up of directional trough cross beds formed by megaripples

(Hayes and Kana, 1976) for mesotidal inlets, but consists of spit platform deposits made up of large-scale Gilbert-type foresets for microtidal inlets (Kumar and Sander, 1974). Proposed sequences of mesotidal flood tidal delta are essentially derived from of Hayes' morphological models (1980) by applying Walther's Law (Hayes, 1980; Hubbard and Barwis, 1976). They are characterized by successions of megaripple cross-bedding with dominantly ebb orientation in the lower part to flood orientation in the upper part. In contrast, coring of microtidal flood tidal delta revealed thick layers of massive sediments (Berelson and Heron, 1985; Boothroyd, et al., 1985; Israel, et al., 1987; Hennessy and Zarillo, 1987). Even where large-scale bedforms occur on the surface, they are not reflected in the internal structure (Hennessy and Zarillo, 1987). Due to the lack of primary structures, interpretation of microtidal flood delta deposits has to depend on other petrographic attributes and on the relation of the deposits to other facies, such as washover deposits.

1.6 The Study Area

The tidal inlet under investigation in this study is located in the northwest portion of the Malpeque Barrier System, Prince Edward Island, Canada, at an approximate latitude and longitude of 46°45'N and 64°00'30''W, respectively (Figure 1-1). Although other inlets, similar

Figure 1-1 Location map for Palmer Inlet. The oblique air photograph was taken on June 24, 1986. Keys: 1 - North Spit; 2 - South Spit; 3 - North Spit Platform; 4 - South Spit Platform; 5 - Main Channel; 6 - South Channel; 7 - North Channel; 8 - Flood Tida' Delta; 9 - Flood Spillover Lobe; 10 -Ebb Spillover Lobe; 11 - Ebb Spit;

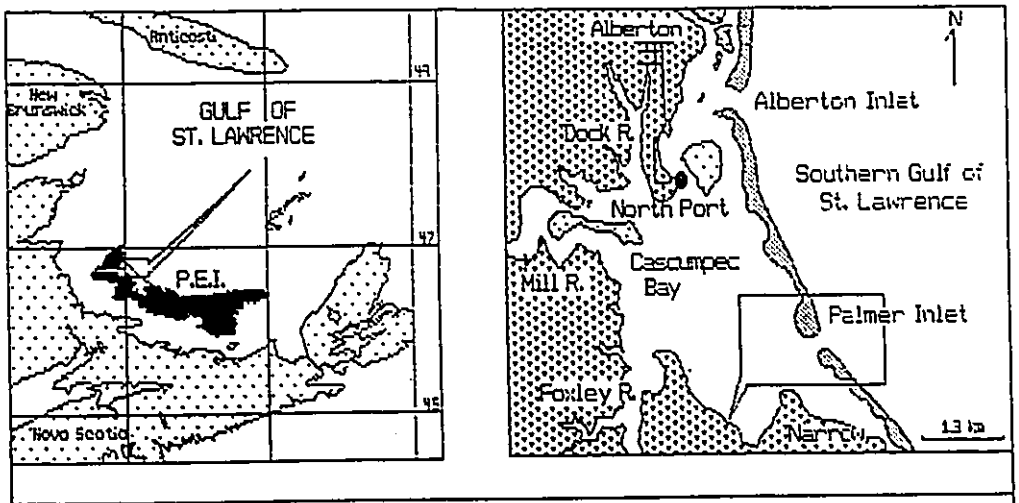
Anticosti
New Brunswick
GULF OF
ST. LAWRENCE
P.E.I.
Nova Scotia
49
47
45
Alberton
N
Alberton Inlet
Dock R.
Southern Gulf of
St. Lawrence
North Port
Cascumpec
Bay
Mill R.
Palmer Inlet
Foxley R.
Narrows
13 km

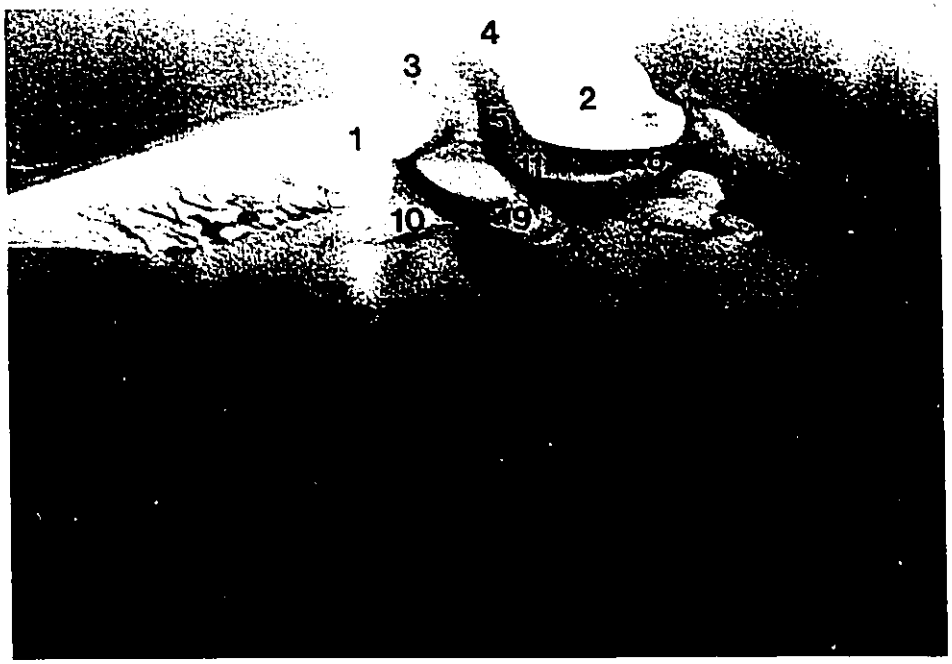
4
3
2
1
10
9

in size and configuration, were considered at the start, Palmer Inlet was chosen because of its natural state, and the proximity to a fishing dock — North Port.

Malpeque Barrier System is a 43 km long sandy barrier chain, broken by four tidal inlets, which connect the two major embayments of western Prince Edward Island to the Gulf of St. Lawrence. Palmer Inlet is one of the two tidal inlets draining the northern embayment, Cascumpec Bay. The hydraulic connection to a second inlet is a complication, which has received little consideration in other inlet studies.

Cascumpec Bay occupies an area of approximate 26 km^2, representing a syncline drowned during the Holocene transgression. There are four river sources to the Bay, but sediment supplies from them are limited due to the small catchment area and low hinterland relief. The inlets are undiluted by fresh water, and the bay is an open water system free from marsh and tidal creeks. The extension of the drowned valleys in the Bay, as suggested by the depth trend, directs a major portion of the Bay tidal prism towards the larger inlet, Alberton inlet, located on the northern end of the Bay. Alberton Inlet provides the major transportation link for a fishing port, North Port. Palmer Inlet is located on the southern edge of the Bay and bounded to the south by the Narrows, a narrow lagoon about 15 km long, and 800-900 m wide, and generally less than 1 m deep.

While the Bay is more than 5 m in its deepest portions, around Palmer Inlet it is less than 1.5 m deep and covered by eelgrass (Zostera marina). The shallower depths around the inlet suggest that Palmer inlet possibly was formed on a topographic high between two river valleys of a former land. Palmer Inlet came into existence before 1935 (Armon, 1975), and has been kept in its natural state ever since. Mixed tides with microtidal range prevail over the area. The coast is exposed to waves generated in the Gulf, but protected from those of the Atlantic Ocean. Waves are produced locally by wind (McCann, 1979).

1.7 Geology History

The surface of Prince Edward Island can be described as gently rolling to flat with local relief seldom in excess of a few tens of metres. The underlying bedrock is dominantly sandstones, with a small amount of siltstone, shale and conglomerates (Poole et al., 1970). These sedimentary rocks were deposited, by rivers, in Late Pennsylvanian and Early Permian times, in oxidizing conditions which gave the rocks their characteristic red-brownish colour and soft cementation. Bedrock has not been found in the field area, although outcrops nearby along Cape Kildare, on Savage Island and in Alberton channel have been identified. The preglacial surface of the Island was developed by erosional drainage systems in the Jurassic-

Tertiary period following the uplift of the Island in the Triassic period (Keen, 1971; Loring and Nota, 1973). The contemporaneous deformation of the bedrock resulted in gentle folds and faults, trending northeast (Prest, 1971).

Pleistocene glaciations left a layer of sandy to clayey tills mantling the preglacial surface, almost everywhere from a few centimetres to some tens of metres thick (Prest, 1973; Prest and Grant, 1969; Grant, 1976). Active ice retreat in early post-glacial deglaciation resulted in invasion of seawater in the west of the Island. Glaciomarine deposits, such as beach, bogs and peat consisting mainly of locally-derived materials, were formed in the area of marine overlap (Prest, 1971; 1973); glacial erratics were scattered on the land surface.

The Early Holocene (13,000-7,000 years B.P.) was a period of regression of sea level in the west due to isostatical rebound (Prest, 1973). The present coastal configuration is the result of Holocene transgression, which began about 4,000 years ago as the eustatic sea level rise gradually overtook the rebound (Grant, 1970). The transgression drowned drainage systems in coastal synclines, producing shallows embayments, which are separated by rugged rocky headlands. Fluvial sediment input into the embayments is small due to the small catchment. Primary sources of sediment are marine erosion of headlands at the shoreline and outcrops of bedrock or glacial deposits offshore (Black,

1987; McCann, 1979). Deposition at the coastline, in response to wind, tide and wave, formed sandy barriers or spits, separating shallow embayments and drowned river valleys from the Gulf. Between the main water bodies, tidal inlets became the main conduits where much of landward transport of sediments takes place (Armon and McCann, 1979).

1.8 Summary

Notable differences as well as similarities in general morphology between the two types of tidal inlets have been identified by previous work. Information on sediment characteristics, however, come mainly from mesotidal inlets, where most of studies were carried out.

Therefore, a typical, small inlet in the Gulf of St. Lawrence was chosen for systematic study of sediment-fluid interaction in a microtidal environment. The basic approach has been to combine field observation with a field-tested numerical model to assure better understanding of sediment and water movement in a typical microtidal environment. Field data collection included aerial photograph, bedform mapping and measurements, collection of grab size samples, digging of trenches, spade-box coring and making resin peels from them, tube-core coring, and echo sounding. Laboratory work and data reduction consisted of opening tube-cores, making resin peels, grain size analysis, analog-digit conversion of echographs and aerial photographs, reduction

and analysis of current data, and plotting of results.

Chapter 2

Physical and Hydraulic Setting

The significant environmental factors controlling inlet sedimentation are winds, waves and related longshore drift, astronomical tides and tidal currents. All these factors change in the course of time: the tide and tidal currents vary in a relatively predictable way, and the local winds and waves vary randomly. For a shallow, semi-closed area like Palmer inlet, these factors are further influenced by the geometry and alignment of the shoreline and basin, and the character of surrounding channels. Shielding of sand shoals may further complicate the tide and flow pattern. As a result, the magnitude of the tides and currents may change considerably with time and space within tidal inlets.

In the following, winds, waves and longshore drift, tides and tidal currents, are described in turn. In presenting the data, numerical and graphical methods have been used for putting the results into perspective. This includes calculations of various statistics and energy density spectra, construction of histograms, and time-velocity and stage-velocity plots.

2.1 Wind Climate

Weather data utilized in this study are 10-minute wind speeds and directions 10 m above the ground, from September 1, 1986 to August 31, 1987. This information was provided by the North Point Wind Station, P.E.I., about 35 km north of Palmer Inlet. Because of its proximity, these data are a close approximation of wind conditions at Palmer Inlet.

Frequencies of wind occurrence by speeds and directions are summarized in Table 2-1, and plotted in Figure 2-1 for the 12-month period studied. The yearly wind pattern shows that the prevailing wind in the study area is offshore from SSW-NW; these westerly winds occur 49.1% of the year. Winds from N-NNE directions form a second mode, occurring 13.3% of the year. Of the 35.1% onshore winds (NNW-ESE), 55.3% is from northern sectors (NNW-NNE), and 30% from southern sectors (ENE-ESE). While westerly winds appear throughout the year, the dominant wind (Figure 2-1) shows a rough shift from NW in September to February, to SE in April and May and then to NE in June to August. This seasonal pattern of winds is a reflection of change in the dominant regional air-mass from midcontinental arctic anticyclones in the winter to maritime extratropical cyclones, originated in the western Atlantic Ocean or in the Gulf of Mexico (Brookes, 1972), in the summer.

Speed data in Table 2-1 show that about 80% of the

Table 2-1 Statistics of wind data, North Point, Prince Edward Island (September 1, 1986 to August 31, 1987)

Speed (M/S)	N	NNE	NE	ENE	E	ESE	SE	SSE	S	SSW	SW	WSW	W	WNW	NW	NNW	Total
Accumulative % (equal to or exceeds the listed value)																	
0-4	6.7	6.6	5.1	3.9	3.5	3.2	6.1	4.4	5.3	6.0	7.2	8.9	9.7	8.6	8.7	6.1	100.0
4-8	4.3	4.0	2.5	1.7	1.6	1.4	2.7	2.1	2.3	2.9	4.3	5.7	6.5	6.6	6.7	4.3	59.6
8-12	1.7	2.0	1.0	0.5	0.3	0.3	0.5	0.3	0.3	0.5	1.3	2.1	2.4	3.1	2.6	1.4	20.3
12-16	0.6	0.7	0.3	0.2	0.1	0.1	0.0	0.0	0.0	0.0	0.1	0.2	0.5	0.7	0.3	0.4	4.2
16-20	0.3	0.2	0.1	0.1	0.0	0.0	0.0	0.0	0.0	0.0	0.0	0.0	0.0	0.0	0.0	0.1	0.8
20-24	0.0	0.0	0.0	0.0	0.0	0.0	0.0	0.0	0.0	0.0	0.0	0.0	0.0	0.0	0.0	0.0	0.0
24-28	0.0	0.0	0.0	0.0	0.0	0.0	0.0	0.0	0.0	0.0	0.0	0.0	0.0	0.0	0.0	0.0	0.0
Percent frequency of > 16 m/s winds																	
	29.2	26.7	10.8	7.2	0.4	3.4	0.0	0.0	0.8	0.0	0.0	0.2	0.2	4.4	3.8	12.7	99.9

Figure 2-1 Annual (12 months) and monthly percentage occurrence of wind directions for each of 16 compass points. Based on 10-minute wind data from North Point Wind Station, Prince Edward Island.

JANUARY

FEBRARY

MARCH

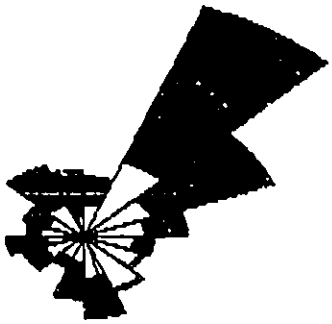

APRIL

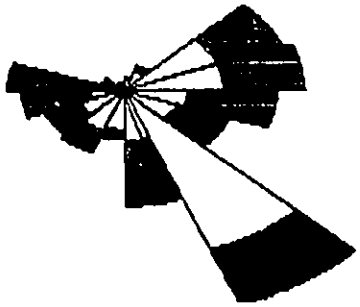

MAY

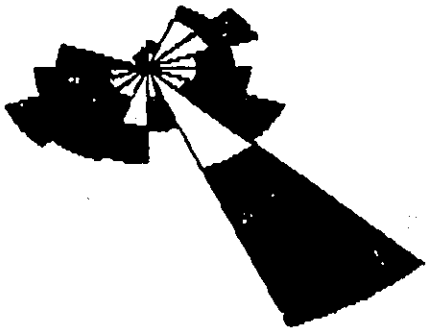

JUNE

JULY

AUGUST

SEPTEMBER

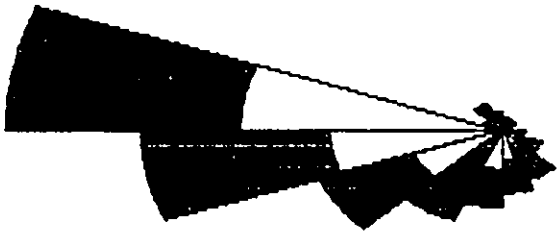

OCTOBER

NOVENBER

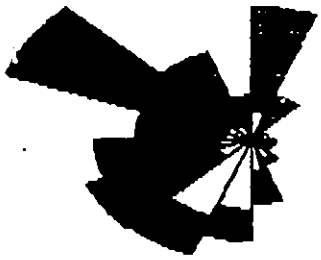

DECEMBER

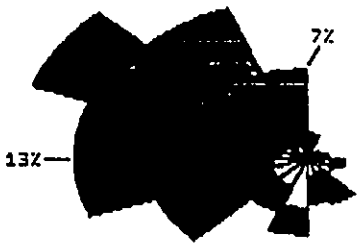

LEGENDS

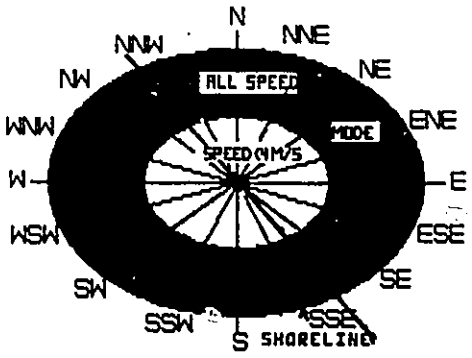

12 MONTHS

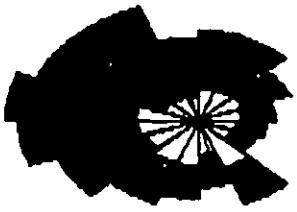

Figure 2-1 Continued.

year, winds blow at speeds of <8 m/s. Storm winds, winds with speed 16 m/s and up, occur less than 1% of the time. Monthly maximum speeds show a similar pattern to that of the wind roses, with higher values occurring in the fall and winter (Figure 2-2). Although most monthly maxima are from west and northeast, the frequency distribution of winds stronger than 16 m/s shows that 90.6% of storm winds are from NNW-ESE directions (Table 2-1). This suggests that stronger winds in the study area are primarily associated with extratropical weather systems, having a strong onshore component in the study area. Further breakdown shows that of these onshore winds, 75.7% come from NNW-NNE, and 12% from ENE-ESE. Both total and >16 m/s wind data thus indicate that onshore winds in the study area are dominated by the northern component.

The summer season from June to August, during which field work were conducted, is a quiescent period with no prominent frontal system passing through the area. Winds were generally mild and steady, and spread fairly evenly throughout the compass. While a sustained quiescent period provided a good and simple condition for field operations and identifying the tidal response, events of higher winds would provide a better spectrum for the understanding of effects of wind-wave conditions. It is in this respect that hindcast for waves employing yearly data is of particular significance.

Figure 2-2 Monthly maximum wind speed, direction at maximum speed, maximum and average temperature from September 1, 1986 to August 31, 1987. Source: North Point Wind Station, North Point, Prince Edward Island.

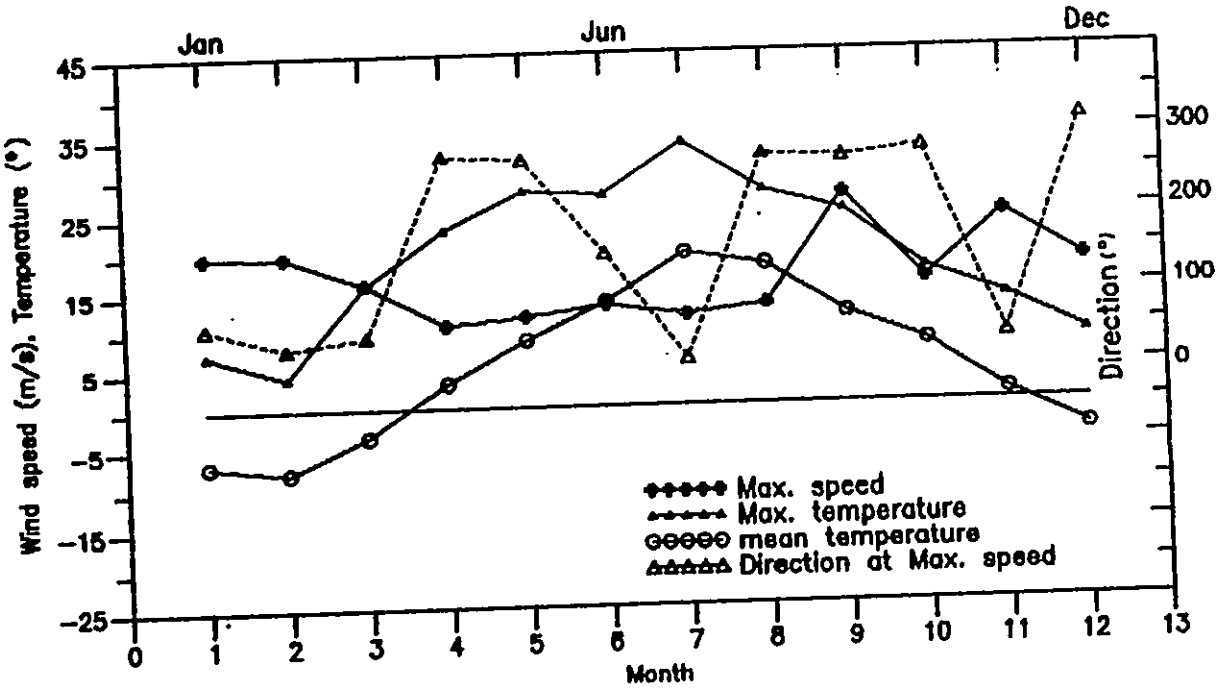
Jan
Jun
Dec
45
35
25
15
5
-5
-15
-25
Wind speed (m/s), Temperature (°)
300
200
100
0
Direction (°)
0
1
2
3
4
5
6
7
8
9
10
11
12
13
Month
Max. speed
Max. temperature
mean temperature
Direction at Max. speed

2.2 Deep Water Waves

Direct measurements of waves in the Gulf with information on both directions and speed are rare. An exception is the set of shipboard observations made by Environment Canada in 1972, and summarized in Summary of Synoptic Meteorological Observations. Available data indicate that swells from the Atlantic Ocean enter the Gulf about 7.4% of the year (Armon, 1975). These swells either continue toward the mouth of St. Lawrence Estuary, or are refracted onto Iles de la Madeleine (Vigeant, 1984). Waves influencing the Malpeque barriers are locally wind-induced in character. The lack of direct measurements made it necessary for early studies of waves to resort to a hindcast method based on either weather charts (Quon et al., 1963) or on wind data collected at land-based stations (Vigeant, 1984; Baird, 1978). While giving the broad picture, the information therein might not be adequate for a study concerning a specific coastal location, as winds in the Gulf region are influenced by coastal topography and proximity. Waves were hindcast for the Malpeque coast by Armon (1975) based on data from Iles de la Madeleine. The Malpeque coast, however, has a wide range of depth of water and fetch due to changes in shoreline orientation. This particularly concerns Palmer inlet, which is partially sheltered by the protruding North Point.

Wind-generated deep wave characteristics were

computed for Palmer Inlet using the Sverdrup-Munk-Bretschneider method (Shore Protection Manual, 1973; Appendix A-1). Calculations were made, using the ice-free nine-month (April to December, Figure 2-2) 10-minute wind data, for the Gulf (NNW to ESE), as well as for Cascumpec Bay (SES to NW). Depth and fetch characteristics, based on average for these directions are given in Table 2-2. For the Gulf, the deep water equations were used, and the duration of winds was assumed infinite, considering that fetch and depth are the main limiting factors of wind growth in the area (Armon, 1975). Shallow water equations were used for calculations of waves in the Bay; duration thus was not considered important. The North Point Station is a coastal station; winds blow over landmass for the sector of 150° to 250°, and over water for the rest. To account for the surface roughness difference, winds out of the former sector were multiplied by 1.43, and the latter by 1.1 as suggested by the Shore Protection Manual (1973). No allowance was made for wave decay and shift in wind directions (Baird, 1978). The calculated significant heights and periods are plotted against wind speeds in Figure 2-3. Their combined effects are presented as wave energy calculated according to $E_o = \rho_w g H_s^2 L/8$ (Shore Protection Manual, 1973), and listed in Table 2-3. In the equation, H_s and L = wave height and length in the shallow water; ρ_w = seawater density; g = gravity constant.

Table 2-2 Fetch and depth characteristics

Direction		Fetch	Depth
Gulf	degree	(m)	(m)
NNW	337.5-360	6,750	4.70
N	360.-22.5	12,000	7.80
NNE	22.5-45.0	282,000	30.30
NE	45.0-67.5	637,500	33.60
ENE	67.5-90.0	375,000	34.90
E	90.-112.5	225,000	32.22
ESE	112.5-135	112,500	5.70
Cascumpec Bay			
SES	157.5-180	2,000	1.0
S	180-202.5	434	0.9
SWS	202.5-225	1,000	0.9
SW	225-247.5	1,600	1.0
WSW	247.5-270	2,000	1.8
W	270-292.5	2,100	2.6
WNW	292.5-315	4,800	2.5
NW	315-337.5	4,400	1.8

Figure 2-3 Computed significant wave heights and periods versus wind speeds for offshore (bayside, A and C) and onshore (gulfside, B and D) sectors.

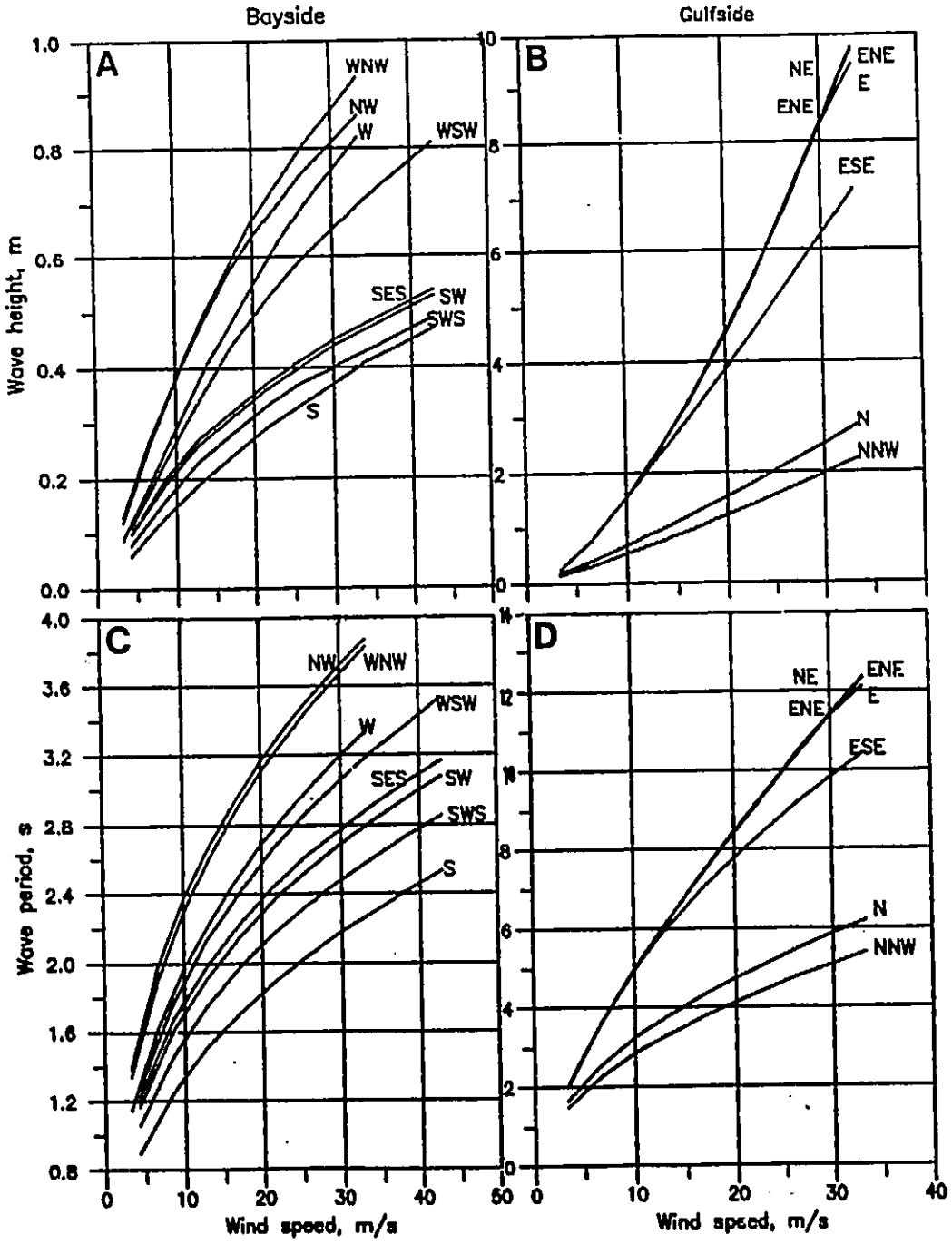
Bayside
Gulfside
A
B
C
D
WNW
NW
W
WSW
SES
SW
SWS
S
NE
ENE
E
ESE
N
NNW
Wave height, m
Wave period, s
Wind speed, m/s
Wind speed, m/s

Table 2-3 Computed total wave energy by speeds and directions, using wind data from April to December, North Point, P.E.I. Speed unit is m/s. Energy unit is 10^9 Kg-m/crest metre; some results are: onshore(southward, N-NNE) = 138.2, onshore (northward, ENE-ESE) = 46.5, offshore (southward, WSW-NW) = 5.16, and offshore (northward, SES-SWS) = 0.36.

Speed (m/s)	N	NNE	NE	ENE	E	ESE	SE	SSE	S	SSW	SW	WSW	W	WNW	NW	NNW	Total
0-4	0.02	0.03	0.03	0.03	0.03	0.02	0.00	0.01	0.00	0.00	0.00	0.00	0.00	0.00	0.00	0.01	0.20
4-8	1.30	7.03	6.17	5.44	6.15	4.90	0.07	0.10	0.02	0.09	0.17	0.15	0.21	0.29	0.25	0.70	33.03
8-12	3.31	17.75	7.85	3.37	5.82	10.38	0.08	0.06	0.02	0.06	0.26	0.41	0.41	1.06	0.62	1.29	52.73
12-16	3.44	11.42	3.78	7.70	0.55	0.42	0.00	0.00	0.00	0.00	0.03	0.10	0.31	1.02	0.14	0.66	29.58
16-20	3.87	20.56	15.06	1.71	0.00	0.00	0.00	0.00	0.00	0.00	0.00	0.00	0.01	0.11	0.05	0.52	41.86
20-24	0.51	60.06	12.89	0.00	0.00	0.00	0.00	0.00	0.00	0.00	0.00	0.00	0.00	0.00	0.01	0.42	73.89
24-28	0.00	8.95	0.00	0.00	0.00	0.00	0.00	0.00	0.00	0.00	0.00	0.00	0.00	0.00	0.00	0.00	8.96
28-32	0.00	0.00	0.00	0.00	0.00	0.00	0.00	0.00	0.00	0.00	0.00	0.00	0.00	0.00	0.00	0.00	0.00
32-36	0.00	0.00	0.00	0.00	0.00	0.00	0.00	0.00	0.00	0.00	0.00	0.00	0.00	0.00	0.00	0.00	0.00
36-40	0.00	0.00	0.00	0.00	0.00	0.00	0.00	0.00	0.00	0.00	0.00	0.00	0.00	0.00	0.00	0.00	0.00
Total	12.43	125.8	45.78	18.25	12.54	15.72	0.15	0.17	0.04	0.14	0.47	0.66	0.94	2.48	1.08	3.60	240.2

On the Gulf side (Figure 2-3b and d), for a given wind speed in the Gulf, the largest waves come from the NNE-E. Waves out of the N-NNW are of smallest dimensions because of short fetches imposed by the North Point. The nine-month averages of wave height and period of all directions are 0.50 m and 2.5 s with the modal height occurring in the 0.3 to 0.91 m class (Table 2-4). Considering that 81% of onshore winds have speeds less than 4 m/s, waves are small most of the year except during the passage of extratropical storms, when winds stronger than 16 m/s could produce waves with heights larger than 3.0 m and periods larger than 7 sec. In terms of wave energy, waves from N-NNW are an order of magnitude smaller than those from NNE-NE (Table 2-3) despite the fact that winds blow more often from the former directions (Table 2-1). Nonetheless, wave energy from north of the direction normal to the shoreline (138×10^9 kg-m/crest metre, Table 2-3) is higher than that from south of the shorenormal (47×10^9 kg-m/crest metre), indicating that around Palmer Inlet, the northern component dominates deep waves in the Gulf.

In Cascumpec Bay, the largest waves are from the WNW and NW direction, and the smallest waves from southerly directions (Figure 2-3a and c). A 16 m/s wind produces a wave of 0.55 m height and 2.8 s from NW, and a wave of 0.28 m and 2.0 s from SW. The average value of calculated waves is 0.18 m and 0.15 sec. Smaller dimensions of waves result

Table 2-4 Frequency % of computed wave heights for four directions

Height (M)	NW 292-337°	N 337-22°	NE 22-67°	E 67-112°
0.00-0.30	3.32	3.84	4.5	3.63
0.30-0.91	5.8	5.1	3.43	2.86
0.92-1.51	4.31	1.83	0.59	0.37
1.52-2.12	1.16	0.46	0.07	0
2.13-2.43	0.09	0.2	0.05	0
2.44-3.04	0.01	0.03	0.05	0
3.05-3.65	0	0	0	0
Total	14.69	11.46	8.69	6.86

in much lower energy level in the Bay, which is about two orders of magnitude smaller than that in the Gulf (Table 2-3). The southern component totals 5×10^9 kg-m/crest metre, while the northern component 0.36×10^9 kg-m/crest metre. Along the lagoon side of the barrier, wave-induced currents are also expected to be towards the south.

2.3 Longshore Currents

2.3.1 Wave Refraction

Deep water waves are linked to the inshore wave climate through shoaling and refraction process. Dobson's numerical method (1967) offers a fast and reasonably accurate means for refraction analysis, and is used in the present study to estimate wave conditions in the vicinity of Palmer inlet. This method is based on the geometrical optics approximation with the assumption, besides neglecting local wind, current and reflection, that wave energy is confined between wave orthogonals. Bathymetric data for wave refraction analysis were obtained from hydrographic Chart 4492, supplemented by nearshore depth-sounder profiles made in 1986. A grid system of 73x73 m mesh size was constructed from these data using the Surfer Contour software. For each given direction, waves of certain period were initiated in deep water, and allowed to propagate across the mesh network at an incremental step of 0.1 grid size. At each step, depth was interpolated from the nearest

four grid nodes using a second degree polynomial approximation. The ray stopped when the wave-breaking criterion was reached (Komar, 1974) or when the depth is less than 1.6 m. Test runs showed that at this depth, refraction began to become unstable. Printed output at every four steps gave wave positions in grid units, the angle, θ, between the wave orthogonal and the shorenormal, and the refraction coefficient, K_r, and the shoaling coefficient, K_s, calculated according to:

$$K_r = \sqrt{(b_o/b)}$$

$$K_s = \sqrt{\{C_o/[C(1+(4\pi D/L)/\sinh(4\pi D/L)]\}}$$

Where b = separation between wave orthogonal; L = wave length; D = water depth and C = wave celerity. Zero subscripts refer to deep water condition.

Refraction analysis has been performed for waves of 3 s, 5 s, and 8 s from the N, NNE, NE, ENE, E. The directions were chosen so that two are from north of the shorenormal (N55°E) and two from south of it. Refraction parameters were collected at Stations I, II, and III (Figure 2-4), chosen to represent locations updrift, central and downdrift of the inlet, respectively. Results are presented in Table 2-5. Included in the table are longshore components of wave energy flux, P_l, calculated as

Figure 2-4 Wave refraction diagrams for waves of 3 seconds from (A) 90°; (B) 57°; (C)33°; (D) 360°. Water depths are in feet. Stations at which wave refraction parameters were collected are indicated in (A): Triangle = Station I: Circle = Station II; Square = Station III.

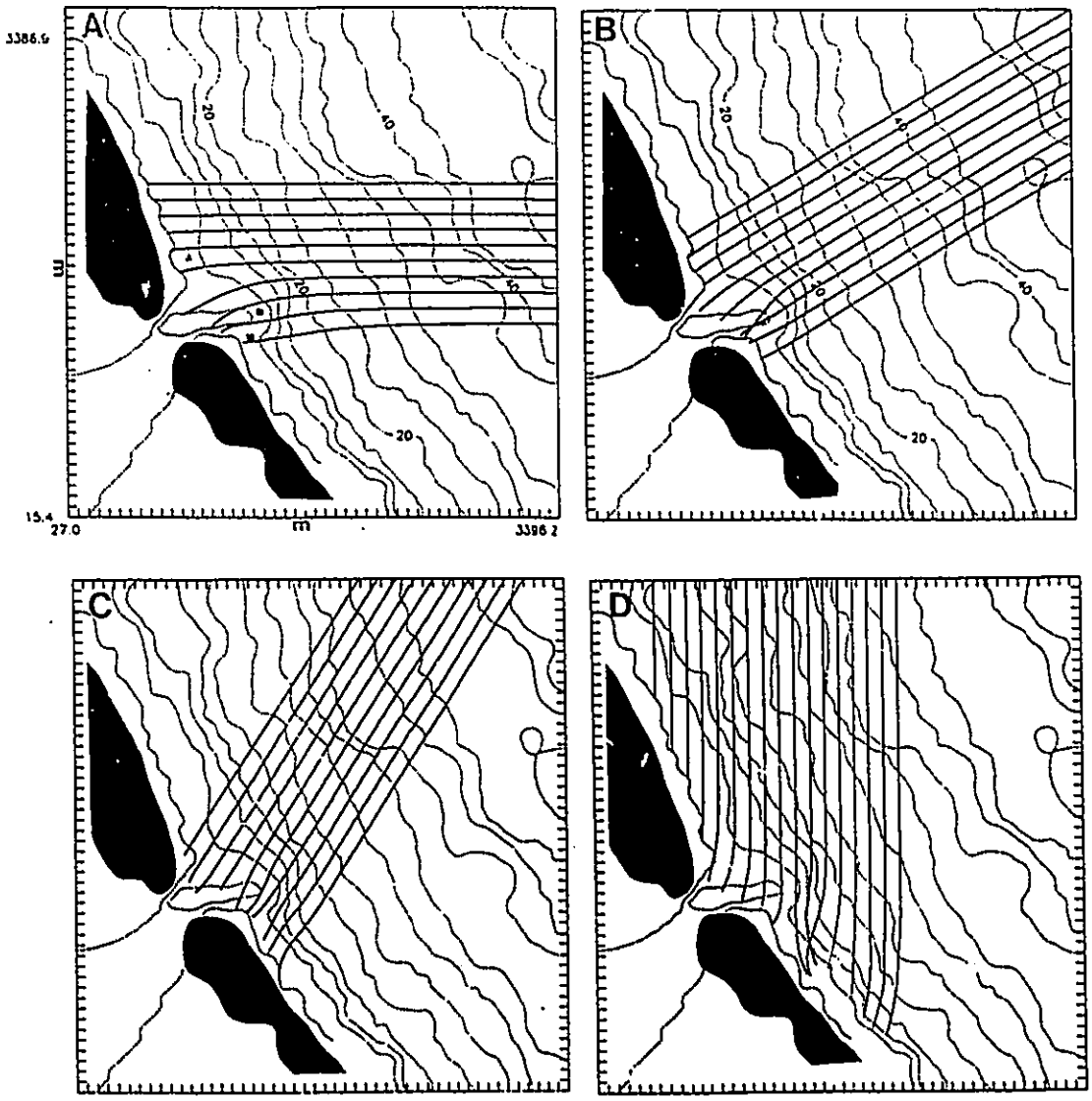
A
B
C
D
3386.9
15.4
27.0
m
3386.2
-20
-40
-60

Table 2-5 Computed wave refraction parameters at stations shown in Figure 2-4. K_r = Refraction coefficient; K_s = shoaling coefficient; K = K_r K_s. θ = Angle between the wave-orthogonal and shorenormal. P_l = Longshore-wave-flux (Kg-m/s/meter of beach front). + = Southward component; - = Northward component

Station Parameters		I K_r	I k	I θ	I P_l	II K_r	II k	II θ	II P_l	III K_r	III k	III θ	III P_l
Period(sec)													
N	3	0.87	0.80	39.40	8.12	1.01	0.96	29.20	11.19	0.98	1.09	27.50	14.82
	5	0.84	0.88	34.80	9.98	1.10	1.21	47.80	23.31	1.16	1.34	20.20	19.69
	8	0.78	1.01	29.10	12.53	1.43	1.75	50.00	58.01	1.31	1.47	11.70	15.17
NNE	3	0.93	0.86	22.10	6.96	1.04	1.01	21.90	10.32	0.97	0.90	14.90	5.49
	5	0.83	0.87	20.30	6.68	1.07	1.13	23.60	14.49	1.07	1.17	8.40	6.25
	8	0.80	1.02	19.70	9.70	1.27	1.36	28.60	26.37	1.19	1.32	-4.60	-4.61
NE	3	0.97	0.89	2.10	0.81	1.01	0.93	4.30	1.81	0.97	0.90	-2.00	-0.77
	5	0.98	1.04	5.20	2.89	1.02	1.06	3.00	1.79	0.97	1.15	-2.50	-1.78
	8	0.91	1.02	7.70	4.02	1.07	1.28	4.40	4.13	1.03	1.21	-7.80	-6.28
ENE	3	0.88	0.82	-13.20	-3.93	0.98	0.87	-20.10	-6.62	0.89	0.82	-15.40	-4.53
	5	0.72	0.78	-7.30	-1.96	1.00	1.21	-9.90	-7.92	1.00	1.11	-7.70	-5.00
	8	0.70	0.83	-6.70	-2.11	1.08	1.19	-6.40	-4.55	1.09	1.27	-14.90	-13.12
E	3	0.81	0.79	-17.40	-4.60	1.02	0.94	-34.00	-11.55	0.94	0.88	-27.60	-8.67
	5	0.80	0.88	-10.10	-3.64	1.14	1.14	-19.40	-12.63	0.97	1.02	-13.40	-6.88
	8	0.73	0.81	-7.40	-2.19	1.17	1.27	-14.80	-13.00	0.92	1.08	-7.80	-4.73
Net longshore					43.27				94.74				5.04

$$P_l = 32.1\ H_{sb}^{5/2} \sin(2\alpha)$$

Where H_{sb} = significant wave height at break, and is approximated by (H_oK) at three Stations; $K = K_r\ K_s$; α = breaker angle between wave crest and shoreline (Vitale, 1980). Since wave refraction and shoaling do not depend on the input wave height, P_l in the Table 2-5 was derived assuming unit deep wave height (H_o = one ft; calculations were carried out in the Imperial System). In the table, positive numbers denote southward components and negative numbers northward components. Samples of wave ray diagrams are given in Figure 2-4 and Figure 2-5 for waves of 3 and 8 s from four directions, respectively.

2.3.2 Results and Discussion

Values of K_r are indicators of convergence (>1) or divergence (<1) of waves at a location due to wave refraction. Table 2-5 indicates that Station I is a location where divergence occurs for all waves from all directions, while Station II basically is a station where wave convergence occurs. The condition is somewhat different for Station III. At this location, waves from ESE to E directions tend to diverge, and those from N to NNE converge. Another observation made from the study is that with the increase of the wave period, K_r values generally increase for convergence but decrease for divergence.

Wave refraction is least pronounced for waves

Figure 2-5 Wave refraction diagrams for waves of 8 seconds from (A) 90°; (B) 57°; (C)33°; (D) 360°. Water depths are in feet.

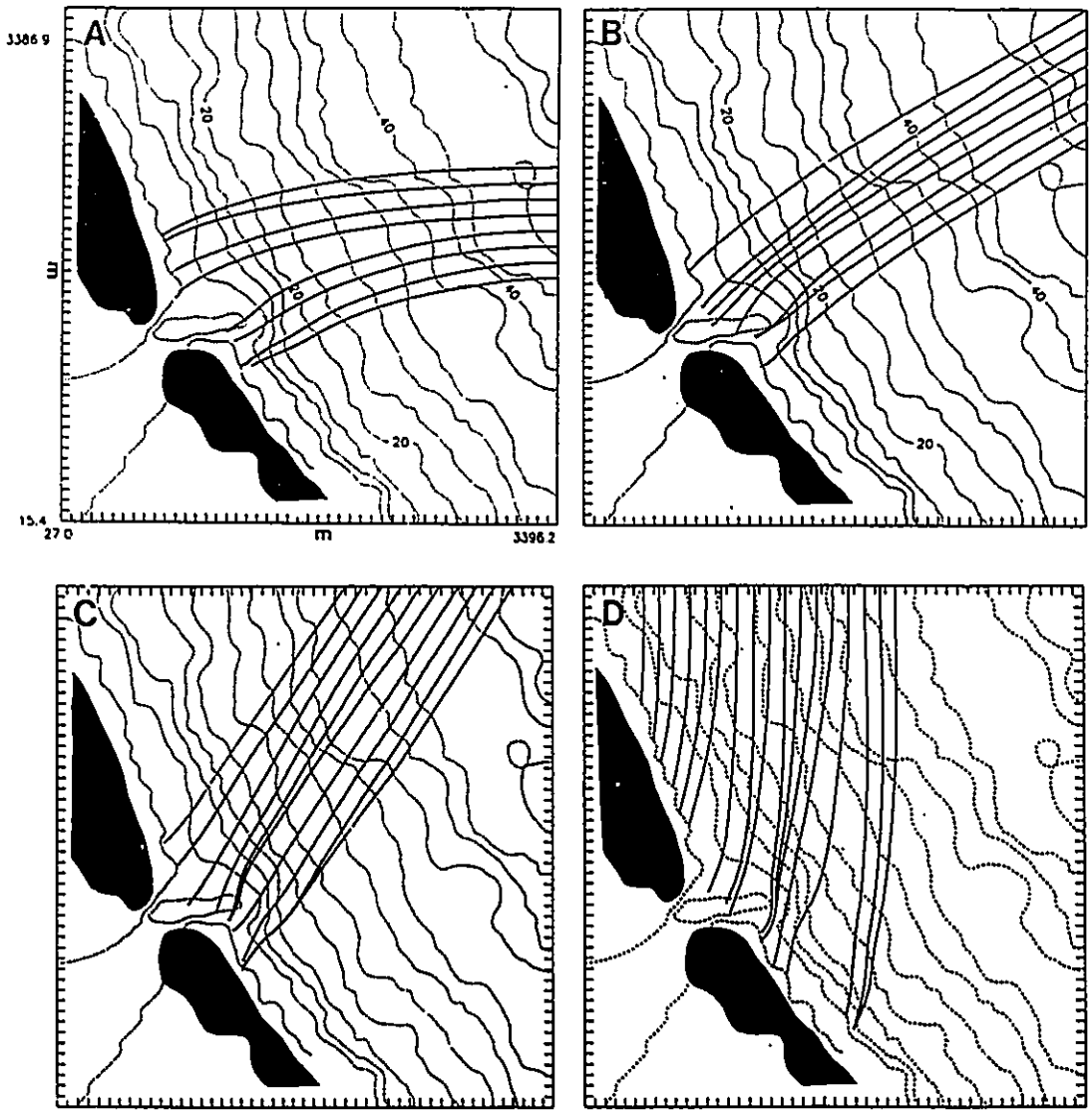
A
B
C
D
3386.9
15.4
27.0
m
3396.2
20
40
60

approaching from NE direction (57°). Values of θ angles for waves from NE are within plus and minus 8° of the shorenormal, indicating a near normal approach of waves from this direction. Changes in direction of wave rays increase both for more northerly and more southerly waves. The longshore energy flux, P_l, however, is basically directed down-coast (toward the south) for waves from the N to NNE, and up-coast (toward the north) for waves from the ENE and E. This suggests that wave-induced inshore currents along this coast are primarily maintained by the oblique approach of incident waves. An interesting fact related to direction changes is the occurrence of negative values of P_l at Station III for waves from NE. In fact, P_l begins to take negative values for waves of 8 s from the NNE direction. This suggests that despite its small size, strong refraction could occur around the ebb terminal lobe when wind and waves are large. The likelihood of landward or even reversal of longshore currents is thus increased for the downdrift side of the inlet. Current reversal due to wave refraction has been observed in many tide-dominated inlets (Goldsmith and Byrne, 1975; Finley, 1975).

The net values of total longshore wave energy flux summed over all directions (Table 2-5) indicates that the highest longshore energy occurs at the central Station II. This is due to the exposure of this Station to waves from all directions, and their general convergence on the

Station. The concentration of energy at this location will prevent extensive seaward growth of the ebb delta. Net P_l values at all three Stations are positive, indicating a general southward directed longshore current along the coast. Although these P_l values are qualitative in the sense that unit H_o values were used, the predominance in frequency of the northern component in both wind and deep wave climate (Table 2-1 and Table 2-5), suggests that the dominance would be in the same direction if actual calculations were carried out.

2.4 Tides

2.4.1 Tide Gaging

Tide records of varied lengths (46 to 70 days) were obtained at three locations (Figure 2-6) representing tides just outside (Beachside station) and inside (Bayside station) the inlet, and in the interior of the bay (North Port station). The Canadian Hydrographic Service (CHS) low water chart datum is taken as the common datum, and a mean water level of 0.53 m assumed throughout the area (O'Reilly, pers. commun., 1986). Representative time-series plots of tides, and tidal difference are given in Figure 2-7. The analog data were digitized hourly over each of the periods with values read to the nearest 0.001 inch. Subsequent least square harmonic analyses yielded a total of 41 tidal constituents for each station. Table 2-6 and Table 2-7

Figure 2-6 Location map for tidal gauging stations, and current meter stations within Cascumpec Bay. ● = Tidal stations: A = Beachside Station; B = Bayside Station; C = North Port Station. ▲ = Aanderaa continuously recording current meter, Station 71-XI. ■ is Marsh-McBirney direct reading current meter, Station M-1.

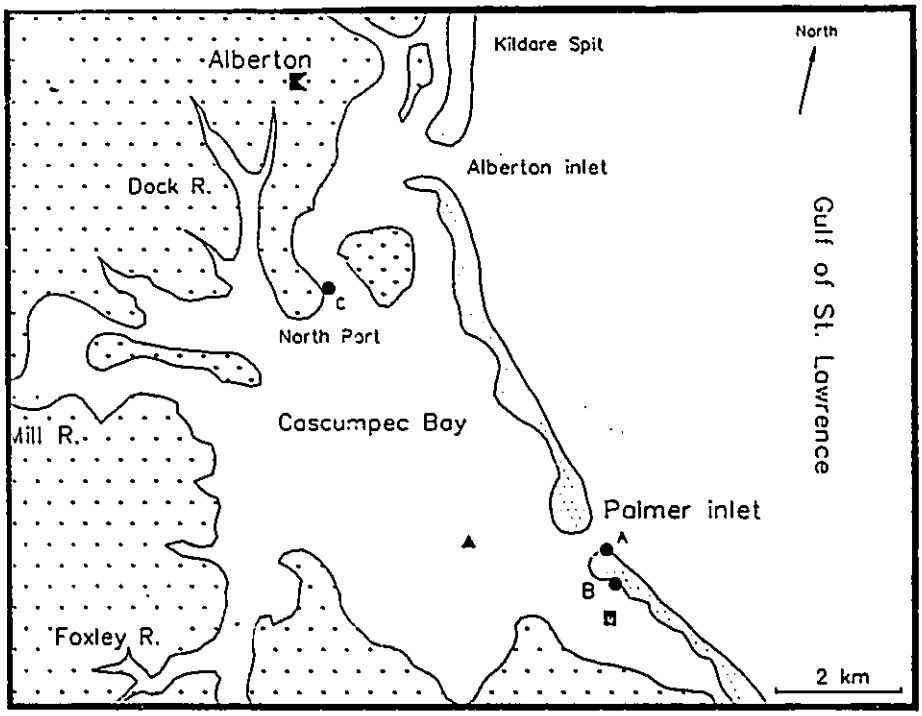
Alberton
Kildare Spit
North
Alberton inlet
Dock R.
Gulf of St. Lawrence
C
North Port
Cascumpec Bay
Mill R.
Palmer inlet
A
B
Foxley R.
2 km

Figure 2-7 Selected time series of bay tides (A), tides at three Stations (B), and tidal differences (C).

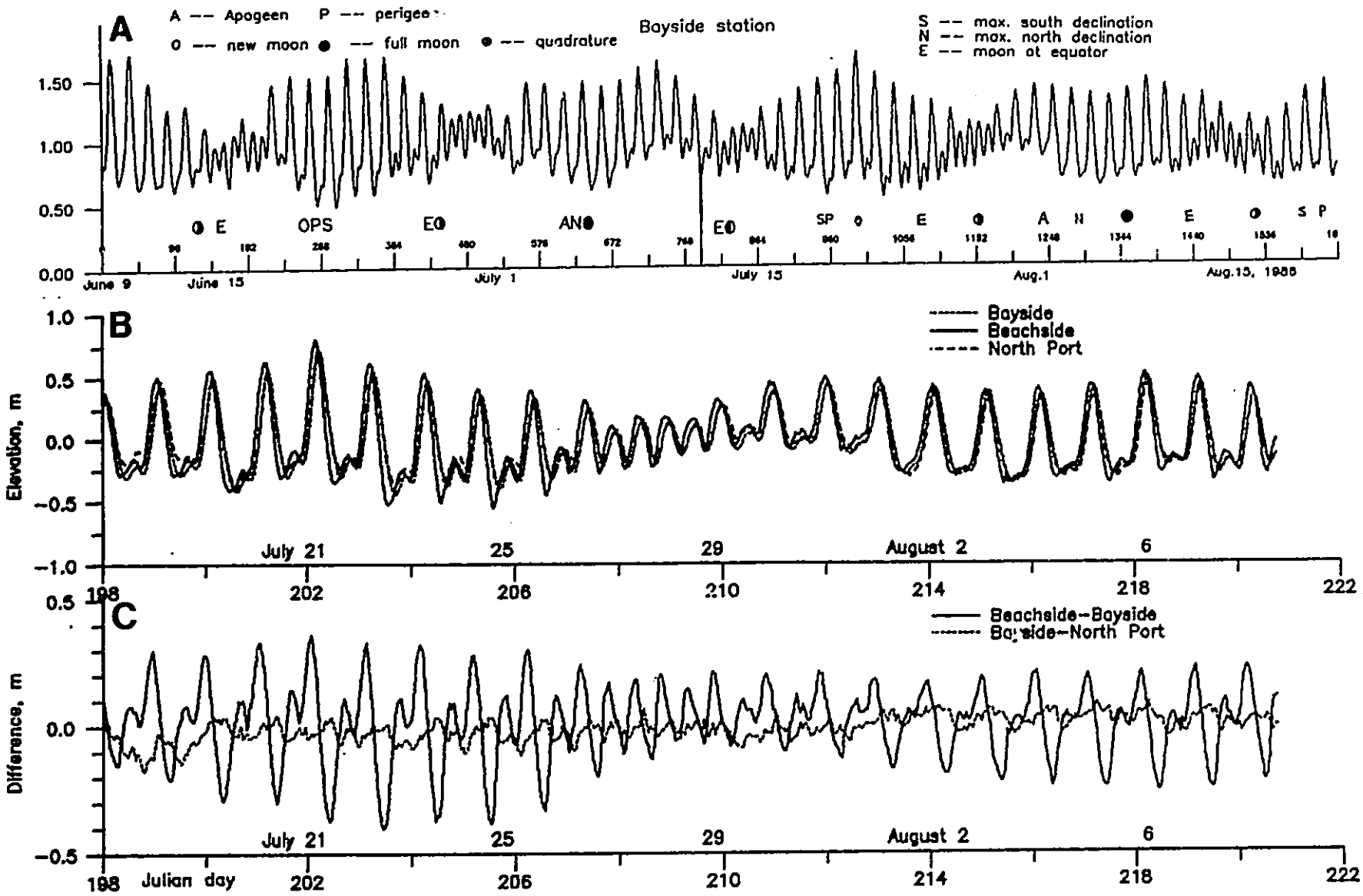
A
A -- Apogeen P -- perigee
0 -- new moon ● -- full moon ● -- quadrature
Bayside station
S -- max. south declination
N -- max. north declination
E -- moon at equator
1.50
1.00
0.50
0.00
June 9
June 15
July 1
July 15
Aug.1
Aug.15, 1988
B
Bayside
Beachside
North Port
Elevation, m
1.0
0.5
0.0
−0.5
−1.0
July 21
25
29
August 2
6
198
202
206
210
214
218
222
C
Beachside−Bayside
Bayside−North Port
Difference, m
0.5
0.0
−0.5
Julian day

Table 2-6 Harmonic constants of fundamental tides and overtides. a = Amplitude in centimetre. θ = Phase angle in degree (Atlantic Standard Time). θ' = Phase angle after nodal modulation and astronomical argument corrections. Data used in the analysis are: Beachside Station = 13:0, July 3, 1986 - 11:0, August 18, 1986. Bayside Station = 19:0, June 9, 1986 - 10:0, August 18, 1986. North Port Station = 18:0, June 19, 1986 - 16:0, August 18, 1986.

Tidal constituents			Locations of tidal stations								
Symbol	Origin	Period(hr)	Bayside			Beachside			North Port		
			a	θ	θ'	a	θ	θ'	a	θ	θ'
						Semidiurnal tides					
M_2	Lunar principal	12.40	13.80	306.20	180.24	17.60	256.50	140.00	12.70	340.70	179.74
N_2	Lunar elliptic	12.70	3.50	251.50	174.89	4.40	345.70	127.01	3.10	353.00	174.49
S_2	Solar principal	12.00	3.56	196.80	256.88	4.70	189.70	189.78	2.80	89.30	239.31
L_2	Solar elliptic	12.00	1.30	157.10	147.98	1.04	297.00	93.94	1.20	123.18	146.45
k_2	Lunisolar declinational	12.00	1.70	345.60	162.88	2.26	314.90	195.78	1.30	227.90	245.31
$2N_2$	Second order elliptic	12.90	0.41	217.30	189.52	0.70	82.60	113.16	0.50	348.10	151.53
						Diurnal tides					
Q_1	Lunar L. elliptic	26.90	2.50	350.30	226.97	1.90	56.50	165.15	2.49	131.80	216.54
O_1	Lunar P. declinational	25.80	19.80	60.70	246.91	20.10	7.60	221.46	18.10	146.00	247.18
P_1	Solar P. declinational	24.10	5.20	270.60	278.12	5.46	283.70	249.48	4.80	229.50	277.04
K_1	Lunisolar declinational	23.90	17.50	224.40	273.22	18.30	214.00	244.58	16.10	173.30	272.14
J_1	Lunar S. elliptic	23.10	0.90	299.55	296.91	1.30	131.80	266.64	1.82	198.70	313.08
$2Q_1$	Second order elliptic	28.00	1.42	272.90	199.86	1.10	215.40	218.72	1.40	162.10	230.17
						Overtides					
M_4	Lunar quarter diurnal	6.20	0.07	50.50	158.51	1.31	319.00	86.46	0.43	101.60	139.77
M_6	Lunar sixth diurnal	4.10	0.07	250.00	237.07	0.20	25.90	145.30	0.10	47.30	284.51
M_8	Lunar eighth diurnal	3.10	0.05	252.60	108.70	0.06	188.70	82.61	0.10	44.30	120.58
S_4	Solar quarter diurnal	6.00	1.13	34.30	154.45	0.12	15.30	15.39	0.09	279.50	219.60
						Fortnightly or monthly tides					
M_m	Lunar monthly	27.56	3.42	215.29	164.64	4.79	96.25	201.29	4.88	138.50	154.81
M_{sf}	Lunisolar fortnightly	14.70	0.87	271.08	96.22	2.60	67.89	183.58	1.56	219.88	169.98

Table 2-7 Harmonic constants of compound tides. For source and legends, see Table 2-6.

Compound tides			Locations of tidal stations								
Symbol	Origin	Period(hr)	Bayside			Beachside			North Port		
			a	θ	θ'	a	θ	θ'	a	θ	θ'
MO_3	$M_2 + O_1$	8.39	1.30	299.09	359.34	1.24	227.52	324.87	1.45	91.40	31.66
MK_3	$M_2 + K_1$	8.18	1.13	114.43	37.24	0.47	172.29	86.39	1.04	140.85	78.80
SK_3	$S_2 + K_1$	7.99	0.55	320.35	69.21	0.57	348.70	19.38	0.17	255.57	144.51
MN_4	$M_2 + N_2$	6.27	0.11	274.27	71.67	0.48	8.61	29.37	0.12	35.21	55.81
SN_4	$S_2 + N_2$	6.16	0.05	38.06	21.52	0.26	67.24	204.58	0.06	241.83	213.42
MS_4	$M_2 + S_2$	6.10	0.32	61.59	355.60	0.75	349.68	233.22	0.14	36.87	26.00
$2MK_5$	$M_4 + K_1$	4.93	0.14	132.57	289.40	0.09	7.08	164.67	0.08	346.79	123.80
$2SK_5$	$S_4 + K_1$	4.80	0.07	95.67	264.58	0.11	116.56	147.30	0.15	76.70	115.70
$2MS_6$	$M_4 + S_2$	4.09	0.08	75.29	243.37	0.29	25.90	152.92	0.16	4.12	192.31
$2SM_6$	$S_4 + M_2$	4.05	0.03	20.46	14.59	0.23	10.39	253.98	0.40	223.99	3.18

list those constituents with amplitude in excess of 0.03 cm. Statistics derived from the raw data or from results of harmonic analyses are listed in Table 2-8.

In the presentation of the results, the following definitions are used (Doodson and Warburg, 1941). Declinational tides are fortnightly variations of tides related to the declinational movement of the Moon. The tide is equatorial if the Moon is at the Equator, and is tropic when the Moon at maximum north or south of the equator. Synoptic tides are similar fortnightly tidal variations, but related to the Moon's rotation around the Earth with spring tides corresponding to the New Moon or the Full Moon position and neap tides to the quadrature position. On the other hand, large, intermediate, and small tides are terms based on the following intervals of tidal ranges, > 0.75 m, 0.45-0.75 m, and < 0.45 m.

2.4.2 Results

Tides at Palmer inlet fall in the microtidal range with mean tidal ranges of 0.56 m, 0.64 m and 0.75 m for the three stations. Corresponding figures for larger tides are 0.94, 1.02 m and 1.08 m. 55% of tides, calculated using data from Bayside Station, are < 0.45 m, 28% in the range of 0.45 - 0.75 m, and 16% > 0.75 m (Figure 2-8). The maxima of higher high water and lower low water occur during large tide periods. At all locations, the four principal tidal

Table 2-8

(A) Tidal statistics calculated from results of harmonic analysis of tides at three stations. HHW = Higher high water; LLW = Lower low water; HLW = Higher low water; LHW = Low high water. DT is defined as

$$DT = \frac{O_1 + K_1}{M_2 + S_2}$$

DT > 3.3	Diurnal tide
DT = 1.5 - 3.0	Mixed, mainly diurnal tide
DT = .25 - 1.5	Mixed, mainly semidiurnal tide
DT = 0 - .25	Semidiurnal tide

(B) Elevation and time difference for HW and LW between gulf and bay tides using data from July 3 to August 18, 1986.

A.

Tidal Parameters	Tidal Beachside	Stations North Bayside	Port
DT	1.72	2.15	2.19
Tidal range			
Large tide	1.08	1.02	0.94
Mean tide	0.75	0.64	0.56
Mean tide			
HHW	0.94	0.92	0.88
LLW	0.19	0.28	0.32
LHW	0.51	0.48	0.47
HLW	0.41	0.41	0.41
Water level			
Large tide			
HHW	1.22	1.17	1.12
LLW	0.14	0.15	0.18

B.

Tide range (m)	Gulf tide - Bay tide Elevation (cm) HW	LW	Time (min) HW	LW
0.15-0.45 m				
Average	4.3	-0.7	49.0	40.9
Maximum	5.2	2.1	85.0	52.5
Minimum	3.4	-5.2	22.5	25.0
St.Dev.	0.6	2.4	19.3	8.9
0.45-0.75 m				
Average	4.1	3.2	46.6	88.6
Maximum	8.0	13.4	90.0	219.9
Minimum	0.3	-3.7	22.5	5.0
St.Dev.	2.3	3.9	16.0	50.4
> 0.75 m				
Average	5.0	5.0	70.8	153.0
Maximum	9.4	15.0	110.0	219.9
Minimum	-2.7	-3.1	25.1	35.0
St.Dev.	3.8	5.7	25.8	62.1
All classes				
Average	4.2	3.3	52.7	93.2
Maximum	9.4	15.0	110.0	219.9
Minimum	-2.7	-5.2	22.0	5.0
St.Dev.	2.8	5.0	24.3	64.1

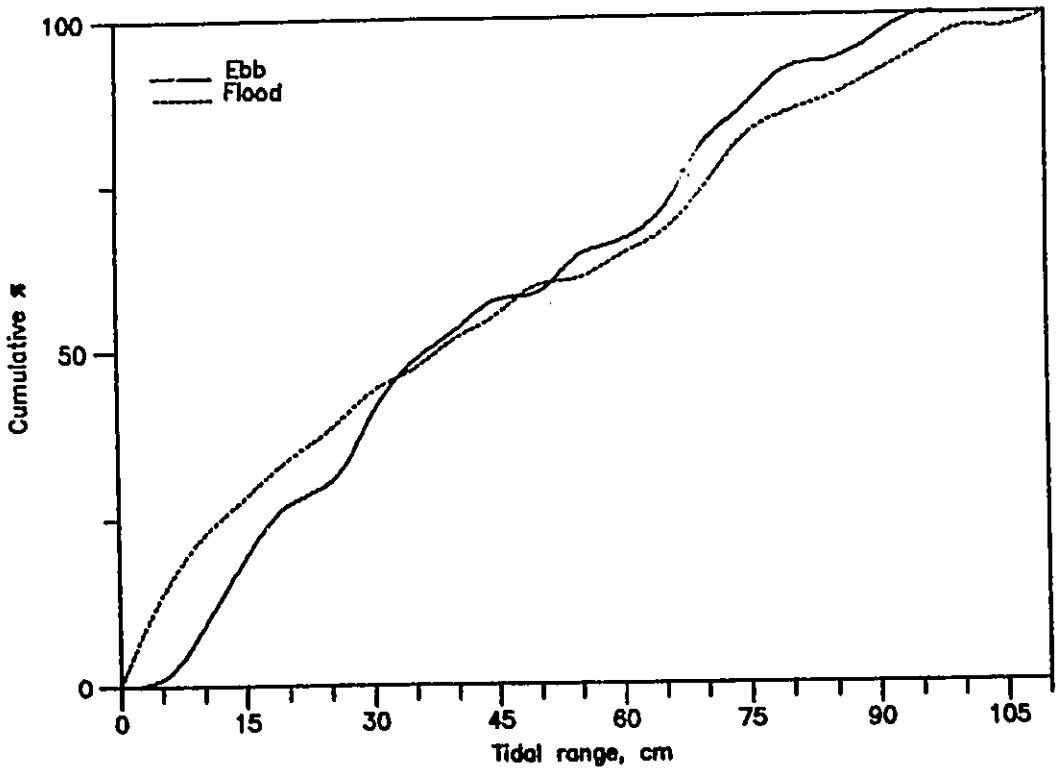
100
50
0
Ebb
Flood
Cumulative %
0
15
30
45
60
75
90
105
Tidal range, cm

Figure 2-8 Cumulative probability distribution of tidal ranges calculated from measured bay tides.

constituents, O_1 and K_1, and M_2 and S_2, comprise of more than 98% of the tidal energy. The dominant diurnal components, K_1 and O_1, account for more than 60% of the energy, and have approximately equal magnitude. The amplitude of M_2 component is, however, about four times larger than that of S_2, indicating the larger influence of the Moon in semidiurnal tides. The calculated ratio between $(O_1 + K_1)$ and $(M_2 + S_2)$ ranges from 1.72 to 2.19, suggesting a mixed but mainly diurnal tide (Wood, 1986). This ratio is larger for the two stations inside the bay, as a result of larger reduction in the semidiurnal constituents. Tides within the bay are more diurnal than those outside.

The fortnightly tide of Palmer Inlet has well defined cycles, similar to the spring-neap variation typical of semidiurnal tides. The difference is that in Figure 2-7a, along with the change in <u>amplitude</u> is a concomitant change in <u>periodicity</u>. The result is that small tides always coincide with periods of predominantly semidiurnal tides with two high/low waters a day, and large tides with those of dominantly diurnal tides. Diurnal inequality occurs both in large and small tide periods. In the former, it is characterized by every second high tide being larger than its predecessor. The first high tide occurs, as either a small bump or a standstill, invariably on the lower part of the rising limb of the major peak. This breaks the continuity of the rising tide, and produces a daily tide

with a long runout following every higher high water. During the small tide period, diurnal inequality is more variable.

The tide undergoes changes as it moves into the inlet. Figure 2-7b shows tides inside the inlet (bay tide) lagging behind the gulf tide with a concomitant reduction in elevation. These changes are not, however, symmetrical between ebb and flood. The average and maximum lag at low water (LW) is 93 min and 220 min, as compared to 53 min and 110 min at high water (HW), respectively. The difference in amplitude between flood and ebb is less obvious with both values close to 3-4 cm. This is because low water values have larger scatter, and in many cases, low water of bay tides reaches an even lower level. These facts are reflected in Figure 2-9, which shows that a better regression with tidal range occurs for ebb than for flood phase lags. Unequal changes between high and low water impart an asymmetry to tides. The asymmetry is characterized by: 1) a steep, short rising limb and a gentler, longer falling limb; 2) a low water truncation especially during large tides. Except the magnitude, similar tidal changes have been observed for the two stations within the bay (Figure 2-7c). Within the period of measurements, difference in elevation between them is less than 3 cm in average. This, for a distance of 6.25 km, gives a slope of water surface of 6.4 to 45 per million.

Figure 2-9A Delay of high and low water of bay tides with respect to those of Gulf tides. Regression equations for each stage are given in the figure. The dotted line is the regression line for low water data. Different tidal ranges are shown by different symbols (see legends).

Figure 2-9B Comparisons of HW and LW level difference between bay and Gulf tides as a function of tidal ranges. Regression is made only for positive numbers, which mean reduction in bay tides. For others, see A.

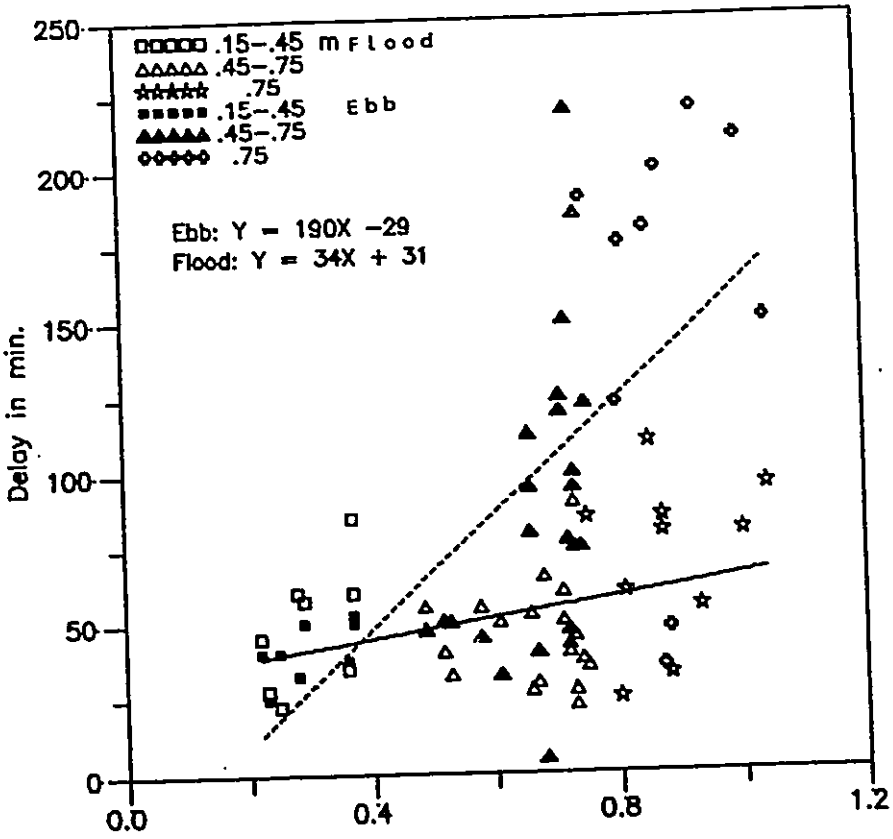
□□□□□ .15–.45 m Flood
△△△△△ .45–.75
☆☆☆☆☆ .75
■■■■■ .15–.45 Ebb
▲▲▲▲▲ .45–.75
◇◇◇◇◇ .75
Ebb: Y = 190X −29
Flood: Y = 34X + 31
Delay in min.
250
200
150
100
50
0
0.0
0.4
0.8
1.2

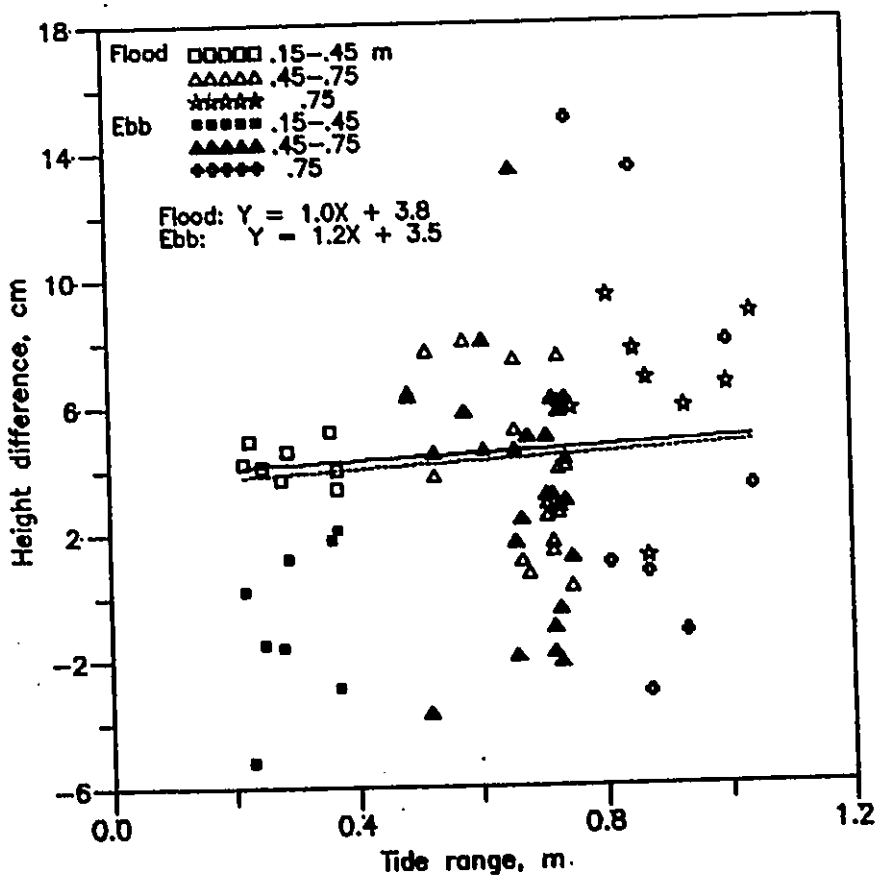
Flood □□□□□ .15–.45 m
△△△△△ .45–.75
☆☆☆☆☆ .75
Ebb ■■■■■ .15–.45
▲▲▲▲▲ .45–.75
◆◆◆◆◆ .75
Flood: Y = 1.0X + 3.8
Ebb: Y = 1.2X + 3.5
Height difference, cm
18
14
10
6
2
−2
−6
0.0
0.4
0.8
1.2
Tide range, m.

The implication is that the surface of the bay can be considered essentially horizontal throughout tidal cycles.

2.4.3 Discussion

It is tempting to attribute the observed expansion and contraction of water levels on a fortnightly cycle to the spring-neap phenomenon, or the synodic movement of the Moon. The astronomical alignment during the months when the field work was conducted, seems to support this notion (Figure 2-7a). In the present astronomical epoch (Wood, 1986, p.248-258), however, June, July and August happen to be the months, in which small tides are associated with the quadrature, and large tides with the new or full Moon. Different associations could occur in other months as the declinational (M_f) and synoptic (M_{sf}) movement differ in period (by 1.11 days every two weeks). Similarly, it is also not right to attribute the fortnightly cycle to a tropic-equatorial sequence.

The fortnightly features at Palmer Inlet can be explained by the 'beat phenomenon', an interaction between two constituents which leads to addition when they are in phase, and subtraction when they are out of phase. The M_f and M_{sf} are the result of beat between O_1 and K_1, and between M_2 and S_2, respectively (Beer, 1983, p.72). At Palmer Inlet, K_1 and O_1 are of almost equal magnitudes. Their beat out of phase leads to almost zero tides, as illustrated in

Figure 2-10a. The two components involved in M_{sf} beat, M_2 and S_2, on the other hand, differ in magnitude by a factor of four. Their beat does not lead to complete cancellation (Figure 2-10b). The addition of the results of the above two beats (Figure 2-10c) reproduces the main features of tides observed at Palmer Inlet. It is thus seen that the fortnightly tides of Palmer Inlet are not a simple tropic-equatorial sequence, nor are they a simple spring-neap sequence. Instead, they are a mixture of them. At times of maximum declination, when K_1 and O_1 are additive, tides are tropic and large. At times of zero declination, M_2 and S_2 become important, and tides are small and mainly semidiurnal. This distinct tropic-to-spring/neap sequence is the result of particular combination of magnitudes of K_1 and O_1, and that of M_2 and S_2 at this particular place. Tides in the Gulf of Mexico are also well-known for their dominantly mixed and diurnal character. The fortnightly cycle there, however, is a one of tropic-to-equatorial transition (Smith, 1983). The difference is that in the Gulf of Mexico, M_2 and S_2 are smaller in respect to the diurnal constituents, and also closer to each other. Their in-phase beat will not lead to complete cancellation as K_1 and O_1 are out-of-phase. The result is that declinational forces dominate throughout.

It is noted that Figure 2-10c also reproduces the main features of daily tides. Diurnal inequality thus also

Figure 2-10 Generation of fortnightly tides as beat between K_1 and O_1 (A), and between M_2 and S_2 (B). Amplitude and phase data taken from measured data in Table 2-6.

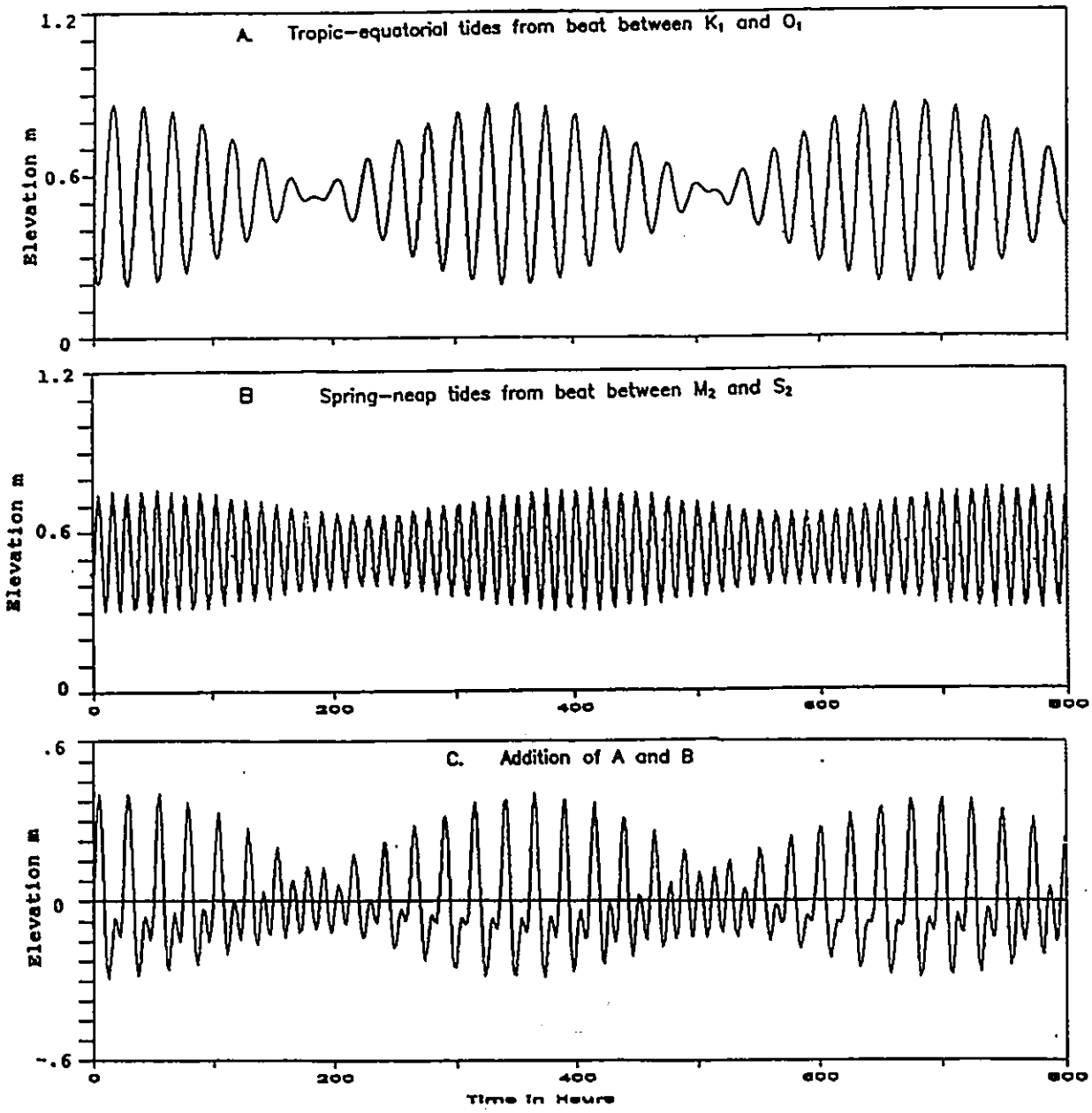
A. Tropic–equatorial tides from beat between K_1 and O_1
B Spring–neap tides from beat between M_2 and S_2
C. Addition of A and B
Elevation m
1.2
0.6
0
.6
-.6
0
200
400
600
800
Time in Hours

can be considered as resulting primarily from the interaction between the four principal tidal components. In other words, the minor peak in the diurnal inequality can be considered as representing the perturbation of the semidiurnal tide on the dominant diurnal tide, instead of perturbations of higher harmonics as in many semidiurnal tide areas.

2.5 Tidal Currents

2.5.1 Data Collection and Reduction

Currents were measured at 26 Stations in various parts of the inlet and the bay using RCM-4 Aanderaa automatic-recording meters mounted on a metal-frame. Nineteen of those generating reliable data are shown in Figure 2-6 and Figure 2-17. Current speeds are the average value of the rotor revolutions every five minutes measured one metre above the bed. High frequency fluctuations up to 10% were observed embedded within the raw data. These random fluctuations were smoothed using a low-pass filter with a cut-off-period of 1 hour, which is smaller than the highest tidal constituent (M_{10}, 2.5 hours) from harmonic analysis of water levels (Table 2-6 and 2-7). Continuous current meter records at three levels were available for only limited hours. This is due to intermittent fouling by seaweeds, especially during the ebb stage when large volumes of seaweed were carried out from the interior of the bay. In addition, a Marsh-McBirney Model 201 portable current meter

and two Endeco 110 remote reading current meters were also used where water depth was too shallow for a metal frame, and for obtaining velocity profiles.

This section will deal with the general features of tidal currents in the area. Current characteristics at particular stations will be discussed in the next chapter when depositional environments are described. Data from the inlet throat, however, will be used as examples to facilitate the interpretation, as they reflect the hydraulics of the system as a whole. Bay tides were utilized wherever the water stage is needed. Bay tides are forced tides, and considered to be more closely related to currents in the inlet channel than the forcing (gulf) tide.

The bottom shear velocity, U_*, was calculated from the logarithmic velocity profile by Inman's (1968) iterating least square method:

$$U = U_*/\kappa \ \ln(Z/Z_0+1)$$

Where U is the current velocity at a depth of Z; κ is von Karman's constant (= 0.4); and the Z_0 is the roughness length. The term U_*/κ is the slope of the velocity profile on a log-linear plot, from which U_* and Z_0 can be calculated.

Various parameters have been used to define the asymmetry between flood and ebb (Allen, 1980; Terwindt and

Brouwer, 1986). In this study, a scheme similar to the latter was used:

$$\text{Strength Index of flood, SIF} = (U_{fm} - U_{1cr})/U_{1cr}$$

$$\text{Strength Index of ebb, SIE} = (U_{em} - U_{1cr})/U_{1cr}$$

$$\text{Velocity Asymmetry Index, VSI} = \text{Abs}(U_{fm}/U_{em})-1$$

Where U_{fm} = maximum of flood currents; U_{em} = maximum of ebb currents; U_{1cr} = critical velocity for sediment movement measured 1 m off the bed.

In order to quantify the asymmetry, it was necessary to calculate transport sediment rates, which take into account of both velocity and duration. Several sediment transport equations are currently in use, the most popular of which among sedimentologists is those of Bagnold (1963) and Engelend-Hansen (1967). Tests using both equations showed that while momentary rates could be quite different, the cumulative result gave values which indicate similar dominance of transport. Gadd et al.'s (1978) modified Bagnold equation as a function of speed 1 m off the bed is:

$$q_s = k(U_1 - U_{1cr})^3$$

The advantage of this equation is that it can be applied directly to the present study using existing data. For this reason, Gadd et al's equation was used in calculation of

transport rate with k = 4.48 10^{-5} g/cm^4/s. The critical velocity at 1 m off the bed, U_{1cr}, was determined, assuming a logarithmic profile, from

$$U_{1cr} = 2.5\ U_{*cr}\ \ln(Z/Z_o)$$

Where Z_o = mean roughness length from measured velocity profile. U_{*cr} = critical shear velocities, which is estimated from Shield's criteria for a water temperature of 20° (Blatt et al., 1984).

2.5.2 Results and Discussion

2.5.2.1 General Features

Raw current data were summarised with histograms grouped into 3 cm/s intervals for various tidal conditions (Figure 2-11). Separately, histograms of large and small tides show rather even distributions over the velocity range without prominent modes. This is particularly true for large tides. The histogram using all data available, however, approaches a normal distribution. Flood and ebb velocities fall within the same range between 0 and 1.2 m/s, and in general, show a similar distribution with fairly uniform decrease in frequency with increasing speeds. A slightly low percent is observed for > 0.3 m/s ebb currents. This is balanced by the somewhat high percent in the lower range (< 0.3 m/s).

Figure 2-11 Histograms of frequency percent of current speeds data at Station 55-I. The interval for current speeds is 3 cm/s.

(A) Large tides, Station 55-I.

(B) Small tides, Station 55-I.

(C) All data. Figures indicated are tidal ranges in metres.

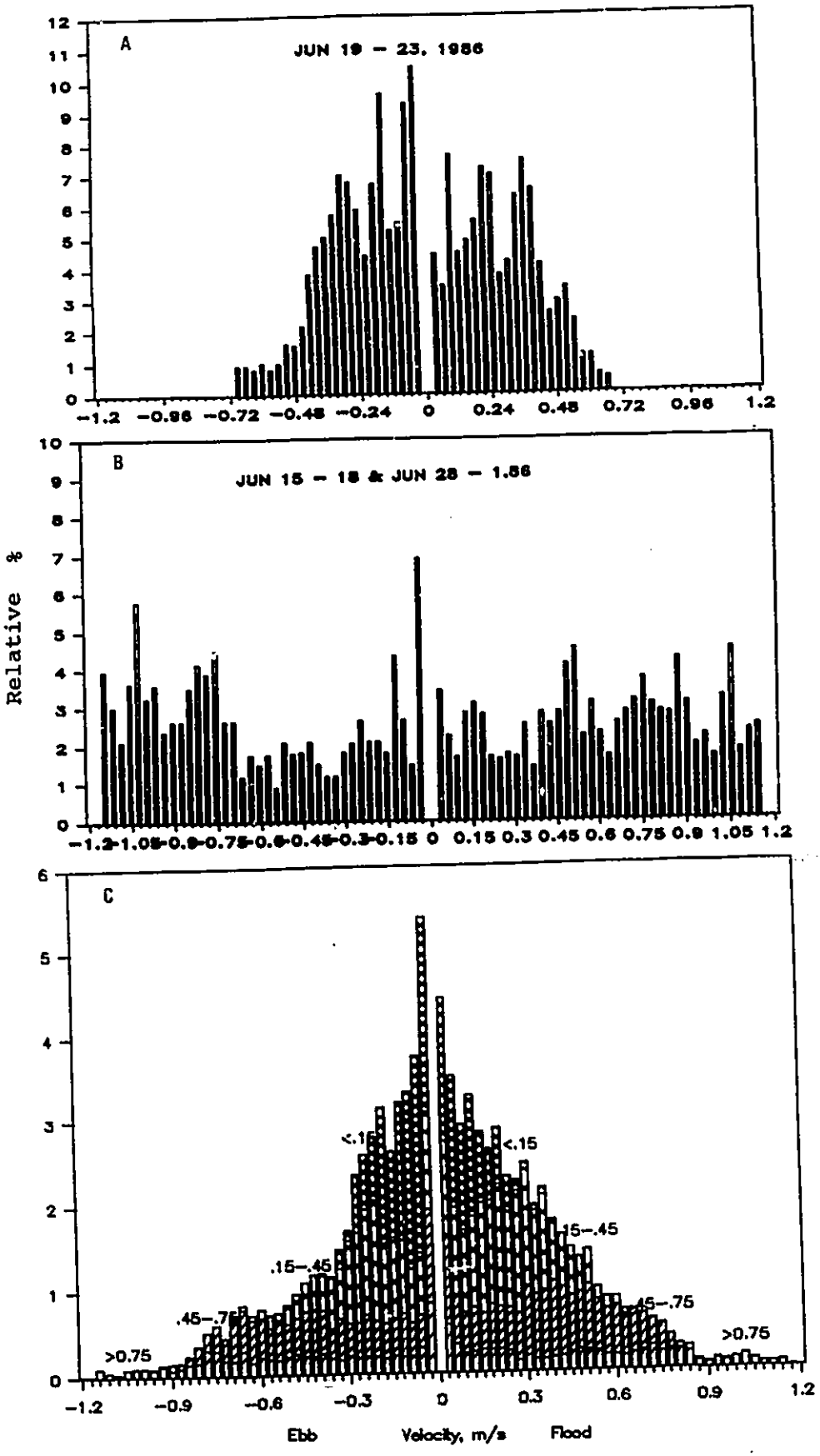
A
JUN 19 – 23, 1986
B
JUN 15 – 18 & JUN 28 – 1.86
Relative %
C
<.15
<.15
.15–.45
.15–.45
.45–.75
.45–.75
>0.75
>0.75
Ebb
Velocity, m/s
Flood

An overview of fortnightly variations of currents is provided by a composite plot using data from different locations in the main channel (Figure 2-12). Despite the frequent discontinuities, the envelop defined by the peak values clearly delineates the expansions and contractions as tidal constituents beat in and out of phase. Like the water level variation, the fortnightly cycle is one of transition from tropic to spring/neap sequence with changes in both magnitude and period. Under tropic tidal conditions, the major ebb and flood phase last about 8-9 hours, and reach 1.2 m/s in speed. At small (spring/neap) tides, ebb and flood last about 6 hours, and the strongest speeds are generally less than 0.5 m/s. Daily variations of currents also follow the general pattern of vertical tides with a strong diurnal inequality. During large tides, the second daily tide is alw[illegible]nger than its predecessor. The difference is usually more than twice for both flood and ebb. The diurnal inequality in small tides is less consistent. The stronger phase usually changes its position in the daily tides. Substantial variations of current velocity with time are expected to have a pronounced effect on sediment movement. Representative plots of sediment transport (Figure 2-13) show that active sand transport is essentially restricted to large tide periods. Currents in the minor tides of large tides are below the threshold of sand movement, and only marginally above it at any time

Figure 2-12 Composite time series of tidal current speeds using data from stations in the main channel. Also plotted are the corresponding bay tides.

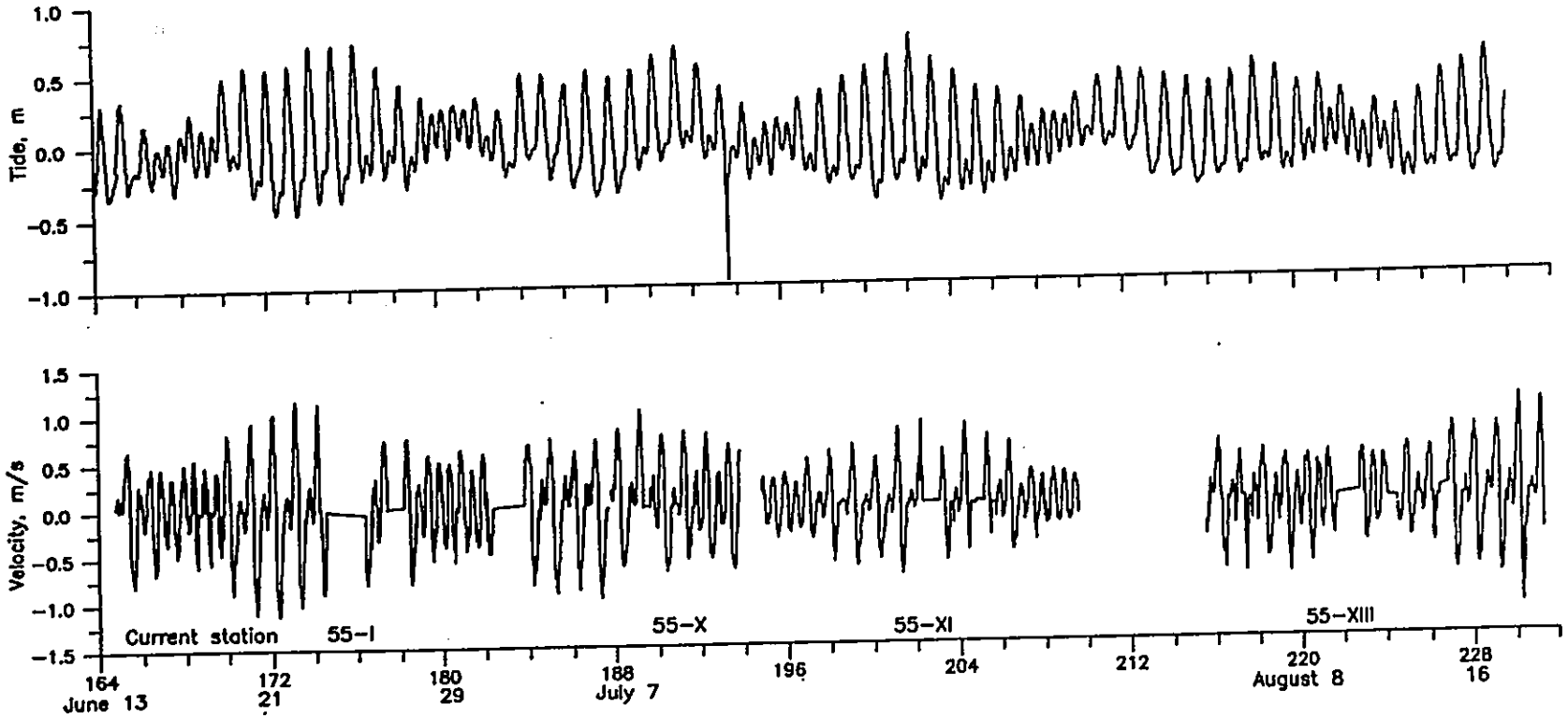
1.0
0.5
0.0
-0.5
-1.0
Tide, m
1.5
1.0
0.5
0.0
-0.5
-1.0
-1.5
Velocity, m/s
Current station
55-I
55-X
55-XI
55-XIII
164
June 13
172
21
180
29
188
July 7
196
204
212
220
August 8
228
16

Figure 2-13 Typical time series plots of current speeds,inlet throat, Station 55-XI, 1986. Also plotted are corresponding bay tides and tidal difference between bay and gulf tides. The calculated velocity asymmetry, current strength index, and sediment transport rates are also shown.

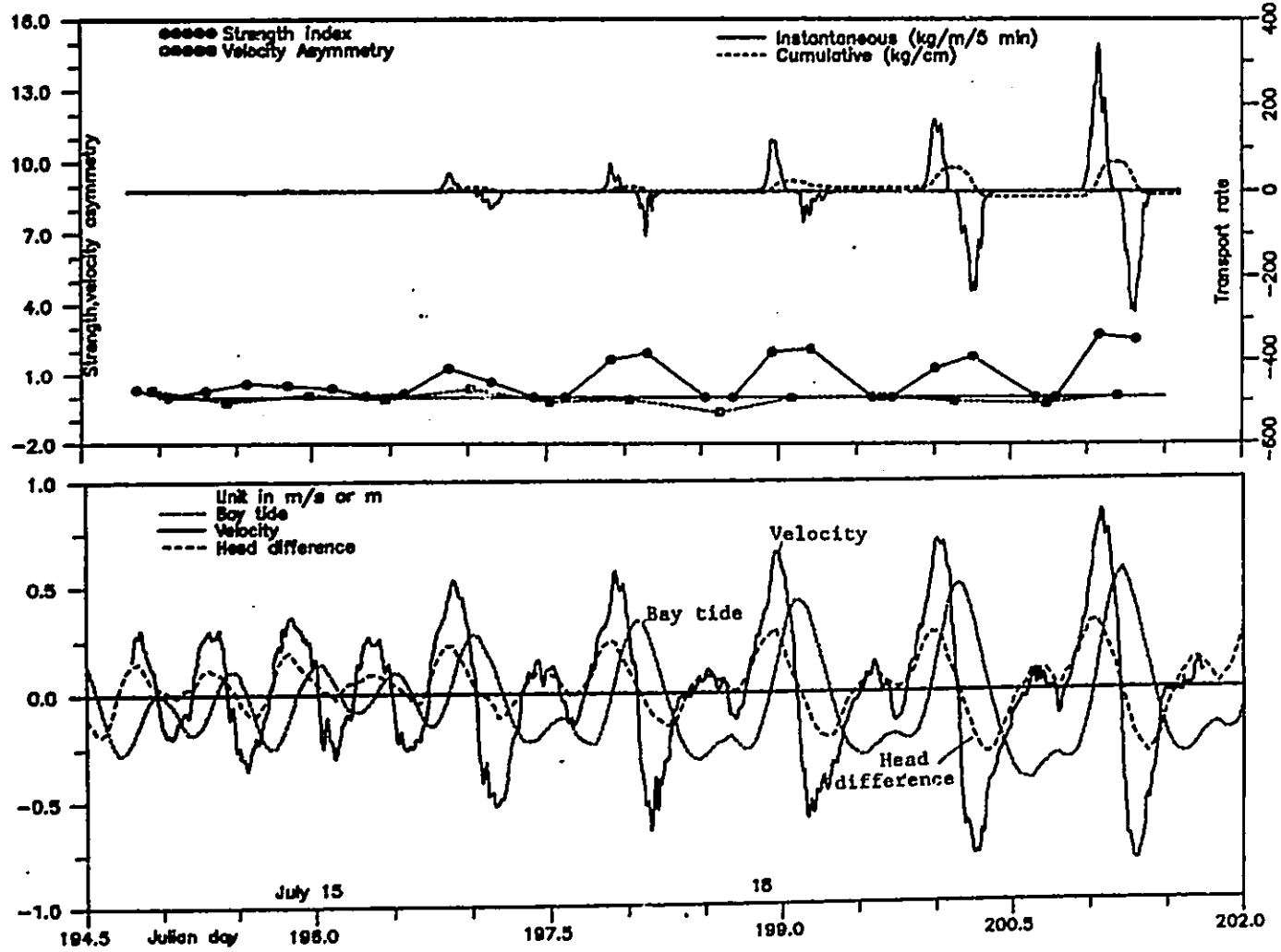
Strength index
Velocity Asymmetry
Instantaneous (kg/m/5 min)
Cumulative (kg/cm)
Strength,velocity asymmetry
Transport rate
16.0
13.0
10.0
7.0
4.0
1.0
-2.0
400
200
0
-200
-400
-600
Unit in m/s or m
Bay tide
Velocity
Head difference
Velocity
Bay tide
Head difference
1.0
0.5
0.0
-0.5
-1.0
July 15
16
194.5
Julian day
196.0
197.5
199.0
200.5
202.0

during small tides.

2.5.2.2 Energy Density Spectrum

The important time scales of currents were shown in an energy density spectrum computed with a Fast Fourier Transformation technique with the mean removed. The longest unbroken record of currents consists of 234 hours measured at Station 55-I in the throat section of the main channel (Figure 2-14A). The data were subsampled to provide hourly data to be consistent with the format of water level data. The resultant bandwidth resolution is 0.0229 cph, and the lowest periodicity resolved is 2.0 hours.

Figure 2-14A shows that various time-scales in water levels are also reflected in velocity field. Dominating the velocity spectrum are the diurnal (band) peak reflecting the effects of O_1 and K_1, and the semidiurnal (band) peak produced by M_2 and S_2. Compared with the tide spectrum measured over the same period of interval, the velocity spectrum shows a general decrease in energy for longer periodicities, and a relatively large increase for shorter periodicities. Also, although the diurnal band still contains more energy, the peak of the velocity spectrum occurs in the semidiurnal band. These features suggest a transfer of energy from longer periodicities into the shorter periodicities. Energy spectra have also been calculated for water levels of a period when both bay and gulf tides are available (Figure 2-14B). It is noted that

Figure 2-14

(A) Energy spectrum density of current velocities and corresponding bay tides. Data from 18:25, June 13 to 12:25, June 23, 1986, Station 55-I, main channel. Sample interval = 1 hour; Bandwidth resolution = 0.0229 cph.

(B) Energy spectrum density of bay tides and tidal difference between bay and gulf tides. Data from 13:00, July 3 to 13:00, July 28, 1986. Sample interval = 1 hour. Bandwidth resolution = 0.008319 cph.

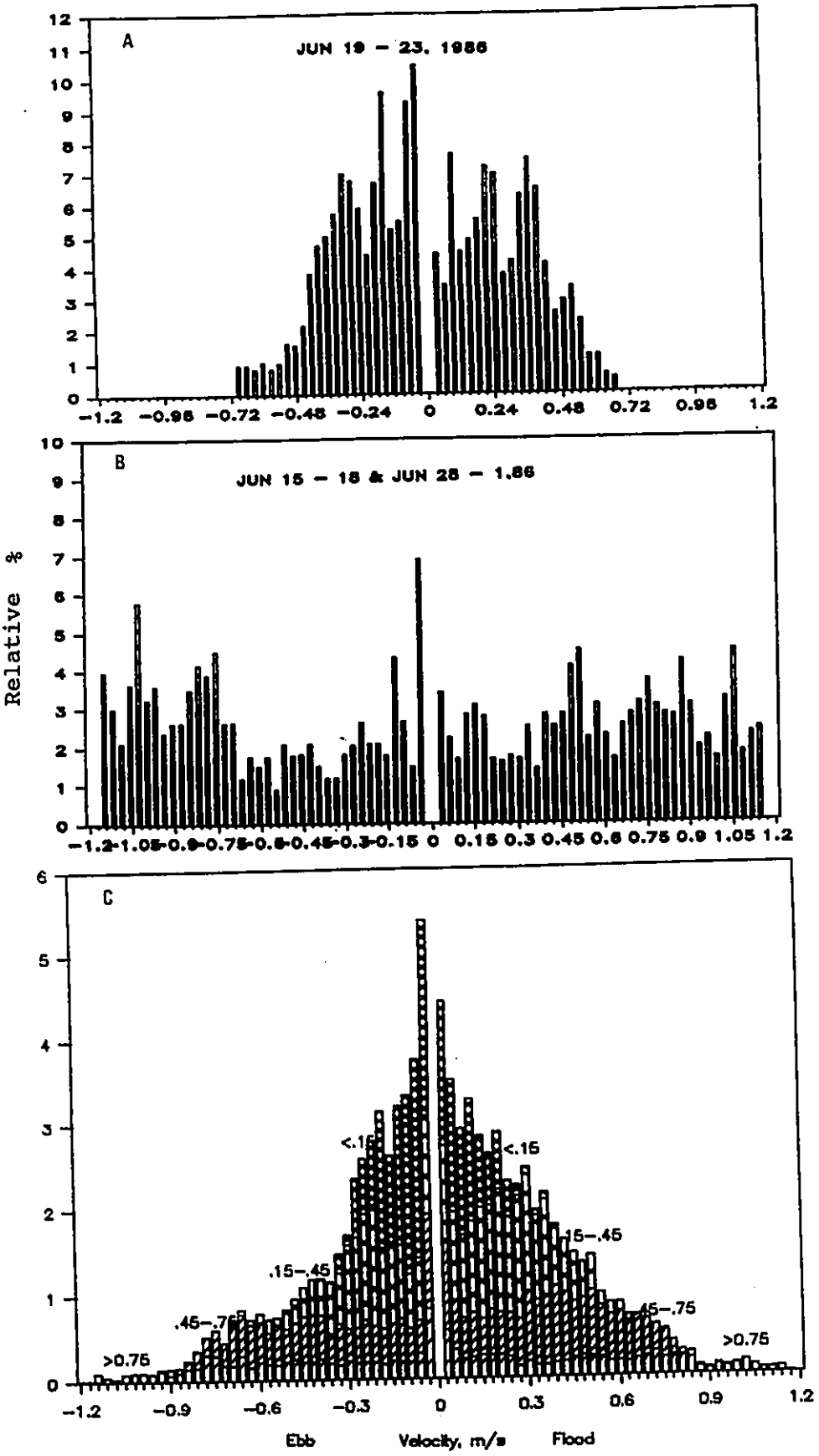
A
JUN 19 – 23, 1986
B
JUN 15 – 18 & JUN 28 – 1.86
Relative %
C
<.15
<.15
.15–.45
.15–.45
.45–.75
.45–.75
>0.75
>0.75
Ebb
Velocity, m/s
Flood

except in scale, the features revealed in Figure 2-14A are also present here. The similarities between water level difference in Figure 2-14B and tidal current in Figure 2-14A is particularly noteworthy. This suggests that tidal currents are more closely related to the water level difference than to the water level per se.

Current data may be plotted against water levels or head difference between gulf and bay tide to provide further insight into the character and relationship of tide and currents in an inlet environment. On such plots for sine waves, assuming flood being positive, an in-phase relationship is represented by a straight line running from upper right to lower left through the (0,0) point. A 90° out-of-phase relationship is represented by an ellipse with the major and minor axes in coincidence with the horizontal and vertical axis, respectively. Figure 2-15 are representative examples of such plots for different tidal conditions. It is seen that velocity-tidal difference curves in Figure 2-15 appear as a squashed figure eight in the first and third quadrants. This suggests an in-phase relationship between velocities and hydraulic head, or in other words, currents in the inlet are driven by the water level difference between the two ends of the inlet. The ellipses described by velocity-stage, on the other hand, suggests an out-of-phase relationship between them. This indicates that tides move through the system in the form of

Figure 2-15 Plots of current speeds versus (bay) tidal stage and head difference between gulf and bay tides for different tidal conditions. Data from Station 55-XI (A, B, C), and Station 55-I (D), main channel. Tidal ranges 0.42 m - 1.0 m. Arrows indicate the sequence from the start of the flood to the end of the ebb. Head data is not available for (D). Note that the separation between the accelerating and the decelerating phase. This suggests a hysteresis in hydraulic head-velocity relationship.

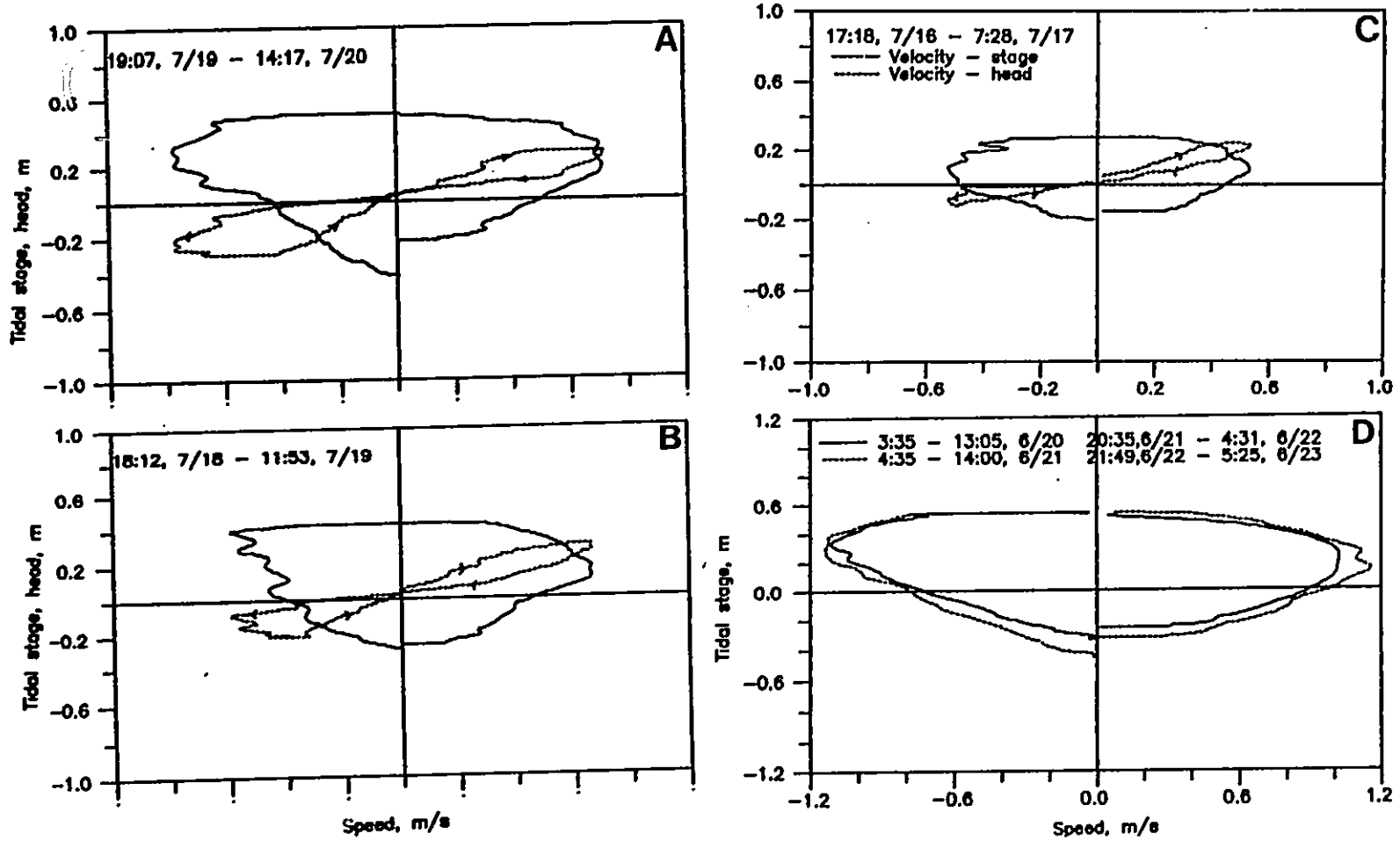
A
19:07, 7/19 – 14:17, 7/20
B
18:12, 7/18 – 11:53, 7/19
C
17:18, 7/16 – 7:28, 7/17
Velocity – stage
Velocity – head
D
3:35 – 13:05, 6/20
4:35 – 14:00, 6/21
20:35,6/21 – 4:31, 6/22
21:49,6/22 – 5:25, 6/23
Tidal stage, head, m
Speed, m/s

standing waves. It is noted, however, the major axis of the ellipses does not coincide with the mean water line. That is, peak velocities are not reached at times when the water level passes through the mean water mark, as is expected for a pure standing wave. The deviation is probably due to a partial reflection of tidal waves on the barrier shoreline, or due to shallow water distortion of tidal waves.

2.5.2.3 Spatial Variations

Tidal currents are highly variable in space. Figure 2-16 (also see Figure 4-11) compares currents measured in the three major channels. The figure shows that currents in the main channel are stronger than those in the South Channel, which are in turn stronger than those in the North Channel. At peak tides (June 23, 1986), the difference could be as high as 0.25-0.4 m/s for the South Channel, and 0.6 m/s for the North Channel. The difference is smaller for small tides. The high current speeds of the South Channel indicate that it is the main water way on the landward side.

Tidal currents of a full tidal cycle of large tides, where available, have been selected from stations of various part of the inlet, and plotted in Figure 2-17. The figure shows current variation across the inlet. At the throat section of the main channel, currents reached a maximum of about 1.15 m/s. They decreased to 0.6 m/s at the entrance

Figure 2-16 Comparisons of time series of current velocities measured in the main channel (Station 55-I), the south channel (Station 71-II) and the north channel (Station 64-II) for two tidal conditions. Also shown are bay tides.

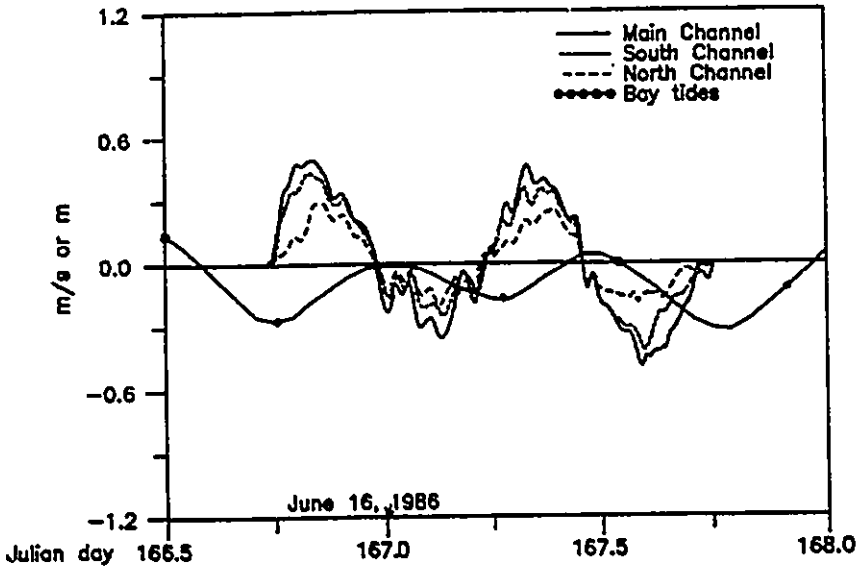
Main Channel
South Channel
North Channel
Bay tides
1.2
0.6
0.0
−0.6
−1.2
m/s or m
June 16, 1986
Julian day 166.5
167.0
167.5
168.0

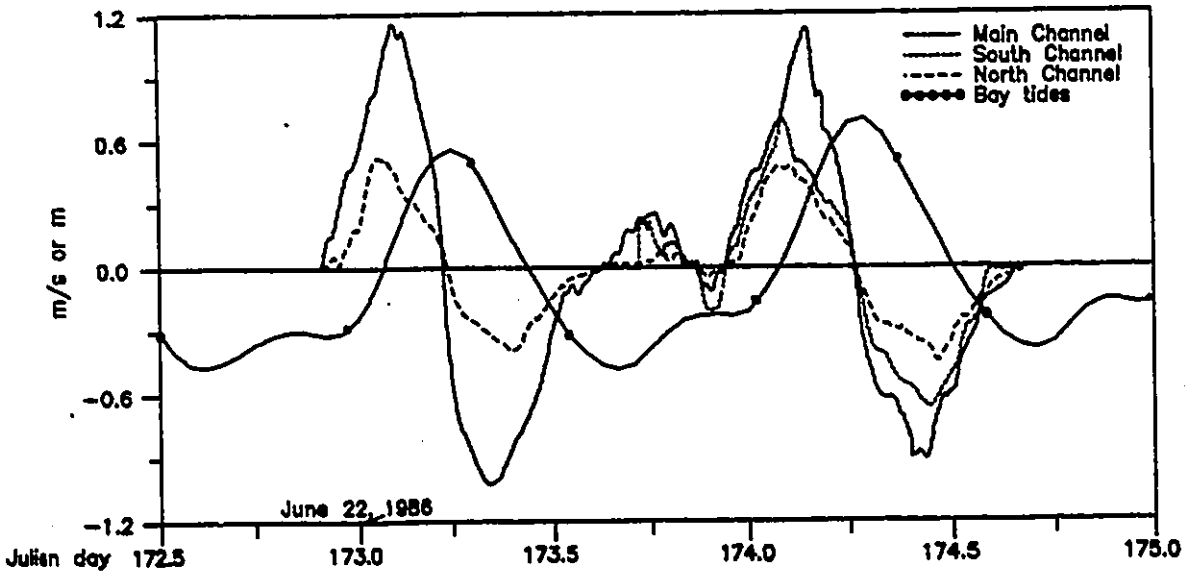
Main Channel
South Channel
North Channel
Bay tides
1.2
0.6
0.0
−0.6
−1.2
m/s or m
June 22, 1986
Julian day 172.5
173.0
173.5
174.0
174.5
175.0

Figure 2-17 Location map for current meter stations, and representative time-velocity curves at selected stations. The vertical scales is metre for tidal curve and m/s for current velocity. The horizontal scale is either in Julian day (e.g., 175.0), or Gregorian day calendar (e.g., June 24). Note Station 71-VI is located outside the picture in the trough of the first nearshore bar; see Figure 3-1A for the location.

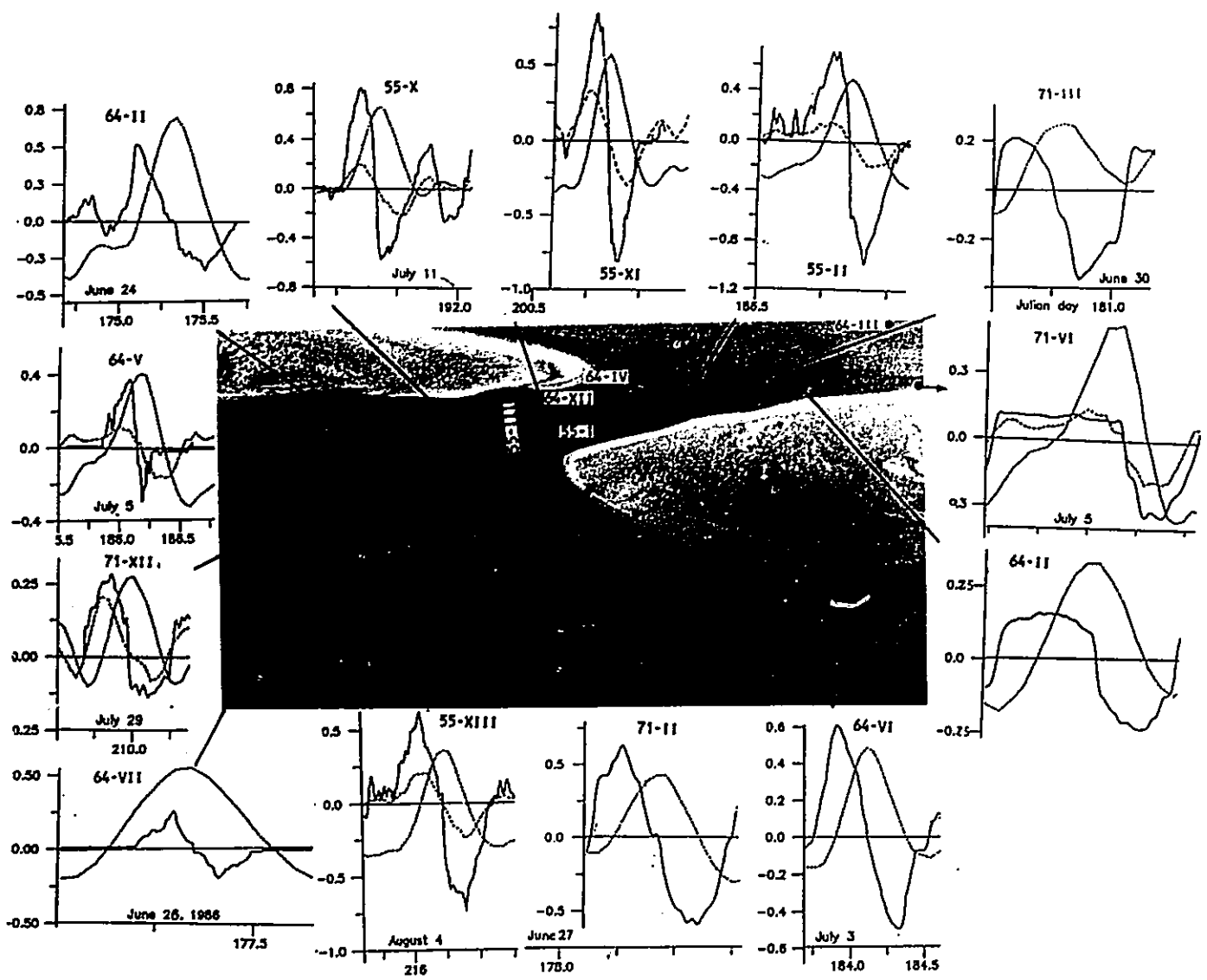
64-II
June 24
55-X
July 11
55-XI
55-II
71-III
June 30
Julian day 181.0
64-V
July 5
64-IV
64-III
64-XII
64-I
71-VI
July 5
71-XII
July 29
64-II
64-VII
June 26, 1986
55-XIII
August 4
71-II
June 27
64-VI
July 3

and on the flood ramp. On the flood tidal delta, velocities of large tides reached about 0.5 m/s on the proximal part, and but less than 0.3 m/s on the distal part. Currents were also measured at two locations within the bay. They both showed a maximum velocity less than 0.1 m/s. The station near the entrance to the Narrows (Figure 2-18A) showed flood currents marginally stronger than ebb currents but having shorter duration. The flow was thus rather balanced at this location. The station located about 0.5 km northwest of the flood delta (Figure 2-18B), however, showed a dominant flood with both larger speed and longer duration. While it is the only set of data available, the pattern it revealed might reflect a drift of tidal water to the northern part of the bay, where the larger, and more efficient Alberton Inlet is located. The lost flood water would not be available for the next ebb. This would introduce an imbalance into the flow field, which is directed away from the inlet.

Taken together, the pattern revealed in the figure is a one that shows currents that decrease away from the throat, and quickly dampen into the bay. The particularly small velocities a short distance into the bay indicate that the flow activity of Palmer inlet is concentrated around the immediate vicinity of the inlet channel. The bay can be considered as a storage basin, in which tidal motion is negligible. This is consistent with the result of water level analysis, which indicates that at any given time,

Figure 2-18 Time series of current velocities measured in the Narrow, Station 71-XI (A), and in the bay, Station M-1 (□). See Figure 2-6 for their locations.

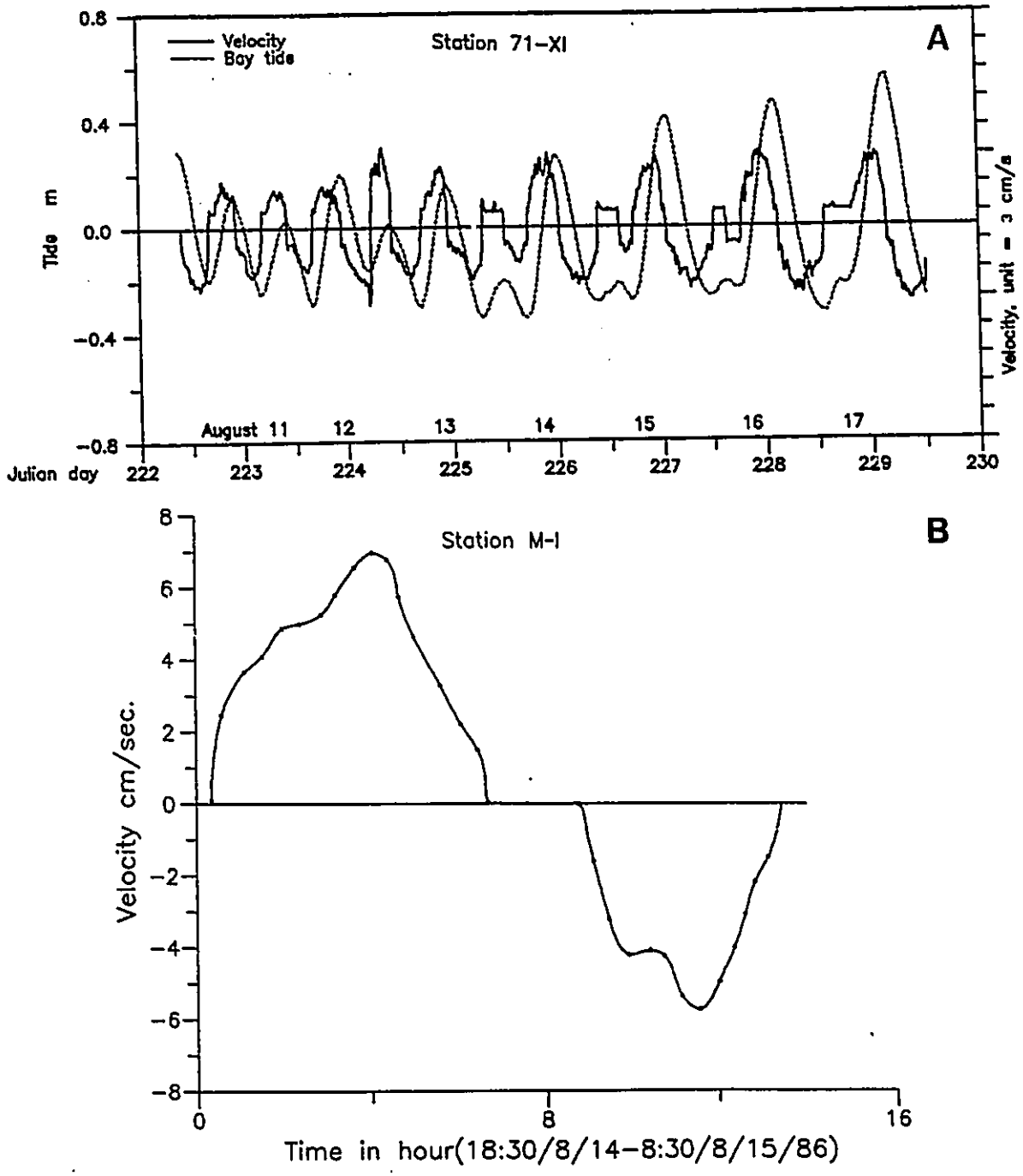
A
Station 71-XI
Velocity
Bay tide
Tide m
Velocity, unit = 3 cm/s
0.8
0.4
0.0
-0.4
-0.8
August 11
12
13
14
15
16
17
Julian day
222
223
224
225
226
227
228
229
230
B
Station M-I
Velocity cm/sec.
8
6
4
2
0
-2
-4
-6
-8
0
8
16
Time in hour(18:30/8/14-8:30/8/15/86)

water levels in the bay can be taken as approximately horizontal.

2.5.2.4 Tidal Asymmetry

Asymmetry between the flood and the ebb flow refers to difference in both speed and duration. Results compiled using 178 flood and ebb phases, during which both tide and current data are available, are summarised in Table 2-9. The table shows that the total average as well as the maximum value of flow strength of flood are equal or nearly equal to the corresponding value of ebb. The average duration of flood is slightly longer. With sediment transport rate being a steep function of speeds but a linear function of duration, the flow at Palmer Inlet can be described as overall rather balanced with only slight indication of flood dominance.

Conditions are somewhat different in different tidal ranges. The > 0.75 m range shows a preference for incoming currents, as flood is dominant in both strength and duration. The opposite is evident for the range of 0.45-0.75 m. In the two lower ranges, there is less persistence in duration and velocity to show preferred dominance. Note that the pattern revealed here is consistent with that showed by the histogram. In terms of sediment transport, which is initiated after a threshold is passed, the above data suggest that the inlet will be overall flood

Table 2-9 Velocity statistics based on 178 flood and ebb phases. Lead is the time difference between maximum ebb velocities and HW. Delay is the time difference between maximum flood velocities and HW.

Tidal range (m) Number of flood Number of ebb		Max. velocity Flood	 Ebb (m/s)	Duration Flood	 ebb (hours)	Phase Delay	 lead (hours)
Minor tides of large tides							
<0.15 m	Average	0.2	-0.2	4.8	3.5	3.0	1.0
17	Maximum	0.4	-0.3	6.6	6.5	5.2	2.6
25	Minimum	0	-0.1	2.8	1.5	2.0	0.4
Small tides							
0.15-0.45 m	Average	0.4	-0.4	5.8	6.1	3.4	2.2
32	Maximum	0.6	-0.7	8.1	8.5	5.1	4.0
24	Minimum	0.2	-0.2	3.8	3.5	2.2	0.5
Intermediate tides							
0.45-0.75 m	Average	0.6	-0.7	8.2	8.4	3.4	2.7
28	Maximum	0.9	-0.9	16	11.1	5.2	4.9
24	Minimum	0.3	-0.4	0.1	6.4	2.2	0.7
Large tides							
>0.75 m	Average	0.9	-0.8	9.8	7.7	3.2	2.4
12	Maximum	1.16	-1.13	15.5	11	4.8	3.8
16	Minimum	0.6	-0.4	6.9	0.4	2.7	1.1
All tides	Average	0.5	-0.5	6.9	6.3	3.3	2.0
178	Maximum	1.15	-1.14	16	11.1	5.2	4.9
	Minimum	0.04	-0.05	0.1	0.4	1.9	0.1

dominated.

The spatial variation of asymmetry in the inlet can be seen in Figure 2-17. In general, at the throat, the flow has rather balanced distribution with slight ebb dominance. The dominance, as indicated by the velocity-asymmetry-index curve, is not persistent from one cycle to the next (Figure 2-13). With increasing distance from the throat, the asymmetry becomes increasingly clear with flood-dominance in the bayward direction, and ebb-dominance toward entrance. This pattern of speed-asymmetry is consistent with that characteristic of tidal inlets in general (O'Brien, 1976). That is, inlet flow of each tidal phase tends to dominate at the discharging end of its path, where the flow assumes the character of a jet. Topographic shielding has also been considered as playing an important role in producing the observed asymmetry (Hayes, 1980; Hine, 1977). The flood tidal delta contributes to flood dominance by providing protection against ebb currents. The reverse is somewhat true for spit platforms, which tend to shield the flow in the channel during flood. The effects of topographic shields are probably best illustrated in the South Channel. In this channel, the ebb flow is observed to dominate the north half, and the flood flow the south half. This division in flow dominance can be attributed to the two shoals, the ebb spit on the north and the flood lobe on the south. These sand bodies provide a shield against the flow

that they are facing.

Another aspect of current asymmetry is the skewness of the time-velocity profile in a complete tidal cycle. This skewness results from the shift of peak velocities away from the midtide point. Overall, the shape-asymmetry of currents at Palmer Inlet is characterized by both flood and ebb maxima displaced toward the high water point (Table 2-9; Figure 2-13). The table shows that the maximum flood current lags high water by 2-3.5 hours, and the maximum ebb current leads high water by 2-3 hours. In details, the above features apply primarily to the main channel. This is demonstrated graphically in representative velocity-stage plots of the throat channel (Figure 2-15), in which the ellipses do not lie completely flat. Instead, they tilt slightly toward the right especially when tides are large. In time-velocity terms (Figure 2-13), this means that flood velocity increases slowly, reaches a peak late in the cycle, and then declined rapidly to high water. In contrast, on the ebb, velocity increases rapidly, reach the peak early in the cycle, and decreases slowly into low water. This shape-asymmetry is better illustrated on the velocity-hydraulic head plots as shown in Figure 2-15. The separation of the accelerating and the decelerating phase in the figure indicates a hysteresis behaviour. The clockwise-loop in the flood halfcycle indicates that the decelerating phase is more efficient, because a given hydraulic head produces a

larger speed, or conversely, a given speed requires a smaller head as opposed to those of the accelerating phase. The reverse is the case for the ebb half, in which the curve describes a counterclockwise loop. In both cases, the peak velocity occurs at a time when the water level is higher, and while the flow is less confined by the sand shoals. Palmer Inlet is clogged with sand around the throat, and lacks well developed bayward outlets, both factors acting to restrict tidal water from entering the channel when the tide is low. Tidal currents in the throat thus will not accelerate at this time, although a small cross-section implies that it would.

A rather different situation is observed in the two channels landward of the inlet. In both channels, measured velocity curves show a steep rising limb and a less steep falling limb (Figure 2-16). This is demonstrated in the figure, in which current velocities measured simultaneously in three channels are plotted together (Figure 2-16). The figure shows that peak velocities in the two landward channels are more deviated away from high water than those in the throat channel. This is significant, because in comparison to the throat channel, this not only means that maximum velocities in these channels occur at a shallower depth, which probably results in higher shear velocities, but also means that it changes the time at which the bottom sand particles reach the threshold of initiation.

2.6 Tidal Deformation and Implication for Sediment Transport

The integration of water level and current data reveals a number of interesting features of tide/currents deformation through Palmer Inlet. Velocity data indicate that both the maximum velocity (Figure 2-19) and shift-from-HW (Figure 2-20) appear to be better correlated with, and a steeper function of tidal ranges for flood than for ebb. Tidal data show similar results as is indicated in Figure 2-9 and by the water level profile of Figure 2-7B. Palmer inlet system as a whole offers more resistance to ebb than to flood flows. Because resistance is a function of water depth, a part of the above inequality can be explained by the difference in water depth experienced during the flood and ebb phase. Around high water, depth is relatively large, and the flow is less confined. Tides move into the inlet with relative ease. Around low water, tides move out against larger friction created by shallow water and a smaller opening of an increasingly narrow channel. The time averaged force of friction would be slightly in favour of the flood flow, and directed towards the bay. This force acts against the long ebb runout inherent in the daily tide. As a result, although daily tides are characterized by stronger ebb, as far as sediment transport is concerned, the tidal regime is more or less balanced.

A second aspect of tidal deformation is related to

Figure 2-19 Plots and linear regressions of maximum flood and ebb velocities versus tidal ranges. In the regression equations, Y represents maximum velocities and X represents tidal ranges.

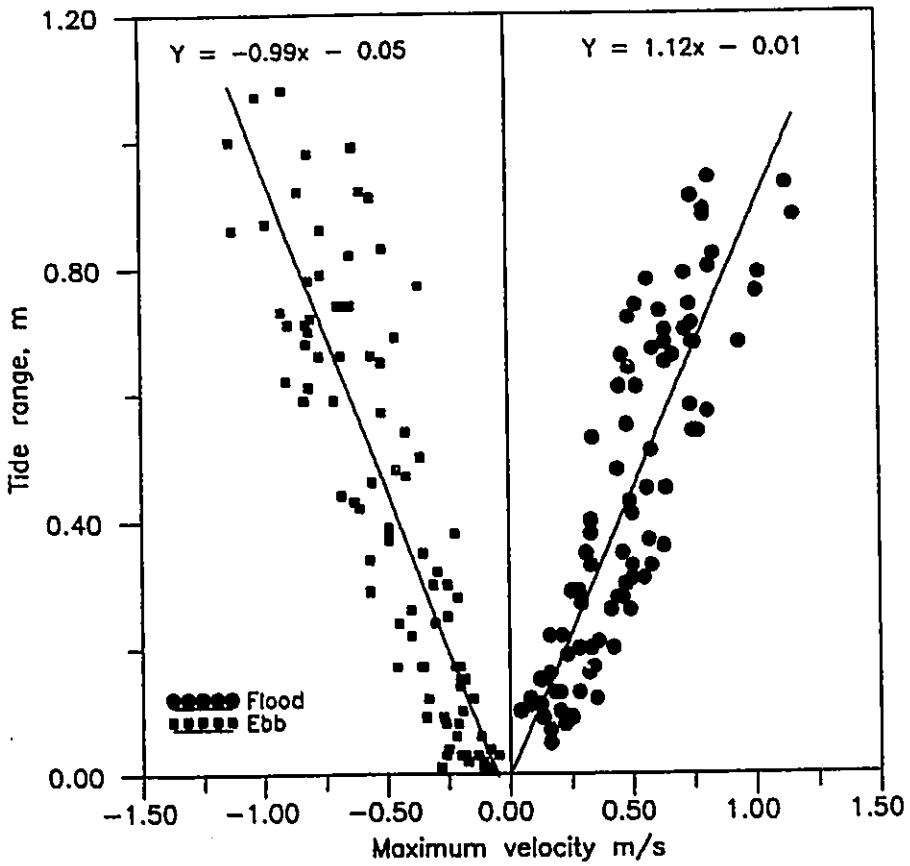
Y = −0.99x − 0.05
Y = 1.12x − 0.01
Flood
Ebb
Tide range, m
1.20
0.80
0.40
0.00
−1.50
−1.00
−0.50
0.00
0.50
1.00
1.50
Maximum velocity m/s

Figure 2-20 Plots and linear regressions of lag (flood) and lead (ebb) versus maximum velocities using data of all tidal ranges.

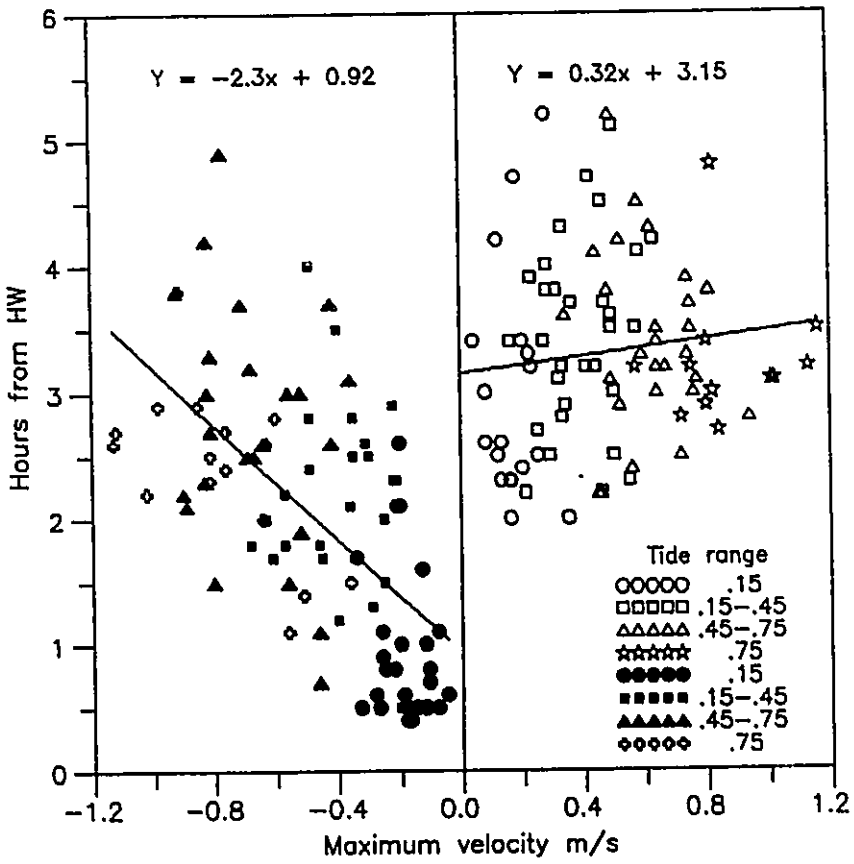
Y = −2.3x + 0.92
Y = 0.32x + 3.15
Hours from HW
Maximum velocity m/s
Tide range
.15
.15–.45
.45–.75
.75
.15
.15–.45
.45–.75
.75
0
1
2
3
4
5
6
−1.2
−0.8
−0.4
0.0
0.4
0.8
1.2

the shape-asymmetry of time-velocity profile. Such phenomena has been observed in many coastal environments. Depending on the geometry of the system (Bayliss, 1979; Penthic, 1980), such asymmetry can take the form from nearer to low water on tidal flats in the Wadden Sea (Postma, 1967), to nearer to high water in the backbarrier tidal creeks in the South Carolina. Both asymmetries occur at Palmer Inlet: the latter resembles that in the throat, and the former resembles that in the two landward channels. The reason for this can only be speculated upon at this stage. Two important factors considered responsible for velocity asymmetry in inlet environment are geometry and friction (Keulegan, 1967). Geometry and bathymmetry are expected to be more important in a shallow, constricted setting. At Palmer Inlet, the clog of large shoals around the throat produces very poor drainage near low waters. In its attempt to flush sand out of the system and maintain equilibrium, flow in the inlet has to reach a relatively high speed when water level is high. Flow in the throat channel can be considered controlled by this effect. In the South or North Channel, where water is shallower, local friction becomes more important. It overcomes the effect imposed by inlet geometry. The resultant shallow water effect tends to shift the peak velocities toward the low water period. This differentiation in asymmetry between different channels has important sedimentological consequences. In the throat

channel, the critical velocity occurs late in the flood and early in the ebb. Thus, there is more time following the critical value in the ebb than in the flood. The potential of more sediment transport under ebb flow is thus increased because particles move farther away from the throat during ebb period than they do during the flood period. An opposite picture of sediment movement occurs in the South and the North Channel. The result of such differences in shape-asymmetry between different channels results in a possible net ebb transport in the throat, and a net flood transport in the two landward channels. This explains the development of Palmer Inlet in the past several decades, which indicates that sediments have been continuously accumulated around the flood delta, while the throat channel has maintained itself relatively free of sediment.

While tides undergo changes through the inlet, these changes are relatively small, as compared with the results of other studies. Reduction in tidal range at Palmer Inlet is 6% for large tides, and 15% for mean tides, whereas at Nauset Inlet, MA. (Aubery and Speer, 1985), Fire Island Inlet, NY (Wong, 1986) and elsewhere, reductions of up to 70% have been reported. This is contrary to what is expected as smaller size of Palmer Inlet would suggest large reduction. Inlet size, however, is only one factor determining tidal response of an inlet-bay system. Tidal period is equally important. Keulegan (1967) suggested that

tidal period is directly proportional to the ability of an ocean tide to fill an interior basin. Tides twice as long in period will be twice easier to move through the inlet. The small reduction at Palmer Inlet, therefore, can be attributed to the dominantly diurnal character of the tides.

2.7 Tidal Inlet as a Filter

Tides undergo changes as they move into shallow water. For water levels, Palmer inlet appears to work as a low-pass filter. As shown in Table 2-6, the semidiurnal frequency, M_2, is preferentially damped as its amplitude decreases from 17.6 cm outside the inlet to 13.8 cm and 12.7 cm within. The corresponding change for O_1 is from 20.1 cm to 19.8 cm and 18.1 cm. A similar low relative change is observed for K_1 as compared with S_2. In the higher harmonics range, those related to K_1 and O_1 (MO_3 and MK_3) experience slightly increase in amplitude; those related to semidiurnal tides, M_2, M_4 and M_6, undergo decrease. These data indicate that the constrictive effect and the narrow channel of the inlet combine to act as a low-pass filter for tidal levels. High semidiurnal frequencies are preferentially filtered, which gives more diurnal-dominated tides within the bay.

The low-pass nature of tidal inlet with respect to tidal levels has been observed and studied in a number of studies (Speer and Aubrey, 1985; Dilorenso, 1986; Isaji et

al., 1985). Corresponding data on current velocities, however, are few in the literature. The limited data obtained at Palmer Inlet suggest that the filtering process reflected in tidal currents is one characterized by transfer of energy from longer period constituents to those of shorter periods (Figure 2-14A). The energy transferred is used to produce shallow water compound tides and overtides. In tidal inlets, changes in water levels and currents may be somewhat different; the latter seems to be more sensitive to, and thus a better indication of local hydraulic process. This is consistent with fluid mechanics requirements, which state that transformation of fluid movement originates in the flow field through energy conservation principle, and is then transferred into water levels through the mass conservation condition.

2.8 Conclusions

The main physical factors - wind, wave and longshore drift, tide and tidal currents - have been examined in this chapter. Winds in the study area are dominantly offshore from the west, and less than 8 m/s. Storm winds (>16 m/s), however, are dominated by onshore winds, especially by those from NNW-NNE sectors. Hindcast waves in the Gulf are of relatively small dimensions during most of the year. The average wave has a height of 0.50 m and a period of 2.5 s. During storms, waves as large as 3 m and 7 s are expected

out of NNE and NE. Large waves from these directions contribute much to a dominance of the north component in deep wave climate, despite the fact that Palmer Inlet is largely shielded by North Point from waves that approach from the NNW and N. Longshore currents in the area are mainly controlled by the oblique approach of incident waves. This allows the translation of the deep wave climate to the inshore region, and there is a dominant southward directed longshore drift on the Gulf side of the barrier. Strong wave refraction does, however, occur around the ebb terminal lobe for large waves from NNE and NE. This could affect the direction of sediment movement on the downdrift side of the inlet. Waves in Cascumpec Bay have a height of 0.18 m in and a period of 1.5 s on average, and are also dominated by the north component.

The tide of Palmer Inlet is microtidal, mixed and mainly diurnal. Similar magnitudes of the O_1 and K_1 component, and large difference between the M_2 and S_2 components result in a distinct fortnightly cycle, which is characterized by a tropic-to-synodic sequence as tidal constituents beat in and out of phase. Large tides are mainly diurnal and tropic, but at small tides, a semidiurnal synodic influence becomes important. The diurnal equality of large daily tides is characterized by every second tide and tidal current being larger than its predecessor, which always occurs on the lower part of the rising limb of the

dominant peak.

Tidal currents are highly variable with time and from one place to the next. The time-variation of tidal currents follows the general pattern of tidal levels with a distinct fortnightly cycle and strong diurnal inequality. Maximum current speeds reach up to 1.15 m/s in tropic (large) tides. Small tides generally produce currents with peak velocities less than 0.5 m/s, and semidiurnal in period. At the throat section, current speed reaches a maximum and is slightly ebb-dominated. Speeds decrease in both directions, and become increasingly skewed with each phase dominating at its discharging end of the throat.

The gulf tide undergoes deformation in its motion into the inlet. While the deformation is small overall in comparison with other similar areas, it is not symmetrical between ebb and flood. The system as a whole provides more resistance to ebb than flood. As a result, although water levels are characterized by long runouts, tide deformation tends to produce more sediment transport on the flood, and create a system which traps sediment within the bay. In the throat channel, the shape-asymmetry of time-velocity profile is characterized by both flood and ebb peaks shifting toward high water so that currents have a steeper accelerating ebb and decelerating flood. An opposite pattern occurs for current velocities in the north and the South Channel. The significance in this difference is that given speed- and

duration-symmetry, this shape-asymmetry alone will induce a net ebb sediment transport in the throat, and a net flood sediment transport in the other two channels. Sediments transported inside the inlet will essentially stay there, and those sediments left in the throat will be flushed out to the sea. This explains why Palmer Inlet, over the past several decades, has developed a large flood delta, but still managed to keep the channel open.

In microtidal tidal inlets, bathymetry plays an important role in controlling flow characteristics and sediment transport. The inlet shoals, functioning as topographic shields, result in longitudinal segregation of tidal currents in the main and South Channel. The sand body at the each end of the channel provides shielding to flow from the incoming end so that each of the flood/ebb flows dominates its discharging end.

Tidal activity is concentrated near the inlet, and quickly damped into the bay. The bay can be considered as a storage basin, and in essence, responses to the forcing of gulf tide in the manner of a simple 'pumping model' (Mehta and Ozsoy, 1979). At any given time, the water level within the bay rises and falls uniformly, and water movement is negligible. It is, however, possible that there is a weak drift of flood water toward Alberton inlet. The lost water is not available for the next ebb, and could contribute to the reduced flushing ability of Palmer Inlet.

Chapter 3

Inlet Morphology and History

3.1 Introduction and General Information

Inlet morphology is determined by a number of large-scale physical parameters. In particular, it reflects the relative importance of tidal and wave energy. As wave height and tidal range vary along a coast (Nummedal et al., 1977), so do the general morphology of tidal inlets and the distribution of their sand bodies. Hayes (1979) recognized, by bivariate plots of the above two parameters, four basic types of inlet/estuary morphology from wave-dominated (Florida coast) through mixed-energy (east coast of United States) to tidal-dominated (Bristol Bay of England or Bay of Fundy).

This chapter examines the general morphology of Palmer Inlet, and its development since 1958. The morphology was ascertained in 1986 and 1987 through area mapping, oblique air photographing, echo-sounding profiles, and low-tide ground reconnaissance. For 1986 and 1987, maps were produced with an alidade and a plane table using the standard technique as described by Compton (p.88-112, 1961). The maps were linked to vertical air photographs through a temporary reference mark used in the survey (Figure 3-1C), which is also identifiable in 1981 photographs. The linkage

Figure 3-1 Oblique air photographs taken in June, 1986. F - flood-oriented sand lobes; E - ebb-spit; FR - flood ramp. 1 - main channel; 2 - south channel; 3 - north channel.

A) Entrance section of the inlet, showing the larger updrift spit platform, the smaller downdrift spit, and their associated channel margin linear bars (cmlb). Note the lobe-shaped ebb terminal lobe (Tl), and the well-developed seaward margin channel. Shell lag deposits are visible in the channel (white streaks).

B) Throat section, showing the north spit platform connected with the flood tidal delta, and the seaward end of the north channel ended at the north spit. Megaripples can be seen on the ebb spit (E) and on the edge of shoals along the main channel (arrow). The arrow in the main channel marks a submerged mud-scarp projecting bayward from the south spit platform. White streaks in the main channel are shell deposits.

C) Bayward section, showing portion of the flood tidal delta close to the inlet throat. Note the lack of bayward outlets for inlet channels, and superimposition of the south channel on two sand lobes. Point 'R' on the north spit is the reference point used in the field survey.

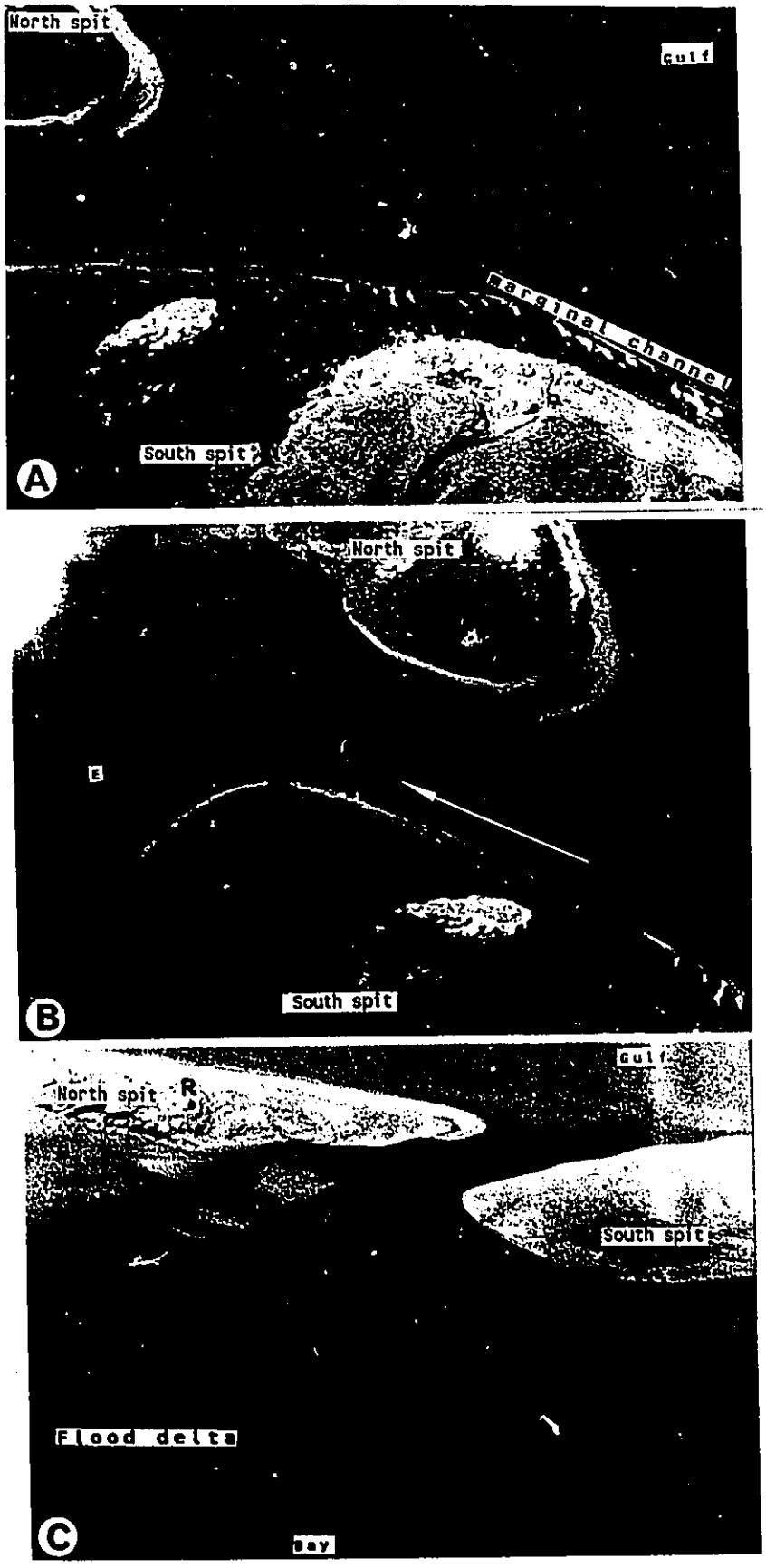
North spit
Gulf
Marginal channel
South spit
A
North spit
E
B
South spit
Gulf
North spit
R
South spit
Flood delta
C
Bay

was also assisted by oblique air photographs after correcting for vertical tilt of the camera using a computer program written by Roggeband (1988). The program is given in Appendix A-2. The historical development of the inlet was determined by comparison of a series of hydrographic sheets, and vertical aerial photographs (Appendix E) digitized using a SUMMASKETCH pad. The use of the same coordinate system, defined by three morphological features recognizable on all photographs, allows ready graphic superimposition, and subsequent calculation of inlet migration and volume changes. It has been realized that the delineation of morphological boundaries on air photographs involved a degree of subjectivity and approximation. The calculation was hence restricted to the updrift side of the entrance region, where the largest changes have occurred. Separation of the spit and the platform is also necessary because of the different thickness involved. In Table 3-1, the average distance of migration is the digitized area divided by the width, that is assumed, averaged over various periods, to be 300 m for the spit and 600 m for the platform. The maximum migration distance is that covered by the seaward tip of the main channels between successive records. The volume is the product of the area and the estimated thickness. Based on the present topography, the average thickness for the spit is assumed to be 1.1 m. This is equivalent to placing the base of the spit at the spring low

Table 3-1 Inlet migration and volumetric calculations from air photographs and field survey data. Calculations were made for the updrift side. [1] - digitized area divided by 600 m for the subtidal channel, and 300 m for the spit. [2] - distance between the seaward tips of the two compared channels. [3] - Negative figures = updrift movement or loss; positive = downdrift movement or gain.

	1958-64	1964-68	1968-71	1971-81	1981-86	1986-87	1958-87
Spit							
Migration distance (m)							
Average[1]	-19[3]	-30	85	2	172	6	265
Rate (m/yr)	-3	-8	28	0	34	6	11
Area (m^2)	-5,799	-9,066	25,553	500	51,597	1,950	79,600
Volume (m^3)	-18,557	-29,011	81,770	1,550	56,757	2,145	142,222
Rate (m^3/yr)	-3,093	-7,253	27,257	155	11,351	2,145	4,904
Spit platform							
Migration distance (m)							
Maximum[2]	144	23	330	207	10	0	709
Average[1]	66	18	156	246	110	8	428
Rate (m/yr)	11	5	52	25	22	8	15
Area (m^2)	40,097	10,947	93,557	147,994	66,559	4,500	363,657
Volume (m^3)	84,204	22,989	196,470	310,787	139,774	9,450	763,680
Rate (m^3/yr)	14,034	5,747	65,490	31,079	27,955	9,450	26,333
Total (m^3/yr)	10,940	-1,500	92,746	31,234	39,306	11,600	31,237

water mark. The average thickness of the subtidal platform used is 2.1 m, the average maximum depth of the main channel.

3.2 Recent Morphology

The Inlet is bounded by two bulbous sand bars (Figure 1-1; Figure 3-1C), the terminus of Conway Sand Hill to the south (south spit) and of Cascumpec Sand Hill to the north (north spit). They are about 300-400 m in width; most of the bar consists of a featureless sand flat, remaining exposed above the water line most of the time except in large tides, when it is flooded by a very thin layer of water (0-20 cm). The flat has a slope of 0.3° dipping toward the land so that the surface on the bayside is usually more moist than that on the gulfside. The spit is fringed by a beach with a slope of 4-7°, which decreases in width from the gulfside into the inlet.

The subtidal extension of the spit is the spit platform (Figure 3-1A and Figure 3-2D), normally covered by a metre or so water at low water. The spit platform on the south side is located beyond the inlet throat, and is considerably smaller in size than that on the updrift side, which extends deep into the inlet, and is connected with the flood tidal delta (Figure 3-1B). The intertidal feature of the platform consists of channel margin linear bars or a series of swash bars especially on the downdrift side in

Figure 3-2 Oblique air photographs taken in August, 1986. (A) and in July, 1987 (Rest). E - ebb-spit; F - flood-oriented sand lobes.

(A) Proximal flood tidal delta, showing two flood-oriented sand lobes (F) and associated tidal creeks. The arrow points to the slightly elevated northern edge of the delta flanking the north channel. Large bedforms can be seen along the southern edge fringing the flood ramp.

(B) Close-up views of the proximal portion of the flood tidal delta, showing bedforms in a tidal creek and along the edge fringing the flood ramp. The slightly elevated northern margin appears white (arrowed).

(C) South channel margin linear bar consisting primarily of swash bars (B and C) with a low central area. Landward migration of swash bars and their attachment to the beach caused the closure of the seaward marginal channel (compare with Figure 3-1A) and seaward progradation of shoreline. Arrows in the (C) and (D) are equivalent in position.

(D) Entrance section, showing the contrasting size of the north and south spit platform separated by the main channel. Note the seaward progradation of the shoreline on the downdrift side (arrowed) due to attachment of swash bars to the beach. Sediment attachment on the updrift side has a larger shore-parallel component, as is indicated by the sandy hooks at the tip of the north spit. The hooks entrap small water pond ('P') behind them. A close-up view of the arrowed area is given in (C).

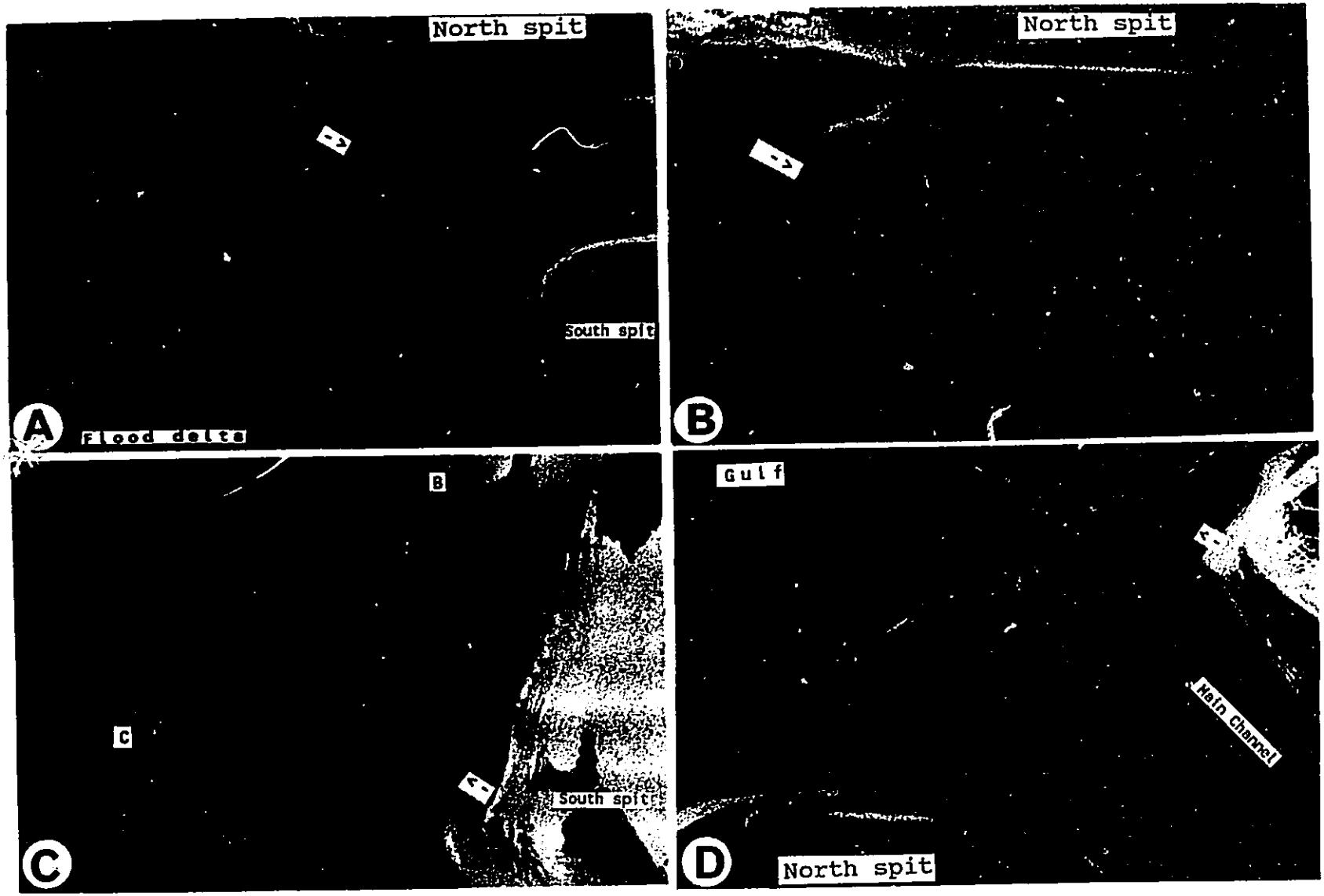
North spit
South spit
A
Flood delta
North spit
B
B
C
South spit
C
Gulf
Main Channel
D
North spit

1987 (Figure 3-2D). While the north channel margin linear bar showed little change, the one on the south side changed in shape from a triangle in 1968 to two separate strings of swash bar with a low, central area in 1987. This suggests that the latter must have experienced an erosional phase in the winter of 1968, and was then rebuilt as constructive summer waves drove sands landward in the form of swash bars. Attachment of swash bars was observed in this period, and this resulted in progradation of the shoreline, and infilling of the margin channel existing on this side of the inlet (compare Figure 3-1A and Figure 3-2D). Connecting the two platforms under the water is a small seaward arc, the ebb terminal lobe with its tip located about less than one km off the shoreline.

3.2.1 Flood Tidal Delta

The flood tidal delta is by far the largest sand body of the inlet. It covers a total area of 1900x900 m^2, is elevated about 0.5 metre above the low water level, and is surrounded by a less than one metre deep bay with dense eelgrass. Morphologically, it is simple, characterized by a large, central lobe devoid of the morphological elements of Hayes' model (1980). Two small sand lobes appear on the proximal part in the air but are barely identifiable on the ground (Figure 3-2A). Their configuration suggests that they are flood products, formed by inflow as spill-over

lobes over the delta. Ebb-formed features are absent from the delta surface but appear in the South Channel as spits (Figure 3-1C). This not only indicates that the South Channel is the main conduit on the bayward side, but also suggests that the ebb flow, starting from rest, can hardly overtop the delta at the present. The flow in the North Channel is impeded on the ebb due to the poor seaward outlet, and forms a slightly elevated, shield-like structure along the northern edge of the proximal delta. It appears relatively white on the photo but again can hardly be recognized on the ground (Figure 3-2B).

3.2.2 Tidal Channels

The tidal channels of Palmer Inlet are shallow and rather sand-congested (Figure 3-1C, and Figure 3-3 and Figure 3-4). The main channel measured about 850 m between the flood ramp landward and the ebb terminal lobe. Although scours upto 3.8 m deep were found, the main channel averages 2.1 m at mean low water along its thalweg, and about 1.2-1.7 m at high water when the subtidal platform is included. At the throat section between profile F and I of Figure 3-4, it is about 190-250 m in width, and 330-410 m^2 in cross-section area. The throat section of the channel scoured into a semicompact, cohesive mud substrate, which occurs as scarps or pinnacles at the bottom. In plan view, the channel is skewed to the south at an azimuth of 95°. In cross-section,

Figure 3-3

(A) Bathymetric map of Palmer Inlet constructed from 1987 field survey and echo sounding profiles. Depth in metres.

(B) Echo sounding profile lines of inlet channels measured in 1987.

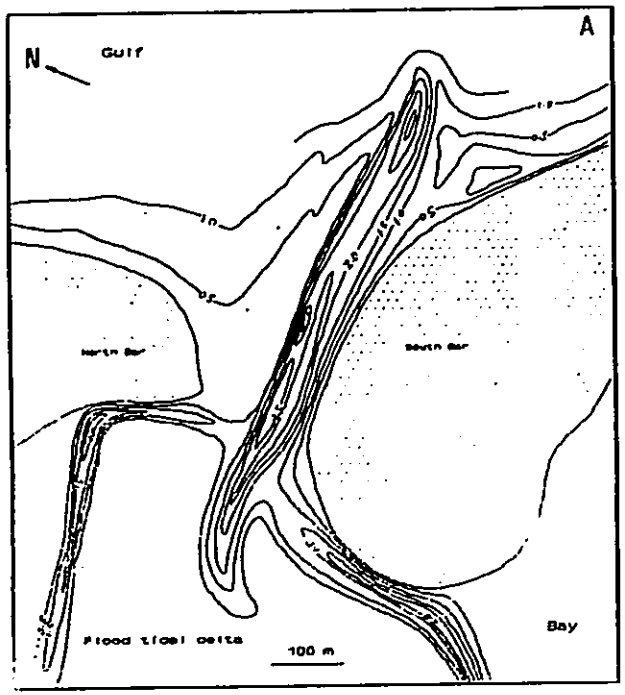
A
N
Gulf
North Bar
South Bar
Flood tidal delta
100 m
Bay

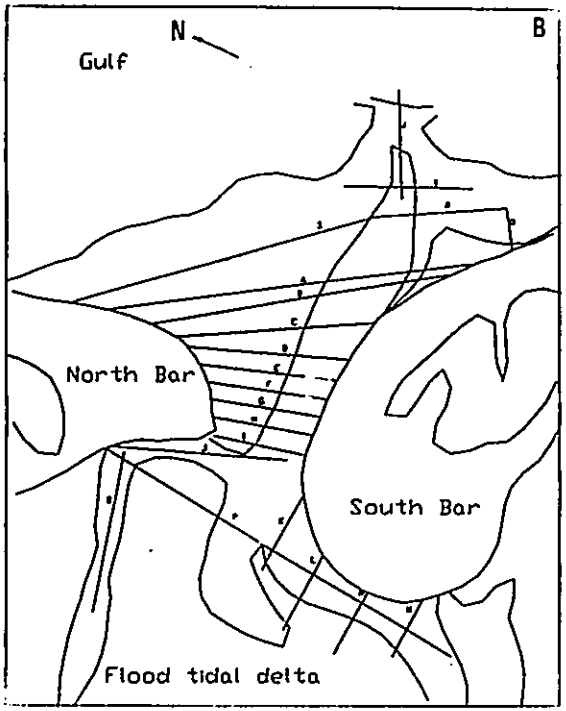
B
N
Gulf
North Bar
South Bar
Flood tidal delta

Figure 3-4 Cross-section profiles of the main channel, reproduced from 1987 echographs. For locations see Figure 3-3B. Solid and dashed lines of each profile are average spring tide high water and low water marks, respectively. The figure in each profile is the channel width at high water mark. Geometric characteristics are given in the inset table. The upper vertical scale is for Profile F-I, and the lower vertical scale is for Profile A-E. CMLB - north channel margin linear bar; SWB - south channel margin linear bar.

Geometric characteristics

Pf.	Width (HWL)	Area (HW)	D_{mean} (HW)	D_{max} (LW)
A	710	971	1.2	1.6
B	575	794	1.3	1.7
C	403	614	1.5	1.7
D	322	480	1.4	2.0
E	286	435	1.5	3.2
F	246	413	1.6	2.9
G	233	395	1.6	2.4
H	190	411	1.7	2.2
I	184	334	1.6	2.2

* Unit in m or m^2

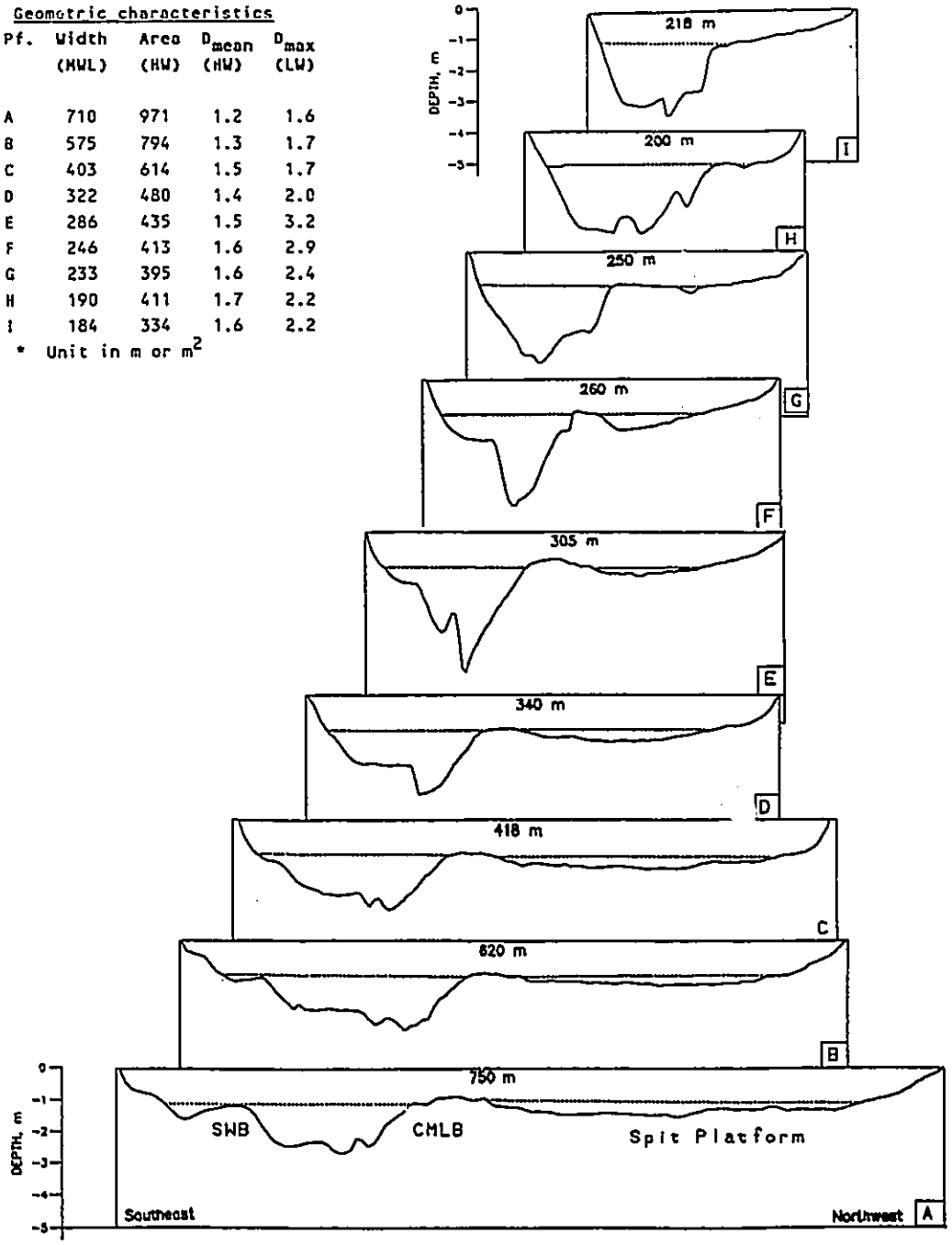

it is asymmetrical with a steeper bank on the north side. With a dominant northerly longshore drift, it would be expected that the northern bank is gentler (FitzGerald and Nummedal, 1983). This suggests that the asymmetry of the cross-section is controlled by the pattern of tidal current related to the curvature of the channel. As in fluvial channels, the main stream of the flow is located closer to the concave (northern) bank.

The main channel bifurcates on the landward side into a south channel and a north channel. The South Channel is superimposed on an ebb-spit on the north and a flood lobe on the south. It has maximum depths of 2.5 metres in its central portion, and shallows to less than one m to both ends. Its steeper bank is located against the south spit. Like the main channel, therefore, it is the curvature of the channel that controls the symmetry of the cross-section. While less sand-clogged, the North Channel lacks well-formed outlets at both ends. At the seaward end, it appears truncated by the north spit at a sharp angle (Figure 3-1B and Figure 3-2A). Although reaching more than 2.0 m at this end, it shallows quickly landward (Figure 1-1 and Figure 3-50), and diminishes within the flood delta. Echosounding and diver-observed mud scarps outcrops at the bottom on the seaward end, indicating that it was a former throat channel, abandoned after the inlet moved to a more southerly position (Figure 3-5).

Figure 3-5 Some cross-section profiles reproduced from 1987 and 1986 echographs. For locations see Figure 3-3B. For explanations see Figure 3-4.

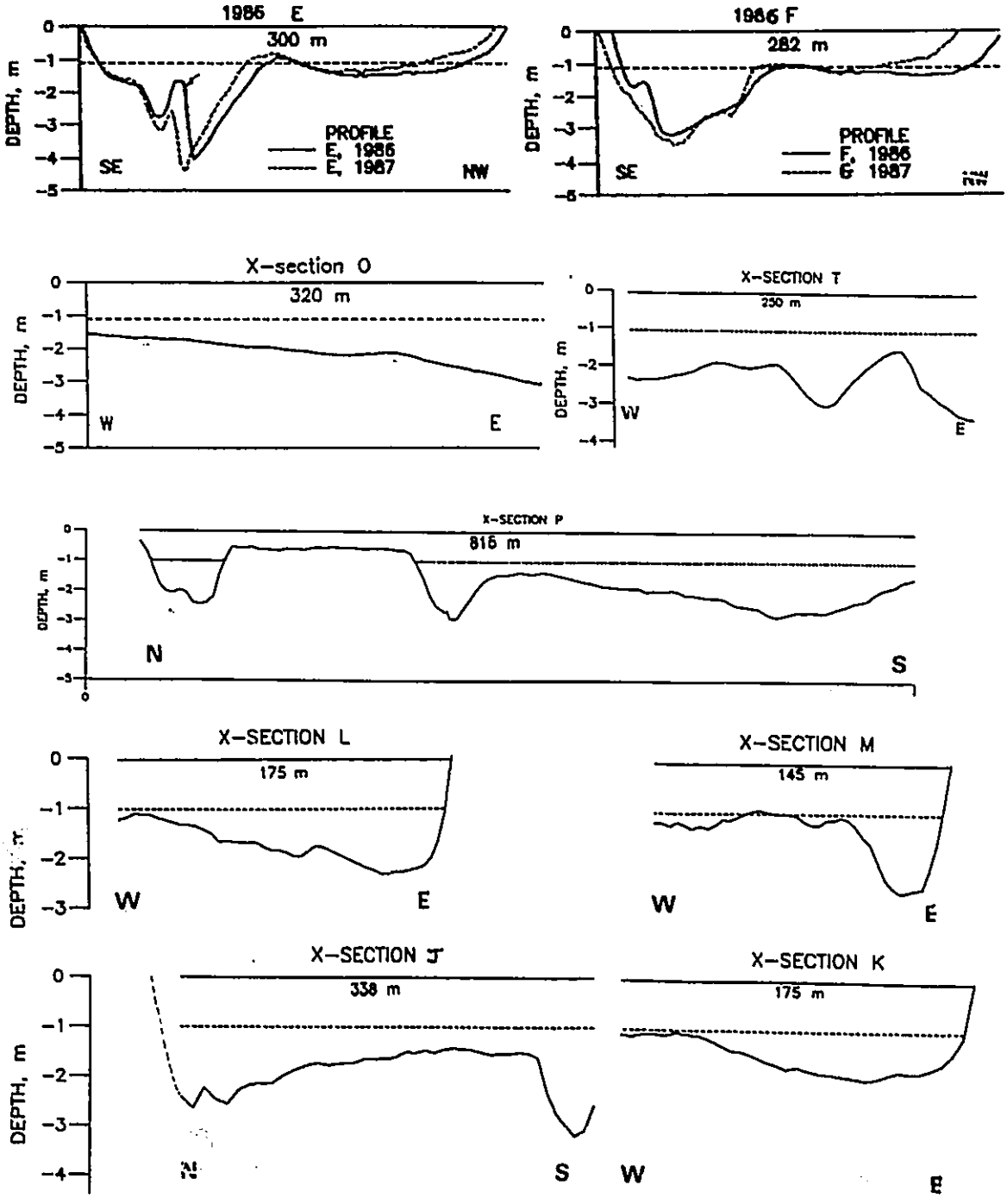
1986 E
300 m
DEPTH, m
SE
NW
PROFILE
E, 1986
E, 1987
1986 F
282 m
SE
PROFILE
F, 1986
G, 1987
X-section O
320 m
W
E
X-SECTION T
250 m
W
E
X-SECTION P
815 m
N
S
X-SECTION L
175 m
W
E
X-SECTION M
145 m
W
E
X-SECTION J
338 m
S
X-SECTION K
175 m
W
E

3.3 Morphologic Changes Since 1958

The earliest vertical air photo available to this study is that of 1958 (Figure 3-6). In 1958, a large subtidal spit platform existed on the south side of the inlet, and the main channel abutted the north spit, trending in northeast direction. The occurrence of a large platform on the south side of the inlet is an unexpected result of a southerly longshore drift. Early study (Armon, 1980) showed, however, that the area was once a subaerial spit on 1935 photo. While the triggering mechanism was not identified, it is apparent that such a change calls for erosion instead of deposition. Its appearance, therefore, does not point to a longshore drift opposite to that of the present one before 1958.

In 1958, the flood tidal delta was covered by a relatively well developed network of tidal creeks, each having a small sand lobe at its discharging end. Judging from the scale, the central creek (the direct extension of the main channel) was the dominant channel bayward of the inlet, but even it did not have a free bayward outlet. This configuration indicates that the flood delta was less elevated at that time. Both flood and ebb flow could overtop it relatively easily, and were less channelized than at present.

Inlet configuration has undergone systematic changes along with a general southward migration of the inlet since

Figure 3-6 Morphology of Palmer Inlet between 1958 and 1987, reproduced from air photos and field survey. Major changes include: the southward migration of the inlet; the shift of the larger spit platform from downdrift side to updrift side; the orientation of the main channel from NE to E; the stabilization of aeolian dune on the north spit; decrease in the number of ebb-oriented sand lobes (ES) and the retreat of flood-oriented sand lobes close to the throat on the flood tidal delta (FS); gradual silting-up of tidal creeks on the northern part and shift of discharge to the south part of the flood delta.

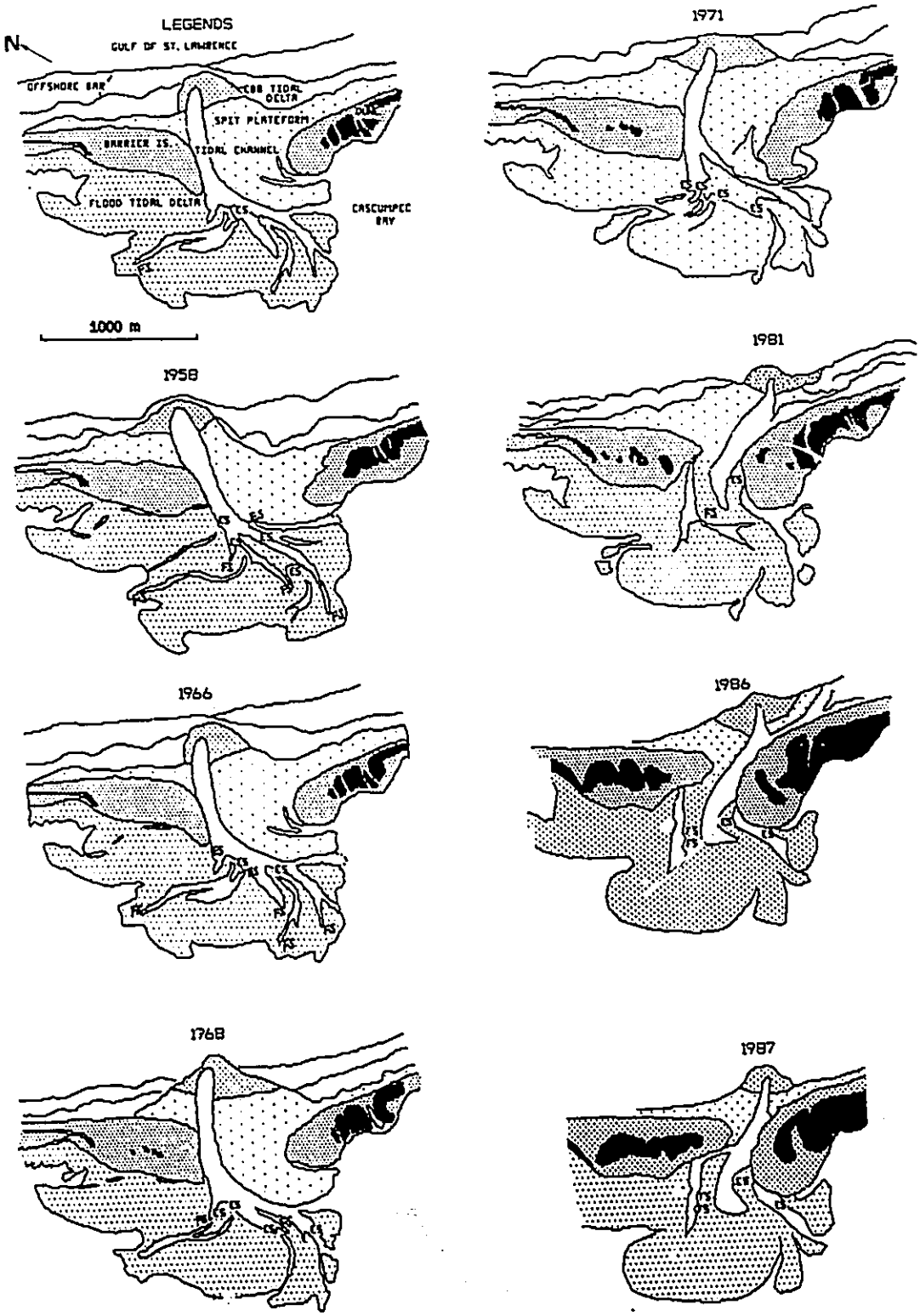
LEGENDS
N
GULF OF ST. LAWRENCE
OFFSHORE BAR
COB TIDAL DELTA
SPIT PLATFORM
DUNE
BARRIER IS.
TIDAL CHANNEL
FLOOD TIDAL DELTA
CASCUMPEC BAY
1000 m
1971
1958
1981
1966
1986
1968
1987

1958 (Figure 3-6 and Figure 3-7). In the following, these changes will be examined in terms of three basic units: the inlet channel, the spit and platform, and the flood tidal delta.

3.3.1 Changes in the Inlet Channel

The main channel experienced a general shift to the south after 1958. The movement was not uniform along its length and in time. Before 1968, the seaward section migrated in a southerly direction, while the throat section migrated in a northerly direction. After 1968, the throat section reversed its migration but still moved at a considerably lower speed than the seaward section; the motion, consequently, was a clockwise rotation. Because of the differential movement between the two ends, the main channel became increasingly bent (1968-1971). A point was finally reached in 1981 when the landward section broke off from the fast moving seaward section. By this time, the inlet had much its present configuration with the main channel trending approximate east-west against the south spit. The broken-off landward section became the present North Channel, and the South Channel assumed the role of the major conduit bayward of the inlet.

The southward migration of the seaward section is the expected result of the dominant southerly longshore drift. A number of factors, however, affect the motion of

Figure 3-7 Comparisons of changes of inlet configuration from 1958 to 1987.

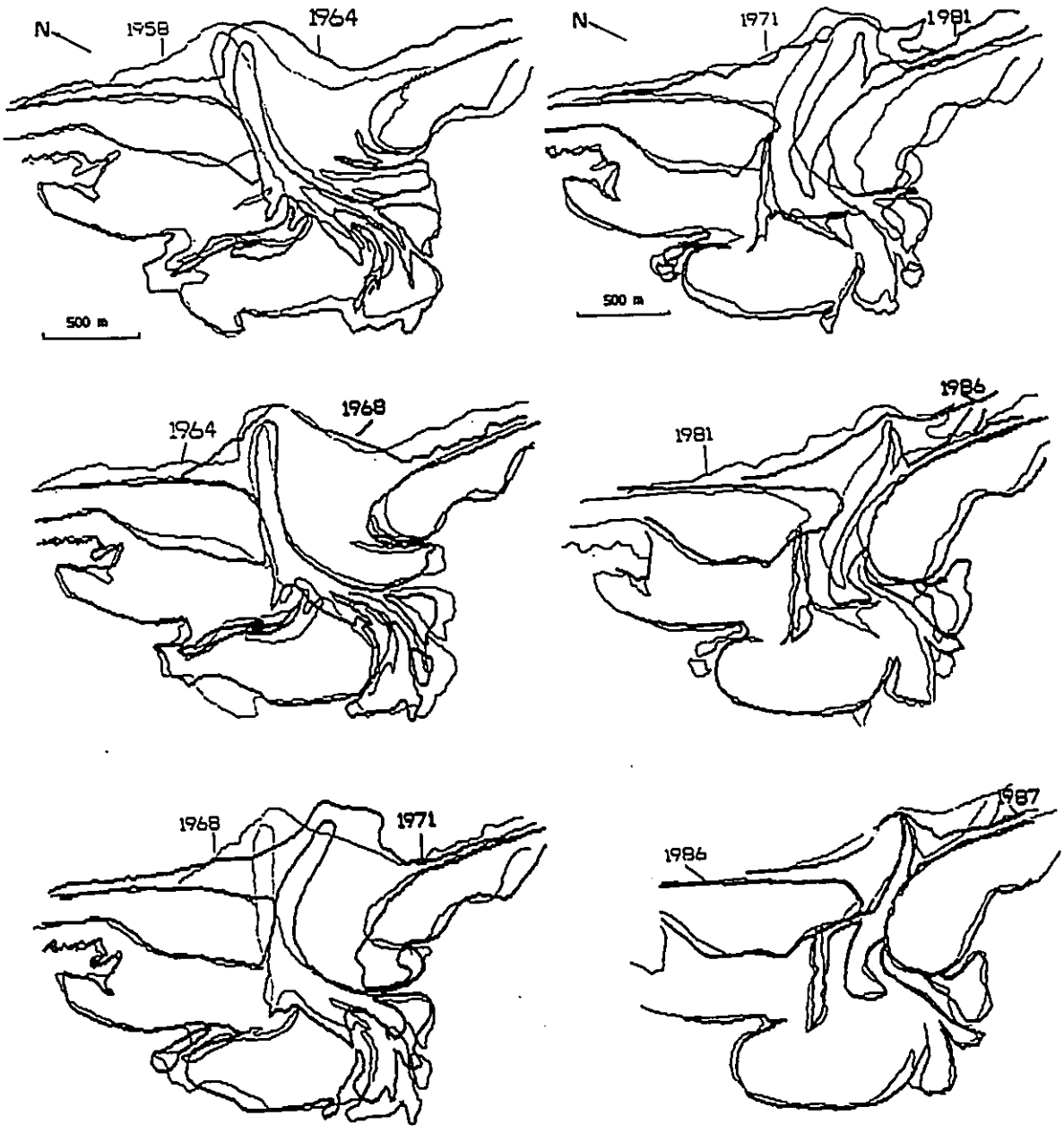
N
1958
1964
500 m
N
1971
1981
500 m
1964
1968
1981
1986
1968
1971
1986
1987

the throat section. The first is the curvature of the main channel. The inlet channel of Palmer Inlet curved to the south with the throat coinciding with the bend. The ebb flow concentrated on its north bank, forcing it to move updrift. This process is similar to the formation of meanders in fluvial channels, and has been used in a number of cases to explain the unusual, updrift migration of inlets (FitzGerald, 1984; Armon, 1980). The second factor is the location and shift with time of the large subtidal platform. This is because the platform serves as an opening for waves to drive sand into the inlet. Before 1971, the large platform was on the downdrift side. Sediments transported into the inlet were deposited on the southern bank of the throat channel. This deposition, in couple with the ebb current, which was strong, forced the channel to move against the dominant longshore drift. The trend was reversed after 1971 as more and more sand was transported into the inlet through the north side of the inlet with the gradual switch of the large platform to the updrift side. This is indicated by the relatively large rates of migration in the periods after 1971. An additional factor that may play a crucial role is related to the fact that the channel is now incised in the mud substrate. It may well be that this was the case as early as 1958. The cohesive mud, which provides more resistance to migration, would prevent the throat from moving as fast as the shallower seaward section.

A marginal channel appeared on the downdrift entrance side of the inlet on 1981 photo. Comparison with the previous photo shows that the location of this marginal channel coincided with that of the downdrift nearshore bar on the 1971 photo. The implication is that the marginal channel probably did not own its origin to tidal scouring. More likely, it was just the trough of a former nearshore bar. Tidal water followed this natural depression when the main channel was gradually switched to this position between 1971 and 1981. This explains why the marginal channel was quickly filled up in the following years by landward-moving sediments as the inlet became relatively stable at that location. Current measurements have showed that tidal flows were generally sluggish in this channel. It is possible that they have never been active over its history.

3.3.2 Spit and Spit Platform

With the downdrift migration of the inlet, the updrift side prograded onto the main channel at an averaged rate of 11 m/yr for the spit, and 15 m/yr for the platform. The north platform in front of the throat did not, however, begin to grow until after 1981 when the dominant platform has completed its course of shifting from the south side to the north side. Before that time, the progradation of the throat was primarily in the form of growth of the spit. On the downdrift side, while the platform was retreated

southward due to erosion, the spit underwent continuous expansion. This is especially evident in the period before 1981, when a major bayward growth took place (1968-1971). While this is unusual, it does lend support to two notions presented above: (1) the 1958-inlet configuration represents a non-equilibrium condition after an erosional event, and (2) the platform serves as a shallow, broad base for waves driving sediments into the inlet.

Subaerially, aeolian dunes began to appear on the north spit, and became stabilized over time. Aeolian dunes first occurred on the bayward side of the spit instead of along the shore line. This is presumably because the surface here was damper, and thus was better able to trap sand, and supporting the growth of plants.

3.3.3 Flood Tidal Delta

The flood delta remained stable in the lateral location, but underwent growth upward as a result of the rotational motion of inlet migration. The latter is indicated by the following changes over the time: (1) Decrease in the number of the small sand-lobe; (2) Retreat of the flood-oriented lobe to a more innerward position. Note that the flood-oriented lobes formed an outer circle, and those of ebb-oriented formed an inner circle before 1964; (3) Shift of the ebb-oriented lobe from on the delta (before 1981) to within the (south) channel (after 1981);

(4) Gradual closure and silting-up of tidal creeks on the northern part, and development of relatively free bayward outlets for the South Channel. These changes indicate an overall reduction in flow activity, and gradual diversion flow (especially the ebb) from central-north part to the southern part of the delta. Sediments carried in by the flood and deposited in front of the flood ramp became increasingly less influenced by the returning flow, which then clogged the inlet at the throat. By the end of 1986, the proximal part of the flood delta was almost completely filled, and became connected with the north spit platform.

3.4 Estimate of Longshore Drift and Inlet Stability

The purpose of a rate of migration calculation is to estimate volume changes over the time, from which the rate of longshore drift can be derived. The volume thus determined represents only the portion of sands intercepted by the inlet within the spit and the platform. Sand trapped in the flood tidal delta, or leaked to the offshore or downdrift cannot be determined. The figure thus derived represents the minimum value of the dominant longshore drift.

Table 3-1 shows that along with the southward migration, the inlet intercepted a total of about 900,000 m^3 sediments, which give a volume rate of longshore drift 31,000 m^3/yr. Similar calculations by Armon (1975) showed

rates of 45,000 m^3/yr for Hardy Channel (1935-1968) and 30,000-50,000 m^3/yr for Alberton Inlet (1765-1845). Considering the smaller size of Palmer Inlet, the figure can be considered in the right order of magnitude.

Using the measured tidal prism (3,125,000 m^3, Table 2, Part II), this longshore drift rate gives Bruun's stability index, P/M, a value of 99 for Palmer Inlet. Inlets with P/M values between 50 and 100 are described by Bruun (1978) as having fair-to-poor stability. The longshore drift, M, used in Bruun's calculation, however, is the annual total net value. Although there is no certain way of establishing this value from this study, some estimates can be derived from Armon's study (1975). Assuming cross-sectional stability for Alberton Inlet and a bar-bypassing mode of sands for Hardy Inlet, Armon arrived at 158,000 m^3/yr and 175,000 m^3/yr of net longshore drift for the two inlets, respectively. The average rate of net longshore drift along U.S. east coast is about 191,000 m^3/yr (250,000 yd^3/yr) to the south (Humphries, 1977). The lower values on Gulf of St. Lawrence coasts are expected, due to the generally low energy level of the Gulf. Palmer Inlet is located between Alberton and Hardy inlets. Taking the average of the above two figures yields a P/M of about 19. This puts Palmer Inlet in the range of poor stability (<50). This result is consistent with the present configuration of the inlet, and with the change of morphology over the past

three decade, which shows that the drainage system is deteriorating.

Another observation can be made from the above air photos is that during the period studied, major water lines did not show detectable shift in the seaward-landward direction. This suggests that the present sea level rise (Grant, 1970) is in equilibrium with the sediment supply at this location.

3.5 Discussion and Summary

Using the calculated average deep water height (0.5 m) and the measured mean tidal range (0.75 m), Palmer Inlet falls in the mixed-energy, wave-dominated region of Hayes's diagram (Figure 3-8). The overall morphology described above resembles the models proposed for this region by Hayes (1979; 1980) and Nummedal and Fischer (1978), characterized by: large flood tidal delta and small ebb tidal delta, bulbous spits, large updrift spit platform extending, shallow channels, and an open bay depleted of marsh and tidal creeks. Also like most microtidal inlets, Palmer inlet showed a general migration in the direction of the dominant longshore drift. The migration records an average rate of about 11-15 m/yr, or a minimum longshore drift of 31,000 m^3/yr to the south.

There are differences, however, between Palmer Inlet and other similar inlets. The downdrift migration of Palmer

Figure 3-8 Plot of wave height versus tidal range. The location of Palmer Inlet is marked by 'P'. General locations of tidal inlets in the southern Gulf of St. Lawrence are shown by the dash-line rectangle; data from McCann (1979). Data for other tidal inlets are from Hayes (1979); Boothroyd (1983), Mason (1981), Shipp (1984), etc.

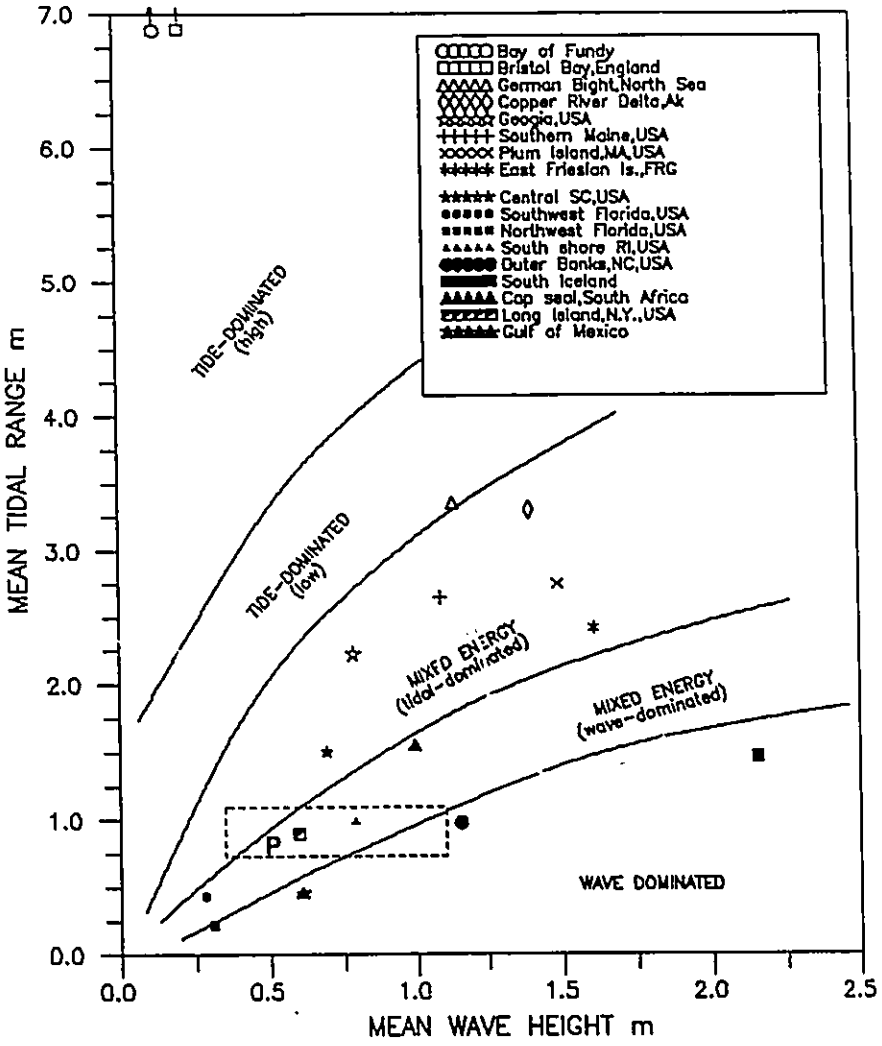
Bay of Fundy
Bristol Bay,England
German Bight,North Sea
Copper River Delta,Ak
Georgia,USA
Southern Maine,USA
Plum Island,MA,USA
East Friesian Is.,FRG
Central SC,USA
Southwest Florida,USA
Northwest Florida,USA
South shore RI,USA
Outer Banks,NC,USA
South Iceland
Cap seal,South Africa
Long Island,N.Y.,USA
Gulf of Mexico
TIDE-DOMINATED (high)
TIDE-DOMINATED (low)
MIXED ENERGY (tidal-dominated)
MIXED ENERGY (wave-dominated)
WAVE DOMINATED
P
MEAN TIDAL RANGE m
MEAN WAVE HEIGHT m
7.0
6.0
5.0
4.0
3.0
2.0
1.0
0.0
0.0
0.5
1.0
1.5
2.0
2.5

Inlet took place in the form of a clockwise rotation with the seaward section of the main channel moving faster than the throat section. This is due to two rather unusual factors at Palmer Inlet. One is the coincidence of the throat with the bend of the hook-shaped channel. The other is resistance provided by burial of the inlet throat in the mud substrate, probably as early as 1958. The rotational motion plays a major role in controlling the inlet development into its present configuration, and is also responsible for other morphological differences observed at Palmer Inlet. Major sand bodies of Palmer Inlet are connected, and cluster around the throat. Most microtidal inlets have sand bodies more displaced away from the throat area (Davis and Hayes, 1984; Boothroyd, 1985; Moslow and Heron, 1979 FitzGerald, et.al., 1984). The flood tidal delta of Palmer Inlet showed essentially no lateral shift over its history. Intercalation of deposits of tidal channels, overwash or lagoon, which was reported in many inlets (Reinson, 1984), is not expected to be common at Palmer Inlet. The flood tidal delta of Palmer Inlet is also particularly quiet, and depleted of ground-detectable morphological elements. This is because the increasing bend of the channel system with the rotational motion leads to an overall flow reduction, as well as separation of flood and ebb flow on the bayward side. Flood sediments deposited inside the inlet becomes consequently less and less affected

by the ebb flow, which results in vertical accretion, and progressively closing of the throat.

The platform provides not only a physical base, but also a source of material necessary for the growth of the spit. This is indicated by the unusual behaviour of the south spit, which underwent consistent expansion with deposition updrift and erosion downdrift of the platform. As the amount of sand driven through the opening provided by the platform is proportional to the size of the platform, it is expected that the growth of the spit and the platform is inversely related. Initially the platform grows on the updrift end of the barrier. The growth of the platform continues to a point that sediment through it is sufficient to start to build the spit on the top of it. When the spit grows, it reduces the area of the platform open to waves, and thus cuts its own sediments supply. This leads to the decline of spit growth, which will start another cycle of development of the platform. The development of the updrift spit-platform of Palmer Inlet between 1971 and 1986 illustrated part of the above process. These observations confirm the studies of Meistrell (1972) and Nielsen et al. (1988). They demonstrated that the spit only starts to form on the top of a prograded platform, and that when the spit's growth declines, the platform's growth begins, and vice versa.

Chapter 4

Depositional Environments

4.1 General Introduction and Terminology

Palmer Inlet has been divided into five depositional environments: (1) Inlet channels; (2) Channel margin linear bars; (3) Subaqueous spit platforms, (4) Subaerial spits; (5) Flood tidal delta. The relative position of these environments with respect to the mean water level and to the throat governs the relative strength of current velocities, waves, winds, as well as other factors at each location, and creates differences in sediment properties. In-site studies of tidal inlets with sufficient information on sediment characteristics are few. The lack of prototype data can be attributed, to a large extent, to the harsh working conditions, and the difficulties of retaining primary structures in the coring process. At Palmer Inlet, the small tidal range and shallow depth have made possible collection of both surface and subsurface sediment data using relatively simple apparatus. This, with the hydraulic data collected concurrently, allows more objective interpretation of sedimentary facies in term of sediment characteristics and hydraulics.

Following a brief description of observational techniques (Section 4.2), each environment will be described

in detail, as it was seen during the field seasons of 1986 and 1987 (Section 4.4 - 4.7). Readers who are not interested in the details may skip the descriptive material and proceed directly to the summary given in Section 4.8 on page 216. The description of each environment follows the following order: dominant processes, texture, bedforms and internal structures, and vertical sequence, in turn. The terminology of large-scale bedforms used is that of Dalrymple et al. (1978). Type I megaripples are those with straight to moderately sinuous crests and troughs without scour pits. Type II megaripples have strongly sinuous to discontinuous crests and deep troughs with scour pits. Stratification is used as a generic term referring to layered structures. Those formed by migration of ripples are referred to as cross-lamination, those by megaripples as cross-bedding, and those by wave-swash as swash-lamination or beach-lamination if formed on the foreshore. Cross beds formed at the front of a migrating bar rather than by flow separation, are termed bar-front foresets. Avalanching-foresets of swash bar origin are called swash-bar foresets. In the description of stratification, an arbitrary scale suitable to this particular inlet is used: <5 cm, small-scale; 5-10 cm, medium-scale; >10 cm, large-scale.

The flow is broadly described as high speed flow if the 1 m/s limit is exceeded, and as low speed flow below. Bed states, on the other hand, are described using a series

of critical values, including the initiation of sand movement, transition from ripple to megaripples, and transition from megaripple to upper plane bed. For a mean size of 0.25 mm, the critical value of U_* for these parameters from Shields (1935), Vanoni (1974), and Liu (1957) in Raudkivi (1976), are 0.014 m/s, 0.045 m/s, and 0.048 m/s, respectively. The corresponding critical velocity at 1 m off the bed, U_{1cr}, converted by assuming a logarithmic profile and mean roughness lengths of 0.0004 m, 0.006 m, and 0.0004 m for three bed states, are 0.27 m/s, 0.57 m/s, and 0.94 m/s, respectively. This result allows the bed state to be judged under the present current data format: in these shallow water depths, velocities of greater than 1 m/s generally correspond to upper flow regime (upper plane bed).

4.2 Collection of Sediment Information

Information about bedforms was obtained through echosounding and diving in subtidal areas, and through tape/Brunton measurement on intertidal flats. For large bedforms, the wave length is the average of the distance between the crests of two bedforms. The height is the average of vertical distances between the trough and the crest involved. For small ripples, six forms are used instead of two. Results of bedform measurements are listed in Appendix C.

Internal structures were studied using spade-type box corers. The corer is 0.3 m in width, and 0.34 m long: it therefore recovers only the top three decimeters of sediment. Because cores were taken at low water, stratification of the uppermost layer (commonly a few centimetres thick) is generally in the ebb direction. Interpretation of internal structures should, however, rely on the deeper layers buried below this surface layer.

Cores up to 2 m long were obtained with 2 or 3 inch-diameter polyvinyl chloride (PVC) tubes. Tube cores were pounded as deep as possible, and were retrieved by use of a specially-made clamp, often with the help of a car jack. Each core was oriented, and referenced to the water level at the time it was made, so that stratigraphic measurements could be carried out later. Cores were split, described, and the working halves were photographed. Resin-peels were made of all spade- and tube-cores to enhance the structures. Locations of cores are given in Figure 4-1.

Grain size samples (Appendix B-1), collected using a funnel-shaped sampler on board or by diving, were subsampled to about 50 grams in the field. In the lab, each samples were treated with hydrogen peroxide and washed through 2 mm and 0.03 mm sieves to separate gravels, muds and sands. Weight percent of sand fractions was obtained by means of an automatically recording settling tube system using about 1 gram of samples. The data were recorded at 0.2 ϕ intervals,

Figure 4-1 (A) Location map for tube-cores. Resin peels of tube-cores 1 to 8 are shown in Figure 4-22, A to H in Figure 4-23, and a to h in Figure 4-24. No resin peels were made of tube-cores B and C. Locations of echosounding profiles are shown as solid lines.

(B) Locations map for spade-cores. Resin peels of spade-core 1 to 3 correspond, respectively, to A to C in Figure 4-20; 4 to 7 to A to D in Figure 4-35; 12 to 15 to A to D in Figure 4-41; 16 to 19 to A to D in Figure 4-46; 20 to 23 to A to D in Figure 4-48, and 24 to 27 to A to D in Figure 4-52. Note spade-core 16 and 19 are given in (A), and 8 to 11 are given in Figure 4-36.

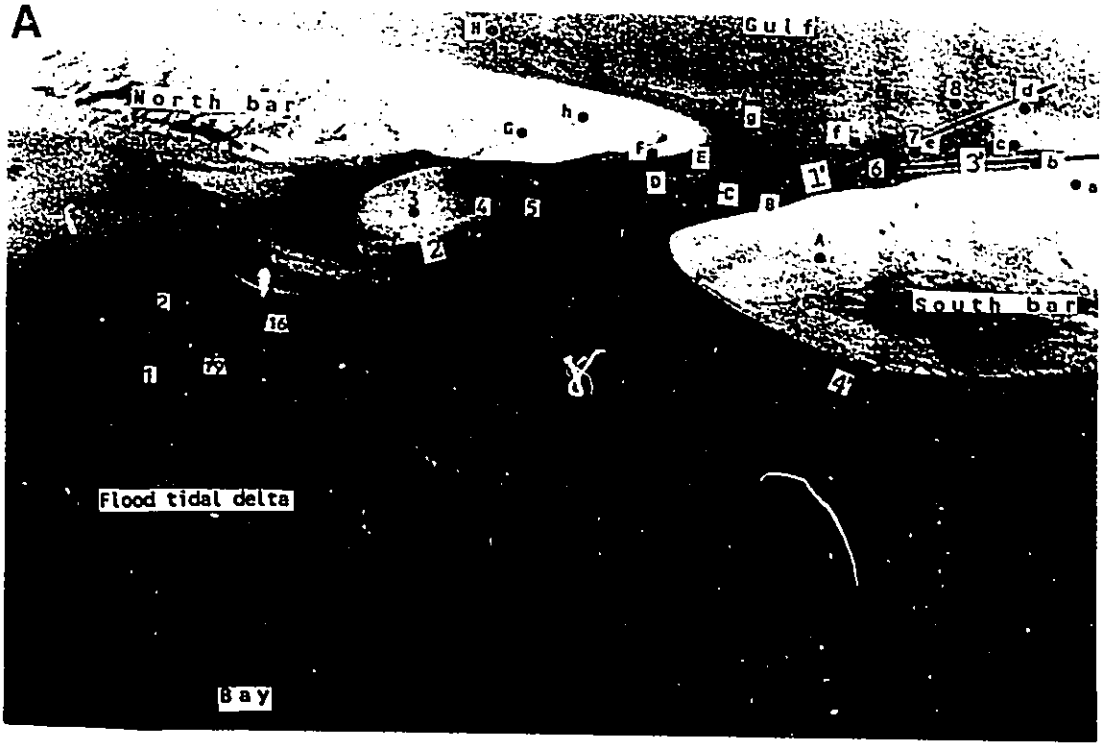
A
Gulf
North bar
South bar
Flood tidal delta
Bay

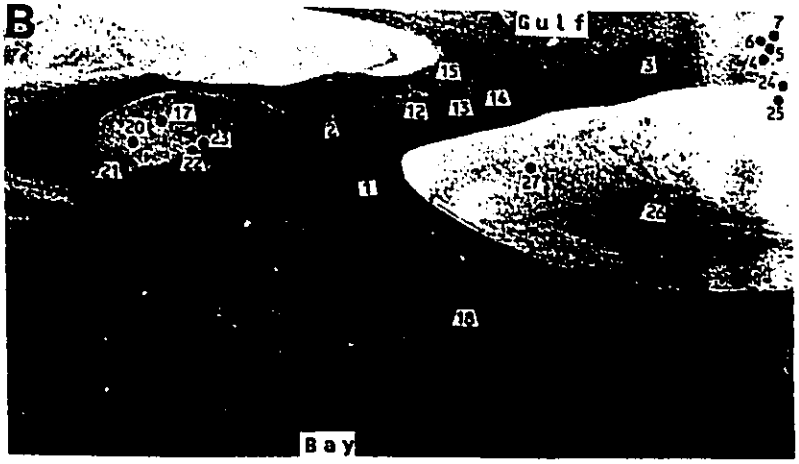
B
Gulf
Bay

and the textural statistics calculated by the moment method. Grains with diameters < 0.03 mm are usually less than 0.1-0.2% of total sediments. Their elimination would not significantly influence the statistics, but significantly reduced working time. Locations of grain size samples are given in Figure 4-2.

4.3 Inlet Channels

Physical Processes Inlet channels extend to the lowest topographic levels of any environments studied and were dominated by tidal currents. The effect of waves is restricted to assisting tidal current in stirring up bottom sediments. Flows in channels were monitored at 12 stations for full tidal cycles during large, mean, and small tidal conditions (for locations see Figure 2-17). This allows the time variation of flows in different parts of channels to be discussed in detail. In the present study, the flood ramp is treated as the landward extension of the main channel.

Main Channel (Including Seaward Marginal Channel) Tidal currents were measured at seven stations in the main channel between the flood ramp and the ebb terminal lobe. Station 55-I and 55-III (Figure 4-3, Figure 4-4 and Figure 2-13 in Chapter 2) were located in the gorge section between Cross Section I and Section D in Figure 3-4. High speed flows occurred during major large tides with both flood and ebb currents reaching 1.15 m/s. Currents were in the megaripple

Figure 4-2 Location map of grain size samples. The prefix, GZ, for each number has been omitted for brevity. The longitudinal profile used in Figure 4-55 is also shown in the figure.

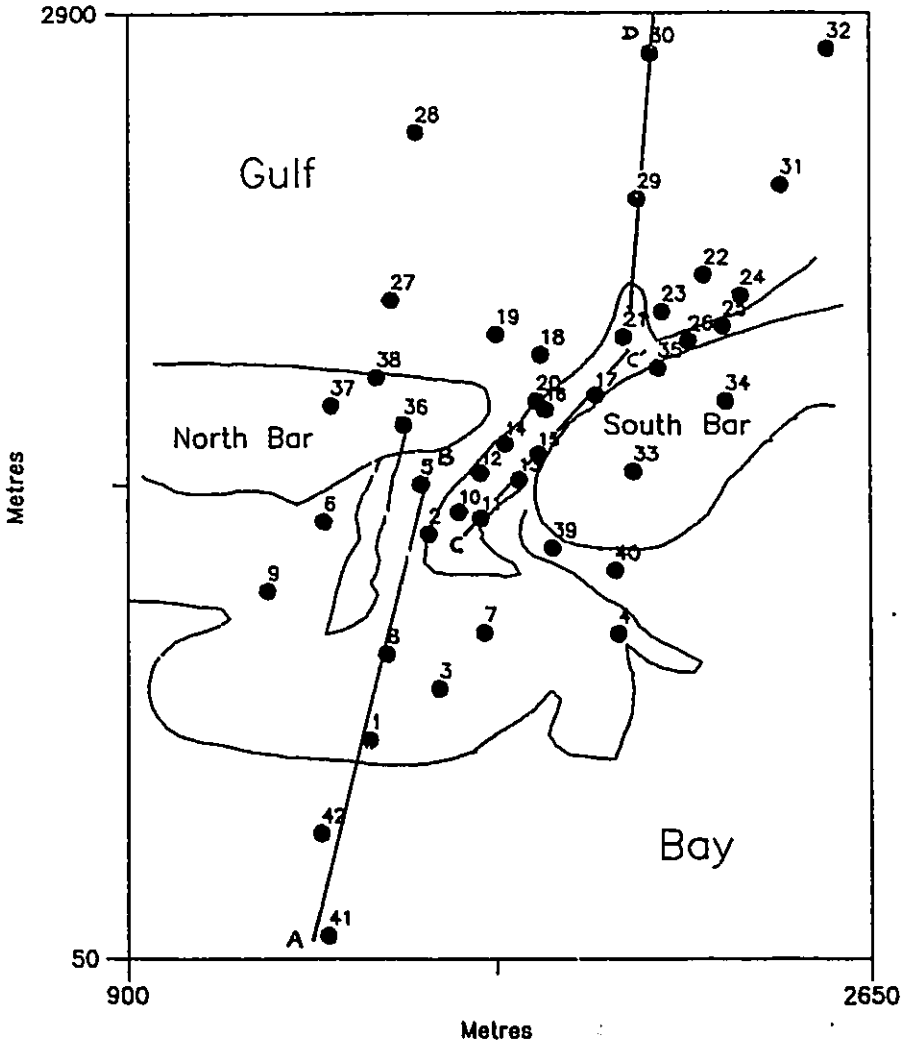
2900
50
900
2650
Metres
Metres
Gulf
North Bar
South Bar
Bay
A
B
C
C'
D

Figure 4-3 Time series of current velocities, bay tides, and tidal difference between bay and gulf tides, Station 55-I, throat section, main channel. For location see Figure 2-17. Also shown are calculated sediment transport rate, and strength index and velocity asymmetry curves.

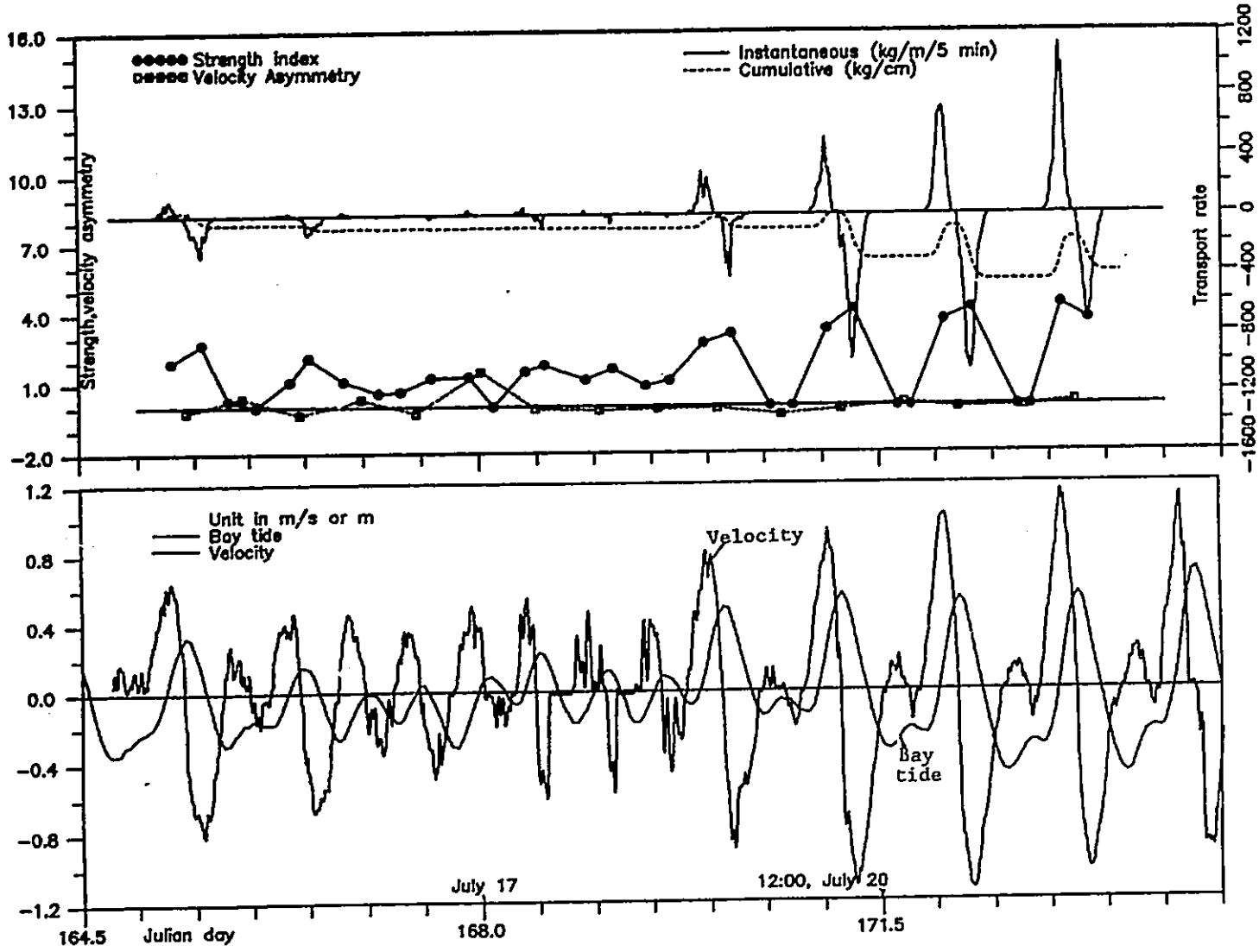
Strength index
Velocity Asymmetry
Instantaneous (kg/m/5 min)
Cumulative (kg/cm)
Strength,velocity asymmetry
Transport rate
16.0
13.0
10.0
7.0
4.0
1.0
-2.0
1200
800
400
0
-400
-800
-1200
-1600
Unit in m/s or m
Bay tide
Velocity
Velocity
Bay tide
1.2
0.8
0.4
0.0
-0.4
-0.8
-1.2
July 17
12:00, July 20
164.5
Julian day
168.0
171.5

Figure 4-4 Time series of current velocities, bay tides, and tidal difference between bay and gulf tides, Station 55-III, throat section, main channel. For location see Figure 2-17. Also shown are calculated sediment transport rate, and strength index and velocity asymmetry curves.

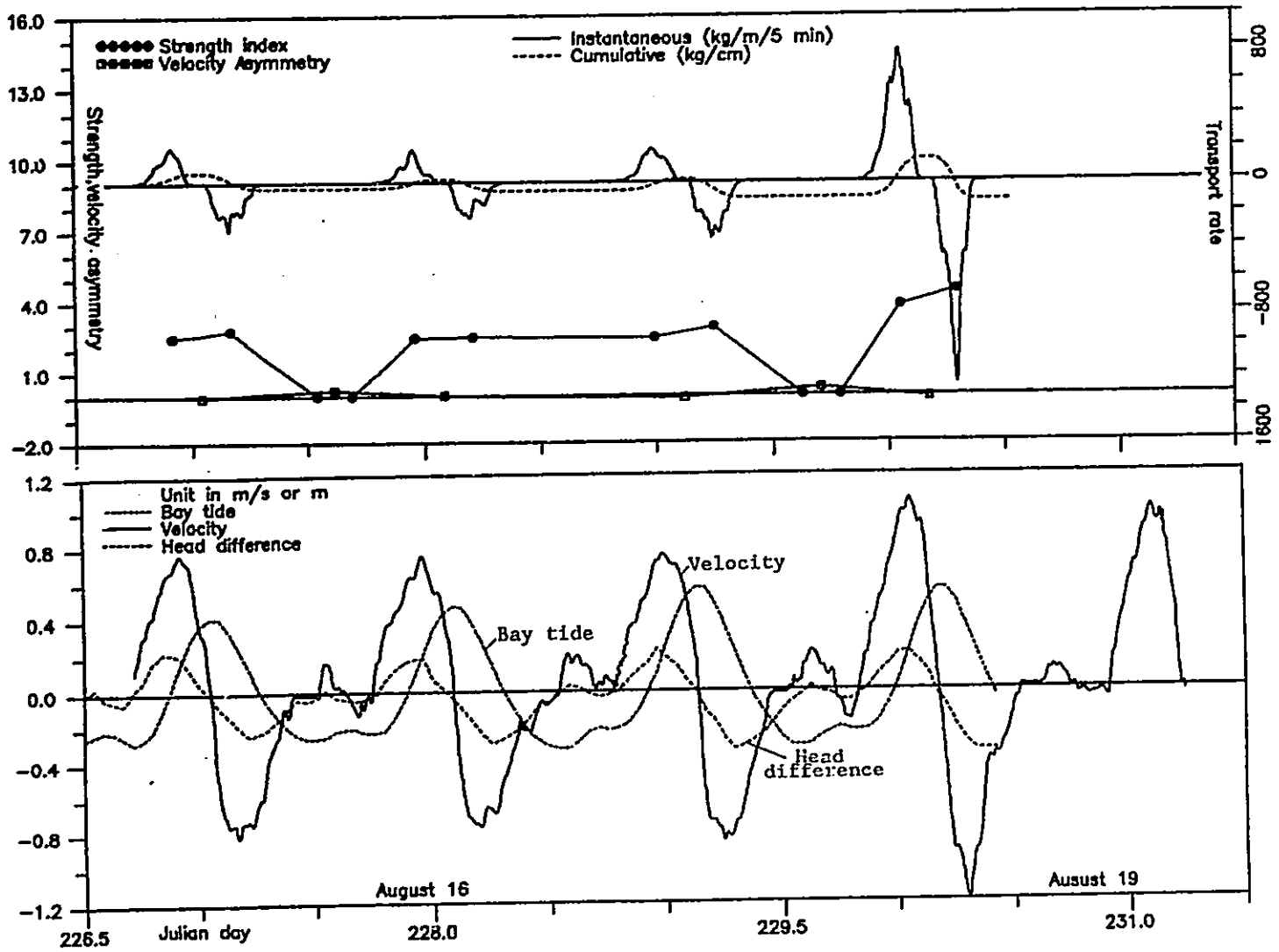
Strength index
Velocity Asymmetry
Instantaneous (kg/m/5 min)
Cumulative (kg/cm)
Strength,velocity asymmetry
Transport rate
16.0
13.0
10.0
7.0
4.0
1.0
-2.0
800
0
-800
1600
Unit in m/s or m
Bay tide
Velocity
Head difference
Velocity
Bay tide
Head difference
August 16
Ausust 19
1.2
0.8
0.4
0.0
-0.4
-0.8
-1.2
226.5
Julian day
228.0
229.5
231.0

range for large to intermediate tides, and dropped to the ripple range for small tides. Although sediment accumulated over the entire period indicated a small amount of net transport in ebb direction, currents were quite symmetrical between the flood and ebb. In fact, velocity dominance of individual cycles, as is indicated by the velocity index curve, was not consistent for both small tides and large tide. The fact that flow dominance varies with the tide range indicates that the direction of net transport could be different depending on the particular time selected. Away from the throat toward both directions, currents drop to the lower flow-regime, and becomes increasingly asymmetrical. Just inside the inlet (Station 55-X, Figure 4-5), the flood was dominant in both individual cycles and cumulative values. The flood speed reached 0.8-1.0 m/s, and ebb 0.6-0.8 m/s. Velocity profiles, measured over three intermediate tides at this location, showed shear velocities following the same pattern as the time-velocity curve, and indicating the dominance of the flood (Figure 4-5B). The maximum shear velocity was about 0.08 m/s for flood and 0.07 m/s for ebb. Shear velocities calculated using three data points, however, suffered from larger error (56%) even at low significance level. The error for estimated roughness length was even larger (151%). For this reason, estimates of the current velocity are preferred over those of the shear velocity. This trend continued further landward with

Figure 4-5A Time series of current velocities, bay tides, and tidal difference between bay and gulf tides, Station 55-X, throat section, main channel. For location see Figure 2-17. Also shown are calculated sediment transport rate, and strength index and velocity asymmetry curves.

Figure 4-5B Time series of shear velocity, roughness length, and Chezy friction factor, calculated from current velocity profiles, Station 55-X, main channel. See next page.

Figure 4-5(A)

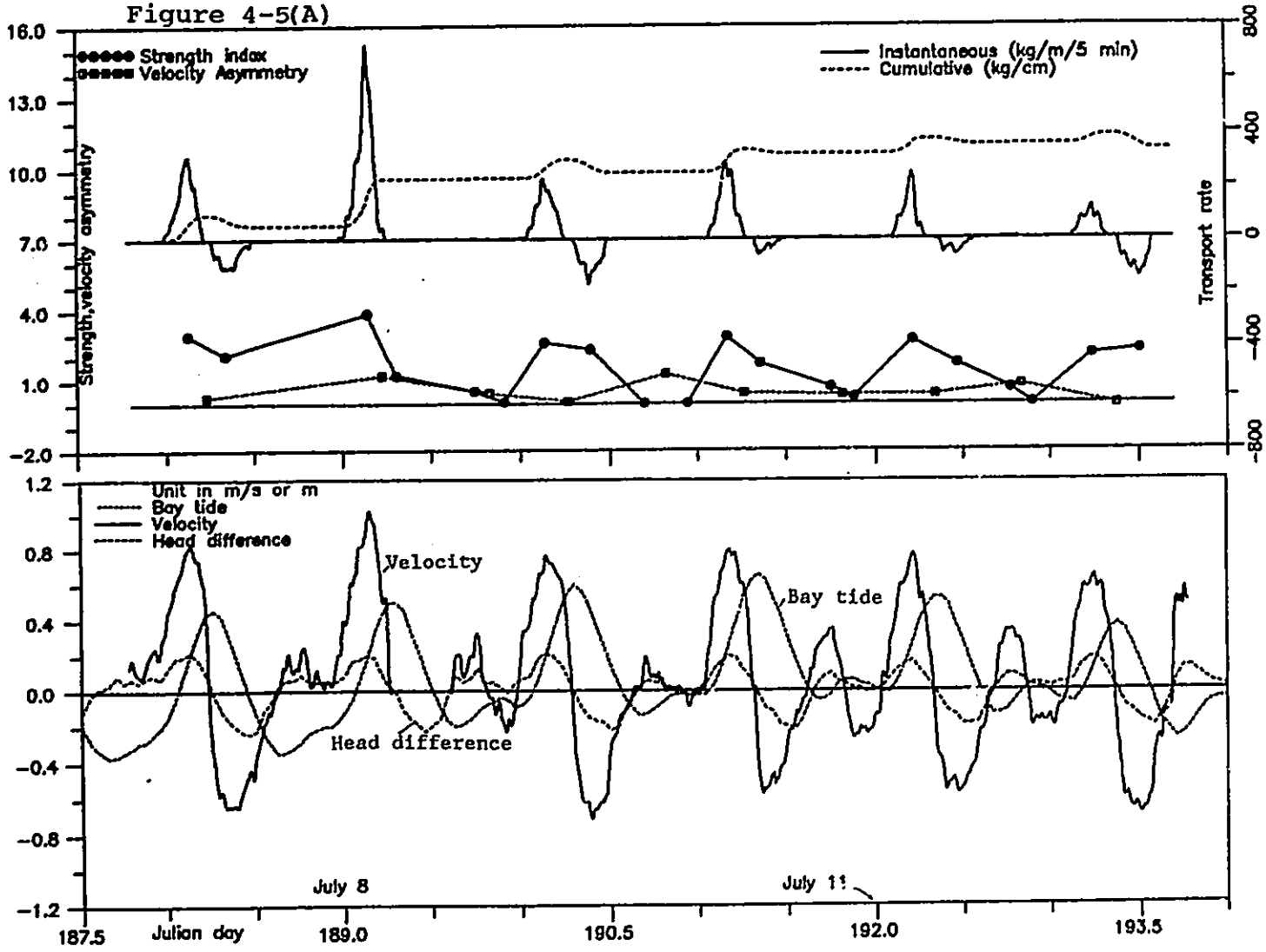
Strength index
Velocity Asymmetry
Instantaneous (kg/m/5 min)
Cumulative (kg/cm)
Strength,velocity asymmetry
Transport rate
16.0
13.0
10.0
7.0
4.0
1.0
-2.0
800
400
0
-400
-800
Unit in m/s or m
Bay tide
Velocity
Head difference
Velocity
Bay tide
Head difference
July 8
July 11
1.2
0.8
0.4
0.0
-0.4
-0.8
-1.2
187.5
Julian day
189.0
190.5
192.0
193.5

Figure 4-5(B)

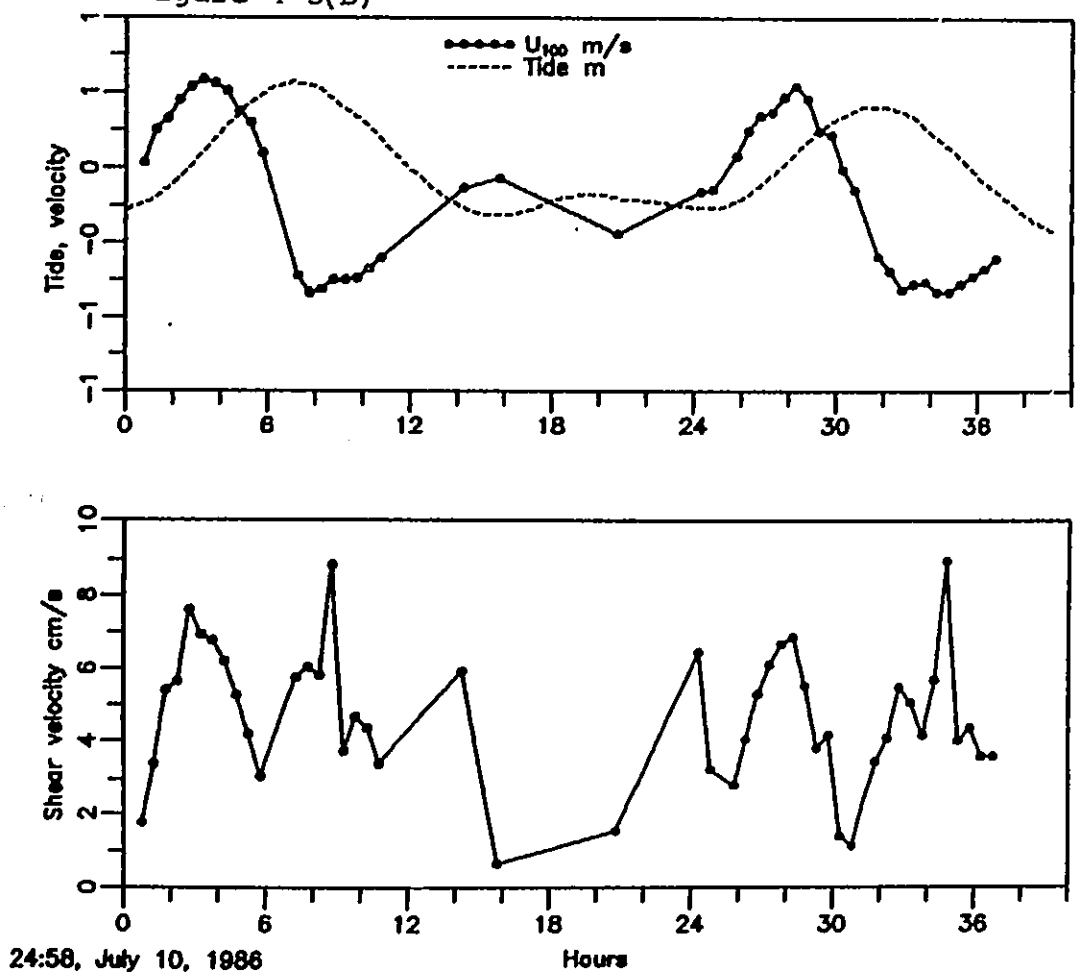
U_{100} m/s
Tide m
Tide, velocity
1
0
-0
-1
-1
0
6
12
18
24
30
36
Shear velocity cm/s
10
8
6
4
2
0
0
6
12
18
24
30
36
24:58, July 10, 1986
Hours

increasing flood dominance. In the middle of the flood ramp, Station 71-XII (Figure 4-6) gave maximum flood speeds of about 0.27 m/s for small tides, and about 0.35 m/s for mean tides. The corresponding ebb value was about 0.12-0.13 m/s. Extrapolations from these values showed that currents in large tides should be able to produce large bedforms.

An opposite trend was observed in the other direction from the throat stations. At Station 55-II (Figure 4-7), about 300 m seaward of the throat, currents of both directions were in the range of megaripples but with apparent ebb dominance, as is showed by both velocity-asymmetry curve and net sediment transport. For large tides, the ebb speeds reached 0.8-1.0 m/s, while the flood speeds were around 0.65-0.75 m/s. Despite the longer duration of the flood, the resultant net sediment transport was in the ebb direction. The trend continued seaward with the further expansion of the flow. At Station 71-III (Figure 4-8), about 200 m seaward of Station 55-II, time velocity curve was characterized by alternations of stronger and longer ebb with weaker and shorter flood current. For the particular tides measured, the maximum flood was about 0.2 m/s and the maximum ebb was 0.4 m/s. Estimation of currents for large tides showed that megaripples should be active during ebb but dormant during flood. Ebb dominance was particularly evident in sediment transport and velocity index curves.

Figure 4-6 Time series of current velocities, bay tides, and tidal difference between bay and gulf tides, Station 71-XII, flood ramp. For location see Figure 2-17. Also shown are calculated sediment transport rate, and strength index and velocity asymmetry curves.

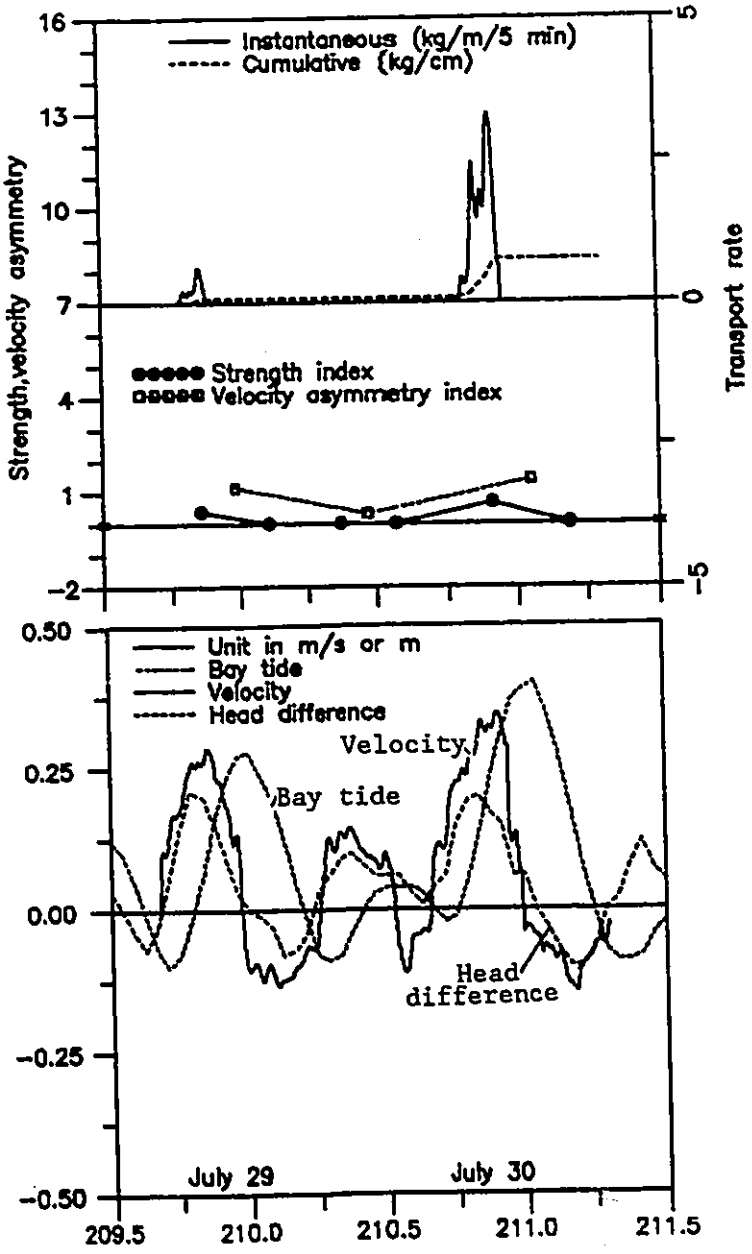
Instantaneous (kg/m/5 min)
Cumulative (kg/cm)
Strength index
Velocity asymmetry index
Strength, velocity asymmetry
Transport rate
16
13
10
7
4
1
-2
5
0
-5
Unit in m/s or m
Bay tide
Velocity
Head difference
Velocity
Bay tide
Head difference
0.50
0.25
0.00
-0.25
-0.50
July 29
July 30
209.5
210.0
210.5
211.0
211.5

Figure 4-7 Time series of current velocities, bay tides, and tidal difference between bay and gulf tides, Station 55-II, main channel. For location see Figure 2-17. Also shown are calculated sediment transport rate, and strength index and velocity asymmetry curves. See text for their definitions.

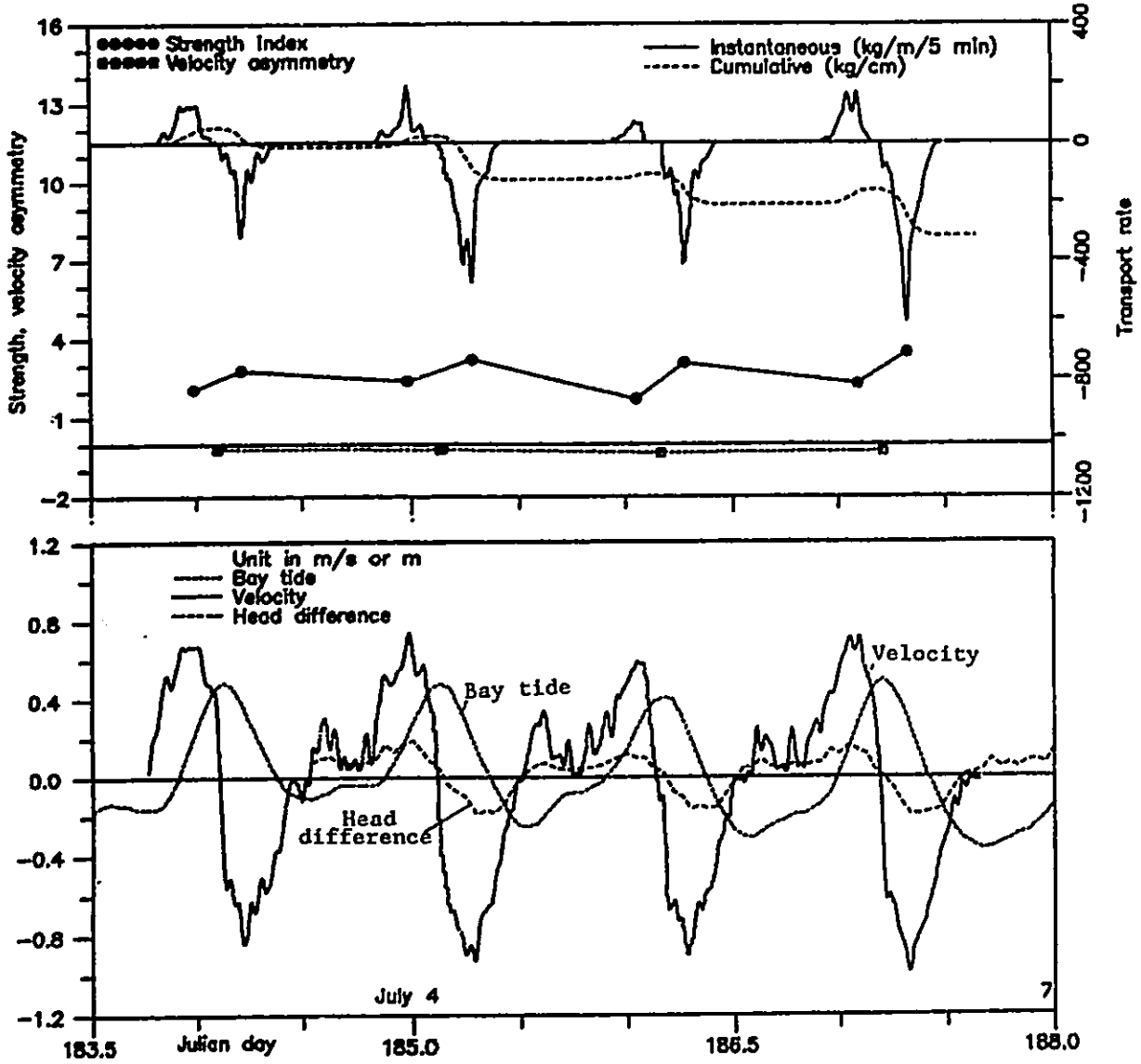
Strength Index
Velocity asymmetry
Instantaneous (kg/m/5 min)
Cumulative (kg/cm)
Strength, velocity asymmetry
Transport rate
16
13
10
7
4
1
-2
400
0
-400
-800
-1200
Unit in m/s or m
Bay tide
Velocity
Head difference
1.2
0.8
0.4
0.0
-0.4
-0.8
-1.2
Velocity
Bay tide
Head difference
July 4
7
183.5
Julian day
185.0
186.5
188.0

Figure 4-8 Time series of current velocities, bay tides, and tidal difference between bay and gulf tides, Station 71-III, main channel. For location see Figure 2-17. Also shown are calculated sediment transport rate, and strength index and velocity asymmetry curves. See text for their definitions.

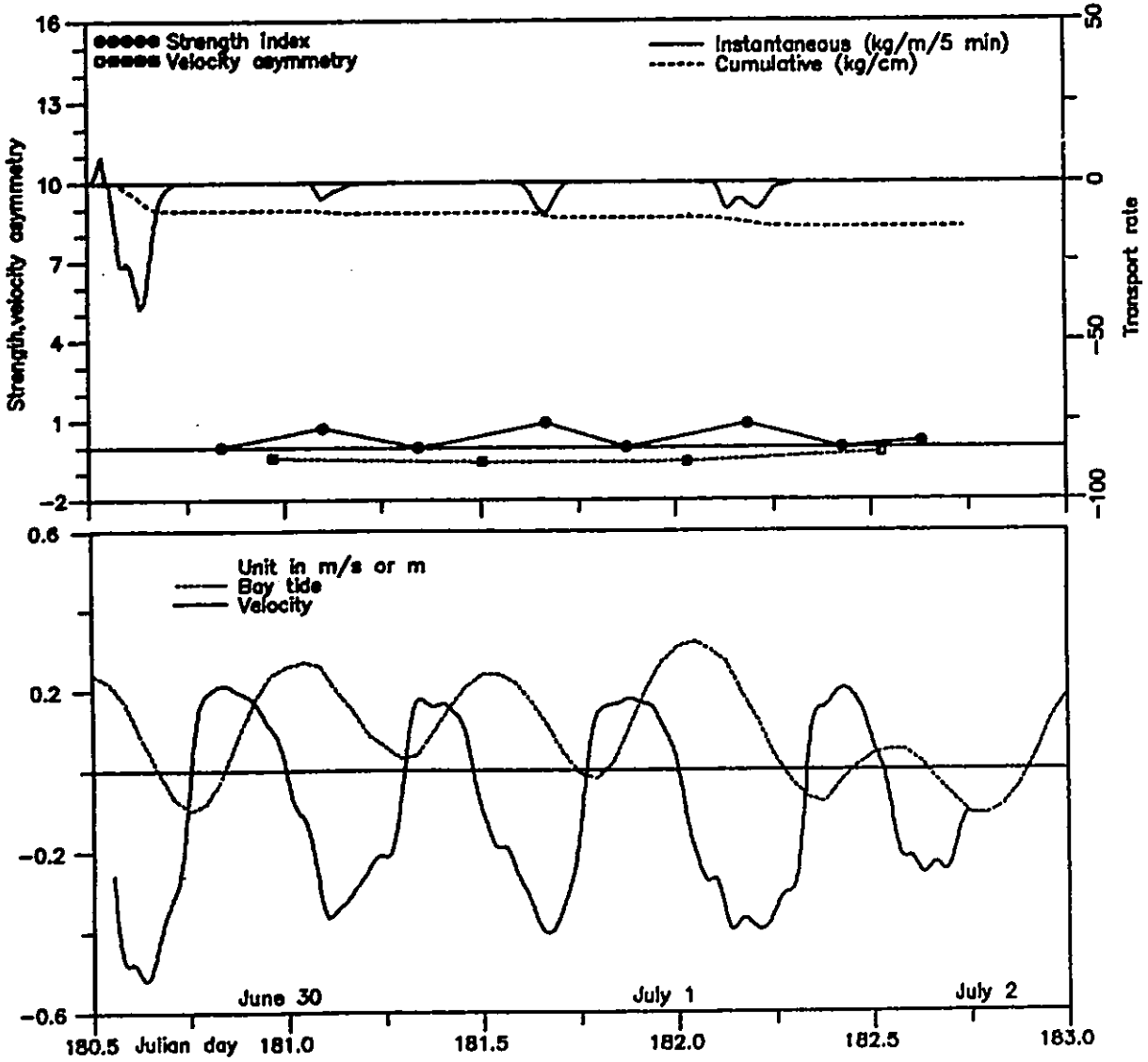
Strength index
Velocity asymmetry
Instantaneous (kg/m/5 min)
Cumulative (kg/cm)
Strength,velocity asymmetry
Transport rate
16
13
10
7
4
1
-2
50
0
-50
-100
Unit in m/s or m
Bay tide
Velocity
0.6
0.2
-0.2
-0.6
June 30
July 1
July 2
180.5
Julian day
181.0
181.5
182.0
182.5
183.0

South Channel The South Channel was the main drainage conduit landward of the inlet. Currents in the South Channel are generally below those defined as high speed flow, and in the megaripple range for large tides. Measurements at three stations showed opposite dominance between the northern and the southern part. Station 55-XIII (Figure 4-9) showed that over the northern part, ebb flow dominated. Peak ebb speeds reached about (.8 m/s, and flood speeds 0.6 m/s for mean to large tides. The net sediment transport is thus directed toward the crest of the ebb spit (Figure 4-9). Sediment carried over the crest, however, will be washed away by currents in the main channel. The ebb dominance in this northern part of the channel occurred because the flood was shielded by the crest of the south-facing ebb spit. Over the slope of the ebb spit, the flow was very turbulent. This was indicated by surface 'boils' especially at late ebb at this location. High turbulence was produced as ebb flows shoaling up the slope with increased bottom shear stresses toward the crest of the spit similar to the process observed over the stossface of large-scale bedforms (Middleton and Southard, 1984, p.7-21).

Station 64-VI (Figure 4-10) was located at the other end of the channel. Measurements here showed that over the southern part, flood flows dominated. For the intermediate tides measured, flood speeds reached 0.6 m/s, and ebb speeds 0.5 m/s. The net sediment transport is thus directed to the

Figure 4-9 Time series of current velocities, bay tides, and tidal difference between bay and gulf tides, Station 55-XIII, northern part of the south channel. For location see Figure 2-17. Also shown are calculated sediment transport rate, and strength index and velocity asymmetry curves. See text for their definitions.

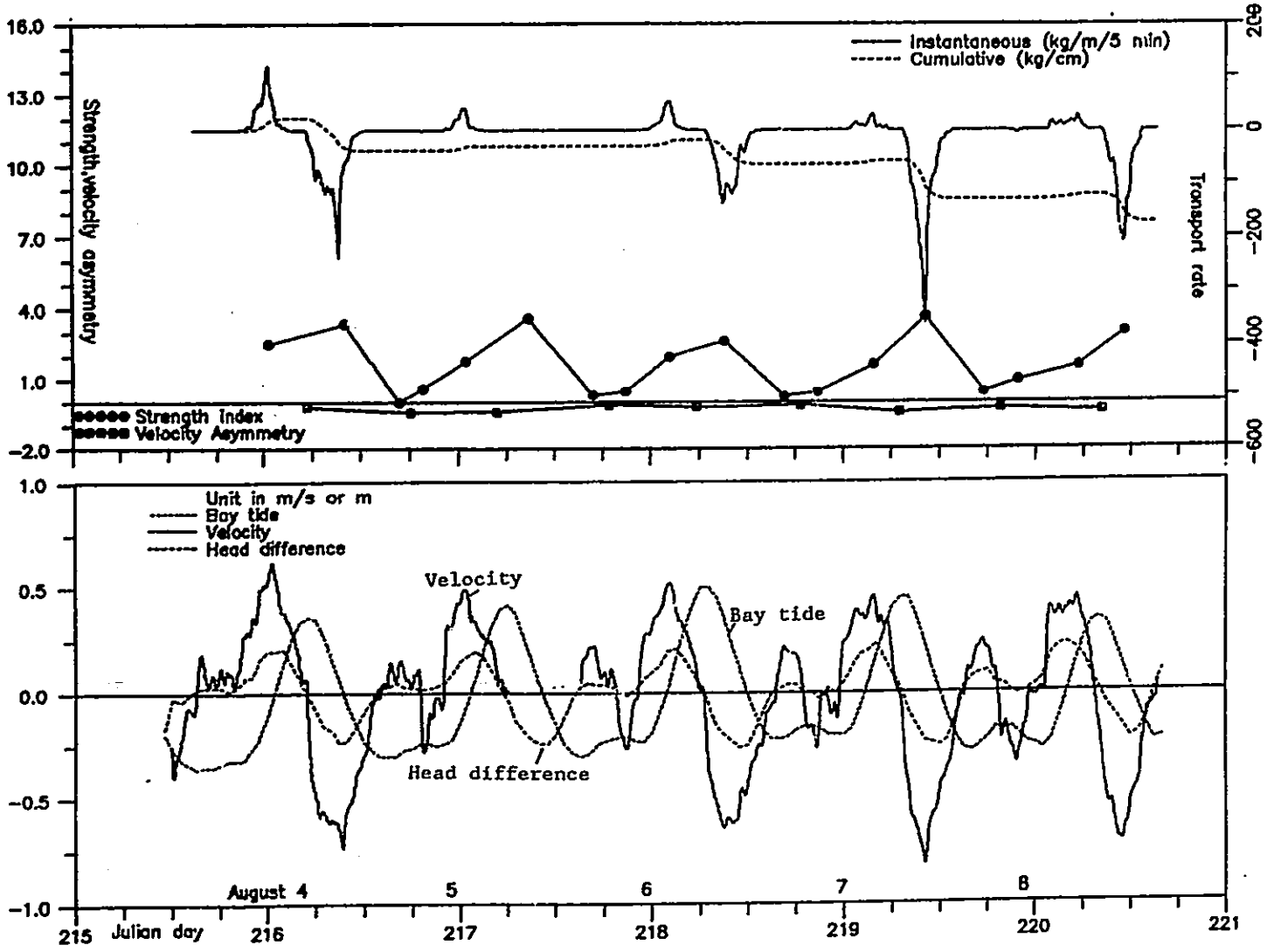
Instantaneous (kg/m/5 min)
Cumulative (kg/cm)
Strength,velocity asymmetry
Transport rate
Strength Index
Velocity Asymmetry
Unit in m/s or m
Bay tide
Velocity
Head difference
Velocity
Bay tide
Head difference
August 4
5
6
7
8
Julian day
215
216
217
218
219
220
221

Figure 4-10 Time series of current velocities, bay tides, and tidal difference between bay and gulf tides, Station 64-VI, southern part of the south channel. For location see Figure 2-17. Also shown are calculated sediment transport rate, and strength index and velocity asymmetry curves. See text for their definitions.

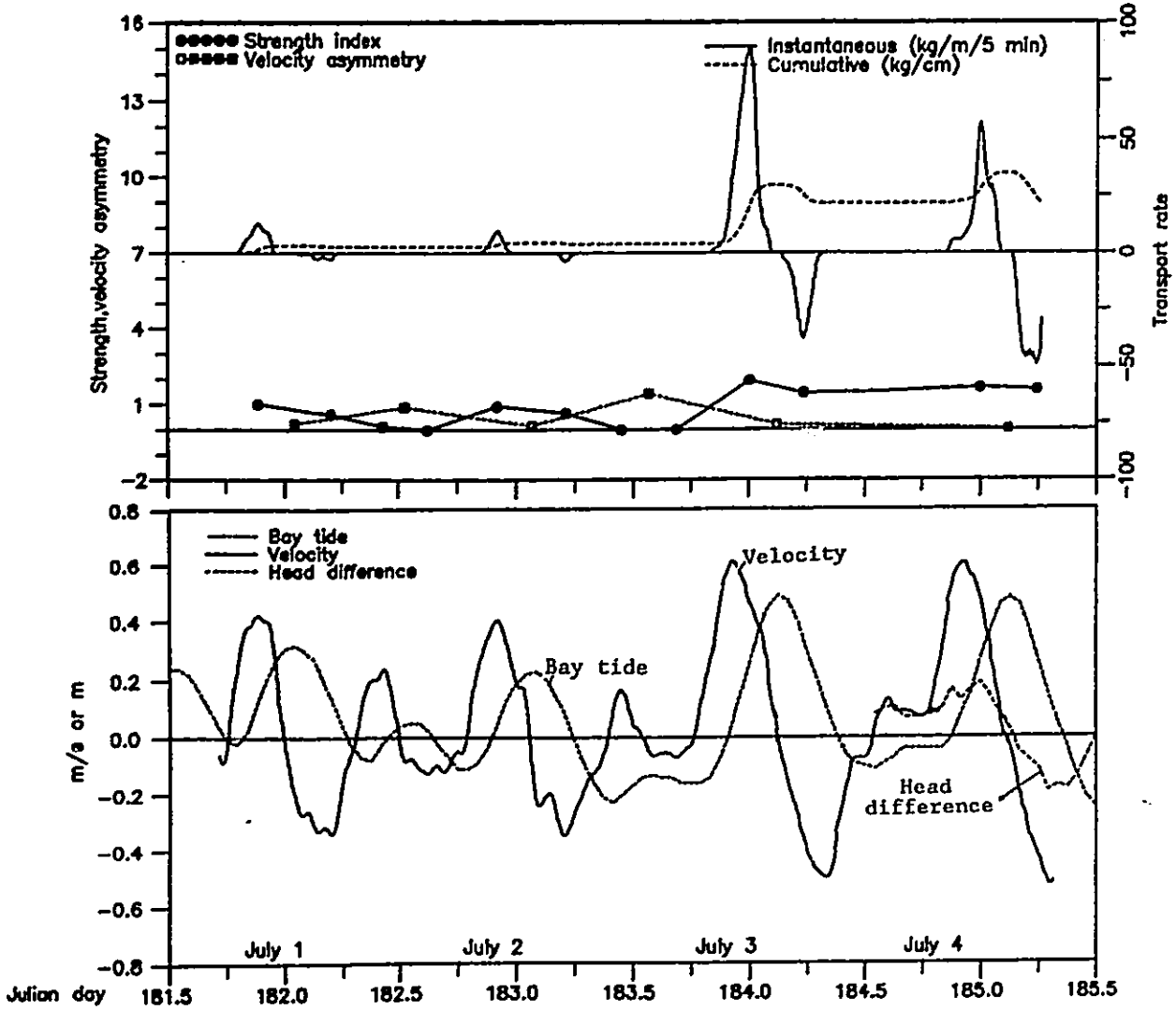
Strength index
Velocity asymmetry
Instantaneous (kg/m/5 min)
Cumulative (kg/cm)
Strength,velocity asymmetry
Transport rate
16
13
10
7
4
1
-2
100
50
0
-50
-100
Bay tide
Velocity
Head difference
m/s or m
0.8
0.6
0.4
0.2
0.0
-0.2
-0.4
-0.6
-0.8
July 1
July 2
July 3
July 4
Julian day
181.5
182.0
182.5
183.0
183.5
184.0
184.5
185.0
185.5

south (Figure 4-10), and since the returning current is weaker on the side, these materials will be contributing to the growth of the flood lobe. The station area here was shielded from the ebb by the north-facing flood lobe until it was submerged to a certain depth. Turbulent boils did not, however, occur on this end as the flow (flood) moved onto the shoal. This was because of the relatively large water depth, and the associated expansion of flow during the flood stage.

Between the two stations, flow was rather balanced. In large tides, flood and ebb both were around 0.7-0.8 m/s (Station 71-II, Figure 4-11). This station was located in front of the outlet of the channel leading to the bay. Flow here represented conditions with little influence of any topographic shield. Currents at this station were generally lower then those in the main channel. The difference was smaller for small tides, and increased with tidal range. For large tides, the difference was 0.15-0.2 m/s. A similar comparison was also made in Figure 2-16.

North Channel The North Channel was flood dominant (Station 64-II, Figure 4-12). The flood speed measured during the largest tide of the season was about 0.5 m/s, and the ebb speed 0.4 m/s, indicating that the tides were not capable of generating large active bedforms. These values were about half of the corresponding values of the main channel (see Figure 2-16). The flood dominance was probably due to two

Figure 4-11 Time series of current velocities and bay tides in the south channel (Station 71-II) and in the main channel (Station 55-I). For location see Figure 2-17.

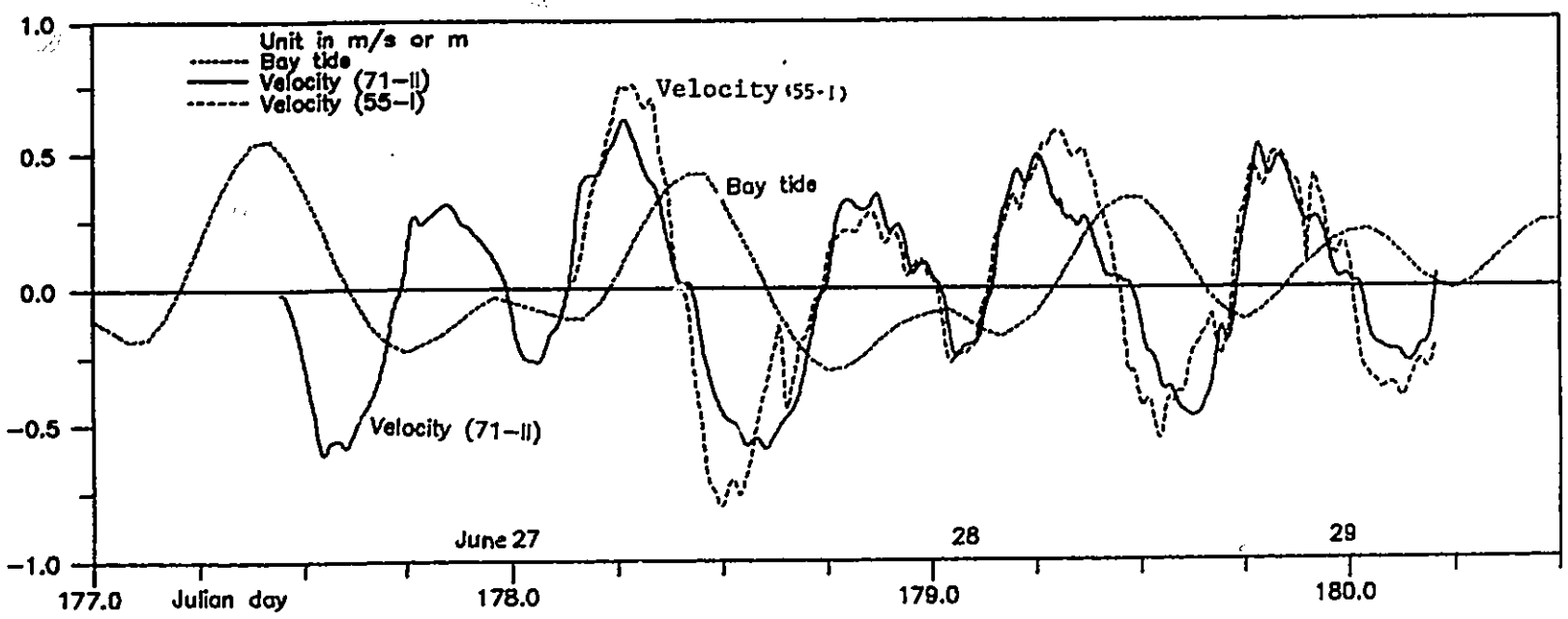
Unit in m/s or m
Bay tide
Velocity (71–II)
Velocity (55–I)
Velocity (55-I)
Bay tide
Velocity (71–II)
1.0
0.5
0.0
−0.5
−1.0
June 27
28
29
177.0
Julian day
178.0
179.0
180.0

Figure 4-12 Time series of current velocities and bay tides, Station 64-I, north channel. For location see Figure 2-17. Also shown are calculated sediment transport rate, and strength index and velocity asymmetry curves. See text for their definitions.

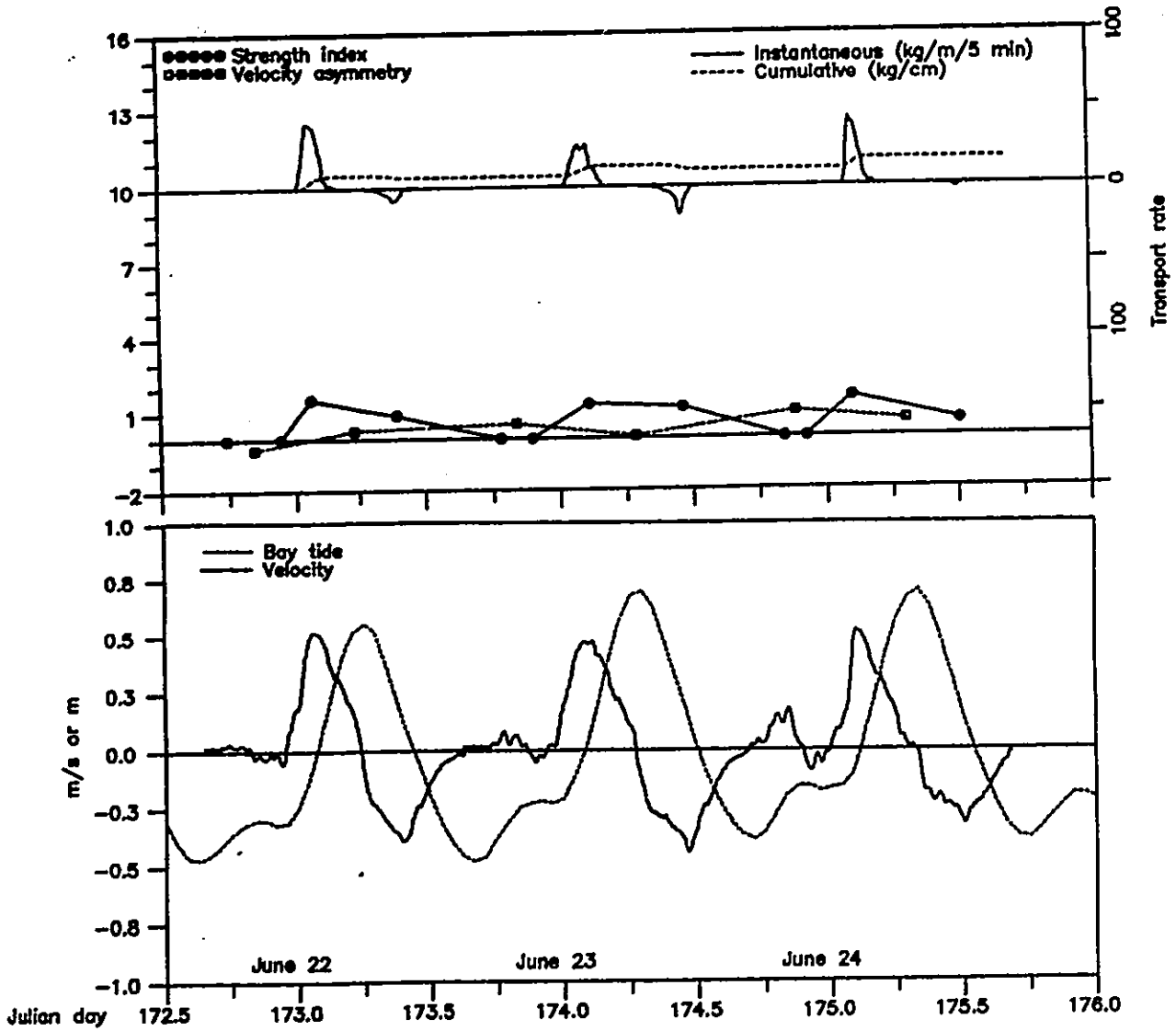
Strength index
Velocity asymmetry
Instantaneous (kg/m/5 min)
Cumulative (kg/cm)
Transport rate
Bay tide
Velocity
m/s or m
June 22
June 23
June 24
Julian day
16
13
10
7
4
1
-2
1.0
0.8
0.5
0.3
0.0
-0.3
-0.5
-0.8
-1.0
100
0
100
172.5
173.0
173.5
174.0
174.5
175.0
175.5
176.0

reasons. One is that the North Channel lacked outlets on the bayward side. The other is its good alignment with the main channel. The majority of the Northern Channel was covered by small current ripples. Very low-amplitude undulations occurred on echographs on the seaward end. Successive profiling, however, indicated that these undulations were not active bedforms responsive to normal tidal flows. Because of its quiescence, the North Channel will not be discussed further.

Seaward Marginal Channel Currents, measured at two locations in the seaward marginal channel, showed dominance of ebb over flood with a characteristic time-velocity pattern. Station 71-IV (Figure 4-13) was located at its seaward end behind the first nearshore bar. The time-velocity curve of this station consisted of relatively peaked ebbs alternating with flat flood plateaus. The ratio of maximum ebb to flood was about 3 with the ebb having peak of 0.35 m/s for large tides. Although the ebb dominance would mean that net sediment transport is out of the channel, the weak current may not be able to combat longshore drift. Station 64-III (Figure 4-14) was located in front of the south channel margin linear bar. The same characteristic time-velocity pattern was observed but to a less degree. Judging from the data measured during small tides, which gave 0.3 m/s for ebb and < 0.2 m/s for flood, currents at this station are just above the threshold of

Figure 4-13 Time series of current velocities, bay tides, and tidal difference between bay and gulf tides, Station 71-IV, seaward marginal channel. For location see Figure 2-17. Also shown are calculated sediment transport rate, and strength index and velocity asymmetry curves. See text for their definitions.

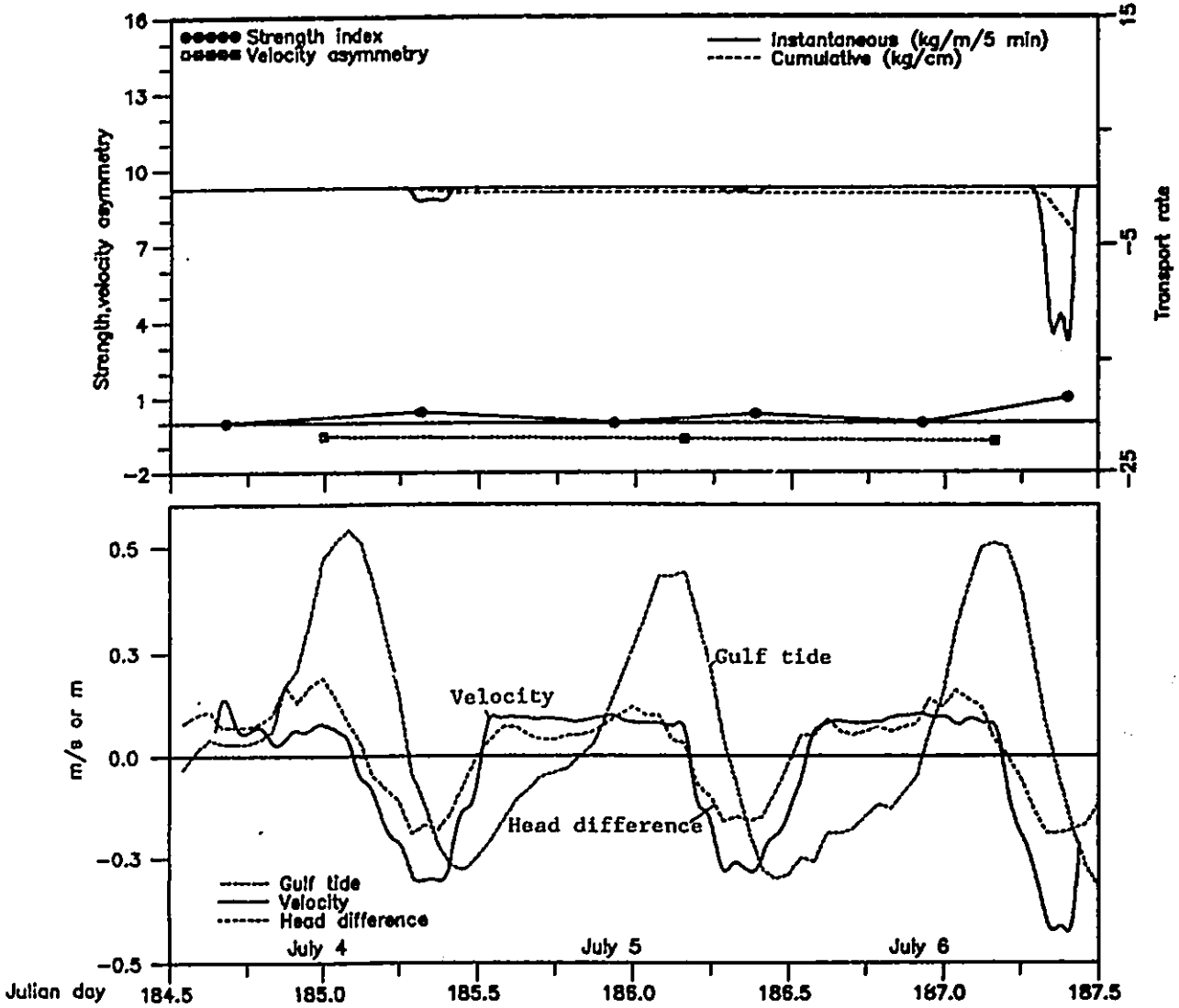
Strength index
Velocity asymmetry
Instantaneous (kg/m/5 min)
Cumulative (kg/cm)
Strength,velocity asymmetry
Transport rate
16
13
10
7
4
1
-2
15
-5
-25
0.5
0.3
0.0
-0.3
-0.5
m/s or m
Velocity
Gulf tide
Head difference
Gulf tide
Velocity
Head difference
July 4
July 5
July 6
Julian day
184.5
185.0
185.5
186.0
186.5
187.0
187.5

Figure 4-14 Time series of current velocities and bay tides, Station 64-II, seaward marginal channel. For location see Figure 2-17. Also shown are calculated sediment transport rate, and strength index and velocity asymmetry curves. See text for their definitions.

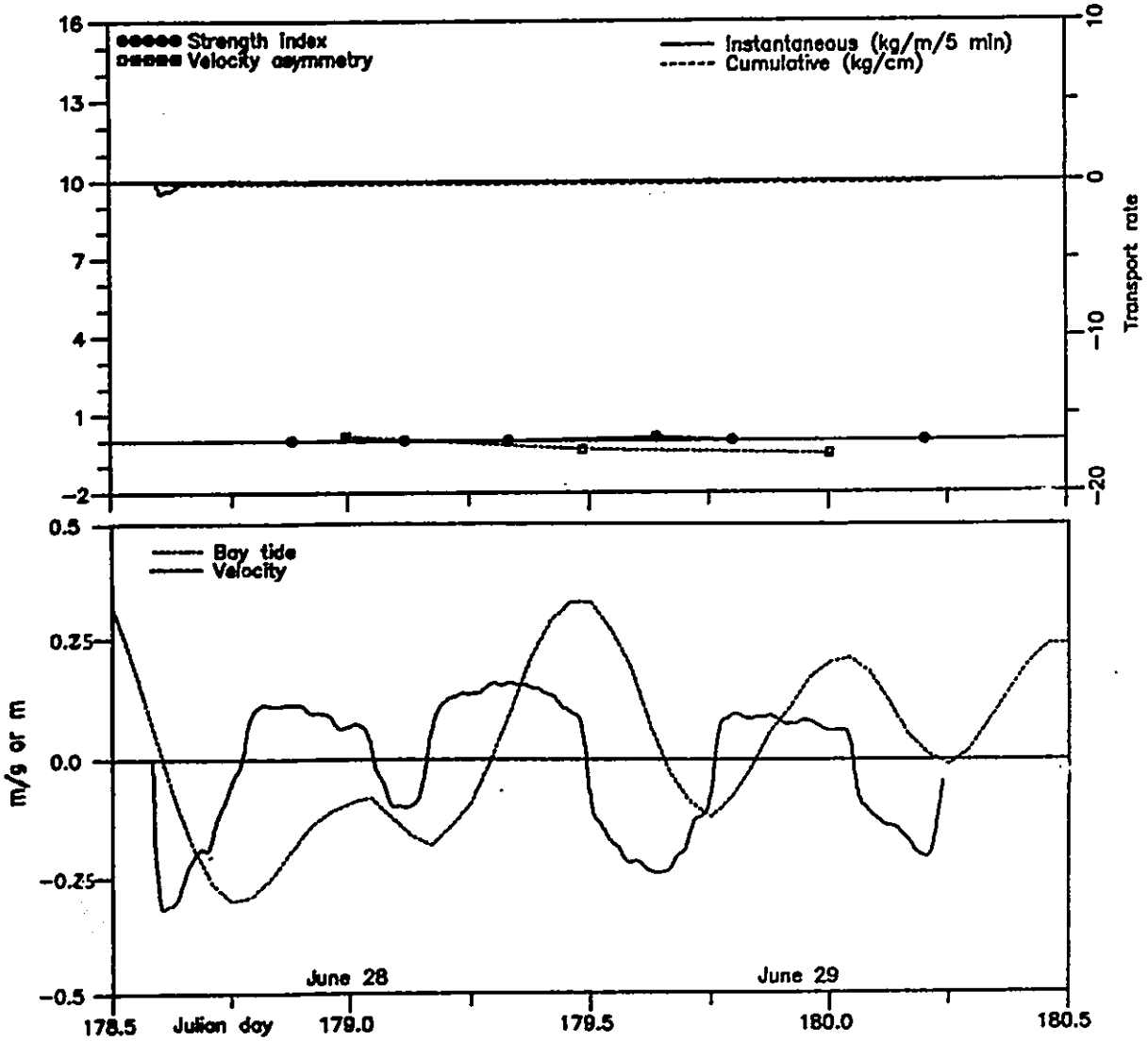
Strength Index
Velocity asymmetry
Instantaneous (kg/m/5 min)
Cumulative (kg/cm)
Transport rate
16
13
10
7
4
1
-2
10
0
-10
-20
Bay tide
Velocity
m/s or m
0.5
0.25
0.0
-0.25
-0.5
June 28
June 29
178.5
Julian day
179.0
179.5
180.0
180.5

producing large bedform. The marginal-channel has been considered as flood-dominated in the mesotidal ebb-tidal model (Hayes, 1980). The reason for the ebb-dominance at Palmer Inlet is probably a combination of small tidal range, and nearshore bathymetry and morphology. The flood-dominance in the mesotidal model is interpreted as due to the inertia of ebb flow in the main channel, which the flood must first overcome as the tide turns. As a result, the early flood takes the marginal route flanking the barrier, where the resistance is the least. The nearshore bar at Palmer Inlet was very close to the shoreline, and emerged at low tide. The early flood is thus blocked by the nearshore bar from entering the marginal channel. By the time the bar is submerged, the flooding of gulf tides has already overcome the ebb inertia in the main channel.

Texture A large percentage of the main channel was covered by a layer of lag deposits up to 0.25 m in thickness. On the seaward end and the shallow bank on the downdrift side, the lag deposits consisted almost entirely of disarticulate bivalves halves (white bands in Figure 3-1A and B). Shells here were often covered with a slimy coat, and rested convex-up. Defining the size in terms of the longest dimension, the average size of shells was on the order of 0.035 m, and the largest one was up to 0.11 m. Toward the throat in the deep thalweg, the lag was shelly gravels and pebbles. They were well-rounded, and made up of red

sandstones, igneous and metamorphic rocks fragments, clean shells and shell fragments, and small amount of interstitial sands. Shells were overall low in species diversity. The great majority of shells (>95%) are thick, beach to nearshore species. They were predominantly the surf clam (Spisula solidissima, Gosner, 1978), and the black clam (Arctica islandica). Other forms included common oysters (Crassostrea virginica), and mussels. Species with thin shell, such as green sea urchins (Strongylocentrotus droebachiensis), sand dollars (Echinarachnius parma) and sea stars (Asterias sp.), which occurred on beach and spit, were not found in the lag. In comparison with other studies (Tye, 1984; Berelson and Heron, 1985; Moslow and Heron, 1978; Reddering, 1983; Kumar and Sanders, 1974; Barwis and Makurath, 1978), the percentage of backbarrier forms of fauna in lag deposits of Palmer Inlet is low. This is attributed to the fact that the Cascumpec Bay is not a biologically productive area. At present, only a few oyster beds exist in the bay. The backbarrier flat is also only sparsely populated.

On the average (Table 4-1), channel sands are high in gravel and mud contents, relatively coarse (2.09 ϕ) and well sorted (0.38 ϕ). The presence of a relatively larger amount of coarse sands extends the coarse tail and enhances the peakedness of the central part of the population. This gives them a negative skewness (-0.21) and relatively large

Table 4-1 Statistics of grains sizes of inlet, bay and nearshore environments. Gravel <-1 ϕ (2 mm). Mud >4 ϕ (0.625 mm). CxI — Percentile of the intersection between C and I populations; IxS — Percentile of the intersection between I and S populations. For definitions of C, I and S populations, see text.

Environment	Four statistics Mz φ	σ φ	Sk	Kg	gravel & mud gravel %	mud %	Characteristics of subpopulations CxI φ	IxS φ	C %	I %	S %
Flood tidal delta (No. of samples = 9)											
Minimum	2.17	0.30	0.73	3.30	0.00	0.06	1.00	2.70	0.00	83.00	2.80
Maximum	2.71	0.49	1.37	7.35	0.36	0.60	1.70	3.10	0.44	97.20	16.00
Average	2.40	0.41	0.99	5.11	0.05	0.25	1.24	2.90	0.09	91.63	8.26
St.dev.	0.15	0.05	0.19	1.09	0.11	0.16	0.19	0.12	0.16	4.91	4.56
Spit platform (including channel margin bar) (7)											
Minimum	1.85	0.29	-1.38	6.74	0.00	0.00	0.80	2.80	0.00	92.00	0.50
Maximum	2.18	0.53	1.54	13.22	1.76	0.35	1.30	2.90	4.30	99.30	2.20
Average	2.06	0.36	0.49	9.75	0.37	0.14	1.03	2.87	0.91	97.59	1.13
St.dev.	0.11	0.08	1.08	2.15	0.61	0.11	0.15	0.05	1.46	2.35	0.51
Inlet channels (12)											
Minimum	1.84	0.24	-1.74	4.21	0.03	0.00	0.50	2.30	0.00	93.30	0.00
Maximum	2.72	0.74	1.59	10.95	3.50	1.96	1.20	3.10	2.60	99.60	2.00
Average	2.09	0.38	-0.21	7.18	0.59	0.21	0.96	2.83	0.61	97.70	1.08
St.dev.	0.23	0.13	0.90	1.73	0.94	0.53	0.19	0.20	0.74	1.77	0.65
Spit (beach, dune and overwash) (7)											
Minimum	2.08	0.24	-0.10	4.81	0.00	0.00	0.70	2.90	0.00	97.00	0.40
Maximum	2.23	0.39	1.64	11.72	0.04	0.12	1.30	2.90	1.13	99.60	2.20
Aveage	2.15	0.33	0.74	6.70	0.01	0.04	1.13	2.90	0.23	98.32	1.28
St.dev.	0.05	0.05	0.48	2.29	0.02	0.04	0.21	0.00	0.41	0.81	0.68
Nearshore-offshore (6)											
Minimum	2.13	0.24	-0.25	1.89	0.00	0.11	1.10	2.90	0.00	65.50	0.20
Maximum	3.18	0.73	1.24	14.78	0.24	6.51	1.60	3.30	0.60	99.80	34.50
Average	2.71	0.47	0.58	5.72	0.10	2.11	1.30	3.10	0.10	84.68	15.40
St.dev.	0.35	0.14	0.48	4.25	0.11	2.20	0.17	0.12	0.22	13.41	13.48
Bay (2)											
Average	3.84	2.51	1.66	6.00	0.62	28.85	-0.30	1.60	0.03	4.05	95.35
St.dev.	0.09	0.14	0.26	1.24	0.11	1.83	0.40	0.10	0.03	3.55	3.35

values of kurtosis (7.18). Channel sands, however, are of high variability. This is indicated by the larger values of standard deviation of the four statistics in Table 4-1, especially that of Mz, σ, and by the large scattering in the bivariate plots employing all data points (Figure 4-15). The high variability of textural characteristics is due, to a large extent, to the mud content which fluctuates, and possesses both the highest and the lowest values of the five inlet environments. The maximum and the minimum values of gravel fraction also occur in channel sands. The high variability indicates the high but variable energy conditions of inlet channels.

The grain size curves of channel sands are characterized by three subpopulations (GZ-13, Figure 4-16; Table 4-1): a minor, poorly sorted traction population (C), a major, well sorted intermittent suspension population (I), and a small continuous suspension population (Middleton, 1976). This indicates that three modes of sediment transport are active in the channel (Moss, 1972; Visher, 1969; Middleton, 1976). The dominant I population occurs between 1 ϕ and 2.8 ϕ. It accounts for 93-99% of the total sediments, and is always well sorted. The C population appears in ten of the twelve samples, but never exceeds 2.6% in content, and always poorly-sorted. The S population is also small, averaging 1% of the samples. In six out of 12 samples, the S population consists of two segments with

Figure 4-15 Bivariate plots of grain size statistics, showing considerable overlapping between various inlet environments. In Plots using logarithmic scales, values equal to zero have been set to 0.01. Bay and nearshore deposits can be distinguished from inlet environments by their high mud and S population, small mean size, poor sorting and small ϕ value of intersection between I and S population.
I - Intermittent suspension population; S - Continuous suspension population.

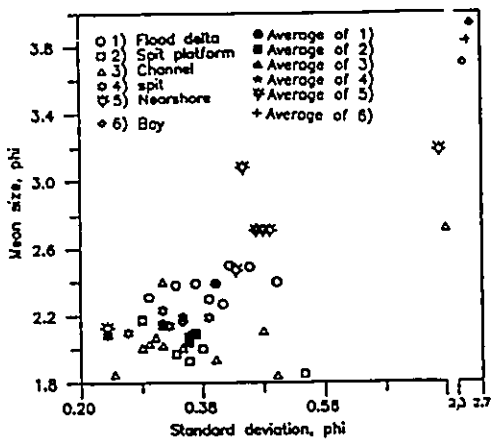
1) Flood delta
2) Spit platform
3) Channel
4) spit
5) Nearshore
6) Bay
Average of 1)
Average of 2)
Average of 3)
Average of 4)
Average of 5)
Average of 6)
Mean size, phi
Standard deviation, phi

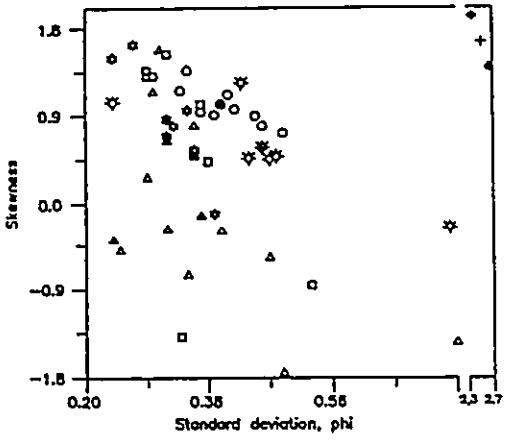
Skewness
Standard deviation, phi

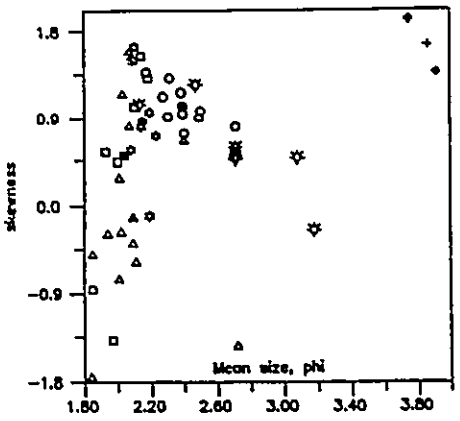
Skewness
Mean size, phi

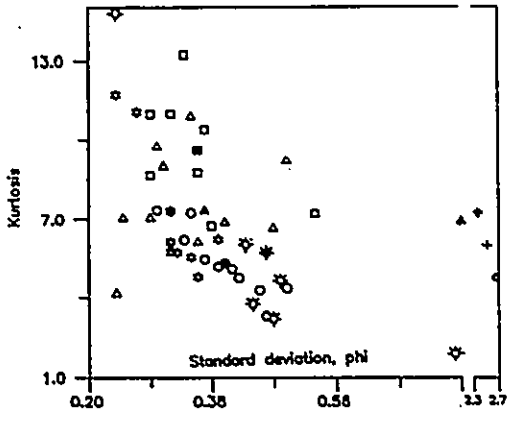
Kurtosis
Standard deviation, phi

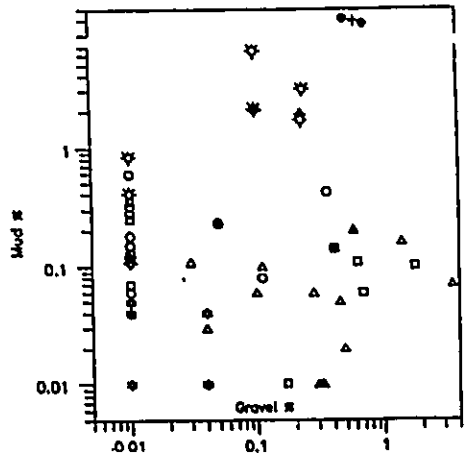
Mud %
Gravel %

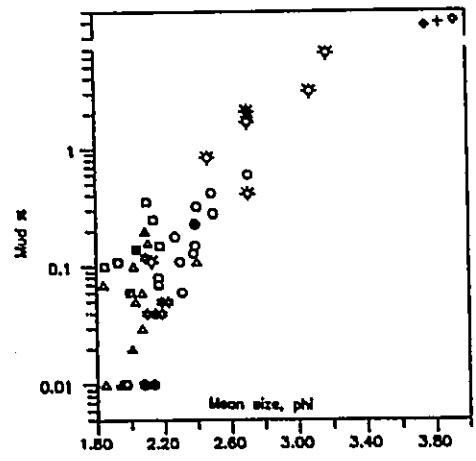
Mud %
Mean size, phi

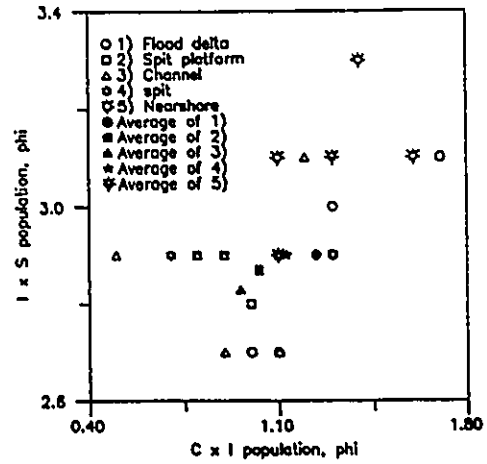
1) Flood delta
2) Spit platform
3) Channel
4) spit
5) Nearshore
Average of 1)
Average of 2)
Average of 3)
Average of 4)
Average of 5)
I x S population, phi
C x I population, phi

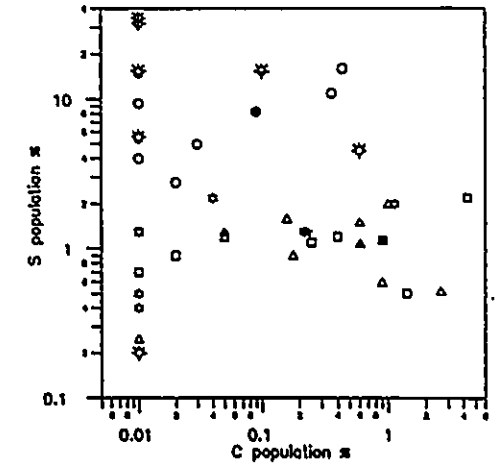
S population %
C population %

Figure 4-16 Representative grain size curves for various inlet environments. Statistics of textures are given for each sample. Titles for vertical axis are given in the lower left figure.

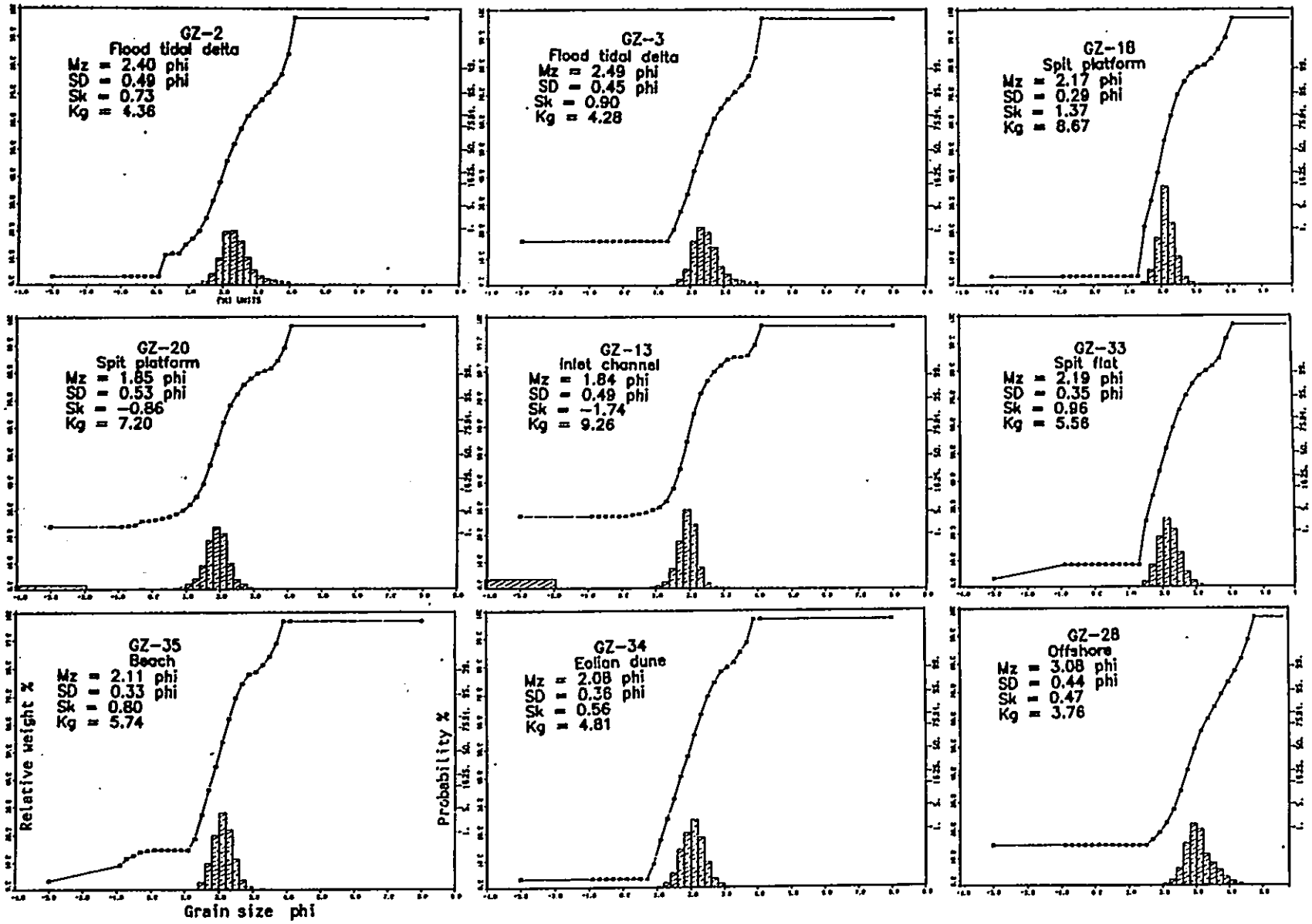
GZ-2
Flood tidal delta
Mz = 2.40 phi
SD = 0.49 phi
Sk = 0.73
Kg = 4.36
GZ-3
Flood tidal delta
Mz = 2.49 phi
SD = 0.45 phi
Sk = 0.90
Kg = 4.28
GZ-18
Spit platform
Mz = 2.17 phi
SD = 0.29 phi
Sk = 1.37
Kg = 8.67
GZ-20
Spit platform
Mz = 1.85 phi
SD = 0.53 phi
Sk = -0.86
Kg = 7.20
GZ-13
Inlet channel
Mz = 1.84 phi
SD = 0.49 phi
Sk = -1.74
Kg = 9.26
GZ-33
Spit flat
Mz = 2.19 phi
SD = 0.35 phi
Sk = 0.96
Kg = 5.58
GZ-35
Beach
Mz = 2.11 phi
SD = 0.33 phi
Sk = 0.80
Kg = 5.74
Relative weight %
Probability %
Grain size phi
GZ-34
Eolian dune
Mz = 2.08 phi
SD = 0.36 phi
Sk = 0.56
Kg = 4.81
GZ-28
Offshore
Mz = 3.08 phi
SD = 0.44 phi
Sk = 0.47
Kg = 3.76

different slopes. This suggests that the material constituting the suspension population did not come from a single, continuous fallout event.

Bedforms of the Main Channel Diver observations showed that the lag bed was completely flat, and not affected by tidal currents. Over a flat bed, the Shields' curve predicts an U_{*cr} of 0.15 m/s or equivalently U_{1cr} of 2.93 m/s for a shell size of 0.03 cm with a density of 2790 kg/m^3. This calculation suggested that lag deposits were not moved by normal tides, or even normal storms. It took large to exceptionally large storms to transport them, and at the same time to flush shells out of the bay. Once emplaced, they were immobile. Those in the low velocity area grew a slimy coat. In the thalweg, the bed was abraded by high speed flow condition. Small particles, including sands continuously brought in and out from adjacent areas, rolled over the bed in high velocity areas, and abraded the lag clean of organic coatings.

In the sandy area around the lag, bedforms were Type II megaripples with well developed scours. They averaged 4.9 m in wavelength and 0.31 m in height. In the landward direction, they changed to the Type I form, and averaged about 4.0 m and 0.21 m in height in the middle of the flood ramp. Toward the entrance, they became smaller, but still have short crests and shallow scour pits, and finally gave way to a flat surface at the ebb terminal lobe. Megaripples

in the main channel did not show visible changes on successive echographs during small tides. Changes during large tides are different between different parts of the channel, with changes compatible with the flow dominance as described above. Figure 4-17 shows a typical profile from the throat to the ebb terminal lobe, and its variation for a large ebb tide. At low water, megaripples were ebb-oriented throughout. At high water, those in the throat reversed and became flood-oriented, while those at the seaward end remained ebb-oriented. In between, megaripples were more or less symmetrical. The slightly ebb dominance of flow at the throat was indicated by clearer ebb-orientation than flood-orientation. Variations of Type I megaripples on the flood ramp are shown in Figure 4-18. It is seen that megaripples higher on the ramp were not affected by the ebb flow, and remained flood oriented at the end of the ebb. Megaripples at the foot of the ramp, however, reversed with the tide.

In the marginal channel (Figure 4-19), megaripples were shown on the bed profile in large tides, but did not show change in orientation with the tide. From the echograph alone, it is not known whether they reacted with the flow. Field observation showed that they were little affected by normal tides. Current data indicate that these megaripples were probably active only near the peak large tide, and remained dormant most of the time during a fortnightly cycle.

Figure 4-17 Bedform profiles of the main channel ('1' in Figure 4-1), July 8, 1986. Megaripples on the landward side reverse their orientation, and those on the seaward side remain ebb oriented. In the middle, megaripples are nearly symmetrical at high water but become ebb-oriented at low water. Lag deposits are dotted. Tidal range = 0.75 m; HW = 6:20; LW = 15:40.

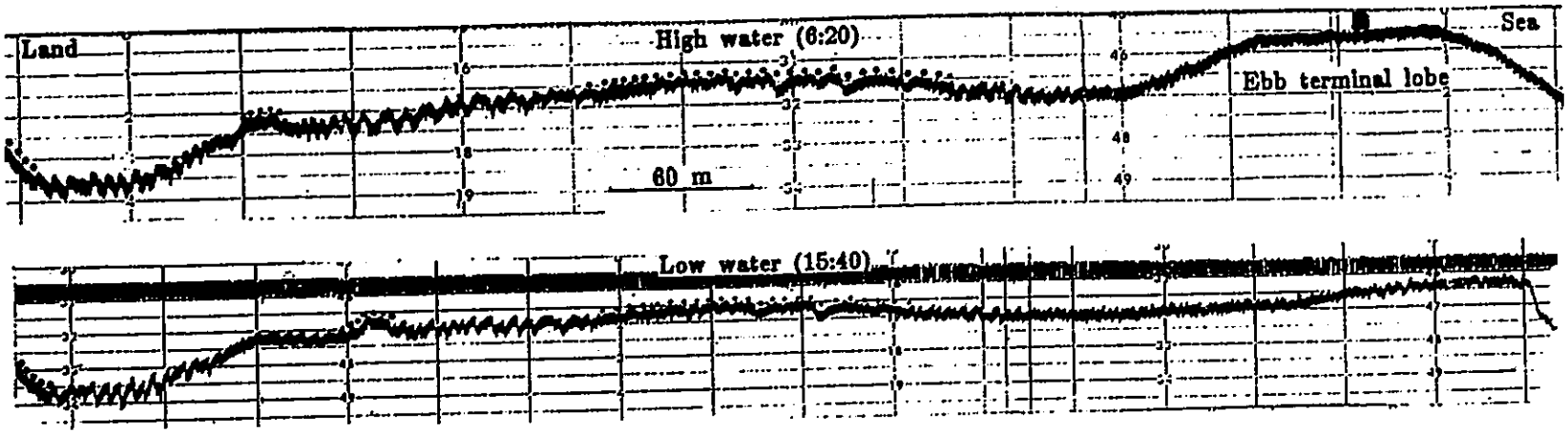
Land
High water (6:20)
Sea
Ebb terminal lobe
60 m
Low water (15:40)

Figure 4-18 Bedform profiles of the flood ramp ('2' in Figure 4-1), July 25, 1986, showing effects of topographic shielding of the flood tidal delta: the flood orientation of megaripples higher on the ramp remains unchanged at low water. Those at the foot of the slope become slightly ebb-oriented. Tidal range = 0.75 m; HW = 8:45; LW = 16:00.

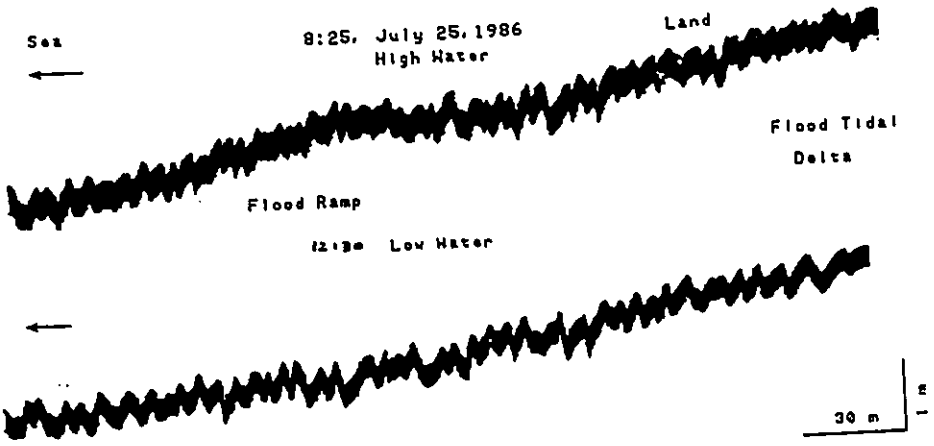
Sea
8:25, July 25, 1986
High Water
Land
Flood Tidal
Delta
Flood Ramp
12:30 Low Water
30 m

Figure 4-19 Bedform profiles of the seaward marginal channel ('3' in Figure 4-1), July 8, 1986. Tidal range = 0.75 m; HW = 6:20; LW = 15:40. Lag deposits dotted.

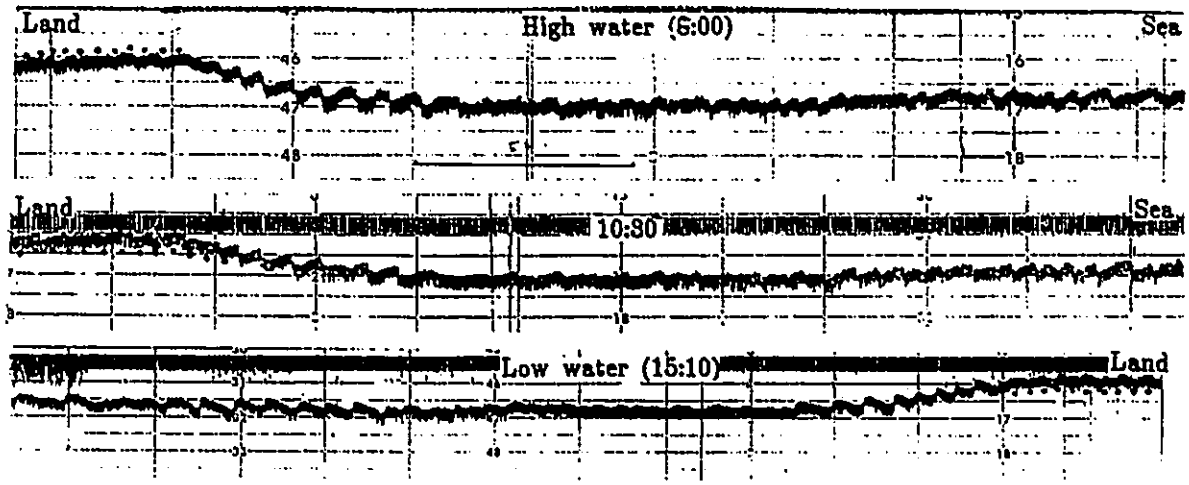
Land
High water (6:00)
Sea
Land
10:30
Sea
Low water (15:10)
Land

Structures of the Main Channel Two spade-cores were taken in the main channel. The one from the throat (Figure 4-20B) showed sets of medium-scale (5-7 cm) trough cross-bedding. Cross-beds were high-angle (16°-33°), and bidirectional. Set of cross-beds were in direct contact, and separated by low-angle boundaries. The dip of beds on both sides of the boundary indicates that they are erosional surfaces of migrating megaripple troughs, rather than reactivation surfaces (Klein, 1970). These cross-beds are apparently megaripple products formed during large tides. It is noted that the preserved deposits were thinner in set thickness than the topmost one just formed (16 cm). The discrepancy in scale between the preserved beds and surface bedforms is consistent with the flow characteristics in this section. With rather symmetrical flow, bedforms moving in both directions eroded one another with equal strength, and only deposits at the bottom of troughs were preserved. Tidal currents during small tides fell below the threshold of megaripples but still above that of ripple formation. They are expected to form ripple lamination, but apparently these structures were reworked by the next large tide. As a result, successive sets of cross-beds were mostly in direct contact with one another.

No spade-core is available on the flood ramp. A tube core taken in the middle of it will be discussed later. The peel near entrance side just penetrated the top layer.

Figure 4-20 Resin peels of spade cores from inlet channels. A, B and C correspond to 1, 2 and 3 in Figure 4-1B, respectively. Structures in the top 5-10 cm have been distorted. Ebb to the right.

(A) Dominantly ebb-oriented trough cross-bedding from the crest of a Type II megaripples, ebb spit, South Channel.

(B) Medium-scaled, bidirectional trough cross-bedding from the stoss-side of a Type II megaripple.

(C) Ebb-oriented trough cross-bedding from the crest of a Type II megaripple, near entrance, main channel.

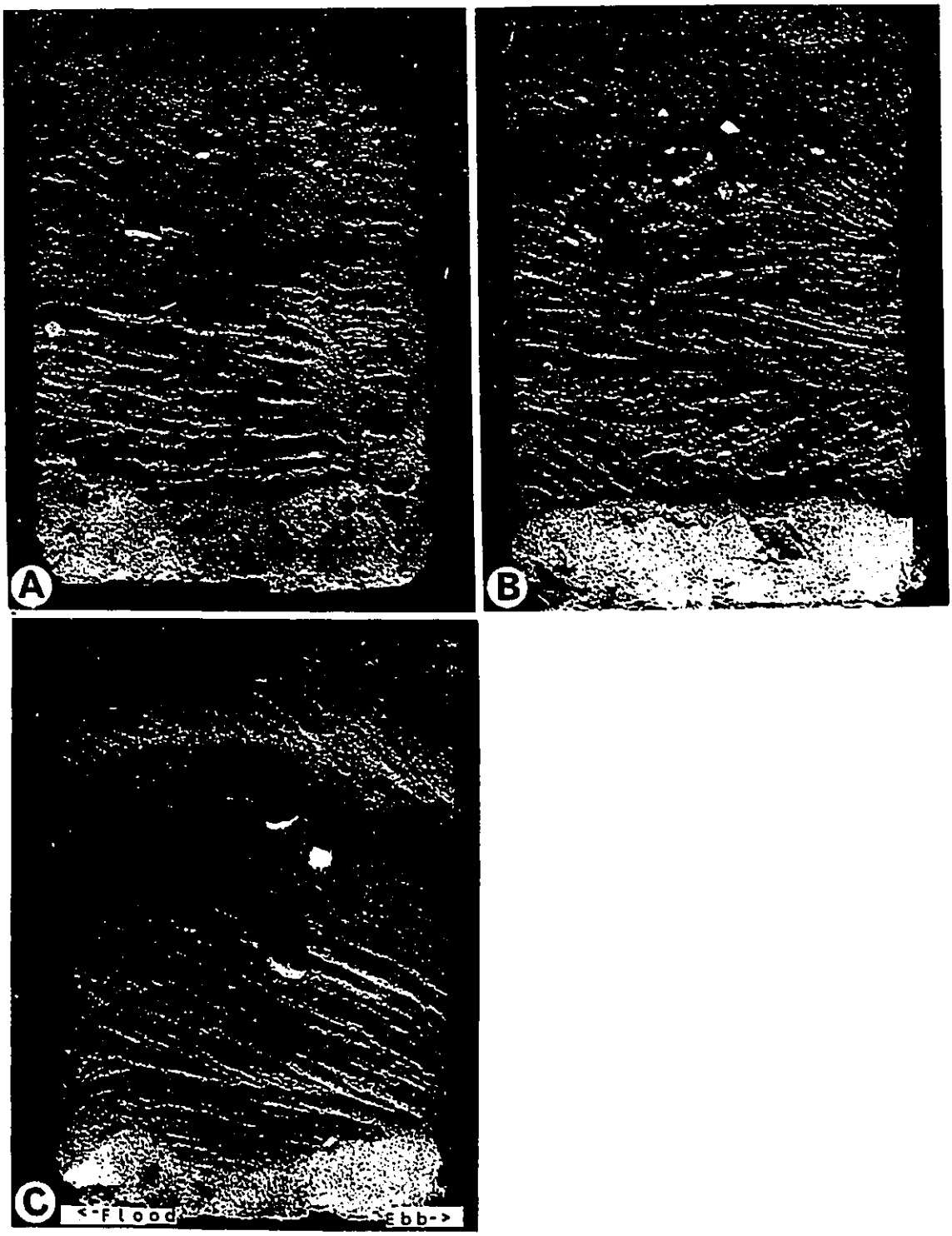
A
B
C
<-Flood
Ebb->

The exposed two layers (Figure 4-20C) both showed trough cross-bedding dipping in the ebb-direction. While the scale of the preserved bedding cannot be determined, an ebb dominated condition seemed indicated. The difference in the dip between the two sets of foresets is interpreted as representing different parts of a bedding set.

Tube-cores from the top of the ebb terminal lobe showed finely structured, and clean fine sands as opposed to those from the channel (8 in Figure 4-22). The dominant structure was parallel to gently dipping, even lamination. Dip was dominantly in landward direction, but ebb-orientation also occurred. Another structure was ripple-lamination, concentrated at the bottom. Overall, such an assemblage of structures is different from the normal megaripple bedding in that they lack erosional set boundaries, and tangential foresets. Instead, they resembled those typical of nearshore bars as described from the landward slope of bars off the New Brunswick coast (Davidson-Arnott and Greenwood, 1974), and as also similar to those revealed in a core taken on top of an updrift nearshore bar in the present study (H in Figure 4-23). Comparison of echo sounding profiles and air photos taken in 1986 and 1987 showed a general landward migration of the innermost nearshore bar, and final merging of the bar with the ebb terminal lobe. This suggested that waves and associated longshore drift were the dominant provider of

Figure 4-21 Grain size data, tube-core (7) of Figure 4-22, main channel. Sample locations are indicated in the core. Mz = mean size; STD = standard deviation.

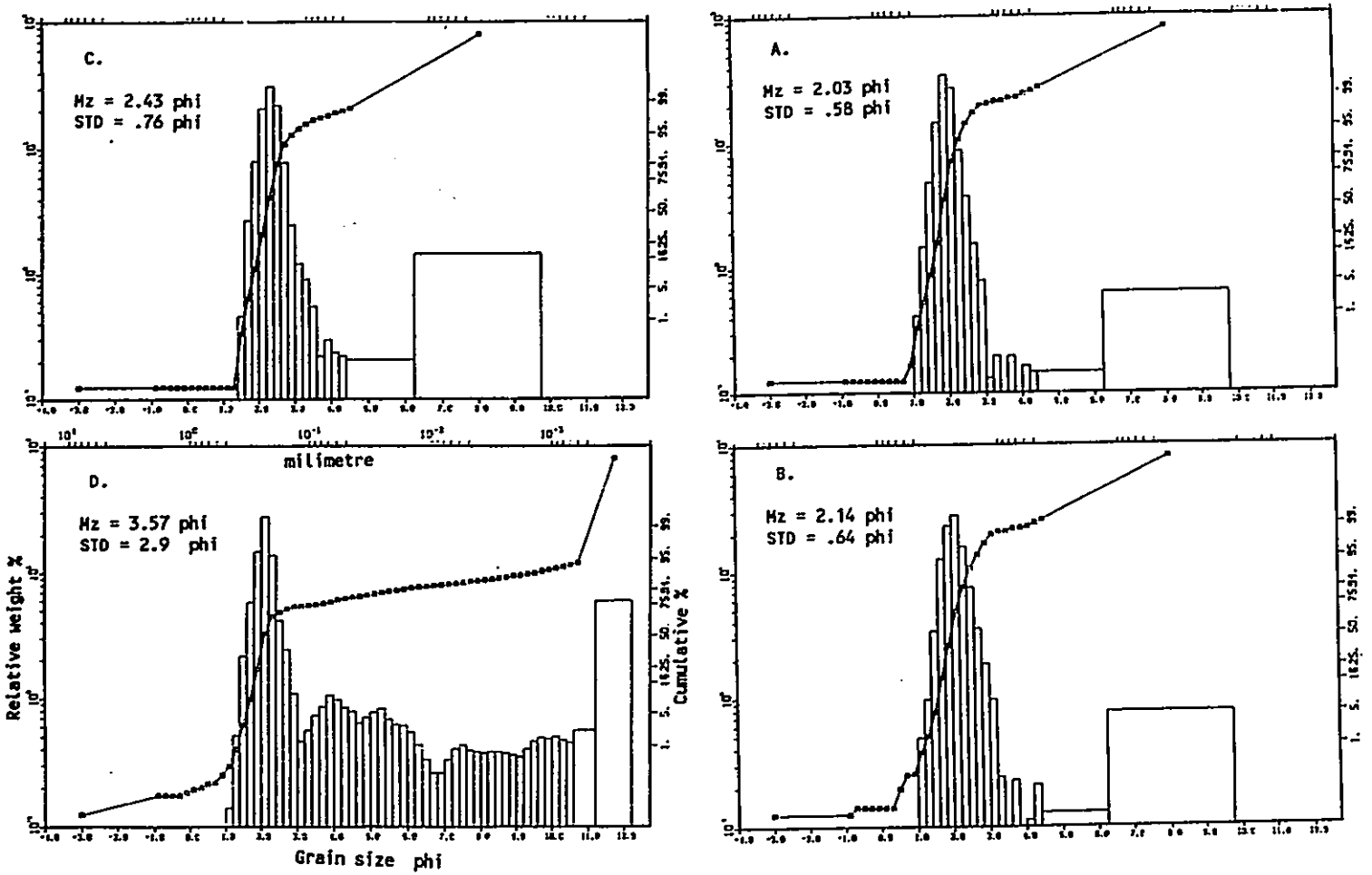
C.
Hz = 2.43 phi
STD = .76 phi
A.
Hz = 2.03 phi
STD = .58 phi
D.
Hz = 3.57 phi
STD = 2.9 phi
B.
Hz = 2.14 phi
STD = .64 phi
millimetre
Relative weight %
Cumulative %
Grain size phi

Figure 4-22 Tube-cores forming a longitudinal stratigraphic profile along the inlet channel. See Figure 4-1 for locations. Numbers below each core are its length in metres; those in the parentheses are the height of the top of the core below the mean water level at the time it was taken. Letters along the core marks the locations of grain size samples as shown in Figure 4-21.


1
2
3
4
5
6
7
8
A
B
C
0.79

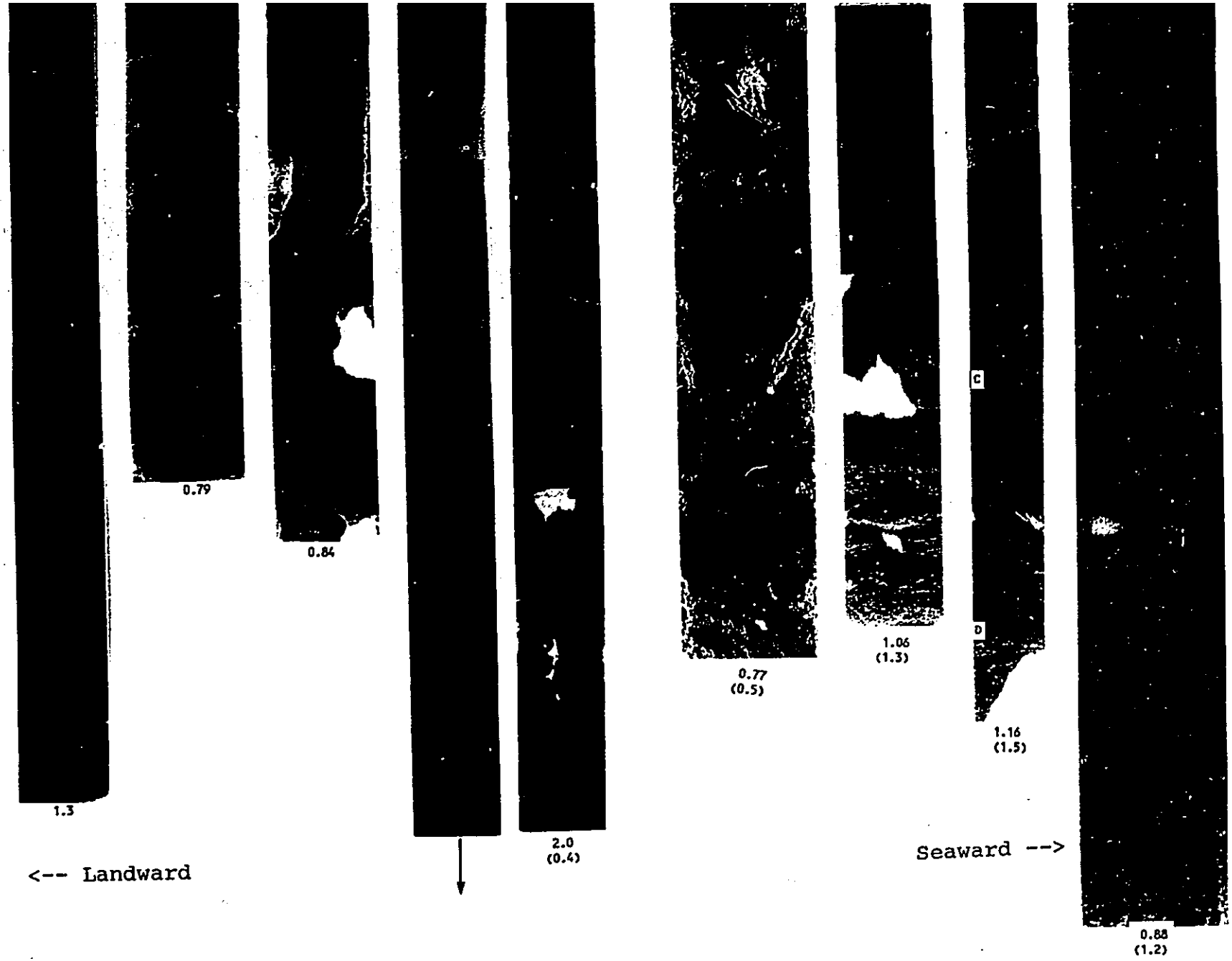
1.3
0.79
0.84
2.0
(0.4)
0.77
(0.5)
1.06
(1.3)
C
D
1.16
(1.5)
0.88
(1.2)
<-- Landward
Seaward -->

sediment to the lobe. Sediments were also supplied by ebb tides from the landward side. These sediments were, however, mostly likely to be reworked by waves as current measurements showed that daily tides were unable to generate bedforms beyond ripples. Based on these considerations, the parallel lamination is interpreted as swash-type plane beds, deposited on top of the ebb lobe as waves break around it. The cross-lamination is formed from wave ripple migration, reflecting relative calm weather, or deeper water.

Vertical Sequence Three cores were taken along the main channel. The core (7 in Figure 4-22) on the entrance side reached the underlying substrate. The substrate was homogeneous, dark-grey to black cohesive mud with root remains. A few thin silt to fine sand layers formed millimetre to centimetre-scaled stratification. The surface of the mud lay at about 2.5 m below the mean water level. Its grain size distribution (Figure 4-21) was very similar to that from the modern bay (Figure 4-25) with four modes occurring at about 2 ϕ, 5 ϕ, 8 ϕ and 10 ϕ. Overlying the mud layer was a shell lag, several centimeters in thickness. The overlying sand portion consisted of relatively fine scale, ripple cross-lamination in the lower half, and ebb-dominated, medium scale cross-bedding in the upper part. The two parts are interpreted as deposits formed before and after the inlet channel moved into this position. The grain size taken at three levels showed a subtle upward coarsening

Figure 4-23 Resin peels of tube cores forming a transverse stratigraphic profile on the entrance side of the inlet. See Figure 4-1A for locations; labels are matched. Numbers below each core are its length in metres; those in the parentheses are the height of the top of the cores above the mean water level at the time it was taken.

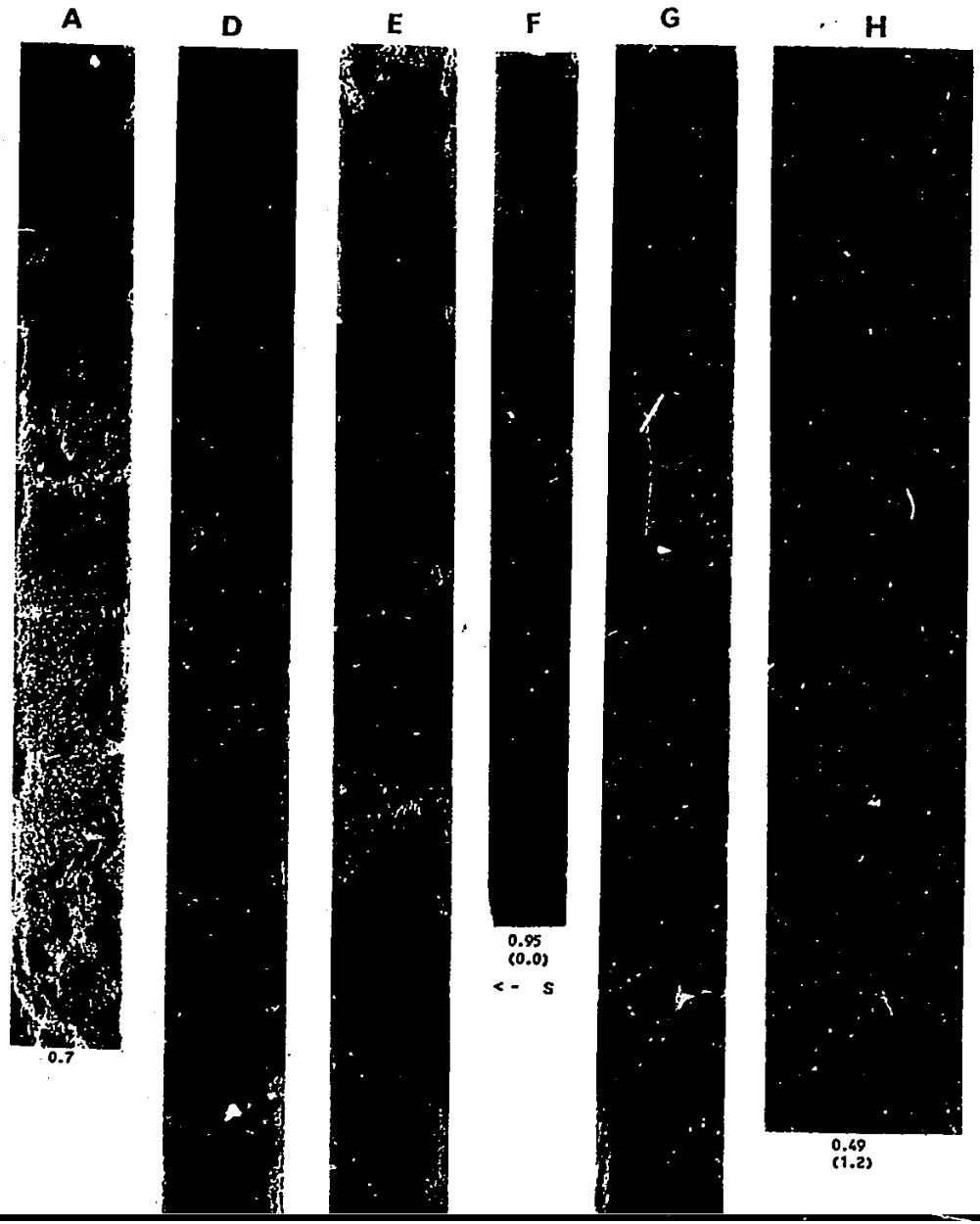
A
D
E
F
G
H
0.7
0.95
(0.0)
< - S
0.49
(1.2)

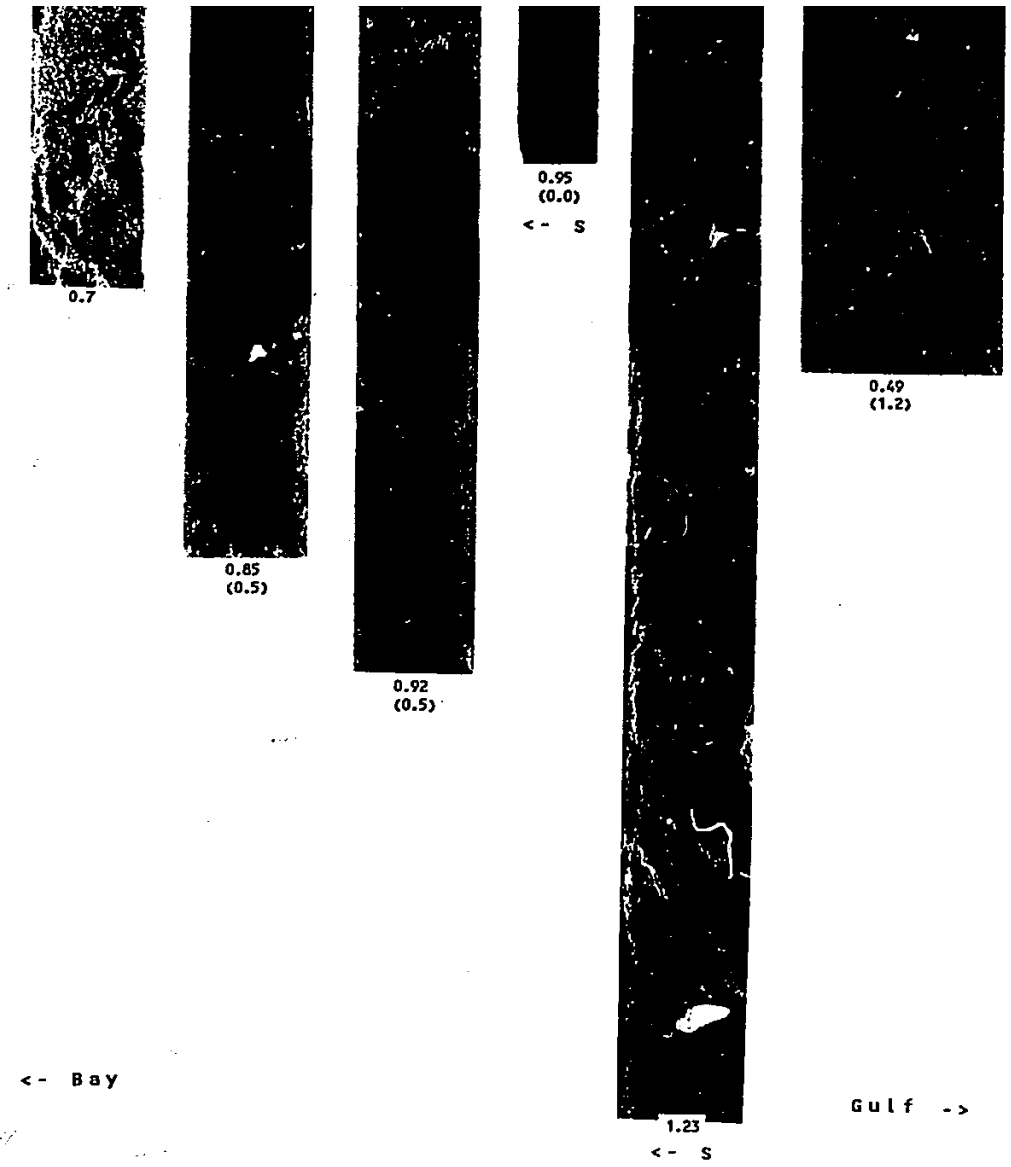
0.7
0.85
(0.5)
0.92
(0.5)
0.95
(0.0)
<- S
1.23
<- S
0.49
(1.2)
<- Bay
Gulf ->

trend (Figure 4-21). This supports the above interpretation, showing channel deposits were slightly coarser than those which were deposited in a nearshore environment.

The core in the middle was taken on the shallow portion on the downdrift side (6 in Figure 4-22). It penetrated the same mud substrate, but at a level 1.8 m below mean water level and without encountering lag materials directly above the mud. Instead, a shell layer, 0.09 m thick, occurred sandwiched between sand deposits. This lag deposit is considered equivalent to that currently exposed in the shallow bank, but has been later buried. The sand portion were characterized by flood-oriented large-scale cross-bedding. It represents deposits formed by megaripples, probably Type I.

The core on the landward side was taken in the middle of the flood ramp (5 in Figure 4-22). The sequence consisted of large-scale, unidirectional cross-bedding dipping in the flood directions in the upper part, and ebb-oriented cross-bedding in the lower part. The bedding of the former was more planar in form but less well defined than that of the latter. Although no grain size data are available, a fining upward trend was visually recognizable. The sequence reflects changes due to the growth of the ramp, and the associated changes in flow characteristics. With currents becoming more and more shielded, there was an

overall decrease in flow strength but an increase in flood influence.

One tube was taken in the marginal channel close to the barrier shoreline (Figure 4-24b). It reached the mud deposits at 1.6 m below the mean water level. No lags were found above the mud. The grain size of the mud was similar to that revealed in the main channel with characteristic quadrimodal distribution (Figure 4-25). The overlying sand deposits were fine in grain size, containing a high amount of silts (Figure 4-25), as well as a small amount of organic relics. Structurally, they lacked clearly defined bedding structures. Some crude small-scale cross-lamination and plane-bed could be seen. The sequence is thus one suggesting that throughout its history, currents have been weak in the marginal channel.

Bedforms of the South Channel The bottom of the South Channel was covered with megaripples. Over the northern half where flow was turbulent, they were Type II forms, about 4.3 m in wavelength and 0.26 m in height, while those on the southern half were Type I forms, about 7.2 m in wavelength and 0.23 m in height. Migration of these bedforms were recorded for different tidal conditions (Figure 4-26 to Figure 4-30). Although the measurements do not constitute a continuous time series, when placed in a correct sequence of tidal range (Figure 4-27), these profiles form a series, in which not only ebb-flood

Figure 4-24 Resin peels of tube cores forming a transverse stratigraphic profile on the landward side of the inlet. Location see Figure 4-1A; labels are matched. Numbers below each core are its length in metres; those in the parentheses are the height of the top of the core above the mean water level at the time it was taken. Letters along the core are sample locations of grain size shown in Figure 4-25 and 4-37.

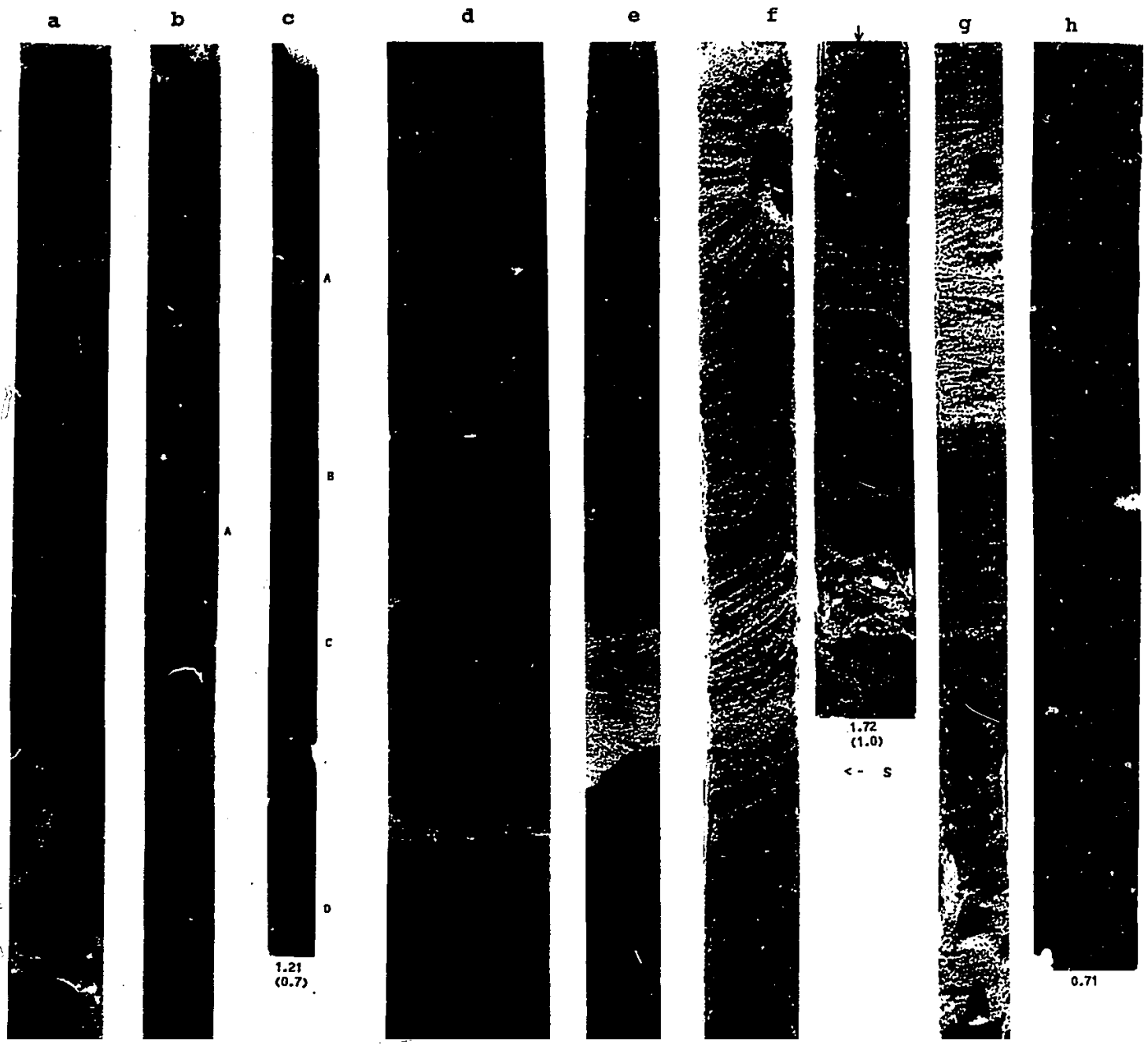
a
b
c
d
e
f
g
h
A
B
C
D
A
1.21
(0.7)
1.72
(1.0)
< - S
0.71

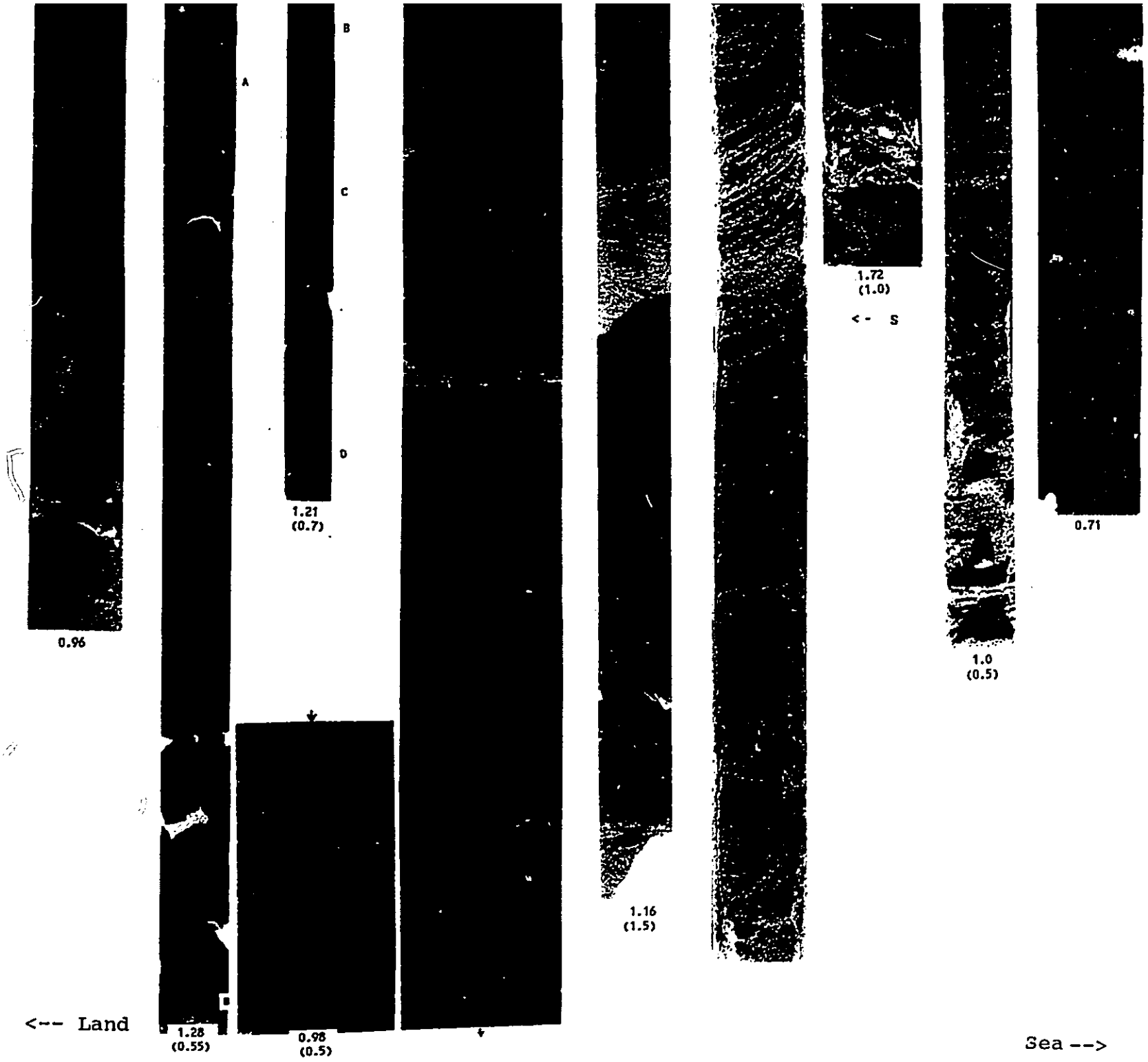
A
B
C
D
0.96
1.28
(0.55)
1.21
(0.7)
0.98
(0.5)
1.16
(1.5)
1.72
(1.0)
< - S
1.0
(0.5)
0.71
<-- Land
Sea -->

[illegible]

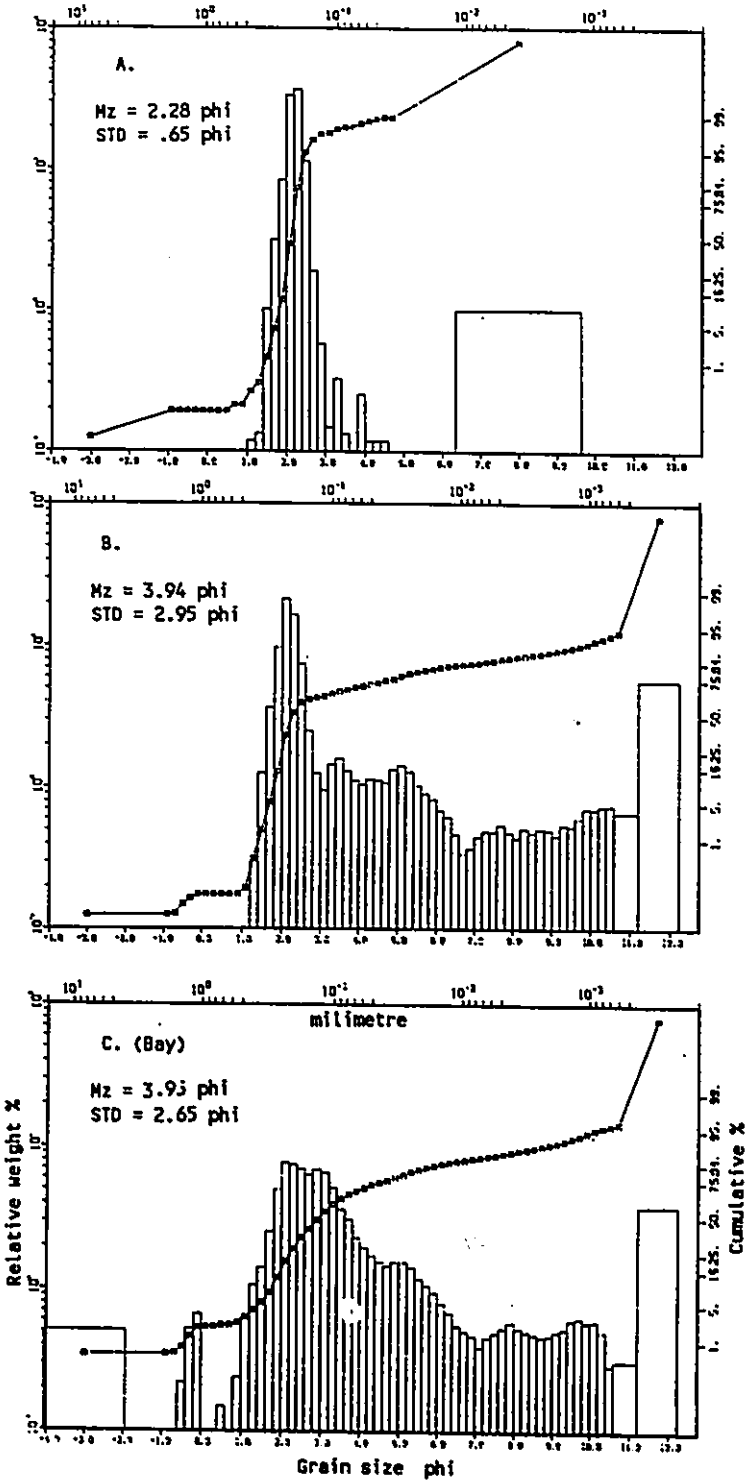
A.
Mz = 2.28 phi
STD = .65 phi
B.
Mz = 3.94 phi
STD = 2.95 phi
millimetre
C. (Bay)
Mz = 3.93 phi
STD = 2.65 phi
Relative weight %
Cumulative %
Grain size phi

Figure 4-26 Bedform profiles of the South Channel ('4' in Figure 4-1), flood tide, June 30, 1987. Tidal range = 0.21 m; LW = 8:00; HW = 13:00.

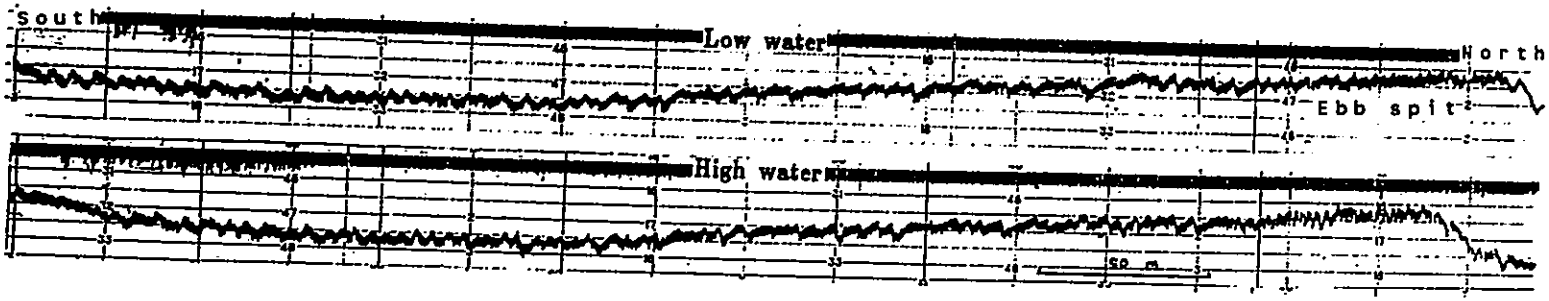
South
Low water
North
Ebb spit
High water

Figure 4-27 Tidal conditions for bedform profiles of Figure 4-28 to Figure 4-30. These profiles were not measured sequentially, but are reorganized here in the order of tidal range so that a complete ebb-flood-ebb cycle can be examined. Tidal range is given in parenthesis. Vertical scale in metre.

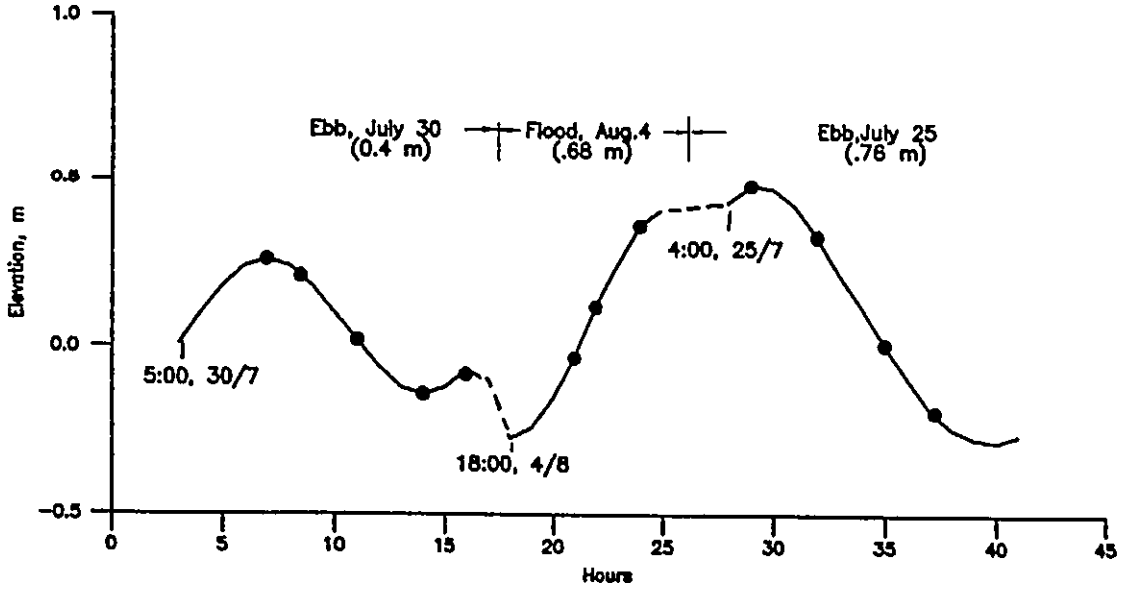
Ebb, July 30
(0.4 m)
Flood, Aug.4
(.68 m)
Ebb,July 25
(.76 m)
4:00, 25/7
5:00, 30/7
18:00, 4/8
Elevation, m
Hours

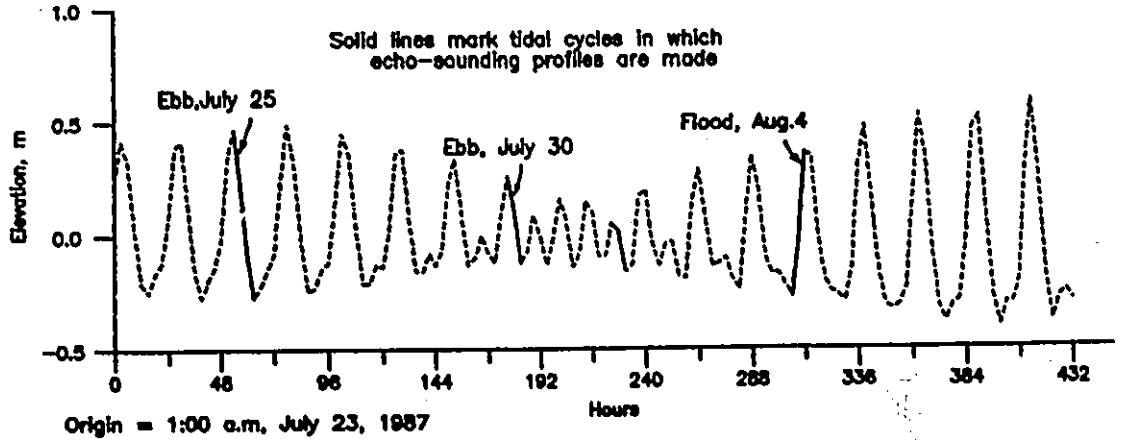
Solid lines mark tidal cycles in which
echo-sounding profiles are made
Ebb,July 25
Ebb, July 30
Flood, Aug.4
Elevation, m
Hours
Origin = 1:00 a.m. July 23, 1987

Figure 4-28 Same profile as Figure 4-26, ebb tide, July 30, 1987. See Figure 4-27 for tidal conditions. Vertical scale in metre. The profile plotted from echographs, and is broken into a northern (right) segment characterized by Type II megaripples, and a southern (left) segment characterized by Type I megaripples. The arrow indicates the flow direction with flood toward left and ebb toward right. Vertical scale in metre.

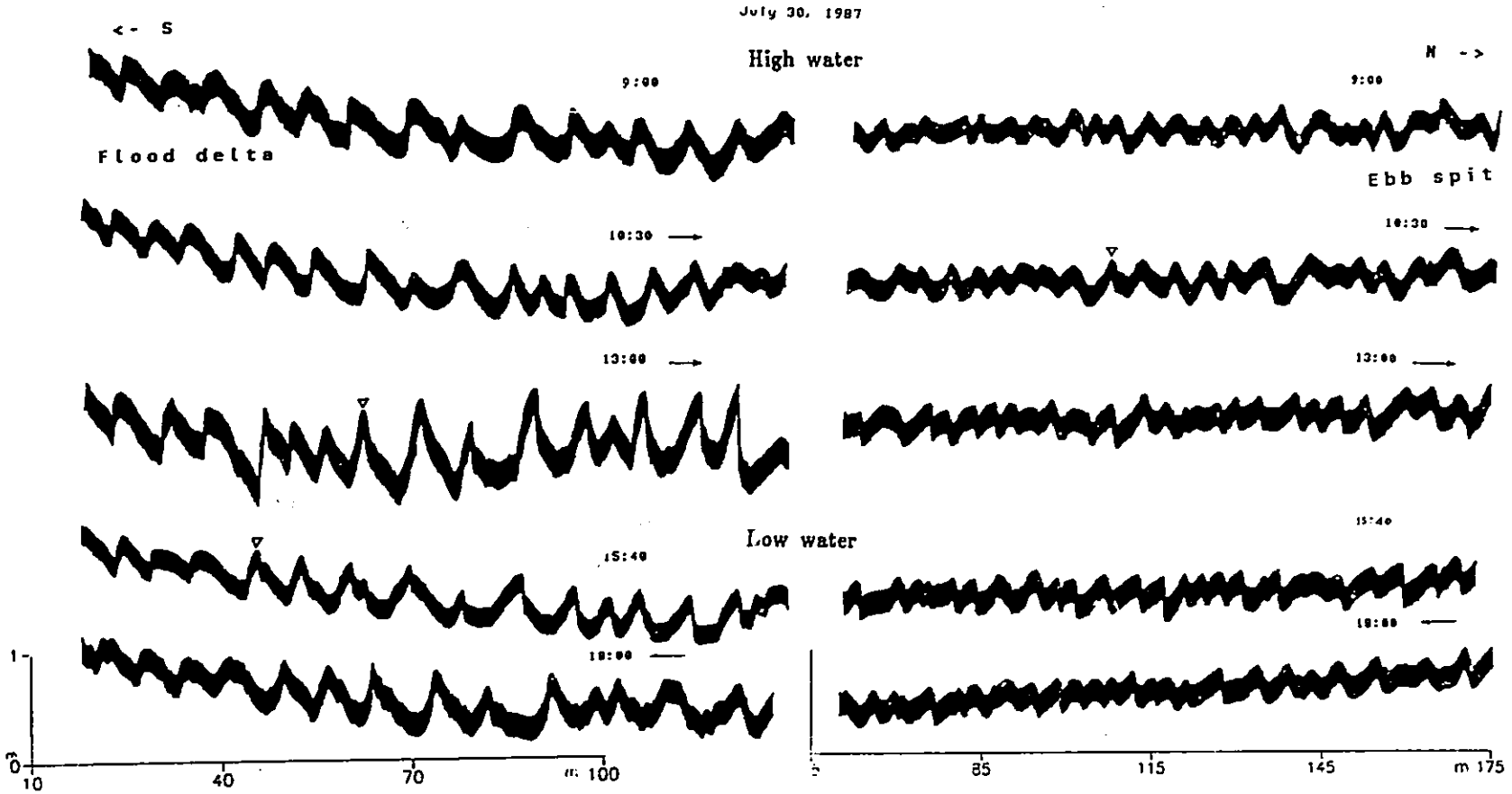
July 30, 1987
<- S
N ->
High water
9:00
9:00
Flood delta
Ebb spit
10:30
10:30
13:00
13:00
Low water
15:40
15:40
18:00
18:00
1
0
10
40
70
m 100
85
115
145
m 175

variation but also some large-small tidal changes can be examined.

In small tides, no apparent change took place between high and low water (Figure 4-26). At a tidal range of 0.4 m, bedforms started to move, and reversed with the tide (Figure 4-28). The reversal, however, started at the crest of the ebb spit, and moved gradually southward with the ebbing tide (13:00 and 15:40). At the end of the low water (15:40), megaripples at the foot of the flood lobe still maintained flood-orientation. A reverse sequence was observed for the following flood tide, which represented a typical intermediate tide situation (18:00 in Figure 4-28 and Figure 4-29). The southernmost bedforms were reversed first (18:00), and reversal proceeded progressively northward. At 22:00 almost five hours after the flooding, the entire sequence became flood-oriented. The same ebb sequence then was repeated in the second ebb, which is typical of large tidal conditions (Figure 4-30). Despite the larger tidal range, the southernmost bedforms remained unaffected. In both ebb sequences, it is observed that in the megaripple Type II field, there was an increase in height as well as irregularity toward the end. Diver observations indicated that the heightening was due to scouring of troughs as flow became more turbulent toward low water.

The above pattern and changes of bedforms are fully

Figure 4-29 Same profile as Figure 4-28, flood tide, August 4, 1987; low water slack = 17:00. See Figure 4-27 for tidal conditions.

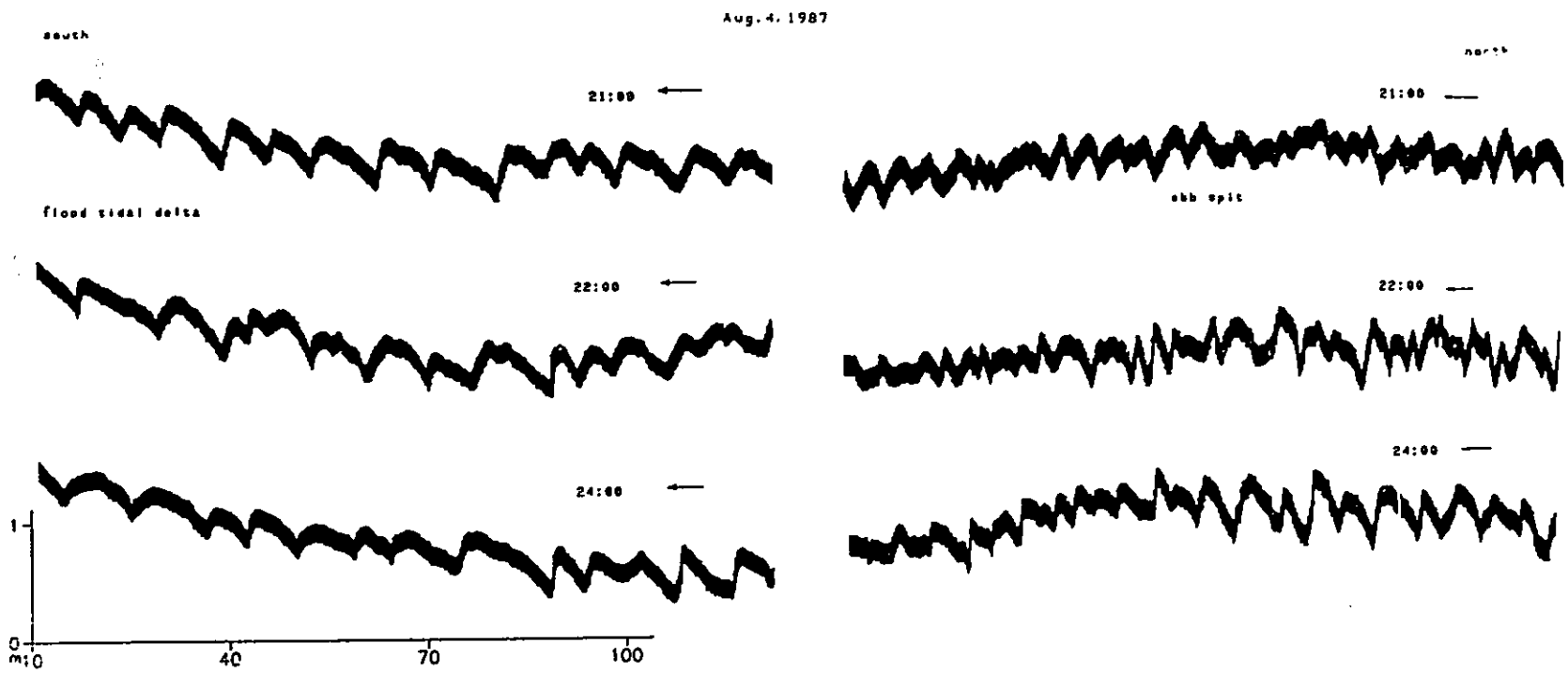
Aug. 4. 1987
south
21:00
flood tidal delta
22:00
24:00
north
21:00
ebb spit
22:00
24:00
1
0
m
0
40
70
100

Figure 4-30 Same profile as Figure 4-28, Ebb tide, July 25, 1987; high water slack = 5:00. See Figure 4-27 for tidal conditions.

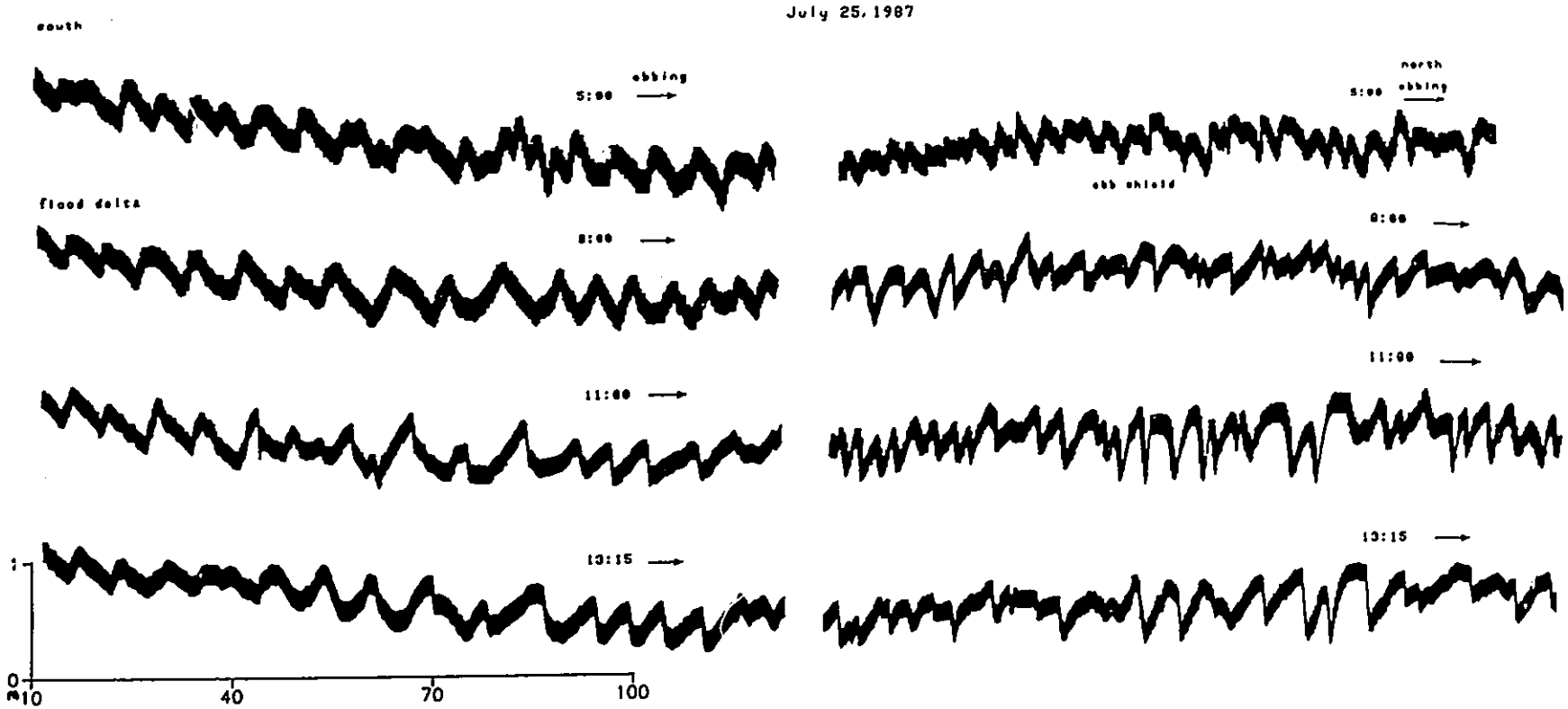
July 25, 1987
south
ebbing
5:00
flood delta
8:00
11:00
13:15
north
ebbing
5:00
ebb shield
8:00
11:00
13:15
1
0
10
40
70
100

compatible with the flow characteristics. The pattern of bedforms recorded in small tides is a reflection of the flow dominance in this channel (Figure 4-26), showing that bedforms in the middle part were nearly symmetrical, while those to the north were ebb-oriented and those to the south were flood-oriented. The fortnightly variation of current was reflected by the alternation of bedform reversing with tide during tropical tides, and drifting into dormancy during synoptic tides. Along with this was an increase in bedform size and irregularity of megaripples from small to large tides especially in the megaripple Type II field. This can be seen by comparing Figure 4-26 and Figure 4-30.

Structures of the South Channel No tube cores were taken in the South Channel. The only spade core was taken near the crest of a Type II megaripple at the foot of the ebb spit (Figure 4-20A). The top set of the core consisted of large-scale, ebb-oriented trough cross-beds. Beneath it there was a small portion of cross-beds, oriented toward the flood. Because of the limited penetration, it is hard to determine the scale and organization of the preserved beds. Judging from the flow and bedform behaviour, they should be similar to those observed in the throat channel, i.e., consisting of sets of medium-scale, bidirectional trough cross-bedding with some indication of ebb dominance.

4.4 Channel Margin Linear Bar

Processes The channel margin linear bar (CMLB) was subject to combined tidal current and wave process with varied strength. In general, along the inner margin flanking the channel, tidal currents were dominant, while on the outer margin, waves were dominant (the south CMLB) or become more important (the north CMLB). Waves were more active on the south CMLB because of its proximity to the gulf. The south CMLB was fronted by a much smaller subtidal shoal, so that waves could reach it with less energy dissipation over the path. Two more factors could have been of significance in the difference. One was wave refraction around the ebb terminal lobe, which contributed additional energy to the downdrift side. The other is that to the dominant NE waves in this region, the south CMLB was a leeside feature, and was somewhat protected by the spit and the spit platform on the north side of the inlet.

Currents were measured near the landward end of the north CMLB (Station 64-XII, Figure 4-31). They indicated that flow at this location was in the lower flow-regime but was able to generate large bedforms in both directions. The flood and ebb were almost asymmetric both in duration and in peak values, both reaching 0.87 m/s with duration of 6.1-6.3 hours. The bar remained emerged for about three hours during both phases. The low asymmetry of currents is very similar to the time-velocity pattern measured in the nearby

Figure 4-31 Time series plot of current velocities, north channel margin linear bar, Station 64-XII.

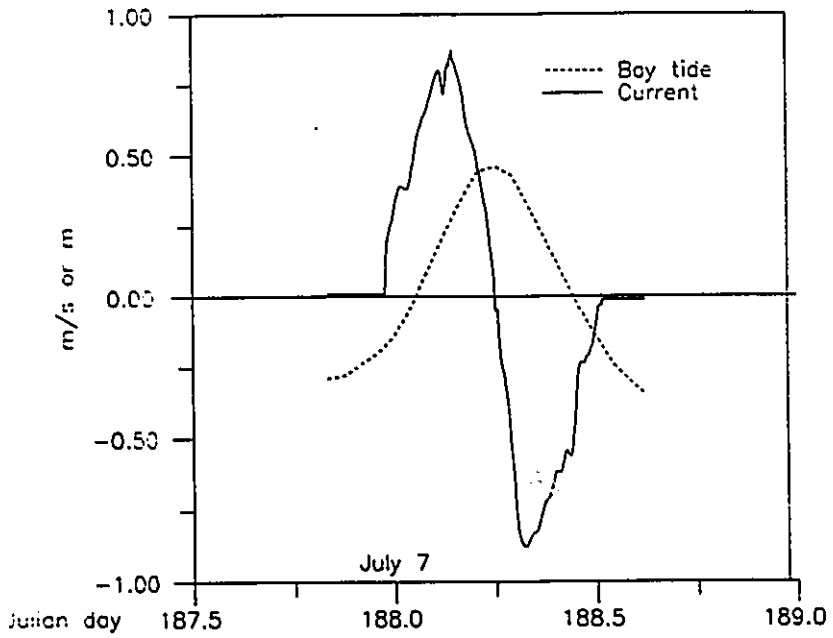
1.00
0.50
0.00
−0.50
−1.00
m/s or m
Bay tide
Current
July 7
Julian day
187.5
188.0
188.5
189.0

channel, but shorter in duration. No currents were measured in other location on the bar. The general pattern, from the throat seaward, should parallel that observed in the main channel (from Station 55-III to 55-I to 71-III. That is, a general decrease in maximum velocity but an increase in ebb dominance and wave influence.

Texture Grain size characteristics of the channel margin bar are similar to that from the nearby spit platform, and will be described in that section.

Bedform of South Channel Margin Linear Bar The south channel margin linear bar showed variation both in overall shape and in elevation between 1986 and 1987. The bathymetric change, albeit small, changed the ratio of time-exposure to swash relative to that of tidal currents, and has had a significant effect on bedform development in this area.

In 1986, the south CMLB was triangular in shape. Bedform distribution was mapped and is shown in Figure 4-32 with some examples illustrated in Figure 4-33. During spring tides, with the inner portion of the bar was covered by poorly-developed megaripples (Figure 4-33A), about 0.7-1.8 m in wavelength, 0.06-0.10 m in height. Their morphology, in particular, the scoop-shaped trough and discontinuous crest, suggested that they were incipient Type II megaripples, abandoned by flow after a short period of high velocity. Away from the channel margin in the seaward

Figure 4-32 Distributions of bedforms on the south channel margin linear bar, 1986. Inset gives the approximate locations. Some examples of bedforms are shown in Figure 4-33 with corresponding relief peels given in Figure 4-35.

(A) Large tide (tidal range = 0.75 m), July 9.

(B) Small tide (tidal range = 0.25 m), June 30.

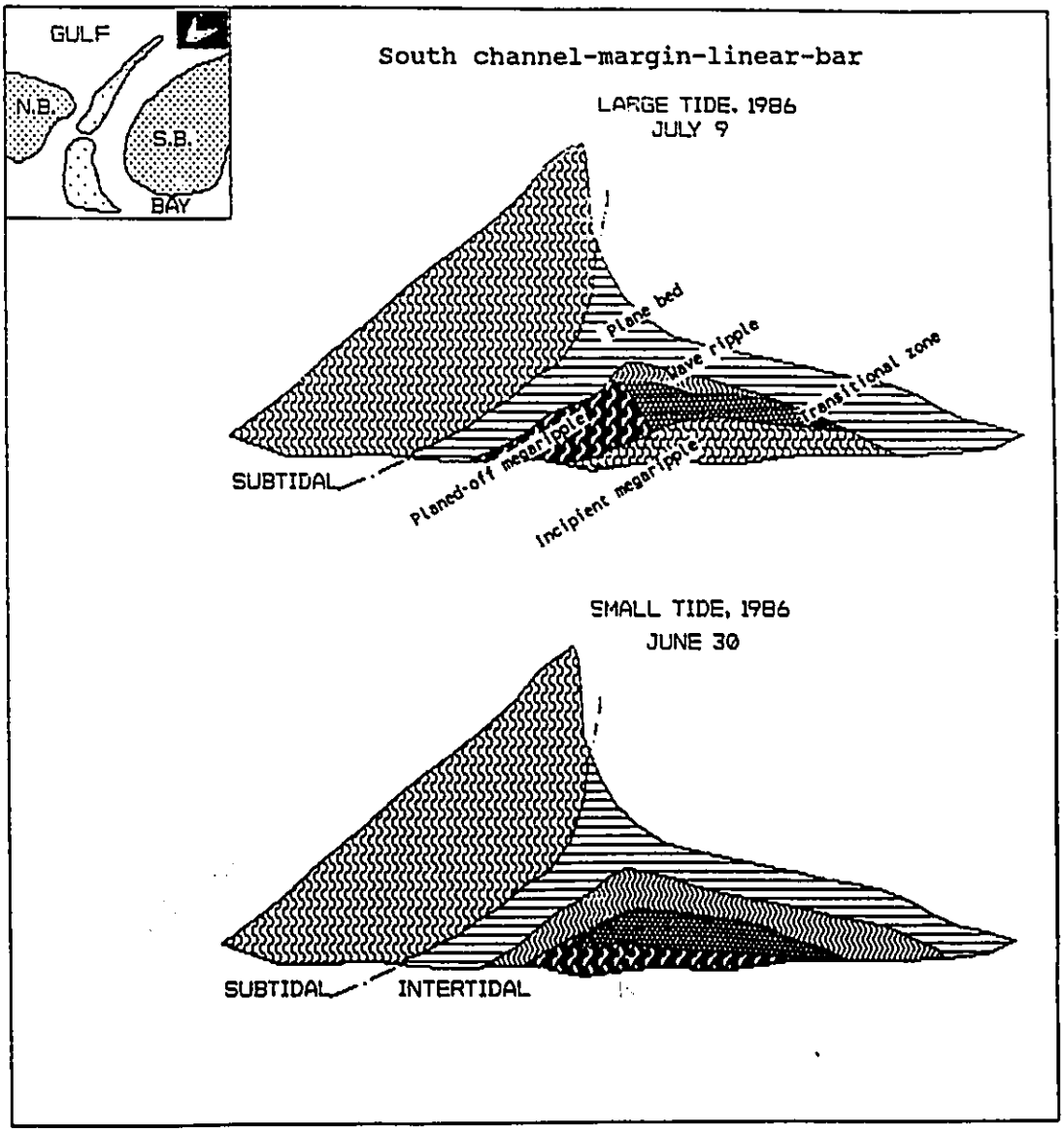
GULF
N.B.
S.B.
BAY
South channel-margin-linear-bar
LARGE TIDE, 1986
JULY 9
Plane bed
Wave ripple
Transitional zone
Incipient megaripple
Planed-off megaripple
SUBTIDAL
SMALL TIDE, 1986
JUNE 30
SUBTIDAL
INTERTIDAL

Figure 4-33 Bedforms of the south channel margin bar, 1986. For locations see Figure 4-32; letters are matched. Gulf to the left.

(A) Incipient megaripples along the inner margin fringing the marginal channel (background). Notebook is 22 cm long.

(B) Planed-off incipient megaripples. View toward the Bay with the boat in the seaward marginal channel.

(C) Zone between incipient megaripples and wave ripples. Pen is 12 cm long.

(D) Wave-ripples on the seaward side. Pen is 12 cm long.

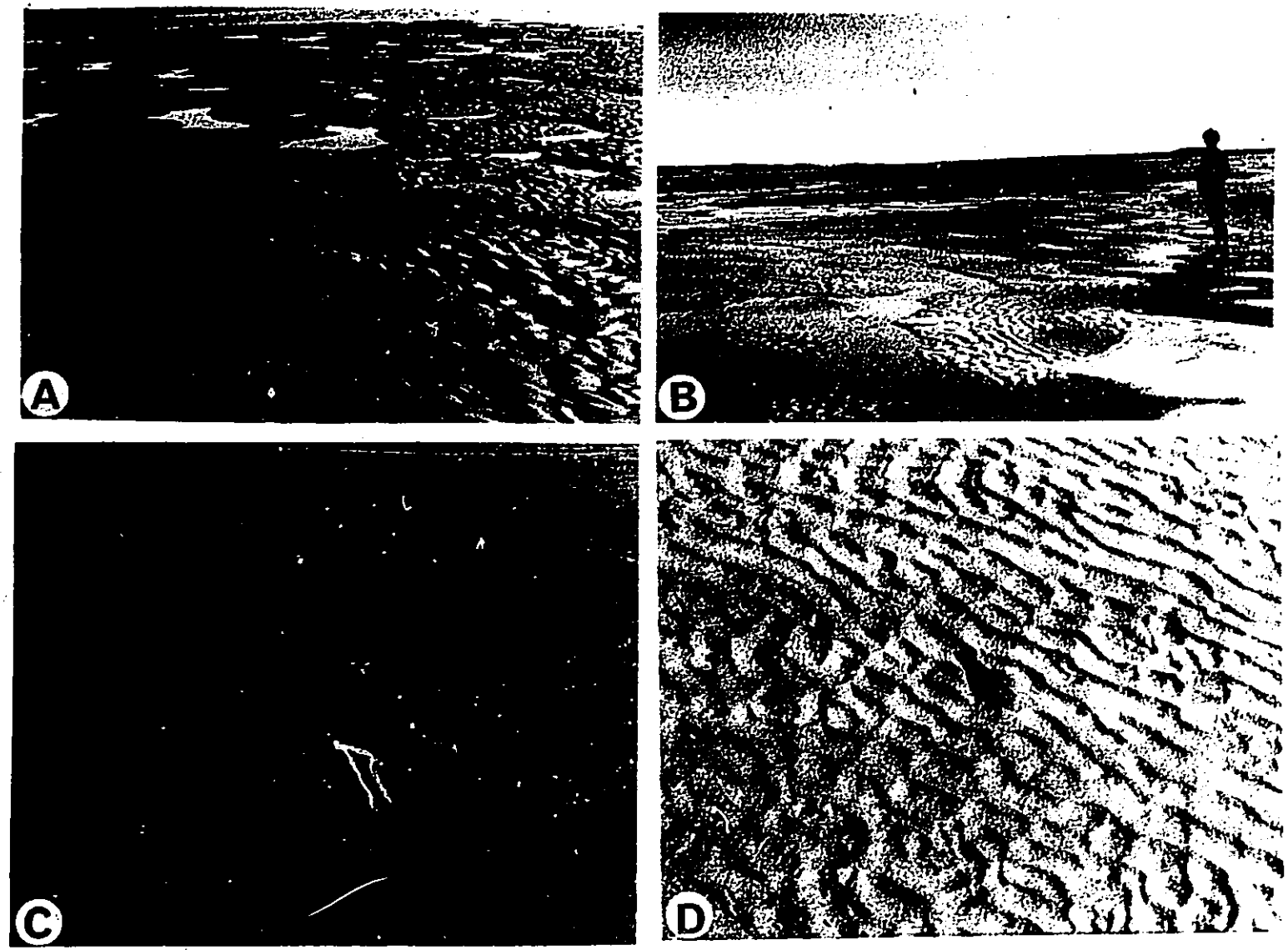
A
B
C
D

direction, there was a systematic change from highly planed-off incipient megaripples (Figure 4-33B) or a transitional zone (Figure 4-33C) through long-crested asymmetrical wave-ripples (Figure 4-33D), to wave-swashed plane beds at the water edge. Away from large tides, megaripples ceased to be active, and were subject to continuous reworking by waves. In small tides, the bar became essentially flat. It was covered largely by wave ripples and swash plane beds. Along the inner portion there were some small bumps, which were reminiscent of previous incipient megaripples (Figure 4-34A).

The internal structure of the south CMLB was basically a combination of small-scale current- and wave-produced structures in varied proportions (Figure 4-35). Corresponding to the surface forms, two types of ripple cross-lamination were recognized. Cross-lamination formed from current-ripples was centimetre-scaled (1-2 cm). It had sharply defined, well-oriented foresets, and rather regular set boundaries (XL, Figure 4-35A). The foresets were concave-upward, and had well developed tangential bottomsets. A few cross-beds dipping in opposite directions were seen (herringbone structure). Cross-lamination of wave ripples was millimetre-scaled. It had a crinkled appearance with faint and wavy foresets and set boundaries in many examples (WL, Figure 4-36A and C). The crinkled appearance is due to lack of persistent dips related to varied

Figure 4-34 South channel margin-linear bar.

(A) Surface feature of the inner portion of the bar flanking the marginal channel (background) near small tide, 1986.

(B) Landwardmost swash bar flanking the seaward margin channel, 1987, looking seaward in northeast direction. Landward migration of swash bar has caused near closure of the marginal channel, and seaward progradation of the beach on the downdrift side. The foreground is the barrier beach of the south spit. The bar surface was covered by wave ripples at the time the photo was taken. Spade-core locations of Figure 4-36 are shown.

(C) Swash bar flanking the main channel (foreground), 1987, looking seaward in east direction. Bar surface is completely flat due to swash action.


A

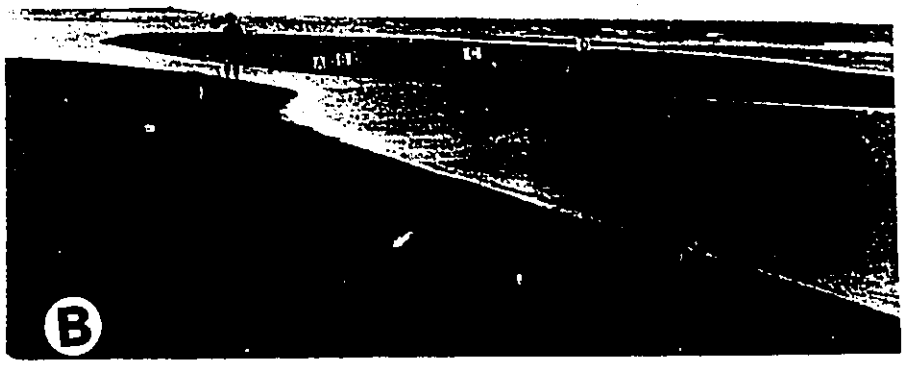
B

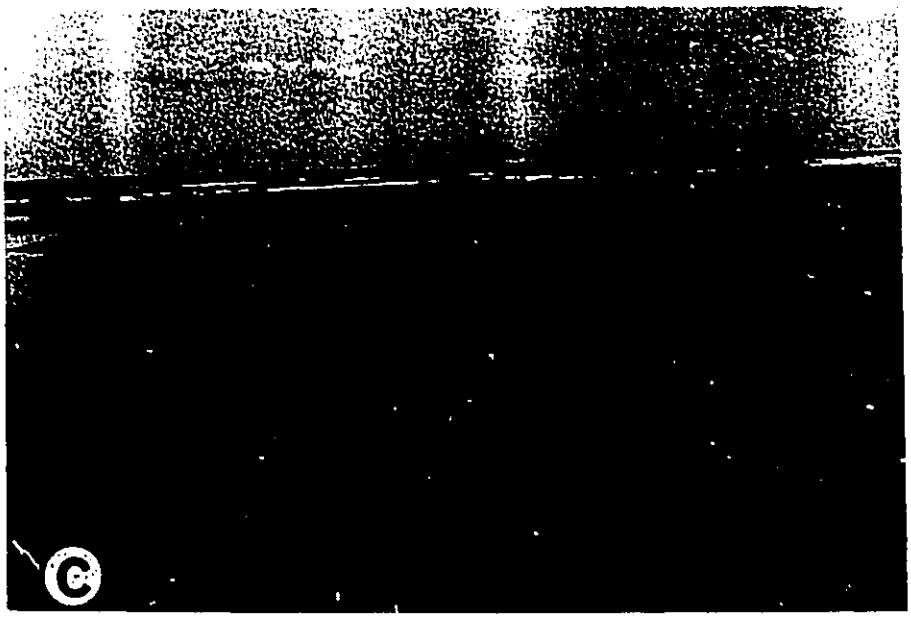
C

Figure 4-35 Resin peels from various fields of the south channel margin linear bar depicted in Figure 4-32. A to D corresponds to 4 to 7 in Figure 4-1B, respectively. Structures are labelled: XL = current-ripple cross-lamination; WL = wave-ripple cross-lamination. See text for the difference between the two types of cross-lamination. Land to the left.

(A) Incipient megaripple field, showing small to medium scale cross-lamination. Note herringbone structures (bidirectional dips).

(B) Transitional zone showing dominance of wave cross-lamination (crinkled). Current-ripple cross-lamination still exists, and swash-lamination begins to occur.

(C) Wave-ripple field, showing crinkled wave cross-lamination, and swash parallel lamination increasing in amount. Set boundaries between different units are numbered. The bottom set of cross-beds is interpreted as small swash bar structures. The boundary is erosional, but are hardly noticeable due to lack of grain size contrast.

(D) Plane bed field, seaward water edge, showing dominance of swash-lamination, and two sets of small swash bar deposits similar to that in (C); note their foresets decreasing in dip upward.

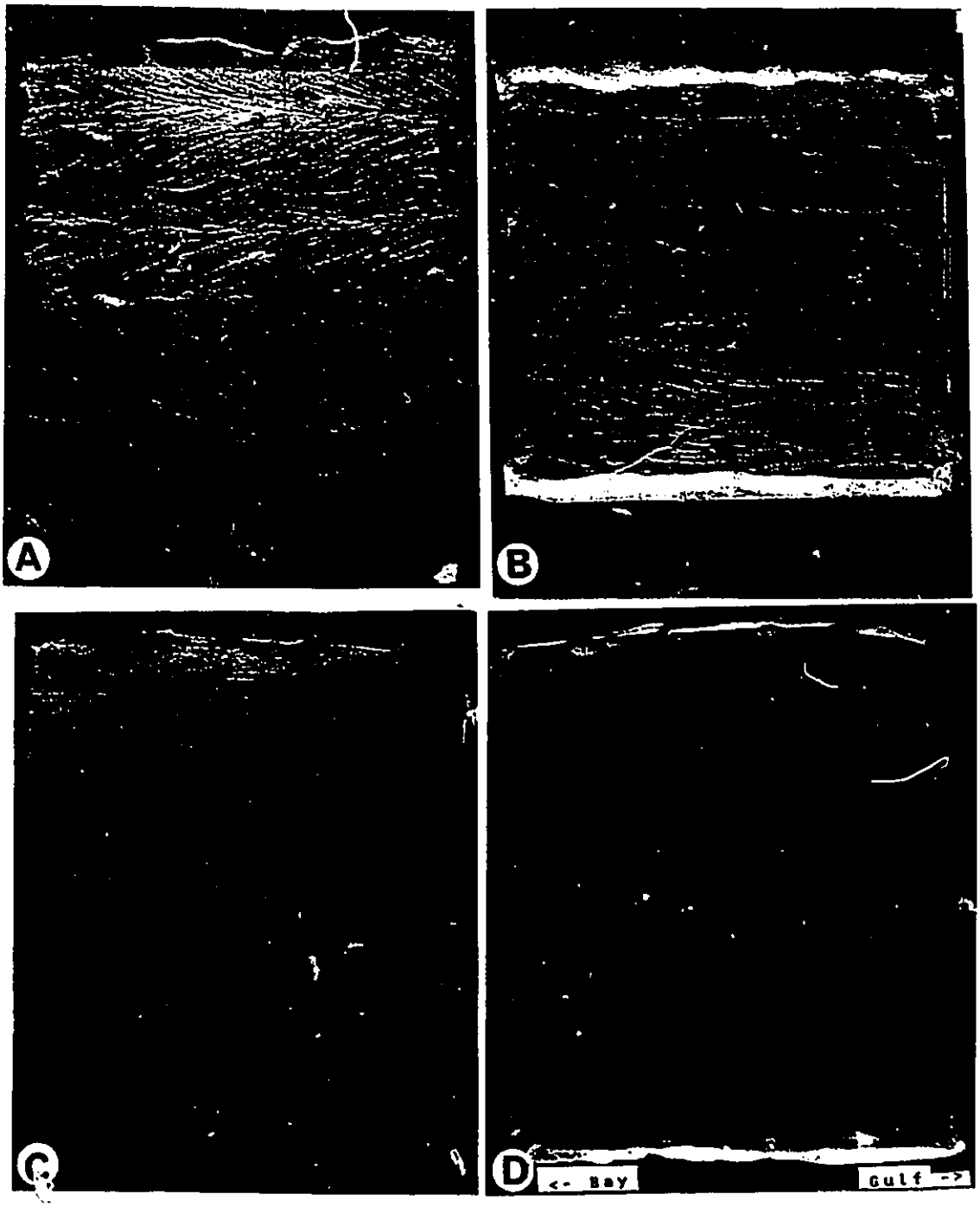
A
B
C
D
<- Bay
Gulf ->
9

Figure 4-36 Selected resin peels from the landwardmost swash bar, south channel margin bar. For locations see Figure 4-34B. Land to the right.

(A) Landward dipping slipface-foresets, under the bar crest. Dips are 15°-25°. Ripple cross-lamination can be observed beneath the foresets.

(B) Slipface foresets, two metres seaward of the bar crest. Note the top layer has been reworked into parallel lamination by waves.

(C) Stoss-side, six metres seaward of the bar crest, showing dominance of stossface parallel lamination. Note a set of slipface occurred at the bottom.

(D) Stoss-side, eleven metres seaward of the bar crest, showing dominance of stossface deposits. Wave ripple cross-lamination occurred at the top and at the bottom.

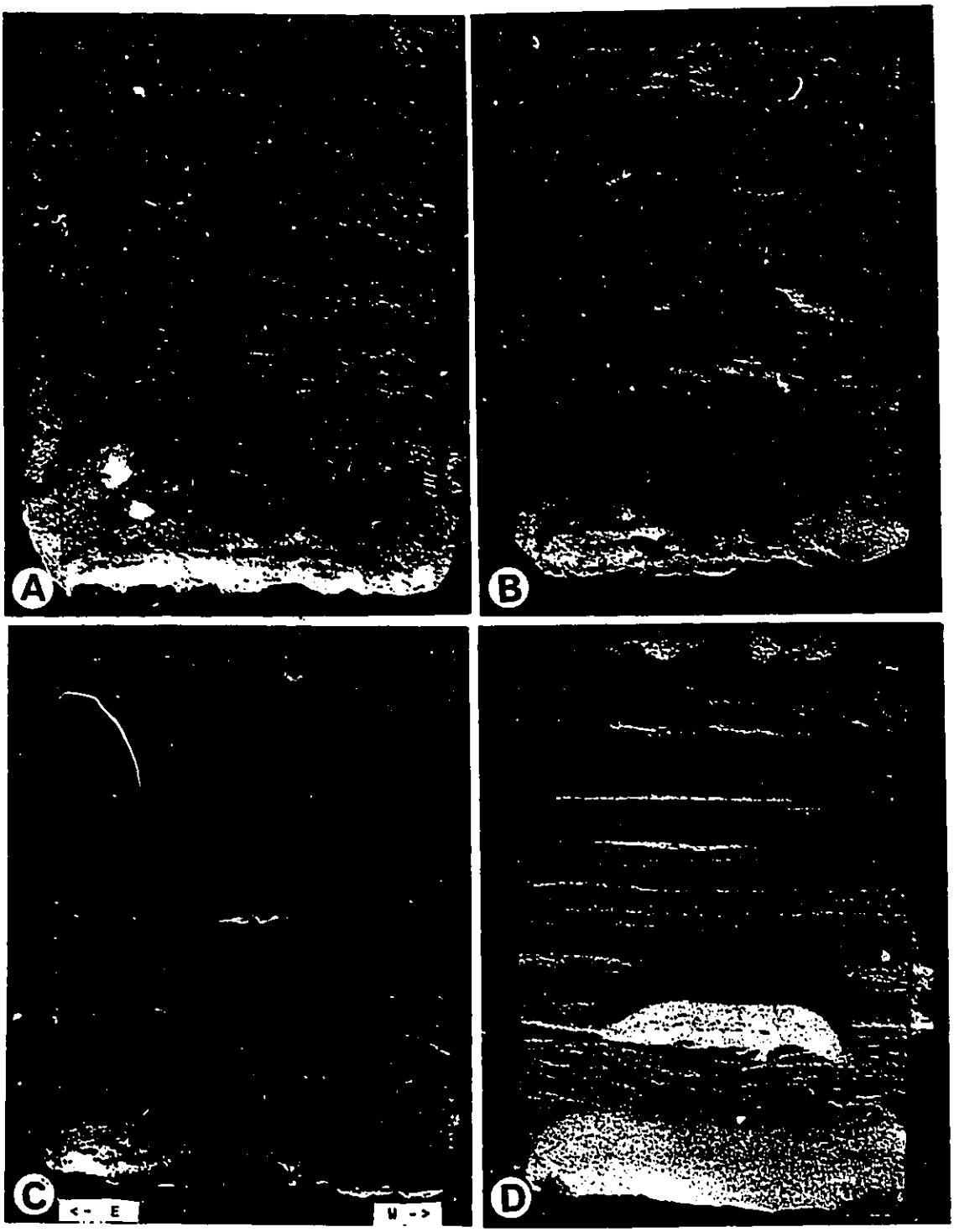
A
B
C
<- E
W ->
D

migration direction of ripples with changing wind conditions.

As with surface features, the internal structure showed a systematic change across the bar. Close to the channel, current cross-lamination with herringbone structures was the dominant structure; wave cross-lamination occurred as intercalations (Peel A). These structures were replaced by crinkled wave-ripple cross-lamination in the middle (Peel B). At this location, current cross-lamination still existed but with reduced size and proportion, and swash-lamination began to occur. Further seaward, they were gradually replaced by swash-generated structure, including plane-beds and swash bar foresets (Peel C), which became the dominant structures at the water edge (Peel D). An interesting structure is the fan-shaped bundles in Peel C and D. These bundles consisted of landward-oriented foresets, sigmoidal in shape and decreasing upward in dips. Similar structures have been reported from modern tidal as well as recent coastal deposits (Boersma and Terwindt, 1981; Beets, et al., 1981). The former authors explained them as a variant of megaripple cross-bedding formed from an abrupt change from foreset (full vortex) deposition to suspension (deceleration) deposition. Beets et al., on the other hand, considered them as wave products. They maintained that such features were formed behind the leeface of migrating coastal ridges under wave-induced upper flow-

regime conditions. Such conditions undoubtedly can occur at Palmer Inlet as waves surge over the seaward edge of the bar. This produces sediment-laden flow which quickly fill in the trough of swash bars at the water edge.

In 1987, with net sediment accumulation on the bar, the entire bar changed into a multiple swash bar complex (Figure 3-2C and D). The sediment input is in the form of swash bars. Formed on the distal part of the platform, the swash bars migrated toward the land, and gained more intertidal exposure. They slowed down and coalesced to form larger bars close to the shoreline, and almost closed the marginal channel (Figure 4-34B). The swash bars in the intertidal zone were lobate in shape, had a gentle seaward slope (2-4°) and a steep landward dipping slip face (26-34°), and were separated from each other by a wide shallow trough. Depending on wave conditions, the bar was either smooth (Figure 4-34C), or covered with wave-ripples (Figure 4-34B).

Two sets of spade-cores (altogether 16) were made on the two landward most bars, among which four were selected for illustration (Figure 4-34). These cores (Figure 4-36) revealed typical swash bar structures (Hayes, 1972; Van de Berg, 1977). These include high-angle (21-27°) landward-dipping foresets of slipface deposits (A and B), restricted to 1-2 m of the crest area, and more abundant low angle seaward-dipping parallel lamination of stossface deposits (C

and D). Since the ratio between these two types of structures depends on the rate of landward migration of the bar with respect to that of reworking by swash and backwash, the small proportion of slipface deposits indicates that swash bar migration at Palmer Inlet was generally low. Nonetheless, they have been found preserved beneath the surface, as shown at the bottom of Peel C. In other cases, underlying the stossface lamination was crinkled wave ripple cross-lamination (D). Basal cross-lamination representing current ripple migration in the bar trough has been found (A). In general, it was poorly developed and absent from most of the cores.

Vertical Sequence One tube core was taken on the south CMLB. It was located in the trough of the landwardmost swash bar facing the closing marginal channel (Figure 4-24c). The core reached the mud deposits at 1.65 m below the mean water level without encountering lag deposits. The overlying sand deposit is interpreted as representing a filling-in sequence of the marginal channel by swash bar deposits. The sequence began with dark mud with similar size characteristic as the modern bay deposits (Figure 4-37), progressed up through medium-scale, tidal current cross-bedding, and was topped by steep, slipface-foresets dipping toward the channel. The middle interval of the sequence is the deposits of tidal current within the marginal channel. It showed an upward decrease in scale and

Figure 4-37 Grain size data of a tube-core in the trough of the landwardmost swash bar (c of Figure 4-24). Sample locations are indicated in the core. Mz = mean size; STD = standard deviation.

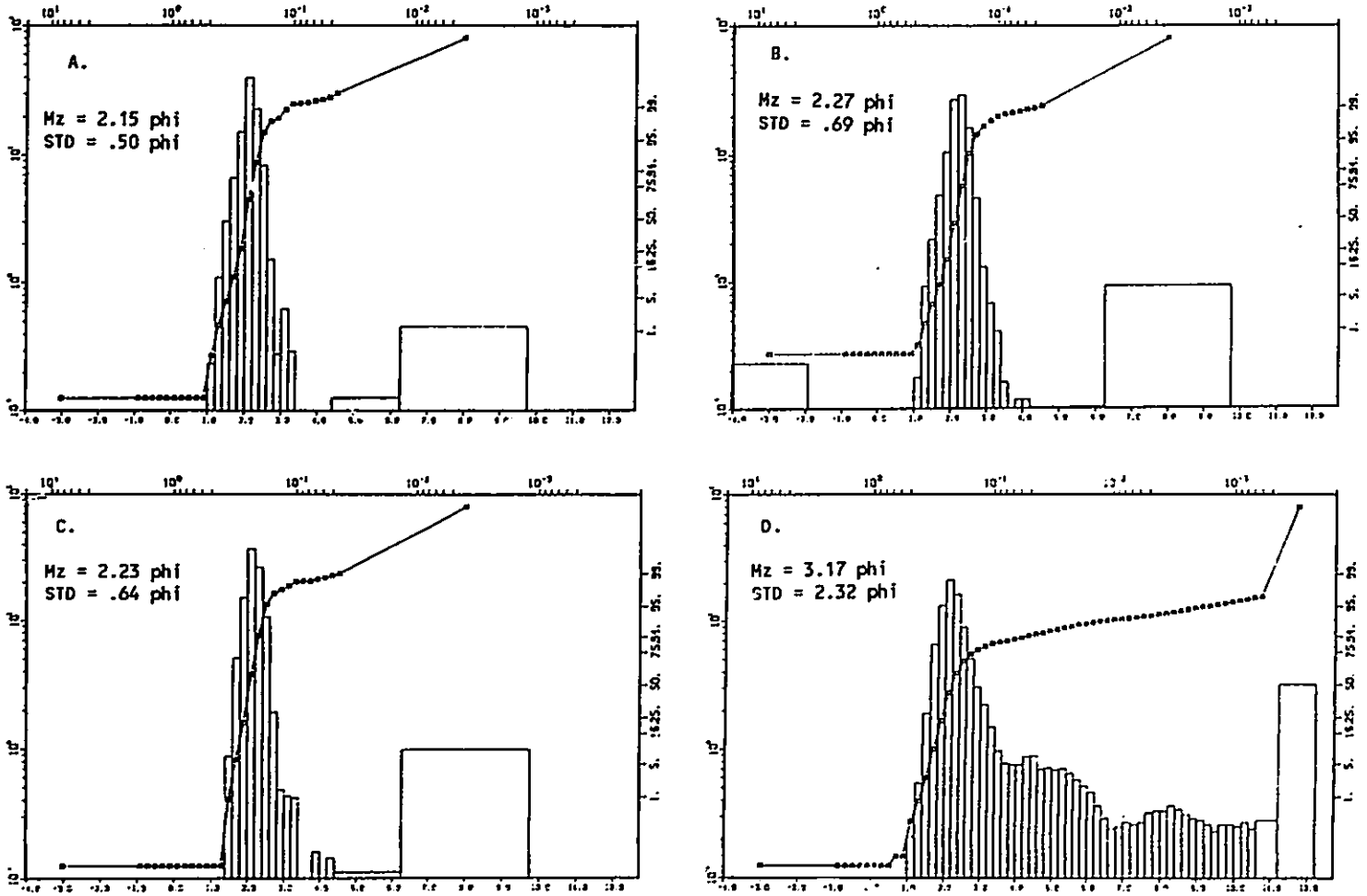
A.
Mz = 2.15 phi
STD = .50 phi
B.
Mz = 2.27 phi
STD = .69 phi
C.
Mz = 2.23 phi
STD = .64 phi
D.
Mz = 3.17 phi
STD = 2.32 phi

clarity of stratification. This is interpreted as reflecting the gradual dying-down of currents in the channel with the sealing-up of the marginal channel. The decreasing flow produced no bedform-related structures but allowed fine material to settle out. The grain size data also indicate that the uppermost swash bar sediments are relatively coarser and well-sorted (Figure 4-37).

Bedforms of the north channel margin linear bar

Figure 4-38 shows a large to small tide variation of surface features of the north CMLB bar in 1987. Some corresponding examples are given in Figure 4-39. The conditions in 1986 were similar. In general, the outer portion and seaward end of the bar were covered with small ripples throughout the cycle. On the upwind margin, there always existed a zone of flat bed produced by swash. Along the inner portion, tidal currents were strong enough to engender large-scale bedforms in large tides, but could only produce small ripples range in small tides. Accordingly, the surface changed from essentially megaripple-sculptured (Figure 4-39) to totally flat with small ripples and swash plane beds (Figure 4-40). In large tides, megaripples were Type II forms on the landward end, averaging 2.34 m in wavelength, 0.18 m in height (Figure 4-39A), and with very irregular crest pattern. They changed to Type I forms with wavelength of 2.7 m and height 0.18 m in the middle (Figure 4-39B). They had straight-crests, and were oriented perpendicular to the

Figure 4-38 Bedform distributions for large, intermediate, and small tidal conditions, north channel margin linear bar, 1987. The inset shows approximate locations. Some examples of bedforms are shown in Figure 4-39 and Figure 4-40. Note that megaripples on the inner portion of the bar replaced by ripples on the outer portion and seaward end. In small tides, the bar surface is essentially flat.

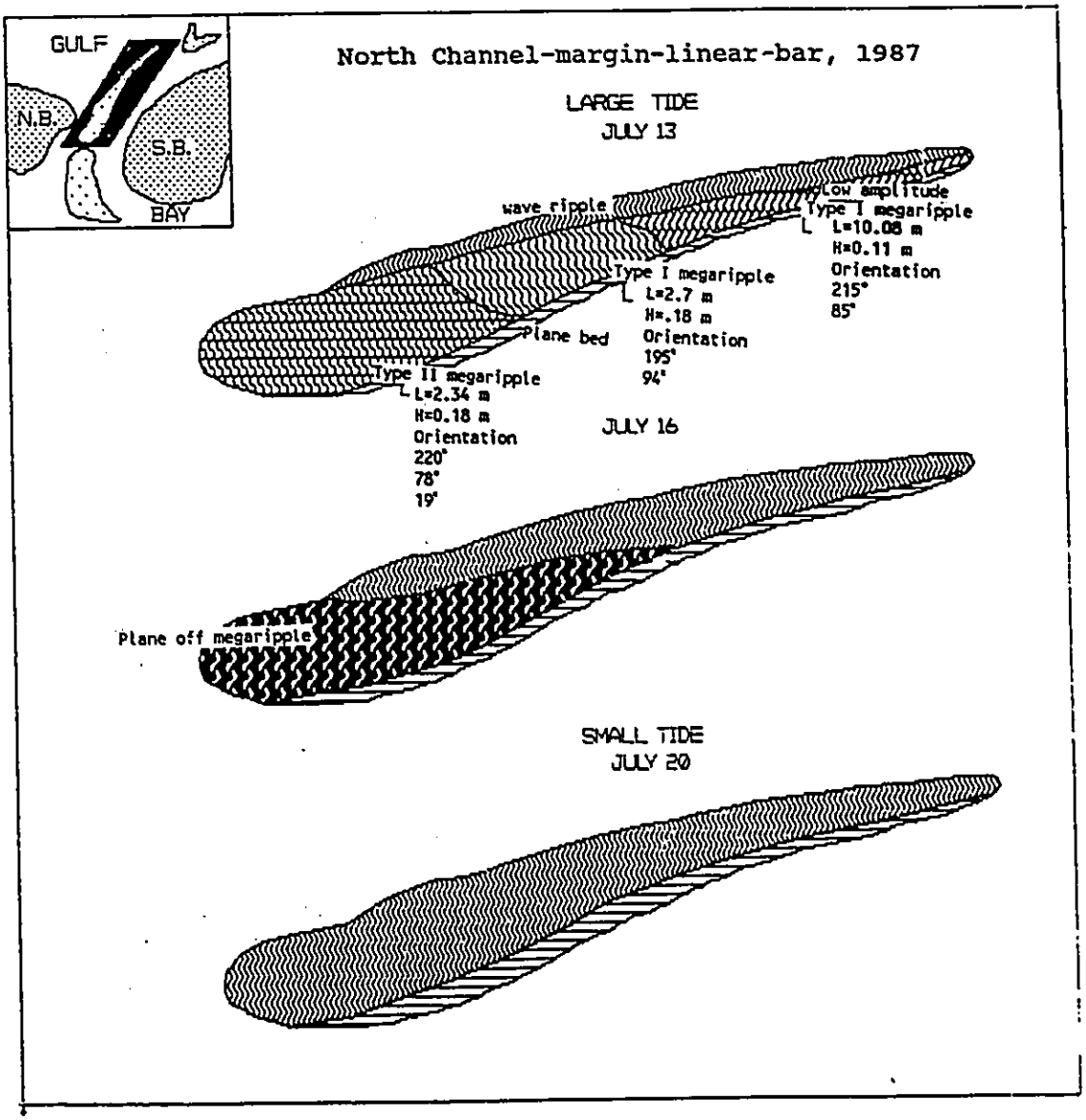
GULF
N.B.
S.B.
BAY
North Channel-margin-linear-bar, 1987
LARGE TIDE
JULY 13
wave ripple
Low amplitude
Type I megaripple
L=10.08 m
H=0.11 m
Orientation
215°
85°
Type I megaripple
L=2.7 m
H=.18 m
Orientation
195°
94°
Plane bed
Type II megaripple
L=2.34 m
H=0.18 m
Orientation
220°
78°
19°
JULY 16
Plane off megaripple
SMALL TIDE
JULY 20

Figure 4-39 Representative examples of bedforms along the inner portion of the north channel margin-linear-bar, 1987. Bedforms are ebb-oriented. View toward the Bay. Main channel on the left hand side.

(A) Type II megaripples, landward end. Note the irregular pattern of crests.

(B) Type I megaripples, central portion. Note that megaripples die out toward right (outer portion of the bar), and change into ripple field (see Figure 4-38). Megaripples are oriented perpendicular to the main channel, and are planed off by waves. Falling-wave-level marks, and ripples formed by late-stage drainage in the trough can be seen.

(C) Same location as (A) but formed in a smaller tide. The Type II megaripples are smaller, and have more regular orientation. Superimposed on megaripples are current-ripples, and ripple-fans in the troughs formed before emergence.

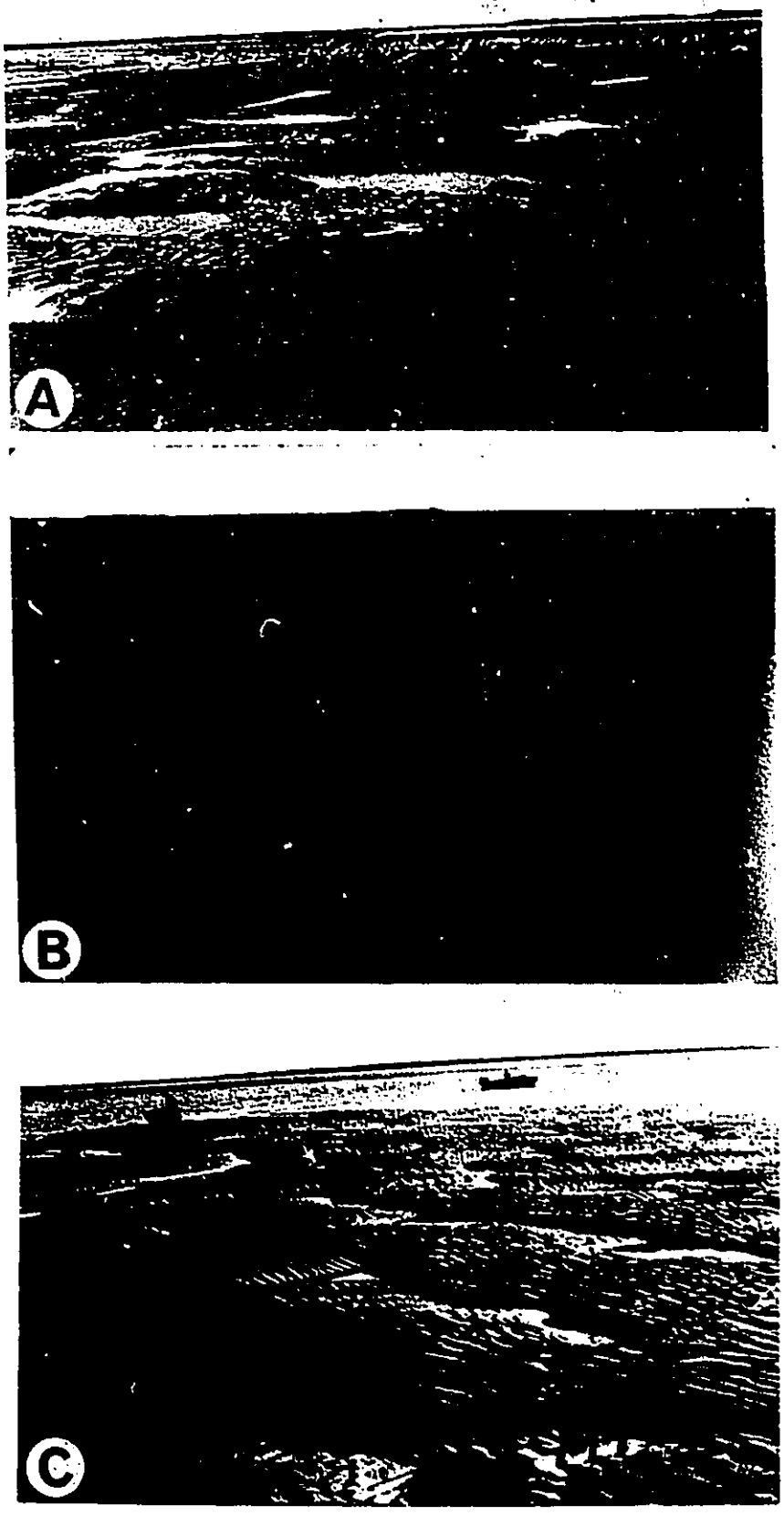
A
B
C

Figure 4-40 Surface feature, small tide, north channel-margin linear bar, 1987. View toward the bay. Main channel on the left side. Shovel 65 cm long.

(A) Near flat surface with megaripple relics. Plane-bed at the water edge indicates wave direction.

(B) Flat surface covered with wave-ripples and swash plane-bed at the water edge.

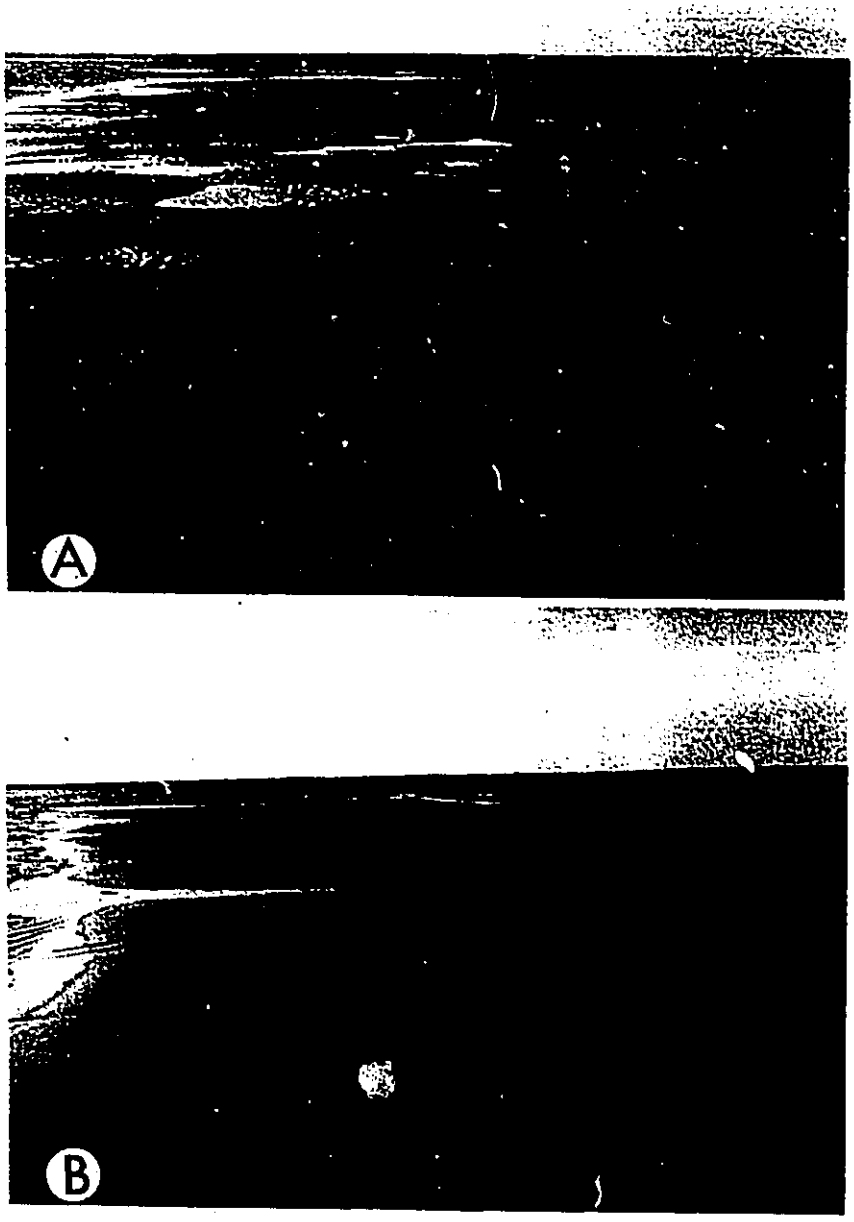
A
B

channel. Toward the seaward end, they further changed to very low-amplitude forms with wavelength of 10 m and height less than 0.11 m. The irregular pattern of Type II megaripples on the landward end was caused by superimposition of more than two sets of intersecting forms with different orientations. This was due to change in flow direction during the ebb tide. The early ebb from the South Channel was able to flow across the bar in NE direction while the tide was still high. It took a more and more easterly direction with the ebb until it became confined by the channel. As the process is controlled by the tidal range, megaripples in smaller large tides (4-39C) were not only less energetic, but also had generally only one orientation, perpendicular to the nearby channel. Late-stage features, such as breaching of megaripple-spurs, run-off microtidal deltas, small current-ripples formed by drainage in the trough, rill-marks and water-level marks, were observed in this area at low tides. Rounding-off of megaripple crests by waves also occurred at low tide but with less intensity as compared with the other side of the inlet.

Internal Structure of the North Channel Margin Linear Bar

Peels from Type II megaripple field near the throat consisted of medium- to large-scale trough cross-bedding, separated by erosional planes (Figure 4-41A). Foresets were ebb-dominated. The flood-oriented beds occurred in the same

Figure 4-41 Resin peels from various parts of the north channel margin linear bar, 1987. A to C corresponds to 12 to 15 in Figure 4-1B, respectively.

(A) Peel from the Type II megaripple field, showing large- to medium-scale trough cross-bedding, separated by erosional surfaces. Both ebb- and flood-oriented beds occur but with ebb dominance.

(B) Peel from the Type I megaripple field, showing bidirectional, large-scale tabular cross-bedding. Late-stage wave reworking produced parallel lamination which truncates cross-beds.

(C) Peel from the seaward end of the bar, showing small- to medium-scale cross-lamination with wavy lower boundaries and herringbone structures.

(D) Peel from the outer portion of the bar, showing small-scale ripple cross-lamination with herringbone structure.

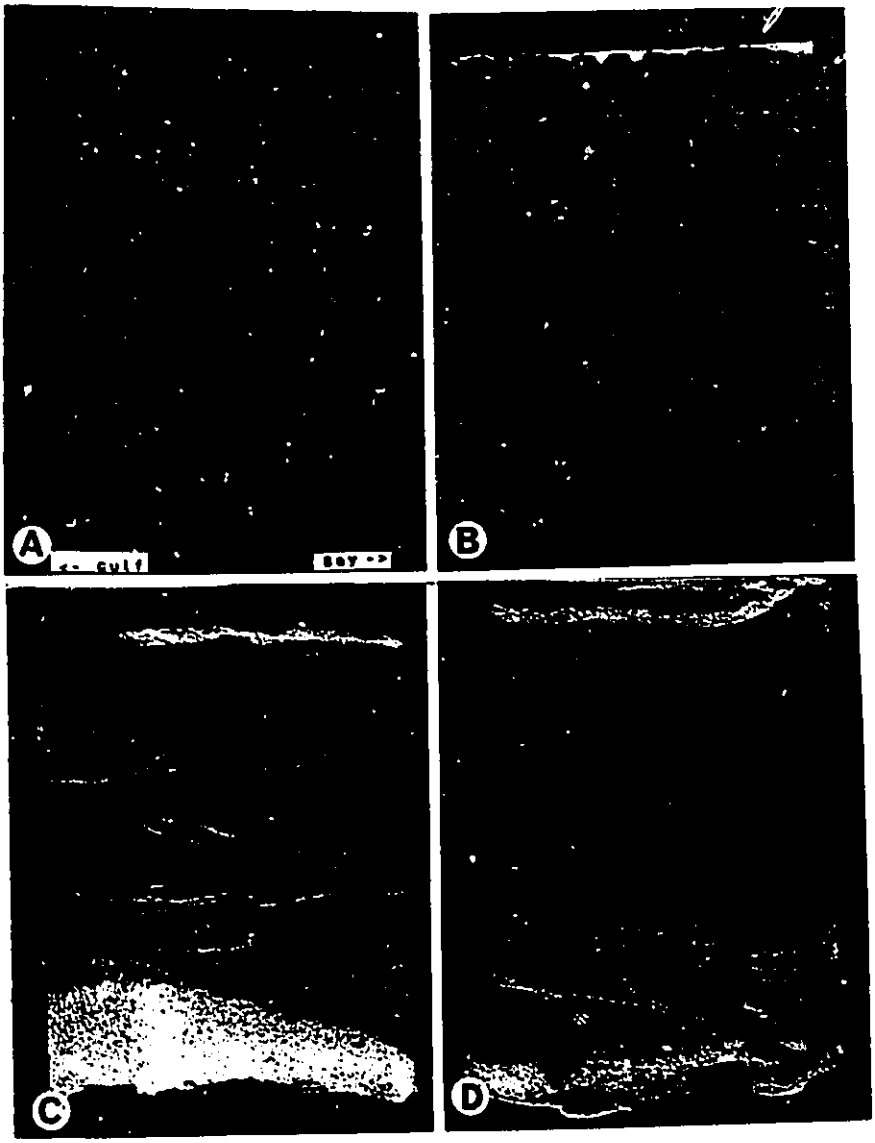
A
B
C
D

level as the ebb set. No reactivation surfaces, however, are observed with superjacent foresets dipping in the same direction. Structures produced by small tides were preserved as centimeter-thick cross-lamination. Peels from Type I megaripple field showed sets of bidirectional, large-scale, tabular cross-beds. Parallel lamination apparently due to late stage wave reworking was found in a few cores, and truncated the tabular cross-beds (Figure 4-41B).

Peels from the ripple field of the seaward end and the outer portion of the bar revealed similar structures (Figure 4-41C and D). The dominant structure was centimetre-scale cross-lamination. The occurrence of herringbone structure, clearly defined concave-upward foreset and well developed tangential bottomsets attest to their tidal current origin. Millimetre-scale wave-ripple cross-lamination occurred but mainly as intercalations. This combination of structures indicates that tidal currents were still the dominant process along the outer portion of the bar even though surface feature suggested otherwise.

Vertical Sequence Tube cores were taken on each end of the bar. The one near the throat was about 0.85 m length, and was taken on the leading slope of the bar just below the low water edge (D of Figure 4-23). Texturally, it consists of fine-medium sand with abundant shell fragments. Structurally, it can be divided into two parts. The upper 0.32 m consisted of large-scale cross-sets. They are

interpreted as avalanche-type foresets, formed as sediments moving landward across the surface of platforms and avalanched down the leading slope. The process is similar to that observed by FitzGerald (1976) at Price Inlet, North Carolina, as swash bars moved onto the CMLB, and were truncated by tidal currents. The lower part of the core consisted of sets of bidirectional, large-scale trough cross-bedding. They are interpreted as tidal cross-bedding, formed by Type II megaripples migrating along the channel bank. The entire sequence thus reflects lateral migration of the inlet as the platform was built and prograded into the main channel. The core taken near the seaward end of the bar was similar but revealed a more complete sequence of inlet migration than the previous core (Figure 4-24f). The core is significant because it is the only core on the updrift side, which reaches the mud substrate. It reached a thin layer of shell lag deposits underlain by the mud deposit at 2.6 m below the mean water level. The overlying sandy deposit was similar to that on the other end in that the upper layer consisted of well developed cross-sets, representing bar-front foresets of the platform. Underlying it there were two sets of cross-bedding. While it is impossible to determine the dip, their appearance suggests that they were produced by megaripples. Below that occurred massive sand, as well as some less-well defined stratified sand at the bottom. Their appearance suggested that they

were small-scale structures, probably cross-lamination and/or parallel lamination. The entire sequence records a complete sequence of events taking place in the course of the main channel moving into the position. When the channel was still to the north, the coring area was an environment in which wave action was important. As the channel moved into the area larger bedform structures were formed by the relatively strong current on the seaward end of the channel. This was succeeded by deposition at its leading edge of the spit platform.

It is noted that in both cores, bar-front foresets were in direct contact with channel cross-beds. The implication is that the shallow channel unit consisting of plane-beds of Fire Island Inlet model (Kumar and Sander, 1974) is absent at Palmer Inlet.

4.5 Spit Platforms

Processes Spit platforms were covered by about 1 m of water at low water, and constantly subject to combined tidal currents and wave processes. Currents measured on both sides of the inlet showed similar time-velocity curve with flood dominance. Typical curves are given in Figure 4-42. On the downdrift side (Station 64-III), the flood current reached about 0.39 m/s for intermediate tides, and ebb current reached about 0.17 m/s. A lower flood to ebb ratio was observed for currents on the north spit platform

Figure 4-42

(A) Time series of current velocities and bay tides, Station 64-III, south spit platform. For location see Figure 2-17.

(B) Time series of current velocities, bay tides and tidal difference between bay and gulf tides, Station 64-IV, north spit platform. For location see Figure 2-17. Also shown are sediment transport rate, and strength index and velocity asymmetry curves(C).

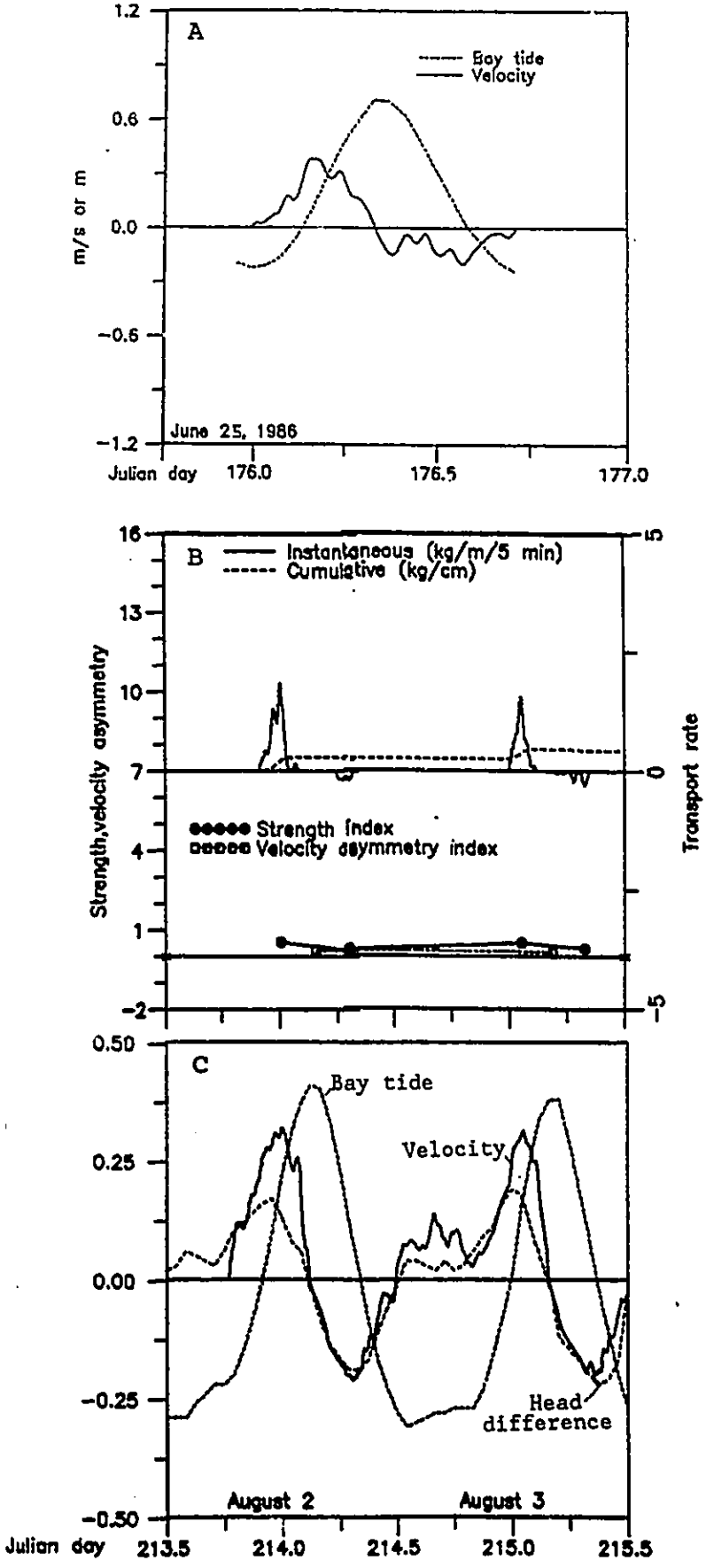
A
Bay tide
Velocity
m/s or m
1.2
0.6
0.0
-0.6
-1.2
June 25, 1986
Julian day
176.0
176.5
177.0
B
Instantaneous (kg/m/5 min)
Cumulative (kg/cm)
Strength,velocity asymmetry
Transport rate
16
13
10
7
4
1
-2
5
0
-5
Strength index
Velocity asymmetry index
C
Bay tide
Velocity
Head difference
0.50
0.25
0.00
-0.25
-0.50
August 2
August 3
Julian day
213.5
214.0
214.5
215.0
215.5

(Station 64-IV). This is probably due to the fact that the platform on the updrift side was influenced by flow from the North Channel, while the downdrift station was located in the front of the south CMLB, which shielded the area from the ebb. Tidal currents on spit platforms are hence within the small ripple bedform stability field.

Waves were important on the spit platform simply because of the proximity to the gulf, and because of constant submergence at small water depths. For the same reasons mentioned in the previous section, waves were more active on the south platform. Large waves with height 0.5 m or over were observed to break around the outline of the ebb lobe, and shoaled onto the platform. Flattening of wave orbit during the shoaling process resulted in a net land-directed sediment transport. The superimposition of waves on tidal currents has been observed to cause an increase in bottom shear stress (Bijker, 1967) and a lowering of the threshold of sediment movement (Hammond and Collins, 1979), thus increasing the rate of sediment transport (Heathershaw, 1981; Pattiaratchi and Collins, 1983). In the present situation, the forward orbital motion of shoaling waves assisted the flood phase but retarded the ebb phase. Such enhancements are expected to be most effective near low water periods, when depth is small and tidal currents are weak (Bijker, 1967). The flood dominance indicated by current records did not include the component of wave

enhancement. It is considered that the rotor of current meters was unable to response to the high frequency wave oscillations. Even if it did, they would have been suppressed by digital filtering.

Texture Seven samples were taken from the spit platforms including the CMLB. These samples resembled the deposits of inlet channels almost in every aspect. On scatter diagrams, these two environments cannot be separated by any parameters. In average values (Table 4-1), they are relatively coarse (2.06 ϕ), well-sorted (0.36 ϕ), nearly symmetric (0.49) and peaked in the central portion (9.75). Three of the seven samples have all three populations with similar relative proportions (GZ-20, Figure 4-16). In particular, the S population of six samples consists of a gentle and a steep segment.

Bedforms of Spit Platforms Wave-ripples were ubiquitous on the subtidal platform. They were 0.02-0.04 m in height, 0.11-0.28 m in length, and mostly symmetrical. Large bedforms were wave-generated swash bars. Swash bars were formed in the distal part of the platform, and migrated toward the land under the influence of the residual shoreward motion of shoaling or breaking waves.

Internal Structure Only three tube cores are available for spit platforms, and none of them reached the mud substrate. The one from the downdrift side was located just in front of the south CMLB at the water edge (Figure 4-24d). It was

0.98 m in length. The sequence consisted of clean, fine sand with few shell fragments. The structure was dominated by small-scale cross-lamination of crinkled appearance, representing deposition of wave ripples in a shallow, nearshore environment. Near the top, there were some cross-sets. Based on the location and their landward orientation, they are considered as the foresets of swash bars. Similarly, the cross-set overlying them but with opposite dips are interpreted as the stossface swash-lamination of swash bars. The entire sequence reflects changes in deposition associated with a shoaling bathymetry in a wave-dominated environment.

Two cores were taken on the north platform. The one on the entrance side (Figure 4-24g) revealed a structure sequence with the lower part consisting of large-scale foresets, similar to the bar-front type foreset revealed on the present edge of the channel margin linear bar. The sequence is therefore interpreted as the preserved lateral migration deposits of the platform. The dominant structure of the upper part was small-scale cross-laminae, representing wave- or combined-ripple products, and some large-scale, high-angle planar beds, interpreted as slipface foresets of swash bars. This part is interpreted as representing the vertical accretion of the platform under water. With the lower part representing avalanching deposits of the platform, the core thus confirms

observations by Meistrell (1972) on the growth sequence of spit and spit platform in a wave tank. Meistrell (1972) demonstrated that the growth of the subtidal platform was characterized by alternation of lateral growth as avalanche-foresets from longshore drift deposited at the head, and vertical accretion of the platform as topset beds.

Similar growth dynamics of platforms can be used to explain the core from the landward side of the platform (E of Figure 4-23). The upper portion of this core consisted of crinkled small-scale cross-lamination. This is interpreted as the topset bed of the platform, equivalent to the upper part of the previous core. The structure of the lower portion was not well developed. Medium- to large-scale cross-stratified sets could, however, be recognized. Their bidirectional dips suggest that they were probably megaripple products. The difference observed between the above two cores suggests that avalanche-foresets of the platform may not necessarily be preserved.

4.6 Flood Tidal Delta

Processes The flood tidal delta was subject to combined tidal and wave action. In comparison with the spit platform, the overall tidal and wave energy levels it experienced were relatively low. Overall, tidal currents were dominated by the flood, and decreased bayward due to the expansion of flow and the resistance provided by the

delta. Relatively high velocity occurred in the proximal part near the throat, especially those areas flanking the main channel and local tidal creeks. Station 64-V (Figure 4-43B) shows that the proximal part of the delta was exposed to current activity for nearly 12 hours for large tides. Flood currents lasted 7.4 hours, and reached 0.6 m/s. Ebb currents lasted less than 4.0 hours and reached 0.3 m/s. The longer flood duration occurred because the station was located on the lee side of the flood delta with respect to the falling tide. Ebb flow was blocked by the delta shortly after high water, and its duration was accordingly curtailed. No data were available for tidal creeks. The flood-oriented configuration of the spill-over-lobes associated with them suggests, however, that currents there should be flood-dominated. Currents measured at the distal part of the delta (Figure 4-43) showed shortened but similar duration between flood and ebb. Measured maximum currents in large tides were about 0.3 m/s for flood, and 0.2 m/s for ebb. Along the distal part of the delta, currents are thus generally below the level generating active ripple migration.

Waves affecting the delta were primarily produced in the bay, and thus were smaller in dimension than those affecting the platform. The waves could touch the bottom, however, because of the small depth of water. Especially in the late stage before the shoal emerged, the waves could

Figure 4-43

(A) Time series of current velocities, bay tides and tidal difference between bay and gulf tides, Station 64-V, proximal flood tidal delta. For location see Figure 2-17.

(B) Time series of current velocities and bay tides, Station 64-VII, distal flood tidal delta. For location see Figure 2-17.

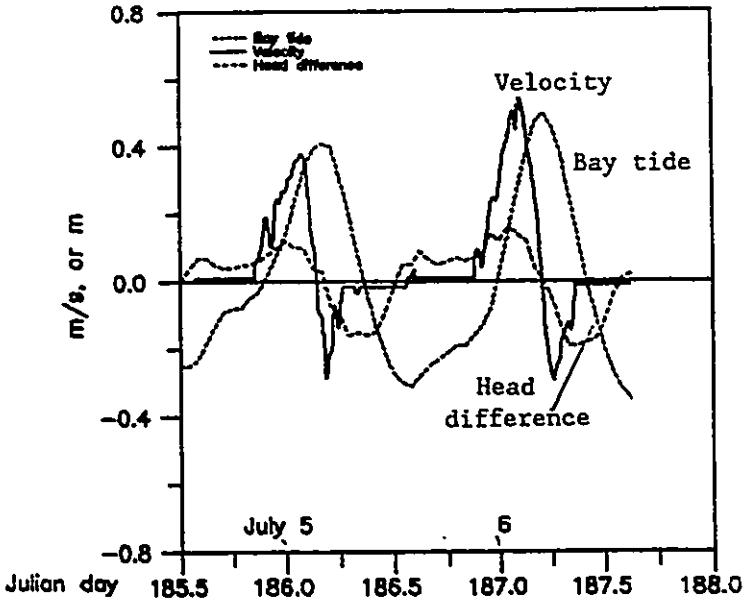
0.8
0.4
0.0
−0.4
−0.8
m/s, or m
Velocity
Bay tide
Head
difference
July 5
6
Julian day
185.5
186.0
186.5
187.0
187.5
188.0

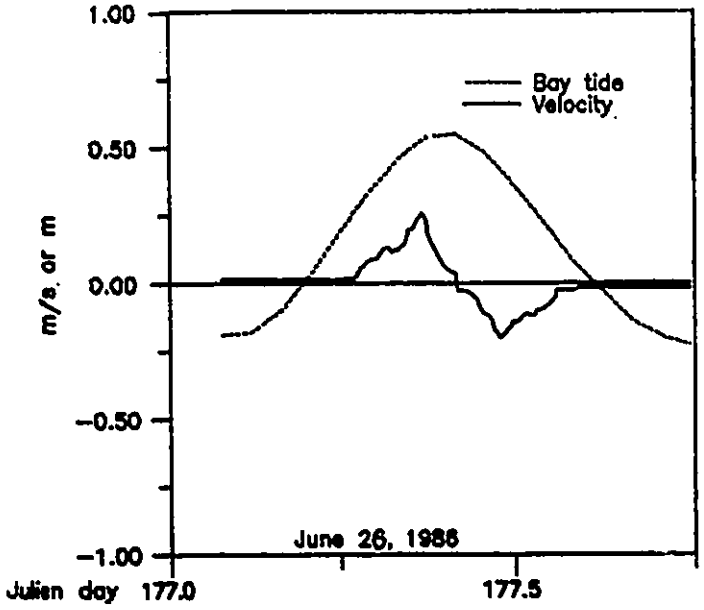
1.00
0.50
0.00
−0.50
−1.00
m/s, or m
Bay tide
Velocity
June 26, 1986
Julian day
177.0
177.5

play an important role in moulding the surface features. Waves from the gulf side can also reach the delta during high waters. As a result, waves on the flood delta were more variable in direction and than those on the spit platforms, and more related to local winds. The association of wave enhancement with a particular phase of tide is not expected on this side of the inlet.

Texture On the average (Table 4-1), the flood tidal delta has, the smallest mean size (2.4 ϕ), the poorest sorting (0.41 ϕ), the largest skewness (0.99) and smallest kurtosis values (5.11). These extreme values are due to the high percent of mud (0.25%) and low percent of gravel (0.05%). On histograms, flood tidal deposits are characterized by a relatively larger fine tail (GZ-2 and GZ-3, Figure 4-16) than deposits of other environments. The C population is missing from the probability plot except in one example, so that the typical grain size curve consists of two populations. In comparison with inlet channels and platforms, the Intermittent Suspension population is lower in content (91%), and the Continuous Suspension population is correspondingly higher (8%). Despite its high content, the S population consists of only one segment, indicating that the flood delta received relatively uniform deposition from suspension.

Bedforms and Internal Structures The most striking feature of the flood delta was probably the small size of the

surface bedforms. Small ripples were the sole form in vast area of the delta. Although limited in size, they were rich in geometric variety. Combined wave-tidal ripples were by far the most common forms. They were 0.08-0.18 m in wavelengths and 0.01-0.02 m in heights, straight-crested, bifurcating, asymmetric and had rounded crests and V-shaped troughs (Figure 4-44A). Symmetric wave-ripples with peaked crests and rounded troughs were also common. They were often found in close association with the above combined-ripples as the latter was reworked by oscillatory waves before emergence (Figure 4-44A). Other variants of small ripples also occurred. Wave-to-wave (Figure 4-44B) or wave-to-current (Figure 4-44C) interaction at high angles produced ladder-back ripples. Orbital motion of waves during emergence could produce flat-crested ripples (Figure 4-45B) by decapitating the existing ripples, or double-crested ripples (Figure 4-44A) by creating new crests with the lowering of water level. Tidal current ripples had very localized distribution as observed at low tides, but were undoubtedly important during flood tides because of the relatively higher velocity. Those observed at low tide were dominantly linguoid forms (Figure 4-45C). They were invariably ebb-directed, and confined to lower surfaces, where late-stage run-off took place. Ripples disappeared on the sand flat behind the north spit. Some relic forms indicated occasional movement (Figure 4-45D). The surface

Figure 4-44 Various types of small ripples, flood tidal delta. Pen measured 12.8 cm long.

(A) Asymmetrical combined-ripples (background) reworked into symmetrical (double-crested) wave-ripples (foreground) on a microtopographic slope.

(B) Ladder-back ripples due to superimposition of two sets of wave-ripples at about 90°. Ripples of both sets are symmetrical with peaked crests and rounded troughs.

(C) Ladder-back ripples due to superimposition of ripples and current-ripples formed by final stage drainage in the existing ripple troughs. Wave-ripple crests are flattened.

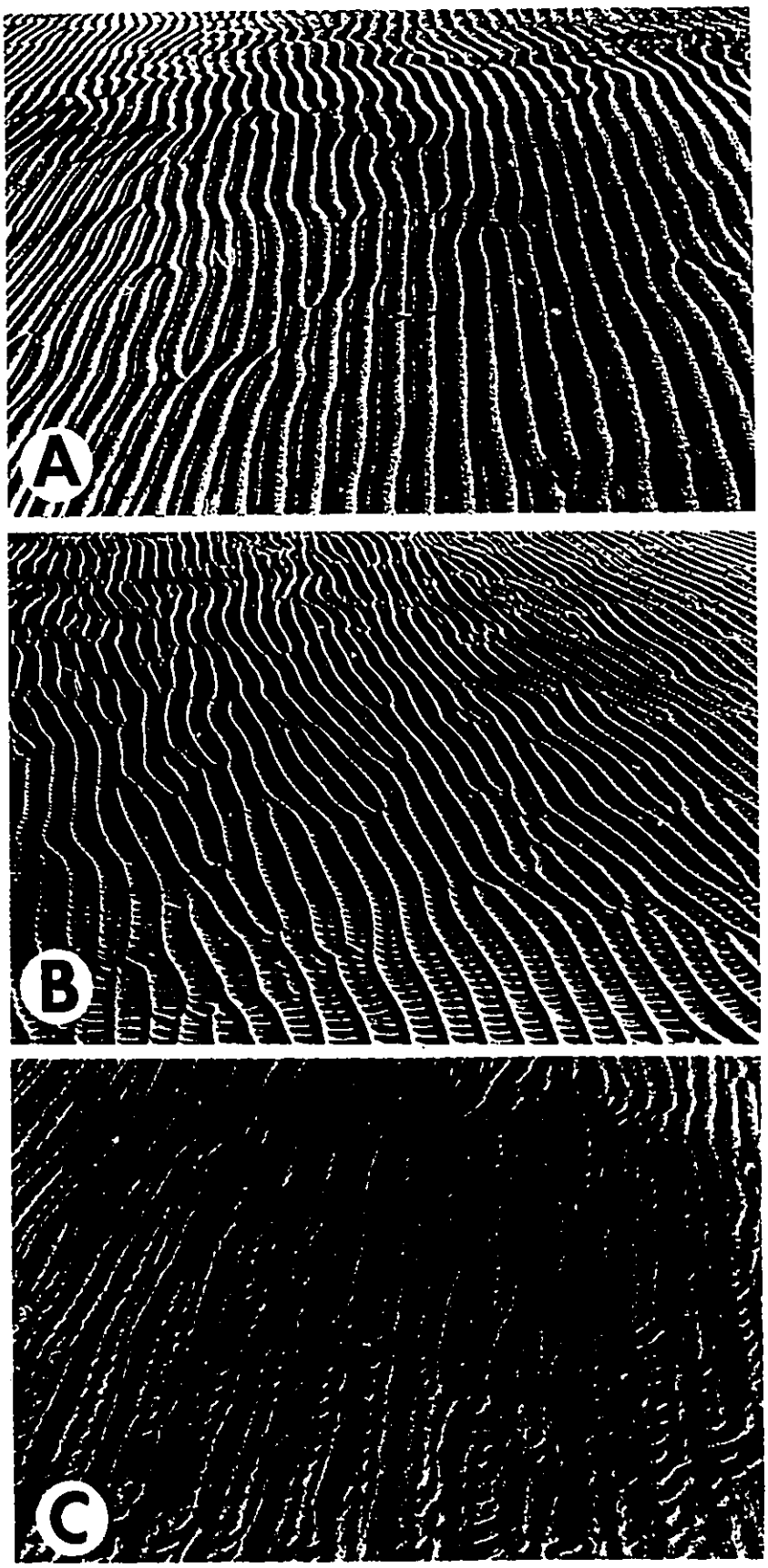
A
B
C

Figure 4-45 Surface features, flood tidal delta. Ball pen 12.8 cm long.

(A) Ladder-back ripples due to superimposition of combined-ripples and current-ripples formed by late stage drainage in the troughs.

(B) Late-stage planed-off small ripples.

(C) Typical linguoid current-ripples with concave stoss faces. Pencil 16 cm long.

(D) Typical surface feature of the flat behind the north spit, showing the algae-bound flat surface. The scale is 15 cm long.

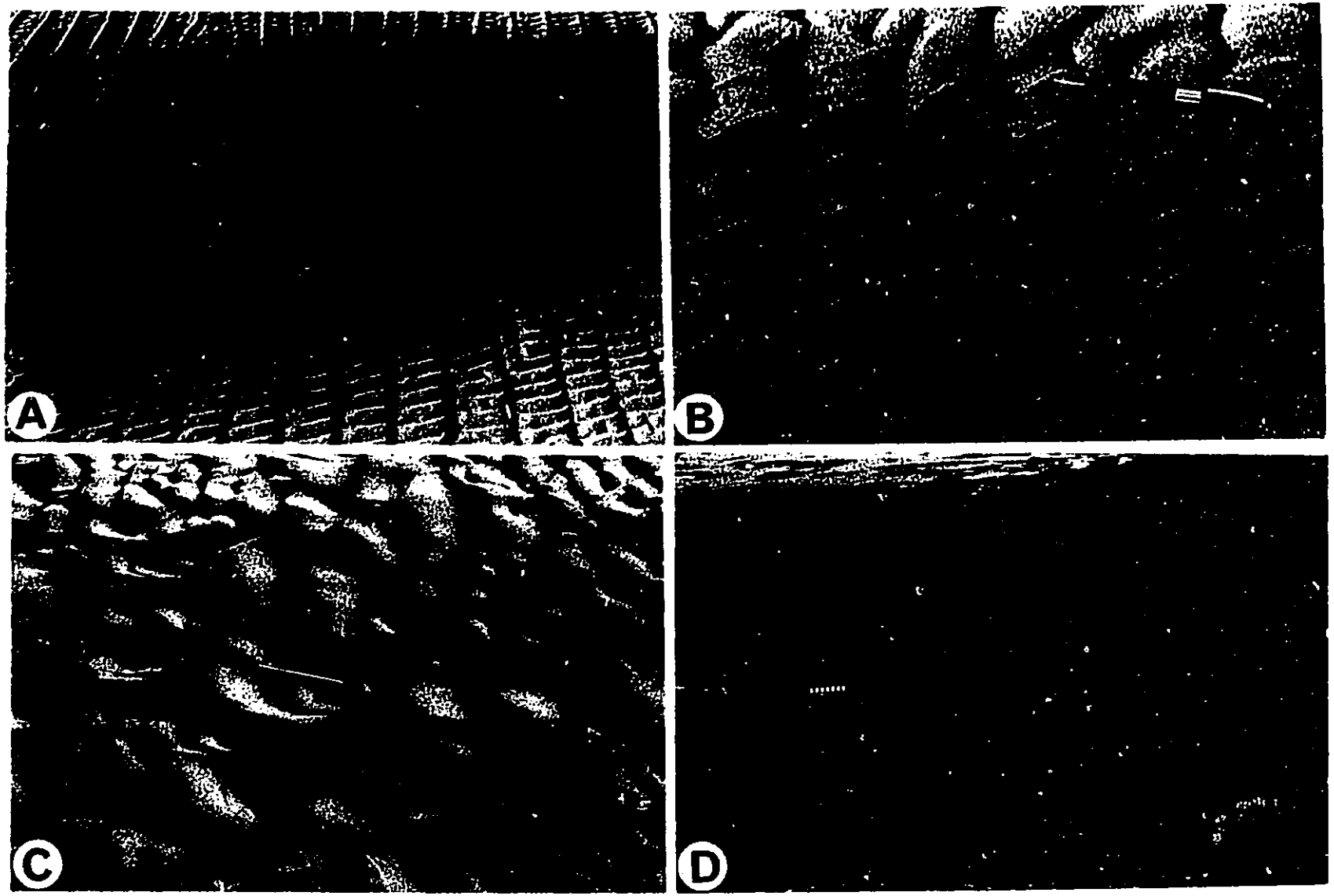
A
B
C
D

here was algal-bound, and hosted a number of sparsely abundant organism. The most common ones included periwinkle (Littorina littorea) and blue mussel (Mytilus edulis), and razor clam (Ensis directus).

Spade-cores taken from various part of the ripple field of the flood delta showed that small ripples were mostly surface features, and were not reflected in the internal structures. Note in Peel B, ripples occurred at the surface but there were no internal laminae. Peels from both the proximal and distal part showed similar structureless sand (Figure 4-46). Trace of lamination did occasionally occur, probably representing relics of structures formed during large tides or more energetic periods. The difference in massive sand between the proximal and distal part was that peels from the former had a warty appearance, while those from the distal part not. This seems to be due to the fact that sands of the proximal delta are relatively well sorted and contain less silt. The good permeability of the proximal sand allows resin to penetrate better, which caused warts during the processes of taking the peel. The peels from the south part showed some relatively well developed cross-lamination (Figure 4-46C). This was because the area was affected by the flow in the South Channel.

Large-scale bedforms were localized along the sides of the proximal part of the delta in areas where, as

Figure 4-46 Resin peels of spade cores from various parts of ripple fields on the flood tidal delta, showing dominance of structureless sands. A to D correspond to 16 to 19 in Figure 4-1.

(A) Proximal portion.

(B) Central portion.

(C) Southern part.

(D) Bayward edge.

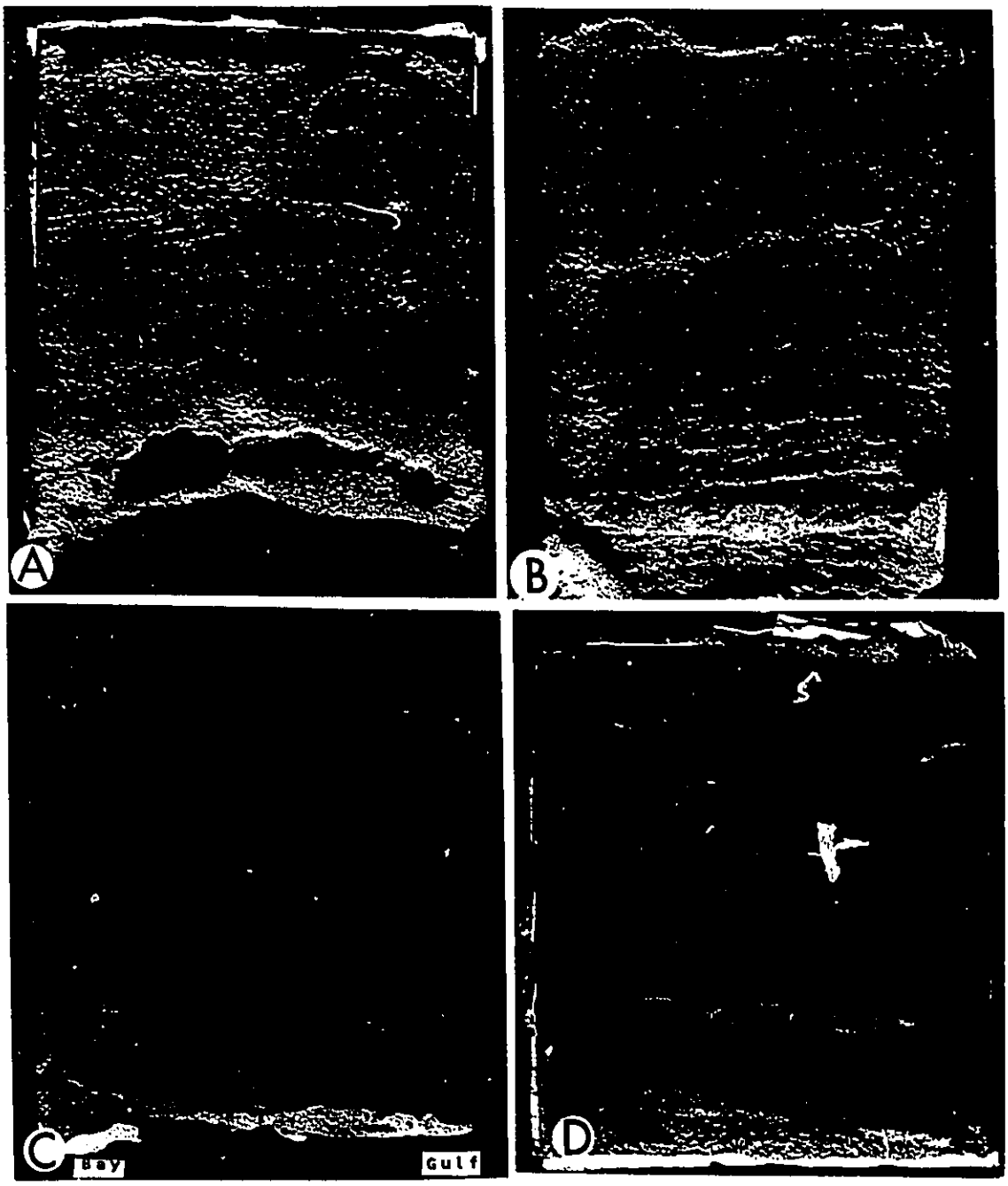
A
B
C
Bay
Gulf
D

described above, short period of high velocity occurred. The crest pattern of large bedforms in tidal creeks suggested that they were Type II megaripples with crests, which were almost leveled with the ground (Figure 4-47B). These bedforms are interpreted as wash-out megaripples formed at the transitional stage as flow changes from lower- to upper flow-regime (Simons, et al., 1965). The high speed flow in tidal creeks occurred when ebb water drained through them, while the surrounding surface was exposed. A high velocity could be reached as is indicated by the turbulent eddies observed in such creeks before emergence. High velocity and extremely shallow depth combined to produce upper flow-regime sheet flow, which prevented crests of bedforms from developing.

Internally, these washed out megaripples consisted of bidirectional, large-scale trough cross-bedding (Figure 4-48B). Flood-oriented foresets were dominant in volume over those oriented in ebb-direction, indicating these creeks were indeed flood-dominated. Figure 4-48A was taken at the edge of the tidal creeks. It showed these cross-bedded tidal creek deposits overlying massive sand of the tidal delta.

Megaripples also occurred along the margin fringing the flood ramp but in very subdued forms. The large bedforms here were Type I forms with low amplitude and straight crests (Figure 4-48E). At large tides, these

Figure 4-47 Surface features, proximal portion of the flood tidal delta, 1987.

(A) South margin, adjacent to the flood ramp (upper left), showing megaripples reworked into low amplitude sand bumps by a small tide. Looking toward the bay. Main channel on the left.

(B) Tidal creek, showing wash-out megaripples with deep scours and angle of repose slipface. Ebb toward low right. Notebook is 19 cm long.

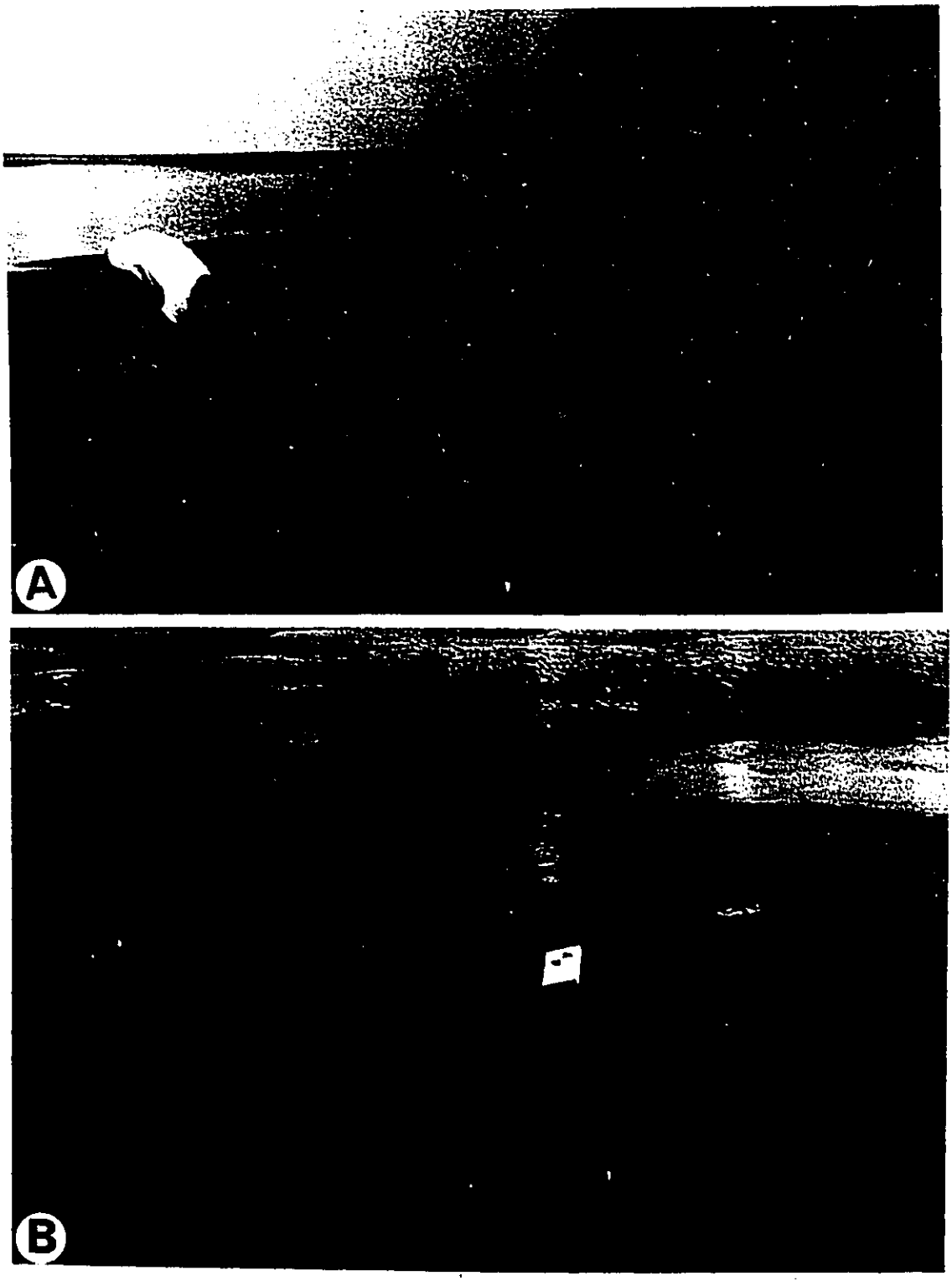
A
B

Figure 4-48 Internal structures and surface features, flood tidal delta. A to D corresponds to 20 to 23 in Figure 4-1B.

(A) and (B) Resin peels from a wash-out megaripple field in a tidal creek, showing bidirectional trough cross-bedding. (A) was taken from the creek margin, which shows cross-beds overlying massive deltaic sand.

(C) and (D) Peel from Type I megaripple field adjacent to the flood ramp (Figure 4-47), showing flood-oriented (W), large-scale tabular megaripple cross-bedding overlying massive sands. Note that the cross-beds formed in large tides were reworked into massive sands (upper part) in small tides.

(E) Type I megaripples, large tide, along the south margin of the proximal delta. Looking toward the bay. Flow was ebbing toward the throat (low right). Location same as Figure 4-47.

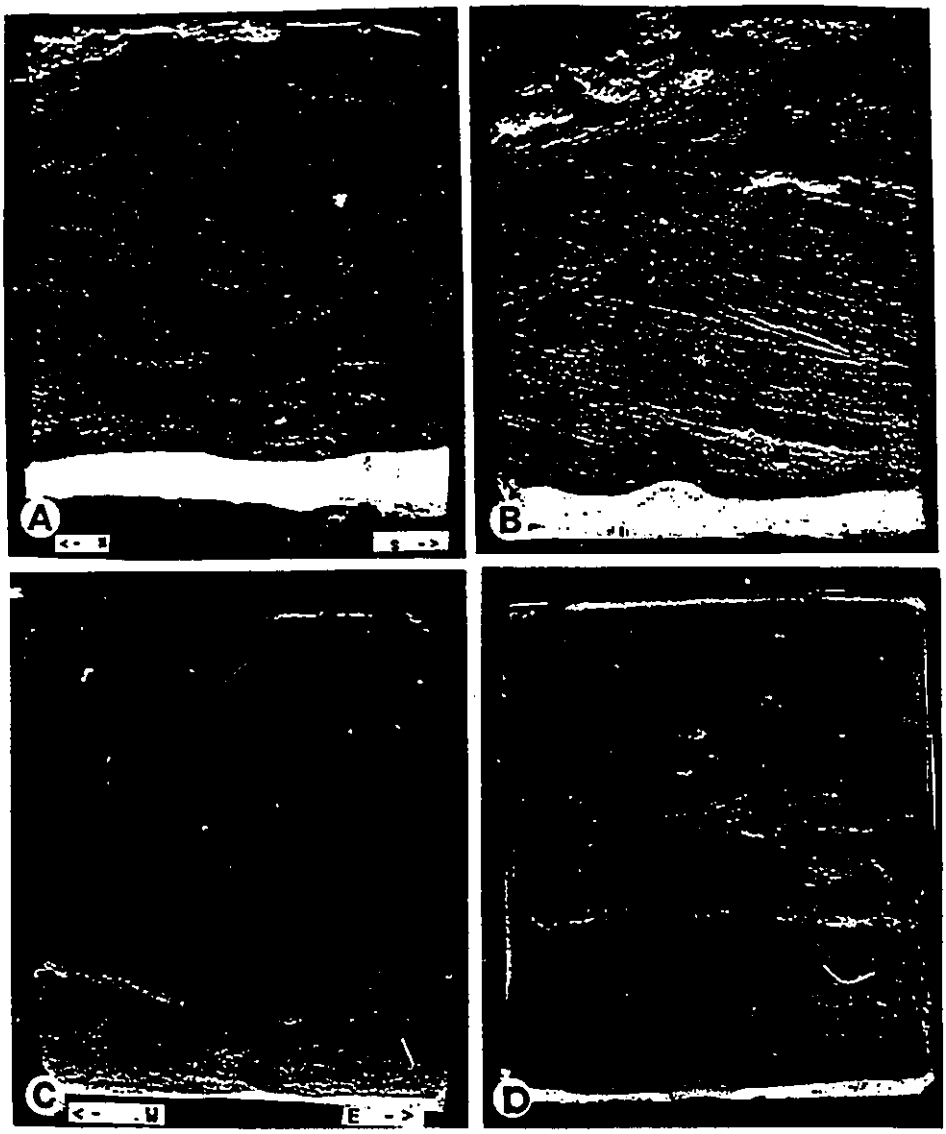
A
B
C
<- W
E ->
D
E

bedforms were relatively well developed, with wavelengths of 2-3 m, and height of 0.15-0.25 m, and maintained a flood orientation at low water. At small tides, they were changed, depending on wind and tide conditions, into low-amplitude 'hump' with still recognizable flood-oriented slipface (0.04-0.06 m), or into simple rounded 'mounds' with no preferred orientation (Figure 4-47A). Measurements using stakes indicated that they did not move until 1-2 tides before the peak of large tides. This sequence is reflected in the internal structures from spade-cores taken at small tides (Figure 4-48 C and D). The large-scale, flood-oriented tabular cross-bedding with tangential foresets were produced by megaripples during large tides. These cross-beds passed gradationally upward into massive sands. It is clear that the upper part of the cross-set has been eroded away by ripples migrating during small tides. These small ripples reworked the megaripple bedding, but did not produce recognizable structures of their own. The bottom half of the two peels were either warty-type massive sands, or crinkled ripple cross-lamination. This suggests that large scale structures would not be common occurrences even along this edge of the flood delta.

Vertical Sequence Four tube cores, up to 2.0 m in length, were taken on the flood delta (1, 2, 3 and 4 of Figure 4-22). These cores revealed that over a vast area and throughout the history of the tidal delta, low energy

condition prevailed. Structureless, massive sands were the overwhelmingly dominant features. Small amount of crinkled cross-lamination, or some incomplete traces of primary structures were observed, and occurred near the proximate part of the delta. Cores from the distal part were invariably uniformly structureless, and increasingly silty.

The core taken at the seaward end of the delta (4 of Figure 4-22) was 2.0 m in length. It penetrated the entire deltaic sand body, and reached the mud substrate. From bottom to the top, it consisted of the following intervals: (1) 0.30 m dark to black mud, containing plant roots and seagrass fibers; (2) Erosional boundary; (3) 0.25 m of crudely-bedded pebbly/shelly coarse sands (lag deposits); (4) 0.25 m of large-scale, high-angle, medium-to-coarse grained cross-beds with shell-fragments; (5) 1.5 m of fine-grained, massive sands with some sort of fine-scale laminated structures embedded in certain intervals. The upward-fining trend in grain size was visually clear. The sand portion as a whole can be explained as consisting of channel deposits overlain by delta deposits as a result of the southward shift of the delta. The large-scale, planar cross-beds are interpreted as active channel deposits, probably formed by migration of large scale Type I megaripples; its ebb-orientation indicates the dominance of ebb flow in the early tidal channel. The overlying sands are normal tidal delta deposits with occasional primary

structures formed during high energy periods. The sequence reflects a decrease in energy level from the base upward with the growth of the delta.

4.7 Spits

Processes The spit environment is the highest topographic unit of inlet environments. It ranges from low water at the beach foot to aeolian foredunes higher than 3-4 m above the barrier surface. The central and major part of the spit is the spit-flat. Other subenvironments include the beach along the water edge and foredunes on the far side of the spit, mostly outside the study area. Tidal currents do not affect the spit directly by producing bedforms. At high water of large tides, however, the flats are wetted, and waves act upon the surface, changing the way the spit-flat reacts to aeolian processes.

Winds affect the spit on a daily basis. They cause effective exchange of sands between subenvironments, and are the dominant process in the formation of foredunes. Waves are the dominant process on the beach, where they produce swash and backwash. Waves propagating into the inlet are refracted, and dissipated over the shallow platform. The beach facing the inlet is thus subject to less wave energy per unit length of the coast than that facing the gulf. This is reflected by a decrease in the width of the beach from the gulf inward. Winds have a limited influence on the

beach due to the limited time between tidal cycles. Without the protection of foredunes, the spit flat can readily be overtopped by water set up during strong wind periods. Though short-lived, such events can transfer large quantities of sediments, and are responsible for the upgrowth of the spit.

Texture Six samples were taken on spits, two from each of the three subenvironments. Mud and gravels were essentially missing from spit sediments. As a result, on the average (Table 4-1), spit deposits had medium values of mean size (2.15 ϕ), skewness (0.74) and kurtosis (6.7), and had the best sorting (0.33 ϕ) of any of the environments studied. Separately, samples from aeolian dunes and overwash were not distinguishable from each other, and as also almost identical to beach deposits in textural statistics. This is expected because the sediments of the three subenvironments were all derived from beach, and because there was active exchange between them. Grain size curves of spit sands are characterized by two subpopulations (GZ-33 and GZ-34, Figure 4-16). Only one sample developed an incomplete C population, which was from beach deposits (GZ-35). The dominant I population accounted for more than 98% of the total sample. In no case was the double 'saltation' population been observed (Visher, 1969). The S population consisted basically of one segment, like that of the flood tidal delta sands.

Bedforms and Structures of Spits

Spit Flat Figure 4-49 shows a typical cycle of changes of surface features of spit flats from prolonged exposure in small tides to large tides when the surface was inundated. Right after large tide, the surface was covered by a layer of loose sand. The highest-portion, represented initially by aeolian dunes, was completely dry and covered by wind-generated ripples. The seaward portion was damp. It captured wind-blown sand, and formed adhesion ripples (Hunter, 1969). These adhesion ripples were small, millimetre-high transverse sand ridges with rather continuous but irregular crestlines (Figure 4-50A-A). They were asymmetric in profile with steeper upwind-facing fronts and flat downwind backs. The low-lying surface on the bayward side was very damp or saturated with water. Small ripples or their relics often occurred on this side, which were formed by wave activity at high water or by drainage during emergence (Figure 4-50B-F). The effect of water content on the development of surface feature was also reflected on a smaller scale controlled by microtopography. Figure 4-50A-C shows diminishing of adhesion ripples from the edge of a small drainage where sand was relatively damp, to the center, where the surface becomes saturated. If, on the other hand, the surface was drier and not evenly wetted, sand captured along the crest of adhesion ripples would not be uniform. The resultant adhesion structures had

Figure 4-49 Changes in surface feature in a large to small tidal cycle, 1984, south spit flat. For locations see inset. See text for explanation.

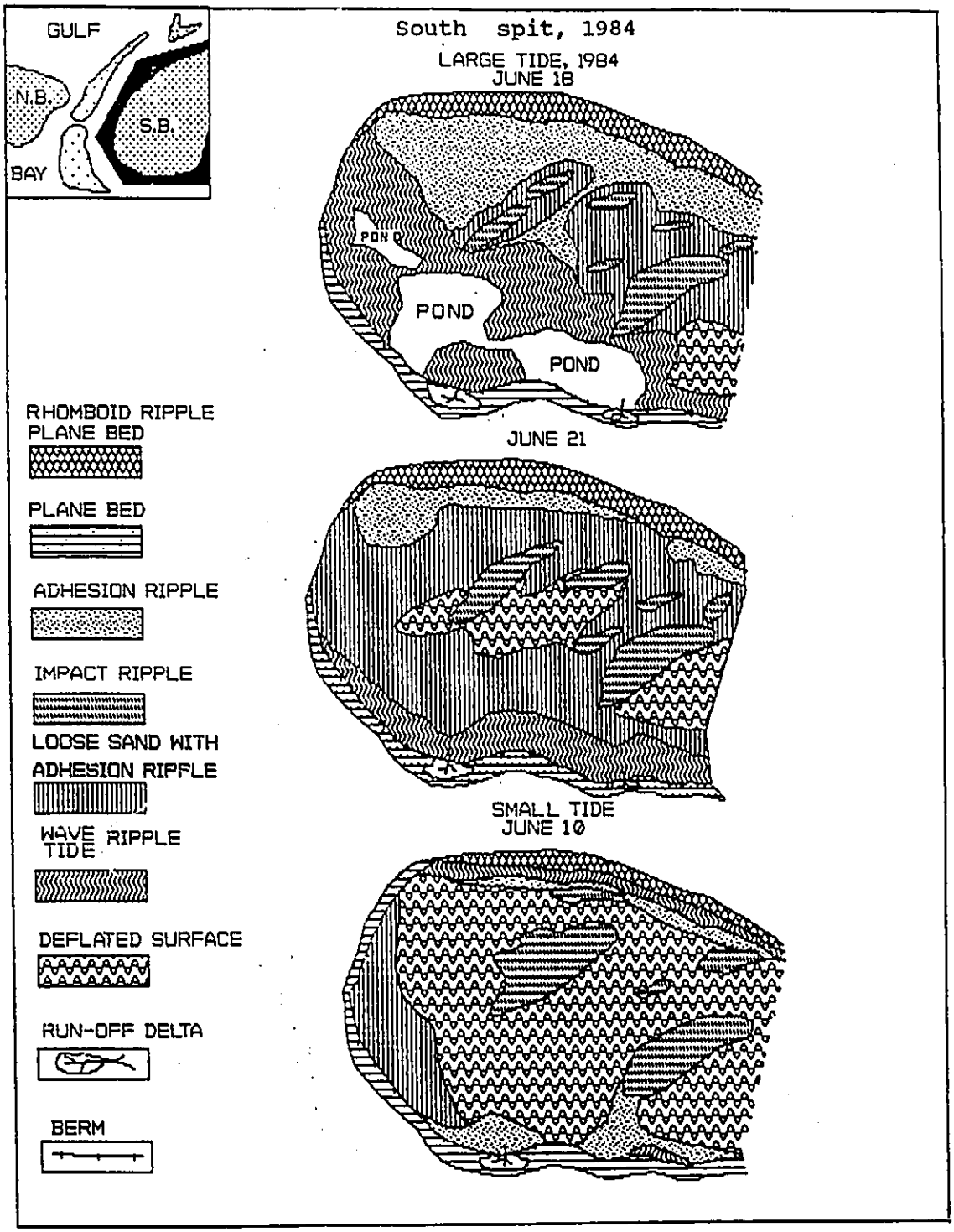
South spit, 1984
LARGE TIDE, 1984
JUNE 18
GULF
N.B.
S.B.
BAY
POND
POND
POND
JUNE 21
SMALL TIDE
JUNE 10
RHOMBOID RIPPLE
PLANE BED
PLANE BED
ADHESION RIPPLE
IMPACT RIPPLE
LOOSE SAND WITH
ADHESION RIPPLE
WAVE RIPPLE
TIDE
DEFLATED SURFACE
RUN-OFF DELTA
BERM

Figure 4-50A Adhesion ripples, south spit-flat.

(A) Adhesion ripples on moist surface, showing continuous but irregular crests. The steeper face points to the upwind direction (bottom). Marker is 12 cm long.

(B) Asymmetrical adhesion-warts, developed on less-moisture ripple surface. The long axis of warts parallels the wind direction. Compare the morphology of these warts with the adhesion ripples in (A). Winds from left to right. Pencil measured 19 cm long.

(C) Changes of adhesion ripples as a function of surface wetness, showing adhesion ripples diminishing toward the entre of a small drainage where sand became saturated. Marker is 12 cm long, and points towards the wind direction.

Figure 4-50B Surface features and internal structures, south spit.
(A) Berm structure of foreshore, gulfside, showing the ridge with a steep, landward slope and a gentle seaward slope, and ripples in the runnel. Note berms are broken by run-off channels. Flights of water level marks occur on the lee slope of the ridge. Notebook measures 15x21 cm.

(B) Rhombohedral ripples on beachface, gulfside.

(C) Air-holes on the upper foreshore, formed as percolating swash water forced interstitial air to the surface of the beach. Pencil is 10 cm.

(D) Parallel lamination, backshore. Lamination is enhanced by alternation of difference mineral layers. Wave ripples occurred on the surface but had very low potential of preservation. Gulf is to the right.

(E) Low tide view of inlet-beach on the downdrift side of the inlet, showing the lower part of the foreshore affected by tidal currents. Looking toward the bay. Main channel on the right.

(F) Washed-off wave-current ripples by water retreating from the bayward sloping surface of the spit.

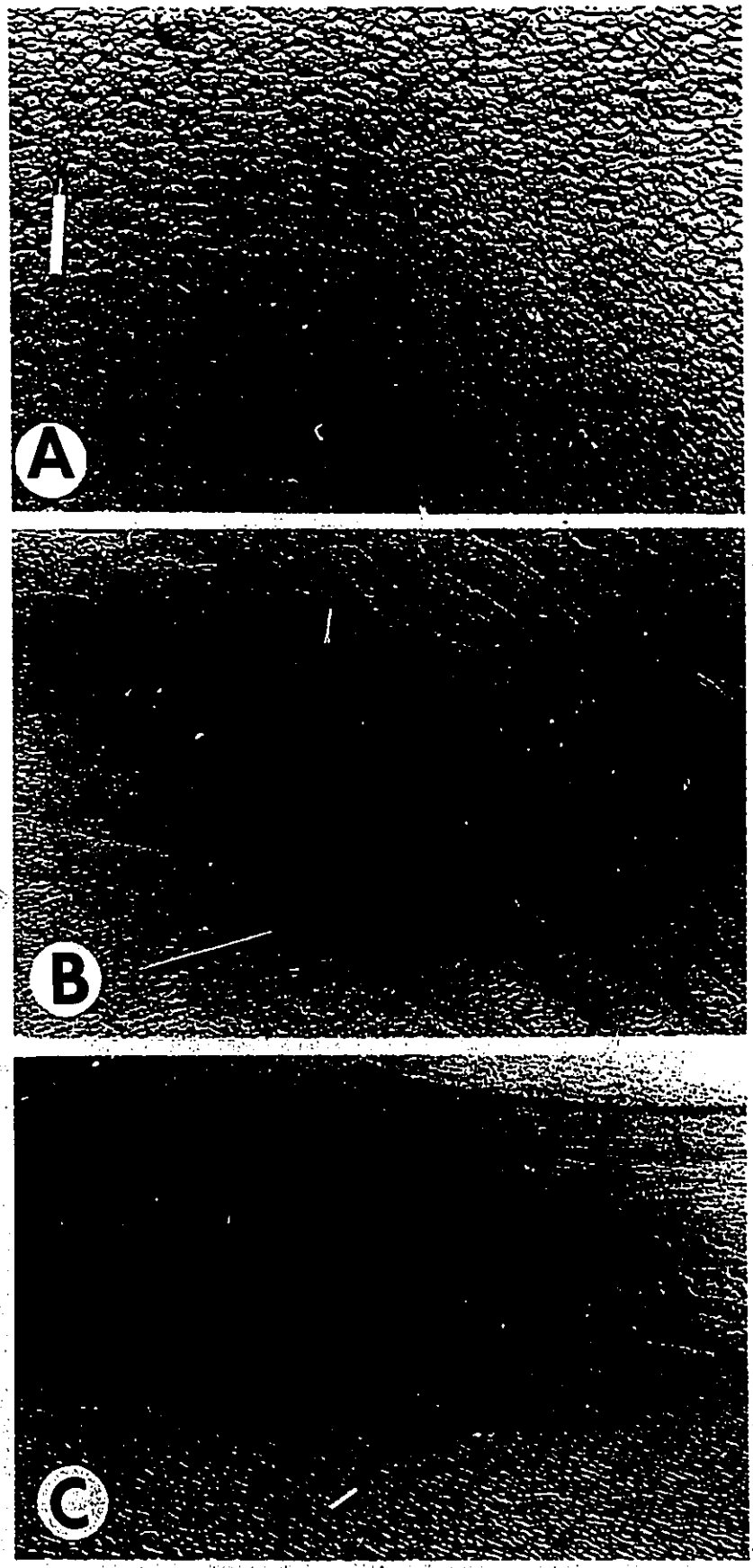
A
B
C

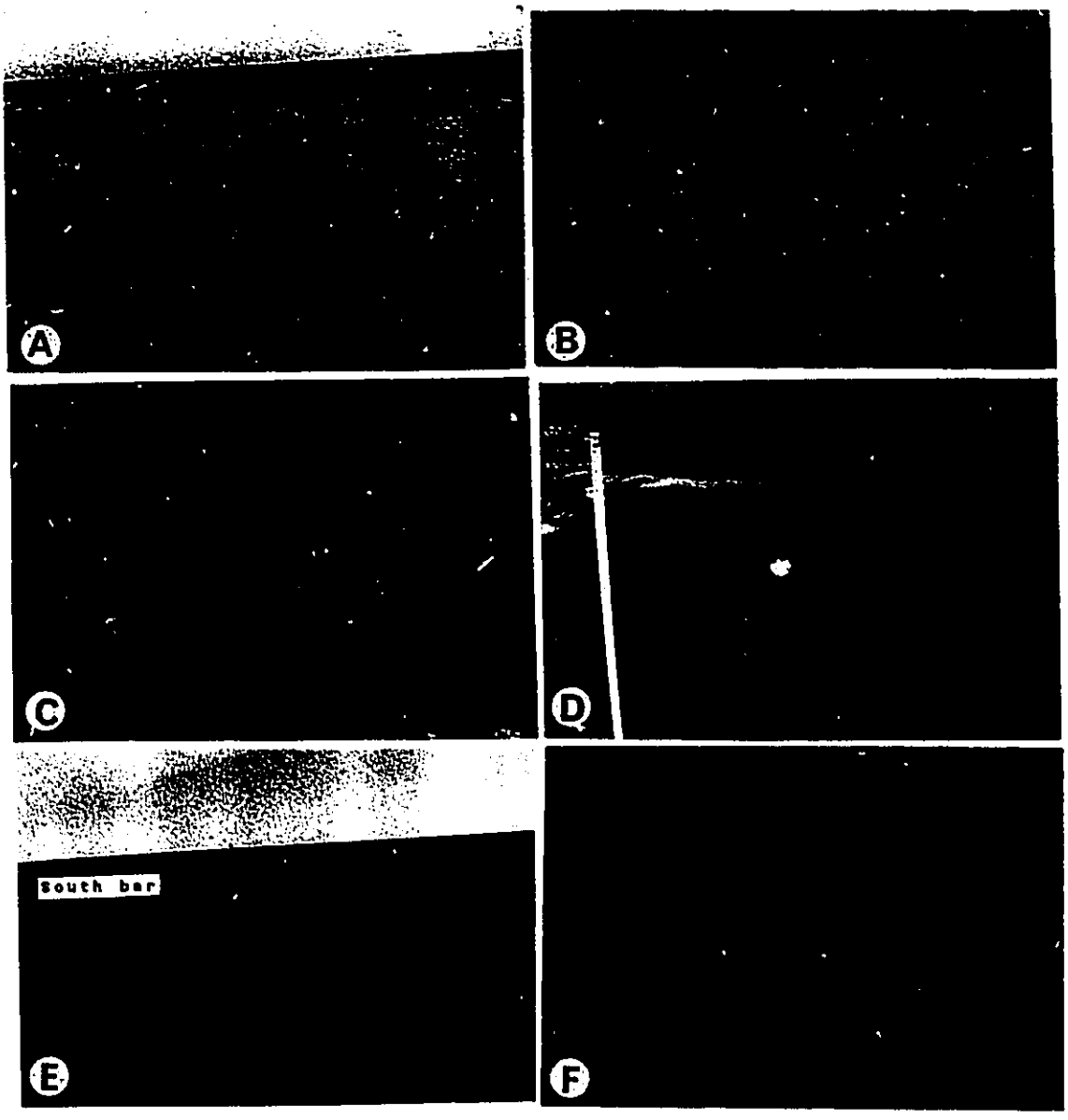
A
B
C
D
South bar
E
F

discontinuous crests and micro-scours in front of the crests, a form that has been called asymmetric adhesion warts by Olsen et al. (1989). The slightly elevated crests of a former ripple field represented a favoured location, upon which adhesion warts were often observed (Figure 4-50A-B).

Toward the small tides, there was an increase in the area of the wind-generated ripples with a corresponding decrease in the area of the adhesion ripples. With further drying up, more loose sands were blown away either back to the beach, or to form an initial aeolian dune on the flat (Figure 4-51C). A wind deflation surface began to develop (Figure 4-51B), and expanded with further exposure (Figure 4-51C). The deflation surface was covered with large shells, shell fragments, pebbles, or other debris (Figure 4-51C). These coarse particles provided shelter for the sand behind them. This led to the formation of wind-sculptured sand-ridges with their tails pointing downwind (Figure 4-51E). Salt-encrustation of small ripples provided similar protection, whereby similar structures could form (Figure 4-51F).

Most, if not all, of the above surface structures were not reflected in the internal structures of the spit flat. Spade-cores taken on the spit-flat were characterized by massive sands and laminated sands (Figure 4-52C and D), interpreted as representing an inactive and an active phase

Figure 4-51 Wind-related features, south spit.

(A) Shallow wedge-shaped cross-bedding of foredunes. Bedding dips toward the bay and away from the inlet (to the right).

(B) Planar bedding of foredunes. Bedding dips toward the bay (into the picture).

(C) Wind deflation surface, spit-flat, showing exhumed shells, pebbles and plant debris, and erosional sand-ridges with the nose pointing to the wind direction. The boundary between the deflated and the non-deflated fields can be noted by the colour change in the distance. Looking toward the Bay. Notebook measured 15x22 cm.

(D) Ripple cross lamination formed by aeolian ballistic ripples on an initial aeolian dune, spit flat. The change of bedding shape is due to change in surface slope.

(E) Closer view of erosional sand-ridges on the deflation surface of (C). The nose of ridges is shell or pebble or other coarse materials, and often tilted toward the wind due to continual erosion of sands by winds along the upwind edge of the ridge. Winds blowing toward the right. Quarter for scale.

(F) Erosional sand-ridge formed on existent ripple surface. Salt encrustation of ripple crest provide protection for sand behind it. Quarter for scale.

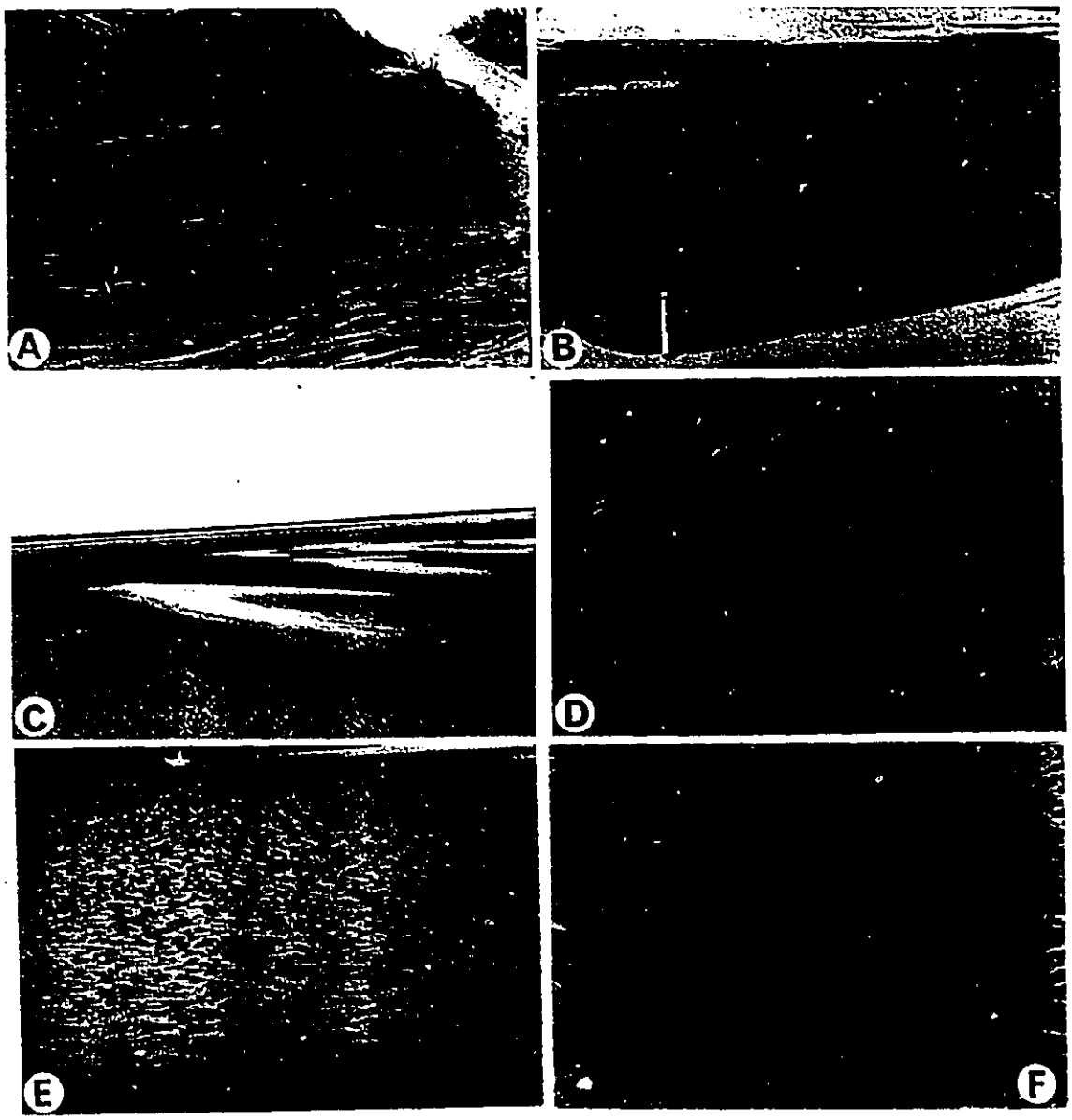
A
B
C
D
E
F

Figure 4-52 Resin peels of spade cores from various parts of the south spit. A to D corresponds to 24 to 27 in Figure 4-1B.

(A) Foreshore, showing seaward-dipping, millimetre-thick beach lamination formed by swash/backwash. Compared with backshore parallel lamination, the beach lamination lack heavy mineral layers.

(B) Internal structure of berm ridge, showing planar, high- angle (20°) foresets, overlying foreshore beach lamination. Note ripples in the runnel of the berm did not produce internal structures.

(C) and (D) spit flat, showing massive sands intercalating with overwash parallel lamination.

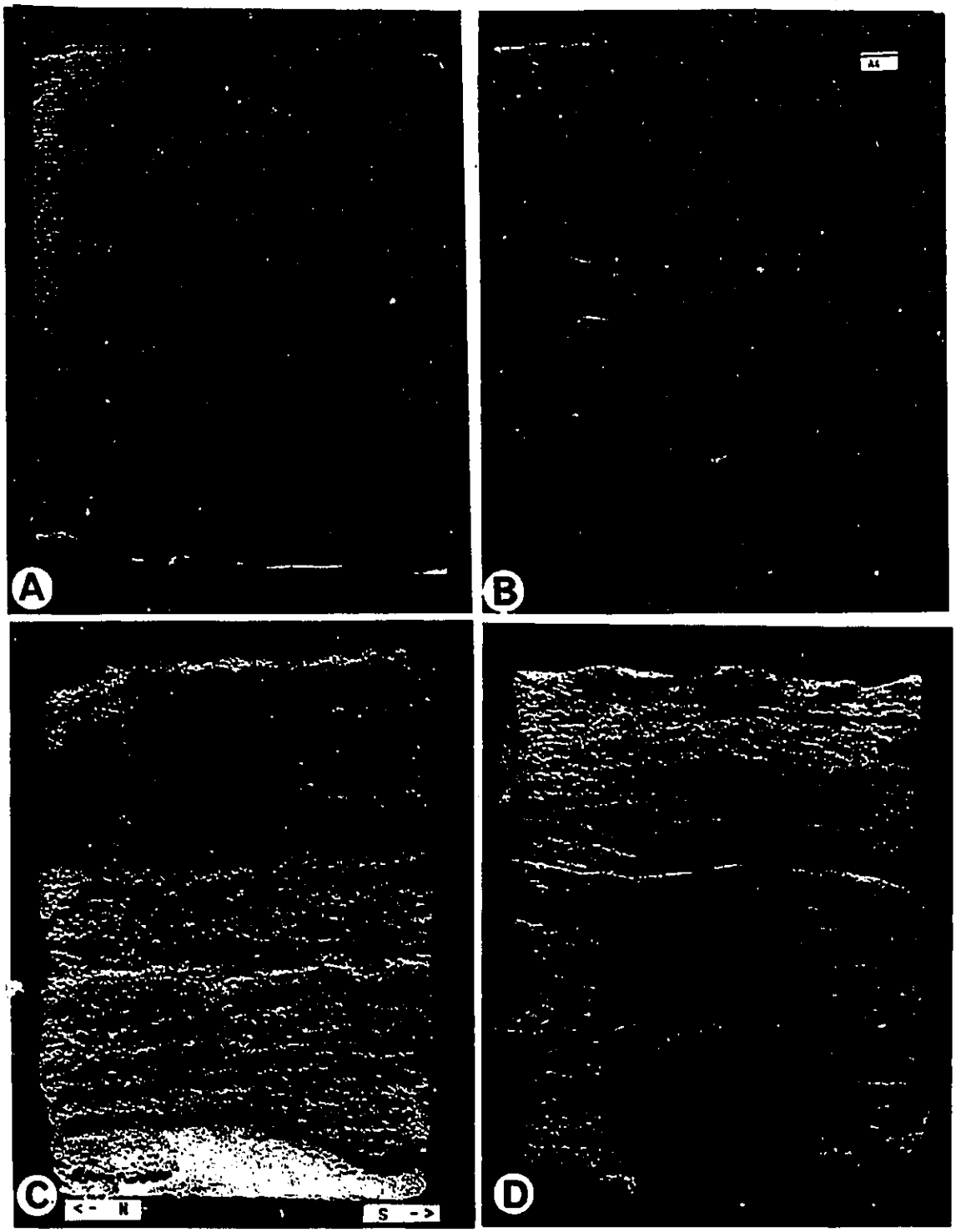
A
B
A1
C
< - N
S - >
D

of the flat deposition, respectively. Laminated sands are interpreted as overwash deposits, formed when storm set-ups and wave surges carrying sediments overtopped the spit in sheet flows. These high energy events could bring in coarse materials, and also created an upper flow regime condition, which deposited plane-beds. This process is similar to that which takes place in normal overwashs breaking through foredunes of barrier islands (Schwart, 1982). The difference is that overwash of the inlet spit is less confined, and thus currents are probably weaker.

The high-energy, active phase was followed by a quite, passive phase, when daily processes set in. The quiet, passive phase acted to redistribute sediment brought in during the previous stage, but usually did not produce any visible structures of its own. The result was the massive sand.

Aeolian processes produced primary structure on initial aeolian dunes, where sand started to be stabilized. Migration of wind-ripples created climbing-ripple cross-lamination over these little mounds (Figure 4-50B-D). Stabilized dunes along the shoreline developed into foredunes. The most common stratification of foredunes is large-scale, shallow wedge-shaped cross-bedding, and planar bedding (Figure 4-51A and B) dipping toward the land. This showed that sands comprising the foredune came mainly from the beach.

Vertical Sequence Four tube cores were taken on the spit surface on both sides of the inlet (Figure 4-23A and G; Figure 4-24a and h). As in the shallow cores, the dominant structures revealed were parallel lamination and massive sands. Layers of coarse materials were observed, such as shells and their fragments, coarse sands, wood or seaweed debris. Three of the four cores showed similar patterns with laminated sand closer to the top, and massive sand closer to the bottom. This suggests an upward change from a low-energy to a high-energy condition. Such a change is considered consistent with the growth of the spit. At a relatively early stage when the spit was still low, small wave surges could top it, which would not produce as strong overwash as when the spit has grown higher.

The core shown in Figure 4-23G penetrated several units of inlet environment on the updrift side. The sequence started with ripple cross-lamination, passed upward into steeply-dipping, planar cross-bedding, and was capped by massive sands. In accordance with the history of the inlet, they can be interpreted by the following sequence of events: (1) Subtidal vertical-accretion of the platform; (2) Lateral extension of the spit over the subtidal platform as sediments were deposited in front of the end of the spit to form the planar cross-bedding; (3) Subaerial growth of the spit.

Beach The beach environment showed surface and subsurface

features similar to those characterizing the open coast beach. The predominant surface feature of foreshore was a current-lineated plane bed (Clifton, 1969). Other features included antidunes and rhomboid ripples (Figure 4-50B-B), air-trapping holes and foam (Figure 4-50B-C), and swash marks made up of seaweeds or drifted wood pieces. The internal structure of beachface consisted almost exclusively of beach laminae (Figure 4-52A), millimetre-thick and dipping toward the water line. Many large shells and shell fragments occurred on the gulf side beach, but did not disturb the laminae. A tube core was taken in the beach on the updrift side of the inlet (Figure 4-23F). It revealed normal spit deposits being reworked into beach lamination at the water edge. Similar processes took place on the beach on the downdrift side of the inlet. Close to its landward end, however, low-amplitude bars were found attached to lower part of foreshore, and continued to the subtidal zone (Figure 4-50B-E). The acute angle of these bars with the ebb current indicated that they were ebb products. Spade-cores taken on them revealed meso-scale cross-bedding, which displayed bipolar movement of sediments in response to both flood and ebb processes.

The shoreward limit of the foreshore was often marked by a berm structure. The berm consisted of a shoreline-parallel beach ridge with a steeper, angle-of-repose landward slope and a gentler seaward slope (Figure

4-50B-A), and a shallow runnel behind it, in which small wave-ripples were oriented at angles with the shoreline. The length of ridges was often broken by small channels, serving as drainage outlets for water overtopping the ridge during high water. Run-off in these drainage channels produced ripples with crests parallel to the waterline. The summer season represented a recovering stage for the beach, with berm ridges climbing gradually up the foreshore with the rise of tides. Peels from the crest area of the berm showed simple high-angle, planar cross-beds, representing slipface deposition during the landward migration. These cross-beds lay directly over beach lamination (Figure 4-52B), indicating ripples in the runnel were not preserved in the deposits. Trenches dug on the foreshore did not reveal slipface deposits of berm structures beneath the surface. This suggests that products of the intermediate stages of ridge migration have been reworked by wave process. In summary, the berm structures at Palmer Inlet are simple, and less differentiated than those found on mesotidal coasts (Dabrio et al., 1982).

The backshore of the beach, which developed in front of the foredunes, was flat, and covered by drifted wood or seaweed, scattered shells and pebbles, and wind and a few wave ripples. Many heavy mineral concentrations were found along the foot of the foreshore due to wind winnowing effects which selectively blow away lighter particles.

Internally, the backshore deposits consist of sand with even lamination enhanced by heavy mineral layers (Figure 4-50B-D). Although ripples rarely occurred on the surface, their lamination was preserved.

4.8 Three-Dimensional Model and Comparisons with Other Studies

The description of the sediment characteristics of various environments sets the stage for constructing a three-dimensional depositional model for Palmer inlet. (Figure 4-53). The three-dimensional model was constructed based primarily on three stratigraphic cross-sections, comprising 22 tube cores (Figure 4-22, Figure 4-23 and Figure 4-24). It reflects the present morphology and surface sediment characteristics. Although no core penetrating the entire stratigraphy is available, short cores at different depths make the record fairly complete. By displaying the relationship between various sediment units, the model has implications for elucidating inlet development and history. The sediment characteristics of Palmer Inlet are, in general, consistent with published work on tidal inlets. Differences, however, exist, and have arised from a number of hydraulic and sediment factors, which are peculiar to the study area. They include: (1) The uniform, fine-grained texture of the sand; (2) The scarcity of mud; (3) The small time-velocity asymmetry; (4) The small

Figure 4-53 Three-dimension model of the stratigraphy of Palmer Inlet. Cores forming the stratigraphic sections are showed in Figure 4-22, 4-23 and 4-24. Typical vertical sequences are given in Figure 4-54.

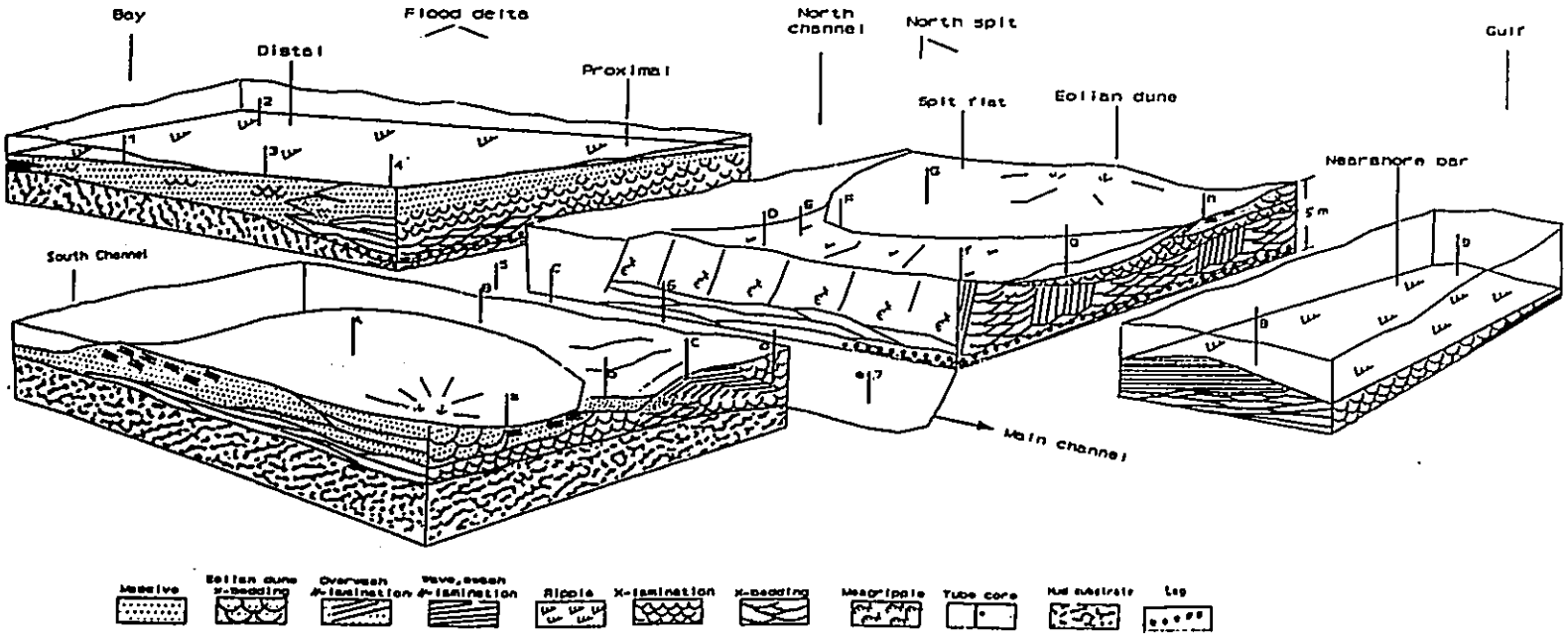
Bay
Flood delta
Distal
Proximal
North channel
North split
Gulf
Split flat
Eolian dune
Nearshore bar
5 m
South Channel
Main channel
Massive
Eolian dune x-bedding
Overwash x-lamination
Wave, swash x-lamination
Ripple
x-lamination
x-bedding
Mesoripple
Tube core
Mud substrate
Lag

tidal range; and (5) The shallow depth of the inlet channels. In the next section, the three-dimensional model is first presented. Three distinct sediment units and their representative stratigraphic sequences are then described.

4.8.1 Three-Dimensional Model

Palmer Inlet depositional system is a two-layered structure with inlet sand overlying the backbarrier mud deposits (Figure 4-53). Lack of sediment supply and relative sea level rise contribute to the following features of the inlet sand. (1) Small thickness. The inlet sand body is about 2 m thick except the updrift side where undercuts reached 4 m. (2) Uniformity of its sediment content. It consists almost exclusively of well-sorted fine sands except at deep scoured base where gravels and shell dominate. (3) Lack of mud. Lack of muds is due to limited river drainage into the bay, and their inability to settle out in the inlet associated environments.

The nature and evolution of this sand body can be understood in the context of the regional Holocene history. The mud substrate is interpreted as of Holocene age and deposited in a shallow, low-energy coastal pond, similar to Cascumpec Bay. The pond was inundated about 4,000 years ago as the eustatic rise of sea level outpaced the rebound of the land in this region (Grant, 1970; 1976). The main evidence for the Holocene age of the mud layer is its low

degree of induration, and the similarities in its characteristics to modern bay deposits. These include the dark color, the cohesiveness and massiveness with occasional sandy- to silty interbeds, and the presence of lagoon-type organic materials. In particular, the quadri-modal size distribution suggests that they have the same source of sediments. More importantly, the mud substrate directly underlies the surficial sand on the downdrift side, and is at the same topographic level as that of the present depositional surface of the bay.

Transgressive condition dominated the region during the late Holocene, which drove sediments alongshore or from offshore over the mud substrate, and formed the Malpeque Barrier Islands. Palmer Inlet was formed about 55 years ago (Armon, 1975), probably by a major storm breach. The breach cut into the Holocene mud, and was covered by shell/gravel lags currently exposed at the bottom of the throat channel. For the past 20 years or so, the inlet has migrated in the direction of dominant longshore drift. As it migrated, sands were deposited on the updrift side and eroded on the downdrift side. In addition, sediments were transported into the inlet to form the flood tidal delta. The stratigraphy depicted in the block diagram hence represents a retrogradational sequence. Due to the difference in their relative movement to the transgression, three sediment units can be distinguished within the system. These units and

their representative sequences are described in the following.

4.8.2 Updrift Inlet-Fill Unit

On the updrift side, the depositional sequence is one reflecting a single inlet-fill. It developed as the spit platform was built and prograded into the main channel, and a spit was constructed on top of it. The inlet-fill sequence at Palmer Inlet (Figure 4-54) is about 3-3.5 m in thickness excluding the foredune unit. It erosionally overlies the mud substrate, and is separated from it by a layer of lag deposits consisting of large shells and pebbles. The shells include forms from both the gulf and the bay. Overall, the sequence fines upward texturally, but except the bottom part, which contain gravels and coarse-sand particles, the sands are well-sorted and uniformly fine-grained. Structurally, the fill-in sequence starts from tidal bidirectional, medium-scale, trough cross-bedding (channel deposits), and passes upward from large-scale bar-front foresets (platform front) to small-scale wave ripple lamination with swash-bar intercalations (platform topset). This is capped by dominantly massive sand with parallel-lamination close to the top (subaerial spit), which may pass upward into large-scale, cross-bedded aeolian dune deposits. Near the throat where currents are strong, the bar-front foresets of the platform front may be replaced by channel

Figure 4-54 Representative vertical sequences of Palmer Inlet. See text for explanation.

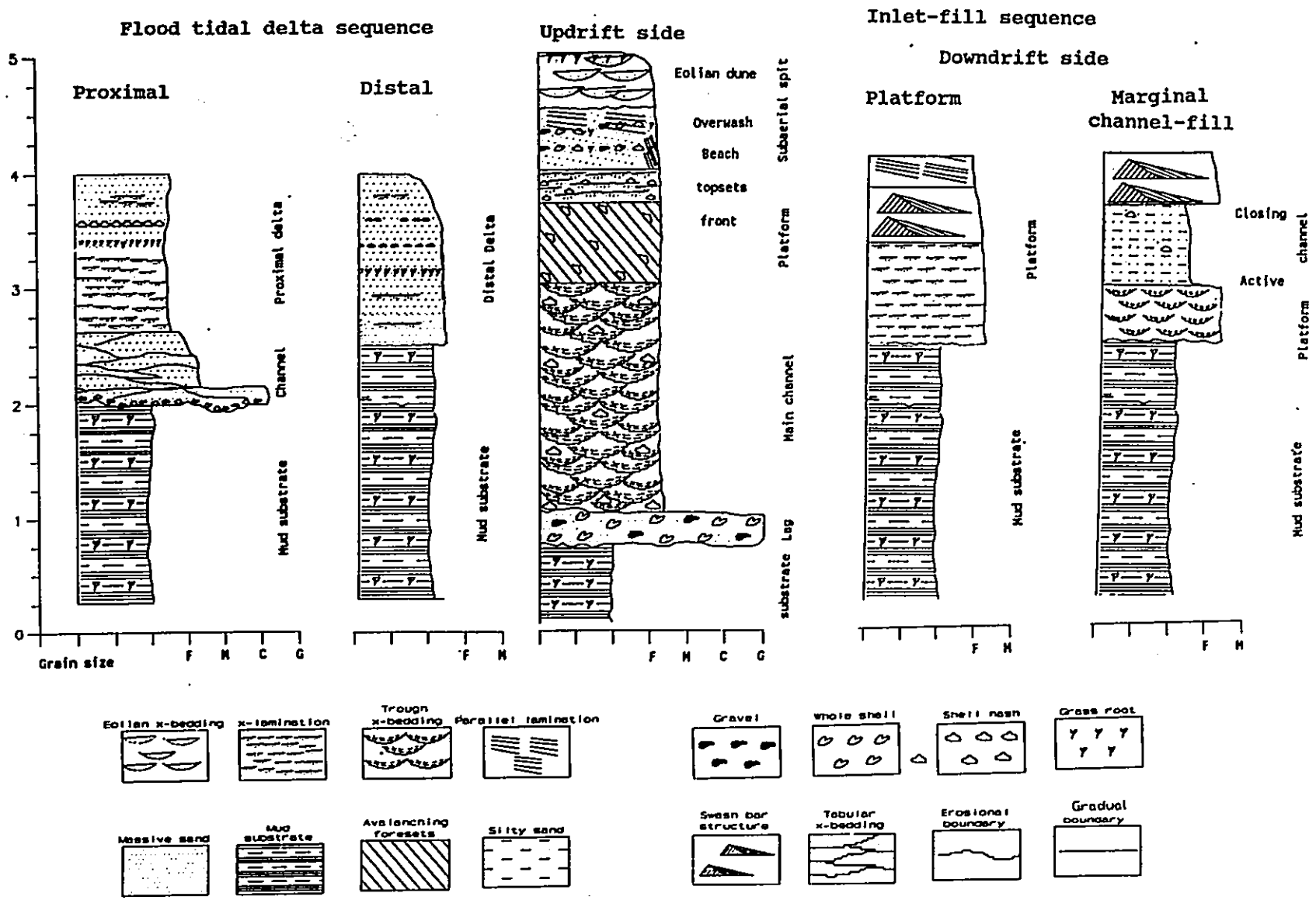
Flood tidal delta sequence
Proximal
Distal
Updrift side
Inlet-fill sequence
Downdrift side
Platform
Marginal channel-fill
Eolian dune
Overwash
Beach
topsets
front
Subaerial spit
Platform
Main channel
substrate Log
Proximal delta
Channel
Mud substrate
Distal Delta
Mud substrate
Platform
Mud substrate
Closing
Active
Platform channel
Mud substrate
Grain size
F M C G
F M
F M C G
F M
F M
0 1 2 3 4 5
Eolian x-bedding
x-lamination
Trough x-bedding
Parallel lamination
Massive sand
Mud substrate
Avalanching foresets
Silty sand
Gravel
Whole shell
Shell hash
Grass root
Swash bar structure
Tabular x-bedding
Erosional boundary
Gradual boundary

deposits. In such a case, megaripples cross-beds are in direct contact with the topset of the platform. On the other hand, the cross-bedding of tidal channel deposits may show dominant flood-orientation toward the landward end and ebb-orientation toward the entrance.

4.8.2.1 Absence of the Shallow Channel Unit

The main channel of Palmer Inlet is shallow. This is responsible for a number of differences of the inlet-fill sequence from the microtidal inlet model (Kumar and Sander, 1974). First, the resultant sequence is much thinner than that of Fire Island Inlet (> 10 m, Kumar and Sanders, 1974). Secondly, in the model, over the deep channel there is a shallow channel unit, consisting of upper plane-bed. Its occurrence has been attributed to the change of flow from lower- to upper-regime with decreasing water depth. Since flow regime is a function of water depth, such differentiation will not occur in a shallow channel. As a result, the shallow channel unit is absent from Palmer Inlet, and megaripple bedding is in direct contact with the avalanche-foresets.

4.8.2.2 The Preservation of Bar-Front Foresets

Another effect of a shallow channel is that the platform directly faces the main channel at its front, while in a deep channel such as the Fire Island Inlet (Kumar and

Sanders, 1974), they form two separated morpho-sedimentary units. At Palmer Inlet, sediments avalanching down the platform front are subject to reworking of tidal currents in the channel. Their preservation depends on the balance between the rate of progradation of the platform, and the rate of reworking by tidal currents. It has been shown that Palmer Inlet migrated much faster at the entrance than at the throat section (Chapter 3), where currents are much stronger. The deposits produced by the progradation of the platform at the entrance side could proceed with little tidal modification. On the landward side, however, they are gradually reworked into tidal bedding by megaripples which migrate along the channel bank. Therefore, if the channel depth is small — less than a few metres, the bar-front foresets of the platform may not be preserved.

4.8.2.3 Absence of Sandwaves

Sandwaves and their associated large-scale tabular cross-bedding have been reported as an important component of inlet deposits (Boothroyd, 1975; Nummedal and Penland, 1981; Reison, 1979; Reddering; 1983; Kumar and Sanders, 1974), but are absent at Palmer Inlet. This is contrary to the observation that sandwaves occur in the same depth-velocity field as Type I megaripples (Dalrymple et al., 1979). The strength of currents and water depth is, however, not the only factors controlling the occurrence of

sandwaves. Boothroyd and Hubbard (1975) reported that sandwaves occur in area where the dominant flow is twice as large as the secondary flow. Such large velocity asymmetry does not exist at Palmer, especially in the major sediment transport conduits. Strong velocity asymmetry occurs toward the both ends of the main channel. In these locations, however, the strength of currents has dropped to a level below that generates megaripples. In addition, the mode of sediment transport is also an important factor (Middleton, pers. comm., 1984): higher bedload transport is conducive to the formation of sandwaves, and higher suspension transport to that of megaripples. Although there are no actual data on the specific mode of sediment transport, the high proportion of fine sands and associated high mobility (Blatt et al., 1980, p.103) suggests that suspension is an important mode of transport in the channel.

4.8.2.4 Absence of Reactivation Surfaces

One of most important features of estuarine/inlet deposits are long, unidirectional bundles of foresets with multiple reactivation surfaces (Klein, 1970; Boersma and Terwindt, 1981). At Palmer Inlet, reactivation surfaces are extremely rare encounters in cores. Reactivation surfaces indicate a dominant transport direction with frequent current reversals. Current reversal at Palmer Inlet takes place at a low frequency, because the major transport event

here takes place during large tides, when tides have only one flood and one ebb a day. More important for the difference is, however, the low degree of time-velocity asymmetry. The low asymmetry, coupled with the small tidal range, means that bedforms in the channel move approximately equal distance in both directions. Each phase tends to erode the previous deposits, and is subject to erosion by the following phase with about the same strength. The structural record left from such process consists, to a large degree, of basal deposits of the trough bedding, instead of unidirectional bundles of foresets with abundant reactivation surfaces.

4.8.3 Downdrift Accretional Unit

The depositional sequence on the downdrift side is a barrier island accretion sequence in the vicinity of an inlet. The accretion results primarily from landward migration of swash-bars, which often involves shoreline progradation and in-filling of the marginal channel. Two sequences can occur (Figure 4-54). Sequence I reflects the upgrowth of the platform conformably over the mud substrate. It is about 2 m thick not including spit deposits, and composed almost exclusively of clean, well-sorted, uniform fine-grained sand. Internally, it is characterized, from bottom upward, by wave-formed small-scale cross-lamination, swash-bar structures and swash-generate parallel lamination.

The change of structure reflects changes in wave processes associated with the shoaling in a wave-dominated environment. With the aggradation of the platform, the major wave process changes from one dominated by symmetrical oscillation, to asymmetrical oscillation produced by shoaling waves with a strong forward motion, and then to a back and forth motion produced by swash and backwash.

Sequence II reflects deposition associated with the closure of the seaward marginal channel close to the barrier island. Structures occur above the mud in the following ascending order: (1) Fine-sand, with tidal cross-bedding produced by active channel deposition; (2) Massive to poorly laminated silty sand produced by inactive channel deposition (3) Fine sand, with large-scale, slipface foresets produced by swash bar deposition.

The inactive channel deposits of the marginal channel in mesotidal inlets consist of highly bioturbated mud and marsh deposits (Tye, 1984). A number of studies (Imperato, et al., 1988; Sexton and Hayes, 1982; Tye, 1984) have showed that such deposits comprise a significant portion of ebb tidal delta accretion in the vicinity of a mesotidal inlet due to frequent changes in its position. The changes in position are due to the intrinsic controls on inlet migration because as the inlet migrates, its hydraulic efficiency decreases, and eventually a threshold is reached, when the old channel is abandoned, and switched to a more

direct course. The marginal channel at Palmer Inlet is rather stable. In fact, as both core and current measurement indicated, the marginal channel has not been very active throughout its history. Also, because of lack of fine material, the materials filling the marginal channel at Palmer Inlet are silts to fine sands instead of clayey marsh deposits. As a result, its product is not volumetrically significant and texturally distinctive within the stratigraphy.

4.8.4 Flood Tidal Delta Sequence

The stratigraphy of the flood tidal delta can also be represented by two types of vertical sequence, each about two metres in thickness. In the proximal part, it is a channel-fill sequence (Figure 4-54). The sequence consists of a fining-upward trend with deltaic fine sands overlying shelly to coarse-grained channel deposits. Structurally, the channel deposit consists of large-scale tabular cross-bedding, changing upward from seaward- to landward-directed. The overlying deltaic deposits are dominantly massive to ripple cross-laminated. The vast majority of the flood tidal delta is a distal sequence, representing in-place upgrowth under weak flow conditions. It consists almost exclusively of uniform, silty sands, and is devoid of primary structures. Shell hash, seagrass, and occasionally relics of lamination may occur.

Reason for Lack of Primary Structures The salient feature of flood deltaic deposits is the massiveness of the sediments, especially considering the fact that ripples are ubiquitous on the surface of the delta, and currents are capable of causing current-ripples movement at least during flood periods. Structureless sands of intertidal shoals have been reported in a number of studies (Jago, 1980; Jago and Hardisty, 1984; De Boer, 1979), and have been attributed to bioturbation, or to air-cavities. At Palmer Inlet, there is only a sparse number of benthonic fauna inhabiting the flood delta, basically some clams (Spisula solidissima) and moon shells. Burrows have been rarely encountered in the cores. Air-filled cavities have been observed on a few occasions (Figure 4-46C and D), but are not common enough to destroy all lamination. The massiveness of the Palmer flood delta is interpreted as syndepositional. The flood delta consists of uniform fine sand, which lacks grain size and mineral contrasts, on which lamination depends. In addition, the expression of lamination is also a function of the degree of hydraulic sorting the flow can provide. It is well-known that particles in the fine-sand range have the lowest threshold values for both entrainment and suspension. The latter also happens to coincide with the threshold for ripple formation (Middleton and Southard, 1978; Blatt et al., 1980, p.136-146). This suggests that ripple migration on the flood delta involves a high degree of suspension, or

a low degree of tractional movement. Such processes will not provide enough sorting for the production of lamination, which is visible within the limited grain size present. The same explanation applies to the spit environment, where massive sand is also a major component of stratigraphy.

Lack of sedimentary structures on the flood delta confirms the results of previous works in wave-dominated inlets (Hubbard et al., 1979; Israel et al., 1987). The interfingering of tidal deltaic sands with mud, such as backbarrier flat, marsh or lagoon deposits, which typify many of micro- and meso-tidal flood tidal delta systems (Israel et al., 1987), however, does not occur at Palmer Inlet. The reason is that fine materials are simply not available at Palmer Inlet. The simple facies observed in vertical sequence also suggests that the depositional history of the flood delta of Palmer Inlet is relatively simple, primarily a single, slow vertical accretion. This is consistent with its morphological history, which indicates that the flood delta is stable in location over the past 55 years (Chapter 3).

4.8.5 Texture as Environment Indicator

The salient feature of sediments of Palmer Inlet is the extreme homogeneity and maturity of grain size. Except the distal flood delta, 97-99% of sediments of Palmer Inlet are concentrated in a narrow range between 1 ϕ and 3 ϕ. The

direct result of this homogeneity is the close similarities in the four size statistics as well as probability curves between various environments within the inlet. As a result, none of these size features are particularly useful as environmental indicators. For example, the average values of the mean size occur between 2.06 ϕ and 2.40 ϕ, and that of the sorting between .33 ϕ and .41 ϕ (Table 4-1). Bivariate plots using these parameters show that inlet environments cannot be separated, except the flood delta which is set apart, though with considerable overlap (Figure 4-15), by the relatively large amount of mud and small mean size.

An important result of the homogeneity of sediments is that the probability plots of Palmer Inlet sediments are characterized by an extremely dominant (95%), well-sorted intermittent suspension population, a small (<2%), moderate sorted continuous suspension population, and a small, or negligible, poorly sorted traction population. Such probability curves do not resemble those of the corresponding environments of Fire Island Inlet (Kumar and Sanders, 1974). They also differ from the typical curves of coastal environments described by Visher (1969), in which the traction population occurs in significant amount in almost all the samples, including those from offshore and aeolian deposits. The maximum shear velocity measured in the main channel of Palmer Inlet is able to transport coarse

sands. The deficiency of C population at Palmer is thus source-controlled. C population materials are not available at Palmer Inlet in the same proportion as at Fire Island, where the sediments are most entirely medium and coarse sand. The source material of the Malpeque Barrier Islands are the sandstones and glacial tills of nearby coastal cliff and the offshore seabed (McCann, 1979; Black, 1984). Most of the sandstones are fine grained, and so are the tills derived from them. Even if coarse sands existed in the source material, most of them could have been lost to the updrift beaches on their way to the inlet.

4.8.5.1 Origin of the Double-Segment of the S Population

The S population of the flood delta and the spit consists primarily of one segment, while that of the inlet channel and the platform consists of two segments with different slopes. The latter is subtidal environment, while the former is intertidal environment, which suggests that this feature is depth-related. That is, the two segments correspond to suspension deposition at high and low water, respectively. The channel and the platform, which are constantly below water, are able to accept both deposits and thus two segments in the S population. Fall out of suspension at low water periods, however, is not available to the flood delta and the spit as they are both emergent during that time.

4.8.5.2 Longitudinal Profile of Grain Size

Among the inlet environment, the flood tidal delta can be reasonably well separated from the rest by its high silt content. On histograms, the flood delta has a stronger fine-tail skewness, and on probability plots it is devoid of C population. As a result of this, a longitudinal profile through the inlet, including the bay and nearshore environments (Figure 4-55), shows changes of size characteristics reflecting the mean energy of the environments. Figure 4-55 shows that from the inlet throat toward both directions with decrease in mean energy, there is generally an increase in mud content and suspension population, and a decrease in mean size and sorting. The diagram clearly shows that the bay and nearshore environments are areas where silts and clay currently accumulate. Mud in the area is as high as 27-30%. This indicates that fine materials are generally unable to settle within the inlet. Instead, they are diverted either to the backbarrier area or washed out to the Gulf. This, plus the low river drainage into the bay, explains why Palmer Inlet is essentially depleted of mud deposits.

4.9 Summary and Conclusions

This Chapter has presented a detailed account of the depositional environments in terms of their sediment characteristics and prevalent hydraulic conditions. Palmer

Figure 4-55 Longitudinal profiles of grain size parameters, including the bay and nearshore environments. See Figure 4-2 for locations. Sample No. 10 is the average of No.10 and 11, No.12 the average of No.12 and 13, No.14 the average of No.14 and 15 and No.16 the average of No.16 and 17.

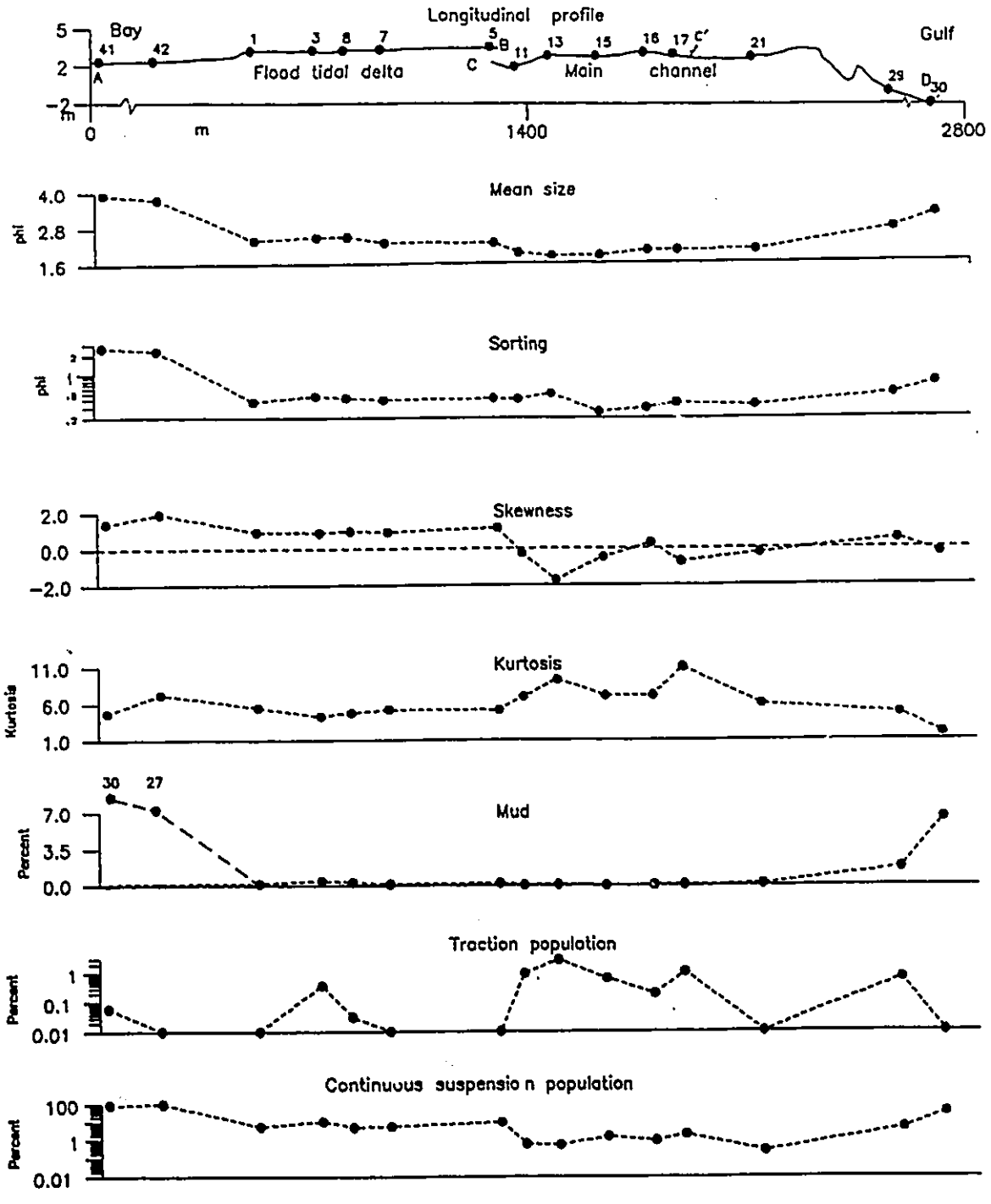
Longitudinal profile
Bay
Gulf
Flood tidal delta
Main channel
A
B
C
C'
D
5
2
−2
m
0
1400
2800
Mean size
phi
4.0
2.8
1.6
Sorting
Skewness
2.0
0.0
−2.0
Kurtosis
11.0
6.0
1.0
Mud
Percent
7.0
3.5
0.0
Traction population
1
0.1
0.01
Continuous suspension population
100
1
0.01

Inlet can be divided into five vertically- and spatially-separated sedimentary environments: inlet channels, channel margin linear bars, spit platforms, spits, and the flood tidal delta. Each environment displays sediment characteristics which reflect the dominant hydraulic regime and its time variation. To a first approximation, tidal currents and megaripples dominate inlet channels. These megaripples are dormant in small tides, and migrate with about equal strength in both directions in large tides. The resultant internal structure is sets of medium-scale cross-bedding in direct contact and lacking reactivation surface. Megaripple scales are larger in the channel behind the barrier (South Channel) than in the main channel despite the shallower depth and weaker currents. Waves dominate the subtidal spit platform, where wave ripples and swash bars are active bedforms. The stratigraphy of the spit platform consists of deposits produced by platform progradation into the channel on the updrift side (bar-front avalanching foresets), and vertical accretion of the platform on the downdrift side. The channel margin linear bar is a transitional zone between tidal currents and waves. Tidal currents are strong enough to engender large-scale tidal bedforms during large tides, but give way to wave processes especially at the seaward end of the bar. The surface changes from essentially megaripple-sculptured (Figure 4-39) to totally flat with small ripples and swash plane beds.

The internal structure of the channel margin linear bar reflects the balance between the rate of progradation of the platform and the reworking of tidal currents. It could be either the bar-front avalanching-foresets where tidal currents are weak (entrance), or megaripple cross-bedding where currents are strong (throat). Both tidal currents and waves are weak on the flood delta, and on the spit, where wind is also active and creates its own surface features. In both areas, although small ripples and other surface features appear on the surface, they do not produce internal structures. Deposits of both environments reflect in-place upgrowth, consisting essentially of massive sands, with the spit containing intercalations of parallel laminae formed by overwashs during storm surges.

Three-dimensional relationships of the environments of the inlet, and the typical vertical sequences are presented in Figure 4-53 and Figure 4-54. The sand body of Palmer Inlet represents a retrogradational sequence formed during late Holocene transgression. The sediment characteristics and the resultant sequences of the sand body are, in general, consistent with published work on other tidal inlets. The differences which exist include: (1) The sand body is thin, about 4 m for the inlet-fill deposits, and 2 m for the rest; (2) It consists almost exclusively of fine sands; lack of a source of fine material results in the absence of mud facies from the flood tidal delta and the

abandoned marginal channel; (3) A large portion of the sand body consists of massive sand (flood tidal delta and spit), or wave-related deposits (downdrift spit platform), and lacks a fining-upward trend in grain size; (4) A relatively complete sequence occurs on the updrift side where the spit platform progrades onto the main channel, and is topped by spit and aeolian deposits; the channel deposits, however, lack large-scale sandwave structures, reactivation surfaces, and a shallow channel unit. These differences arise from a combination of factors which are peculiar to the study area. They include: (1) The uniform, fine-grained texture of the sediment, and lack of mud deposits; (2) The low time-velocity asymmetry of tidal currents; (3) The small tidal range; (4) The shallow channel depth.

Chapter 5

Hydraulic Interpretation of Sediment Characteristics

5.1 Characteristics and Modeling of Suspended Sediments

5.1.1 Data Collection

Suspended sediments (Appendix B-2) were collected using a self-made apparatus (Figure 5-1) at locations shown in Figure 2-17 (hollow circles, Chapter 2). The apparatus was made of aluminum frame with four suspended sediment traps mounted at 0.06, 0.3, 0.7 and 1.0 m above the bed (Figure 5-1). The traps were made of 30 μm-mesh plankton netting bags, 25 cm long and 10 cm diameter. During each deployment, the frame was secured by pounding two pipes into sand bed. Sample bags were replaced every hour. 17 deployments were made using this device during three ebb tides, yielding 68 suspended samples. Two bed material samples were taken at the sample sites during slack waters. All samples were subject to size analysis using the same method as described in Chapter 4 for bed sediments.

Concurrent velocity profile measurements were made using a Marsh-Mcbirney Model 201 current meter at intervals of 15 min. For each profile, velocities were measured at five levels with fix ratios to the water depth: .15, .24, .37, .58 and .90 (Hayter & Mehta, 1979; Appendix D-1). This gives appropriate weighting to values close to the bed, and

Figure 5-1 Schematic view of instrument frame for suspended sediment sampling. The metal frame was made of aluminum bars, and anchored on the bed with three metal pipes, 4.4 cm in diameter. The inset shows a plankton-net clamped on a sawed-off 3'' PVC tube.

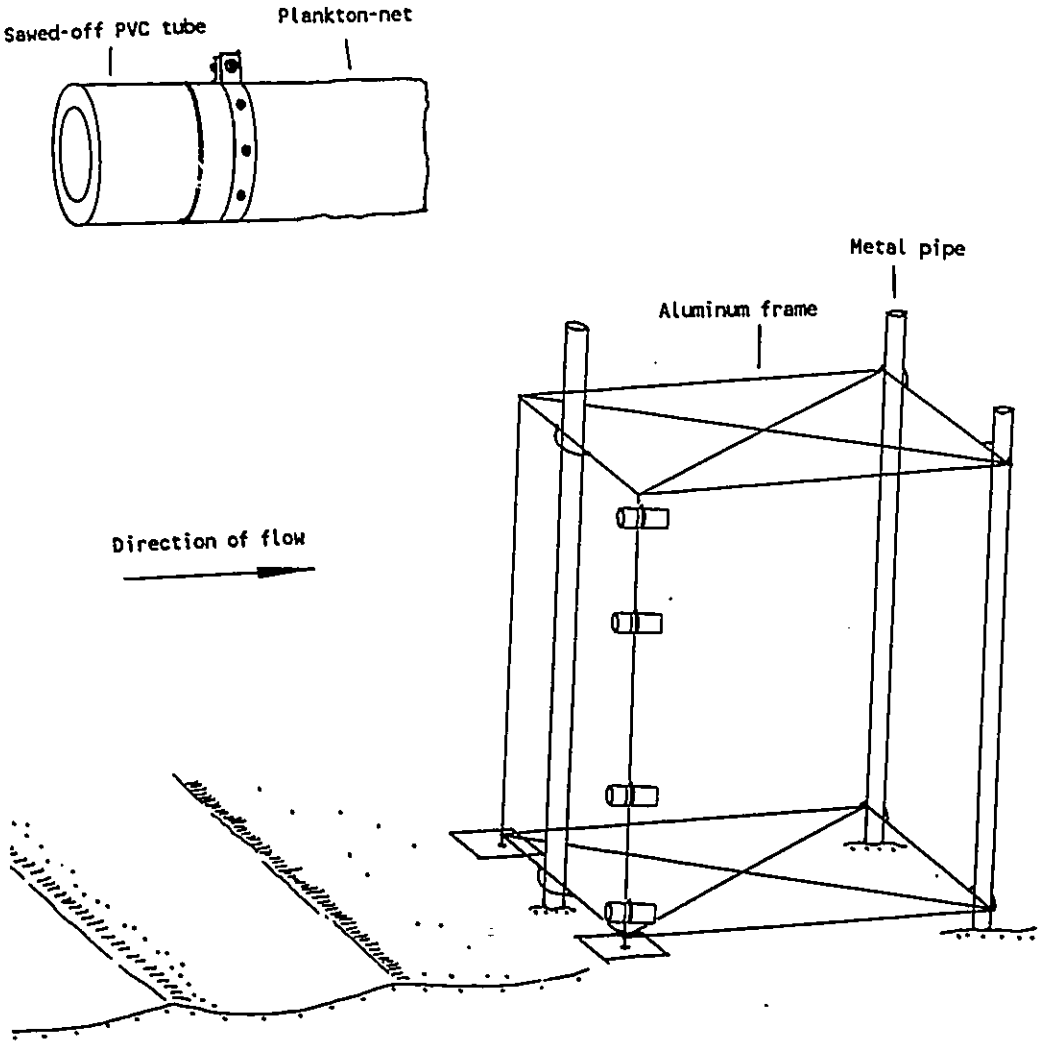
Sawed-off PVC tube
Plankton-net
Metal pipe
Aluminum frame
Direction of flow

on velocity-log depth plots, creates evenly-spaced points as shown in Figure 5-2. U_* was calculated from each profile using the same method as described in Chapter 4. More than 90% of profiles showed fits to the Wall of Law that are statistically significant at the 95% confidence level.

5.1.2 General Characteristics and Their Variations

The statistics of size analyses of suspended sediments are given in Table 5-1. In general, suspended sediments can be easily distinguished from bed sediments (Table 4-1, Chapter 4) by four statistics. They have a finer mean size (2.56 phi), and a poorer sorting (0.45 phi) than all five inlet environments. This is due to their high percentage of mud. The all-profile-averaged value of muds is 4 %, higher than even nearshore samples by a factor of 2. The high mud percent introduces a long fine tail to the size distributions. This, coupled with the generally absence of coarse tails, gives rise to a high, positive skewness (1.88), and together with the dominance of a central, intermittent subpopulation (I) gives a large kurtosis (10.16).

The cumulative curve of suspended sediments closely resembles that of channel bed samples in overall shape (Figure 5-3) with a predominant intermittent suspension (I) subpopulation and subordinate continuous suspension populations (S). The difference is that the S subpopulation

Figure 5-2 Typical near-bed velocity profiles during the two ebb tides of suspended sediment measurements. Time of measurement is noted for each profile. The five elevations of each profile were pre-set at fixed ratios to the flow depth rather than at fixed heights off the bed.

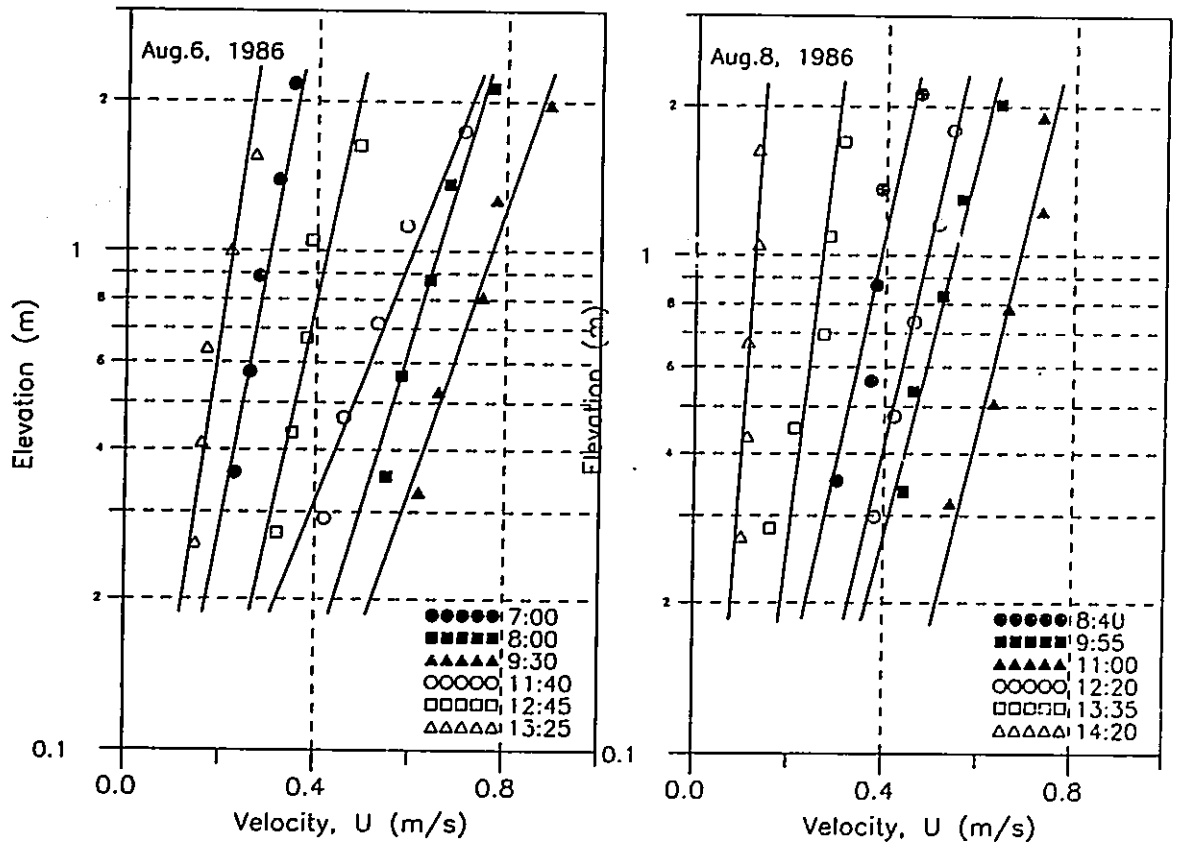
Aug.6, 1986
Aug.8, 1986
Elevation (m)
Velocity, U (m/s)
0.0
0.4
0.8
0.1
1
2
7:00
8:00
9:30
11:40
12:45
13:25
8:40
9:55
11:00
12:20
13:35
14:20

Table 5-1 Textural statistics of suspended sediments at four depths, calculated from 44 samples collected in August 6 and August 8, 1986.

Depth above bed	Statistics	Mean ϕ	Sorting ϕ	Skewness	Kurtosis	Sand %	Mud %
6 cm	Average	2.25	0.31	1.41	11.17	99.67	0.34
	St.dev.	0.09	0.03	0.36	3.07	0.22	0.22
	Maximum	2.37	0.35	1.87	16.65	100.00	0.65
	Minimum	2.13	0.28	0.78	7.20	99.36	0.00
30 cm	Average	2.51	0.40	2.30	12.47	98.44	1.57
	St.dev.	0.10	0.04	0.55	3.93	0.72	0.72
	Maximum	2.63	0.45	3.30	19.26	99.22	2.42
	Minimum	2.38	0.35	1.78	8.61	97.58	0.79
30 cm	Average	2.66	0.51	2.13	9.58	95.64	4.36
	St.dev.	0.14	0.13	0.39	3.32	3.43	3.43
	Maximum	2.83	0.75	2.70	14.56	98.68	10.97
	Minimum	2.46	0.39	1.55	5.27	89.04	1.32
100 cm	Average	2.83	0.60	1.69	7.44	90.27	9.73
	St.dev.	0.27	0.19	0.80	4.31	10.64	10.64
	Maximum	3.28	0.94	2.87	15.05	98.14	29.78
	Minimum	2.53	0.43	0.53	2.03	70.23	1.86
Average of 4 levels	Average	2.56	0.45	1.88	10.16	96.00	4.00
	St.dev.	0.15	0.09	0.52	3.66	3.75	3.75
	Maximum	2.77	0.62	2.68	16.38	99.01	10.95
	Minimum	2.38	0.36	1.16	5.78	89.05	0.99

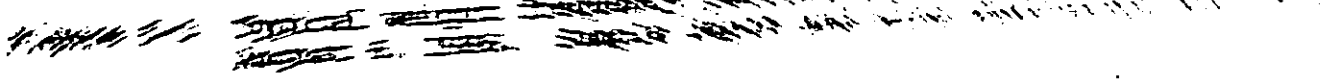

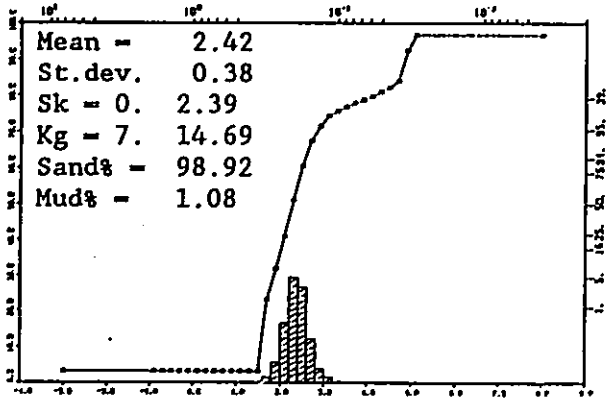

Depth = 0.3 m

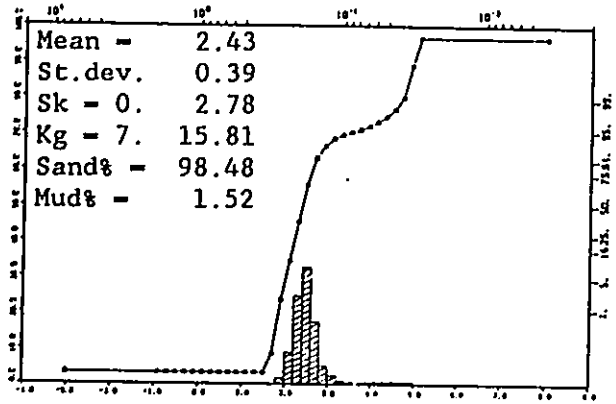

Depth = 0.7 m

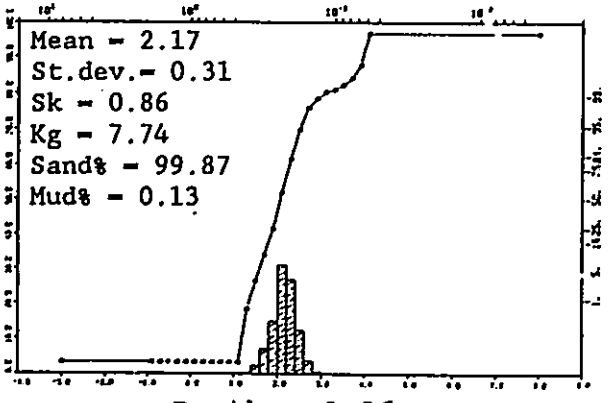

Depth = 0.06 m

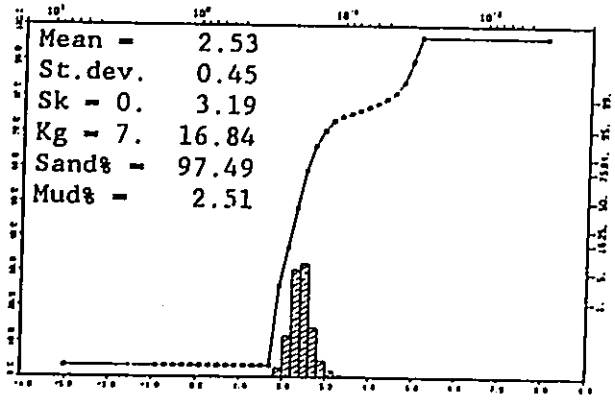

Depth = 1 m

Figure 5-3 Typical weight frequency percent of suspended sediments, 9:30, August 6, 1986. Sample depth and size statistics are shown.

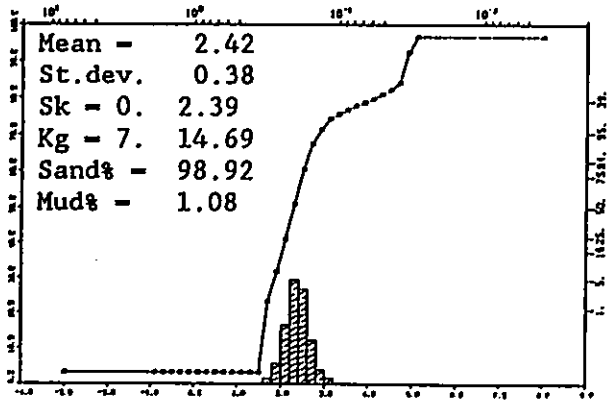

Depth = 0.3 m

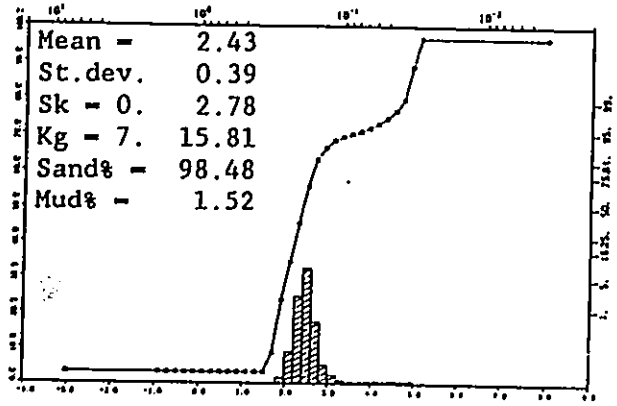

Depth = 0.7 m

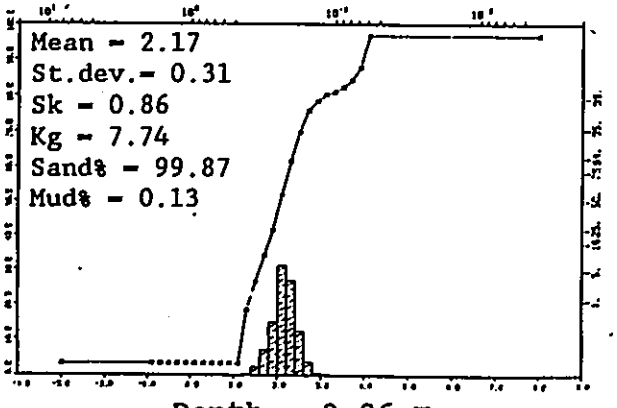

Depth = 0.06 m

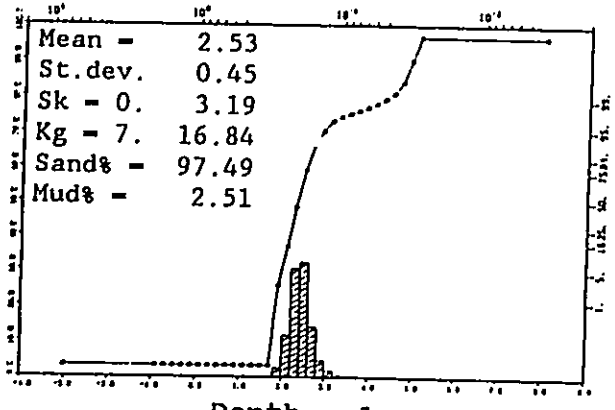

Depth = 1 m

of suspended sediments accounts for about 10 %, considerably higher than that of channel deposits (<2%). In particular, finer-than-4.1 phi particles amount to several percent in suspended sediments with observed values upto 30%. These fines are, however, missing in channel deposits. This suggests that the two S populations are of different origins; the one appeared in the water is not, or at least the majority of it is not indigenous to the channel bed. The fact that fine materials were washed out of Palmer Inlet (Section 4.8.5, Chapter 4) indicates that finer-than-4.1 phi particles are derived from backbarrier and nearshore areas, where they are abundant. For a particle of 5.1 phi in diameter (settling velocity = 0.75 mm/s), it takes about 45 min. to settle through a flow of 2 m depth. This will take it 1300 m down the stream assuming a flow speed of 0.5 m/s. This simple calculation shows that for most of the time when concentrations are relatively high, these fine materials could not settle out onto the (channel) floor. The only time this is possible is the late waning and slack tides. The concentration then, however, is very low, and not expected to have any effect on the size distributions of the bed material. The role of these fine materials to inlet flow can be likened to 'wash load' in a fluvial system: they are present in the water column (with the coming and going of the tide), but not in the bed. In a fluvial channel where a wide spectrum of particle sizes are available, the

grain size of suspended sediment reflects the textural composition of the bed. The above observation indicates that this may not be true in tidal inlets. This is significant as it has direct bearing on how the Rouse suspension equation is to be applied to the latter environments.

5.1.3 Variations of Size Parameters

Besides the overall characteristics, the measurements of suspended sediments also allow examination of their variations vertical in the water column, and over time through a tidal cycle. Variations of suspended sediments with depth show results (Figure 5-4), which are in accordance with diffusion theory, i.e., a balance between settling flux and turbulence generated at the bed:

(1) From the bottom upward, percentage in the sample mud increases consistently, from about 0.34% at 6 cm to 10% at 100 cm. Sand percentage exhibits a reverse trend.

(2) As a result of (1), the mean size decreases with height off the bed, from about 2.25 phi to 2.83 phi. This is accompanied by a deterioration in sorting as standard deviation increases from 0.31 phi to 0.6 phi.

(3) Variations of kurtosis are less consistent but generally become smaller upward, an effect showing the influence of increasing mud percentage. The smaller kurtosis at the lowest level results from the small traction

Figure 5-4 Variations of grain size parameters of suspended sediments with depths. Size parameters are average values of the same elevation. Ordinate is depth in m in logarithmic scale.

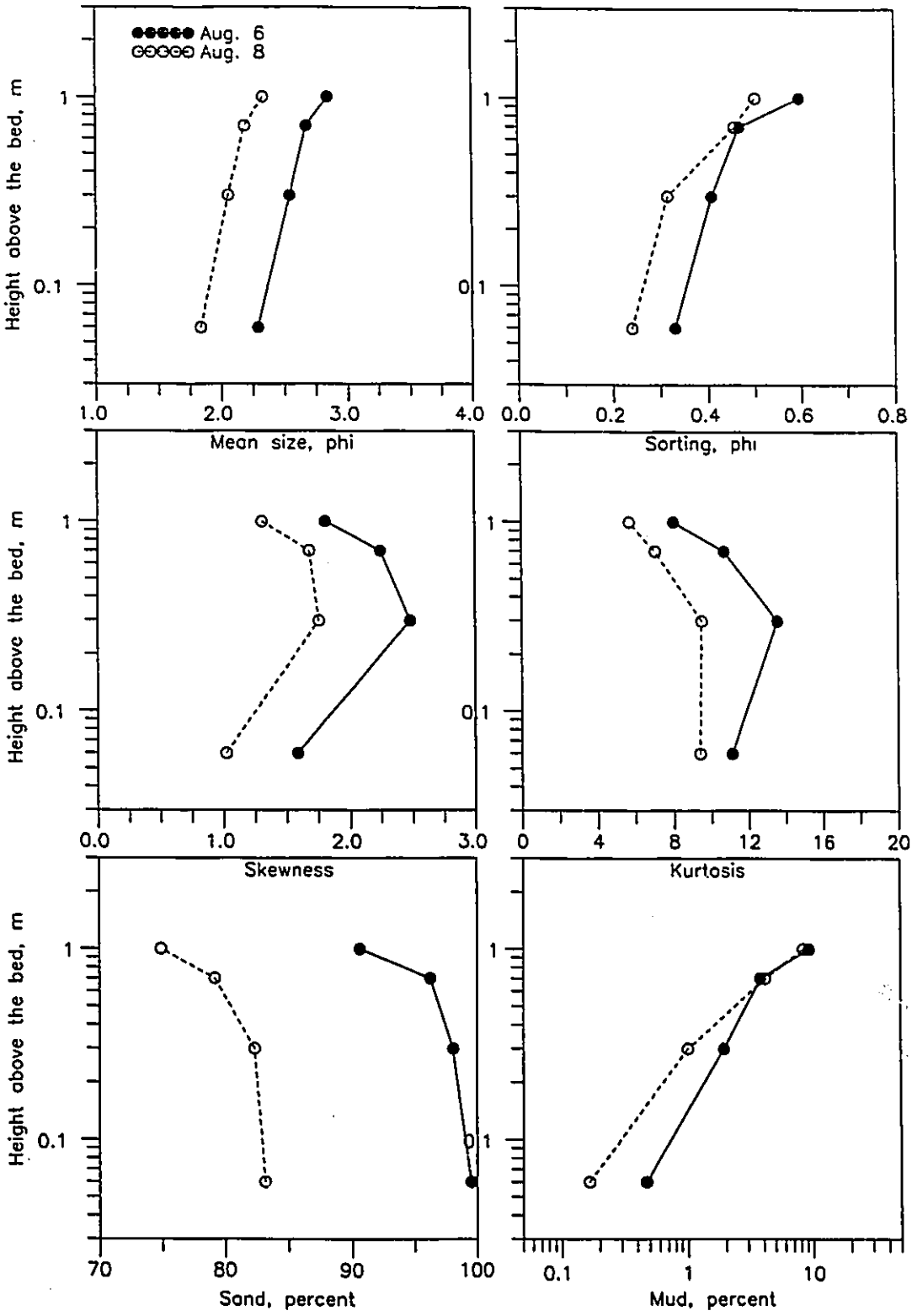
Aug. 6
Aug. 8
Height above the bed, m
1
0.1
1.0
2.0
3.0
4.0
0.0
0.2
0.4
0.6
0.8
Mean size, phi
Sorting, phi
0.0
1.0
2.0
3.0
0
4
8
12
16
20
Skewness
Kurtosis
70
80
90
100
0.1
1
10
Sand, percent
Mud, percent

subpopulation occurring sometimes at that level. By extending the tail on the coarse side, it offsets the 'peakness' of the central portion of the size distribution, thus decreasing the value of kurtosis.

(4) Variations of skewness exhibits a similar pattern to that of kurtosis. The same reason cited above can be used to explain the smallest value next to the bed. The upward trend exhibited by other points is a little perplexing in view of the increasing mud content in this direction. It probably results from the fact that skewness is more sensitive to the tail and to interdependency of size classes, especially their proportionalities, than kurtosis.

Similar systematic changes can also be observed over time as the current strength changes. As shown in Figure 5-5 and Figure 5-6, with increasing shear velocity, there is an increase in mean size and a corresponding decrease in standard deviation with accompanying increase in sand percent and decrease in mud percent. Changes in values of skewness and kurtosis are in good correspondence with what would be expected with the addition or exclusion of mud. Such changes, however, seem to be more synchronized for August 6, where the coarsest sand occurs at the same time as the maximum U_* (about 11:30). In August 8, a delay of about 1 hour exists. A possible explanation could be that the value of the maximum U_* at 11:30, August 6, is overestimated. This would shift the maximum velocity to a

Figure 5-5 Variations of grain size parameters of suspended sediments with time, August 6, 1986. Size parameters are depth-average values for each deployment. Also shown are shear velocities as well as tides and depth-average current speeds.

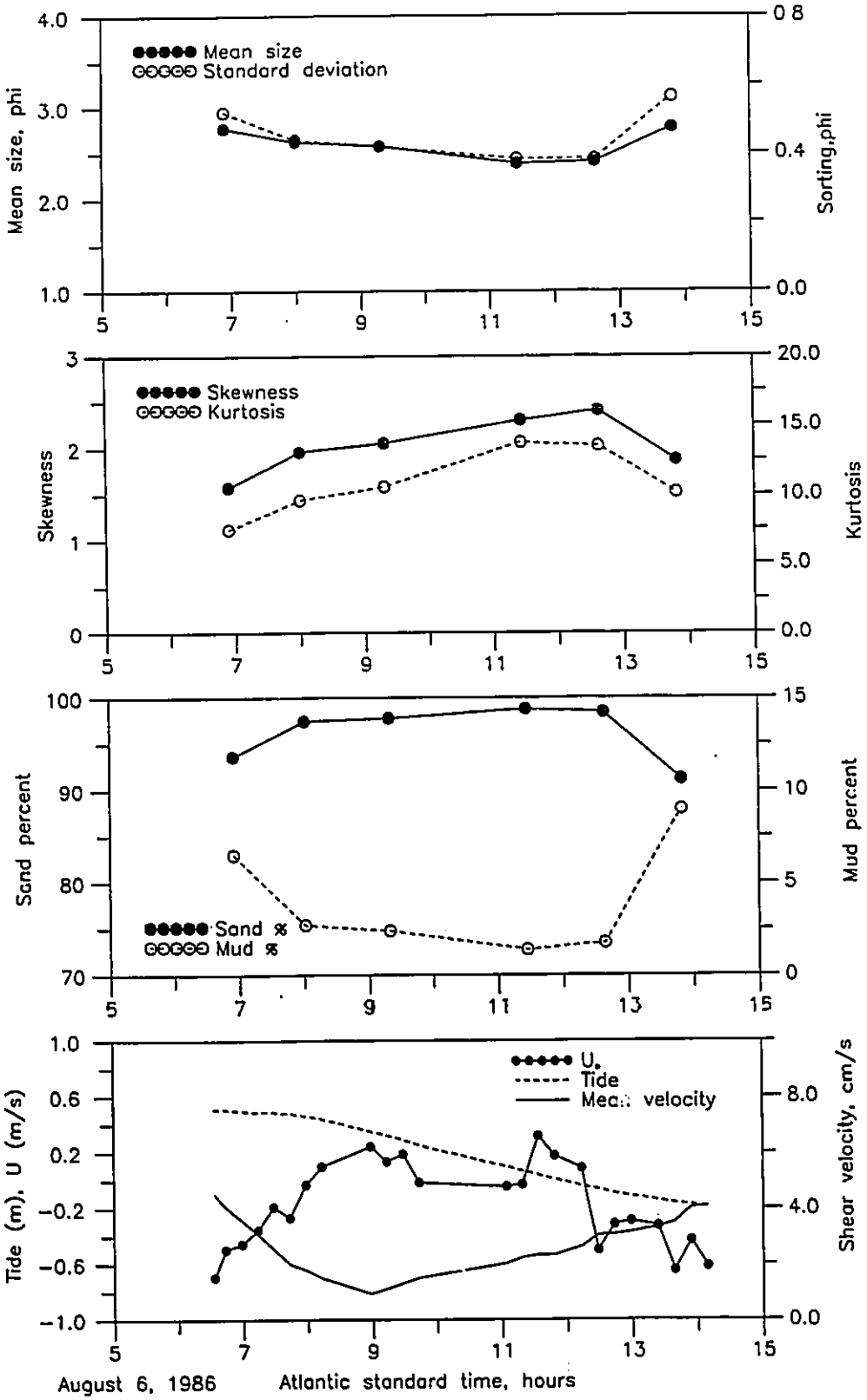
Mean size
Standard deviation
Mean size, phi
Sorting,phi
Skewness
Kurtosis
Sand %
Mud %
Sand percent
Mud percent
U*
Tide
Mean velocity
Tide (m), U (m/s)
Shear velocity, cm/s
August 6, 1986
Atlantic standard time, hours

Figure 5-6 Variations of grain size parameters of suspended sediments with time, August 8, 1986. See Figure 5-5 for other explanations.

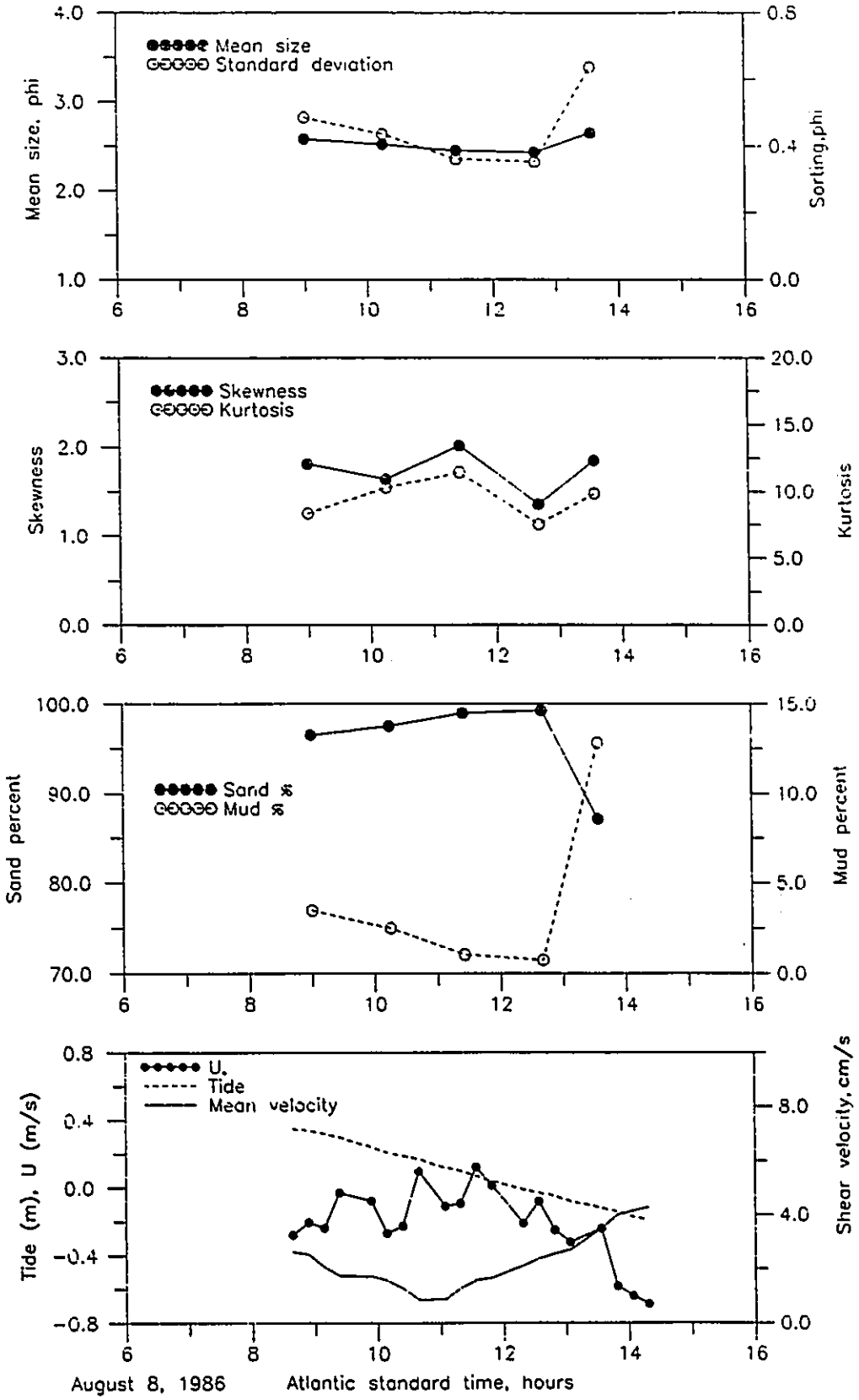
Mean size
Standard deviation
Mean size, phi
Sorting,phi
Skewness
Kurtosis
Sand %
Mud %
Sand percent
Mud percent
U,
Tide
Mean velocity
Tide (m), U (m/s)
Shear velocity, cm/s
August 8, 1986
Atlantic standard time, hours

stage an hour earlier (Figure 5-5), thus bringing the result in line with that of August 8. The difference also could, however, be a reflection of difference in the suspension process during different tidal conditions (Figure 2-7). With the limited data available, the true reason cannot be determined.

5.2 Calculations of Size Distribution of Suspended Sediments from Bed Material

In a study of hydraulic interpretation of grain size distributions, Middleton (1976) used bed material to calculate the size distributions of sediments in suspension using the Rouse equation. He suggested that this is possible provided that the wash load is excluded, and that a reference sample is available which is close enough to the bed that its size distribution can be assumed the same as that in the bed. In the present study, the same method is used to predict suspended sediment distributions for comparison with the measured data at Palmer Inlet. As sediment samples are usually taken at the bed, it will be of great convenience that they can be directly used in the predictions. A new form of Rouse equation thus was developed, which accepts input directly from the bed.

5.2.1 Rouse Equation and Its Modified Form

The existing theory describing suspended sediment

concentrations of a turbulent flow is that of Rouse equation (1937):

$$C = Ca \left(\frac{D - Y \quad a}{D - a \quad Y}\right) \frac{W}{\kappa U_*} \qquad \text{— (1)}$$

Where D = total water depth; Ca = sediment concentration at a reference level a; C = sediment concentration at distance Y off the bottom; W = particle settling velocity; κ = Von Karman's constant, and U_* = shear velocity acting on the bed. If weight percent rather than weight is used, the same equation can be used to predict size distribution of either bulk or each size class of suspended sediments. It is of practical significance that the required concentration, Ca, can be chosen at the bed. At y = 0, however, Rouse equation approaches infinity. This is inherited from the assumption of a logarithmic velocity profile in deriving the equation. The infinity problem of the velocity profile was overcome by Rossby (1932), Sutton (1953) and Mehta and Christensen (1983) by introducing a +1 into the logarithmic term,

$$\frac{U}{U_*} = \frac{1}{\kappa} \ln \left(\frac{Y}{Z_o} + 1\right) \qquad \text{— (2)}$$

Equation (2) can be used to derive a new form of

Equation (1):

$$\frac{C}{Ca} = \left(\frac{(D-Y)}{(D-a)} \frac{(a+Z_o)}{(Y+Z_o)} \right) \frac{W D}{\kappa U_*(D+Z_o)} \qquad \text{— (3)}$$

Figure 5-7 shows comparisons of results calculated using Equation (3) and Rouse equation. For small Z_o values (< 0.5 cm), results from the two equations are almost identical. Above 0.5 cm, the new equation overestimates slightly. Rouse equation was based on the assumption of a plane bed. Occurrence of bedforms increases turbulence and lifting forces for suspension. In this sense, Equation (3) appears to be closer to natural conditions. Equation (3) eliminates the infinity problem, and has the advantage of requiring no measurements above the bed. In the following, it is used to predict size distributions of suspended sediments from samples taken at the bed.

5.2.2 Preparation and Procedure of Computations

As noted above, the S subpopulation of suspended and bed sediments are of different origins. The S population should be separated and excluded from bed samples. This can be done by one of the existing graphic (Cassie, 1954; Middleton, 1988) or numerical methods (Clark, 1976; Sheridan et al., 1987). In the present study, a simpler approach was used because of the extremely small quantities involved. It

Figure 5-7 Comparisons of profiles of suspended sediment concentrations calculated using Rouse equation (solid lines) and Equation (2) (dotted lines). Roughness length is 0.2 cm for the upper graph, and 1.0 cm for the lower graph. Flow depth of 2 m is used.

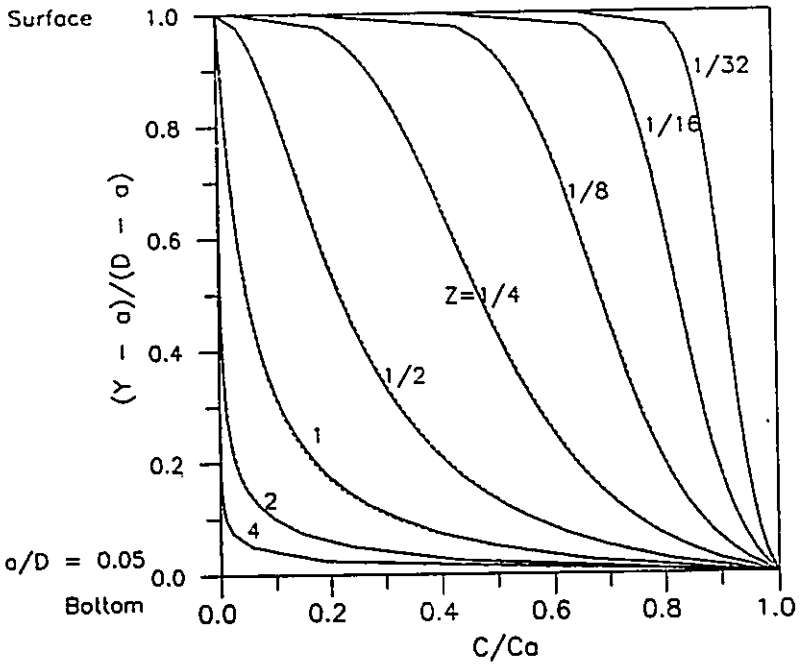
Surface
1.0
0.8
0.6
0.4
0.2
0.0
(Y - a)/(D - a)
1/32
1/16
1/8
Z=1/4
1/2
1
2
4
a/D = 0.05
Bottom
0.0
0.2
0.4
0.6
0.8
1.0
C/Ca

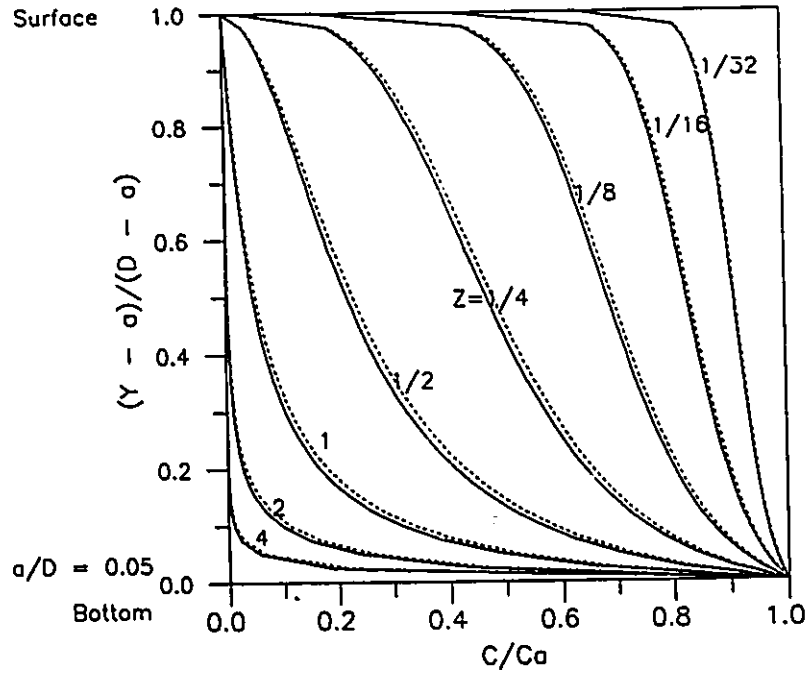
Surface
1.0
0.8
0.6
0.4
0.2
0.0
(Y - a)/(D - a)
1/32
1/16
1/8
Z=1/4
1/2
1
2
4
a/D = 0.05
Bottom
0.0
0.2
0.4
0.6
0.8
1.0
C/Ca

was done by first extending the line of the I subpopulation on the probability paper, and then re-reading cumulative percent off that extended line at 0.2 ϕ intervals upto 99.99%. The last percentile thus derived was taken as the upper limit, whose cumulative percent was noted as N. Anything beyond this was treated as not indigenous and discarded. The cumulative frequency of each size class was then re-calculated to 100% by multiplying a factor of 100/N.

Using re-calculated data of bed sediments, relative weight percent of C was calculated at 0.2 phi intervals for four depths of each profile where suspended samples were taken. For each deployment, two sets of calculations were made using (1) average U_*; and (2) maximum U_*, respectively. The settling velocities were calculated from van Rijn (1984) using mid-class phi values for conditions of sediment density of 2.65 g/cm^3, fluid density of 1.0 g/cm^3, and viscosity of (0.01005 cm unit). No correction was made to the Von Karman constant due to sediment concentration (Vanoni, 1977). Results of are shown in Figure 5-8 and Figure 5-9 with predicted data plotted against measured ones.

A direct way to compare the goodness of fit of results is by computing a chi square as a sum over (predicted weight % - observed weight %)^2 divided by observed weight % (Jarrett and Kraft, 1989). In the present study, the expression was used without the power of 2 in

Figure 5-8 Comparisons of predicted and observed size distributions of suspended sediment for model (1) (A) and model (2) (B), August 6, 1986. Model (1) uses average U_*. Model (2) uses maximum U_*. The vertical axis is relative weight in percent. Time and elevations at which samples were taken are shown. Also shown is the bottom sample used in modeling.

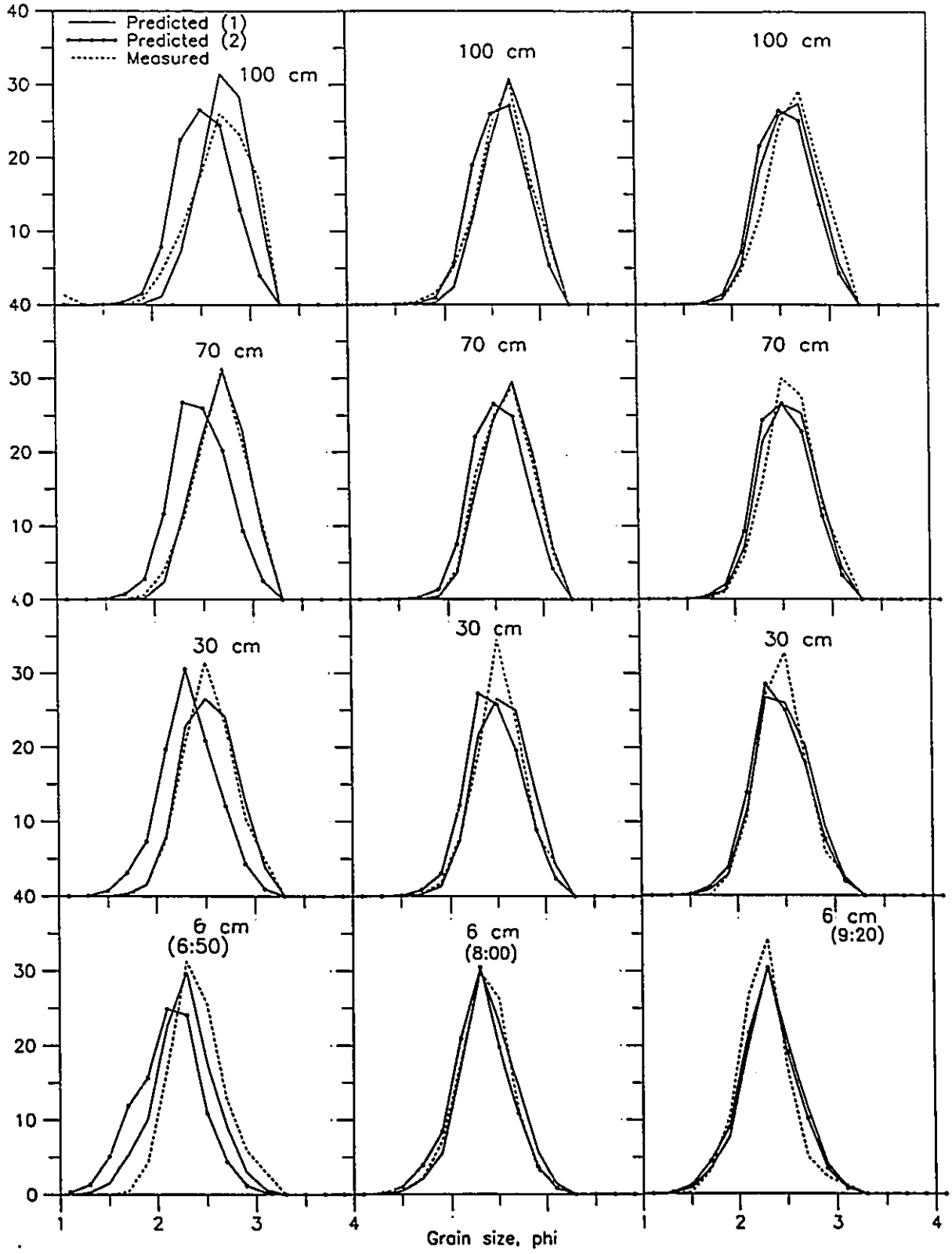
Predicted (1)
Predicted (2)
Measured
100 cm
100 cm
100 cm
70 cm
70 cm
70 cm
30 cm
30 cm
30 cm
6 cm (6:50)
6 cm (8:00)
6 cm (9:20)
40
30
20
10
0
1
2
3
4
Grain size, phi

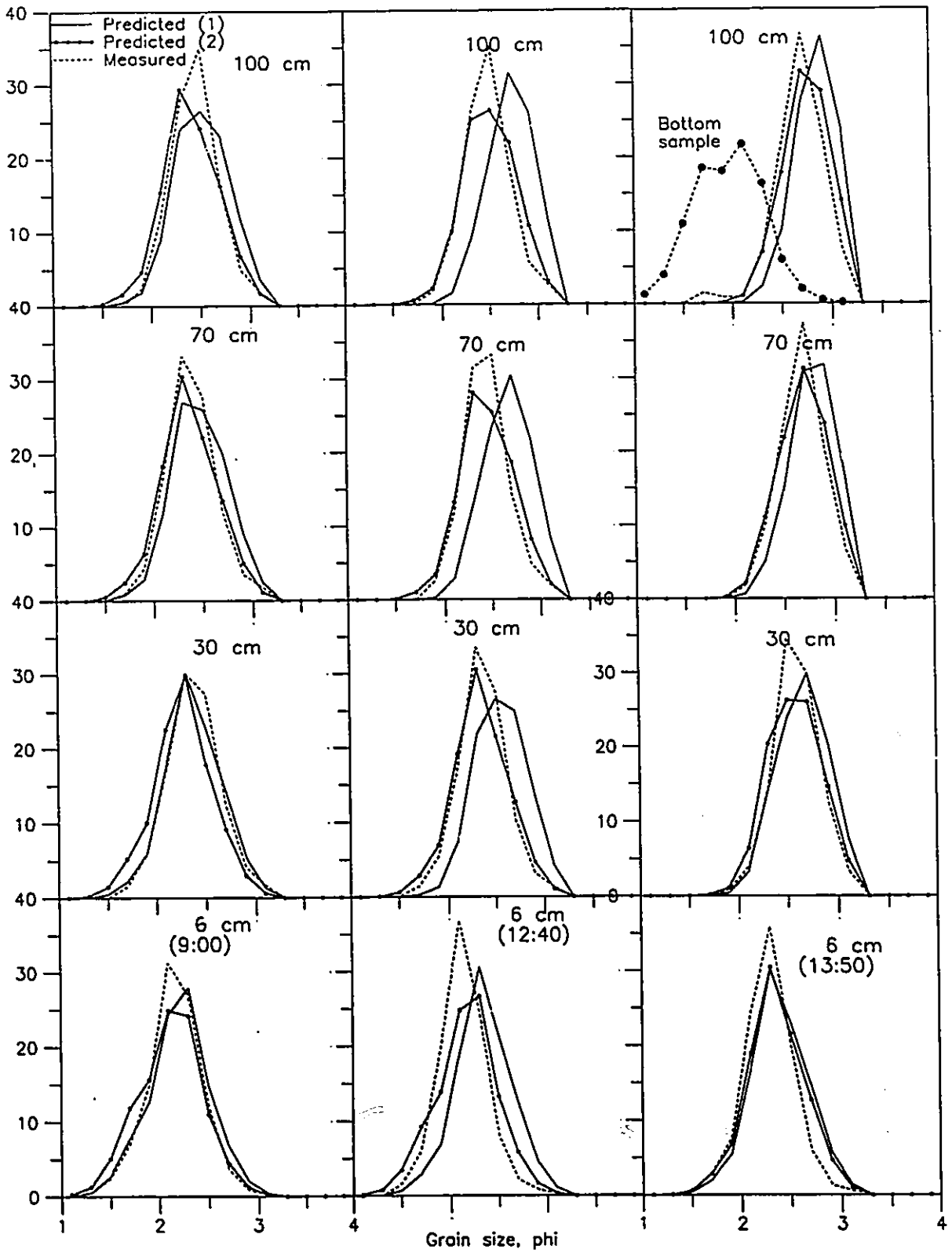
Predicted (1)
Predicted (2)
Measured
100 cm
100 cm
100 cm
Bottom sample
70 cm
70 cm
70 cm
30 cm
30 cm
30 cm
6 cm (9:00)
6 cm (12:40)
6 cm (13:50)
Grain size, phi

Figure 5-9 Comparisons of predicted and observed size distributions of suspended sediment for model (1) (A) and model (2) (B), August 8, 1986. Model (1) uses average U_*. Model (2) uses maximum U_*. The vertical axis is relative weight in percent. Time and elevations at which samples were taken are shown. Also shown is the bottom sample used in modeling.

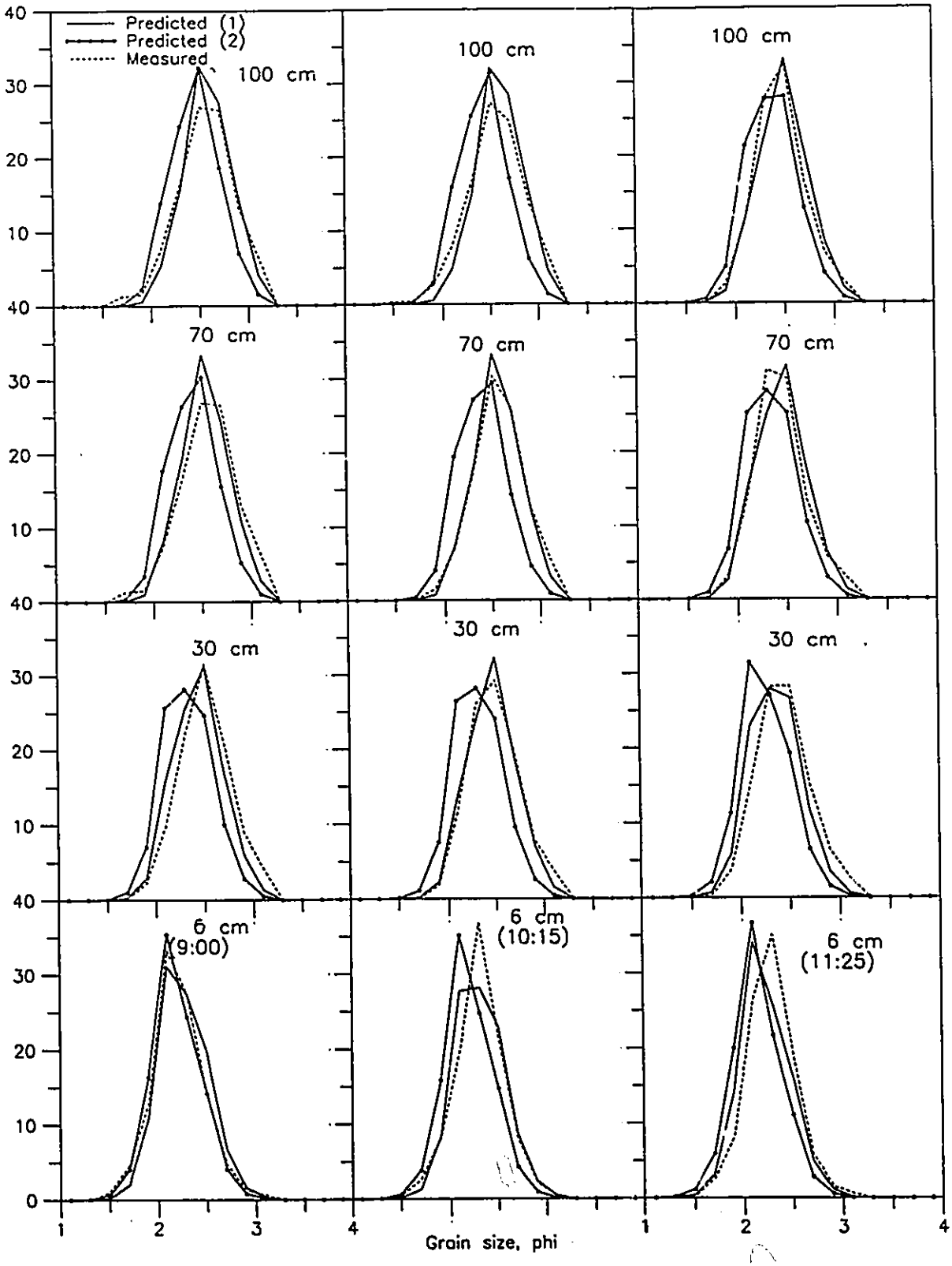
Predicted (1)
Predicted (2)
Measured
100 cm
100 cm
100 cm
70 cm
70 cm
70 cm
30 cm
30 cm
30 cm
6 cm (9:00)
6 cm (10:15)
6 cm (11:25)
Grain size, phi

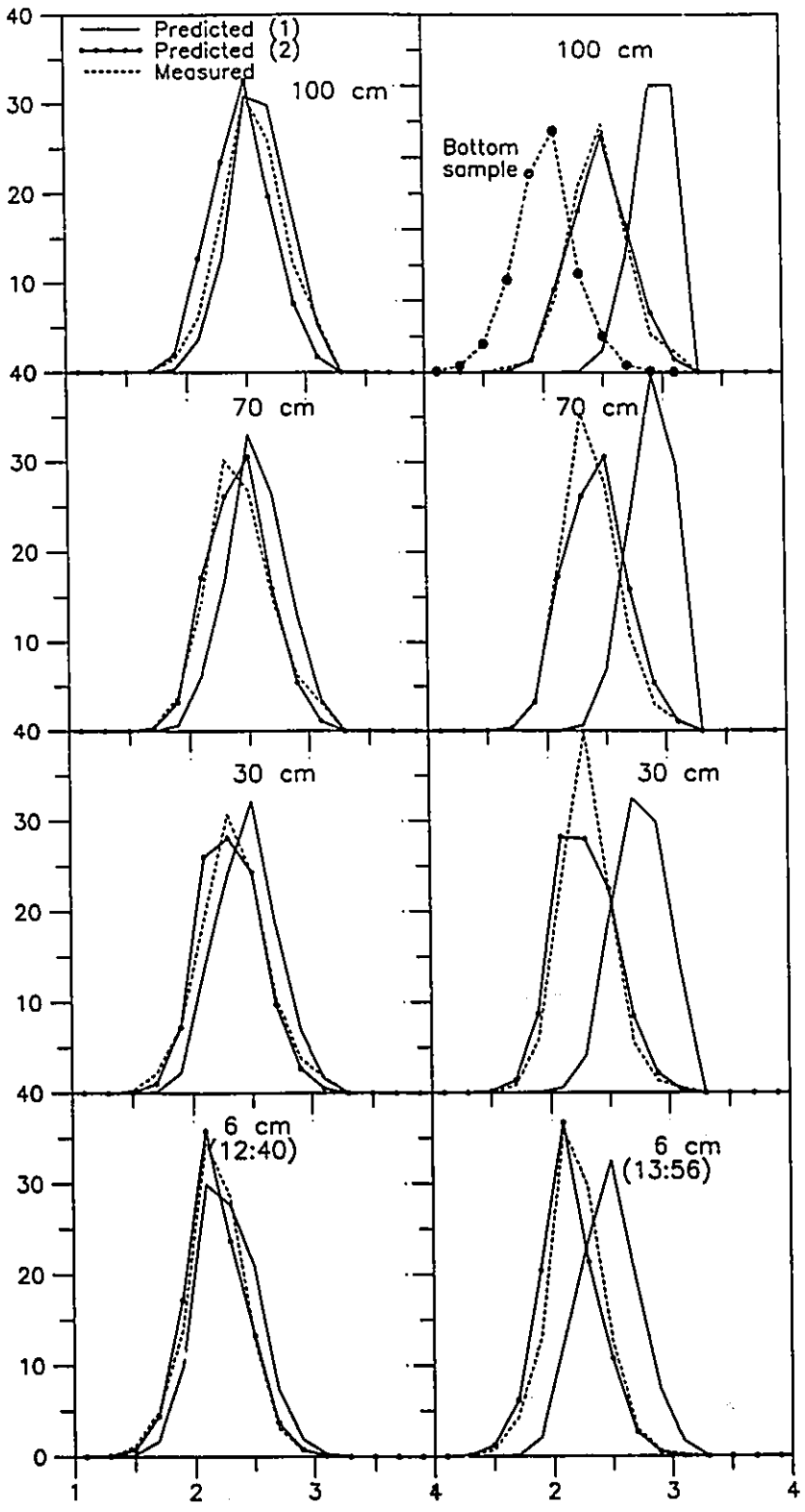
Predicted (1)
Predicted (2)
Measured
100 cm
100 cm
Bottom sample
70 cm
70 cm
30 cm
30 cm
6 cm (12:40)
6 cm (13:56)
40
30
20
10
0
1
2
3
4

order to retain the sign. Differences were calculated for each size class (Figure 5-10). They were then summed over all classes for each sample (solid dots in Figure 5-11), and further over (four) depths for each deployment (cross dots).

5.2.3 Results of Calculations

The first impression on the results of the modeling is its wide variations. The similarity of modeled and observed size distributions ranges from closely following each other in overall shape to showing major departures in both peaks and in lateral positions. The difference factor for individual size class, as a measure of goodness of fit, spreads over four orders of magnitudes with about 55% of the values falls between -0.4 and 0.4. The smallest is less than plus or minus 0.01, but values as high as 30 occur (Figure 5-11). It is noted that large departures occurred primarily toward the very ends of the size distributions, where the weight percent of the observed samples is extremely low. The average difference, excluding these end points, was recalculated to be 0.1, decreasing by a factor of three but still not to be considered small. Difference summed over all classes are equally varied, range from as small as -0.01 to overestimating by a factor of up to 231; the majority are within plus and minus 1-2.

For both tidal conditions, the departure appears generally small around mid-tides as the flow is strongest,

Figure 5-10 Frequency distributions of the difference factor, calculated for each size class by $(C_p - C_o)/C_o$, where C_p = predicted weight %; C_o = observed weight percent. Some statistics are shown.

(A) Results of model (1) and model (2) combined. Two averages shown correspond to (1) all data; (2) all data except those > 3, which mainly occur at the two ends of size distribution when the weight % of the observed samples are extremely small.

(B) Using model (1) results for accelerating flows, and model (2) results for decelerating flows.

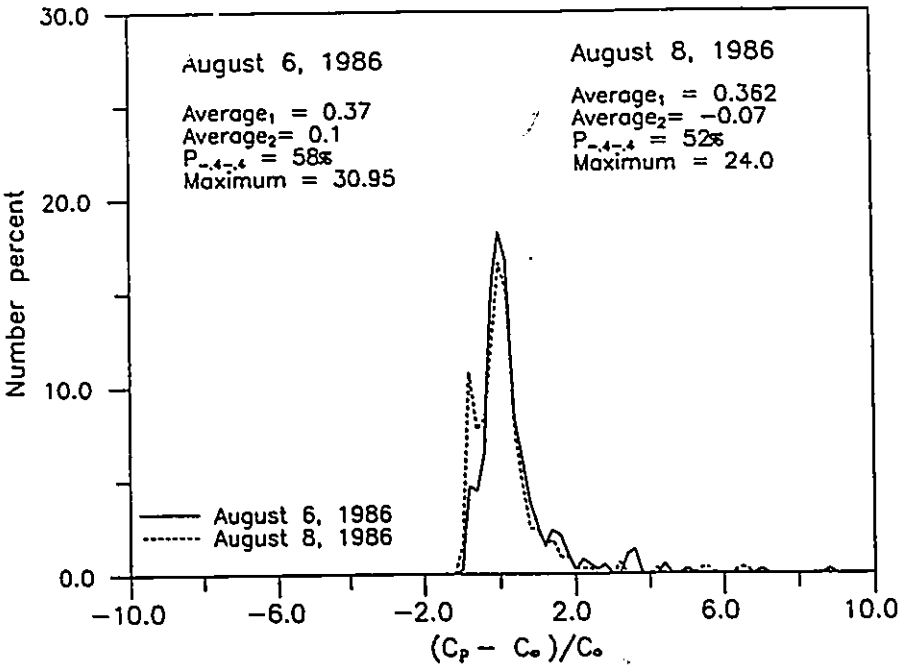
30.0
20.0
10.0
0.0
Number percent
August 6, 1986
Average1 = 0.37
Average2= 0.1
P-.4-.4 = 58%
Maximum = 30.95
August 8, 1986
Average1 = 0.362
Average2= −0.07
P-.4-.4 = 52%
Maximum = 24.0
August 6, 1986
August 8, 1986
−10.0
−6.0
−2.0
2.0
6.0
10.0
(Cp − Co)/Co

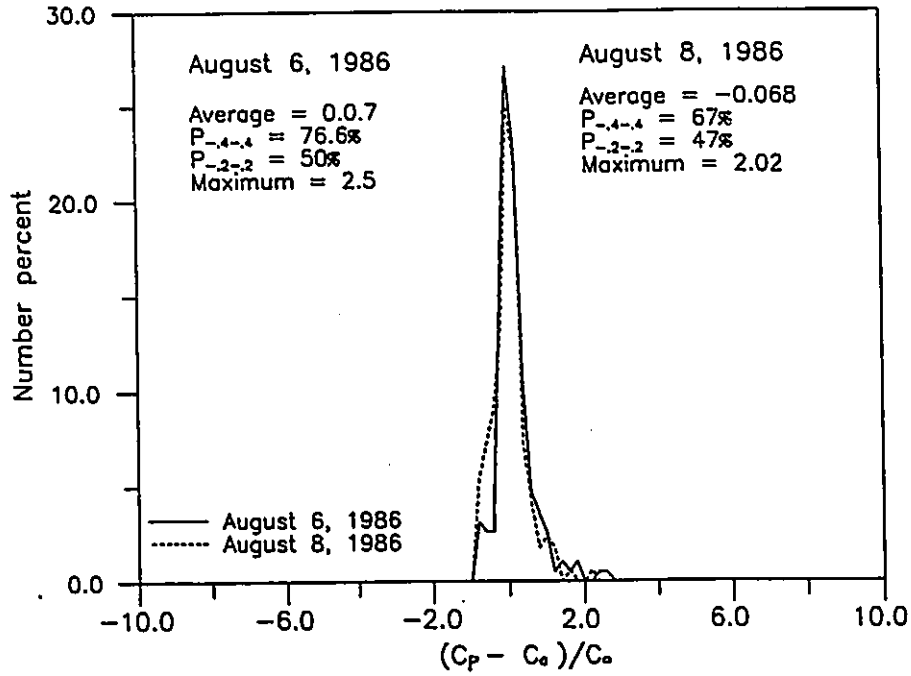
30.0
20.0
10.0
0.0
Number percent
August 6, 1986
Average = 0.0.7
P-.4-.4 = 76.6%
P-.2-.2 = 50%
Maximum = 2.5
August 8, 1986
Average = −0.068
P-.4-.4 = 67%
P-.2-.2 = 47%
Maximum = 2.02
August 6, 1986
August 8, 1986
−10.0
−6.0
−2.0
2.0
6.0
10.0
(Cp − Co)/Co

Figure 5-11 Difference factor (summed over size classes) between observed and predicted weight % for model (1) using average U_* and model (2) using maximum U_*. The large crossed circles are profile differences summed over four samples at z = 6, 30, 70 and 100 cm. The number by the arrow in the upper left graph refers to offscale data points. Note the scale changes.

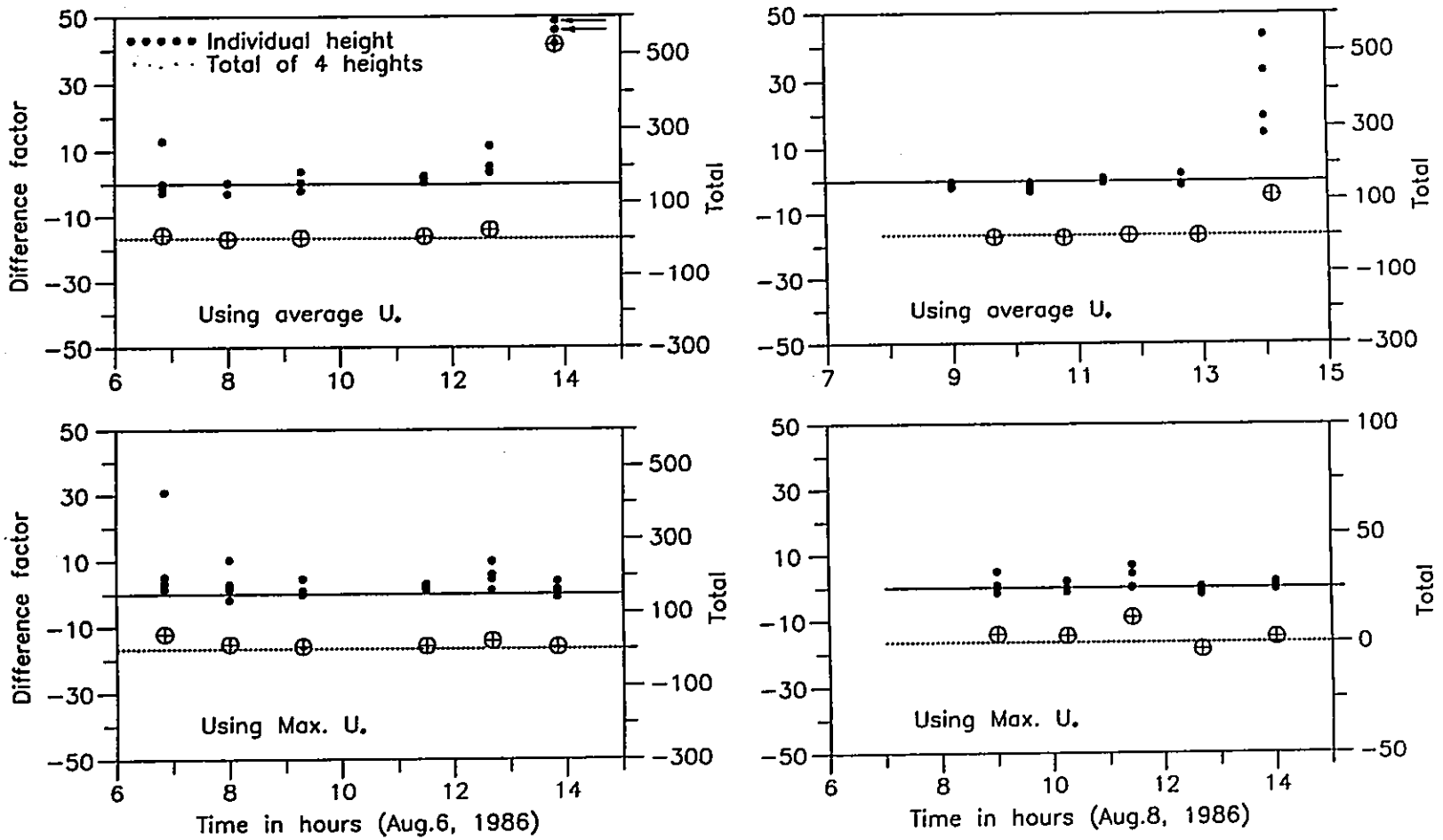
Individual height
Total of 4 heights
Difference factor
Total
Using average U.
Using Max. U.
Time in hours (Aug.6, 1986)
Time in hours (Aug.8, 1986)

and increases toward both directions with reduced speeds. Different phase relationships can be observed, however, between predicted and measured curves for the two models. For model (1) (solid lines), larger departures occur at late stages of tides (12:40 and 13:50 for August 6, and 13:56 for August 8), when differences reach 525 and 110. For model (2) (dotted solid lines), on the contrary, larger departures occur at earlier stages (6:50 for August 6, and 9:00 for August 8). On size distribution plots (Figure 5-8 and 5-9), this is shown by a consistent shift with time of dashed lines (observed) from more closely coinciding with solid lines to more closely coinciding with dotted solid lines. Such changes can be observed for both August 6 and August 8.

5.2.4 Explanation of Different Phase Relationships

In unsteady flows, sediments often do not response in phase to the variation of hydraulics (Allen, 1978). Instead, they exhibit a delay (Allen, 1973; Allen, 1976; Terwindt and Brouwer, 1986; Dyer, 1980) when plotted against, for example, current velocities. The delay theory implies that the response is not directly related to the force at the time the measurement was made, but a function of past history. In the case of suspension process, sediments measured at some instant at some height above the bed represent a time-integration of particles dislodged earlier but still moving in the water column. To represent

this integration, an appropriate parameter should be used. Such a parameter will apparently be different for the early tide when the flow is accelerating and for the late tide when it is decelerating. For accelerating flows, it should reflect the condition of earlier lower speeds due to the nature of the flow. Of the two parameters, $U_{*_{avg}}$ is therefore a better representative than $U_{*_{max}}$ would. For decelerating flows, the reverse will be true. That is, with past flow being stronger, $U_{*_{max}}$ will be a better choice.

Based on above considerations, difference factors were recalculated using model (1) results for accelerating flows and model (2) results for decelerating (Figure 5-10). As is expected, the goodness of fit is improved significantly: the percentage of difference between plus and minus 0.4 increases to 77% and 67% for the two days, respectively. About 50% of the samples now fall between -0.2 and 0.2 with an average of 0.07. For a sample consisting of 8-10 size classes, this gives a sample error of 56-70 %.

5.2.5 Sources of Errors

Compared with other studies, deviations of the present study are relatively large. Sternberg et al. (1986) found that the observed suspended sediment in San Francisco Bay could be predicted 68% within plus and minus 0.25, 10% or higher than the present study. A number of reasons could

cause the difference. First, sediment monitoring is a more difficult operation in the present environment where flows are relatively swift. The mounting of instruments also presents problems because of artificially induced scouring, or perturbations of the flow field around. Secondly, many boundary effects neglected are more seriously violated. With large-scale bedforms existing on a shallow water floor, the uniformity of flow assumed by Rouse equation is less valid in the present case. The same is true for Von Karman's constant and fluid viscosity. The presence of higher concentrations of sediment in suspension in the fluid can change the characteristics of the flow, which in turn can affect the sediment in motion (Vanoni and Nomicos, 1959; Thron and Parson, 1980). The sampling apparatus is another possible source of errors. The metal frame and the traps mounted in close proximity undoubtedly interfered with flows, hence distorting sediment paths. The plankton netting bags used in this study provided further impedance to water passing through, especially toward the end of each deployment when they are relatively clogged.

Furthermore, the calculations assumed a time-independent size composition of the bed material. In reality, this is not true. Repetitive suspension and differential settling of particles could cause layering of bed sediments with fine particles concentrated closer to the surface (Hamilton, et al., 1980). The availability of these

particles for suspension thus varies with tides. Less of them will be available during high velocity periods than during lower velocity periods as water-bound fine sediments settle back to the bed. On the other hand, continuous erosion during suspension would provide armouring for the bed as coarser particles were left behind. This effect is also a function of time, and may further complicate the situation.

5.2.6 Summary of Suspended Sediments

Suspended sediments at Palmer Inlet differ from bed samples by their small mean size, poor sorting, and large positive skewness and kurtosis. They show expected variations with current speeds and heights off the bed as observed in turbulent flows. Comparisons of size data of suspended and bed sediments indicate that inlet flows are more a process of removal rather than addition of fine particles to the system as observed in, for example, tidal flats. The finer-than-4.1 phi particles, which are virtually absent in the bed, make up a large portion of the S subpopulation of suspended sediments. These materials are thus derived from outside (backbarrier and nearshore), and the two S subpopulations of suspended and bed sediments are not formed by the same suspension processes. They move through the inlet during each tide like the 'wash load' in rivers, present in the water column but not to be

incorporated into the bed.

The method proposed by Middleton (1976) provides an easy way to calculate size distributions of suspended sediments from bed material. The calculated results from this study show good general agreement in the overall shape of size distribution with the measured samples. The individual values could be predicted within an accuracy of 60%. With a number of possible sources of error involved, such figure can be considered reasonably good. The results also showed that caution must be exercised in applying the method to unsteady flows when sediment samples were taken over an extended period of time. The choice of an appropriate velocity parameter is very important under such conditions. The two models, using $U_{*_{avg}}$ and $U_{*_{max}}$ as input hydraulics respectively, showed different phase relationships between predicted and measured size distributions. Better correlations occurred during the early stage for the model using $U_{*_{avg}}$, and during the late stage of tides for the models using $U_{*_{max}}$. This is interpreted to be the result of lag effects, as it suggests that accelerating flow should be described by a relatively lower value and decelerating flow by a higher value, as if suspended sediments remember the 'past history' of flow.

5.3 Characteristics of megaripples as individuals

Tidal bedforms have been used to establish range of

tides and flow speeds of paleo-environments where tidal influence prevails (Allen, 1981). In this study, bedforms are studied at two levels, i.e., as individuals and as groups. In this section, bedforms are studied by using bivariate plots of (1) wave lengths and heights, and (2) current speeds and water depths. Grain size is not included in the analyses because of its narrow range. Summaries of tidal bedforms have been made by a number of authors (Costello and Southard, 1981; Amos and King, 1984; Dalrymple et al. 1978). These studies are based on much more data, but consist mainly of measurements from large-scale systems, primarily macro- and meso-tidal estuaries/inlets and shorefaces. It is interesting to see how the results of the present study of a single small tidal inlet fit into the framework established from these summaries.

5.3.1 Wavelengths versus Heights

Plots of wave lengths versus heights have been used as a means of examining spectral gaps and classifying bedform phases (Costello and Southard, 1981; Heathershaw and Codd, 1985; Amos and King, 1984; Mann and Swift, 1981). Such plots at Palmer Inlet show similar results to those found elsewhere. This is illustrated on a log-log plot (Figure 5-12A). The figure shows expected linear trend of wave heights increasing with wave lengths from small ripples to megaripples. The rate of increase follows closely the

Figure 5-12 Log-log plots of wave lengths versus heights of megaripples with (A) or without (B) ripple data. These data are compared with summaries of other authors as shown as straight lines in the figures.

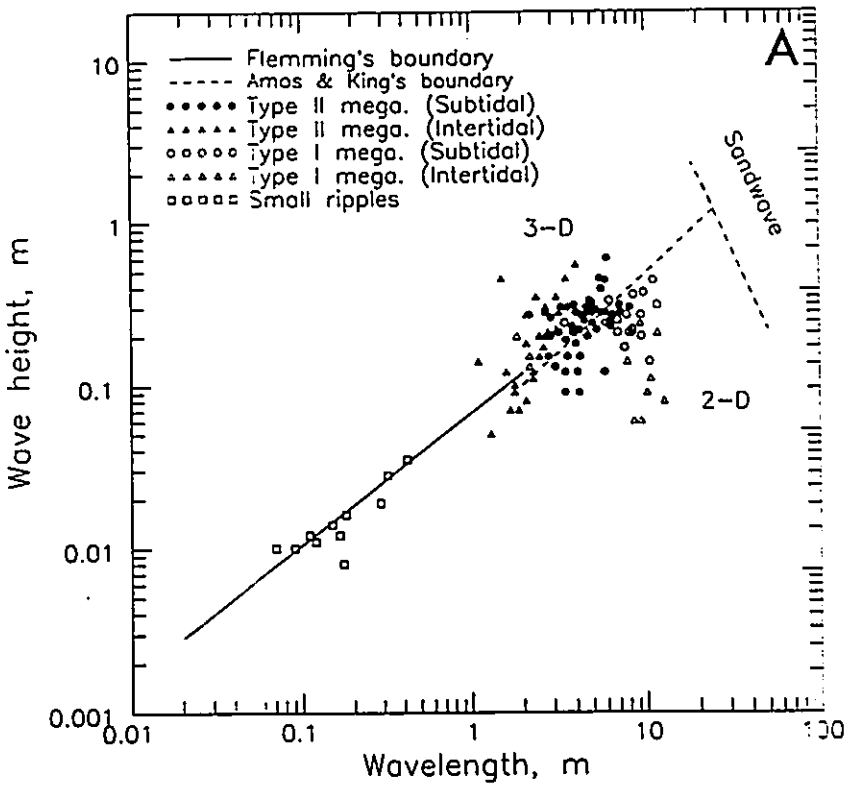
A
Flemming's boundary
Amos & King's boundary
Type II mega. (Subtidal)
Type II mega. (Intertidal)
Type I mega. (Subtidal)
Type I mega. (Intertidal)
Small ripples
3-D
2-D
Sandwave
Wave height, m
Wavelength, m
10
1
0.1
0.01
0.001
0.01
0.1
1
10
100

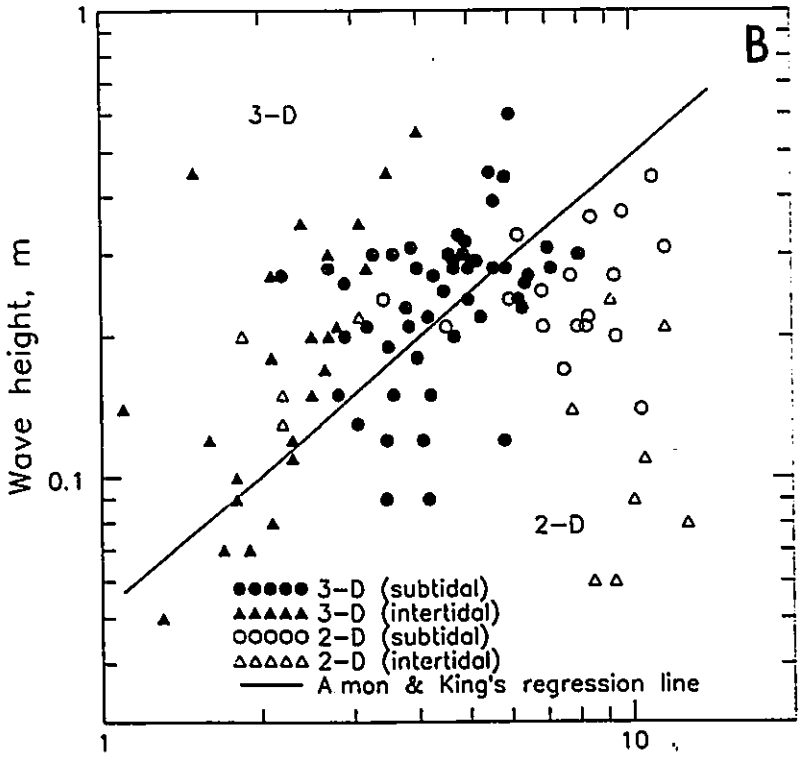
B
3-D
2-D
3-D (subtidal)
3-D (intertidal)
2-D (subtidal)
2-D (intertidal)
Amon & King's regression line
Wave height, m
1
0.1
1
10

regression line of Flemming (1988) calculated from 1491 data points from various locations. Despite the scatter, megaripples fall within a field, which conforms with their global occurrence (Amos and King, 1984), and can be separated from small ripples by a discontinuity at a wave length of around 1 m. These results provide support for the observation that values of the two parameters, i.e., wave lengths and heights, differ for different bed phases. This is true irrespective of locations and origins. These two parameters are therefore good indicators for differentiating between megaripples, sandwaves and small ripples.

The high degree of scatter exhibited by megaripples is due, to a large degree, to some outliers in both the Type I and Type II field. Inspections show that these outliers are mostly from the intertidal north channel linear bar. In particular, those of Type I outliers are from the seaward end, and those of Type II outliers from the landward end of the bar. Chapter 4 described that at the landward end of the bar, flows undergo expansion; speeds are usually below the threshold of megaripple creation. Low-amplitude, subdued bedforms, however, form at this location probably as a result of long-term accumulation under the influence of the strong ebb-dominated flows. These bedforms assume the morphology of Type I megaripple. On the other hand, the convergence of flow and rapid change in its directions created high turbulence at the landward (throat) of the bar

before emergence. The bursts of turbulence, though short lived, scoured pits in the troughs. The resultant bedforms assumed morphology of Type II megaripples. In either case, outliers are probably not equilibrium forms.

In the study of bedforms using wave lengths and heights, a distinction is often made between Type I and Type II megaripples. This is considered as reflecting changes in kinematic structure of flows at higher velocities. Data from Palmer Inlet show that such distinctions cannot be made without a great amount of ambiguity. Figure 5-12B shows that while Type I and II megaripples are roughly distributed into two fields, there is considerable overlapping across the line roughly interpreted as the boundary by Amos and King (1984). This agrees with results of Dalrymple et al. (1978) and Amos and Kings' summary. Consequently, wave lengths/heights are not distinct indicator for differentiating the two types of megaripples. The overlapping, however, appears primarily as subtidal Type II megaripples distributing into the Type I field; there are less Type I megaripples distributing into the Type II field. The pattern appears to suggest a rather consistent underestimates of heights or overestimates of wave lengths in the field. Such underestimates could result from ambiguous morphology and resultant incorrect identification of bedforms. This is in line with above observations about intertidal 'outliers'. They together point out the

difficulties in identifying equilibrium and non-degraded forms in microtidal inlets. This will be further discussed in the next section when velocities and stability fields are considered.

5.3.2 Flow Speeds versus Depths

Another commonly used method for distinguishing Type I and Type II megaripples is to plot speeds against depths under which they are formed. Such a plot is constructed in Figure 5-13, using peak depth-averaged current velocities and corresponding depths as the horizontal and the vertical axis, respectively. The figure shows expected distribution along the horizontal axis: Type I megaripples at the lower speed end and Type II megaripples at the higher speed end. Based on the observation that water depth has little influence in flows deeper than 0.5 m, and ignoring several straying points, a vertical line was drawn. This separates the diagram into two stability fields with the boundary at 0.65 m/s. Boundary values separating Type I and Type II megaripples were given by several authors. Their figures range from 0.7 to 0.8 m/s (Costello and Southard, 1981; Boersma and Terwindt, 1981; Terwindt and Brouwer, 1986; Dalrymple et al., 1978). The lower value at Palmer Inlet can be attributed to a tendency to misidentify Type II bed phases arising from the ambiguous morphology of subtidal bedforms. Plots such as Figure 5-13 can be used to

Figure 5-13 Distinction of Type I and Type II megaripples by current speed versus water depth plots. Current speeds are peak depth-average values, and depths are corresponding average values. Dotted lines are visually best fit boundary between the two fields, while taking into consideration that water depth has little influence above 0.5 m. See Figure 5-12 for legends in details.

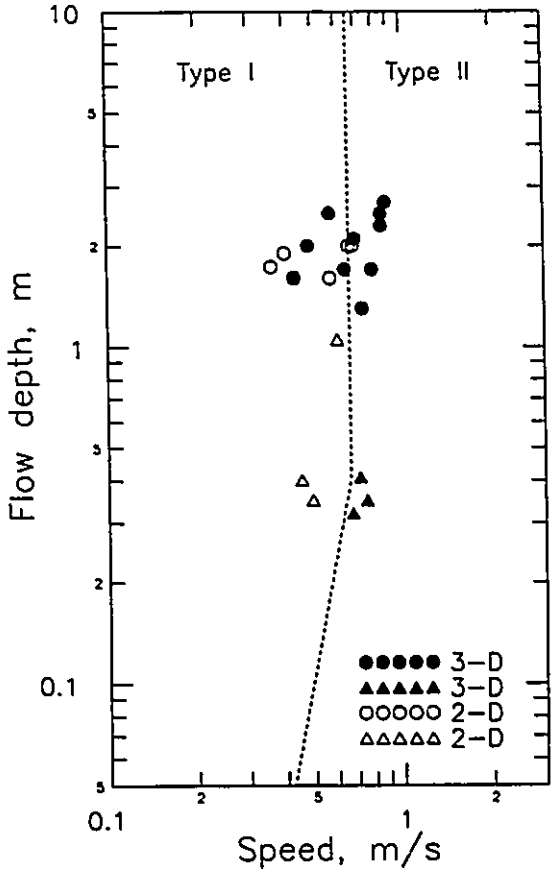
10
5
2
1
0.5
0.2
0.1
Type I
Type II
Flow depth, m
●●●●● 3-D
▲▲▲▲▲ 3-D
○○○○○ 2-D
△△△△△ 2-D
0.1
2
5
1
2
Speed, m/s

construct stability fields of bed phases provided bedforms used are equilibrium forms. To identify equilibrium bedforms, simultaneous morphological and hydraulic information are needed. Unfortunately, the two groups of observations are made at different times. For macro- or meso-tidal inlets, this is not a serious problem. This is because megaripples in those areas are active and able to develop close to equilibrium throughout the course of fortnightly cycles. The bundle structure indicates that even during neap tides, there is enough sediment transport to generate relative balanced megaripples. Stability diagram constructed for those areas were found to fit well with phase diagrams known from flumes and rivers (Dalrymple, 1984; Terwindt and Brouwer, 1986). The problem becomes significant for microtidal inlets, however. This is because the degree of equilibrium of bedforms is expected to be lower due to generally low tidal current speeds. At Palmer Inlet, active megaripples occur primarily around the major portion of large tides. They are expected to be subject to modifications by subsequent tides as current speeds decline almost to zero in small tides. Degraded and disequilibrium bedforms with ambiguous morphology are thus relatively widespread. This makes classification by existing criteria difficult. In the field, there is a tendency to classify anything with less continuous crestlines and uneven troughs as Type II forms. The result is an underestimate of the

current speeds needed to form Type II bed phases. The three or four Type II megaripples straying deep into Type I field in Figure 5-13 are clear evidence of such incorrect identifications in this microtidal inlet. It is also noted that degradation of Type II megaripples at Palmer Inlet is characterized by an infilling of troughs as tides change from large to small tides. Overestimates of bed states are thus accompanied by underestimate of heights, which leads to the intrusion of Type II forms into Type I field in Figure 5-12B.

5.4 Group Characteristics of Megaripples

The echo sounding of bed profiles gives a spatial series of megaripples. The spatial series contains information reflecting properties of megaripples as a group. This provides us with another tool of studying different types of megaripples and possibly their differences.

At this second Ievel, bedforms are treated as populations, and their group attributes are studied using time series analysis. Time series technique has been applied to dunes of river flows (Nordin 1971; Nordin and Alert, 1966; Ashida and Tanaka, 1967; Crickmore 1967; Squarer, 1970), and recently, to large-scale bedforms produced by tidal flows on shelves (Ozasa, 1974) and in estuaries (Balig and Hudspeth, 1981). Studies of this kind are of practical importance as direct observations in such

areas have proved hazardous if not altogether impossible, and as echo sounding has been increasingly becoming a standard procedure in field operations.

In the present study, the time series method is applied to echo sounding profiles of megaripples in the South Channel of Palmer Inlet. The basis of the method is to calculate variance spectra in frequency domain, and cross- and auto-correlation in the time domain. The first section introduces briefly such methods used in the analyses. The procedures used to eliminate nonstationarities after analogue to digital conversion was then presented. The above mentioned three types of functions were then calculated for Type I and Type II megaripples separately. The results are then discussed, and compared to each other with the known information from field observations. At a more general level, they are also compared with existing theories in the literature, and their validity in tidal inlets discussed.

5.4.1 Time Series Analysis

While designed for the treatment of random data as a function of time, time series analysis applies equally well to recordings of bed elevations as a function of space. The difference is that the resulting unit is 'cycles per unit length' (wave number) rather than 'cycles per unit time' (frequency). Detailed descriptions of computation of cross-

and auto-correlation functions and variance spectra are given in Press, et al. (1986) and Marple (1988). Reference on this subject is also made to Otnes (1978), Ramirez (1985), and Jarrett and Kraft (1989).

The crosscorrelation and autocorrelation function are similar in that they are used to study the relationships between two series, [X] and [Y] in the former case and [X] and [X] in the latter case. The correlation is calculated at steps (time or distance), separated by a certain interval, Δt. In the crosscorrelation case, the discrete form of this calculation is:

$$R_{xy}(k) = \frac{1}{N - k} \sum_{t=1}^{t=N-k} X_t \, Y_{t+k} \qquad \text{— (4)}$$

Where t = 1, 2, 3, ... n representing X(t) and Y(t), sampled at intervals over a total distance of $N\Delta t$. The calculation can be done for intervals between k = 0 and k = $m\Delta t$, which is the maximum displacement or lag. The value of crosscorrelation function, which falls between plus and minus 1, is directly proportional to the degree of, in the present case, geometric similarity between the two series. If the two series were both pure sine waves, the crosscorrelation would be a cosine wave of the same period and of amplitude of 1. On the other hand, if they were totally random, the crosscorrelation would form a random

trend fluctuating around zero. This property can be utilized in the bedform analysis, as Type I and II megaripples have been observed differing in morphology and regularity in the plan view.

While the cross- and auto-correlation function are used to establish relationships or the existence of a periodicity or periodicities of one or two series, the variance spectrum is used to disclose the frequencies and amplitude of these components, which compose the series. The variance spectrum for a discrete data, $x(k\Delta f)$, can be calculated by the Discrete Fourier Transform method (DFT):

$$x(k\Delta f) = \Delta t \, \Sigma X(n\Delta t) \, e^{(-j2\pi k\Delta f n\Delta t)} \qquad \text{— (5)}$$

Where n and k = 0, 1, 2, ..., N-1. Δf = frequency sample interval. A quick version of Equations (5) is the Fast Fourier transformation (FFT), which reduces the number of evaluations of DFT by taking advantage of symmetric and periodic properties of the series (Ramirez, 1985). In variance spectrum, a series consisting of a pure sine wave appears as a single vertical line at that frequency, while random noise consists of all possible frequencies of the same variance. Bedform profiles, no matter how regular they may appear, fall between these two extremes. Studies of their spectra would provide valuable information about the presence or absence of certain frequencies. The structures

revealed by the spectra have genetic implications, as people found in studies of wind waves and turbulent flows (Phillips, 1958; Batchelor, 1953).

5.4.2 Procedures of Data Preparation

The data used for the analyses were digitized echo profiles of bedforms in the South Channel (Figure 4-1, Chapter 4). Twelve profiles representing three ebb tidal conditions were used in the analyses. The raw profiles contain two types of nonstationarities which must be eliminated: size changes of megaripples along the profile, and a general topographic slope upon which they are superimposed. The former was eliminated by dissecting each profile into a Type II megaripple dominated north segment, and a Type I dominated south segment (Bendat and Piersol, 1966) (Figure 5-14A and B). The latter was eliminated by passing the dissected profiles through a high-pass digital filter (Tatsusaburo Isaji personal communication, 1986) with a cut-off wave length of 50 m. Figure 5-14 shows that the artificial peak introduced by the topographic slope to the lower end of spectrum graph (Figure 5-14D) was corrected; the cyclic pattern was also recovered in the autocorrelation function (Figure 5-14C). The digitizing interval is 0.16 m and 0.23 m for the south and north segment, respectively. The maximum lag used in calculation of the correlation functions was 10% of the record (Otnes, 1978). This gives a

Figure 5-14 A sample showing the effects of a general topography slope before and after detrending, using a high-pass filter with a cut-off wave length of 50 m.

(A) and (B) Bisected original profiles. The original profile was superimposed on a general slope consisting a ebb spit to the right (north) and a flood tidal lobe to the left (south).

(C) and (D) showing effects of detrending. The correlogram (C) before detrending appears as a steadily declining curve. The periodic signal contained in the profile is revealed after the trend is removed. The oblique straight line is the regression between the horizontal distance, x, and zero-crossings of autocorrelation function in terms of number of megaripples, y. The slope creates a large peak at the low wave number end in the spectrum (D) (solid line). After detrending (dash line), this peak is eliminated. Hino's (1966) concept of a spectrum consisting of an equilibrium high wave number subrange and an unstable low wave number subrange is also illustrated in the figure. The boundary between the two subrange is defined by K_o, which can be estimated from K_o = 0.15/water depth.

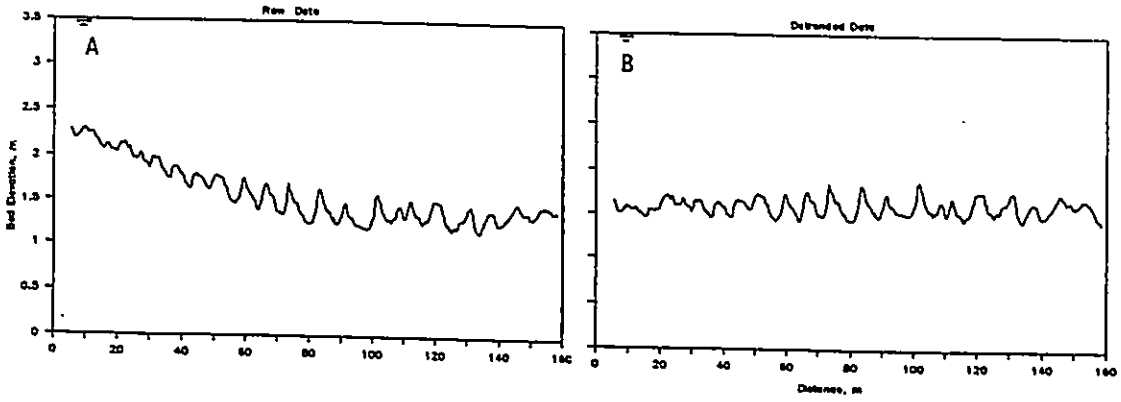
Raw Data
A
Bed Elevation, m
Detrended Data
B
Distance, m

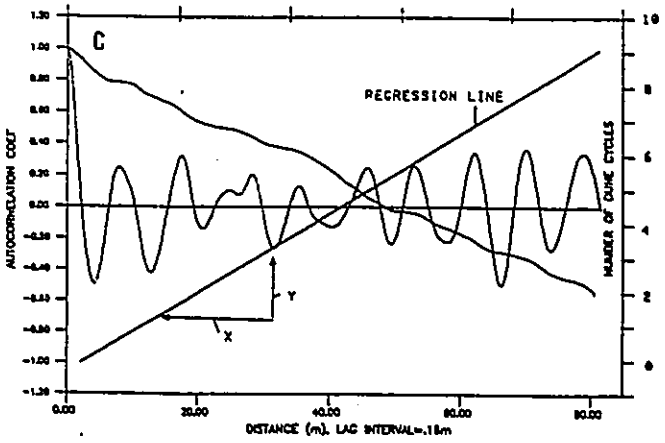
C
REGRESSION LINE
AUTOCORRELATION COEF
NUMBER OF DUNE CYCLES
Y
X
DISTANCE (m), LAG INTERVAL=.18m

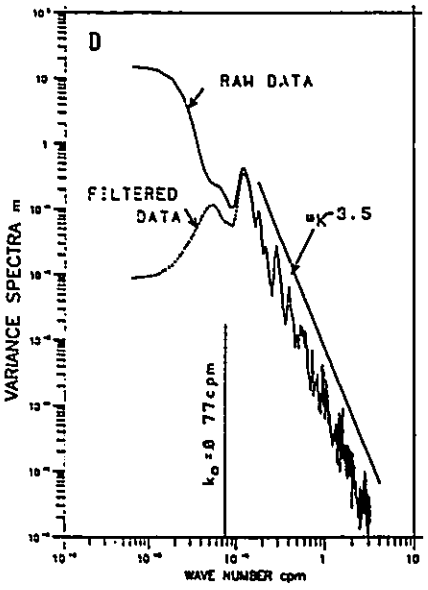
D
RAW DATA
FILTERED DATA
k^-3.5
VARIANCE SPECTRA m
WAVE NUMBER cpm

highest wave number of 1/0.32-1/0.46 cpm (or wave length = 32-46 cm), and a spectral bandwidth resolution of 0.045 - 0.065 cpm.

5.4.3 Results and Discussion

Two pairs of correlograms, that is plots of autocorrelation coefficients against lags, are presented in Figure 5-15. The autocorrelation function falls from an initial maximum value, and become stable in cyclic oscillation. Such pattern is characteristic of a stochastic, periodic process (Rock, 1988). Megaripples as a population can thus be considered as consisting of many sinusoidal waveforms of different periods and amplitudes and superimposed with random noise. The autocorrelation values of the north segment (dash lines) are smaller, and contains more zero-crossings than those of the south segment (solid lines), indicating that megaripples in the north segment are smaller and less regular than those in the south. This is consistent with field observations (Figure 4-28), which showed that in the north with prominent scour pits are short crested, echelon-arranged Type II megaripples superimposed on the ebb spit. They form in response to the highly turbulent flow at this location as tidal currents flow over the shallow ebb spit. Further away from the inlet throat in the south, the flow is less constrained and thus less agitated. Bedforms here are long crested, two-dimensional

Figure 5-15 Examples of correlograms for Type I megaripples (solid line) and Type II megaripples (dash line). The autocorrelation function drops more quickly for Type II megaripples, and assumes smaller value than Type I megaripples.

(A) Profile PD-5 (Type I megaripples, solid line) and Profile PD-6 (Type II, dash line), ebb tide, July 30, 1987. Tidal range = 0.4 m.

(B) Profile PD-21 (Type I megaripples, solid line) and Profile PD-22 (Type II megaripples, dash line), ebb tide, July 25, 1987. Tidal range = 0.76 m.

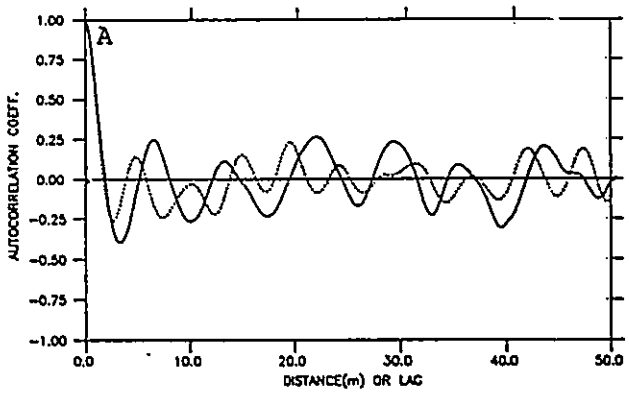
A
1.00
0.75
0.50
0.25
0.00
-0.25
-0.50
-0.75
-1.00
AUTOCORRELATION COEFF.
0.0
10.0
20.0
30.0
40.0
50.0
DISTANCE(m) OR LAG

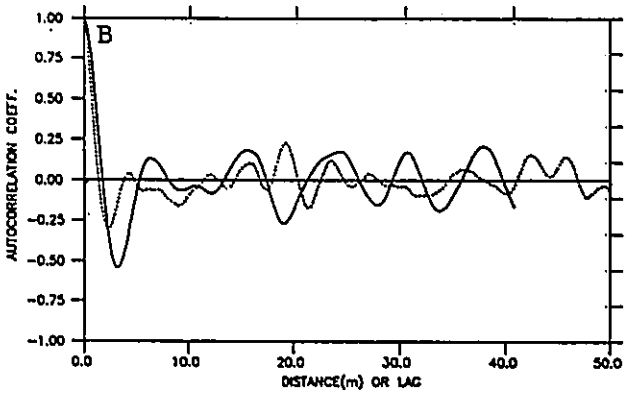
B
1.00
0.75
0.50
0.25
0.00
-0.25
-0.50
-0.75
-1.00
AUTOCORRELATION COEFF.
0.0
10.0
20.0
30.0
40.0
50.0
DISTANCE(m) OR LAG

Type I megaripples. Since the autocorrelation coefficient is a measure of the geometric 'self-similarity' of the bedforms, the regularly-shaped Type I megaripples are expected to give larger similarity values than the irregular Type II megaripples.

Spectral functions display the frequency structure, that is, the relative proportions of sinusoidal components of a given wave number, which comprise the total variance of the measured profiles. Figure 5-16 shows that the variance of Type II megaripples is spreads over a wide range of wave numbers, and is less peaked than the variance of Type I megaripples. This is because their less regular morphology requires more harmonic components to fully describe them. While there is some difference in magnitudes, the basic pattern of spectrum structures remains basically unchanged for the two populations both between different stages of tides and between different tidal conditions (July 25 versus July 30). This suggests that while the two types of megaripples both change their orientations with the stage or change their shapes with the range of tides, they maintain their respective characteristics. There are no major changes from Type I to Type II megaripples (or vice versus) as the tidal range changes. Bed configuration fields shaped during large tides can thus be considered as relatively long-lived, with each field conserving its basic features even during small tides. This is significant as it

Figure 5-16 Typical variance spectra of Type I and Type II megaripples for three ebb stages. The spectral function of Type II megaripples is more dispersed, and less peaked than Type I megaripples. The overall structure of the spectrum does not show significant changes between the two stages. The slope of the spectra in the equilibrium subrange falls in the range of -3 to -3.8.

(A) Type I megaripples in the south segment (PD-3, PD-5 and PD-9), ebb tide, July 30, 1987. Bay tidal range = 0.40 m.

(B) Type II megaripples in the north segment (PD-4, PD-6 and PD-10), ebb tide, July 30, 1987

(C) Type I megaripples in the south segment (PD-19, PD-21 and PD-25), ebb tide, July 25, 1987. Bay tidal range = 0.76 m.

(D) Type II megaripples in the north segment (PD-20, PD-22 and PD-26), ebb tide, July 25, 1987.

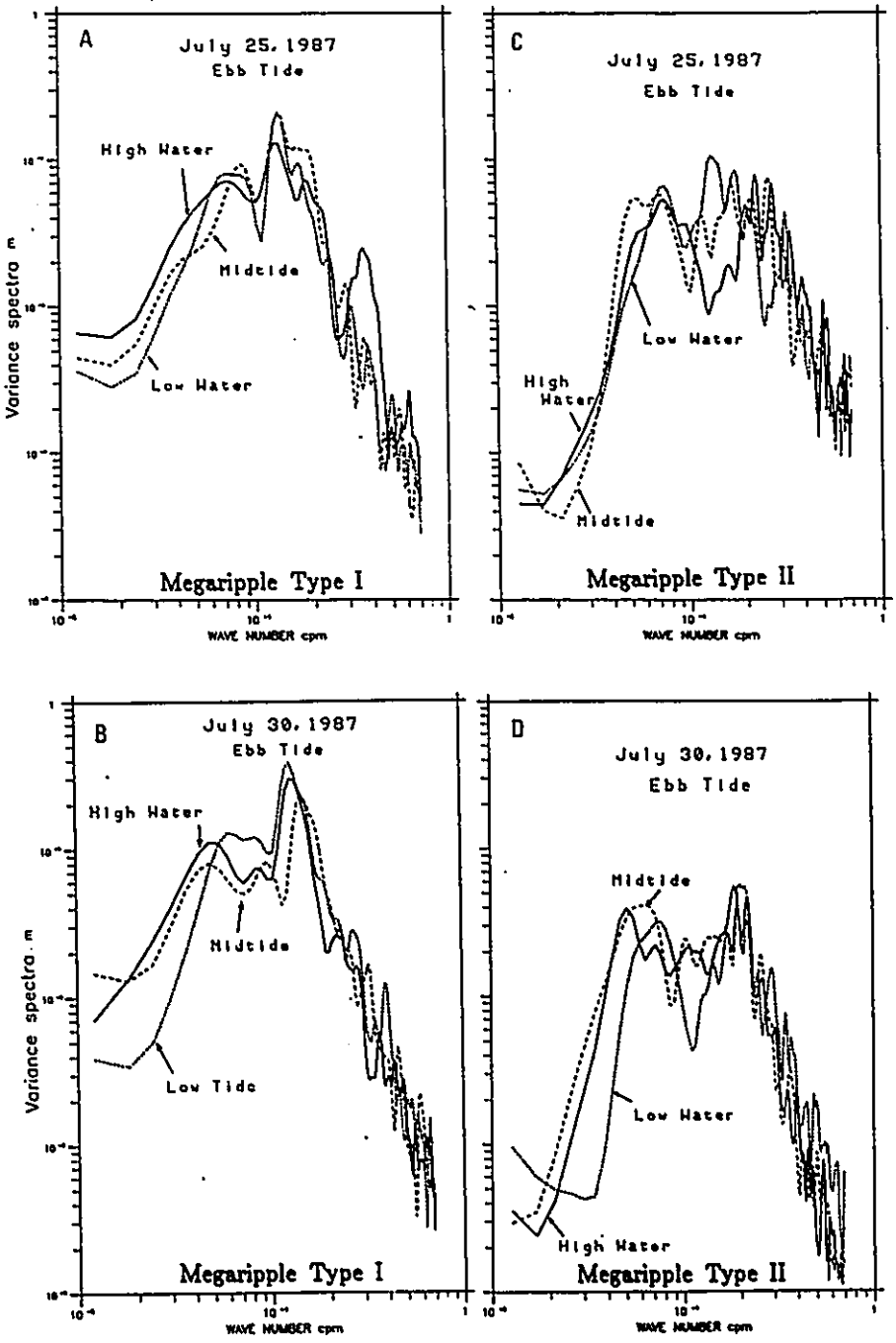
A
July 25, 1987
Ebb Tide
High Water
Midtide
Low Water
Megaripple Type I
C
July 25, 1987
Ebb Tide
Low Water
High Water
Midtide
Megaripple Type II
B
July 30, 1987
Ebb Tide
High Water
Midtide
Low Tide
Megaripple Type I
D
July 30, 1987
Ebb Tide
Midtide
Low Water
High Water
Megaripple Type II
Variance spectra, E
WAVE NUMBER cpm

reinforces the conclusion of the last section about the difficulty of identifying equilibrium forms at Palmer Inlet, and the possibility of underestimating the hydraulic conditions used to form relict bedforms.

The spectral characteristics of Palmer Inlet megaripples are very similar to those of unidirectional bedforms (Hino, 1968; Shen and Cheong, 1977). The spectra of Figure 5-16 can be divided into two subranges. In the high wave number range, the logarithm of the variance decreases linearly with the logarithm of the wave number; the regression slopes are in the range of -3.0 to -3.8. Hino (1968), based on dimensional analysis, found that the spectrum of the high wave number range of unidirectional bedforms is a -3 power function of the wave number. He explained this by the hypothesis that waveforms in this subrange form a 'cascade' that is in equilibrium with the formative flows. A comprehensive summary (Shen and Cheong; 1977) of data from field and flumes (Crickmore, 1970; Nordin and Algert, 1966; Jain and Kennedy, 1974) put the spectral slope in the range of -3 to -4. Spectra in the lower wave number range do not follow straight lines. This, according to Hino (1968), suggests that waveforms in this subrange are still in developing stage, and there is further transfer of energy between the bed and the flow. The group characteristics of bedforms produced by unidirectional flows therefore appear to be similar in a general way to those

produced by tidal flows despite difference in size and genesis.

The smallest wave number for the equilibrium subrange, K_o, defines the boundary between the above two fields, in which bedforms are at different stages of development. Based on experimental data, Hino (1968) found that this value can be estimated as K_o = 0.15/flow depth. K_o values calculated for the samples chosen are 0.065-0.087 cpm. The wave number at which maximum spectral amplitude attains are 0.12-0.15 cpm, larger than the critical wave number, K_o. The majority of spectrum power of these profiles are thus contained in the equilibrium subrange, in which bedforms are fully-developed. In a study of sandwaves in the South Slough Estuary, Coos Bay, Oregon, Balig and Hudspeth (1981) found that the maximum spectral amplitudes are at wave numbers below the smallest wave number of the equilibrium subrange, K_o. As this is a low energy estuary, they explained this to be indicative of a slow process of sandwave growth, and further inferred that it is the catastrophic events such as storms, not hydrodynamics of average flows, that govern their development. Using the same argument, the development of megaripples at Palmer Inlet can be explained as a dynamic, high-energy process, that is dominated by the day-to-day tidal processes rather than by storm events.

To examine megaripples characteristics in the third

dimension, longitudinal profiles were measured along three lines parallel to each other in the South Channel during the high tide of August 4, 1986. Cross-correlation functions were constructed using these profiles (Figure 5-17), from which lateral variations of megaripples can be examined. Figure 5-17 shows that coefficient values are several times larger for megaripple Type I than those for Type II. As the crosscorrelation functions measure, in this case, the lateral continuity of bedforms, the result is consistent with the fact that megaripples in the north segment are short crested, and those in the south are long crested. Comparison of Figure 5-17 with Figure 5-16 and Figure 5-15 indicates that the two types of megaripples can be better separated by crosscorrelation functions than by autocorrelation or spectral functions.

5.4.4 Identifying Equilibrium Megaripples in Microtidal Inlets

Results of above studies indicate that differences in morphology of the two types of megaripples as individuals as defined by Dalrymple et al. (1978) have corresponding reflections in their properties as assemblages. Being less regular in shapes and relatively smaller in size, Type II megaripples have relatively smaller autocorrelation coefficients, and their spectral variance spreads out more than that of Type I megaripples. The difference, however,

Figure 5-17 Crosscorrelograms of megaripples measured along three longitudinal profiles in the South Channel, high water, August 4, 1987. Tidal range = 0.66 m. Larger values of cross-correlation coefficient indicate that megaripples in the south segment (A and B) are laterally more consistent than those in the north segment (C and D). For profile locations see Figure 3-1A in Chapter 3.

(A) PD-17 versus PD-27.

(B) PD-17 versus PD-29.

(C) PD-18 versus PD-28.

(D) PD-18 versus PD-30.

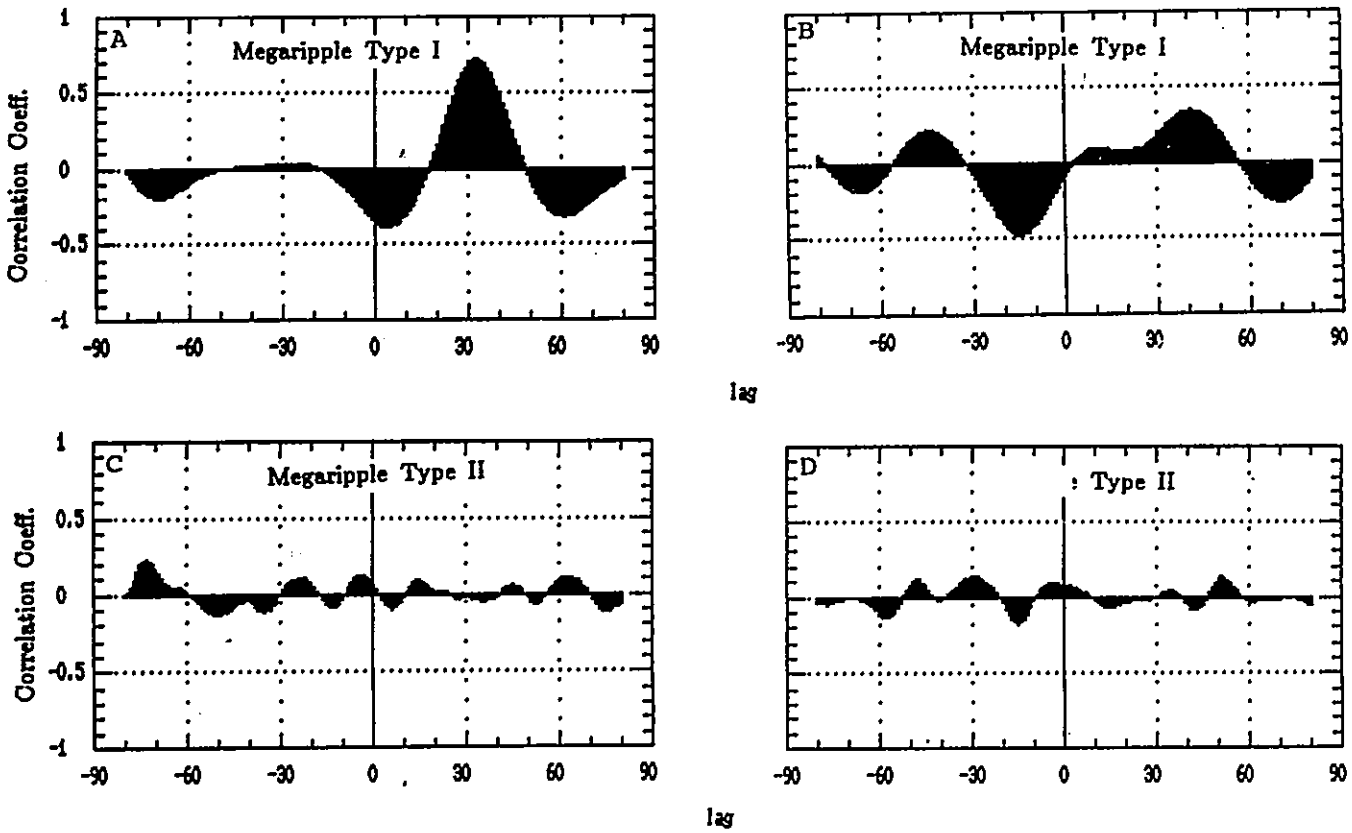
A
Megaripple Type I
B
Megaripple Type I
C
Megaripple Type II
D
Type II
Correlation Coeff.
Correlation Coeff.
1
0.5
0
-0.5
-1
-90
-60
-30
0
30
60
90
lag
lag

is small. The use of the variance spectrum to differentiate different bed phases is thus limited. The difference in group properties between Type I and Type II megaripples is best displayed in crosscorrelation functions when two adjacent series are compared. As an indicator of bed phase, crosscorrelation is thus a more useful tool than the other two functions. Morphological criteria used in classification of the two types of megaripples (Dalrymple, et al., 1978) appears to be useful not only in terms of individual properties, but also in terms of population characteristics. Spectral distributions of megaripples are rather consistent irrespective of tidal stages and tidal conditions. On the one hand, this supports the observation that basic characteristics of each field of megaripples are conserved through the alternation of large and small tidal cycles, and thus could pose identification problem in this microtidal inlet. On the other hand, it also suggests that the time-series methods used are not, capable of distinguishing disequilibrium forms from equilibrium forms.

The megaripple fields of Palmer Inlet have a spectral structure similar to those formed by rivers. The spectrum consists of an equilibrium high wave number subrange in which bedforms are fully developed, and an unstable low wave number subrange in which they are still growing. Within the equilibrium subrange, the spectrum follows Hino's '-3 power law'.

The fact that the majority of the total energy of megaripples is contained in the equilibrium subrange indicates that tidal inlets are a high energy, dynamic environment. The bedform development is controlled by daily tidal flows. This is different from the spectrum structure of bedforms in lower energy regimes, in which the majority of bedform energy is contained outside the equilibrium subrange.

Part I References

Adams, C. E. W., Wells, J. T., and Coleman, J. M., 1982. Sediment transport on the central Louisiana continental shelf: Implications for the developing Atchafalaya river delta. Contributions in Marine Science, 25, 133-148.

Allen, J. R. L., 1981. Paleotidal speeds and ranges estimated from cross-bedding sets with mud drapes. Natures, 293, 394-396.

Allen, J.R.L., 1980. Sand waves: a model of origin and internal structure. Sedimentary Geology, 26, 281-328.

Allen, J. R. L., 1976. Time lag of dunes in unsteady flow: an analysis of Nasner's data from the R. Weser, Germany. Sedimentary Geology, 15, 309-321.

Allen, J. R. L., 1973. Phase differences between bed configuration and flow in natural environments and their geological relevance. Sedimentology, 20, 323-329.

Amos, C. L., and King, E. L., 1984. Bedforms of the Canadian eastern seaboard: a comparison with global occurrences. Marine Geology, 57, 167-208.

Armon, J. W., 1975. The dynamics of a barrier island chain, Prince Edward Island, Canada. Ph.D thesis, McMaster University, Hamilton, 546p.

Armon, J. W., 1980. Changeability of small flood tidal deltas and its effects, Malpeque. In McCann, S.B., ed., The Coastline of Canada, Geological Survey of Canada Paper 80-10, 65-79.

Armon, J. W., and McCann, S. B., 1979. Morphology and landward sediment transfer in a transgressive barrier island system, Southern Gulf of St. Lawrence, Canada. Marine Geology, 31, 333-344.

Ashida, K. and Tanaka, K., 1967. A statistical study of sand waves. Proceedings, 12th Congress, International Association of Hydraulic Research, 2, 103-110.

Aubrey, D. G. and Speer, P. E., 1985. A study of non-linear tidal propagation in shallow inlet/estuarine systems

Part I: Observations. Estuarine, Coastal and Shelf Science, 21, 185-205.

Bagnold, P. A., 1963. Mechanics of marine sedimentation. In: Hill, M.N., ed., The Sea, 3., Wiley-Interscience, New YorK, N,Y., 507-582.

Baird, W.F., 1978. Wave climate analysis for selected locations in the Gulf of St. Lawrence and Lake Superior. Marine Directorate, Department of Public Works, Ottawa.

Baliga, B.R., and Hudspeth, R.T., 1981. Evaluation of sand waves in an estuary. Journal of the Hydraulics Division, American Society of Civil Engineering, HY2, 161-178.

Batchelor, G. K., 1953. The theory of Homogeneous turbulence. Cambridge University Press.

Bayliss-Smith, T.P., Healey, R., Lailey, R., Spencer, T., and Stoddart, D.R., 1979. Tidal flows in salt marsh creeks. Estuarine and Coastal Marine Science, 9, 235-255.

Beer, T., 1983. Environmental Oceanography: An introduction to the behaviour of coastal waters. Pergamon Press Ltd., 262p.

Beets, D. J., Roep, T. B., and Jong J. De., 1981. Sedimentary sequences of the sub-recent North Sea coast of Western Netherlands near Alkmaar. In: Nio, S.D., Shuttenhelm, R.T.E., van Weering, Tj.C.E., ed., Holocene marine sedimentation in the North Sea Basin, Special Publication No.5 of International Association of Sedimentologists. Blackwell Scientific Publications, Oxford, London, 133-145.

Bendat, J.S., and Piersol, A.G., 1966. Measurement and analysis of random data, John Wiley and Sons, Inc., New York, N.Y., 390p.

Berelson, W. M., and Herson, S. D., 1985. Relations between Holocene flood tidal delta and barrier island inlet fill sequences: Back Sound-Shackelfork Banks, North Carolina. Sedimentology, 32, 215-222.

Bijker, E. W., 1967. Some considerations about scales for coastal models with moveable beds. Delft Hydraulic Laboratory Report, No.50, 142p.

Black, J. A., 1987. The Geomorphology of north coast of Prince Edward of Island. Shore and Beach, 55 (1), 41-47.

Blatt, J., Middleton, G. V., and Murry, R., 1980. Origin of Sedimentary Rocks, 2nd edition, Prentice-Hall, Englewood Cliffs, 782p.

Boersma, J. R., and Terwindt, J. H. J., 1981. Neap-spring tide sequences of intertidal shoal deposits in a mesotidal estuary. Sedimentology, 28, 151-170.

Boothroyd, J. C. and Hubbard, D. K., 1975. Genesis of bedforms in mesotidal inlets. In Cronin, L.E., ed., Estuarine Research, Vol. 2, Geology and Engineering. Academic Press, New York, 217-234.

Boothroyd, J. C., and Hubbard, D. K., 1974. Bed form development and distribution pattern, Parker and Essex Estuaries, Massachusetts, Miscellaneous paper 1-74, U.S. Army, Corps of Engineers, Coastal Engineering Research Centre, Fort Belvoir, Virginia, 55p.

Boothroyd, J. C., 1985. Tidal inlets and tidal deltas. In Davis, R.A., ed., Coastal Sedimentary Environments, Springer-Verlag, New York, Inc., 445-525.

Boothroyd, J. C., Friedrich, N. E., and McGuinn, S. R., 1985. Geology of microtidal coastal lagoons: Rhode Island. Marine Geology, 63, 35-76.

Brookes, I., 1972. The physical geography of the Atlantic provinces. In Macpherson, A.G., ed., The Atlantic Provinces, Studies in Canadian Geography, University of Toronto Press, Toronto, 45p.

Bruun, P., 1978. Stability of Tidal Inlets, theory and engineering. Elsevier Scientific publishing Company, 510p.

Burnside, C. D., 1979. Mapping from aerial photographs. Granada Publishing Ltd., 304p.

Byrne, R. J., De Alteris, J. T., and Bullock, P. A., 1974. Channel stability in tidal inlets: A case study. Proceedings of 15th conference on Coastal Engineering, American Society of Civil Engineering, Copenhagen, Chapter 92.

Cassie, R. M., 1954. Some uses of probability paper in the

analysis of size frequency distributions. Australian Journal of Marine and Freshwater Research, 5, 513-522.

Clark, M. W., 1976. Some methods for statistical analysis of multimodal distributions and their application to grain-size data. Mathematical Geology, 8, 267-280.

Clifton, H. E., 1969. Beach lamination - Nature and origin. Marine Geology, 7, 553-559.

Compton, R. R., 1961. Manual of field Geology. John Wiley & Sons, Inc., New York, 363p.

Costello, W. R., and Southard, J. B., 1981. Flume experiments on lower-flow-regime bed forms in coarse sand. Journal of Sedimentary Petrology, 51, 849-864.

Crickmore, J.M., 1967. Measurement of sand transport in rivers with special reference to tracer methods. Sedimentology, 8, 175-278.

Crickmore, J.M., 1970. Effect of flume width on bed-form characteristics. Journal of the Hydraulics Division, American Society of Civil Engineering, HY2, 453-495.

Cronin, L. E., ed., Estuarine Research, Vol. 2, Geology and Engineering. Academic Press, New York, 587p.

Dabrio, C. J., 1982. Sedimentary structures generated on the foreshore by migrating ridge and runnel systems on microtidal and mesotidal coasts. Sedimentary Geology, 32, 141-151.

Dalrymple, R. W., 1984. Morphology and internal structure of sandwaves in the Bay of Fundy. Sedimentology, 31, 365-382.

Dalrymple, R. W., Knight, R. J., and Lambiase, J. J., 1978. Bedforms and their hydraulic stability relationships in a tidal environment, Bay of Fundy, Canada. Nature, 275, 100-104.

Dalrymple, R. W., 1984. Morphology and internal structure of sandwaves in the Bay of Fundy. Sedimentology, 31, 365-382.

Dalrymple, R. W., Knight, R.J., and Lambiase, J.J., 1978. Bedforms and their hydraulic stability relationships

in a tidal environment, Bay of Fundy, Canada. Nature, 275, 100-104.

Dalrymple, R. W., 1977. Sediment dynamics of macrotidal sand bars, Bay of Fundy. Ph.D thesis, Department of Geology, McMaster University, Hamilton, 635p.

Davidson-Arnott, R. A. D., and Greenwood, B., 1974. Bedforms and structures associated with bar topography in the shallow water wave environment, Kouchibouguac Bay, New Brunswick, Canada. Journal of Sedimentary Petrology, 44, 698-704.

Davis, R. A., and Hayes, M. O., 1984. What is wave dominated coasts? Marine Geology, 60, 313-329.

de Mowbray, T., and Visser, M. J., 1984. Reactivation surfaces in subtidal channel deposits, Oosterchelde, Southwest Netherlands. Journal of Sedimentary Petrology, 54(3), 811-824.

De Boer, P. L., 1979. Convolute lamination in modern sands of the estuary of the Oosterschelds, the Netherlands, formed as the results of entrapped air. Sedimentology, 26, 283-294.

DeAlteris, J. T., and Byrne, R. J., 1975. The recent history of Wachapreague inlet, Virginia. In Cronin, L.E., ed., Estuarine Research, Vol. 2, Geology and Engineering. Academic Press, New York, 167-182.

DeLorenzo, J. L., 1986. The overtide and filtering response of deep inlet/bay Systems. Unpublished manuscript.

Dobson, R. S., 1967. Some applications of a digital computer to hydraulic engineering problems. Department of Civil Engineering, Stanford University, Technical Report 80, 163p.

Doodson, A. T., and Warburg, H. D., 1941. Admiralty Manual of Tides. Published by the Hydrographic Department, Admiralty, London. 270p.

Engelund, F., and Hansen, E., 1967. A monograph on sediment transport in alluvial streams. Technisk Vorlag, Copenhagen, 62p.

Finley, R. J., 1975. Morphologic development and dynamic processes at a barrier island inlet, North Inlet, South Carolina. Ph.D thesis, Department of Geology, University of South Carolina, 272p.

FitzGerald, D. M., Fink, L. K., and Lincoln, J. M., 1984. A flood-dominated tidal inlet. Geo-Marine Letters, 3, 17-22.

FitzGerald, D. M. and Nummedal, D., 1983. Response charac teristics of an ebb-dominated tidal inlet channel. Journal of Sedimentary Petrology, 53, 833-845.

Fitzgerald, D. M., 1976. Ebb-tidal delta of Price Inlet, South Carolina: Geomorphology, physical processes, and associated inlet shoreline changes. In: Hayes, M.O., and Kana, T.W., ed., Terrigenous Clastic Depositional Environments, Technical Report No. 11-CRD, University of South Carolina, Columbia, II-143-II-157.

FitzGerald, D. M., 1982. Sediment Bypassing at mixed energy tidal inlets. 18th Conference of Coastal Engineering, American Society of Civil Engineers, 2, 1095-1118.

FitzGerald, D.M., 1984. Sedimentation processes along the East Friesian Islands, West Germany. Proceedings of 19th coastal Engineering Conference of Civil Engineers, Huston, Texas, 3051-3066.

Gadd, P. E., Lavelle, J. W., and Swift, D. J., 1978. Estimates of sand transport on the New York Shelf using near bottom current meter observations. Journal of Sedimentary Petrology, 48, 239-252.

Goldsmith, V., and Byrne, R. J., 1975. The influence of waves on the origin and development of the offset coastal inlets of the southern Delaware Peninsula, Virginia. In Cronin, L.E., ed., Estuarine Research, Vol. 2, Academic Press Inc, New York, 183-200.

Grant, D. R., 1970. Recent coastal submergence of the Maritime Provinces, Canada. Canadian Journal of Earth Science, 7, 676-689.

Grant, D. R., 1976. Late Wisconsin ice limits in the Atlantic Provinces of Canada with particular reference to Cape Breton Island, Nova Scotia. Geological Survey of Canada, Paper 76-1c, 289-292.

Greenwood, B., and Davis, R. A., 1984. Hydrodynamics and sedimentation in wave-dominated coastal environments. Marine Geology, 60(1-4), 473p.

Hamilton, D., Sommerville, J.H., and Standford, P.N., 1980. Bottom currents and shelf sediments, Southwest of Britain. Sedimentary Geology, 26, 115-138.

Hammond, T. M., and Collins, M. B., 1979. On the threshold of transport of sand-sized sediment under the combined influence of unidirectional and oscillatory flow. Sedimentology, 26, 795-812.

Hayes, M. O., 1972. Forms of sediment accumulation in the beach zone. In: Meyer, R.E., ed., Waves on beaches and resulting sediment transport, 4. Academic Press, New York, N.Y., 297-356.

Hayes, M. O., 1975. Morphology of sand accumulations in estuaries. In Cronin, L.E., ed., Estuarine Research, Vol. 2, Geology and Engineering. Academic Press, New York, 3-22.

Hayes, M. O., 1979. Barrier island morphology as a function of tidal and wave regime. In Leatherman, S.P., ed., Barrier Islands from the Gulf of St. Lawrence to the Gulf of Mexico. Academic Press, New York, 1-27.

Hayes, M. O., 1980. General morphology and sediment patterns in tidal inlets. Sedimentary Geology, 26, 139-156.

Hayes, M. O. and Kana, T. W., 1976. Terrigenous clastic depositional environments. Technical Report No.11-CRD, Coastal Research Division, Department of Geology, University of South Carolina, 302p.

Hayter, E. J., and Mehta, A. J., 1979. Verification of changes in flow regime due to dike breakthrough closure. Coastal Structures '79, 729-746.

Heathershaw, A. D., 1979. The turbulent structure of the bottom boundary layer in a tidal current. Journal of Geophysics Research, 58, 395-430.

Heathershaw, A. D., and Codd, J. M., 1985. Sandwaves, internal waves and sediment mobility at the shelf-edge in the Celtic Sea. Oceanographica Acta, 8(4), 391-402.

Heathershaw, A. D., 1979. The turbulent structure of the bottom boundary layer in a tidal current. Journal of Geophysics Research, 58, 395-430.

Heathershaw, A. D., 1981. Comparisons of measured and

predicted sediment transport rates in tidal currents. Marine Geology, 42, 75-104.

Heathershaw, A. D., and Codd, J. M., 1985. Sandwaves, internal waves and sediment mobility at the shelf-edge in the Celtic Sea. Oceanographic Octa, 8(4), 391-402.

Hennessy, J. T., and Zarillo, G. A., 1987. The interrela tion and distinction between flood-tidal delta and washover deposits in a transgressive barrier island. Marine Geology, 78, 35-56.

Heron, S. D., Moslow, T. F., Berelson, W. M., Herbert, J. R., Steele III, F. A., and Swanson, K. R., 1984. Holocene sedimentation of a wave-dominated barrier-island shoreline: Cape Lookout, North Carolina. Marine Geology, 60(1-4), 413-434.

Heward, A. P., 1981. A review of wave dominated clastic shoreline deposits. Earth Science Reviews, 17, 223-276.

Hine, A. C., 1975. Bedform distribution and migration patterns on tidal deltas in the Chatham Harbour Estuary, Cape Cod, Massachusetts. In Cronin, L.E., ed., Estuarine Research, vol. 2, Academic Press Inc., New York, 235-252.

Hino, M., 1968. Equilibrium-range spectra of sandwaves formed by flowing water. Journal of Fluid Mechanics, 34, 565-573.

Hodge, J. A., 1982. Three-dimensional study of a modern flood-tidal delta in South Carolina (Abstract). American Association of Petroleum Geologists Bulletin, 66, 582-583.

Hoyt, J. H., and Henry, V. J., 1967. Influence of island migration on barrier island sedimentation. Geological Society of American Bulletin, 78, 77-86.

Hubbard, D. K., Oertel, G., and Nummedal, D., 1979. The role of waves and tidal currents in the development of tidal-inlet sedimentary structures and sand body geometry: examples from North Carolina, South Carolina and Georgia. Journal of Sedimentary Petrology, 49, 1073-1092.

Hubbard, D. K., and Barwis, J. N., 1976. Discussion of tidal inlet sand deposits: example from the South

Carolina coast. In Hayes, M.O./Kana, T.W., ed., Terrigenous Clastic Depositional Environments, Tech. Report No. 11-CRD, University of South Carolina, Columbia, II-158-II-171.

Humphries, S. M., 1977. Morphological equilibrium of a natural tidal inlet. Coastal Sediments '77, 5th Symposium of the Waterway, Port, Coastal and Ocean Division of American Society of Civil Engineers, 734-753.

Hunter, R. E., 1969. Eolian microridges on modern beaches and a possible ancient example. Journal of Sedimentary Petrology, 39, 1573-1578.

Imperato, D. P., Sexton, W. J., and Hayes, M. O., 1988. Stratigraphy and sediment characteristics of a mesotidal ebb-tidal delta, North Edisto Inlet, South Carolina. Journal of Sedimentary Petrology, 58(6), 950-958.

Inman, D.L., 1968. Sediments: Sediment properties and mechanics of sedimentation. In: Shepard, F.P., ed., Submarine Geology. Harper and Row, New York, N.Y., 557p.

Isaji, T., and Spaulding, M., 1981. A simplified model for assessing the impact of breachway modifications on coastal pond circulation and flushing dynamics. Proceedings of Ocean 81. Boston, Massachusetts, 824-828.

Israel, A. M., Ethridge, F. G., and Estes, E. L., 1987. A sedimentological description of a microtidal, flood-tidal delta, San Luis Pass, Texas. Journal of Sedimentary Petrology, 57(2), 288-300.

Jago, C. F., and Hardisty, J., 1984. Sedimentology and morphodynamics of a macrotidal beach, Pendine sands, SW Wales. Marine Geology, 60, 123-154.

Jago, C. F., 1980. Contemporary accumulation of marine sand in a macrotidal estuary, Southwest Wales. Sedimentary Geology, 26, 21-49.

Jain, S.C. and Kennedy, J.F., 1974. The spectral evolution of sedimentary bed forms. Journal of Fluid Mechanics, 63 (2), 301-314.

Jarrett, J., and Kraft, A., 1989. Statistical analysis for decision making. Allyn and Bacon, 712p.

Keay, P. A., 1975. Inlet stability: A case study, Kouchibouguac Bay, New Brunswick. M.S. thesis, University of Toronto, 87p.

Keen, M. J., 1971. An outline of the development of the Gulf of St. Lawrence. In Hassen, E.M., ed., the Second of St. Lawrence workshop, Bedford Institute of Oceanography, 111-130.

Keulegan, G.H., 1967. Tidal flows in entrances water level fluctuations of basins in communications with seas. T.B. No. 14, Committee on tidal hydraulics, U.S. Army, Corps of Engineers, Vicksburg, Miss.

Klein, G. de V., 1970. Depositional and dispersal dynamics of intertidal sand bars. Journal of Sedimentary Petrology, 40(4), 1095-1127.

Knight, J. R., 1977. Sediments, bedforms and hydraulics in a macrotidal environment, Cobequid Bay (Bay of Fundy), Nova Scotia. Ph.D thesis, Department of Geology, McMaster University, Hamilton, 693p.

Komar, P. D., 1976. Beach Processes and sedimentation. Prentice-Hall Inc., New Jersey, 429p.

Kumar, M., and Sander, J. E., 1974. Inlet sequence: a vertical succession of sedimentary structures and textures by lateral migration of tidal inlets. Sedimentology, 21, 491-532.

Leatherman, S. P., 1979. Migration of Assateague island, Maryland, by inlet and overwash processes. Geology, 7, 104-107.

Lincoln, J. M., and FitzGerald, D. M., 1988. Tidal distor tions and flood dominance at five small tidal inlets in Southern Maine. Marine Geology, 82, 133-148.

Loring, D. H., and Nota, D. J. G., 1973. Morphology and sediments of the Gulf of St. Lawrence. Bulletin of Fisheries Resource Board, Canada, Bull. 182, Ottawa, 147p.

Lynch-Blosse, M. A., and Kumar, N., 1976. Evolution of downdrift offset tidal inlets: A model based on the Brigantine inlet system of New Jersey. Journal of Geology, 84, 165-178.

Mann, R. G., and Swift, D. J. P., 1981. Size classes of flow-transverse bedforms in a subtidal environment,

Nantucket Shoals, North American Atlantic Shelf. Journal: Geo-Marine Letters, 1, 39-43.

Marple, S. L. Jr., 1988. Digital spectral analysis with applications. Prentice-Hall, Inc., Englewood Cliff, New Jersey, 488p.

Matsushita, P. N., 1986. Hydraulics and sedimentation in a microtidal inlet, north shore, Prince Edward Island. M.S. thesis, Department of Geography, University of McMaster, Hamilton, 290p.

McCann, S. B., 1979. Barrier islands in the Southern Gulf of St. Lawrence, Canada. In Leatherman, S.P., ed., Barrier Islands from the Gulf of St. Lawrence to the Gulf of Mexico. Academic Press Inc., New York, 29-63.

Mehta, A. J., and Christensen, B. A., 1983. Initiation of sand transport over coarse bed in tidal intracourse. Coastal Engineering, 7, 61-75.

Meistrell, F. J., 1972. The spit-platform concept: laboratory observation of spit development. In Schwartz, M.L., ed., Spits and Bars, 225-283.

Middleton, G. V., 1988. Graphic dissection of grain-size distributions. Unpublished manuscript, 26p.

Middleton, G. V., 1976. Hydraulic interpretation of grain size distributions. Journal of Geology, Vol. 84, 405-426.

Middleton, G. V., and Southard, J. B., 1984. Mechanics of Sediment movement. Tulsa, Okl., Soc. Econ. Paleontologists Mineralogists, Short Course 3, 401p.

Middleton, G. V., 1976. Hydraulic interpretation of sand size distributions. Journal of Geology, 84, 405-426.

Moslow, T. F., and Heronn, S. D., 1979. Quaternary evolu tion of Core Banks, North Carolina: Cape Lookout to New Drum inlet. In Leatherman, S.P., ed., Barrier Islands from the Gulf of St. Lawrence to the Gulf of Mexico. Academic Press, New York, 211-236.

Moslow, T. F., and Heron, S. D., 1978. Relict inlets: preservation and occurrence in the Holocene stratigraphy of southern Core Banks, North Carolina. Journal of Sedimentary Petrology, 48, 1275-1286.

Moslow, T. F., and Tye, R. S., 1985. Recognition and characterization of Holocene tidal inlet sequence. In Oertel, G.F. & Leatherman, S.P., ed., Barrier Islands. Marine Geology (Special Issue), 63, 129-151.

Moslow, T. F., and Tye, R. S., 1982. Stratigraphic varia tions of wave and tide dominated tidal inlets. Abstracts with programs of Geological Society of American (NE/SE section), 14, 66p.

Moss, A. J., 1972. Bed load sediments. Sedimentology, 18, 159-219.

Nielsen, L., Johannessen, P., and Surlyk, F., 1988. A late Pleistocene coarse-grained spit-platform sequence in northern Jylland, Denmark. Sedimentology, 35, 915-937.

Nordin, C.F.Jr., 1971. Statistical properties of dune profiles. Geological survey professional paper 562-f, 41p.

Nordin, C.F.Jr., and Algert, J.H., 1966. Spectral analysis of sandwaves. Journal of the Hydraulics Division, American Society of Civil Engineering, 92, HY5, 95-114.

Nordin, C.F.Jr., and Algert, J.H., 1966. Spectral analysis of sandwaves. Journal of the Hydraulics Division, American Society of Civil Engineering, 92(HY5), 95-114p.

Nummedal, D., and Fischer, I.A., 1978. Process-response models for depositional shorelines: the German and the Georgia Bights. Proceedings of 16th coastal Engineering Conference of Civil Engineers, 1215-1231.

Nummedal, D., and Penland, S., 1981. Sediment dispersal in Norderneyer Seegat, West Germany. In: Nio, S.D., Shuttenhelm, R.T.E. and van Weering, Tj.C.E., ed., Holocene Marine Sedimentation in the Northe Sea Basin., Special Publication No.5 of International Association of Sedimentologists. Blackwell Scientific Publications, Oxford, London, 187-210.

Nummedal, D., Oertel, G.F., Hubbard, D.K., and Hine, A.C.,III, 1977. Inlet morphology — Cape Hatteras to Cape Canaveral, In Proceedings of Coastal Sediments 77, Charleston, S.C., Nov. 2-4, 1977.

O'Brien, M. P., 1976. Notes on tidal inlets on sandy shores. General Investigation of Tidal Inlets, Report No.5, Coastal Engineering Research Centre, Fort Belvoir, Virginia, 26p.

Oertel, G.F., and Leatherman, S.P., eds., 1985. Barrier Islands. Marine Geology (Specical Issues), 63, 419p.

Olsen, H., Due, P. H., and Clemmensen L.B., 1989. Morphology and genesis of asymmetric adhesion warts — new adhesion surface structure. Sedimentary Geology, 61, 277-285.

Otnes, R. K., and Enochson, L, 1978. Applied Time Series Analysis — Basic Techniques, New York: John Wiley and Son Inc., 449p.

Owen, E. H., 1977. Temporal variation in beach and near shore dynamics. Journal of Sedimentary Petrology, 74(1), 168-190.

Ozasa, H., 1974. Field investigation of large submarine sand waves. Coastal Engineering in Japan, 17, 156-183.

Pattiaratchi, C. B., and Collins, M. B., 1983. Sediment transport under waves and tidal currents: A case study from the Northern Bristol Channel, U.K. Marine Geology, 56, 27-40.

Penland, S., Boyd, R., and Suter, J. R., 1988. Transgres sive depositional systems of the Mississippi Delta Plain: A model for barrier shoreline and shelf sand development. Journal of Sedimentary Petrology, 58(6), 932-949.

Penthic, J.S., 1980. Velocity surges and asymmetry in tidal channels. Estuarine and Coastal Marine Science, 2, 331-345.

Phillips, O.M., 1957. On the generation of surface waves by turbulent wind. Journal of Hydraulics Division, American Society of Civil Engineering, 92 (HY 5), 95-114.

Pierce, J. W. 1969. Tidal inlets and washover fans. Journal of Geology, 51, 230-234.

Poole, W. H., Sanford, B. V., Williams, H., and Kelley, D. G., 1970. Geology of southeastern Canada. In

Douglas, R.J.W., ed., geology and economic minerals of Canada. 5th edition. Geological Survey of Canada. Economic Report 1, 229-304.

Postma, H., 1967. Sediment transport and sedimentation in the estuarine environment. In: G.A. Lauff, ed., Estuaries. Washington, DC, Amer. Assoc. Advancement of Sci., 158-179.

Press, W. H., Flannery, B. P., Teukolsky, S. A., and Vetterling, W. T., 1986. Numerical recipes: The art of scientific computing. Press Syndicate of the University of Cambridge, 818p.

Prest, V. K., and Grant, D. R., 1969. Retreat of the last ice sheet from the Maritime Provinces — Gulf of St. Lawrence region. Geological Survey of Canada, Paper 69-33, 15p.

Prest, V. K., 1973. Surficial deposits of Prince Edward Island. Geological Survey of Canada, Map 1366A.

Prest, V. K., 1971. Geology of Malpeque-Summerside area, Prince Edward Island. Geological Survey of Canada, Paper 71-45, 21p.

Quon, C., Keyte, F. K., and Pearson, A., 1963. Comparison of five years hindcast wave statistics in the Gulf of St. Lawrence and lake Superior. Bedford Institute of Oceanography Report 63-2, 59p.

Ramirez, R. W., 1985. The FFT fundamentals and concepts. Prentice-Hall, Inc., 178p.

Reddering, J. S. V., 1983. An inlet sequence produced by migration of a small microtidal inlet against longshore drift: the Keurbooms Inlet, South Africa. Sedimentology, 30, 201-218.

Reinson, G.E., 1984. Barrier island and associated strand-plain systems. In Walker, R.G., ed., Facies Models. Geoscience Canada Reprint Series 1, Second Edition, 119-140.

Reinson, G. E., 1980. Variations in tidal-inlet morphology and stability, northeast New Brunswick. In McCann, S.B., ed., The Coastline of Canada, Geological Survey of Canada, Paper 80-10, 23-39.

Reinson, G. E., 1977. Tidal current control of submarine morphology at the mouth of the Miramichi estuary,

New Brunswick. Canadian Journal of Earth Science, 14, 2524-2532.

Reison, G. R., 1979. Longitudinal and transverse bedforms on a large tidal delta, Gulf of St. Lawrence, Canada. Marine Geology, 31(3/4), 279-296.

Rock, N. M. S., 1988. Numerical geology — A source guide, glossary and selective bibliography to geological uses of computers and statistics. Lecture Notes in Earth Sciences, No. 18, Springer-Verlag, Berlin, 427p.

Rosen, P., 1979. Eolian dynamics of a barrier island system. In Leatherman, S.P., ed., Barrier Islands from the Gulf of St. Lawrence to the Gulf of Mexico. Academic Press Inc., New York, 81-98.

Rossby, C. G., 1932. Conditions on kinematic similarity. Meteorology papers, Massachusetts Institute of Technology, 1(4), 9-14.

Rouse, H., 1937. Modern conceptions of the mechanics of fluid turbulence. Transaction of American Society of Civil Engineers, 102, 463-543.

Schwartz, R. K., 1982. Bedforms and stratification characteristics of some modern small-scale washover sand bodies. Sedimentology, 29, 835-850.

Seelig, W. N., Harris, D. L., and B.E., Herchenroder, 1977. A Spatially Integrated Numerical Model of Inlet Hydraulics. GITI Report No.14, U.S. Army Coastal Engineering Research Centre, Fort Belvoir, Virginia, 100p.

Sexton, W. J., and Hayes, M. O., 1982. Tidal inlet bar-bypassing with respect to coastal engineering and tidal inlet stratigraphy. Proceeding of 18th Coastal Engineering Conference, Cape Town, South Africa, American Society of Civil Engineering, 2, 1479-1495.

Shen, H.W. and Cheong, H.F., 1977. Statistical properties of sediment bed profiles. Journal of the Hydraulics Division, American Society of Civil Engineering, 103, HY11, 1303-1315.

Sheridan, M. F., Wohletz, K. H., and Dehn, J., 1987. Discrimination of grain-size subpopulations in pyroclastic deposits. Geology, 15, 367-370.

Sheridan, M. F., Wohletz, K. H., and Dehn, J., 1987. Discrimination of grain-size subpopulations in pyroclastic deposits. Geology, 15, 367-370.

Simon, D. B., Richardson, E. V., and Nordin, J. S., 1965. Sedimentary structures generated y flow in alluvial channels. Soc. Econ. Paleont. Mineral. Spec. Publ. 12, 34-52.

Smith, N.P., 1983. Tidal and low-frequency net displacement in a coastal lagoon. Estuaries, 6(3), 180-189.

Speer, P. E., and Aubrey, D. G., 1985. A study of non-linear tidal propagation in shallow inlet/estuarine systems Part II: Theory. Estuarine, Coastal and Shelf Science, 21, 207-224.

Squarer, D., 1970. Friction factors and bed forms in alluvial channels. Journal of the Hydraulics Division, American Society of Civil Engineering, 96, HY4, 995-1017

Sternberg, R. W., Cacchione, D. A., Drake, D. E., and Kate K., 1986. Suspended sediment transport in an estuarine tidal channel within San Francisco Bay, California. Marine Geology, 71, 237-258.

Sutton, O. G., 1953. Micrometeorology. McGraw-Hill, New York, N.Y., 333p.

Terwindt, J. H. J., and Brouwer, M. J. N., 1986. The behaviour of intertidal sandwaves during neap-spring tide cycles and the relevance for paleoflow reconstructions. Sedimentology, 33(1), 1-32.

Terwindt, J. H. J., 1981. Origin and sequence of sedimentary structures in inshore mesotidal deposits of the North Sea. In Nio, S.-D., ed., Holocene marine sedimentation in the North Sea Basin. International Association of Sedimentologists, Special Publication No.5, 4-26. Blackwell Scientific Publications, Oxford, 515p.

Thorn, M. F. C., and Parson, S. J., 1980. Observed tidal variations in apparent values of Von Karman's constant. Abstract of marine Studies GP meeting on Shelf and Nearshore Dynamics and Sedimentation, London, 3-4 December.

Tye, R. S., 1984. Geomorphic evolution and stratigraphy of Price and Capers Inlets, South Carolina.

Sedimentology, 31, 675-695.

U.S. Army Coastal Engineering Research Centre, 1973. Shore protect manual. U.S. Government Printing Office, Washington, D.C., 1, 4-180.

Uhlir, D. M., Akers, A., and Vondra, C. F., 1988. Tidal inlet sequence, Sundance Formation (Upper Jurassic), north-central Wyoming. Sedimentology, 55, 739-752.

van de Kreeke, J., 1984. Stability of multiple inlets. Proceedings of 19th coastal engineering conference, ASCE, 1360-1370.

van den Berg, J. H., 1977. Morphodynamic development and preservation of physical sedimentary structures in two prograding recent ridge and runnel beaches along the Dutch coast. Journal: Geological Mijnbouw, 56, 156-202.

van Rijn, L. C., 1984. Sediment transport, Part II: Suspended load transport. Journal of Hydraulic Engineering, 110(11), American Society of Civil Engineers, 1631-1639.

Vanoni, V. A., 1977. Sedimentation Engineering. Manuals and reports on engineering practices, American Society of Civet Engineers, 54, 745p.

Vanoni, V. A., and Nomicos; C. N., 1959. Resistance properties of sediment laden streams. Journal of Hydraulic Division, 85, American Society of Civil Engineers, 75-107.

Vigeant, G., 1984. Explanatory guide to climatological charts of the St. Lawrence (River and Gulf). Environmental Canada, 14p.

Visher, G. S., 1969. Grain size distributions and depositional processes. Journal of Sedimentary Petrology, 39, 1074-1106.

Vitale, P., 1980. A guide for estimating longshore transport rate using four SPM methods. Coastal Engineering Technical Aid No. 80-6, U.S. Army Coastal Engineering Research Centre, 16p.

Wong, K.C., 1986. Sea level fluctuations in a coastal lagoon. Estuarine, Coastal and Shelf Science, 22, 739-752.

Wood, F. J., 1986. Tidal dynamics: Coastal flooding, and cycles of gravitational force. D. Reidel Publishing Company, 558p.

Part II

Hydraulic Characteristics of Palmer Inlet

— Numerical Simulations

Introduction

Palmer Inlet is characterized by an extensive flood delta and a small ebb delta. The morphology indicates a dominance of sediment transport in the flood direction. In apparent contradiction, daily tides are characterized by a long runout, suggesting that the dominant sediment transport is in the ebb direction. Related to this is the characteristic tidal distortion, showing that the bay tide rises more quickly but falls more slowly than the tide just outside the inlet entrance. Part I postulated the causes for such observations. While intuitively appealing, the interpretations lacked the physical basis, and did not provide insight into the underlying mechanisms that generate these phenomena.

Part II of the thesis attempts to look at the answers of the above phenomena. The approach is to combine a numerical inlet model with the field data to conduct 'what-if-analysis' about effects of various parameters on inlet responses. The calculations provide a basis for understanding the mechanisms that control tidal deformations observed at the study site. The field-tested model is further used as a predictive tool for analysis of inlet hydraulics and stability. This provides a better understanding of the inlet behaviour demonstrated by the

field data.

The physics of inlet processes are first presented in Chapter 1 by introducing the basic equations of inlet dynamics. This is followed by a review of various inlet models currently available in the literature. The review emphasizes the different approaches these models used, and the major findings. An implication is that despite these efforts, the problems raised in the present study are not addressed.

Seelig's (1977) spatially-integrated inlet model used for the present study is then introduced in Chapter 2. The application of the model has two phases. In Phase one, reported in Chapter 3, the model was first run as a test for transient effects. It involved input of cyclic tides of both diurnal and semidiurnal periods. The interval at which the output repeated itself was determined. Step by step parametric studies were then performed using idealized but still realistic inlet geometries. Factors investigated include the size of the flood tidal delta and the spit platform, the slope of the bay wall, the surface area of the bay, the cross section area of inlet channels, friction, effect of a second inlet channel, etc. Emphasis is particularly given to the role they play in inducing tidal asymmetry.

The model is then applied to Palmer tidal inlet in Phase two, reported in Chapter 4. First, the model was

calibrated using predicted data of water levels of July 19-21. The friction factor was used as the main tuning parameter. The model was adjusted until optimal agreement was achieved between the predicted and measured data. After the calibration, as reported in Chapter 5, the model was used to calculate equilibrium curves by combining it with van de Kreeke's stability model. Part II is concluded with a summary.

Chapter 1

Inlet Modelling

1.1 Basic Inlet Equations

In inlet modelling, the two variables to be solved are usually the flow speed (or discharge) and the bay tide. At any instant, these two variables are a function of a combination of the geometric and dynamic parameters of the system. The geometric parameters include the shape and bathymetries of the internal basin and inlet channels. The friction and the acceleration due to gravity form the dynamic parameters, which also include the sea tide and its rate of changes.

Inlet modellers used these factors to form two equations based on two basic laws of fluid mechanics. They are the law of conservation of momentum and the law of the conservation of mass. The two equations formed are the equation of motion or the dynamic equation, and the equation of continuity. To predict tides or currents, these two equations must be solved simultaneously.

The inlet equations take two different forms depending on the assumption made about the tidal motion in the bay. The first form assumes that the bay is deep but relatively small. The flooding, or 'hydraulic filling' (Mehta and Ozsoy, 1978), of such a basin is relatively

quick. In the basin, the tide has the form of a standing wave, and water levels rise and fall uniformly. The inlet model for this type of basin is called the 'pumping model' (Bruun, 1978). The other form assumes that the bay is large in the lateral extent, but shallow in depth. The filling of such a basin thus cannot be instantaneous as in the previous model. There are lags in phase and reduction in amplitude of tides in the basin. In this case, the tide appears as progressive waves. Under this condition, the shallow water long waves model must be used (King, 1974; Van de Kreeke, 1972; van de Kreeke and Cotter, 1974).

The division between these two basic models is usually specified by a dimensionless quantity representing the ratio of the travelling time the tide takes to cover the longest dimension of the bay to the period of the tide (Mehta and Ozsoy, 1978). Roughly, however, they correspond to the two morphodynamic inlet models conceptually familiar to sedimentologists (Hayes, 1979). Mesotidal inlets are characterized by relatively large bays filled with marshlands. The tide has to fill the dendritic network of creeks before filling the basin. Numerous studies have documented amplitude reduction and phase lags usually associated with a progressive wave (Boon, 1975; Bayliss-Smith, et al., 1979; Robinson, et al., 1983). For mesotidal inlets, the long wave model thus applies (Aubrey and Speer, 1985). On the other hand, back barrier lagoons of

microtidal inlets are relatively small and open. Tides are often found filling the basin with no significant phase difference between different parts of the bay (Isaji and Spaulding, 1981; DeLorenzo, 1986). In this case, the pumping model is more appropriate.

1.1.1 Dynamic Equations

The equation of motion governing the inlet dynamics of both pumping and long wave inlet model is a simplified Navier-Stokes' equation. With respect to the coordinate system of Figure 1, the cross-sectionally averaged, one dimensional form of the equation is:

$$\underset{(1)}{\frac{\delta(Q/A_c)}{\delta t}} + \underset{(2)}{\frac{\delta(Q^2/A_c^2)}{\delta x}} + \underset{(3)}{g\frac{\delta h}{\delta x}} + \underset{(4)}{\tau} = 0 \qquad \text{— (1)}$$

Q = inlet water discharge

h = water surface elevation above datum

g = gravitational acceleration

x = distance along the longitudinal axis of the inlet

τ = cross-section mean bottom shear stress along x axis

A_c = inlet gorge cross section area

Equation (1) describes the momentum or force balance between the various terms, which have the following

Figure 1 Schematic depiction of an inlet-bay system, showing the relationship between the hydraulic head and the other dynamic terms U = cross section averaged current velocity. Q = total discharge. A_c = inlet gorge section area. A_s = inlet cross section area at the entrance end. A_b = inlet cross section area at the rear end.

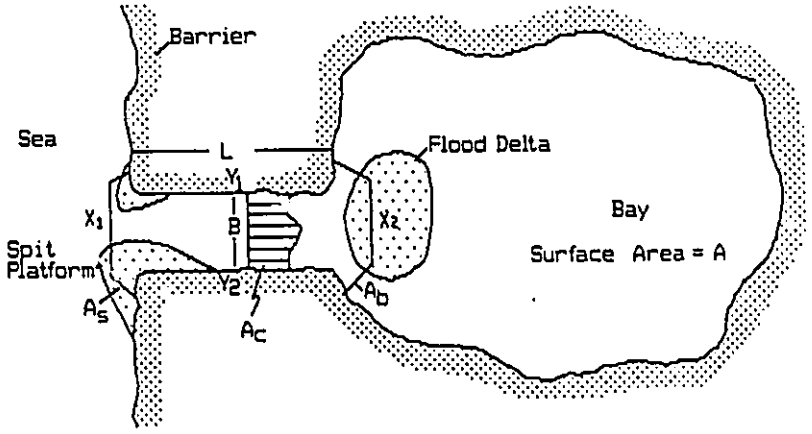

PLAN

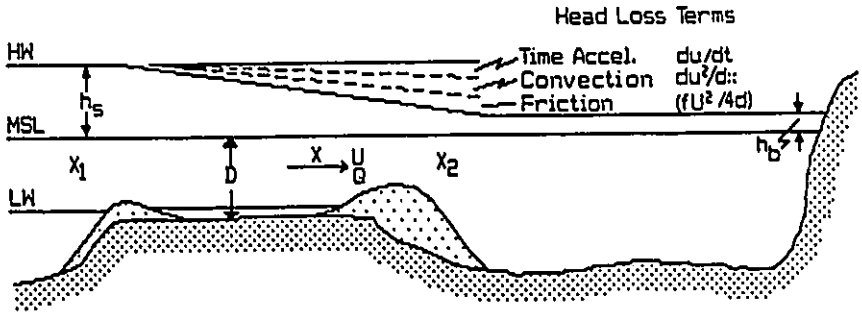

PROFILE

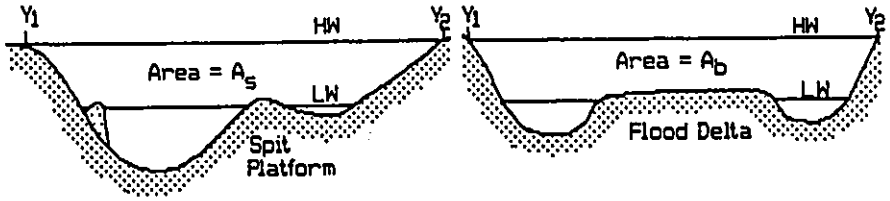

CROSS SECTION

meanings. Term (1) represents the inertial force, or time-acceleration of the tide due to change of flow with respect to time. Because semidiurnal and diurnal tides are low-frequency fluctuations, this term is generally considered small (Mehta, 1978). Term (2) is the advection, or space-acceleration. It represents the force due to change of flow with space. It arises from the variation in cross-section areas along the channel axis. It thus vanishes where the channel is prismatic, but could be significant where there is divergence and convergence, especially if the length is short. Term (3), $g\ \delta h/\delta x$, is the hydraulic head due to the water level difference between the two ends of the inlet. It takes different signs depending on whether the tide is flooding or ebbing. Term (4) is the friction term. It appears as a stress force acting on the bottom. Its magnitude is directly proportional to the roughness of the channel, but inversely proportional to the water depth.

It is noted that the dynamic equation takes different forms for the long wave model and the pumping model. This is because in Equation (1), h and Q are functions of both distance and time for the former. For the pumping model, the two variables are a function of time only. One is thus a partial differential equation, and the other an ordinary differential equation.

1.1.2 Continuity Equations

The continuity equation describes the mass balance between the flow coming in and going out. For the long wave model, it must reflect the fact that water level rises where tidal creeks contract, and falls where expansion occurs. The one-dimensional form of the equation is:

$$\frac{\delta Q}{\delta x} + B \frac{\delta h_b}{\delta t} = 0 \qquad \text{— (2)}$$

Where B = channel width. Again, Q and h are functions of both distance and time.

The internal bay in the pumping model serves only to store water. The continuity equation thus can be simplified into a storage equation. The storage equation describes that the water passing through the inlet is equal to the change in the volume of water in the basin. In mathematic form, this is:

$$Q = A \frac{\delta h_b}{\delta t} \qquad \text{— (3)}$$

Where A = bay surface area. h_b = bay tide elevation. Equation (3) does not consider other sources of water either into or out of the bay, such as those of rivers or rain. If there are such sources, they should be included in the equation.

1.2 Literature Review of Solution of Inlet Equations

The solution of either inlet model involves solving simultaneously the dynamic and the continuity equation mentioned above. Because of the nonlinearity related to the quadratic Q terms, the exact analytical solution cannot be achieved without simplifications. The first analytical solution to the pumping inlet model was achieved by Brown (1928). Brown used sine curves as forcing tides in the solution. He also neglected the flow acceleration, and linearized bottom friction. While correctly produced the general pattern, this model predicted no asymmetry of bay tides. This apparently differs from real situations, and is of little value for the analysis of net sediment transport.

Also using an analytical method, Keulegan (1967) relaxed Brown's linear assumption about friction. By approximating the friction with a quadratic law, he was able to produce nonsinusoidal bay tides despite that assumption that the forcing tide was still a sine wave. Most significant, however, was the introduction by the author of a dimensionless parameter:

$$K = \frac{T}{2\pi a_o} \quad \frac{A_c}{A} \quad \frac{\sqrt{(2ga_o)}}{\sqrt{(F)}} \qquad \text{— (4)}$$

Where T = tidal period; a_o = tidal amplitude; F = impedance or total resistance that includes friction and entrance/exit

loss (O'Brien and Clark, 1974). By lumping various factors together, this parameter provides a convenient measure of the ease with which the tide fills a basin. For this reason, it is called the Coefficient of Repletion. Keulegan's method produced still predicted no asymmetry in net sediment transport because the flow coming in and going out is same. It applies also only to small inlets with simple geometries (O'Brien and Clark, 1974). This is due to the following assumptions used in the solutions:

(1) Flow is steady, i.e., du/dt = 0;

(2) Both the bay surface area and the inlet cross-sectional area do not change with tide;

(3) The cross sectional areas of the inlet channel are constant along its axis;

(4) The forcing tide is a semidiurnal sine wave;

(5) The depth of the inlet channel is much greater than the tidal range.

Subsequent workers refined Keulegan's model by eliminating one or more of the above assumptions. Using analytical and numerical method respectively, King (1974) and Mehta and Ozsoy (1978) incorporated the time acceleration, du/dt, in their model, thus relaxing assumption (1). They both concluded that in large inlets, where water flow is less restricted, the inertial effects are non-negligible. The result is that bay tides are

synchronized with the ocean tides. The incoming water could continue to flow even after the ocean tide had reversed its direction. These effects explained why at some large inlets the slack waters did not coincide with the time, at which the ocean and bay tide were crossing each other.

Forcing tides of nonsinusoidal forms were used by DiLorenzo (1986) and by Semdin and Forney (1970). This was achieved by introducing harmonic overtides. In both cases, the analytical solution was used. The inclusion of overtides improved agreement between the predicted and measured tides. They have also been found responsible for producing irregular fluctuations observed in the velocity field (Semdin and Forney, 1970), and introducing asymmetries into the sediment transport (DiLorenzo, 1986). The latter author also studied time-velocity asymmetries, and presented the results with charts/graphs, in which fields of flow dominance were defined.

Assumption (2) and (3) were relaxed by Mota Oliveira (1970) and King (1974) in their studies using a pumping model and by Boon (1975), Boon and Bryne (1981) and Aubrey and Speer (1985) in long wave models. The inclusion of varying geometries entailed the use of a numerical approach in all five studies. Their studies showed how higher harmonics and net sediment transport resulted from interactions between various terms in inlet equations due to changes in the bay surface or inlet cross section areas.

They found that changes in bay surface area resulted in tidal asymmetries with longer rising tides and shorter but stronger ebbs. In inlets with extensive tidal flats, this is the main control on net transport directions. On the contrary, variations in cross-section areas favour the rising tide, and produce a stronger flood flow. Such changes are more prominent where the ratio of the tidal amplitude and the channel depth is large.

Huval and Wintergerst (1977) proposed a generalized Keulegan's model by relaxing all five assumptions. By dividing the system into a network of subchannels and subsections, they are able to handle complex, irregular bathymetry, and present the result in plan views. In this sense, the model is quasi-two dimensional. The method they used in constructing the network grid is one that assumes that the subchannels at a cross section are of equal cross-section areas. This implies that each cell has an equal share of the total discharge. Generally, this is not an accurate representation of flow distribution in the inlet, nor is it possible to draw the grid graphically in such a way.

Seelig et al. (1977) rectified the above limitation of Huval and Wintergerst's model (1977) by introducing a Weighing function. This was based on the recognition that the fraction of a flow allocated to a cell should be proportional to the ratio of the resistance that cell

experienced to the total resistance of the entire section. In computation, this was achieved by calculating the frictional resistance using Manning's equation, and then assigning it to each cell with recourse to Ohm's law. This reduced the work of constructing the flow net to computer routines. As the inlet equations are first applied to each cell and then integrated across the entire net, Seelig et al.'s method is called a spatially-integrated model.

The above brief review shows that a great many of inlet models exists. They range from relatively simple one-dimensional models with restrictive assumptions, to relatively complex, quasi-two dimensional model. As a result of these efforts, a great deal of knowledge has been achieved about hydraulic behaviour of tidal inlets. While results of these studies may be valid for the cases studied, however, they may not be immediately applicable to other cases. This depends upon the questions being asked and upon the complexity of the inlet conditions. On the coast of the Gulf of St. Lawrence, small tidal inlets tend to develop large flood tidal deltas and large spit platform that restrict inlet communications. They form an unusual class of tidal inlets on a coast where tides are characteristically diurnal. These unique factors have not been previously studied, and their effects remain unknown.

Chapter 2

Seelig et al's Spatially Integrated Inlet Model

Seelig et al.'s numerical model (1976, Appendix A-3) represents the elaboration of current methods in inlet modelling. By discretizing the system and adopting a spatially-integrating approach, this method is capable of dealing with irregular geometries, multiple inlets, storms, etc. The model has been tested in a number of field studies (Sorensen and Seelig, 1976; Isaji and Spaulding, 1981), and proved to be accurate and effective. Seelig et al.'s model is used in the present study. In the following, its development is introduced.

2.1 Assumptions

To applied Seelig et al.'s model, a number of requirements must be met. First of all, it is a pumping model. This requires that the water level in the bay rises and falls relatively uniformly over the whole area. This occurs when the length and width of the embayment is much less than the tidal wavelength (Mehta and Ozsoy, 1978), as defined by the following expression:

$$T \sqrt{(gD)} >> L_b$$

Where T = tidal period; D and L_b are depth and length of the bay. The average depth of Cascumpec Bay at mean water level is about 2.3 m. The diurnal tide thus has a wavelength of 418 Km and semidiurnal tide 214 Km. They are two orders of magnitude larger than the length of the bay, which is about 6.3 Km.

Coriolis force due to the rotation of the earth and stratification of flow due to salt water intrusion are two factors neglected in the model. Coriolis force is proportional to the dimensions of the system, and to the speed of the flow involved. Harris and Bodine (1977) found that for typical inlets with width less than one mile and maximum currents less than 2 m/s, the Coriolis force is negligible. The width and velocity scale of Palmer Inlet are well within these limits. Both Palmer Inlet and Cascumpec Bay are shallow water bodies, water depths being of the same order as the tidal range. Consequently, the water is well-mixed. This was proved by the measurements of vertical salinity profiles.

Effects of wind stress and wind waves, which are also assumed negligible in the model, are difficult to assess. The shallow depth of Palmer Inlet suggests that these forces could reach the bottom, and affect the mean tidal flow. The effects are uncertain and difficult to incorporate into the program. This is expected to constitute the major source of error in applying this model

to the present study. However, as illustrated in Chapter 2, Part I, at Palmer Inlet wind and wind-generated waves on the gulf side are stronger than those on the bayside due to the limited fetch and shallow depth there. The inclusion of wind-related effects should be on the average in favour of the flood current.

2.2 Derivation of Equations

To arrive at simplified equations that can be incorporated into computer routines, Equation (1) is first integrated over the inlet length between sea and bay:

$$\int_{X_1}^{X_2} \frac{\delta (Q/A)}{\delta t}\, dX + \int_{X_1}^{X_2} \frac{\delta (Q^2/A^2)}{\delta X}\, dX + \int_{X_1}^{X_2} g \frac{\delta h}{\delta X}\, dX + \int_{X_1}^{X_2} \tau\, dX = 0 \qquad \text{— (5)}$$

The integration of the first term is

$$\int_{X_1}^{X_2} \frac{\delta (Q/A)}{\delta t}\, dX = \frac{\delta Q}{\delta t} \int_{X_1}^{X_2} \frac{\delta X}{A} \qquad \text{— (6)}$$

The integration of the second term is

$$\int_{X_1}^{X_2} \frac{\delta (Q^2/A)}{\delta X} dX = \frac{1}{2} \left(\frac{1}{A_b^2} - \frac{1}{A_s^2}\right) Q^2 \qquad — (7)$$

The treatment of advection in this way assumes that the potential head loss due to the acceleration of flow into the entrance is equal to the head gain as the water exits at the other end. However, part of the energy must be lost due to eddies and turbulence related to this entering and exit process. To account for this energy loss, Keulegan (1967) and other authors (Dean, 1983) use the following empirical equation instead:

$$\int_{X_1}^{X_2} \frac{\delta (Q^2/A)}{\delta X} dX = (K_{en} + K_{ex}) \frac{|Q|Q}{A^2} \qquad — (8)$$

in which K_{en} and K_{ex} are the entrance and exit loss coefficient, respectively. Typical values for K_{en} are 0.05-0.25 and K_{ex} is usually taken as unity. The absolute sign is used to account for changes in the direction of the flow.

The integration of the third term is

$$\int_{x_1}^{x_2} g \frac{\delta h}{\delta X} dX = g (h_s - h_b) \qquad \text{— (9)}$$

The bottom stress per unit area is evaluated by Manning's equation:

$$\tau = \frac{g n^2 |Q| Q}{D^{0.33} A^2} \qquad \text{— (10)}$$

Where n = Manning's friction factor.

Substituting Equation (6), (7), (8) and (9) into (5) and reorganizing results in the following equation:

$$\frac{dQ}{dt} = - \frac{1}{I} (K_{en} + K_{ex}) \frac{Q^2}{A^2} - \frac{1}{I} (h_b - h_s) - \frac{E}{I} \qquad \text{— (11)}$$

Where

$$I = \int_{x_1}^{x_2} \frac{\delta X}{A} \qquad \text{— (12)}$$

and

$$E = \int_{x_1}^{x_2} \tau \, dx \qquad \text{— (13)}$$

2.3 Implementation and Construction of the Grid System

To implement the model, a means of relating the equations to the physical system is needed. This is achieved by constructing a grid system (Figure 2). The number of subchannels, IC, and subsections, IS, in the grid is determined by the complexity of bathymetry. Simple inlets need small numbers. In the deep parts where flow is strongest, the grid should be more densely spaced. The breakdown of the system into discrete cells makes two changes to Equation (11):

(1) It converts the two integral operations in Equation (12) and (13) into the form of summations;

(2) It transfers the cross-section averaged quantities into cell averaged quantities. For example, A now is A_{ij} and n is n_{ij}, where i and j refer to the cell bounded by the i^{th} section and j^{th} channel.

For each inlet there is an Equation (11), and for each bay there is a continuity Equation (3). This set of simultaneous equations is solved using a fourth order Runge-Kutta-Gill technique in a time marching procedure in the

Figure 2 Grid representation of a typical inlet channel. The grid system (plan diagram) consists of three channels (IC = 3) and four sections (IS = 4). The application of input geometries to grid cells is shown in the block diagram for cell $c_{i,j}$. The subscript i is the index for sections and the subscript j is the index for channels. B is the width, L is the length and A is cross section area. Parameters with primes are measured values applied at cell boundaries. Hydraulic parameters, such as Manning's n, are applied at the centroid.

Inlet Grid Representation

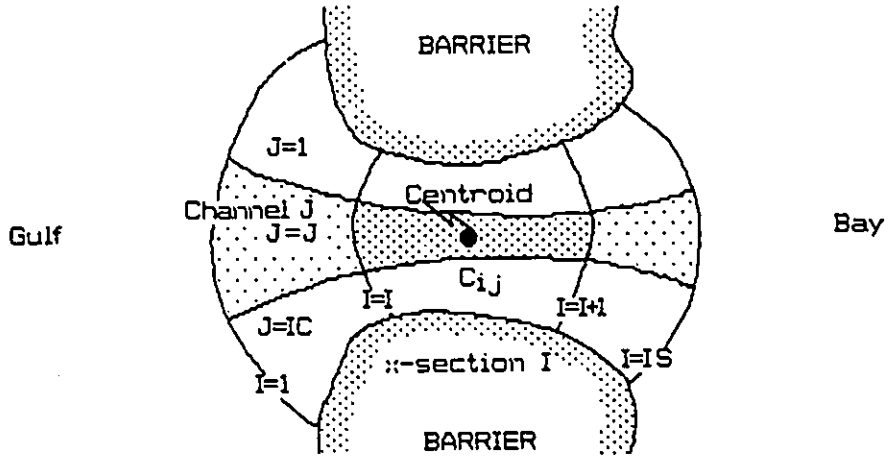

PLAN

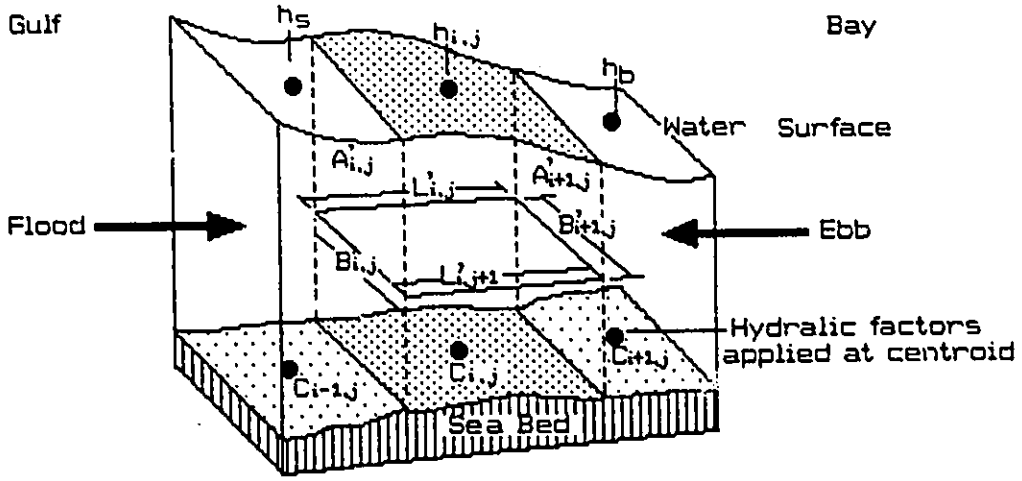

BLOCK

Cell Geometries (at Centroid) :

$$A_{ij} = (A'_{ij} + A'_{i+1,\,j}) / 2$$

$$B_{ij} = (B'_{i,j} + B'_{i+1,\,j}) / 2$$

$$L_{ij} = (L'_{ij} + L'_{i,j+1}) / 2$$

$$D_{ij} = A_{i,j} / B_{i,j}$$

following sequence:

(1) Measured boundary values, including widths, depths and lengths are assigned to each cell. All initial values of hydraulic variables are set to zero at time = 0. This unrealistic condition will be overcome by operating the model through an initial transient period.

(2) Hydraulic factors are evaluated for each cell starting from the first cell in the most seaward row (Figure 2). The program then works its way across the row to the last cell in this row, and moves down to the second row after interpolating the new local water level based on friction loss. This procedure continues until the last cell of the most landward row is reached. At this point, the information is spatially integrated and the coefficients of the differential equation are determined.

(3) $\delta Q/\delta t$ and dh/dt calculated at $t = 0$ are used to computed Q and h. The latter values are then used as inputs for the next time step, $t = \Delta t$.

(4) Step (2) and (3) are repeated as the time advances. The result is a time history of bay water elevations, and inlet discharges or velocity at the end of the time cycle.

Chapter 3

Parametric Study

3.1 Idealized Inlet System

The spatially integrated model is an effective tool for 'what-if-analysis'. In this method, the value of one parameter is allowed to change over a pre-determined range while those of others are kept constant. The effects of each of the possible important factors can thus be examined with least influence of other factors. 'What-if-analysis' was performed on ten parameters in this section. They include the flood tidal delta, the spit platform, the bay surface area and bay wall slope, the throat cross-section area and its slope, friction, effects of a second inlet, etc. To facilitate the calculation, an idealized inlet system is used as the base condition. This is illustrated in Figure 3. The base condition consists of a short, straight middle channel, and 45° funnel-shaped compartments at each end. The grid system consists of seven sections and three channels whose dimensions are given in the figure. The gorge section is modelled as 250 m wide and 2 m deep. The total length is about 560 m. For the base condition, the bay surface area at mean water level, A_{msl} is set at 10^7 m^2. Based on results of other inlet modelling (Chen and Hembree, 1977; Seelig, 1977), Manning's n is approximated

Figure 3 Idealized inlet system used as the basis for parametric studies. It consists of a straight gorge channel with a 45° funnel-shaped compartment at each end. The superimposed grid net consists of seven sections and three channels. The cells used to simulate the effects of the flood tidal delta and spit platform in the parametric study are stippled. Geometric values for each cell are given in the table, in which I refers to the section and J to the channel. Note that there are J+1 times I-1 values of length. The gorge cross section area is about 500 m^2 and the total straight length of the inlet channel is 560 m.

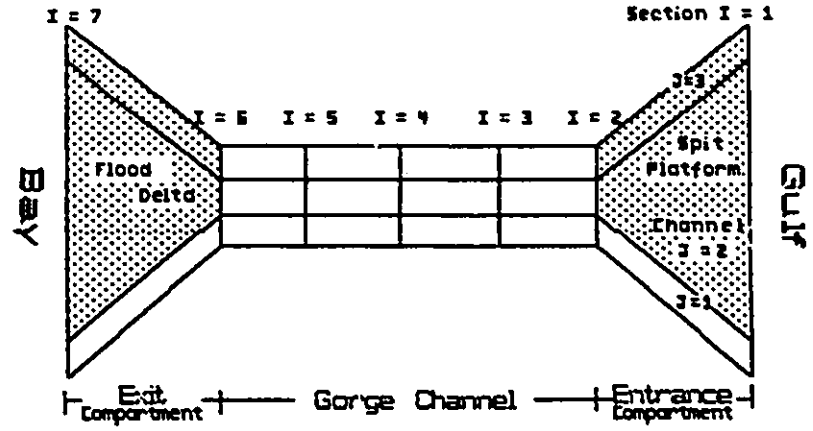

Table of Cell Geometries

J / I	Depth, m			Width, m			Length, m			
	1	2	3	1	2	3	1	2	3	4
1	2	2	2	83	283	83	141	141	141	141
2	2	2	2	83	83	83	70	70	70	70
3	2	2	2	83	83	83	70	70	70	70
4	2	2	2	83	83	83	70	70	70	70
5	2	2	2	83	83	83	70	70	70	70
6	2	2	2	83	83	83	141	141	141	141
7	2	2	2	83	283	83				

using the following relationships (Masch et al., 1977)

$$n = 0.03 \qquad D > 1.2 \text{ m}$$

$$n = 0.055 + 0.005\,D \qquad 0 < D < 1.2 \text{ m}$$

Where D is the mean sea level depth of the channel. For all parametric studies, diurnal tides with amplitude of 55 cm were used as the forcing tide.

It should be pointed out that the base system is modelled on the typical configuration of small inlets on the gulf coast. In particular, it reflects the dimensions as well as physical characteristics of Palmer Inlet. Therefore, although it is idealized, its applicability to the questions in concern is not lost.

3.2 Tests of the Model

To start the model, water levels on both end of the inlet must be specified and applied. This requires an arbitrary initial value (zero in this study) be assigned to the forcing tide. The error introduced by this arbitrary value induces a start-up transient effect in the system response. The transient effect will, however, diminish as dominant operating forces take over. The time interval required to overcome the start-up effect varies with the system properties involved. Thus, before the parametric studies can be performed, the model has to be tested to determine this time interval.

Measured tidal data are not conducive to this

purpose as they vary from cycle to cycle in range and period, therefore, the monochromatic tide is used. Use of a sine wave form ensures that the input data returns to the starting value at the end of each cycle. Response of two successive cycles should thus repeat each other, once the transient effect has been overcome.

Besides the diurnal tide, semidiurnal sine curves with an amplitude of 25 cm were also used as a forcing tide. For each tidal condition, tests were run for five tidal cycles. The output of surface elevation and mean gorge currents was sampled at 1/3 hourly intervals. The percentage difference was between corresponding points of two consecutive cycles. The results are shown in Figure 4 and Figure 5. In the figures, E stands for ebb velocity; F for flood velocity; and T for tidal elevation. The subscripts are the number of cycles. Also plotted in the figures are the four terms of the dynamic equation normalized by the largest term. The tests, as well as other model calculations, wee made on the VAX 6400 at McMaster University. The time step used for integrations of all runs was 150 seconds.

Figure 4 and 5 show that the model is well-behaved under the present configurations. This is indicated by the output that maintains faithfully the pattern of the input data without measurable perturbations throughout the testing period. This suggests that no significant error has

Figure 4 Test results of inlet hydraulics using diurnal tide input. The amplitude (a) of the tide is 0.55 m and the period (p) is 24.8 hr. Manning's n = 0.03. E stands for maximum ebb current, F for maximum flood current and T for tidal range. The figures in subscripts are numbers of tidal cycles and the values are percent difference between the corresponding parameters of two successive cycle. Note that except for F_{1-2} which is the percent difference between the maximum flood current of the first cycle and the second cycle, all the values are three decimal numbers. Also shown are relative magnitudes of four dynamic terms normalized by the largest term. It is noted that the system is strongly friction dominated.

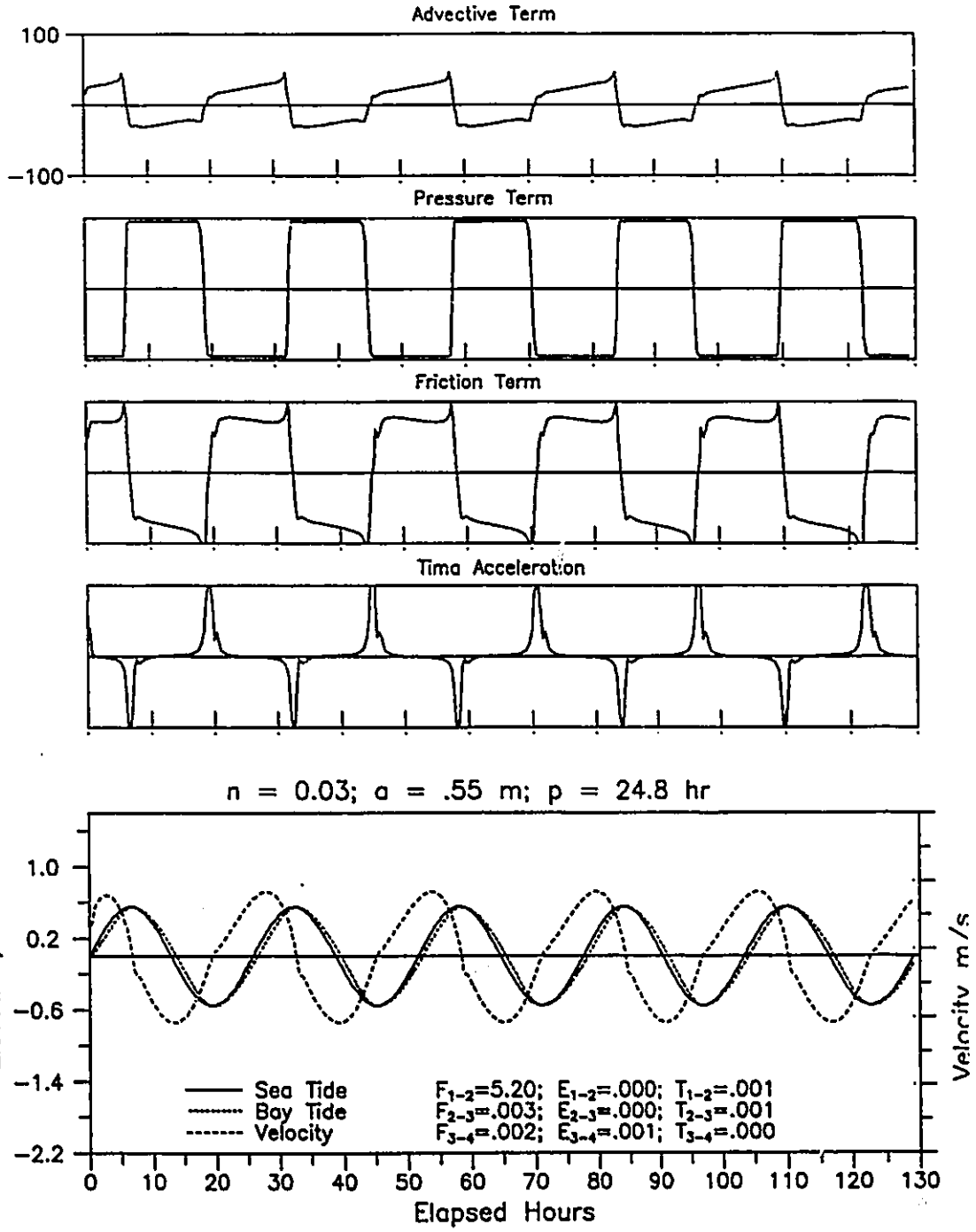
Advective Term
100
−100
Pressure Term
Friction Term
Time Acceleration
n = 0.03; a = .55 m; p = 24.8 hr
1.0
0.2
−0.6
−1.4
−2.2
Elevation, m
Velocity m/s
Sea Tide
Bay Tide
Velocity
F1-2=5.20; E1-2=.000; T1-2=.001
F2-3=.003; E2-3=.000; T2-3=.001
F3-4=.002; E3-4=.001; T3-4=.000
0
10
20
30
40
50
60
70
80
90
100
110
120
130
Elapsed Hours

Figure 5 Test results of inlet hydraulics using semidiurnal tide input. The amplitude (a) of the tide is 0.25 m and the period (p) is 12.4 hr. Manning's n = 0.03. E stands for maximum ebb current, F for maximum flood current and T for tidal range. The figures in subscripts are numbers of tidal cycles and the values are percent difference between the corresponding parameters of two successive cycle. Note that except for $F_{1\text{-}2}$ which is the percent difference between the maximum flood current of the first cycle and the second cycle, all the values are three decimal numbers. Also shown are relative magnitudes of four dynamic terms normalized by the largest term. The system is strongly friction dominated.

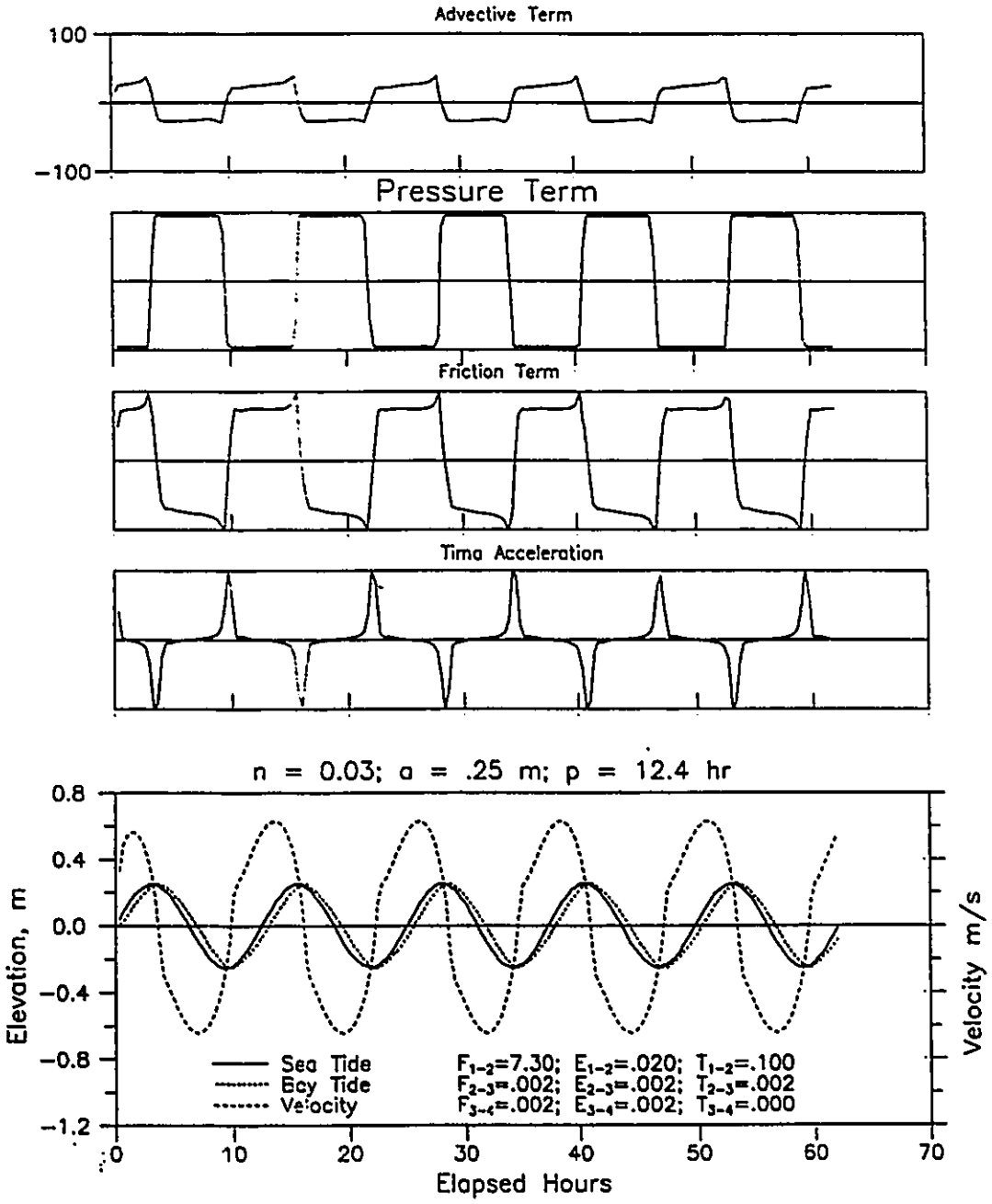
Advective Term
100
−100
Pressure Term
Friction Term
Time Acceleration
n = 0.03; a = .25 m; p = 12.4 hr
0.8
0.4
0.0
−0.4
−0.8
−1.2
Elevation, m
Velocity m/s
Sea Tide
Bay Tide
Velocity
F1-2=7.30; E1-2=.020; T1-2=.100
F2-3=.002; E2-3=.002; T2-3=.002
F3-4=.002; E3-4=.002; T3-4=.000
0
10
20
30
40
50
60
70
Elapsed Hours

accumulated. Such an error would occur if the basic assumptions for the model were inappropriate.

The model also can be considered as extremely stable. For both tests, there are almost no measurable transient effects for water elevations right from the start. The relative difference in tidal range between the first and the second cycle, T_{1-2}, is as low as 0.001% and 0.1%. In fact, they are beginning to disappear only 2 hours after the model was started. The transient effect for current response is slightly longer, but still within the first half tidal cycle as is exemplified by the zero E_{1-2} values. The differences after the first cycle are all five-decimal-point figures.

The reason that the model appears extremely stable is because the base condition is clearly friction dominated. The higher the friction, the sooner it should be able to dampen the transient effect. This proposition is supported by two facts. First, the transient effect on both water levels and current speeds diminished more quickly in the semidiurnal case than the diurnal case. This is shown by comparing the corresponding values in Figure 4 and 5. The temporal inertial is larger — thus less friction dominated — for tides of shorter periods. Second, a separate test was run using the same condition as that of Figure 4 only with friction reduced by two orders of magnitude (Figure 6). The resultant F_{1-2} value is the largest of all three tests.

Figure 6 Test results using the same conditions as that of Figure 4 except that Manning's n = 0.0003. Symbols are the same as in Figure 4. Note that in this case, the friction term is practically zero, while the advective term and time acceleration term are increased. All the calculated values are larger than those in Figure 4.

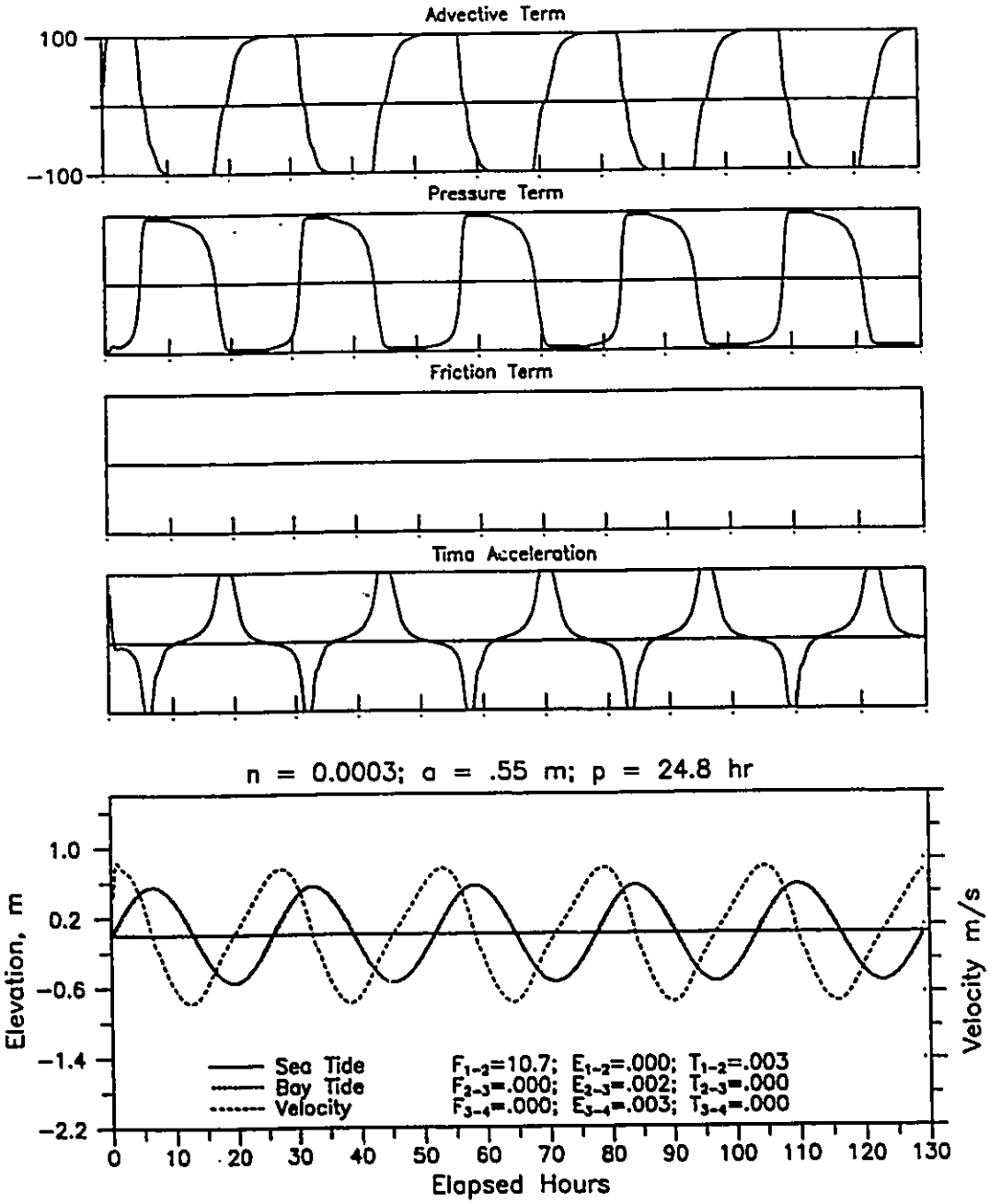
Advective Term
100
-100
Pressure Term
Friction Term
Time Acceleration
n = 0.0003; a = .55 m; p = 24.8 hr
1.0
0.2
-0.6
-1.4
-2.2
Elevation, m
Velocity m/s
Sea Tide
Bay Tide
Velocity
F1-2=10.7; E1-2=.000; T1-2=.003
F2-3=.000; E2-3=.002; T2-3=.000
F3-4=.000; E3-4=.003; T3-4=.000
0 10 20 30 40 50 60 70 80 90 100 110 120 130
Elapsed Hours

Note that the friction term is practically zero. The transient effect was notably longer in this run.

From the above tests, it is concluded that the second cycle no longer depends on the initial condition. The output from that moment on can be considered truly representative of what the real responses would be. It is therefore determined that in the following tests, models are allowed to operate for two tidal cycles. The results of the first cycle are discarded. Only the output of the second cycle was used for evaluations.

3.3 Parametric Studies

The base condition (Figure 3) is modelled as an example of a class of inlets characterized by a throat clogged with sand. The main interest here is to examine the effects of the flood delta and the spit platform in such systems. The ease of operating the program, however, provided enough incentives to carry on similar investigations on other related parameters. These parameters include bay surface area and bay wall slope, inlet cross section area, friction, inlet bank slope, leakage, etc. As many lagoons and embayments are drained by two inlets as is the case in Cascumpec bay, the effects of a second inlet were also examined.

For each run, the model was started from the base condition. The value of the parameter in question was

stepped through a prescribed range, while values of other variables were kept constant. At each step, results of the second cycle of tidal elevations and current speeds were saved for analysis. These included bay tidal range, superelevation, net sediment transport, as well as time-velocity asymmetry. Following Boothroyd's definition (1985), velocity asymmetry is defined as the difference between the flood and ebb peak velocity, and time asymmetry as the shift of these peaks away from their respective midpoints of bay tides (midtides). Superelevation or bay setup is defined as the difference in the mean water level of the bay and that of the ocean (Seabergh and Sager, 1976). As a measure of whether the communication with the sea is deteriorating or improving, superelevation is a good indicator of the overall effect of a parameter on the system. Its value was calculated as the sum of the maximum and the minimum bay tidal elevation. The net sediment transport is used as an indicator of flow dominance. Following the Bagnold's (1963) definition, the rate of sediment transport was computed as the 3rd power of the mean tidal current. It was then integrated over the flood and ebb portion of the cycle to give the volume of transport for flood, Q_f, and ebb, Q_e. Net sediment transport was expressed in terms of

$$Q_n = \frac{Q_f - Q_e}{Q_f + Q_e} 200\%$$

The use of the cube of the mean flow velocity appears to be conservative for estimate of flow dominance. It has been proposed that the bed load transport in tidal inlet may be characterized by maximum velocities raised to the fifth or even higher power (ASCE Task Committee, 1975; Engelund-Hansen, 1967; Bruun, 1978; Costa and Isaacs, 1975). The use of a higher order relationship, however, will affect the magnitude but not the sense (sign) of the results. It also should be pointed out that because of the idealization of the system, the absolute values of the output are of less significance. It is the trend or the pattern of the resultant curves that provides basic information about the hydraulic nature of the parameter and the system. These caveats should be kept in mind as the results are discussed.

3.3.1 Effects of the Flood Tidal Delta

The flood tidal delta is modelled as an intertidal sand body in the rear compartment as stippled in Figure 3. The effect of its size on the tidal responses was modelled as decreasing water depth in those stippled cells to simulate the growth of the delta in elevation. The range of changing water depth is from 0 m to 1.9 m. The output was sampled at four points as shown in the insets of Figure 7.

Figure 7 Inlet responses to varying flood delta sizes. All units are dimensionless.

a. Effects on net sediment transport with further shoaling of the area adjacent to the flood delta. The flood delta is 1.9 m in thickness. With further shoaling of this area (compared with Figure 7c), there is an increase in ebb transport ability in the system except in the area where the flood delta is located.

b. Dimensionless bay tidal range and superelevation. a_o = Ocean tidal range, b_o = bay tidal range and r^o = superelevation. With the growth of the flood delta, the bay tidal range decreases and the superelevation increases.

c. Change of net sediment transport with the flood tidal delta size. The net sediment transport of the flow is calculated as:

$$\frac{Q_f - Q_e}{Q_f + Q_e} \quad 200\%$$

Where q_f and q_e are volumes of transport calculated as the integral of the 3rd power of the mean velocity for flood and ebb, respectively. Sample locations shown in the inset. For gorge section (Empty circles), U is the section mean velocity. For the rest, U is cell Mean velocity. The flood transport in the rear compartment (Solid and empty triangles) increases consistently with the growth of the delta. In the other three locations, the transport curve increases first, but has a slight drop close to the end.

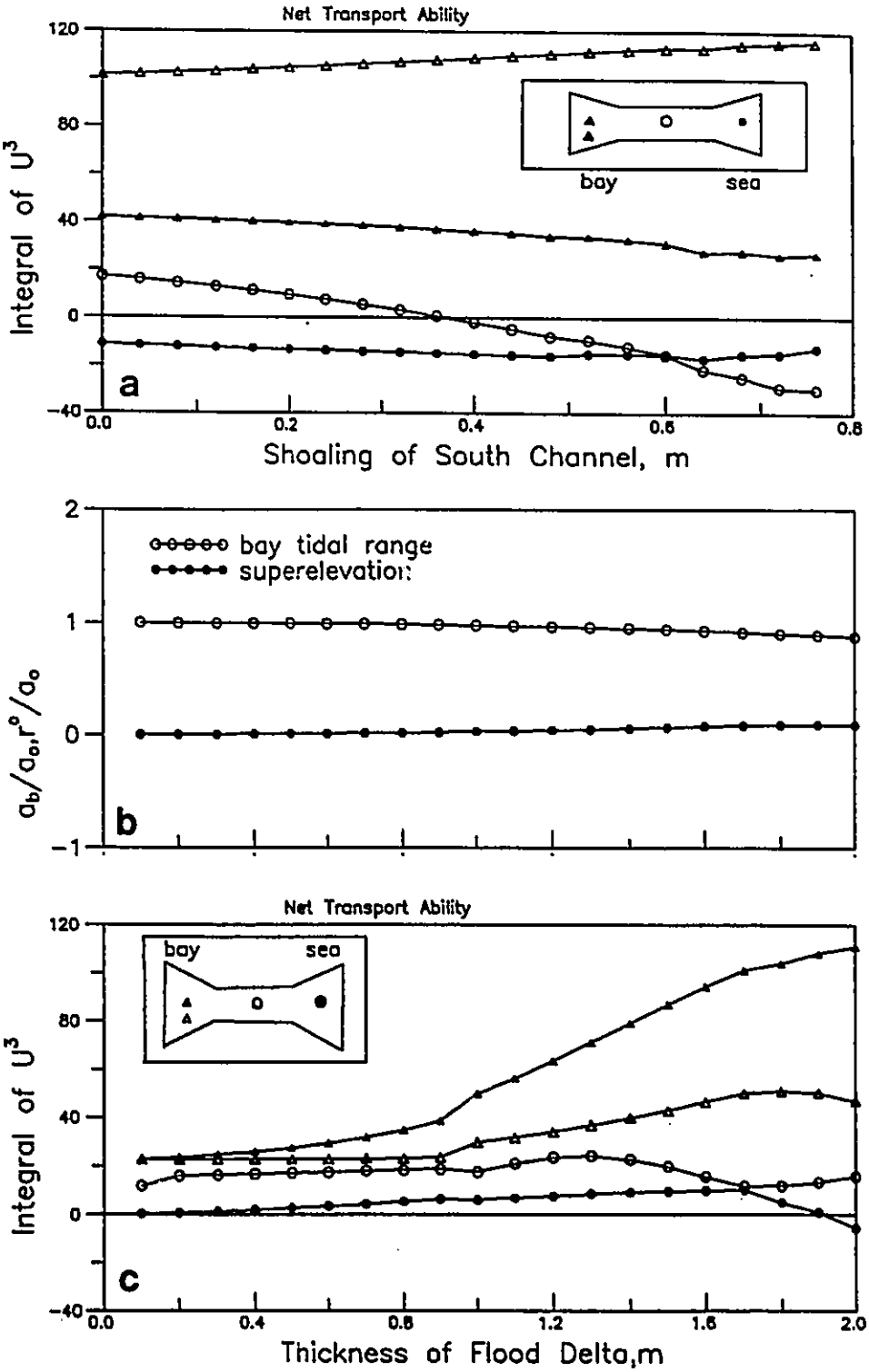
Net Transport Ability
120
80
40
0
−40
Integral of U³
bay
sea
a
0.0
0.2
0.4
0.6
0.8
Shoaling of South Channel, m
2
1
0
−1
bay tidal range
superelevation
$a_b/a_o, r^o/a_o$
b
Net Transport Ability
120
80
40
0
−40
Integral of U³
bay
sea
c
0.0
0.4
0.8
1.2
1.6
2.0
Thickness of Flood Delta,m

The results at the gorge section (hollow circles) are the cross section means. The rest is the cell mean. The results are given in Figure 7 and Figure 8a. The selected time series of tides and velocities in Figure 8a are those when the delta is 0.2 m and 1.8 m in thickness. Figure 7c shows the net sediment transport as a function of the thickness of the flood tidal delta.

Overall, the presence of the flood delta enhances the ability of the flow to transport sediment into the bay, and reduces its ability to transport sediments seaward in both the shoaling and the channel areas. In the rear compartment where the delta is located (solid triangle, Figure 7c), the net sediment transport curve rises steadily to the right. The flood transport ability has been raised four times the initial values by the time the delta is 1.8 m in thickness. In the other three areas, this is still true but occurs at a much reduced level. The trend exhibited by these latter curves also is different: instead of rising steadily, they rise first and then fall in varying degrees close to the end of the lines. It seems that as the flood delta grows higher, the flood bias occurring at earlier stages is reduced or possibly reversed.

To explore this further, a separate run was performed. In this run, the area of the delta is allowed to expand. This is simulated by changing the depth of the area surrounding the flood delta from 2 m to 1 m, while the water

Figure 8 Calculated time series of bay tides and inlet velocities at the throat. Values of peak velocities and durations (in parenthesis) are shown. Also shown are input tides. Values of parameters at which the samples were taken are shown in legends.

a. Effects of the flood tidal delta. With the growth of the flood tidal delta, the flood becomes shorter in duration (11.4 and 10.7 hr) and larger in magnitude (0.8 and 1.36 m/s); the ebb is longer (14.0 and 14.7 hr) but weaker (-0.7 and -1.27 m/s). In addition, as the delta growth from 0.2 m to 1.8 m in thickness, the time at which flood midtide occurs changes from 26.84 to 28.17 hr, the flood peak velocity time from 26.5 to 27.33 hr, the ebb midtide time from 39.5 to 40.5 hr and the ebb peak velocity from 40.84 to 43.67 hr. Therefore, the time asymmetry associated with the flood tidal delta is characterized by a shift of the peak flood velocity away from HW and a shift of the peak ebb velocity toward LW.

b. Effects of the spit platform. At early stages (0.2 m), the growth of the spit platform favours the flood current (0.79 m/s for the flood current versus -0.71 m/s for the ebb current). As the spit platform matures (1.8 m), the ebb current becomes dominant (-1.43 m/s for the ebb versus 1.14 m/s for the flood). At the same time, the time at which flood midtide occurs changes from 26.84 to 27.84 hr, the flood peak velocity time from 26.5 to 27.11 hr, the ebb midtide time from 39.5 to 40.67 hr and the ebb peak velocity from 40.67 to 42.5 hr. There is a shift of both peak velocities away from HW.

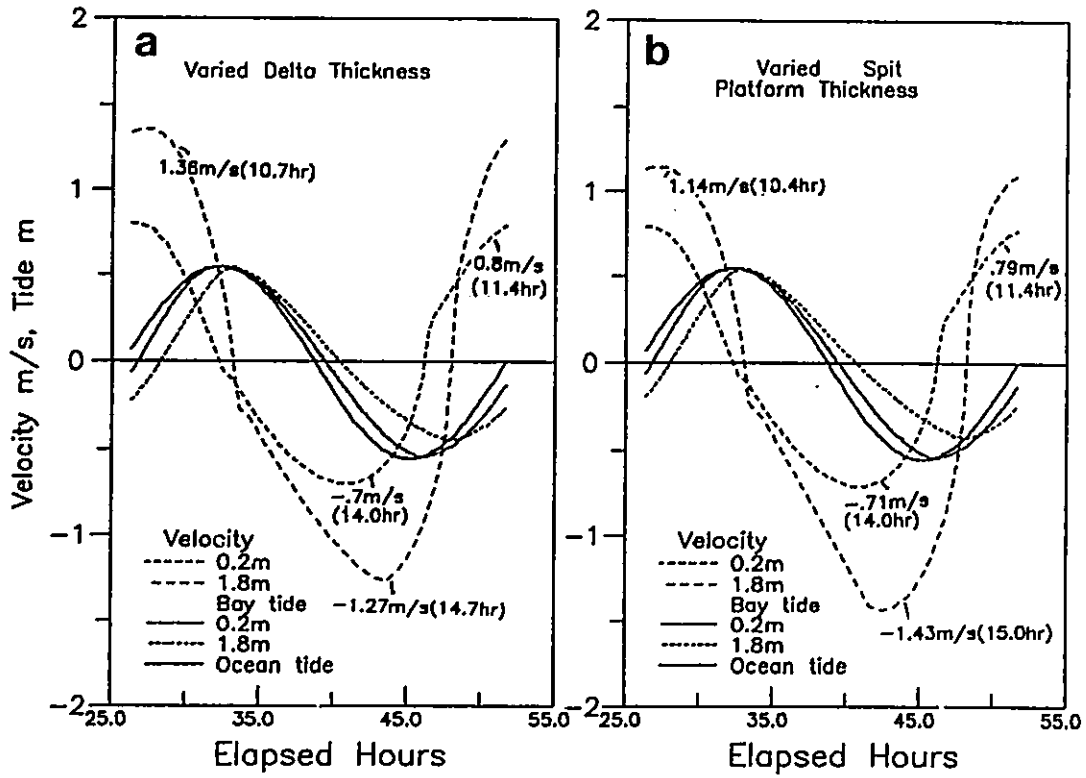
a
Varied Delta Thickness
b
Varied Spit
Platform Thickness
Velocity m/s, Tide m
Elapsed Hours
Elapsed Hours
1.38m/s(10.7hr)
1.14m/s(10.4hr)
.8m/s
(11.4hr)
.79m/s
(11.4hr)
-.7m/s
(14.0hr)
-.71m/s
(14.0hr)
-1.27m/s(14.7hr)
-1.43m/s(15.0hr)
Velocity
0.2m
1.8m
Bay tide
0.2m
1.8m
Ocean tide
2
1
0
-1
-2
25.0
35.0
45.0
55.0

depth in the stippled area was kept at 0.5 m. The results are shown in Figure 7a. It is seen that except in the flood delta area, the trend of the sediment transport curves did change. Instead of rising, all three curves decline slightly. It is interesting to note that the sediment transport curve of the throat section passes below the zero-line, suggesting that the further shoaling of the rear compartment actually improving the flushing ability of the flow in the gorge channel. This is somewhat surprising as intuition would suggest that the ebb transport ability of an inlet will deteriorate as its rear is continuously sand-clogged.

The emplacement of the flood delta offers resistance to the flow. Therefore, there should be a reduction in amplitude and delay in phase of the bay tide. They do reduce, as shown in Figure 7b where a_b/a_o ratios shows a steady decline, and in Figure 8a where the three tidal curves successively decrease in heights and increase in phase lag. However, it is noticed (Figure 8a) that much of the amplitude reduction is due to a sharp truncation at low water. The high water in effect remains unchanged in elevation. Delay at low waters is also more severe than that at high waters.

The parameter of superelevation is a measure of symmetry of communication between the bay and sea, and thus can be used as an indicator of the overall effect of that

factor on the system. In Figure 7b, this curve rises slightly to the right (Figure 7b). This indicates a continuous pile-up of water in the bay, hence the rise of the mean sea level. The rise in the bay mean water level must be related to an overall deterioration of the communication during the ebb. Hence, while the effect of the emplacement of the flood delta could be slightly different in different parts of the inlet, as for the system as a whole, it favours the flood.

This flood-favouring tendency is also reflected by the two gorge velocity curves in Figure 8a. For both curves, the flood current is shorter in duration (11.4 and 10.7 hours) but larger in magnitude (0.8 and 1.36 m/s); the ebb flow is longer (14.0 and 14.7 hours) but weaker (- 0.7 and - 1.27 m/s). An indicator of the degree of velocity asymmetry can be calculated as the percentage difference between the flood and the ebb. The duration difference is normalized using the tidal period, and the velocity difference normalized using the mean value of the flood and ebb velocity. The two figures for duration are 10.1% and 15.5%, and for the peak velocity are 13.3% and 6.8%. In each pair, the first figure is that when the delta thickness equals 0.2 m, and the second that when the thickness equals 1.8 m. It is interesting to note that as the flood tidal delta grow higher, the velocity discrepancy actually becomes smaller (6.8% versus 13.3%). This is compatible with the

result (Figure 7a) that the gorge net transport curve reverses to favour the ebb as the delta expands. The above velocity asymmetry is also reflected in the phase relationship between peak velocities and midtides. At a delta thickness of 0.2 m, the peak flood occurs 0.34 hr. earlier than the flood midtide, and the peak ebb occurs 1.34 hr. later than the ebb midtide. At a delta thickness of 1.8 m, the two values change to 0.84 hr. and 3.17 hr. Therefore, the time asymmetry associated with the growth of flood tidal delta (Figure 8a) is characterized by a shift of the peak flood away from high water, and that of the peak ebb toward low water. The ebb peak, however, moves at a faster speed than the flood peak does. The results are that the ebb become stronger as it tends to be accommodated by a smaller cross section.

3.3.2 Effects of the Spit Platform

The spit platform is also modelled as an intertidal sand body in the entrance compartment as shown by the stippled areas in Figure 3. The effects of changing its size were examined in a similar manner as for the flood delta, i.e., by reducing the water depth over its area. Results were sampled at similar locations, and shown in Figure 9c and Figure 8b. In the latter, the samples selected are those for the spit platform of 0.2 m and 1.8 m in thickness.

Figure 9 Inlet responses to varying spit platform sizes. All units are dimensionless.

a. Effects on net sediment transport ability with varying thickness of both flood delta and spit platform. Note the similarity in trends of the curves in this Figure and those in Figure 9c. This indicates that the spit platform plays a more important role in affecting inlet responses that the flood tidal delta. Sample locations shown in the inset. Except in the gorge channel (empty circles), flows are everywhere in favour of the flood current.

b. Dimensionless bay tidal range and super-elevation. a_o = Ocean tidal range, b_o = bay tidal range and r^o = superelevation. With the growth of the spit platform, the bay tidal range decreases and the superelevation increases.

c. Net sediment transport. For its definition, and other explanations, see Figure 7c. The flood transport in both rear and entrance compartment increases consistently. There is, however, an increase in ebb transport at the throat (Empty circles) as the spit platform grows over 1.0. Note the scale difference between this figure and Figure 7c.

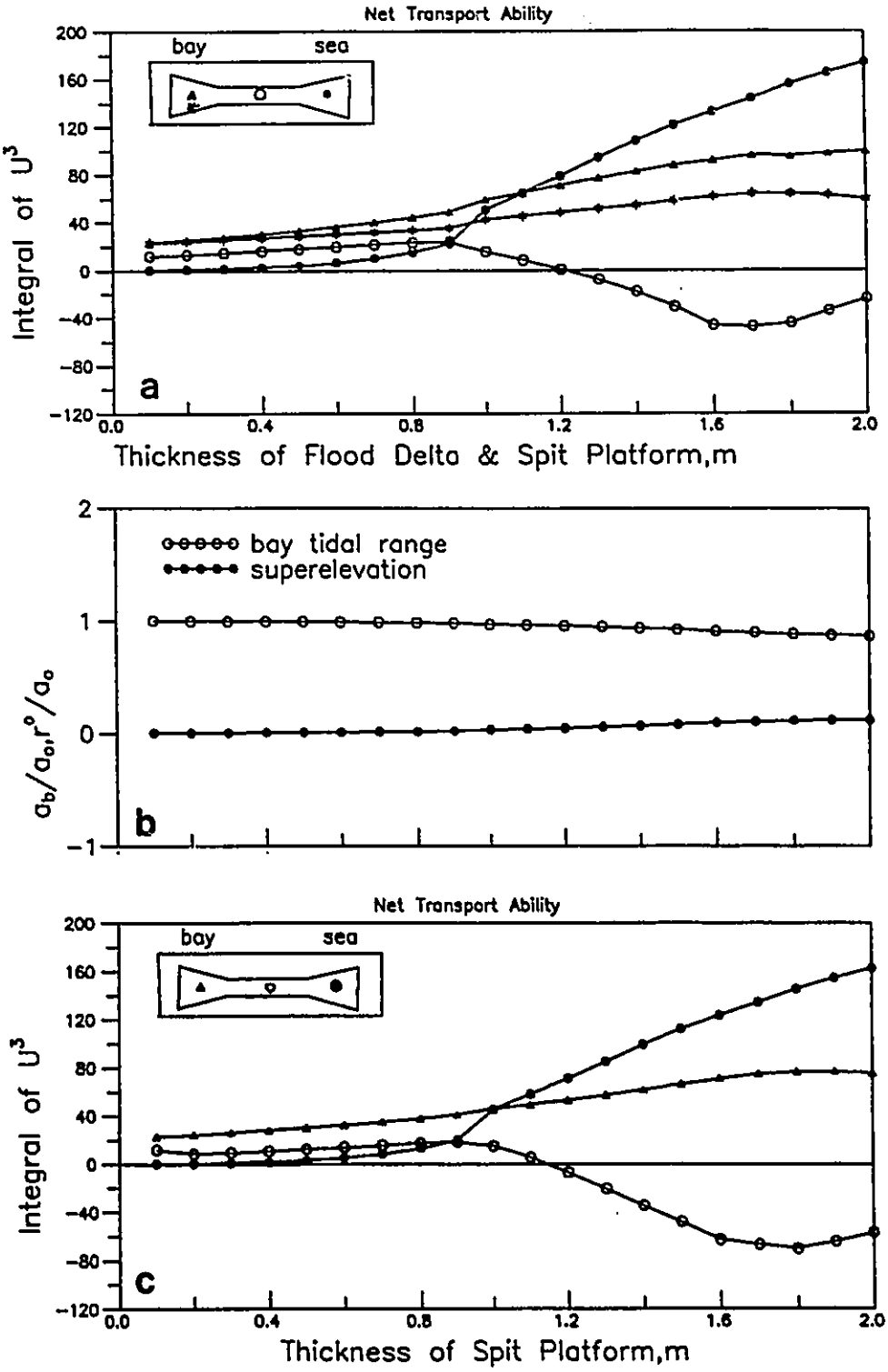
Net Transport Ability
bay
sea
Integral of U³
200
160
120
80
40
0
-40
-80
-120
0.0
0.4
0.8
1.2
1.6
2.0
a
Thickness of Flood Delta & Spit Platform,m
bay tidal range
superelevation
a_b/a_o, r°/a_o
2
1
0
-1
b
Net Transport Ability
bay
sea
Integral of U³
c
Thickness of Spit Platform,m

In general, the effects of the presence of the spit platform on tidal responses are similar to those observed for the flood tidal delta. These include consistent decrease in the amplitude of tides, delay in phase, and increase in mean bay water level, as well as in the tidal asymmetry produced. All these changes, however, appear to be more aggravated in the case of the spit platform, indicating that it has a larger effect than the flood delta. At all four locations sampled (Figure 9c), the values of the net sediment transport are larger than the corresponding ones in Figure 7c. Note the scale difference between the two Figures. This is particularly well demonstrated by the trend of the curve of the gorge section: it rises first and then drops below the zero-line, much like that shown by the extra run in Figure 7a. The same comparisons can be made using the tidal current curves (Figure 8). The ebb current when the spit platform is 1.8 m thick is both strong (-1.43 m/s) and longer (15.0 hours) than the corresponding flood (1.14 m/s and 10.4 hours).

It is expected that the effect of the presence of both the spit platform is additive, but the basic pattern should be preserved. This is shown in the Figure 9a as well as in Figure 17a. In the test, the water depth in both regions of the sand bodies was allowed to change. It is seen from the figures that in the two shoaling areas, the flood transport ability is improved. In the gorge channel,

the curve crosses the zero-line, and becomes ebb-dominated in the latter half. This is because the spit platform has a larger influence than the flood delta. Fig 16a shows that when the two sand bodies are 1.8 m thick, the ebb in the gorge is stronger (- 1.36 m/s) and longer (14.9 hr.) than the flood (1.21 m/s and 10.5 hr.).

3.3.3 Effects of the Bay Wall Slope

Bay wall slope, ß, as suggested by Mota Oliveira (1970) is defined as the difference between bay surface areas at high and low water normalized by the bay tidal range. This definition when incorporated into the relationship

$$A = A_{msl} + \beta\, h_b$$

results in a linear variation of bay surface area with the bay tide. Several authors have investigated the effects of this parameter (Mota-Oliveira, 1970; Huval and Wintergerst, 1977). It is interesting to see what effects it has on the present system. In the computation, ß was allowed to vary from 0 to 1.5 at step of 0.075. The results are presented in Figure 10, and 11b. The samples selected in Figure 11b are those for the slope equal to 0.15 and 1.25.

Result of the present study support observations of the previous studies that the variation in bay surface area

Figure 10 Inlet responses with increasing bay wall slope, ß. Units are dimensionless.

a. Dimensionless bay tidal range and superelevation. a_o = Ocean tidal range, b_o = bay tidal range and r^o = superelevation. Although not visible, the bay tidal range shows slight increase and the superelevation shows slight decrease.

b. Net sediment transport. For its definition, and other explanations, see Figure 7c. The flood transport in both rear and entrance compartment increases consistently. The ebb transport shows steady increase at all locations in the inlet channel.

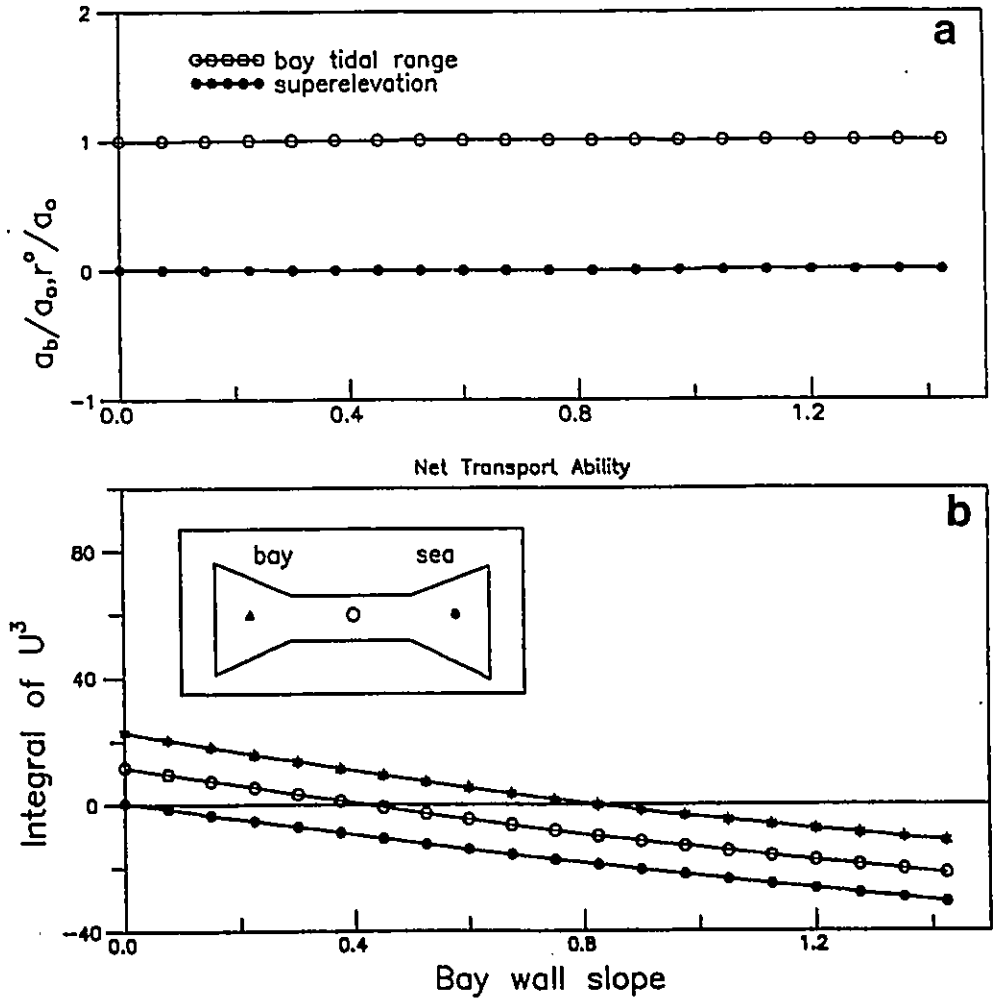
a
bay tidal range
superelevation
$a_b/a_o, r°/a_o$
2
1
0
−1
0.0
0.4
0.8
1.2
Net Transport Ability
b
bay
sea
Integral of U^3
80
40
0
−40
0.0
0.4
0.8
1.2
Bay wall slope

Figure 11 Calculated time series of bay tides and inlet velocities at the throat. Values of peak velocities and durations (in parenthesis) are shown. Also shown are input tides. Values of parameters at which the samples were taken are shown in legends. In the computations, the depth of the inlet channel is kept at 2 m, and Manning's n at 0.03.

a. Varying bay surface area at mean water level. The two time series selected are those when the bay surface area is 1.01 10^7 and 8.51×10^7 m^2. Increase in the bay surface area increases inlet channel flow velocity and decrease the bay tidal range.

b. Varying bay wall slope. The two time series shown are those for slopes of 0.15 and 1.25. Increase in the slope favours the ebb current, but also moves the peak flood and ebb velocity toward HW. Note that the low water at $\beta = 1.25$ leads that at $\beta = 0.15$, while the two high waters nearly overlaps, indicating that with increasing variation in the bay surface area with the time, the flow becomes more efficient at LW than at HW.

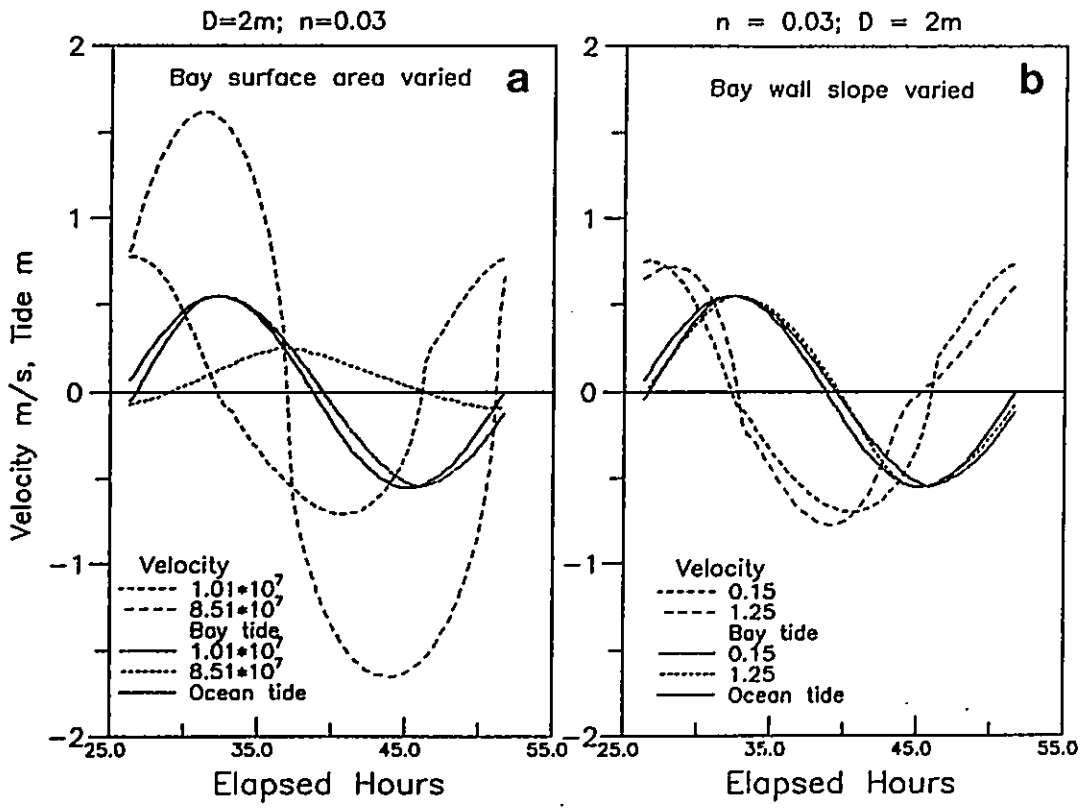
D=2m; n=0.03
Bay surface area varied
a
n = 0.03; D = 2m
Bay wall slope varied
b
Velocity m/s, Tide m
Elapsed Hours
Elapsed Hours
Velocity
1.01*10^7
8.51*10^7
Bay tide
1.01*10^7
8.51*10^7
Ocean tide
Velocity
0.15
1.25
Bay tide
0.15
1.25
Ocean tide
2
1
0
−1
−2
25.0
35.0
45.0
55.0

increases the ebb flow and decreases the flood flow. Figure 10a shows the steady decrease of flood transport ability with increase in ß at all locations. Figure 11b shows that flood currents are longer but weaker and ebb currents are shorter and stronger.

The reason for the above effect has been argued qualitatively by Fitzgerald and Nummedal (1983) from continuity consideration (refer to Equation 3). They stated that in a system with extensive marshlands, which correspond to a large ß value, the draining of the basin is most effective near the end of the ebb interval. This is because during that time, it has the least volume of water to drain. On the other hand, the infilling is least effective near high water, as the volume is the largest to fill at this moment.

The same conclusion can also be reached using an argument based on friction. According to Mehta and Ozsoy (1978) and King (1974), the total resistance of an inlet system to the flow can be expressed by a dimensionless damping coefficient:

$$K_1 = \frac{A}{A_c} \frac{a_o F}{2 L} \qquad \text{— (14)}$$

That is, the total resistance is directly proportional to the A/A_c ratio. For the present purpose,

consider the situation where only the bay surface area, A, varies; that is A_c is a constant. The bay surface area at any instant is the sum of a mean value, A_{msl}, and a time-varying component, A'. Then, the K_1 value is less at low water than at high water, since A' is smaller at low water and larger at high water. The result is the same as the previous conclusion: the flow is more efficient for the ebb.

The variation of bay surface area, however, does not create the low tide truncation, and the stronger low water delay that were observed in the previous two cases. Figure 11b shows that as ß increases, there is almost no change in the tidal range for the two bay tidal curves. The low water point of the second bay tide curve in fact moves slightly leftward toward the ebb midtide so that phase leading occurs. On the other hand, high water remains delayed. This corroborates the above argument that the discharge of the inlet is more efficient at low water than at high water. It is also interesting to note that the time asymmetry associated with time varying bay surface area is characterized by shift of both flood and ebb peak velocities toward high water (Figure 11b).

In line with the ebb-favoured trend, there is a set-down of mean water level, and an increase of tidal range of bay tides. While not graphically visible in Figure 10b, the numerical figures indicate that the a_b/a_o ratio increases from 1.099 to 1.105, and the r^o/a_o ratio decreases from

0.0057 to 0.0035. Overall, changes in the bay area thus improve the communications between the bay and the sea during the ebb phase.

3.3.4 Effects of Bay Surface Area and Inlet Cross Section Area at Mean Water Level

The effects of the bay surface area at mean water level, A_{msl}, and the inlet gorge cross section area at mean sea level, A_{co}, were investigated separately by allowing their values to vary from 5,000,000 m^2 to 100,000,000 m^2, and from 2 m^2 to 2665 m^2, respectively. The results are discussed together here. This is because these two parameters are closely (reciprocally) related in their effects on inlet hydraulics (refer to Equation 4). An increase in A_{msl} will have the same effect as a decrease in A_{co}. Results are shown in Figure 12 and Figure 11a. In the computations, the bay wall slope and the inlet bank slope were kept constant. That is, there is no variation of the bay surface area and inlet cross section with time.

Figure 12b shows that with increases in the mean bay surface area, the tidal range decreases, and the mean sea level increases in the bay. This is expected, since a larger A_{msl} area means a thinner layer of water in the bay if the total amount of water infilling the bay is the same. That is, a small bay tidal range. A more distributed water volume, however, is less effective than a more concentrated

Figure 12 Inlet responses to increasing mean bay surface area, A_{msl}. Units are dimensionless.

a. Dimensionless bay tidal range and superelevation. a_o = Ocean tidal range, b_o = bay tidal range and r^o = superelevation. The figure shows that the bay tidal range decreases, and the superelevation increases.

b. Net sediment transport. For its definition, and other explanations, see Figure 7c. With the increase in bay surface area, the net sediment transport rises (flood-favoured) first to a peak, then reverses to favour the ebb. At the peak, the flushing ability of the inlet is a minimum.

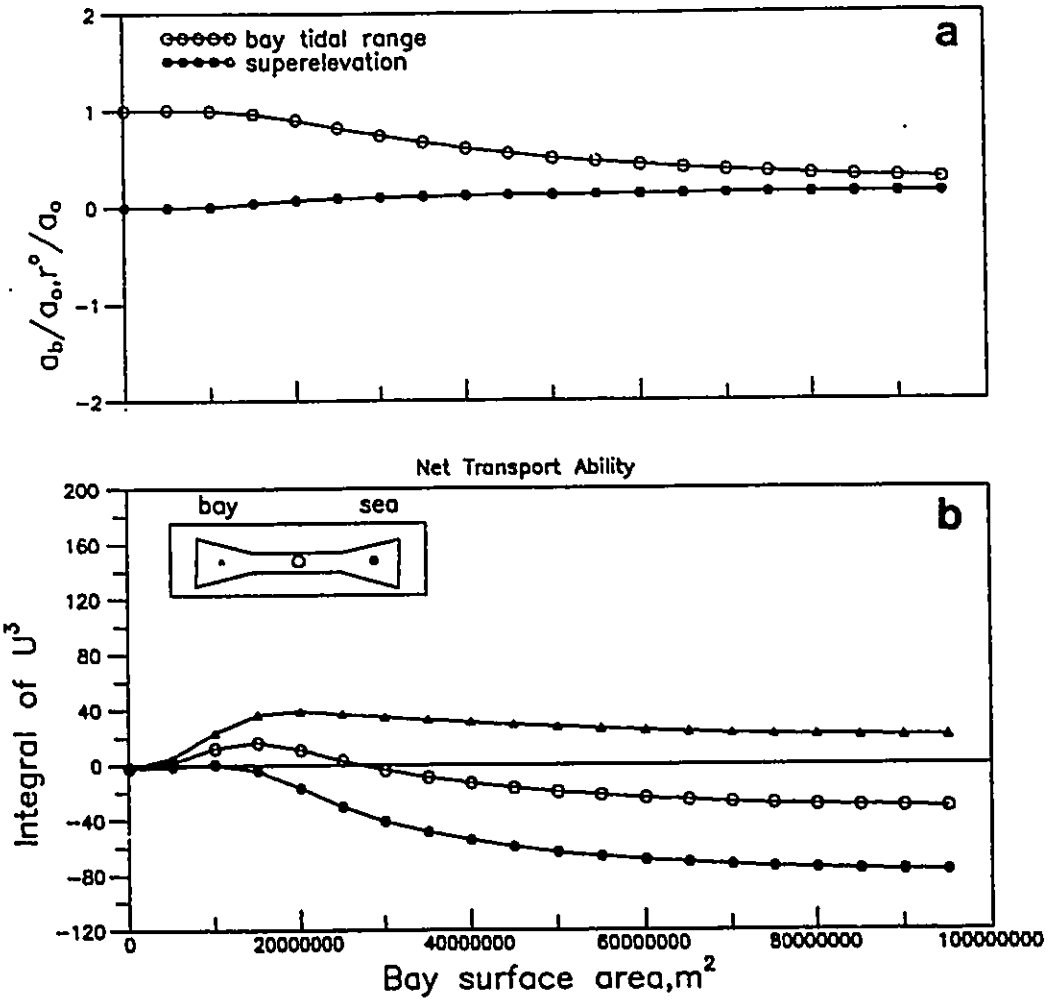
a
bay tidal range
superelevation
$a_b/a_o, r^o/a_o$
2
1
0
−1
−2
Net Transport Ability
b
bay
sea
Integral of U^3
200
160
120
80
40
0
−40
−80
−120
0
20000000
40000000
60000000
80000000
100000000
Bay surface area, m^2

one is in terms of the draining of the bay. A portion of the water will be left in the bay, which causes the positive superelevation of the bay water. Effects of increase in inlet cross-section area, A_{co}, are opposite. As shown in Figure 11a, the gorge mean velocity increases. This will increases the bay tidal range. With both factors effective, the change in A_{msl} obviously dominates.

As A_{co} and A_{msl} are reciprocally related, either of them may be used to illustrate the effect on the sediment transport. A_{co} is used in the following discussion as shown in Figure 13b. The sediment transport curve selected is that of the gorge section. A logarithmic scale is used to show the details at the lower end. The figure shows that the net sediment transport ability is not a monotonous function of the cross section area. As the cross section changes from extremely small to extremely large, the transport curve rises, then falls and then rise again. The trough between the peaks is where the ebb is most dominant. The pattern thus indicates the existence of an optimal configuration at which an inlet is most efficient in flushing sand out of the system. The two points, A and B, at which the transport curve intersects the zero line, are of significance. The crossing also occurs at the very beginning and the very end. These latter two points, however, are different, although they are also points of zero transport. They merely reflect the conditions that

Figure 13

a. Inlet stability plot using model-generated maximum inlet current velocities versus inlet cross-section areas. $A_{msl} = 10^7$ m^2. Manning'n = 0.03. In this case, the maximum velocity reaches the maximum at $A_{msl} = 100$ m^2.

b. Net sediment transport at the gorge as a function of inlet cross-section areas. The net sediment transport is calculated as the integral of U^3. See Figure 7c for its definition. Note that the region above the zero line is flood dominated, and the region below is ebb dominated. The lowest point of the curve, at which the inlet has the best flushing ability, defines two areas: a stable area to the right (negative feedback), and an unstable area to the left (positive feedback). In the stable area, the inlet has the ability to restore itself to the equilibrium point B against changes in cross section area caused by, e.g., storm actions. In the unstable area, however, such changes tend to be reinforced so that the inlet moves away from the equilibrium point A.

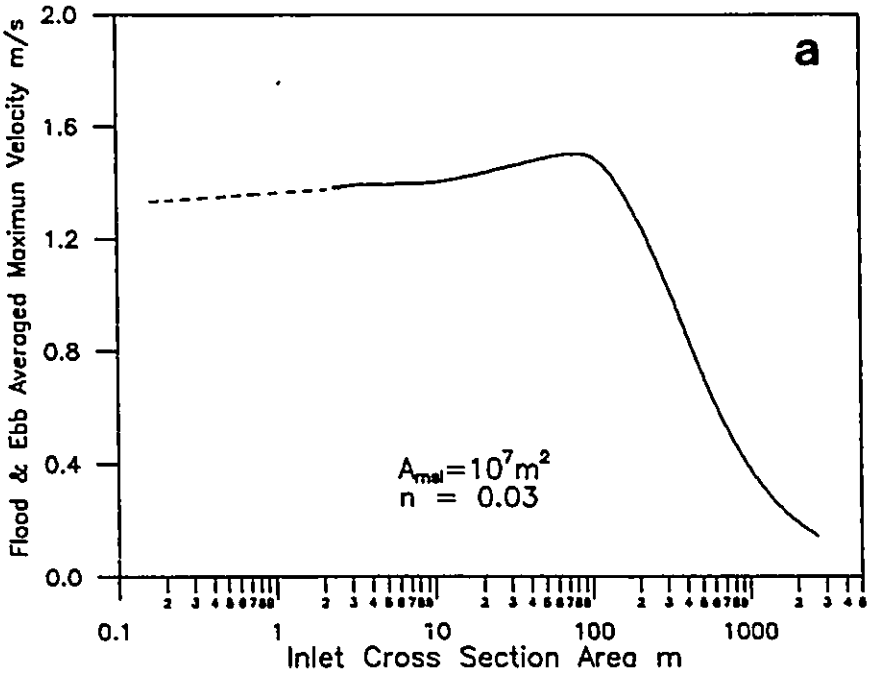
a
Flood & Ebb Averaged Maximum Velocity m/s
2.0
1.6
1.2
0.8
0.4
0.0
$A_{msl}=10^7 m^2$
n = 0.03
0.1
1
10
100
1000
Inlet Cross Section Area m

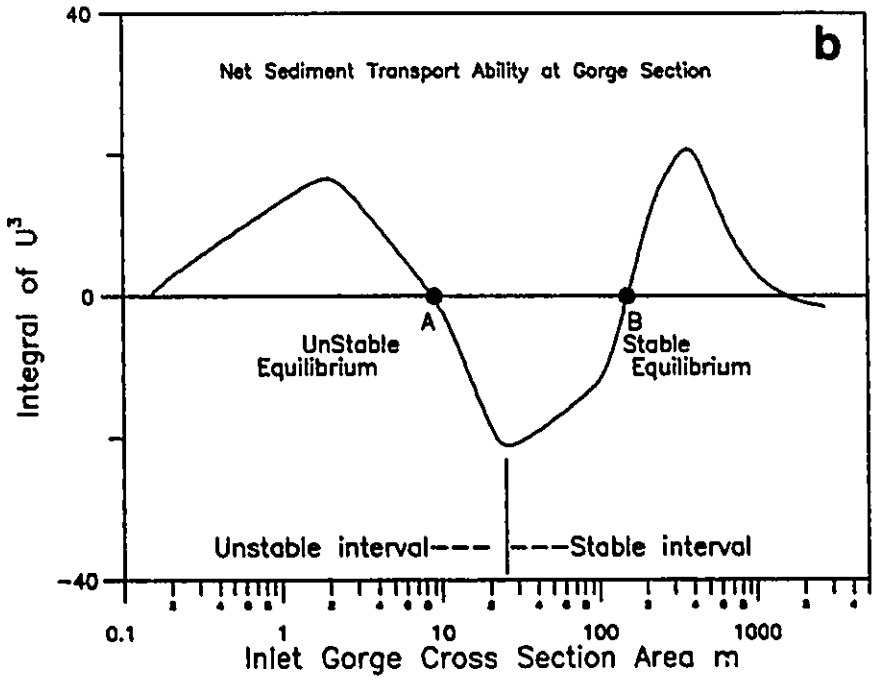
b
Net Sediment Transport Ability at Gorge Section
Integral of U^3
40
0
-40
A
B
UnStable
Equilibrium
Stable
Equilibrium
Unstable interval---
---Stable interval
0.1
1
10
100
1000
Inlet Gorge Cross Section Area m

the velocity approaches zero as A_{co} approaches 0 or approaches infinity. Points A and B, however, indicate a dynamic balance between deposition and erosion. That is, they are non-scouring and non-shoaling points, or equilibrium points. The nature of these two points is, however, different in terms of the relationship between the flushing ability of the flow and the change of A_{co}. Around point A, the flushing ability increases with the increase in A_{co}. Around B, the reverse is true. Such relationships determine the inlet responses to silting or scouring of the channel related to sediment transport. This will be explored in the Synthesis section of this chapter.

Because of the reciprocal relationship, two systems with different A_{msl} and A_{co} values could behave similarly as long as the ratio between the two parameters is the same. To illustrate this point, a 3-D graph is constructed in Figure 14. It uses the A_{co} and A_{msl} as the horizontal axes, and the net sediment transport as the vertical axis. A ridge is shown in the graph. The apex of the ridge represents the flood dominated region, and it follows a linear trend. To reveal the ratio between A_{msl} and A_{co} at which the flushing ability is the worst, a linear regression was made of this trend with A_{co} as the dependable variable. The result showed a high correlation between A_{msl} and A_{co} (Figure 15a) with R2 = 0.99. The slope of the regression equation is 0.00003, and intercept 36. At A_{co} = 0, A_{msl} must

Figure 14 Block diagram, showing relationship between the net transport at the gorge (vertical axis) and bay surface area, A_{msl}, and the inlet cross section area, A_{co}, at mean water level. The two diagrams are the same one viewed from different angles. The peaks of curves, at which the flood transport ability is the maximum, form a linear trend. The values of the bay surface area and inlet cross section area at these peaks were used in the regression in Figure 15a.

E
-30
-10
10
Ab ot MSL, x20000m
783
1463
2143
2823
1000
650
Ac. N
300
650
1000
2823
2143
1463
783
Ab ot MSL, x20000m
W

Figure 15

a. Regression analysis of the mean bay surface area, A_{msl}, on the inlet cross section area, A_{co}. The solid line was forced to pass through the origin to satisfy the fact that the inlet current velocity is zero at $A_c = 0$.

b. Escofier's conceptual model for relationship between the inlet maximum velocity and cross section area. O'Brien's equilibrium curve is superimposed, along which the inlet is in the equilibrium state. For a given inlet conditions, the maximum velocity reaches a peak value at a critical inlet cross section area, A_{cri}. A_{cri} defines a stable (negative feedback) and an unstable (positive feedback) region. In the stable region, changes in the cross section area set up forces that tend to restore the change. In the unstable region, changes in the cross section area set up forces that tend to reinforce the change. Four examples are given to illustrate the above idea, in which (+) means increase; (-) means decrease. Note the general similarity between this graph and Figure 13b.

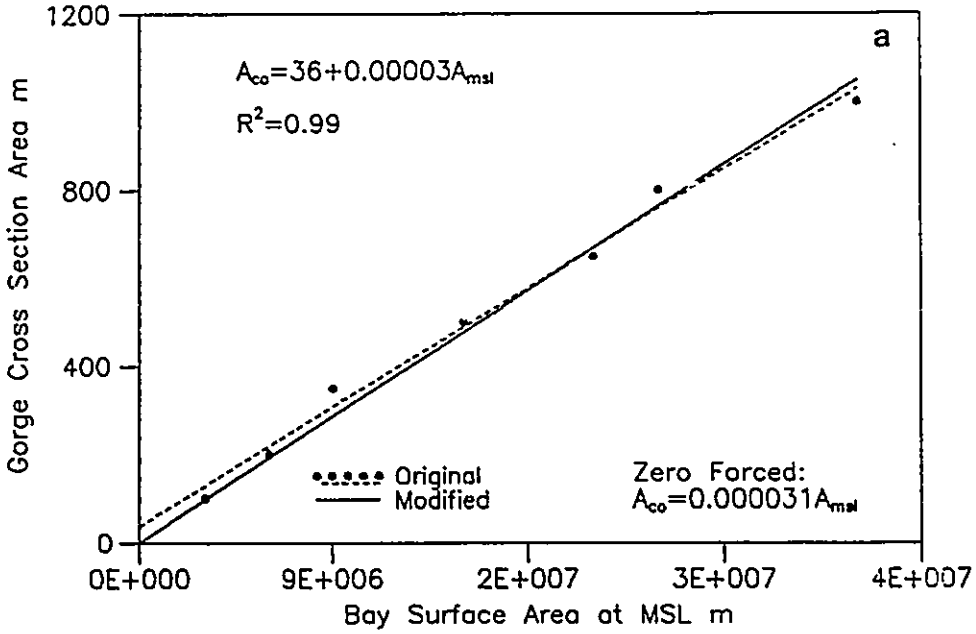
a
$A_{co}=36+0.00003A_{msl}$
$R^2=0.99$
Original
Modified
Zero Forced:
$A_{co}=0.000031A_{msl}$
Gorge Cross Section Area m
1200
800
400
0
0E+000
9E+006
2E+007
3E+007
4E+007
Bay Surface Area at MSL m

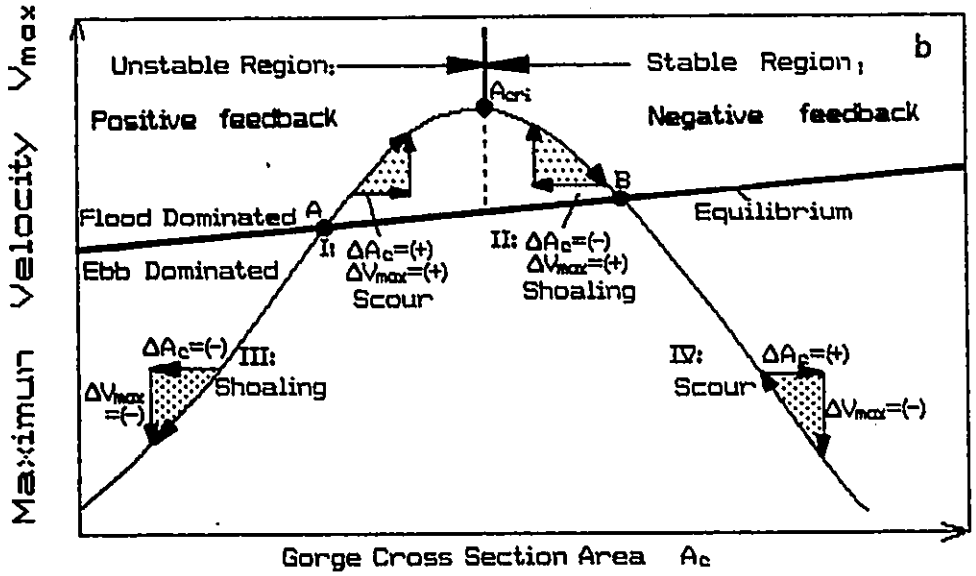
b
Unstable Region:
Positive feedback
Stable Region:
Negative feedback
A_{cri}
Flood Dominated
Ebb Dominated
A
B
Equilibrium
I: $\Delta A_c=(+)$ $\Delta V_{max}=(+)$ Scour
II: $\Delta A_c=(-)$ $\Delta V_{max}=(+)$ Shoaling
III: $\Delta A_c=(-)$ $\Delta V_{max}=(-)$ Shoaling
IV: $\Delta A_c=(+)$ Scour $\Delta V_{max}=(-)$
Maximum Velocity V_{max}
Gorge Cross Section Area A_c

be zero. The regression line is then forced to pass through the origin. The modified slope that gives the minimum residue error is 0.000031. This means that an inlet-bay system is most likely to be closed, when its cross section area is 0.000031 times the bay surface area. It is expected that other hydraulic characteristics are similarly correlatable to the A_{co}/A_{msl} ratio.

3.3.5 Effects of Friction

Friction values were allowed to change from 0 to 0.048. The results are shown in Figure 16 and 17b. Effects of friction on tides propagating in shallow water are well known. Similar effects are observed in the present study. That is, the friction retards the trough more than the crest of the incoming tide. The resultant tide has a steep rising limb, and a gentle falling limb. The tidal currents have a larger forward (flood) velocity of shorter duration, and a smaller backward (ebb) velocity of longer duration. The net sediment transport is thus flood-dominated (Figure 16a). Also, there will be more water moving in than being carried out. Therefore, the mean water level of the bay increases. The dissipation of energy due to friction causes a reduction in the bay tide.

Friction also causes a larger amplitude reduction and phase delay for low water as compared with high water. Within the range tested, however, the reductions are not as

Figure 16 Inlet responses to increasing Manning's n. Units are dimensionless.

a. Dimensionless bay tidal range and superelevation. a_o = Ocean tidal range; b_o = bay tidal range; r^8 = superelevation. The bay tidal range decreases and the superelevation increases.

b. Net sediment transport. For its definition, and other explanations, see Figure 7c. Increase in friction favours the transport ability of the flood current at all locations.

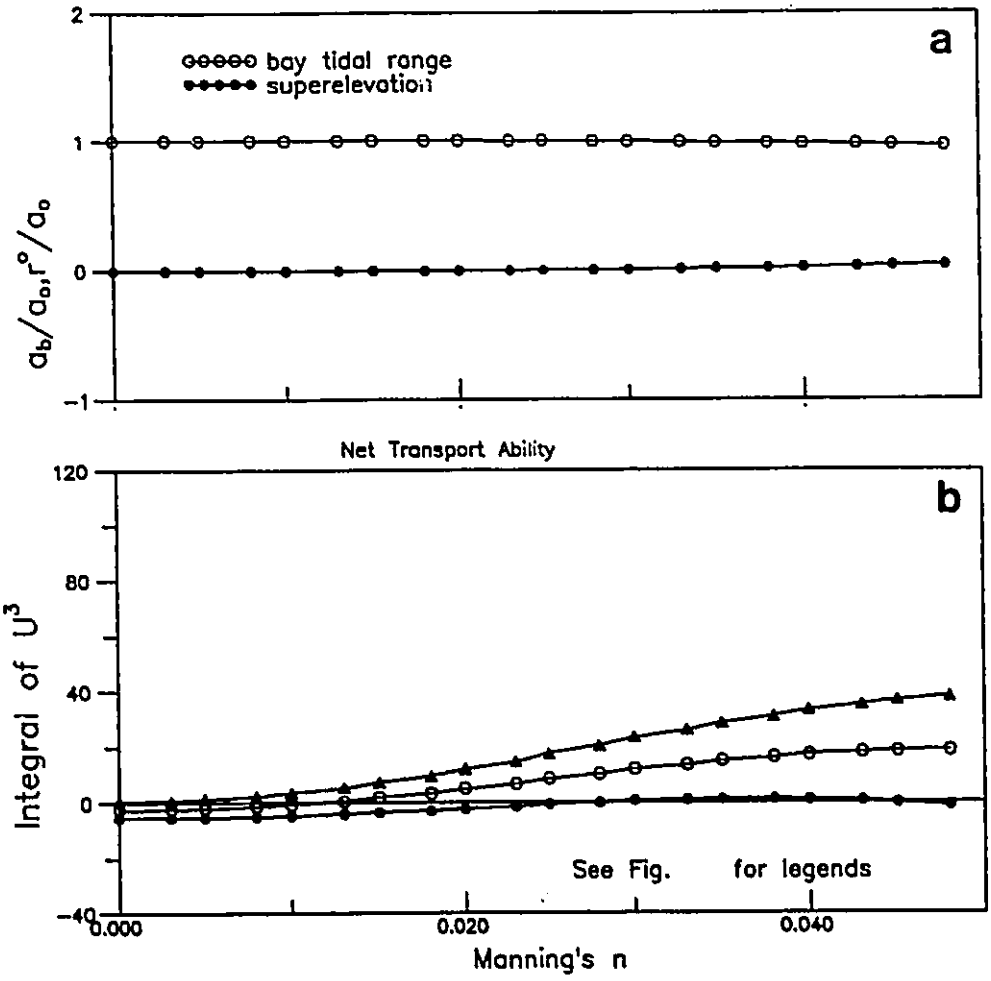
a
bay tidal range
superelevation
$a_b/a_o, r^o/a_o$
2
1
0
−1
Net Transport Ability
b
Integral of U^3
120
80
40
0
−40
See Fig. for legends
0.000
0.020
0.040
Manning's n

strong as those caused by the large sand bodies (Figure 8). It is also seen that the above observations about the effects of friction effects are similar in different parts of the inlet, and thus friction did not cause the 'rise-then-fall' variations seen in Figure 8. This is indicated by all three curves in Figure 17a rising to the right consistently.

The sense of time asymmetry associated with friction is rather different from that associated with the flood delta and the spit platform. In this case, both the flood and the ebb peak velocities shift toward high water. As shown by the figures in the caption of Figure 17b, as friction increases from 0.0025 to 0.045, the peak flood shifts closer to high water by 0.67 hr., and the peak ebb moves closer by 0.17 hr. The peak flood moves at a faster speed. This is because of higher impedance at low water than at high water. Note that despite the relative movement, the velocity peaks are still on the 'far side' of the midtides. That is, in absolute terms they are still away from the high water.

3.3.6 Effects of a Second Tidal Inlet

Palmer Inlet is one of the two openings that connect the Cascumpec bay to the sea. To examine the effect of the presence of a second inlet on the existing one, a new opening was introduced into the base system of the model.

Figure 17 Calculated time series of bay tides and inlet velocities at the throat. Values of peak velocities and durations (in parenthesis) are shown. Also shown are input tides. Values of parameters at which the samples were taken are shown in legends.

a. Thickness of the flood delta and spit platform = 0.2 m and 1.8 m. In the computations, the bay surface area (10^7 m^2) and Manning's n (0.03) are kept constant. As the sand bodies grow to 1.8 m, the ebb current becomes both stronger (1.36 m/s) and longer (14.9 hr) than the flood (1.21 m/s and 10.5 hr). Also, the time at which the flood midtide occurs changes from 26.84 to 28.50 hr, the flood peak velocity time from 26.67 to 27.84 hr, the ebb midtide time from 39.5 to 41.33 hr and the ebb peak velocity from 40.84 to 42.33 hr. The time asymmetry is characterized by both the flood and ebb peak velocities moving away from HW.

b. Manning's n = 0.0025 and 0.045. In the computations, the depth of the inlet channel (2 m) and bay surface area (10^7 m^2) are kept constant. Increase in Manning's n favours the flood current. In both cases, the flood is stronger (0.74 m/s and 0.78 m/s) than the ebb (0.64 m/s and 0.76 m/s). As the friction increases from 0.0025 to 0.045, the time at which flood midtide occurs changes from 26.84 to 27.17 hr, the flood peak velocity time from 26.0 to 27.34 hr, the ebb midtide time from 38.84 to 39.84 hr and the ebb peak velocity from 40.17 to 41.0 hr. The time asymmetry is characterized by the flood and ebb peak velocity moving toward HW.

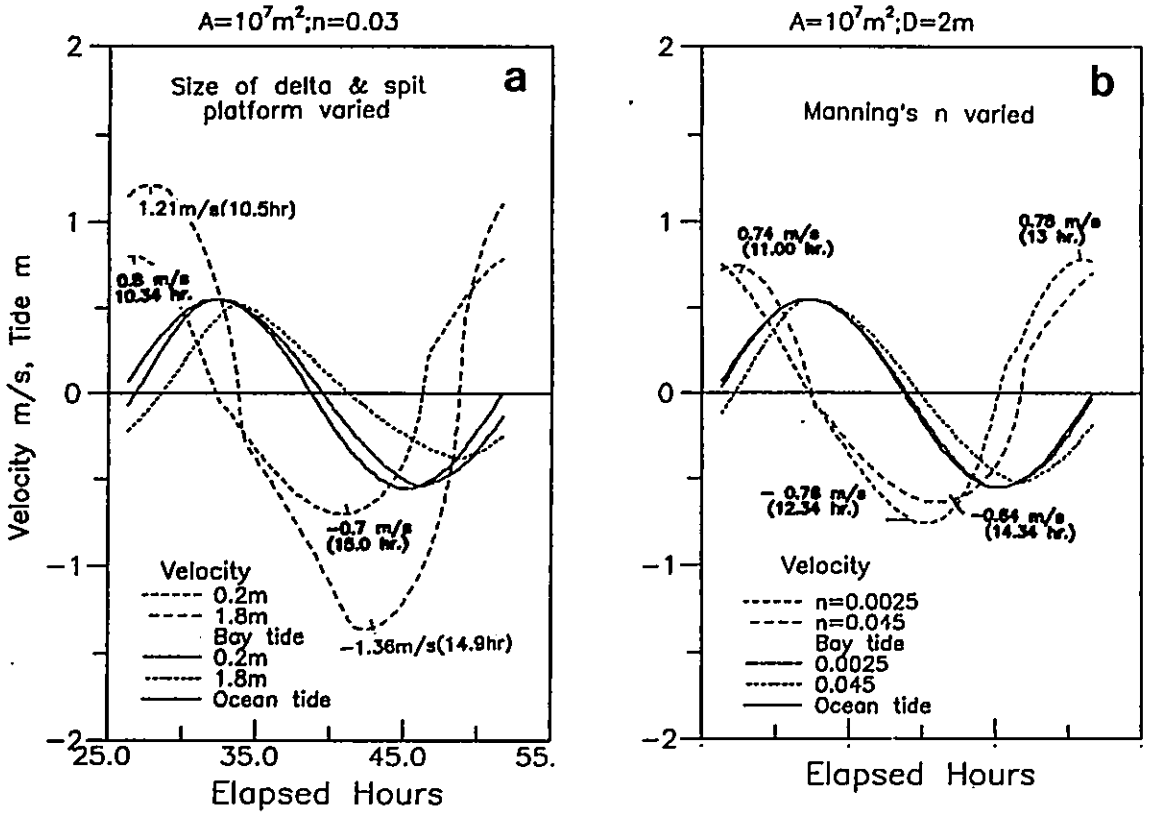
A=10^7m^2;n=0.03
Size of delta & spit platform varied
a
1.21m/s(10.5hr)
0.8 m/s 10.34 hr.
-0.7 m/s (18.0 hr.)
-1.36m/s(14.9hr)
Velocity
0.2m
1.8m
Bay tide
0.2m
1.8m
Ocean tide
Velocity m/s, Tide m
Elapsed Hours
A=10^7m^2;D=2m
Manning's n varied
b
0.74 m/s (11.00 hr.)
0.78 m/s (13 hr.)
-0.78 m/s (12.34 hr.)
-0.64 m/s (14.34 hr.)
Velocity
n=0.0025
n=0.045
Bay tide
0.0025
0.045
Ocean tide
Elapsed Hours

To simplify the procedure, a simple grid system was used for this opening. The grid system consists of only one prismatic channel and two sections with length of 800 m and depth of 3.4 m. These dimensions are modelled after the companion inlet of Palmer Inlet, Alberton Inlet. The same scheme of Manning's n used for the existing inlet was adopted for this new system. Effects of two aspects of the second inlet were examined. One is changes in size, and the other is change in distance away from the first inlet.

Varying Size The effect of changes in size of the new inlet was modelled by varying its width from 50 m to 715 m. This corresponds to areal changes from 170 m^2 to 2430 m^2. Results are presented in Figure 18 and Figure 19b. The two curves in Figure 19b are those whose width is 120 m and 645 m.

The effects of introducing a second inlet are twofold. First, it takes away part of the tidal prism originally available to the existing inlet. The larger its size, the bigger this effect. The result is an apparent decrease in current velocities of the existing inlet with the increase of its size (Figure 18c; Figure 19b). Secondly, the addition of the second inlet to the system increases the total cross section area. The result is better communications between the bay and the sea, and therefore, a decrease in superelevation, an increase in amplitude, and reduction in phase lag of the tide in the

Figure 18 Inlet responses to increasing width of a second inlet. Units are dimensionless. In the computations, the bay surface ($2.2\ 10^7\ m^2$), Manning's n (0.03) and the depth of Inlet I (2 m) are kept constant.

a. Flood and ebb maximum velocities of Inlet I and II. Note that current velocities at both inlets decrease with the increase in the width of the second inlet.

b. Dimensionless bay tidal range and superelevation. a_o = Ocean tidal range; b_o = bay tidal range; r^8 = superelevation. With the increase in the width of the second inlet, the bay tidal range increases and the superelevation decreases.

c. Net sediment transport. For its definition, and other explanations, see Figure 7c. Note that increase in the width of the second inlet increases the transport ability of the ebb current at all locations.

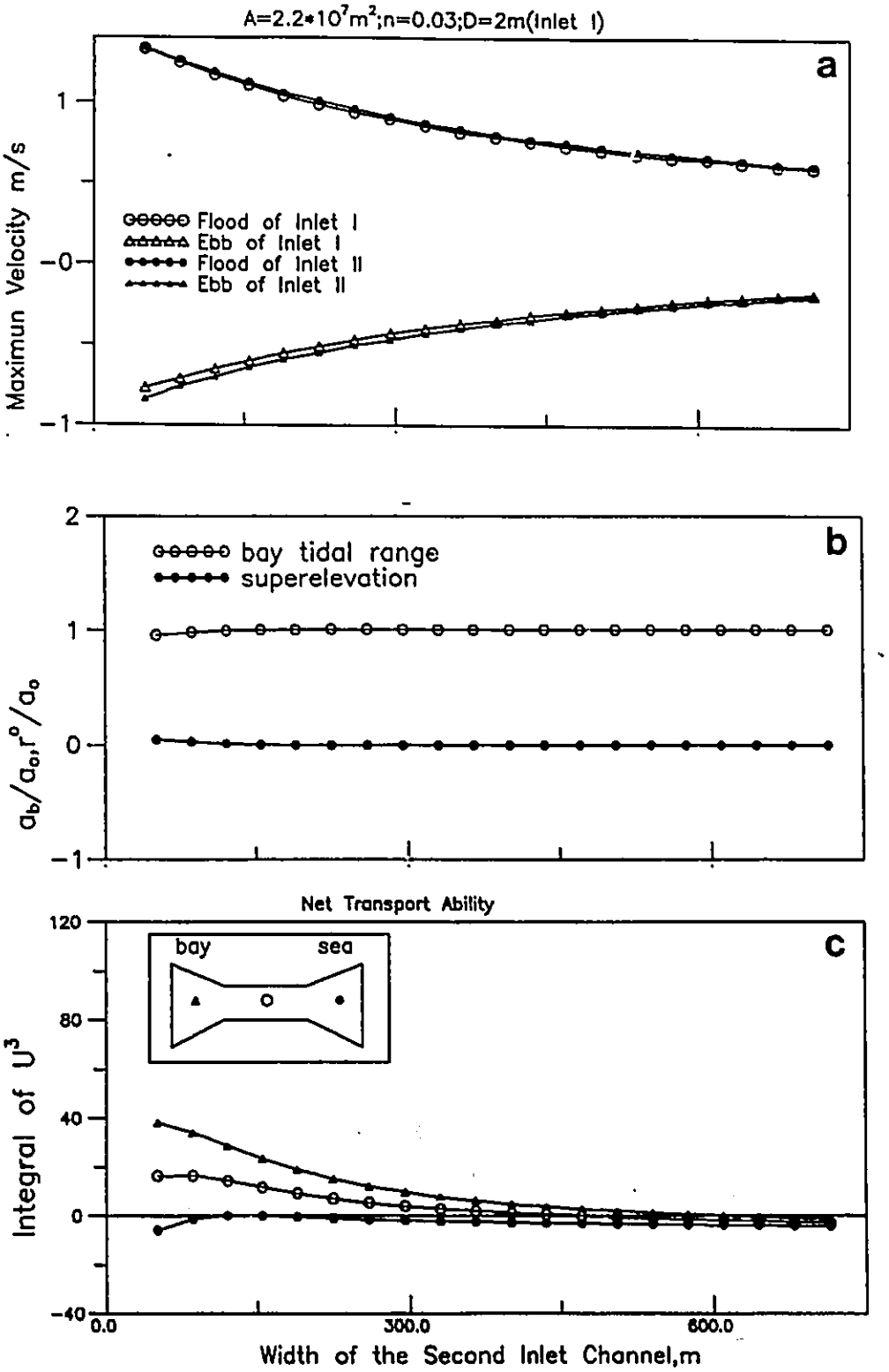
A=2.2*10^7m^2;n=0.03;D=2m(Inlet I)
a
Maximun Velocity m/s
1
0
-1
Flood of Inlet I
Ebb of Inlet I
Flood of Inlet II
Ebb of Inlet II
b
2
1
0
-1
bay tidal range
superelevation
a_b/a_o,r°/a_o
Net Transport Ability
c
120
80
40
0
-40
bay
sea
Integral of U^3
0.0
300.0
600.0
Width of the Second Inlet Channel,m

Figure 19 Calculated time series of bay tides and inlet velocities at two selected parametric values. Also shown is the input ocean tide. In the computations, the bay surface ($2.2\ 10^7\ m^2$), Manning's n (0.03) and the depth of Inlet I (2 m) are kept constant.

a. Varying phase lags of tides of Inlet II with respect to tides of Inlet I. The selected two time series are those when the phase lag is 6 min and 51 min. Note that both flood and ebb velocities increase with the increase in phase lag, while the bay tidal range remains unchanged.

b. Varying width of the second inlet. The selected two time series are those of Inlet I when the width of Inlet II is 120 m and 645 m. Note that there is a large decrease in inlet velocity with the increase in the width, while the bay tide remains basically unchanged in magnitude.

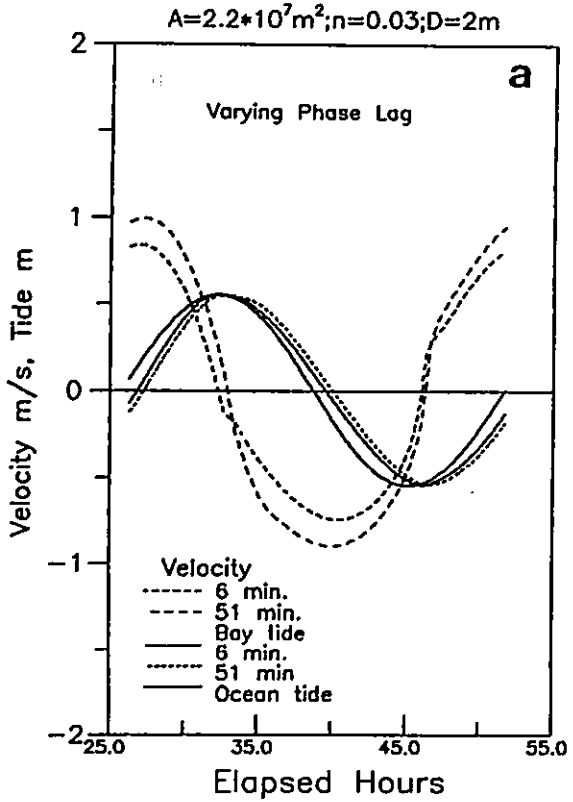
A=2.2*10⁷m²;n=0.03;D=2m
a
Varying Phase Lag
Velocity m/s, Tide m
2
1
0
−1
−2
25.0
35.0
45.0
55.0
Elapsed Hours
Velocity
6 min.
51 min.
Bay tide
6 min.
51 min
Ocean tide

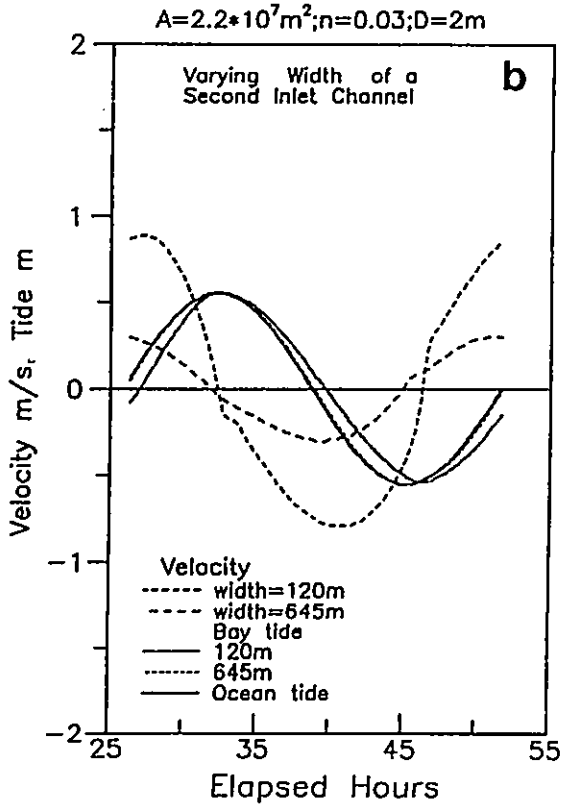
A=2.2*10⁷m²;n=0.03;D=2m
b
Varying Width of a
Second Inlet Channel
Velocity m/s, Tide m
2
1
0
−1
−2
25
35
45
55
Elapsed Hours
Velocity
width=120m
width=645m
Bay tide
120m
645m
Ocean tide

bay. As indicated in Figure 19b, at width of 645 m, the bay tidal curve almost overlaps the ocean tide.

Figure 18a shows that with the increase in the width of the second inlet, the ebb transport ability of inlet currents is improved at all locations. This effect is somewhat unexpected, because with part of the incoming water captured by the second inlet, the ebb should show a decrease in the first inlet. While this might be true, another factor that is also in effect is the decrease in the current strength, as was mentioned above. The reduction in speed reduces the frictional effect through the square law relationship between speed and friction. Because the base condition is friction dominated, this latter factor tends to have a larger effect on the system. The increase in the ebb flow shown in Figure 18a is therefore an indirect result of reduced speeds in the first inlet.

Varying Distance For tides travelling along the coast, the time that tides arrive at the two sites is different. The distance effect can thus be simulated by assigning a phase lag to the forcing tide between the two inlets. It was assumed in the model that the tide came from the direction of the first inlet towards the second inlet. The phase lag was applied to the second inlet. The range of the phase lag used is from 0.0 to 0.228 in radian. For tides with a period of 25.8 hours, this is equivalent to 0 to 56 minutes, respectively. The rate of propagation of tidal wave in

shallow water can be approximated by $\sqrt{(g\ D)}$. Assuming a water depth of 5 m, the above figure of phase lags can be transformed into a horizonal distance of up to 23 km. In the test, the cross section area of the second inlet used was the same as that the existing inlet, that is 500 m^2. The results are presented in Figure 20 and Figure 19a. The selected samples in Figure 19a are those when the lag equals 6 min. and 15 min.

The change in the distance between the two inlets affects the inlet channel flows of both inlets. Figure 20a shows that as the distance increases, the current speed of the first inlet increases, and that of the companion inlet decreases. This can be easily explained as the second inlet being moved constantly farther away from the 'tidal source', and the inlet upstream gets a larger share of the water. Because of the reason, it can be concluded that as the inlets move apart, it is the current at the inlet downstream of the tide that is reduced in speed.

The sediment transport ability of the ebb, however, shows a slight improvement at both inlets (Figure 20c). This is also indicated by the reduction in the duration of the ebb current as shown in Figure 19a. Regardless of the tidal direction, moving an inlet away from its companion thus tends to improve the way they coexist. This has important geological implications, and will be discussed in the synthesis section.

Figure 20 Inlet responses to varying phase lag of tides at Inlet II with respect to tides at Inlet I. Unit are dimensionless. In the computations, the bay surface ($2.2\ 10^7\ m^2$), Manning's n (0.03) and the depth of Inlet I (2 m) are kept constant.

a. Flood and ebb maximum velocities of Inlet I and II. Note that as the phase lag increases, the current velocity of the first inlet increases and that of the second inlet decreases.

b. Dimensionless bay tidal range and super-elevation. a_o = Ocean tidal range; b_o = bay tidal range; r^o = superelevation. With the increase in phase lag, the bay tidal range and superelevation remain completely unchanged.

c. Net sediment transport at Inlet I. For its definition, and other explanations, see Figure 7c. The transport ability at the gorge of Inlet II is also indicated (Asterisk). Note that increase in the phase lag favours the transport ability of the ebb current at all locations in the existing Inlet I. At the same, the ebb transport ability of Inlet II also improves despite the decrease in current velocity (see Figure 20a).

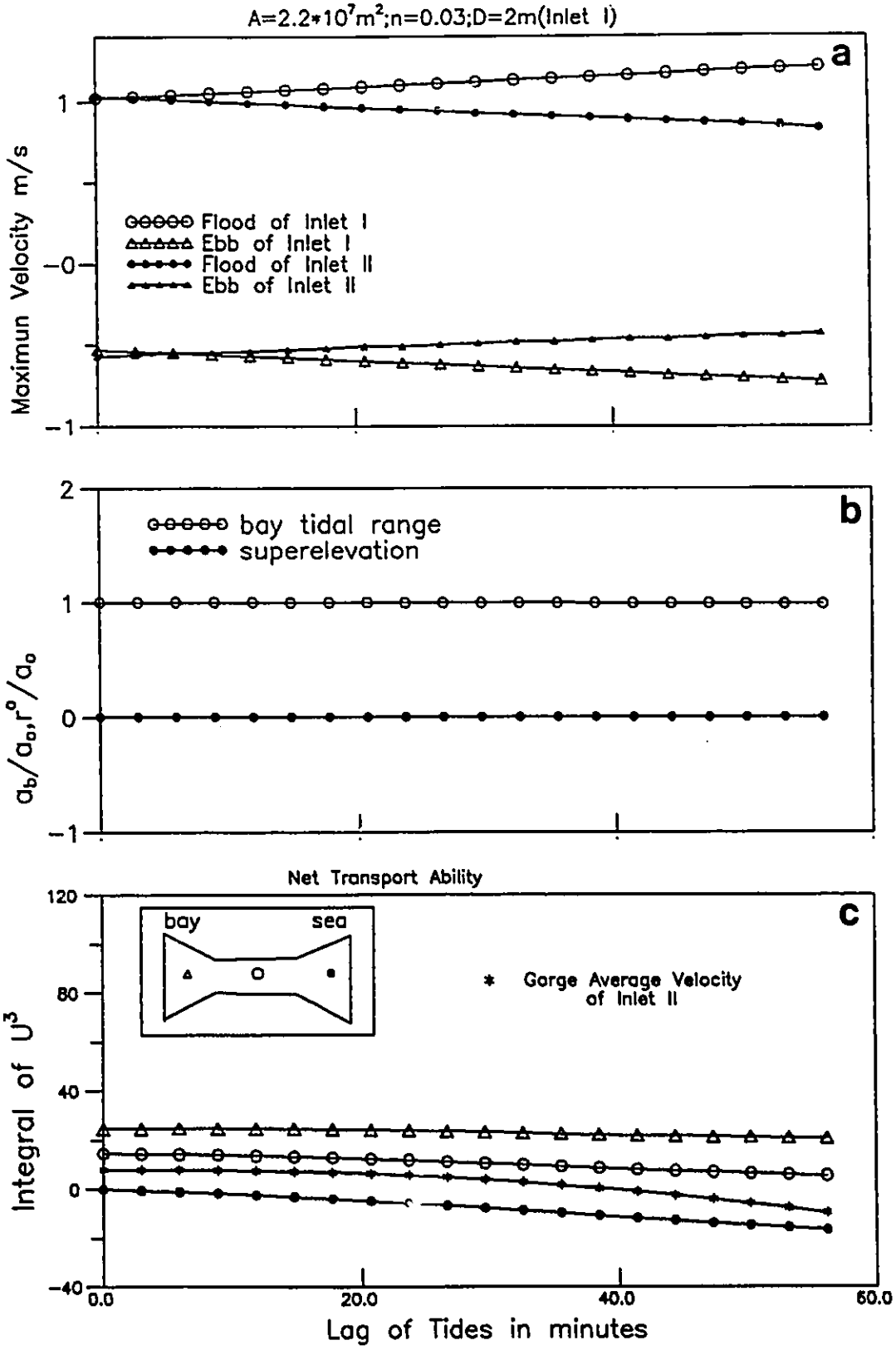
A=2.2*10⁷m²;n=0.03;D=2m(Inlet I)
a
Maximun Velocity m/s
1
0
−1
Flood of Inlet I
Ebb of Inlet I
Flood of Inlet II
Ebb of Inlet II
b
2
1
0
−1
$a_b/a_o, r^o/a_o$
bay tidal range
superelevation
Net Transport Ability
c
120
80
40
0
−40
Integral of U^3
bay
sea
Gorge Average Velocity of Inlet II
0.0
20.0
40.0
60.0
Lag of Tides in minutes

Unlike the previous case of varying width, however, without all the changes at the two inlet proper, changing the distance between the two inlets does not seem to affect the overall bay response. In Figure 20b, it is seen that the bay tidal range and the superelevation remain almost horizontal.

3.3.7 Effects of Other Parameters

Besides the above parameters, the effects of two other parameters were also examined. One is the loss of water in the bay to sinks other than the inlet. Such sinks may be channels which connect the bay to the adjacent lagoons. The Narrow in Cascumpec Bay is one of such examples. The other parameter is the change in slope of the inlet channel bank. The portion of incoming water lost to other sinks will not be available to the outgoing current. This results in a decrease in ebb current velocities and enhancement of flood transport ability at all locations of the inlet (Figure 21b). The effect of changing inlet bank slope, which results in change of cross section area with time, is relatively minor for the current system. Except at an early stage, changes in bank slope basically have no effect on net transport ability (Figure 21a).

3.4 Synthesis and Discussion

Many interesting observations have been made in the

Figure 21 Effects of changing inlet channel bank slope and water leakage on net sediment transport ability.

a. Net sediment transport ability versus inlet bank slope. Effects of changing inlet bank slope is insignificant.

b. Net sediment transport ability versus leakage. Leakage is the volume of sea water lost to other sinks, which is no longer available to the ebb flow. As would be expected, this situation favours the flood flow at all locations in the inlet.

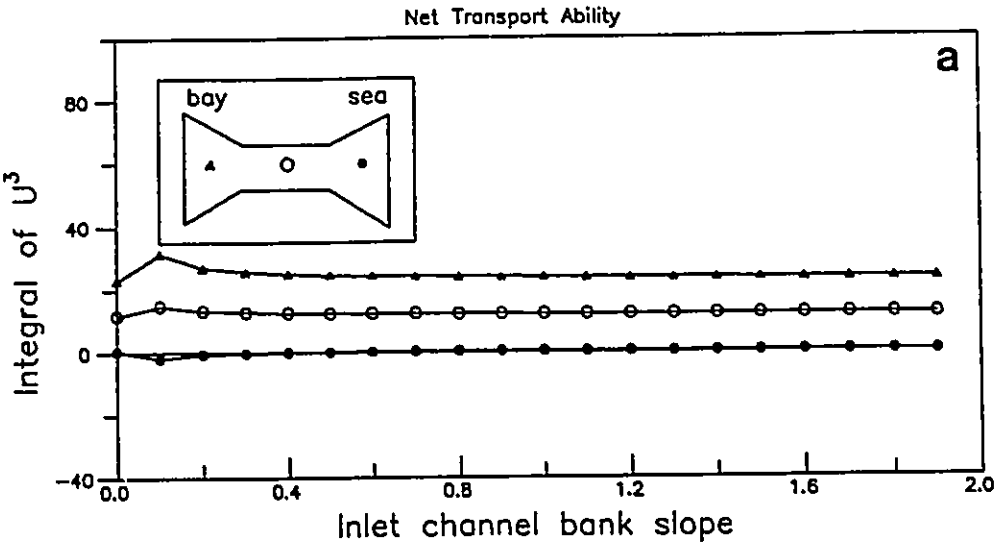
Net Transport Ability
a
bay
sea
80
40
0
-40
Integral of U³
0.0
0.4
0.8
1.2
1.6
2.0
Inlet channel bank slope

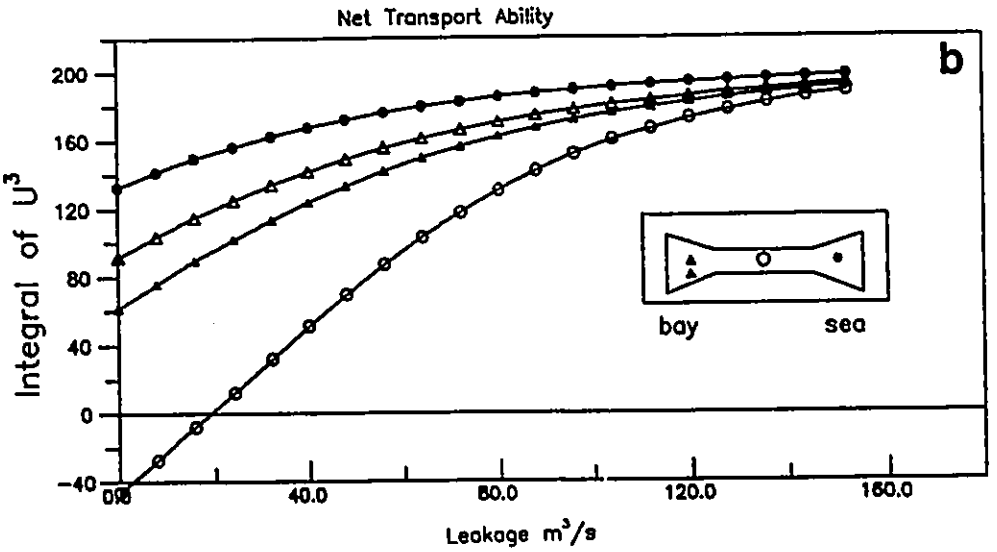
Net Transport Ability
b
200
160
120
80
40
0
-40
Integral of U³
40.0
80.0
120.0
160.0
Leakage m³/s
bay
sea

parametric studies. A number of them have been discussed along with the presentation of the results. Some topics particularly relevant to the present study are discussed further in this section. As the model was configured after a class of tidal inlets, the discussion is presented with respect to small tidal inlets in general. It is, however, equally applicable to Palmer Inlet in particular, as this inlet is a representative member of the class. The particular application to Palmer Inlet, however, is deferred to the next chapter.

3.4.1 Controlling Factors of Tidal Distortions in Small Tidal Inlets

By comparing the relative magnitude of the four dynamic terms, this study showed that in small tidal inlets where water depths is not much larger than the tidal range, friction is the dominant factor. This observation is consistent with many previous studies. The present study, however, found that the two intertidal sand bodies, the flood delta and the spit platform, play more important roles than friction in systems that are clogged by sand. The reason for this can be seen from the comparison of the effects they each produced, and from how these effects fit with the actual observations.

Both friction and the sand bodies affect the resistance the system exerts on the flow. The sand bodies

produce this by changing the water depth over them as the tide fluctuates. This is because the resistance is a function of water depth. Because of their large size, a great portion of the system resistance, in effect, comes from the two sand bodies. This can be seen from the difference in magnitude they produced in the sediment transport curves.

Probably what is more important about these sand bodies is the fact that their existence changes the cross-section area as they are emerged and submerged. These changes are not only large in magnitude, but more importantly, non-linear both <u>in time</u> and <u>in space</u>. They could further interact with other non-linear terms to produce large asymmetrical effects. Friction, on the other hand, does not have this effect. Its effect depends on the bottom roughness, and is rather uniformly applied across the system.

Because of the above reason, the spatial pattern of the effects associated with the friction and the sand bodies are different. Friction alone works invariably in favour of the flood, and against the ebb. This is so regardless of the locations within the inlet. The apparent result of this is deterioration and quick closure of the system. The effects produced by the flood delta and the spit platform, however, are not uniform. In the shoaling areas, the effect favours the flood. In the throat channel, it is slightly in

favour of the ebb. Such a pattern of flow asymmetries has been observed at Palmer Inlet as well as many other similar areas (Stauble, et al., 1989). This is very significant as it probably explains why many microtidal inlets survive for a long time after the flood tidal delta and spit platform are well developed. Its applications to Palmer Inlet will be explained in the next chapter.

3.4.2 Reason for Flood-Dominance in Microtidal Inlets

It is seen that although the flood delta and the spit platform affect the inlet flow differently at different locations, the overall effect (Section 3.3.1 and 3.3.2) of these sand bodies on the system is one that retards the ebb more than the flood. The bay tide is characterized by a short steep flood, a long gentle ebb, and large low water truncations. It is noted that such a pattern is very similar to the measured tides at Palmer Inlet, shown, for example, in Figure 4-7 of Chapter 4.

In mesotidal inlets, the ebb flow is usually the dominant phase. Fitzgerald and Nummedal (1983) explained this as due to the existence of the marshlands, and the resultant difference in drainage efficiency between high and low water caused by it (see Section 3.3.3). A similar qualitative explanation can be offered here for the observed flood-dominance produced by the two sand bodies. In the present case, it is the flood delta and spit platform,

instead of the marshlands, that introduce drastic change in the cross-section area of the inlet. Referring to the storage equation (Equation 3), the rate of change of the bay water level, dh/dt, is proportional to A_c, the cross-section area at the throat. A_c can be related to the two sand bodies through the relationship of $(A_s + A_b)/2$, i.e., as the average between the cross-section areas of the sand bodies. This latter value is obviously small when the sand bodies are emerged, and large as they are submerged by the tide. Then, as far as the bay is concerned, the inlet is most efficient near high water, as it offers the largest cross-section area and the least resistance to the incoming gulf tide. The reverse is true for the low tide. The situation is thus exactly the opposite of the explanation Fitzgerald and Nummedal (1983) used to explain the ebb dominance in mesotidal inlets. If it is true that the ebb-dominated flow of mesotidal inlets is due to the existence of the marshlands, then it also can be said that the flood-dominance often observed in the microtidal inlets is due to the presence of the flood tidal delta and/or the spit platform.

3.4.3 Reason for Larger Effects of the Spit Platform

While both act in favour of the flood, it has been noted that the spit platform has a larger effect on inlet hydraulics than the flood tidal delta. The reason for the

difference lies in the relative positions of the two sand bodies in the inlet, and in how such positions affect the way the sand bodies interact with the tide. Equation (14) describes the overall impedance of the system. After making the same substitution as in the previous section, the equation becomes:

$$K_1 \approx \frac{A}{A_c} \approx \frac{2A}{A_b + A_s} \qquad \text{— (15)}$$

At any instant, A_b and A_s are sums of two components: the mean water level and the fluctuations with tides, A_b' and A_s', respectively. Due to the friction dominated nature of the inlet used in the tests (Figure 4 and 5), the bay tidal range is always smaller than that of the ocean tides. That is, A_b' is smaller than A_s'. Because the spit platform is located on the seaward side, it primarily interacts with A_s. The flood delta is located in on the landward side, and primarily interacts with A_b. The effects of the sand bodies on the system are dual: by changing the friction and by changing the cross-sectional area. These two effects are thus both expected to be larger for the spit platform owing to its proximity to the ocean tide.

3.4.4 Time Asymmetry of Tidal Currents

The model results indicate that time asymmetry related to the flood delta and the spit platform is characterized by shift of the peak velocity of both flood and ebb away from the high water. At Palmer Inlet, the peak velocities at the gorge section were observed to show a shift in the opposite direction. Although the varying bay wall slope, ß, tends to produce the asymmetry needed, the effect is much less than required to overcome the changes caused by other factors. The time asymmetry associated with friction is the same as that associated with the sand bodies, and cannot be used to explain the observed asymmetry. It is possible that the observed time asymmetry at Palmer Inlet is more a result of the characteristics of the Gulf tide than that of tidal deformation. A separate run was conducted to explore this possibility. In this run, the forcing tide used is a combination of O_1 and M_2 with the latter lagging behind by 50°. The amplitudes used are 20.1 cm for O_1 and 17.55 cm for M_2. These values are taken from results of harmonic analysis for tides at Beach Station (Table 2-6, Part I). Both flood delta and spit platform are allowed to vary from 0 to 1.9 m. The result is shown in Figure 22, in which figures of midtides and peak velocities are also indicated. The characteristics of the forcing tide did play an important role in creating the asymmetry observed at the throat. The main feature of observed time

Figure 22 Calculated time series of bay tides and inlet velocities for thickness of the flood delta and spit platform = 0.2 m and 1.8 m. $O_1 + M_2$ is used as the input tide (solid line). The amplitudes of O_1 and M_2 used are 20.1 and 17.6 cm, respectively. The values are taken from harmonic analysis of tides at Palmer Inlet (Table 1, Part I). The times for midtides and peak velocities are marked and their values given. It is observed that with this type of tide input, the flood and ebb peak velocities move toward HW.

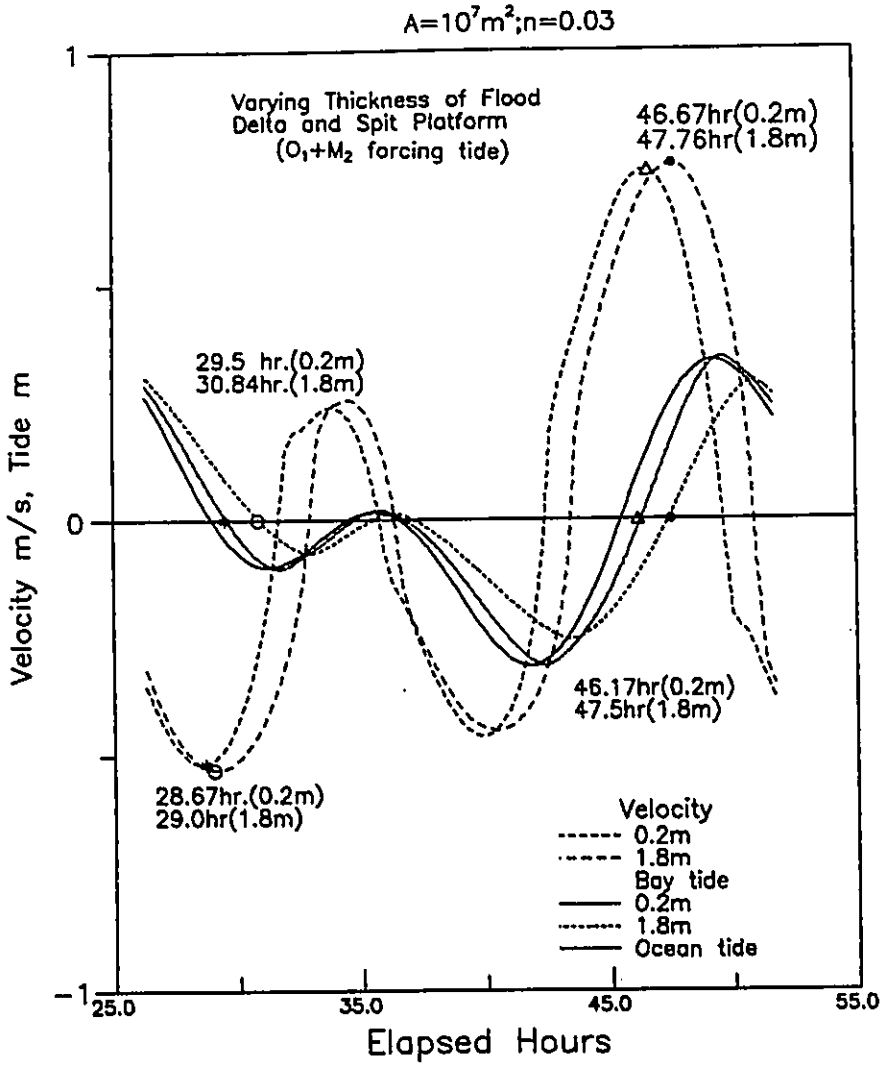
A=10⁷m²;n=0.03
Varying Thickness of Flood Delta and Spit Platform
(O₁+M₂ forcing tide)
46.67hr(0.2m)
47.76hr(1.8m)
29.5 hr.(0.2m)
30.84hr.(1.8m)
46.17hr(0.2m)
47.5hr(1.8m)
28.67hr.(0.2m)
29.0hr(1.8m)
Velocity
0.2m
1.8m
Bay tide
0.2m
1.8m
Ocean tide
1
0
−1
25.0
35.0
45.0
55.0
Velocity m/s, Tide m
Elapsed Hours

asymmetry is reproduced. The ebb peaks lead their midtidal stages by 0.83 hr. and 1.84 hr. for sand body thickness of 0.2 m and 1.8 m, respectively. The corresponding figures for the flood peak are 0.5 hr. and 0.26 hr., but with the midtide in the lead. That is, the peaks of both the flood and the ebb move toward high water.

3.4.5 Relationship between the Flushing Ability and Inlet Cross Section Area

The hydraulic relationship between the flushing ability of an inlet and its cross section area is illustrated in Figure 13. Making use of this figure, the reaction of the inlet cross section to a sudden external disturbance can be examined. Such a disturbance may be a major increase in wave activity and associated littoral drift during storm condition, a situation that is quite typical in microtidal inlet areas.

Figure 13b shows that the net sediment transport curve passed through the zero line at A and B as the inlet evolves from an extremely small to an extreme large cross-section. At points A and B, the sediments deposited in the channel are equal to those which are scoured. That is, A and B are equilibrium points. The two points, however, differ in the way they response to a force that tends to alter the balance. The curve around B is an ascending one. For any small deviations from the equilibrium around this

point, the inlet tends to restore itself to the original B condition. For example, assume A_{co} is reduced as a result of deposition in the inlet by a major storm. The reduction in A_{ac} moves the inlet downward along the curve. This move it into a zone in which the ebb is dominated. Subsequent erosion will remove the sediment deposited, and cause it to move back to point B. Likewise, an increase in A_{co} at point B moves the inlet into the flood dominated region. Subsequent deposition brings it back toward B as well. Because of this ability to maintain a stable cross section, point B is a stable equilibrium point.

On the contrary, point A is an unstable equilibrium point. The curve around A is a descending one. Any disturbance in this region reinforces changes that move the system further away from point A. For instance, a decrease in A_{co} moves the inlet into a flood dominated region. The ensuing deposition causes A_{co} to decrease further, until closure takes place. The trend of increasing the A_{co} is the opposite. It moves the inlet further and further away from the A point, as it is moving into a more and more ebb dominated zone.

The above results are very similar to those shown in Escoffier's (1940, 1977) stability diagram (Figure 15b). This figure has been widely used for inlet stability analysis. Escoffier used the maximum velocity as the hydraulic parameter, and thus did not define a field of

erosion and deposition in the figure. Comparing Figure 15b and 13b shows that point A and B are the corresponding equilibrium points. The region above the equilibrium line in Figure 15b is therefore the region of ebb dominance, and that below the region of flood dominance. On the other hand, the maximum velocity is more easily obtainable than the net sediment transport. As an exercise, a similar diagram (Figure 13a) using maximum velocities as the vertical axis is produced using the base condition of the present inlet model. For this particular system, the peak of the maximum velocity occurred at the inlet cross section area of about 110 m^2.

3.4.6 Coexistence of Two Inlet Systems

The results of the parametric studies for the dual inlet system have geological implications. It is seen that if there are two inlets connecting the same bay, with the distance between them increasing, the flushing ability of both inlets is improved without changing the tidal prism. It thus seems that if there are two inlets side by side competing for the tidal prism, they tend to move as apart as possible, before they settle down into mutual equilibrium. Bruun (1967) indicated that tidal inlets have the ability to maintain the highest flushing power with the least energy loss. The spatial adjustment between two inlets can therefore be viewed as a natural tendency for two tidal

inlets to maintain their separate identity, and to seek for a position, at which they each have their highest flushing ability. This is probably the reason why many double inlet-bay systems have inlets situated at the two opposite ends of the bay.

Chapter 4

Calibration of the Model and Its Application to Palmer Inlet

4.1 Introduction

Before a numerical model can be applied to a particular system, it must be calibrated. That is, one or more parameters are adjusted in the model until best fits between measured and predicted values are obtained. In this Section, the calibration of the spatially integrated inlet model to the Palmer-Alberton-Cascumpec Bay system is presented. Bennett (1976) stated that the calibration for a model in which only water level measurements were used for boundary conditions, was best performed at the maximum values of the discharges to ensure that the amplitude of the predicted and measured discharges were the same. Seelig (1976; 1977) recommended that after calibration for discharge or velocity, the results should be further checked using tidal elevation data. Following these recommendations, the calibration in the present study was carried out by matching amplitudes of both tidal discharges and elevations. The parameters used for achieving the match are Manning's n, and the entrance and exit energy loss coefficients, K_{en} and K_{ex}. The system is modelled as a two inlet system. Although it would be much simpler if the system could be portrayed as a single inlet system, this is

not possible because of the uncertainty in dividing the tidal prism between the Palmer and Alberton Inlet.

4.2 Procedure of Calibration

A flowchart of the basic procedures of calibration is given in Figure 23. Given the boundary conditions and the measured data, the model was first calibrated against the measured discharge data using Manning's n as a tunable parameter. This was done by operating the model with an initial set of Manning's n, checking the results, and then re-running using a different set of friction factor. The friction factor was scaled up if the observed maximum discharges were larger than the computed ones, and scaled down if the opposite was observed. This process was repeated until a good agreement was obtained. The calibrated Manning's n was obtained at this stage. The calibration then preceded to the check of tidal elevations. The same 'trial and error' approach was followed until the amplitude of measured tides was reproduced as closely as possible. The parameters used for fine tuning at this stage were the flood and ebb entrance and exit loss coefficient, K_{en} and K_{ex}. Changes in K_{en} and K_{ex} values affect the calibration results in the previous stage, and a balance has to be struck to achieve satisfactory matching of both discharges and tidal elevations.

Figure 23 Flow chart for inlet model calibration. The model is first calibrated against discharge, Q(t), by varying Manning's n in stage I. After the discharge is reproduced as closely as possible, Manning's n is retained and the calibration is carried on to stage II. In stage II, the entrance and exit loss coefficients, K_{en} and K_{ex}, are adjusted to match the predicted bay tidal elevations to the measured bay tides.

Calibratioin procedure

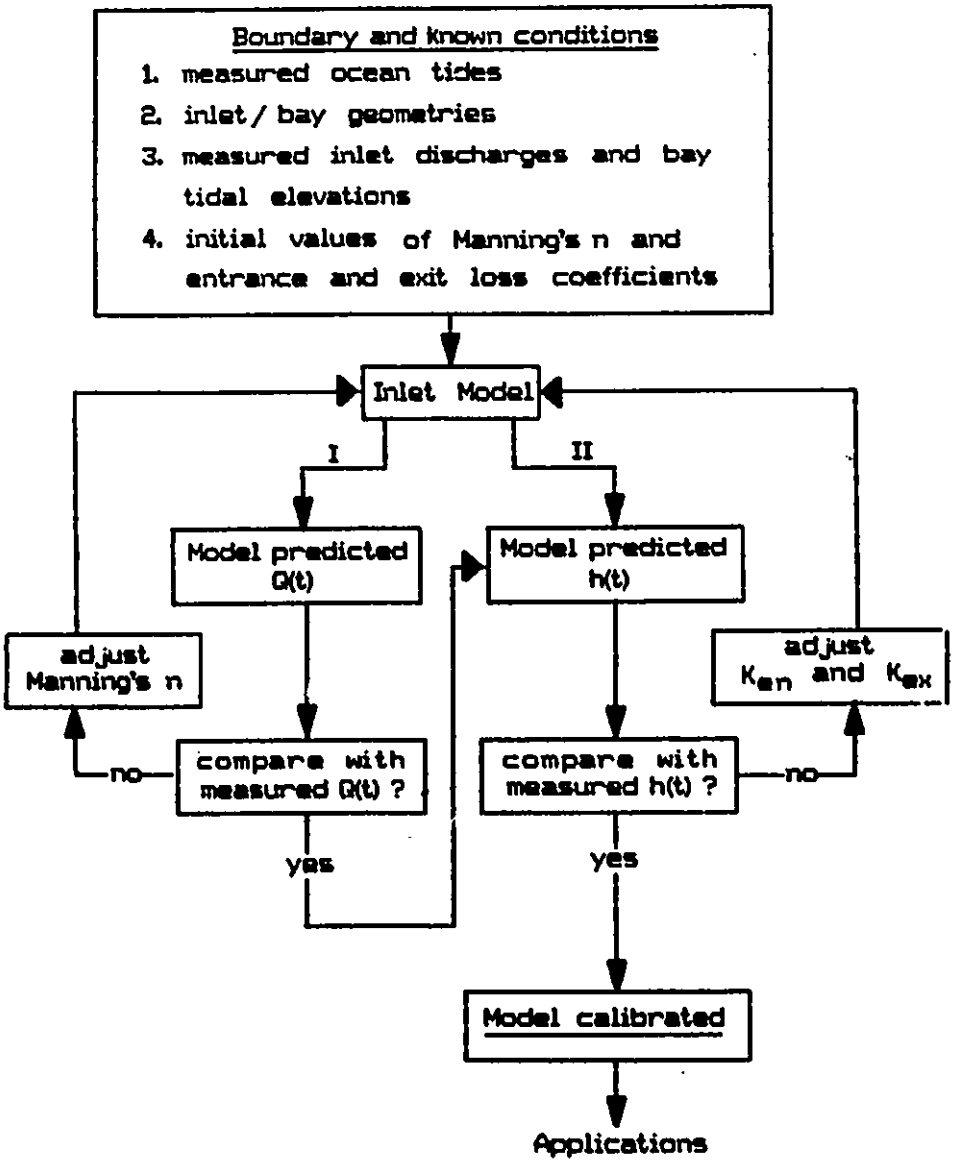

4.3 Boundary Conditions

In order to calibrate the model, boundary conditions must be specified explicitly. The boundary conditions required in this study are open water boundary conditions and submerged seabed boundary conditions. They are either measured data or stated as defined functions of known parameters.

The submerged seabed boundary conditions for the two tidal inlets are represented by the two grid systems shown in Figure 24. The grid system for Palmer Inlet consists of seven sections and six channels, and that for Alberton Inlet consists of seven sections and five channels. The section is denoted as I and indexed from the gulf to the bay. The channel is denoted as J and indexed from left to right. A cell is defined as cell(I,J). Therefore, cell(4,3) refers to the cell located in section 4 and in channel 3. The two grid nets were constructed based on the 1986 bathymetric survey using a precision depth sounder, Raytheon DE-719B. Altogether 31 cross sections were obtained for Palmer Inlet, and 8 cross sections for Alberton Inlet. Simultaneous measurements of sea levels were used to reduce the sounding depths to mean water levels. The grid net for Alberton Inlet and the two most seaward cross sections of Palmer Inlet were constructed using data scaled from the Canadian Hydrographic Survey sheet 4492 (edition of June, 1983). Each cross section echograph was first digitized and then

Figure 24 Flownet of Palmer and Alberton Inlet used for model calibration and applications. The flownets were constructed using 1986 depth sounding records, airphotos and 1980 hydrographic survey chart 4492. A cell can be identified as cell(I,J), in which I refers to the section and J to the channel. The transverse section and longitudinal profile referred in the text are hatched and stippled respectively. The cross section at which the discharge was measured on June 20-21, 1986, was located 15 m seaward of section five of Palmer inlet. The two triangles mark the locations where current velocities were measured simultaneously in the two inlets for two tidal cycles. The dot marks the location where continuous velocity measurements were made one metre off the bottom for model calibration.

Flownet of Alberton Inlet

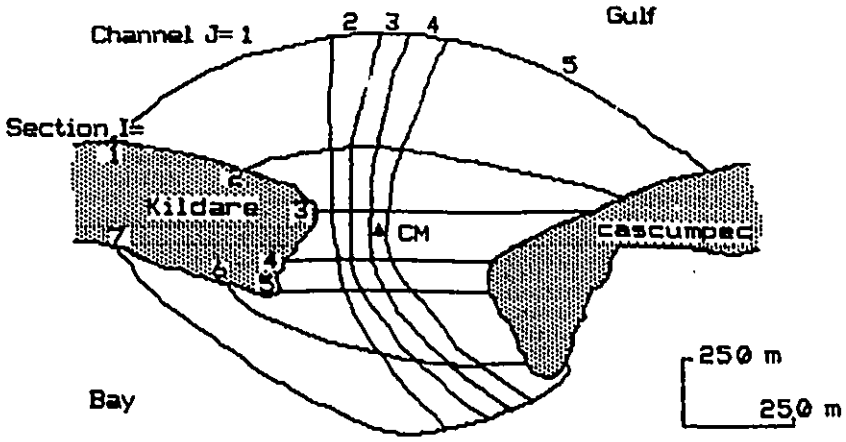

Flownet of Palmer Inlet

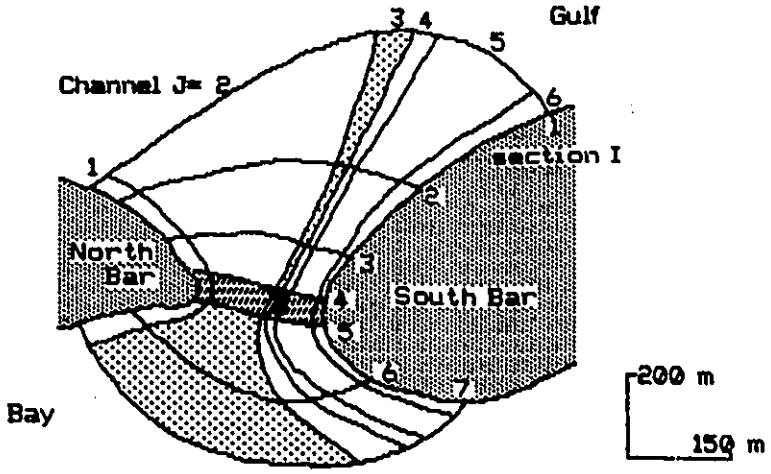

segmented into channels using the procedure described by the computer subroutine NET of Seelig's model (1976). This program uses a weighting function to distribute fractions of the total discharge to each grid cell in a cross section so that flow resistance in each channel is minimized. The values of cell dimensions thus determined are tabulated in Table 1.

The measured discharges used in the calibration were obtained in June 20 to June 21, 1986 at Palmer Inlet. This is the only period when cross sectional velocity measurements were undertaken. No such measurements were made in Alberton Inlet. Because Palmer Inlet is relatively narrow, the 'taut line' method was used for the cross section measurement. This is illustrated in Figure 25. A 2/3 inch thick nylon rope was run all the way across the throat section, and held taut by two stakes at each end of the line. The boat was hooked for and aft to the taut line by swivels and rings so that it could slide freely along the line. Three stations were marked on the rope. At about 40 minutes intervals, a trip was made to cover the three stations. At each station, a vertical velocity profile was measured at four prescribed depths using an Endeco 110 remote reading current meter. Each profile took about 3-4 minutes. Each cross section covering three stations took 40 minutes on average. A total of 25 cross sections were obtained for a complete flood-ebb tidal cycle in June 20-21,

Table 1 Cell dimensions used in model calibrations

Palmer Inlet

Channel J= 1								
Section I								
Depth	1	0.9	0.7	2.0	1.6	0.6	1.7	
	2	0.9	0.7	1.6	1.8	0.7	1.0	
	3	0.8	0.6	2.2	1.9	1.4	1.0	
	4	0.7	0.6	2.3	2.7	1.8	1.1	
	5	0.6	0.5	2.3	2.6	1.9	1.2	
	6	1.5	0.4	1.7	1.7	1.4	1.3	
	7	1.3	0.4	1.0	1.9	1.5	1.3	
Width	1	42.20	487.40	53.30	38.00	186.10	52.50	
	2	37.60	287.60	17.30	13.30	68.70	32.90	
	3	30.40	159.90	12.10	14.20	39.30	16.30	
	4	41.00	116.00	12.00	13.90	36.20	19.20	
	5	27.80	75.90	11.80	13.60	53.00	21.60	
	6	39.30	245.50	44.20	30.70	46.20	20.60	
	7	45.40	454.60	86.80	23.50	66.10	33.40	
Length	1	52.6	61.5	293.9	311.5	317.6	282.1	256.0
	2	111.8	120.5	178.2	179.4	176.9	177.3	177.9
	3	38.5	62.7	111.8	114.6	115.6	115.3	106.5
	4	94.2	87.7	66.0	63.7	64.0	67.5	76.2
	5	92.0	105.9	174.2	180.5	174.5	134.4	112.7
	6	87.4	94.7	174.4	174.9	163.8	145.9	135.1

Alberton Inlet

Channel J = 1						
Section I						
Depth	1	1.3	5.3	4.3	3.4	1.3
	2	1.1	5.9	5.6	5.0	1.1
	3	3.9	6.8	6.8	6.6	2.2
	4	2.7	5.2	5.7	5.7	2.3
	5	3.4	4.2	4.3	5.9	3.6
	6	1.3	5.0	4.8	5.3	3.0
	7	1.1	5.4	5.3	5.3	2.8
Width	1	651.5	116.4	65.9	91.6	791.1
	2	208.2	50.0	55.5	47.9	560.8
	3	27.4	46.3	35.7	40.2	476.4
	4	122.3	30.2	30.3	31.8	260.3
	5	153.9	47.2	47.2	70.5	193.4
	6	443.4	97.2	63.0	71.3	133.9
	7	1,053.0	107.7	69.7	59.0	150.2
Length	1	328.4	457.9	474.8	470.8	466.7	220.4
	2	238.6	247.7	251.4	250.9	252.8	102.4
	3	207.9	205.0	202.4	206.1	204.4	301.8
	4	152.5	153.6	159.2	155.2	171.7	161.9
	5	130.2	233.9	269.2	289.5	280.5	223.4
	6	292.6	348.7	293.7	247.8	218.3	118.1

Figure 25 Schematic diagram, showing measurement of cross section velocity using Endeco 110 current meter. Vertical profiles of velocity were measured at three stations along the taut line. The cross section was partitioned so that each subsection extended laterally half the distance from the preceding vertical profile to half the distance to the next vertical. The discharge for each subsection was the product of the mean velocity calculated from the velocity profile and the subsection area. The mean velocity of the shallow portion was determined by the equation suggested by Jarrett (1976). Besides profiling, the current velocity one metre off the bed was continuously monitored with Aanderaa RCM-4 meter. W = width; D = depth; I, II and III are section numbers. For location see Figure 24.

Inlet Gorge Cross Section

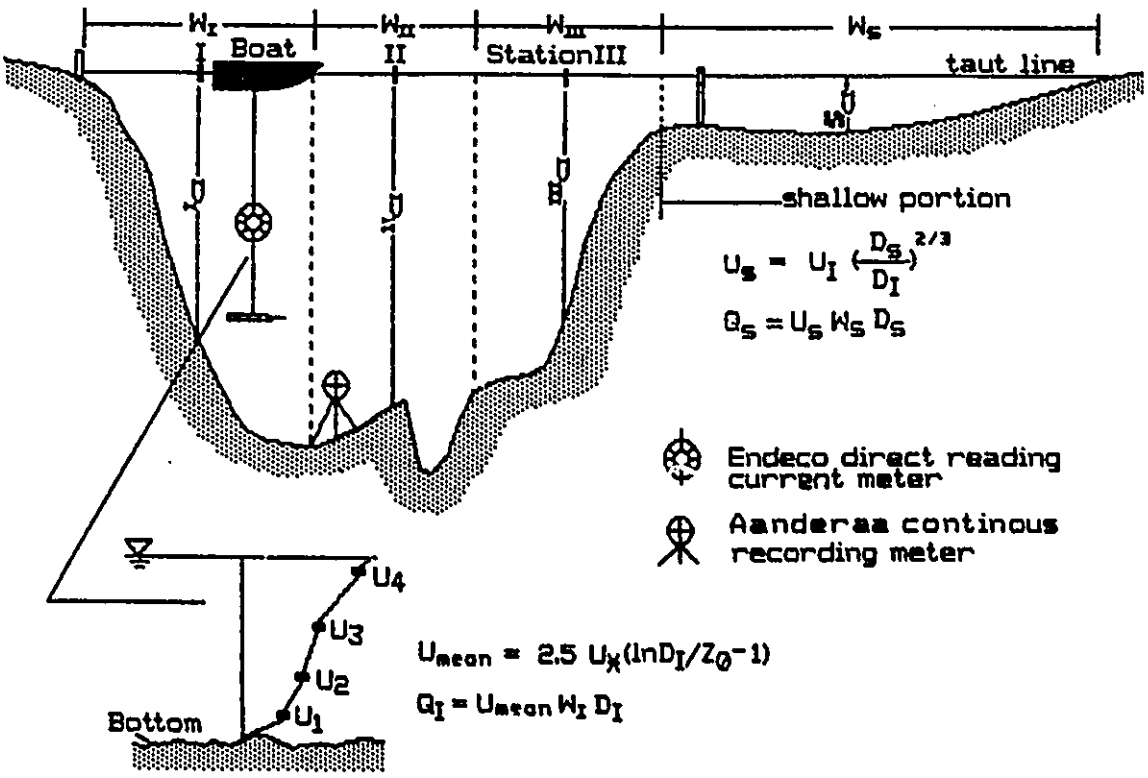

1986. Time series of tidal discharges was obtained using the following procedure (refer to Figure 25):

(1) The cross section was divided into four subsections, of which three had a vertical profile located in the middle. No current measurements were made in the fourth one, because during most of tidal cycle it was too shallow to be accessible by the boat;

(2) The measured velocity is plotted against the logarithm of depth for each vertical profile. The profile mean velocity, U_{mean}, was determined from the best fitted line using the four readings. The mean velocity of the shallow portion, where no measurements were made, however, has to be estimated with the relationship suggested by Jarrett (1974)

$$U_s = U_I \ (D_s/D_I \ )^{2/3}$$

U_s = average current velocity in the shallow portion;

U_I = average current velocity of the I^{th} measured section;

D_s = average depth of the shallow portion;

D_I = average depth of the I^{th} measured section.

(3) The subsection discharge, Q_I, was determined by multiplying the profile mean velocity by the subsection area, which was the product of the subsection width and

depth, i.e., $Q_I = U_{mean} W_I D_I$;

(4) The instantaneous cross section discharge, Q, was computed by summing up the discharges for the four subsections, ΣQ_I

From the calculated Q, the cross section mean velocity, U_m, can be determined by the relation

$$U_m = Q/A_c$$

Where A_c is the throat cross section area obtained from the digitized profiles using a program written by Frank Feuton (University of Toronto, Department of Geology, personal communication, 1987).

The measured discharge and cross section mean velocity using these procedures are shown in Figure 26. These values were used for discharge calibrations of the model. Also shown in the same figure are the predicted gulf tidal elevations and corresponding variations in the throat cross section areas of Palmer Inlet, which were used to calculate the discharge and mean velocity.

Concomitant with the velocity profile measurements, current velocities were also monitored continuously one meter off the bottom using an Aanderra current meter (Station 5572-I, see Figure 25). The location of the meter corresponds to cell (4,4) of the grid net for Palmer Inlet (dot in Figure 24). The current was recorded at five minute

Figure 26 Measured gorge cross-section areas, discharges and mean current velocities, 19:30, June 20 to 13:45, June 21, 1986, Palmer inlet. These data were used for model calibration. The discharges are calculated from vertical velocity profiles measured at three stations using the Endeco 110 direct reading current meter. The basic procedure for calculations were described in the text and illustrated in Figure 24. Also shown are predicted gulf tides and variations of throat cross-section area for the period.

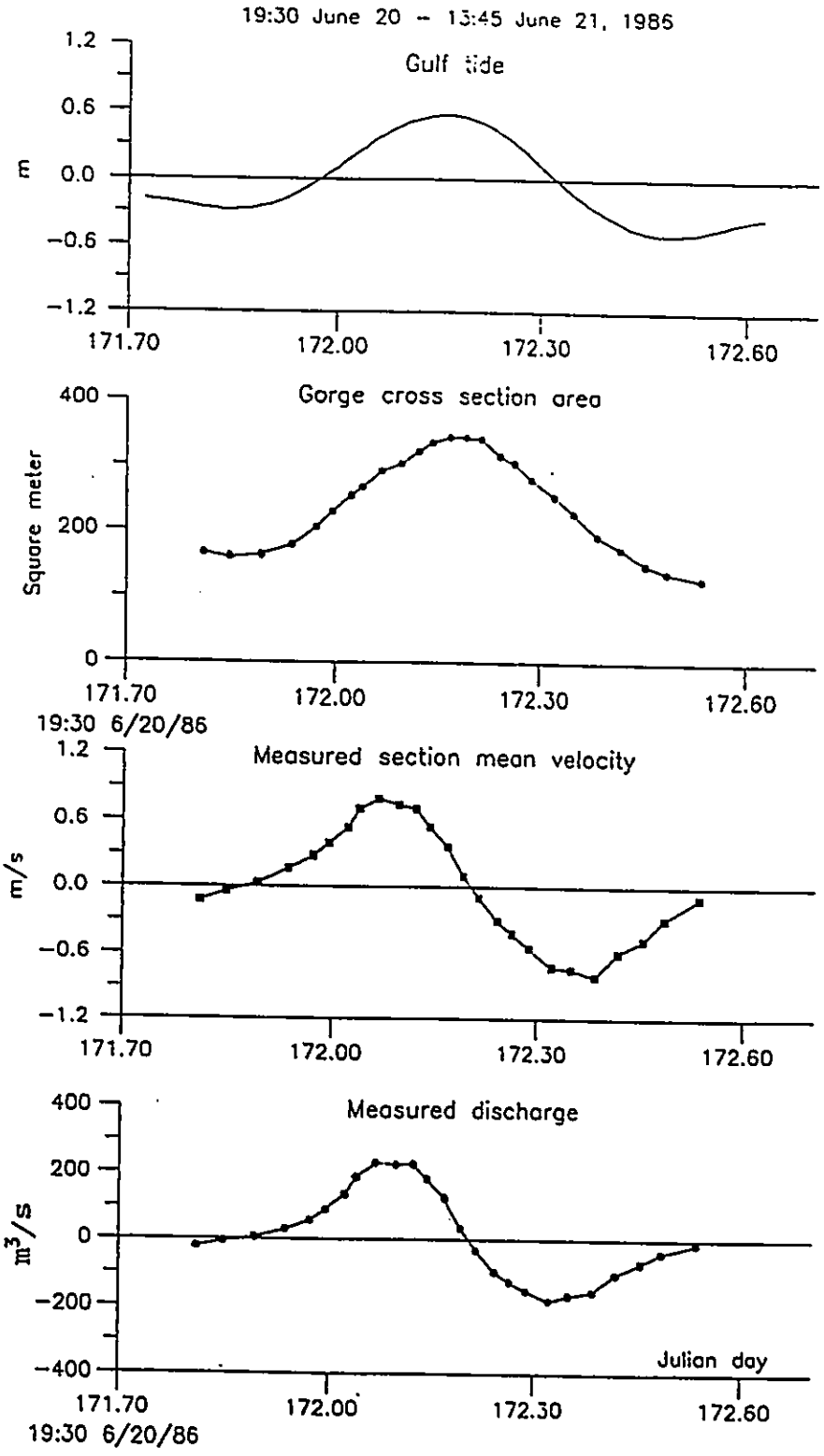
19:30 June 20 -- 13:45 June 21, 1986
Gulf tide
m
1.2
0.6
0.0
−0.6
−1.2
171.70
172.00
172.30
172.60
Gorge cross section area
Square meter
400
200
0
171.70
19:30 6/20/86
172.00
172.30
172.60
Measured section mean velocity
m/s
1.2
0.6
0.0
−0.6
−1.2
171.70
172.00
172.30
172.60
Measured discharge
m³/s
400
200
0
−200
−400
Julian day
171.70
19:30 6/20/86
172.00
172.30
172.60

intervals. The raw data set was first a Fast Fourier Transform with a cut-off period of 1.0 hour. The arithmetic mean of 12 data points was then taken to yield hourly averaged values. After such reductions, the data are believed to be relatively free of high frequency fluctuations. The resultant hourly average velocity was compared with the velocities predicted for section (4,4) by the model.

Measured gulf tides have to be specified as open-water boundary conditions. The Beachside tidal station at Palmer, however, was fouled by sands for the period when discharges were measured. Thus, no real measured gulf tidal data were available for calibration. The forcing tides were therefore generated from tidal constants obtained by harmonic analysis of the data for the Beachside tidal station. The predicted tide, shown in Figure 26, has a flood range of 0.86 m and ebb range of 1.07 m. The use of predicted tides as forcing tides introduced uncertainties into the calibration. Both measured and tide-constant predicted bay tides, however, are available, thus providing data for qualitative checks of the uncertainties.

Initial values of Manning's n as well as flood and ebb loss coefficients, K_{en} and K_{ex}, had to be assigned to start the calibration. Manning's n was prescribed as a function of deptn as given in the equation on p. 23, Chapter 3. The recommended values of n_1 and n_2 are retained as

starting values. The values of K_{en} and K_{ex} depend on the shape of the inlet. Conventionally, they both start as unity.

Values of other pertinent variables prescribed as boundary conditions for the calibration are as follows:

A_{msl} (bay surface area at mean water level) = 2.6 10^7 m^2;

Q_f (river discharge input) = 1.0 m3/s.

α (inlet channel slope) = 0.0

The use of a grid net which divides the inlet channel into individual cells justifies the use of α = 0.0. Changes due to the channel slope have been largely accounted for by changes in topography between cells. As proved in the test of the model in Chapter 3, α has little effect on inlet hydraulics (Figure 21a). There are four tributaries providing fresh waters into the Cascumpec Bay. Only Mill River is monitored by Environmental Canada (Sta. 01CA003). The daily mean runoff for June 20 and 21 is 0.27 and 0.25 m^3/s (Environmental Canada, 1986). Therefore, as a first approximation, the total runoff into Cascumpec bay was estimated to be 1.0 m^3/s. The bay surface area was digitized using Hydrographic Survey sheet 4492 (1980 edition).

4.4 Results of Calibration

n_1 and n_2 values after calibration are 0.035 and 0.0 respectively for all cells. This is equivalent to a Manning's n value of 0.035. This value falls in the range found by other inlet modellers. For example, the calibrated Manning's n is 0.027 for Masonboro inlet, North Carolina (Huval and Wintergerst, 1977), 0.037 for inlet-harbours of Great lakes (Sorensen and Seelig, 1976), and 0.047 for Indian River inlet, Delaware (Keulegan, 1967; Seelig, 1977). The flood and ebb energy loss coefficients, K_{en} and K_{ex}, after calibration are 0.5 and 1.0 respectively. Dean (1983) reported that K_{ex} is usually unity, while typical values for K_{en} are 0.05-0.25. The entrance coefficient, however, depends on the shape of inlet entrance. A less streamlined entrance has a higher value of K_{en}.

The results of the calibration are presented in Figure 27 to 29 and Table 2. Overall, the agreement between the measured and predicted flow/tides can be considered to be very good. The tidal elevation calibration is considered excellent for the second cycle (Figure 27). The measured bay tides (dot-trace in Figure 27) follow the model-predicted elevations (short dash line) faithfully, there being an almost exact match in both phasing and amplitude. Table 2 shows that both the tidal range and high water/low water elevation match exactly for the second cycle in the test. For the first cycle, however, there are delays in

Figure 27

a, b, c, d Output of relative magnitudes of advection, time acceleration, friction and pressure terms in the inlet equations for Palmer inlet from model calibration. The terms are normalized by the largest terms. It is seen that the currents in Palmer inlet are predominantly controlled by head and friction effects. The inertial effect is only significant for a short time near slack waters. The advection term is also not important during most of time but increases slightly toward the slack water.

e. Comparison of measured and predicted bay tides from model calibration. Also plotted are forcing gulf tides and predicted bay tides calculated from tidal constants of harmonic analysis. The agreement between the measured and predicted tide is excellent for Cycle II. Predicted tides underestimated the measured tides for Cycle I. This, however, can be attributed to the used of harmonic-predicted gulf tide as the forcing tide rather than to the computational scheme of the model. This is because the fit between the predicted and harmonic-predicted bay tides is excellent.

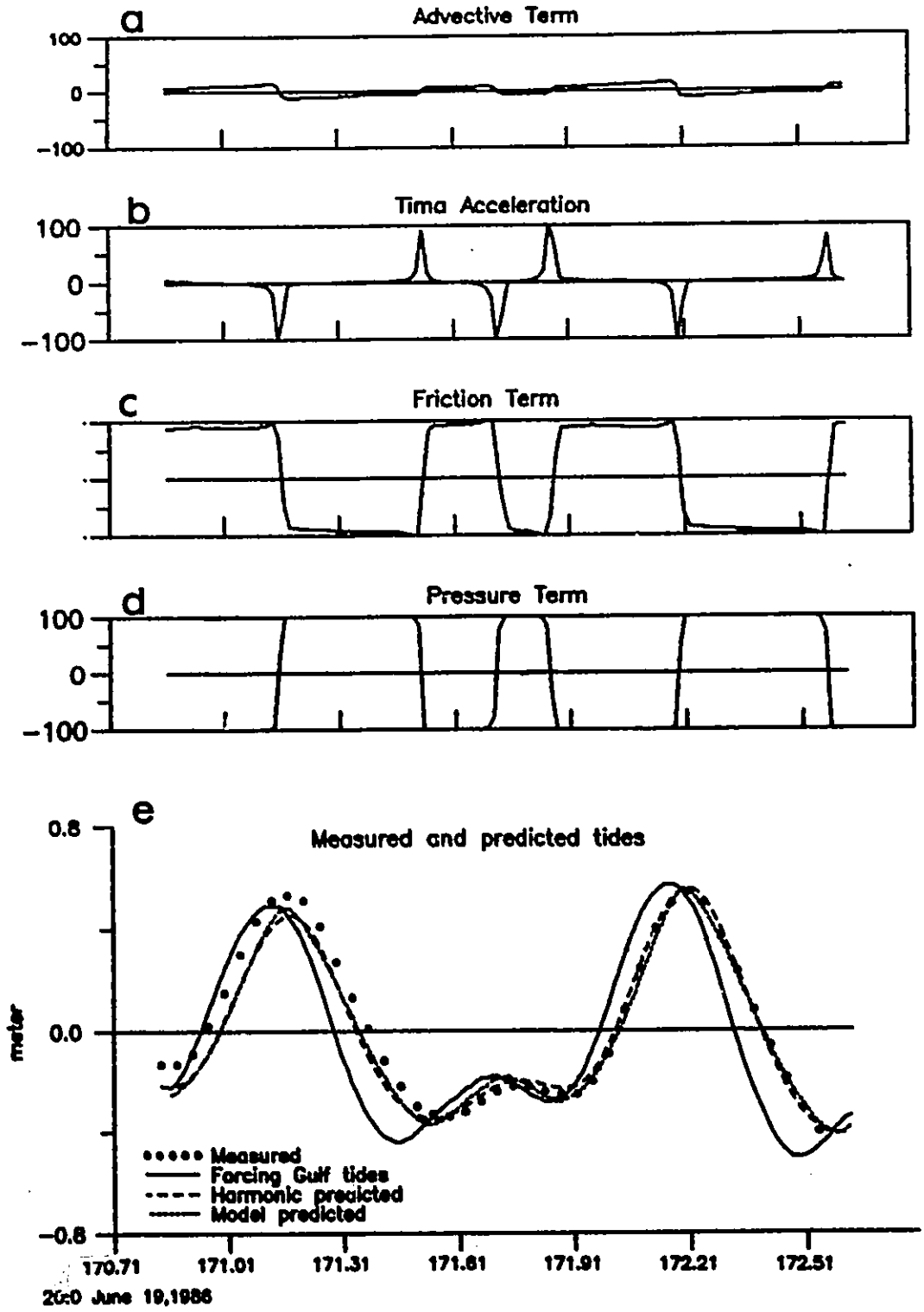
a
Advective Term
100
0
-100
b
Tima Acceleration
100
0
-100
c
Friction Term
d
Pressure Term
100
0
-100
e
Measured and predicted tides
0.8
0.0
-0.8
meter
Measured
Forcing Gulf tides
Harmonic predicted
Model predicted
170.71
171.01
171.31
171.61
171.91
172.21
172.51
20:0 June 19,1986

Table 2 Summary table of results of model calibration

		Cycle I		Cycle II	
		Measured	Predicted	Measured	Predicted
		Cascumpec bay tide, m			
Bay tide	HW	0.45	0.48	0.55	0.55
	LW	-0.35	-0.37	-0.41	-0.41
	Range	0.80	0.86	0.96	0.96
		Peak current velocity, m/s			
Palmer					
Gorge	Flood		0.64		0.71
	Ebb		-0.65		-0.70
U(4,4)	Flood	0.89	0.97	1.03	1.06
	Ebb	1.10	-1.04	-1.14	-1.13
Alberton					
Gorge	Flood		0.68		0.75
	Ebb		-0.70		-0.75
U(4,4)	Flood		1.06		1.17
	Ebb		-1.12		-1.21
		Peak water discharge, m^3/s			
Palmer					
Gorge	Flood		187.31	230.50	219.03
	Ebb		-152.22	-181.20	-171.00
Q(4,4)	Flood		51.80		57.80
	Ebb		-50.00		-54.50
Alberton					
Gorge	Flood		959.71		1,079.94
	Ebb		-901.38		-979.88
Q(4,4)	Flood		117.50		130.90
	Ebb		-116.60		-126.20
		Tidal prism, m^3/tidal cycle			
Palmer					
	Flood		4,300,000	3,300,000	3,200,000
	Ebb		3,600,000	2,950,000	3,600,000
Alberton					
	Flood		26,000,000		17,000,000
	Ebb		23,000,000		24,000,000

* (4,4) refers to cell(4,4) in Figure 24

the zero-crossing and underestimations in amplitude. As a whole, the disagreement decreases from the first cycle to the second cycle, a fact reminiscent of the start-up transient effects. The bay tides (long dash line) calculated using the results of harmonic analysis from lthe Bayside tidal station, however, match the model-predicted tides satisfactorily over the entire calibrated interval. This negates transient effect as a cause and suggests that the source of discrepancies might lie in the use of predicted tides as forcing tides. Spectrum and coherence analysis (not presented in this thesis) of measured tidal and wind data indicated that in this microtidal, shallow water environment, tidal elevations are regularly influenced by meterological conditions. Real gulf tides could be significantly different from the harmonics-predicted tides on days when winds or waves are strong. This is considered as responsible for the discrepancies in the tide calibration.

In Figure 28, the measured and predicted discharge and cross section mean velocity are compared. The agreements are not as good as for the tidal level calibration, but still can be considered as satisfactory. The model values show consistent underestimates of the measured discharge and velocities for the flood and ebb (Table 2). Disagreements in phasing are also evident. Larger deviations observed in tidal flows are expected,

Figure 28 Comparison of measured and predicted discharges (a), and cross-section mean current velocities (b). Note that the patterns of fit are very similar for the two graphs. The agreement between the measured and predicted can be considered very good. The amplitudes are only slightly under-estimated by the model. Phase matching is less satisfactory; but the discrepancies in the phase are uniformly distributed in the flood and ebb — the model overpredicts both during the early acceleration stage of the flood and during the late deceleration stage of the ebb. The net effect is thus insignificant if one or more tidal cycles are considered.

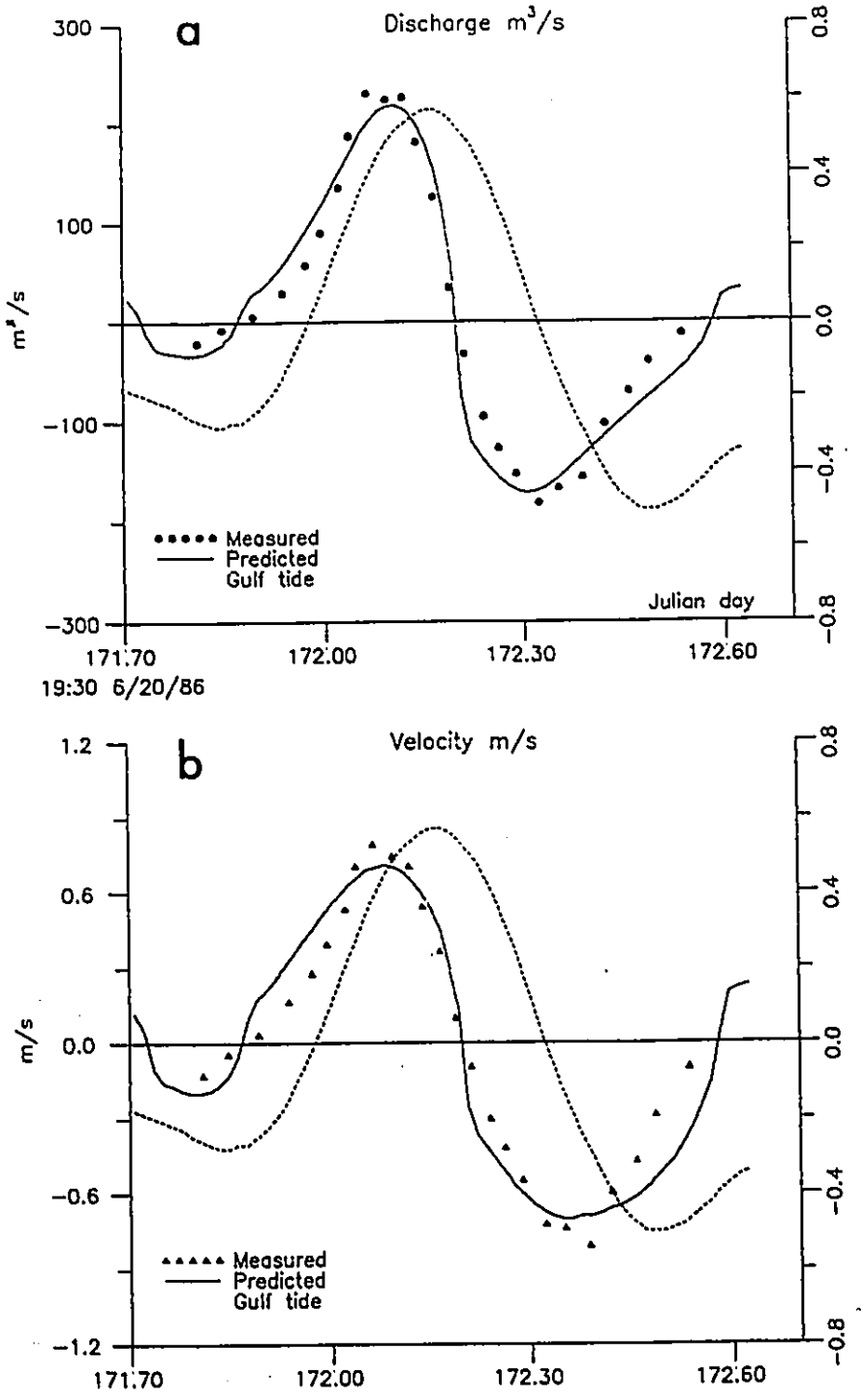
a
Discharge m³/s
300
100
−100
−300
m³/s
0.8
0.4
0.0
−0.4
−0.8
Measured
Predicted
Gulf tide
Julian day
171.70
19:30 6/20/86
172.00
172.30
172.60
b
Velocity m/s
1.2
0.6
0.0
−0.6
−1.2
m/s
0.8
0.4
0.0
−0.4
−0.8
Measured
Predicted
Gulf tide
171.70
172.00
172.30
172.60

since they are more sensitive to errors than the tide. There are no major discrepancies in amplitude and timing, however, and the general pattern of the time history is reproduced. Considering the possible errors associated with flow measurements and especially the uncertainties in the estimations of discharges for the shallow portion of the channel, the agreement between the measured and the predicted discharge/velocity can be considered unexpectedly good. This can be attributed partly to the forcing data used. Because of the use of the predicted forcing tides, no random fluctuations other than astronomical sources are present in the model-predicted discharge/velocity. On the other hand, turbulent fluctuations in measured discharges were also largely filtered out by the several averaging processes (profile and cross sectional averaging). Because both the calibrating and calibrated data were 'artificially' smoothed beforehand, the relatively good agreement between measured and predicted discharges is not surprising. Overestimation of the predicted discharge/velocity is relatively uniform for the flood and ebb (Figure 28). This uniformity suggests that the errors of model predictions will be insignificant as far as the net effect is concerned.

Figure 29a compares the model-predicted cell (4,4) velocities with velocities measured one metre off the bottom using the Aanderra current meter. It covers two major flood-ebb cycles and a minor one (due to diurnal inequality)

Figure 29

a. Comparison of measured and predicted current velocity at cell(4,4), Palmer inlet. The velocity was measured one metre off the bed using an Aanderaa current meter in the throat section (dot in Figure 24). The agreement between the measured and predicted velocity is considered good for the two major tidal cycles. For the minor tide, however, the model overestimates the measured velocities by a factor of more than two. Based on the additional investigations mentioned in the text, the overestimation is believed owing to some unknown factor inherent to the model computational scheme.

b. Predicted tidal discharge for Alberton and Palmer inlet. The peak discharges are listed at appropriate places. Numbers in the parenthesis of the legend are tidal prisms for the last flood-ebb cycle (Cycle II). The positive numbers are flood tidal prism and the negative numbers are ebb tidal prisms. The model predicts that Alberton inlet carries 5.3 times more water during the flood and 6.7 times more water during ebb than Palmer inlet. These Figures are comparable in order of magnitude to the measured tidal prisms from this study and Armon's study (1975).

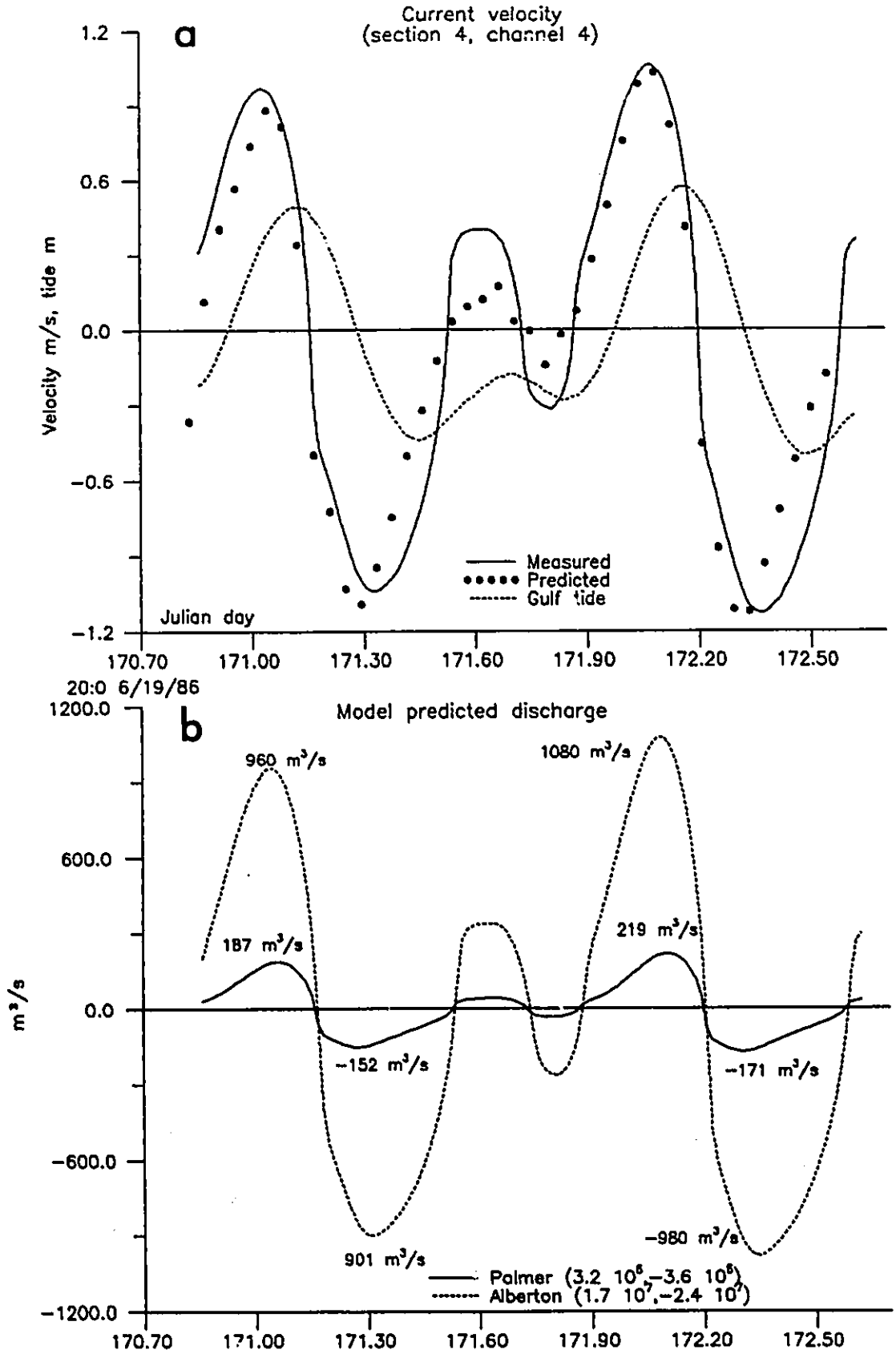
a
Current velocity
(section 4, channel 4)
1.2
0.6
0.0
−0.6
−1.2
Velocity m/s, tide m
Measured
Predicted
Gulf tide
Julian day
170.70
171.00
171.30
171.60
171.90
172.20
172.50
20:0 6/19/86
b
Model predicted discharge
1200.0
600.0
0.0
−600.0
−1200.0
m³/s
960 m³/s
1080 m³/s
187 m³/s
219 m³/s
−152 m³/s
−171 m³/s
901 m³/s
−980 m³/s
Palmer (3.2 10⁶,−3.6 10⁶)
Alberton (1.7 10⁷,−2.4 10⁷)

from 20:0 June 19 to 14:0 June 21. It is seen that the match between the calculated and measured velocities is satisfactory for the two major cycles both in amplitudes and phasing. The largest difference in amplitude occurs at the ebb maximum of the first cycle (Table 2) with the measured underpredicted by only 6 cm/s. The deviation in time history between the two series has similar pattern as that for the discharge. The model considerably overpredicted the velocity amplitude by a factor of 2 (Figure 29a) for the minor tide, although the agreement of phasing is excellent. Additional sensitivity tests indicated that no realistic values of Manning's n could lead to velocities as low as those measured without totally invalidating the calibration. The use of the predicted gulf tide was again suspected as the cause. Harmonic analysis of tidal data produced the differences between the measured tides and harmonic-predicted tides. These are checked to see that residuals for the minor tide are in the range of 0 to 4 cm, smaller than the residuals for the major tides (8 to 12 cm). Bay tidal results were used, since no gulf data are available for the period concerned. After these investigations, it was believed that the discrepancy was caused by some unknown factor inherent in the model. Whatever the factor might be, it seems that the model tends to overestimate for periods of small tidal ranges. It follows that the model probably also overestimates when the current velocity is low. This is

partly confirmed while looking back at Figure 28. In the Figure, the calculated curve tends to overestimate the measured one mainly in the early acceleration stage of the flood and late deceleration stage of the ebb.

Since close correspondences between the model and the prototype data were obtained, reasonably high confidence can be placed on other results about inlet hydraulics generated during calibration. These results include the four hydrodynamic terms, which indicates the hydraulic nature of the inlet. The output of current transport ability at selected grid cells, were also calculated. They are plotted in Figure 29b, 30 and 31 and partially listed in Table 2. These data can be used as to indicate the flow dominance at various locations in the inlet.

4.5 Hydraulic Nature of Palmer Inlet

The four terms constituting the dynamic equation of motion were calculated in the process of calibration. The pertinent data are presented in Figure 27a, b, c, and d. At each time step, each term was normalized using the largest term. Their magnitudes are thus relative. This, however, does not diminish their value as indicators for the hydraulic nature of Palmer Inlet.

Figure 27 shows that the flow in Palmer Inlet is predominantly controlled by the head or pressure term, i.e., the tidal difference between the two ends of the inlet

channel. This term is the driving force of the inlet process, and is to be balanced by the other three terms. Of the remaining three terms, the bottom friction is most significant. This is expected for a system like Palmer Inlet, because shallow depths and a constricted throat are both factors of creating high resistance to the flow. Inlet processes at Palmer Inlet thus can be described as 'tidally-driven and frictionally-dominated'. The effects of these terms dominate during most of the tidal cycle. They become less important only for a short time near the slack waters. At slacks, the bay tidal curve and gulf tidal curve intersect, the head difference being zero. Almost at the same time, current velocities come to standstill, and so does the bottom stress since it is directly proportional to velocities.

Time acceleration and advection terms are often considered negligible, and thus omitted from computations. While generally true, Figure 27a and b show that this does not apply to the slack periods. The advection term reaches the highest values just before and after the high water. This is because the large cross-section during these periods is able to maintain relatively large water discharges even with diminished velocities. On the contrary, the time inertial term reaches a maximum right at high and low water slacks. At these points, all other terms vanish. The flow is the least steady near slacks.

4.6 Flow Dominance pattern at Palmer Inlet and its Significance

The dominance of the tidal current at a location can be represented by the net sediment transport rate. Following the definition given in Chapter 3, the third power of the current velocity, U^3, is used to calculate sediment transports. Instantaneous rates of transport at six cells were calculated along a transverse section (section 4, cross hatched cells in Figure 24), and a longitudinal section (stippled cells in Figure 24), respectively. These rates were further used to calculate the cumulative transports as U^3dt for the flood-ebb cycle for all twelve cells. Results of three cells for each section are selected, and plotted in Figure 30b, c, d and 31b, c, d. The net transport ability over the cycle tested is indicated by the end point of the curves. A negative value of the end point indicates that the net transport is in the seaward direction; a positive value indicates a landward direction. Note that different scales are used for the vertical scale due to the large difference in the cell velocity. In the calculation, time integrations of U^3 were also performed for the flood and the ebb separately. The percent differences between the flood and ebb summation, scaled to 200%, were used as a general measure for flow dominance. These values are plotted in Figure 30a and Figure 31a. The flow dominance for each cell should be compatible with the values of the end point of the

Figure 30

a. Transverse section (Section 4, Figure 24) of flow dominance. Flow dominance was calculated as the percent difference between the time integral of U^3 for flood and that for ebb. Therefore, positive values indicate flood dominance and negative values ebb dominance. The change from flood dominance in the spit platform to ebb dominance in the thalweg of the inlet channel is evident. The southern bank is also slightly flood dominated.

b, c and d. Time histories of the accumulative values of U^3 for cell(4,2), (4,4) and (4,6) respectively. The end points of these curves indicate the net transport resulting from the current. Seaward net transport is indicated for a cell if the end point ends below the zero line; conversely, if the end point is above the line landward net transport is indicated. The results in these graphs are compatible with Figure 30a.

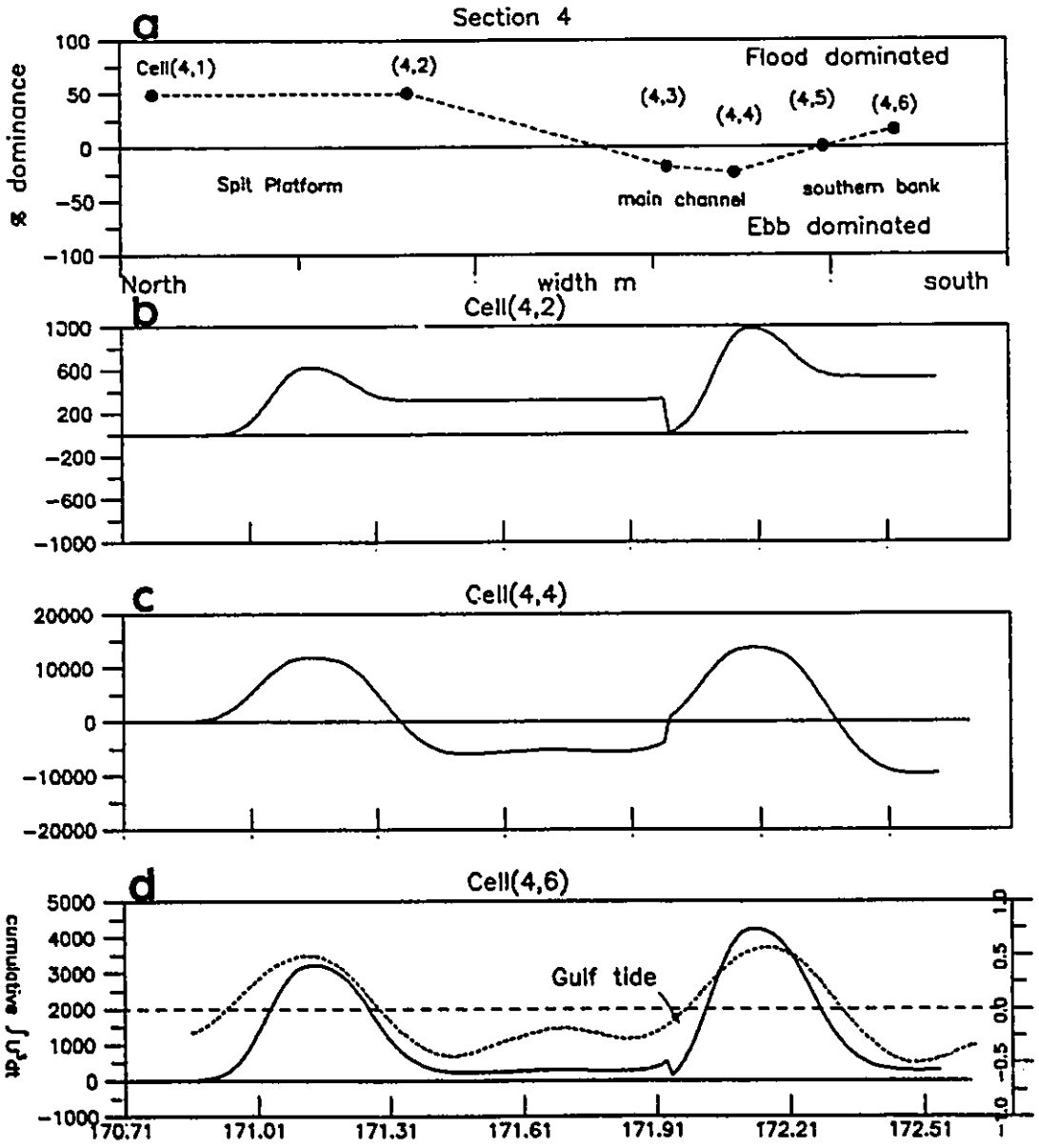
a
Section 4
Flood dominated
Ebb dominated
Cell(4,1)
(4,2)
(4,3)
(4,4)
(4,5)
(4,6)
Spit Platform
main channel
southern bank
% dominance
North
width m
south
b
Cell(4,2)
c
Cell(4,4)
d
Cell(4,6)
Gulf tide
cumulative ∫ J_s dt
170.71
171.01
171.31
171.61
171.91
172.21
172.51

Figure 31

a. Longitudinal profile of flow dominance. For cell locations, see Figure 24. Flow dominance was calculated as indicated in Figure 30a. There is a change from flood dominance in the flood tidal delta to ebb dominance in the seaward entrance of inlet.

b, c and d. Time histories of the accumulative values of U^3 for cell(1,3), (4,3) and (5,2) respectively. The end points of these curves indicate the net transport results of the current. Seaward net transport is indicated for a cell if the end point ends below the zero line; conversely, landward net transport is indicated. The results in these graphs are compatible with those in Figure 31a.

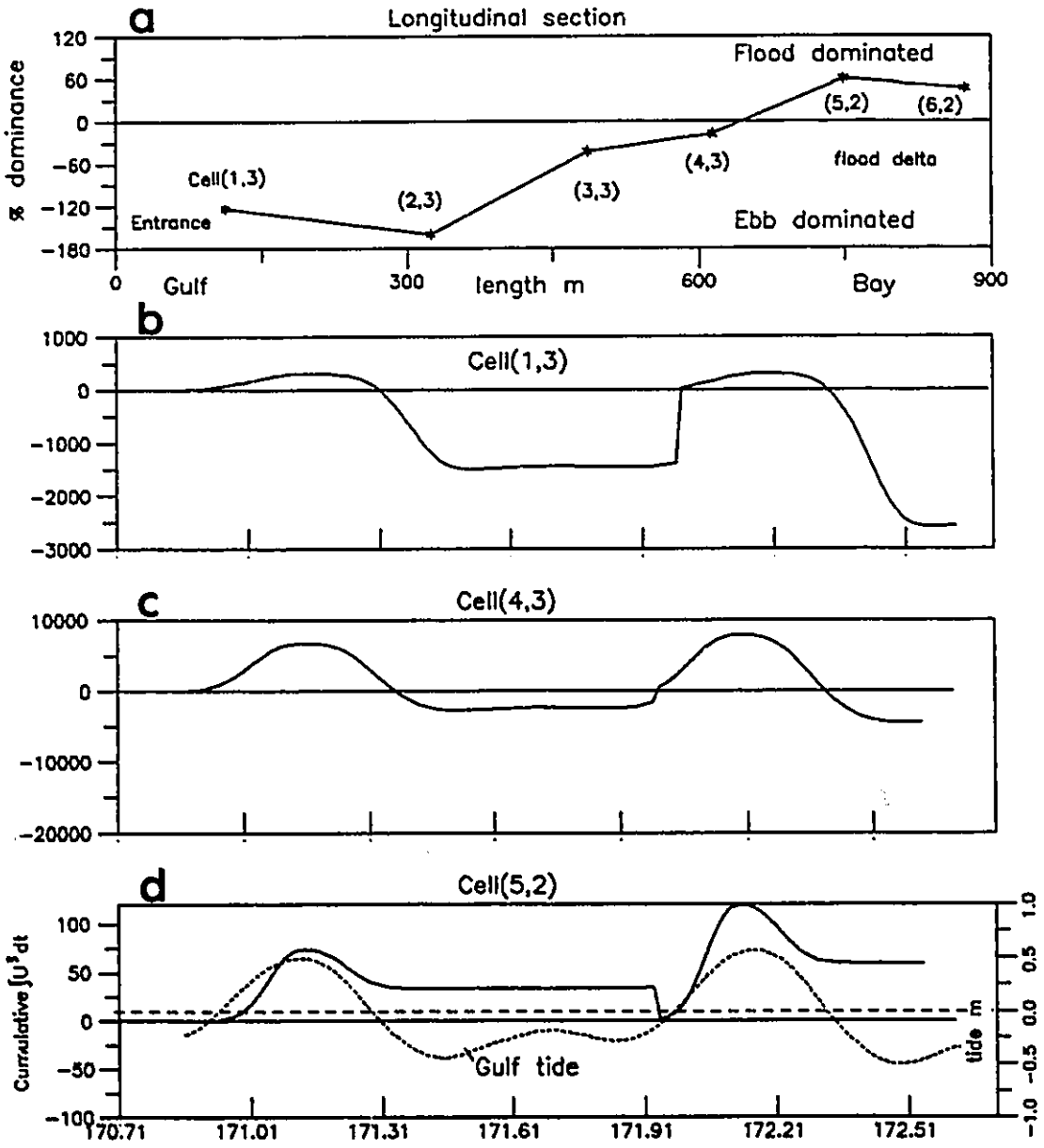
a
Longitudinal section
% dominance
120
60
0
-60
-120
-180
Flood dominated
(5,2)
(6,2)
(4,3)
flood delta
Cell(1,3)
(2,3)
(3,3)
Entrance
Ebb dominated
0
Gulf
300
length m
600
Bay
900
b
Cell(1,3)
1000
0
-1000
-2000
-3000
c
Cell(4,3)
10000
0
-10000
-20000
d
Cell(5,2)
Cumulative ∫U³dt
100
50
0
-50
-100
Gulf tide
tide
1.0
0.5
0.0
-0.5
-1.0
170.71
171.01
171.31
171.61
171.91
172.21
172.51

cumulative curve.

The first impression about these Figures is that the sense of the net sediment transport is not uniform across the inlet, but varies from location to location. The variation, however, follows a pattern, which appears to be very much a function of water depth. Along the transverse section (Figure 30a), the spit shoal (cell(4,1) and cell(4,2)) is strongly flood-dominated; at no time does the cumulative curve fall below the zero line (Figure 30b). On the other hand, the thalweg of the channel (cell(4,3), cell(4,4)) is ebb-dominated. Around the midtide of the ebb, the net transport (indicated by the cumulative curve in Figure 30c) was already in the ebb direction. The right bank of the channel, represented by cell(4,6) is also flood dominated. Therefore, from the deepest portion of the channel to the shallow banks on both sides, there is a transition from ebb dominance to flood dominance.

Flow dominance and associated cumulative transport in the longitudinal direction (Figure 31) exhibit a similar pattern. The deep part of the channel is dominated by ebb currents. The ebb dominance increases in the seaward direction from cell(4,3) to cell(1,3) (Figure 31a). During most of tidal cycles, the net transport in cell(1,3) is in the seaward direction (Figure 31b). In the landward area, where the flood tidal delta is located, the net sediment transport is in the flood direction.

The overall pattern of the net sediment transport suggests that topography plays an important role in controlling flow dominance at Palmer Inlet. In general, the shallow area is dominated by flood currents, while the deep part of the channel is dominated by the ebb currents. In the longitudinal direction, the ebb dominates the seaward part of the inlet and the flood dominates the bayward part. These observations are in line with the general pattern of measured current data, as is illustrated in Figure 2-17 in Chapter 2. Inlet morphology, bedform data and sedimentary structures also support these observations.

The above flow dominance pattern is very similar to that found in the parametric studies. Parametric studies show that such a pattern owes its origin to the existence of the flood delta and the spit platform, and that their overall effect is in favour of the flood. The same conclusion can be made for the present case of Palmer Inlet. This observation is very important as it provides an explanation for the contradiction observed at Palmer Inlet, mentioned in the Introduction. That is, a large flood delta exists in a tidal system that is ebb-dominated. The existence of the sand bodies favours the flood; this creates a force that is directed inward. This force acts against the ebb, which thus becomes more or less balanced with the flood. With waves pushing bayward, the sediment transport regime is then flood-dominated. This combined inward force

is strong enough to transport sediment past the inlet gorge. The delta region is flood-dominated, and there is little sediment transported around it during the ebb. Sediments once deposited in the delta region will stay there. The rear compartment is thus a sediment storage area.

Sediments left in the throat channel tend to be flushed back to the sea, because of the slightly ebb-dominated flow there. This accounts for the continuous growth of the flood delta, and other similar shallow shoals. It also explains why the main channel of Palmer Inlet can keep itself relatively open even though the system as a whole is clogged with sand.

4.7 Tidal Division between Palmer and Alberton Inlet

Tidal division here refers to the ratio between the tidal prisms carried by Alberton Inlet and Palmer Inlet. The tidal prism represents the total water carried into the bay during each of the half tide, and is thus an important parameter in inlet characterization. The model results indicated that Alberton Inlet carried about five to seven times more tidal prism than Palmer Inlet. Table 2 (Cycle II) and Figure 29b show that Alberton Inlet carries a tidal prism of 1.7 10^7 m^3 for the flood and 2.4 10^7 m^3 for the ebb and have peak discharge 1079 m^3/s and -979 m^3/s respectively. The corresponding figures for Palmer Inlet are 3.2 10^6 m^3 and -3.6 10^6 m^3 for tidal prisms and 219 m^3/s

and -171 m^3/s for discharges. These figures can be questioned, however, since the model was only adjusted for Palmer Inlet. No currents were measured in Alberton Inlet during the calibrated periods. There were data measured during other period, however. For the purpose of comparison, discharges were calculated from these data. Currents were measured simultaneously in Alberton and Palmer Inlet (triangles in Figure 24) for a small tide in Aug. 10 to 11, 1986 (tidal range = 0.45 m) and for a medium tide in Aug. 15 to 16, 1986 (tidal range = 0.76 m). These data were converted to those of tidal ranges equivalent to that of Cycle II of the calibration. In the conversion, it is assumed that the velocity measured 1 meter off the bed represent the cross section mean values and the relationships between tidal range and maximum velocities developed in Chapter 4, Part I, apply to the entire cycle. These relationships are:

(1) Max. speed = 1.04 (tidal range) + 0.11 for floods;

(2) Max. speed = 0.97 (tidal range) - 0.16 for ebbs.

Thus, for example, the ebb tidal range of Cycle II is 1.07 m, whereas the ebb range for Aug. 15-16 is 0.81 m. The velocities calculated from (2) with these tidal ranges are 1.19 m/s and 0.94 m/s, respectively. The ratio between them is 1.19/0.94 = 1.26. The velocities measured during that ebb period were then multiplied by 1.26. The resultant velocities were multiplied by a constant cross section area

of 1300 m^2 for Alberton Inlet and 280 m^2 for Palmer Inlet. The discharges thus calculated for flood and ebb are plotted in Figure 32, together with the measured velocity and the gulf tide.

Figure 32 shows that the 'measured' tidal prisms are of the same order of magnitude as the predicted ones. The 'measured' flood tidal prisms for the two measurements are 2.6 10^7 m^3 and 1.7 10^7 m^3 for Alberton and 3.6 10^6 m^3 and 2.1 10^6 m^3 for Palmer Inlet. The tidal division ratio is 7-8. The ebb prisms are 1.8 10^7 m^3 and 3.0 10^7 m^3 for Alberton Inlet and 3.4 10^6 m^3 and 4.1 10^6 m^3 for Palmer Inlet, which gives a tidal division ratio of 5-7. Armon (1975) conducted a simultaneous cross section measurements of current velocities at Alberton and Palmer during a medium ebb tide on July 24, 1974. His calculations gave an ebb prism of 2.1 10^7 m^3 for Alberton and 3.4 10^6 m^3 for Palmer Inlet, the former carrying 6.2 times more water than the latter. Therefore, despite the uncertainties involved, the general similarity and correspondence in these values encourage faith in the capability of the model to predict the right order of magnitude for tidal prism both in absolute and relative terms. It is thus believed that Alberton Inlet carries about 6-7 times of more water than Palmer Inlet in communication with the gulf. In exchange of sediments and nutrients with the gulf and controlling salinity and temperature of the bay, Alberton Inlet plays a

Figure 32

a and c. Simultaneously measured velocities of Alberton and Palmer inlet for a small tide, August 10-11, 1986 (a) and a medium tide, August 15-16, 1986. Current meter stations are marked in Figure 24 (triangles). Currents were measured one metre off the bottom using an Aanderaa CM4 meter. Currents in Alberton inlet were stronger than those in Palmer inlet. Also plotted are predicted gulf tide.

b and d. Estimated discharges and tidal prisms (Figures) for Alberton and Palmer inlet based on data in Figure 32a and c. They are used for comparison with the predicted tidal prisms. The tidal range and the maximum velocity relationships developed in Part I are used to convert the measured velocities to those of the same tidal range as Cycle II of the calibration of the model. The resultant velocities are then multiplied by the cross-section areas, assumed constant for both of the inlets, to obtain the discharges. Tidal prisms are time integral of discharges for the flood and ebb half-cycle.

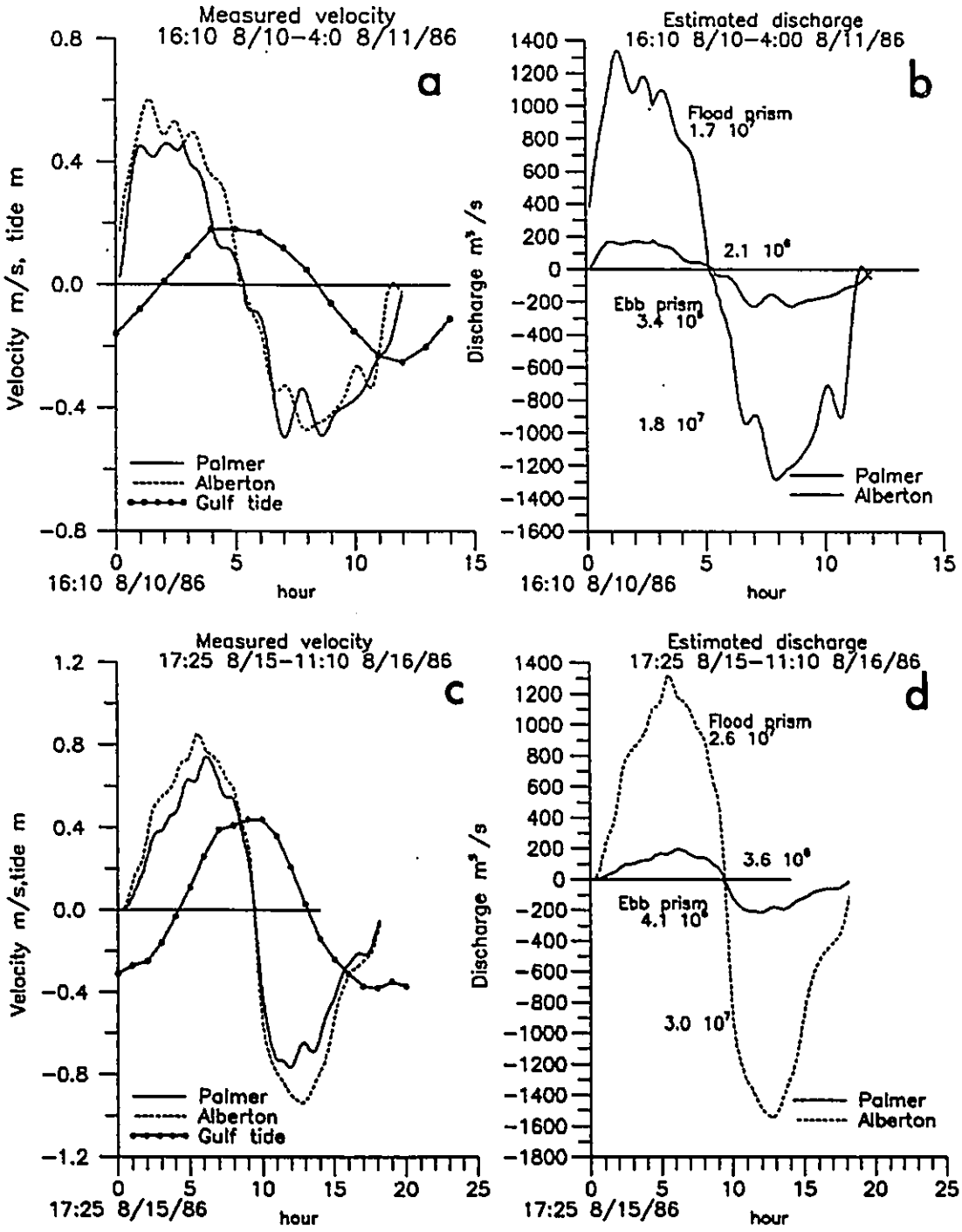
Measured velocity
16:10 8/10–4:0 8/11/86
a
Velocity m/s, tide m
Palmer
Alberton
Gulf tide
16:10 8/10/86
hour
Estimated discharge
16:10 8/10–4:00 8/11/86
b
Discharge m³/s
Flood prism
1.7 10⁷
2.1 10⁶
Ebb prism
3.4 10⁶
1.8 10⁷
Palmer
Alberton
16:10 8/10/86
hour
Measured velocity
17:25 8/15–11:10 8/16/86
c
Velocity m/s,tide m
Palmer
Alberton
Gulf tide
17:25 8/15/86
hour
Estimated discharge
17:25 8/15–11:10 8/16/86
d
Discharge m³/s
Flood prism
2.6 10⁷
3.6 10⁶
Ebb prism
4.1 10⁶
3.0 10⁷
Palmer
Alberton
17:25 8/15/86
hour

much more important role than Palmer Inlet.

4.8 Summary

Results of calibration using data of June 19-21, 1986 indicate that the present model satisfactorily predicted the major aspects of tidal hydraulics for the Palmer-Alberton-Cascumpec Bay system. Computed tidal stage and inlet discharge/velocity agreed well with those measured both in amplitude and phasing. The most serious differences occur during minor tides or weak flow periods. This is attributed to the limitations inherent in the development of the model. Although the cause was not identified, the effect of such limitations is overestimation. Consequently, the model solutions will be more reliable if large tides are used. The errors associated with the model predictions are fairly uniformly distributed in the flood and ebb, therefore, in the long run, the net effect of inlet hydraulics will be less affected.

In addition, it is found that the use of the predicted tide as inlet boundary condition did not introduce any major discrepancies. On the contrary, it tends to smooth the output and thus improve the fit if the measured data are also averaged quantities. Confidence in model predictions can further be enhanced if applications are applied on a long time basis.

Palmer Inlet is friction-dominated. The unsteady

effect due to the oscillatory tide becomes important only for a short period near slacks. In the system, tidal deformation is primarily controlled by the two large sand bodies, the large flood delta and the spit platform. The overall effects of these sand bodies is two-fold: (1) They enhance the flood flow; (2) They create a net sediment transport pattern which is characterized by an ebb-dominated deep channel, and a flood-dominated shoaling area. This explains why a large flood tidal delta exists in Palmer Inlet, while the tide is ebb-dominated. According to the pattern of flow dominance, the flood delta area is a sediment sink, and will continue to grow. The reason Palmer Inlet did not close as quickly as is suggested by its sand-clogged appearance is because the main channel is slightly ebb dominated.

Based on the above determinations, it was decided that in subsequent stability analysis, the predicted tides would be used as the forcing tides. The stability analysis of the dual-inlet system would be carried out only for a large tide, as large tides are the dominant force controlling the stability of inlets. Sediment transport calculations are carried out for a complete large-small tidal cycle of 14 days. To reduce errors at weak flows, threshold values for initiation of sands were applied.

Chapter 5

Stability analysis

5.1 Introduction

Inlet numerical models can be used to generate hydraulic data for inlet stability calculations. Such applications have been used in a number of studies (Mason, 1981; O'Brien and Dean, 1972; van de Kreeke, 1985; Mehta and Brooks, 1973; etc.). An important aspect of stability calculations is to assess the impact of changing flow conditions in the inlet on ecosystems in the bay. Cascumpec Bay is the host to a local fishing harbour, and is the habitat and breeding ground for a number of shell- and marine-fishes. An unstable system will be detrimental to the survival of animals and plants, and to the accessibility of the port as well. While Palmer Inlet has shown evidence of continuing entrapment of littoral sand within the system, a prediction of its inevitable closure based solely on local data is still too speculative. This is because its stability is tied with that of Cascumpec Bay and Alberton Inlet, which for the past 200 years, have shown remarkable stability. A more reliable prediction cannot be made without consideration of the dual-inlet system as a whole.

In this Chapter, the calibrated inlet model is applied to stability analysis of the Palmer-Alberton-

Cascumpec Bay system. In this analysis, the term stability refers to the cross-section stability (Raju et al., 1979), not the locational stability, which was discussed in Part I based on historical and morphology information.

In the following, various methods described in the literature for use in inlet stability analysis are first reviewed (Section 5.2). The review indicates that for a single bay system connected to the sea by more than one inlet, a combination of Seelig's hydraulic model and van de Kreeke's stability model is necessary. The procedure for such a method is then introduced in Section 5.3. In Section 5.4, the results of calculations are presented, and their significance discussed. Section 5.5 is the summary of this Chapter.

5.2 Literature Review

Tidal inlets having a stable cross- section area reflect a dynamic balance between the force of waves attempting to close the inlet and that of tidal flows tending to maintain it (Bruun, 1978). In describing inlet stability under such regime, a number of criteria has been proposed. Bruun and Gerritsen (1960) and Bruun (1965, 1978) proposed a ratio, i.e., the annual total littoral drift (M) and the tidal prism (P), as a measure of the stability. They observed the following relationship (Bruun et al., 1973):

$P/M > 150$	good stability
$50 < P/M < 150$	fair stability
$P/M < 50$	poor stability

The gorge section of the inlet where current speeds reach maximum, however, is usually protected to some extend from wave action, and is primarily maintained by the scouring ability of tidal currents. Other criteria were thus proposed considering only tidal effects (O'Brien, 1969; Mehta and Hou, 1974; Escoffier, 1977). Most authors take the maximum cross section mean velocity, U_{max}, or maximum bottom stress, τ_{max}, as the representatives of this tidal effect (Bruun et al., 1973; 1978; van de Kreeke, 1985). They found that an inlet is stable if the following relationship is satisfied:

$0.9 \text{ m/s} < U_{max} < 1.1 \text{ m/s}$ (Bruun, 1978)

$3.5 \text{ N/m}^2 < \tau_{max} < 5.5 \text{ N/m}^2$ (Bruun, 1978)

O'Brien (1969), Johnson (1973) and Jarrett (1974) argued that tidal effects can be better represented by a time-integrated, rather than an instant, quantity. The quantity they proposed to use is the tidal-cycle-integrated discharge, or tidal prism. Regression analysis indicated that this quantity can be closely correlated to cross sections of the equilibrium inlets in the following form:

$$A_c = b\ P^n$$

The value of coefficients, b and n, however, vary for different tidal and wave conditions between various coasts. Some samples of are given in Table 3 (Jarrett, 1976):

Table 3 Values of b and n

coast	b		n
	SI unit	English unit	
Atlantic	$2.26\ 10^{-5}$	$0.37\ 10^{-6}$	1.07
Pacific	$8.95\ 10^{-6}$	$1.91\ 10^{-6}$	1.10
Gulf of Mexico	$7.00\ 10^{-4}$	$3.51\ 10^{-4}$	0.86

The stability of an inlet, however, is not static (Winton, 1979; Bruun, 1978), but subject to alterations which can be the result of any of the following factors, or a combination of them: 1) Spitting into two or more branches of the inlet channel (Bruun and Gerritsen, 1960); 2) Abnormal deposition/erosion during storms (van de Kreeke, 1985); 3) Changes in the bay area; 4) Opening or changing conditions of an accompanying inlet; and 5) Daily or seasonal fluctuations of tides (Mehta and hou, 1974; Byrne et al., 1974). Change in the cross section area from the equilibrium state will result in corresponding changes in the inlet current velocity. This concept was used by

PAGINATION ERROR.

TEXT COMPLETE.

ERREUR DE PAGINATION.

LE TEXTE EST COMPLET.

NATIONAL LIBRARY OF CANADA.

CANADIAN THESES SERVICE.

BIBLIOTHEQUE NATIONALE DU CANADA.

SERVICE DES THESES CANADIENNES.

Escoffier (1940) in inlet stability analysis. Its modified version, with the equilibrium A_c α P relationship superimposed (Escoffier, 1970; O'Brien and Dean, 1972) was illustrated in Figure 15b, Chapter 3. The basic idea of the diagram is recapitulated here. The diagram is divided into two areas by a vertical line passing through the peak of the curve. An inlet to the right of the line is stable, because it has the ability to counteract any changes, deposition or erosion, and brings the inlet its original stage at point A. An inlet to the left of the line does not have that ability, and therefore is unstable. Point A is a stable equilibrium point, and point B an unstable equilibrium point.

Van de Kreeke (1984 and 1985) expanded Escoffier's concept to include a bay, which is connected to the ocean by two or more inlets. For a dual inlet-system, the stability diagram is a three dimensional variation of Figure 15b. This is qualitatively illustrated in Figure 33a. The 'closure' and 'equilibrium' curves of Figure 15b are replaced by equilibrium surfaces. The two surfaces intersect at a line, whose projection onto the horizontal plane forms the equilibrium curve, at which $U_{max} = U_{eq}$, i.e., inlets are in the equilibrium state. As in the single inlet case, the line (dot-dash, Figure 33a) divides a stable and unstable area. Therefore, point 1 on the graph is in the unstable area (left of the dot-dash line), and the inlet it represents is in the shoaling state, and will be eventually

Figure 33

a. Block diagram showing closure surface and equilibrium stress surface for a double inlet system (van de Kreeke, 1985). Note that there is a similar diagram pertinent to Inlet II. The equilibrium curve is the projection of the intersect line of the two surfaces onto the horizontal plane. It consists of all the loci at which true equilibrium is attained. The dot-dash line passing through the peak of the equilibrium curve divides an unstable area (to the left) and a stable area (to the right) for Inlet I. Following the same reasoning as in Figure 14b, point 1 is unstable and will shoal and close. Scour will occur at point 2 and shoaling occur at point 3; but both will become stable as they reach the equilibrium curve.

b. Equilibrium curves for Inlet I and Inlet II (van de Kreeke, 1985). The cross hatched area represents the co-stable area in which the conditions of equilibrium for both inlets exist simultaneously.

a

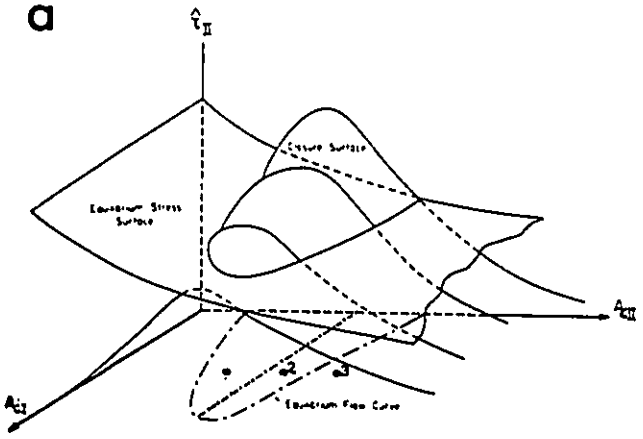
$\hat{\tau}_{II}$
Equilibrium Stress Surface
Failure Surface
A_{cII}
A_{cI}
Equilibrium Flow Curve

b

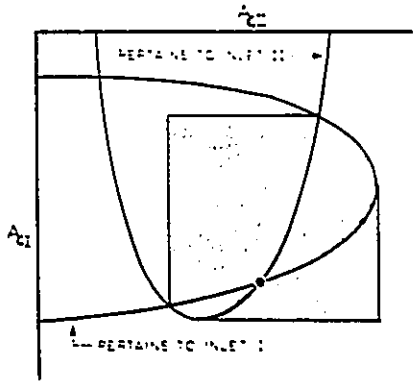
$\dot{\gamma}_{cII}$
A_{cI}

closed. Points 2 and 3 are in the stable area (right of the dot-dash line), and inlets represented by them will either scour (point 2) or shoal (point 3) until the equilibrium curve is reached. Figure 33a, however, represents the result of only one inlet (Inlet I). A similar diagram can be constructed for Inlet II. The superimposition of the these two diagrams defines a common stable area, within which the two inlets coexist in an equilibrium state. This common area is shown as cross-hatched in Figure 33b.

The various empirical diagrams for inlet equilibrium described above are rough estimations of inlet stability of inlets. They are convenient measures for quick calculations of stability and can be used if available data is limited. If there are enough data, hydrodynamic calculations using one of the existing models can be used for more accurate evaluations. For example, O'Brien and Dean (1972), Dennis et al. (1978) and Mason (1981) used Keulegan's hydraulic model in conjunction with the stability relationship between U_{max} and A_c, developed by Escoffier (1940), to calculate the stability of four Florida inlets. Escoffier and Walton (1979) studied the stability of two inlets in the Gulf of Mexico and on the Atlantic coast of Florida using a linearized hydraulic model instead. Most of the existing studies, however, dealt with single inlet systems.

5.3 Stability Calculation

The successful calibration of the Palmer Inlet model using field data provides the basis for conducting a stability analysis for the Palmer Inlet system. The basic boundary values used in the calibrated model are retained for the present study. They include the geometries of the two inlets, and Manning's friction factor (0.035) (Figure 24 and Table 1). The numerical model was used to generate U_{max} at various cross-section areas. The output was then fed into the stability model.

Because the system under investigation is a dual-inlet one, the stability model chosen is that of van de Kreeke. van de Kreeke used maximum bottom shear stresses in his diagram. U_{max} was used in the present study because it is the direct output of the numerical model.

To calculate U_{eq} values, i.e., U_{max} at equilibrium, a relationship defining the equilibrium state is needed. The relationship used for this purpose is $A_c \alpha P$ developed for the Gulf of Mexico (Jarrett, 1976):

$$A_c = 7\ 10^{-4}\ P^{.86} \qquad \text{— (16)}$$

The choice of this particular relationship is based on the similarity between the Gulf of Mexico and the Gulf of St. Lawrence. Both areas are wave-dominated; and in both areas, tides are microtidal and have strong diurnal

inequality. Equation (16) is incorporated in the hydraulic model in the following way.

By definition,

$$P = \int_0^{T/2} A_c U \, dt = \int_0^{T/2} Q \, dt$$

Assuming a sine curve for the velocity, U, then

$$U = U_{max} \sin (2\pi t/T)$$

The integration thus yields

$$P = \frac{A_c \, U_{max} \, T}{\pi} \qquad \text{— (17)}$$

Where T = diurnal tidal period = 24.8 hrs. Keulegan (1967) introduced a correction coefficient, C_k, in the denominator of Equation (17) to account for error induced by the sine velocity curve assumption. Keulegan and Hall (1950) found $C_k = 0.86$ gave good agreement with tidal prism determined from current measurements. Introducing C_k and substituting Equation (16) into Equation (17) for P, reorganizing for U_{max} gives

$$U_{max} = U_{eq} = 0.141 \, A_c^{.163} \qquad \text{— (18)}$$

In addition, at each step with a new A_c value, the shape of the cross section has to be specified in order to calculate inlet-channel width and water depth to solve the inlet equation. A number of empirical width/depth relationships are available for choice (Escoffier, 1977; Winton, 1979). Using regime theory adapted from river hydraulics, Escoffier (1977) gave the width/depth relationship for inlets by the formula

$$A_c = A_{c\ new}\ (D/D_{new})^{5/2}$$

Winton (1979) plotted width, W_c, against depth at mean sea level, D, for inlets along the U.S. coastline. The regression line is described by

$$D = 1.164\ W_c^{.19} \qquad \text{for } W_c > 150 \text{ m}$$

The channel in this study, however, was discretized into small cells. As a result of the discretization, the shape of the cells is less irregular than that of the original A_c section. Therefore, instead of using one of the above relationships, in this study, cells are assumed to have (1) constant rectangular cross sectional shape and (2) constant width/depth aspect ratio (same as the present configuration).

With all the above relationships specified, the

calibrated inlet model was used to calculate U_{max} and U_{eq} for cross section areas of

A_{c1} = 15 m^2 to 4800 m^2 — Alberton Inlet

A_{c2} = 10 m^2 to 2800 m^2 — Palmer Inlet

At each run of the model, the cross section area of one inlet, say A_{c2}, was chosen to be constant; A_{c1} was then stepped through the prescribed range (14-19) and the corresponding U_{max} and U_{eq} were calculated. By systematically changing the A_{c2} value, a series of such runs produced a family of closure curves of $U_{max} \alpha A_{c1}$ and equilibrium curves of $U_{eq} \alpha A_{c1}$ for Alberton Inlet (Figure 34). The calculation was then reversed by fixing A_{c1} and generated two similar sets of curves pertinent to Palmer Inlet. These closure curves were used to produce the block diagrams of closure surfaces and equilibrium surface for each of the inlets (Figure 35 and Figure 36) using the commercial software Design Cad 3-D.

5.4 Results and Discussion

The equilibrium curves for Palmer and Alberton Inlet were plotted together in Figure 37. This was produced by projecting the intersect lines of the closure and equilibrium surface for each inlet (Figure 35 and 36) onto

Figure 34 Closure curves for Alberton inlet. For each given cross-section area of Palmer inlet (values given in the legend), the model stepped through a prescribed range of cross-section area (15-4800 m^2) and calculated the corresponding cross section mean maximum velocities for Alberton inlet. Note that for each closure curve, there is a corresponding equilibrium line, calculated using equation (16); but for clarity, only two equilibrium lines are plotted. Note also that the equilibrium line (not shown in the graph) for A_c of Palmer inlet of 2210 m^2 lies far above the corresponding closure curve (solid circle), indicating that there will be no stable area for Alberton inlet if Palmer inlet is as large as 2210 m^2 in cross-section area. There is a similar family of curves for Palmer inlet.

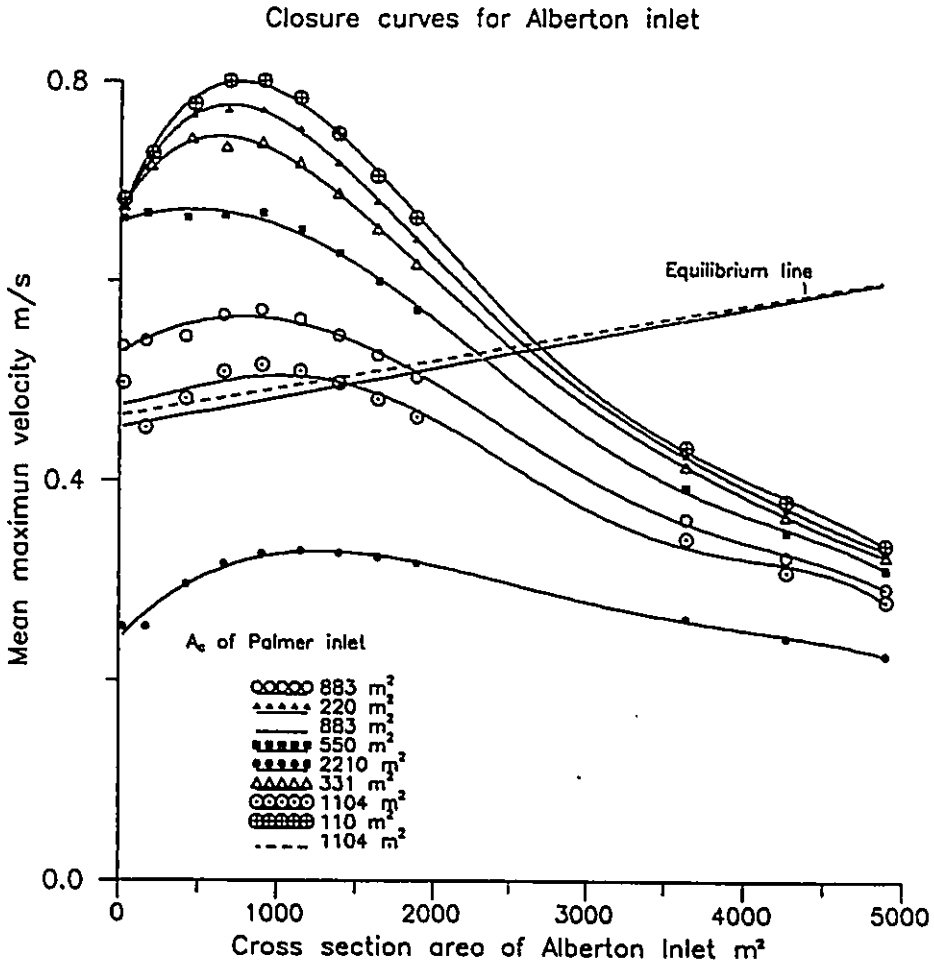
Closure curves for Alberton inlet
0.8
0.4
0.0
Mean maximun velocity m/s
Equilibrium line
A_c of Palmer inlet
883 m²
220 m²
883 m²
550 m²
2210 m²
331 m²
1104 m²
110 m²
1104 m²
0
1000
2000
3000
4000
5000
Cross section area of Alberton Inlet m²

Figure 35 Closure surface and equilibrium surface for Alberton inlet. The block diagram was constructed based on the data shown in Figure 34. The equilibrium curve is the projection, onto the horizontal plane, of the intersection between the equilibrium line and the closure curve in Figure 34. The equilibrium curve consists of all the points where true equilibrium exists for Alberton inlet. The dot-dash line divides an unstable area (to the right) and a stable area (to the left).

Closure surface for Alberton inlet

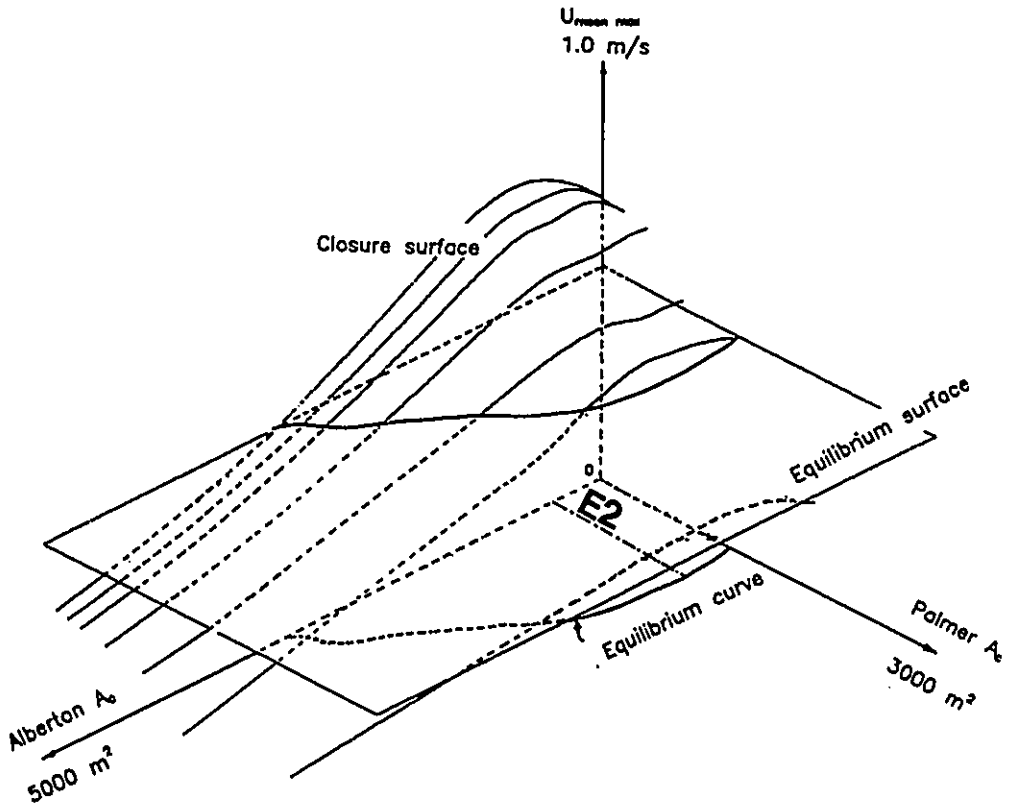

Figure 36 Closure surface and equilibrium surface for Palmer inlet. See Figure 35 for other explanations. The dot-dash line, E1, divides an unstable area (to the left) and a stable area (to the right).

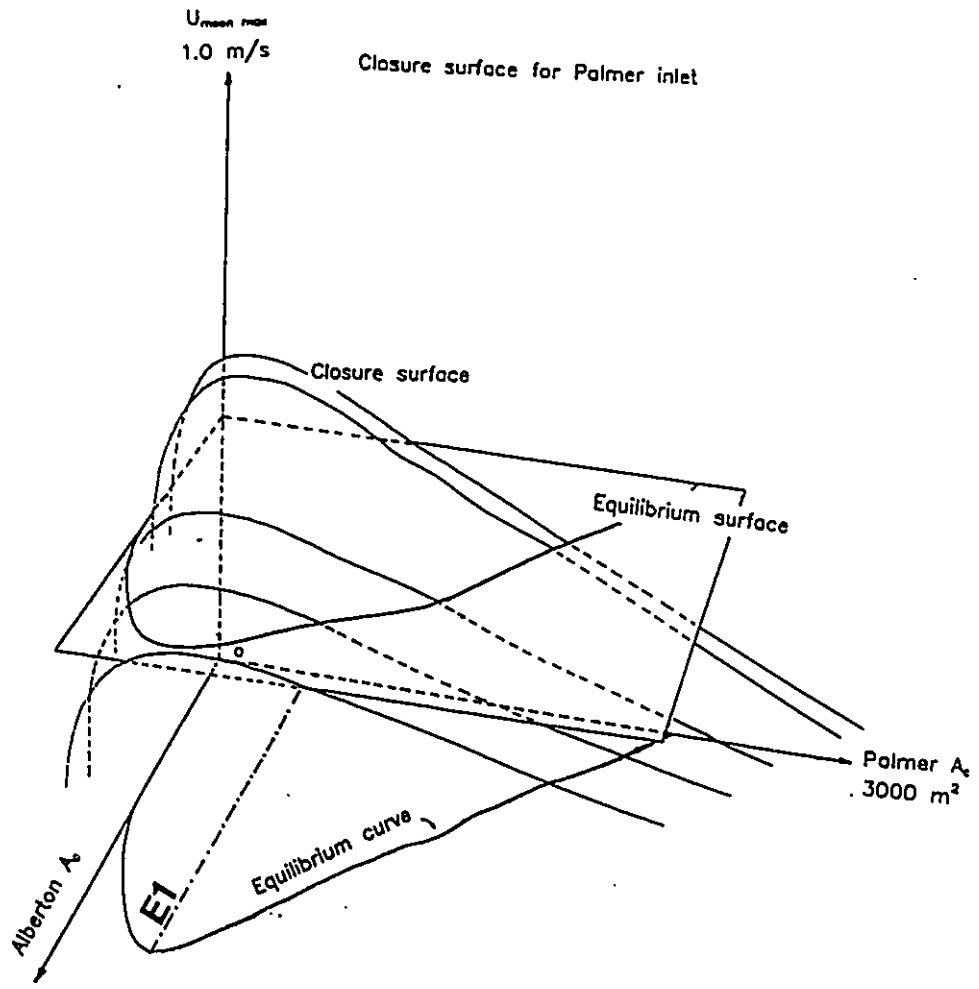
$U_{mean\ max}$
1.0 m/s
Closure surface for Palmer inlet
Closure surface
Equilibrium surface
Palmer A_c
3000 m²
Alberton A_c
Equilibrium curve
E1

Figure 37 Equilibrium curves for Alberton inlet and Palmer inlet. E1 and E2 correspond to the same lines as in Figure 36 and 35. The dash-line rectangle encircle the area in which the two inlets are co-stable. The cross-circle marks the position of Alberton and Palmer inlet in 1986. It falls outside the co-stable area, indicating that the Palmer-Alberton-Cascumpec bay system was not in equilibrium in 1986. The arrow indicates the possible path of evolution of the system if the tendency of acquiring an equilibrium is assumed. The path is a movement away from the co-stable zone. This shows that Cascumpec bay is able to support only one permanent inlet of cross-section area comparable to that of Alberton inlet.

Equilibrium curves for Palmer and Alberton inlet

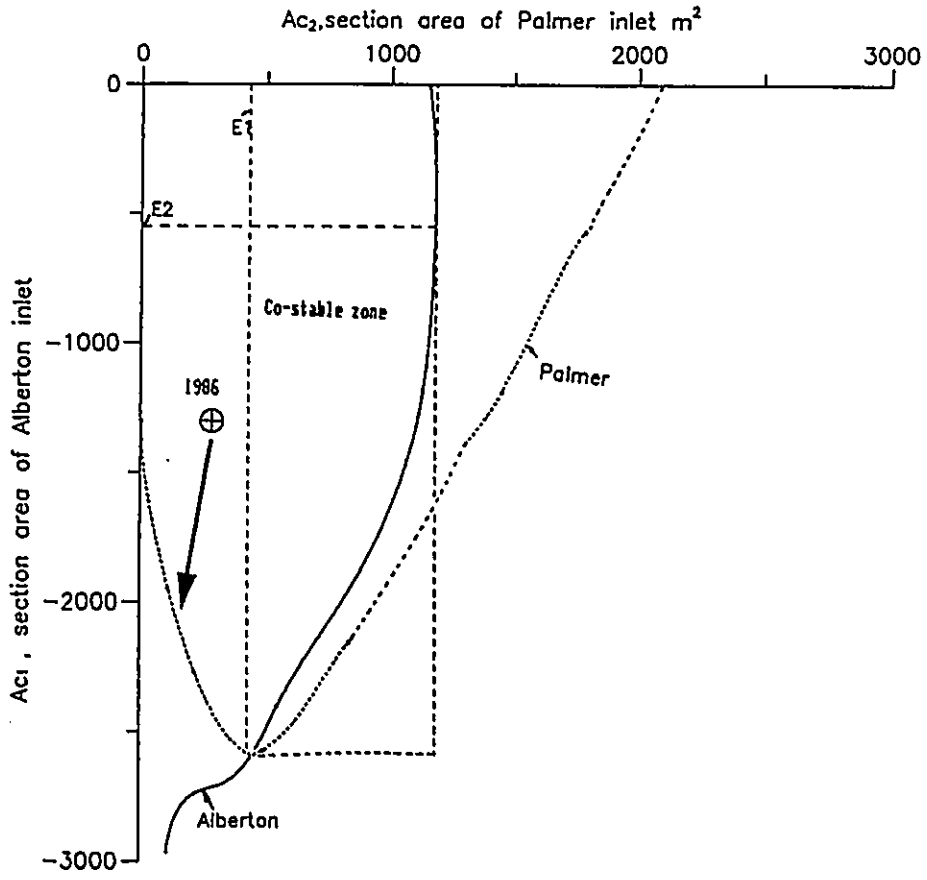

the same (horizontal) plane. The two lines that pass through the peaks (marked with E_1 and E_2) represent the critical cross-section area; they divided the diagram into a stable zone and an unstable zone for each of the two inlets. In 1986, the cross section area of Alberton Inlet was about 1300 m^2 and that of Palmer Inlet is 280 m^2. The locale of this combination is marked with the crossed circle.

Figure 37 shows that the stable areas for each of the inlets overlap to form a co-stable zone (the area bounded by the dashed-lined rectangle). This co-stable zone represents the loci, where conditions of equilibrium for both inlets exist simultaneously. The figure indicates that the conditions of an equilibrium Palmer-Alberton-Cascumpec Bay system for a combination of A_{c1} and A_{c2} do exist. This condition, however, is not satisfied by the 1986 data. This is because the crossed circle falls outside the co-stable area. Armon in 1979 measured the cross section area of Palmer and Alberton Inlet and found they were 365 m^2 and 1600 m^2 respectively. The 1987 survey indicated that the cross section area of Palmer Inlet was 250 m^2, slightly less than that in 1986, while Alberton Inlet remained essentially unchanged. Data points with these combinations still fall outside the co-stable zone. It thus appears that during the past decade, this double inlet system was in not in equilibrium with the existing hydraulic environment.

The diagram can be use to examine the stability of

each inlet separately. The diagram shows that Palmer is located in the unstable region of its own equilibrium curve (to the left of line E_1, Figure 37), whereas Alberton Inlet is located in its stable area (to the right of line E_2). It thus follows that the observation that the system as a whole is not in an equilibrium state is due to the instability of Palmer Inlet. This instability is due, specifically, to the insufficient cross-section area of Palmer Inlet.

For the system to achieve an equilibrium condition, the cross section area of Palmer Inlet must be increased. This naturally requires a corresponding decrease in the cross-sectional area of Alberton Inlet if no change in tidal prism is assumed. Geological evidence, however, indicates that this did not occur in the past. It also highly unlikely that it will occur in the future. On the contrary, in its effort to bring the system into the equilibrium, Alberton Inlet will capture some tidal prism from Palmer Inlet. This will cause an increase in the cross section area of Alberton Inlet. The result will be a further deterioration of Palmer Inlet. That is, the system will follow, in its effort to achieve equilibrium, the path as shown by the arrow in Figure 37. Therefore, in the absence of drastic changes in inlet reorganizations, such as 1), 2), 3), 4) listed in the review section, Palmer Inlet will ultimately be closed.

The cross section area of an inlet of a stable

system depends on the tidal volume it shares. The direction of the arrow in Figure 37 indicates that the Palmer-Alberton-Cascumpec system is moving away from the co-stable area (the rectangle) in order to attain system equilibrium. This means that although Cascumpec Bay is able to support two inlets (because of the existence of the co-stable area), its present size and tidal prism can only maintain one permanent stable inlet of a size comparable with that of Alberton Inlet. In the event that storm surges breach the barrier after the closure of Palmer Inlet, the openings will be closed by subsequent normal wave actions and associated littoral drift, as long as Alberton Inlet remains as it is. Such event possibly happened in 1845 when, as Armon (1975) documented, there were two inlets opened directly into the bay. The closure of these inlets is good evidence that Cascumpec bay is capable of supporting only one stable inlet of a size comparable with that of Alberton. One of these ephemeral inlets had a life span of 67 years, existing from 1845 to 1912. Palmer Inlet is probably just such a temporary inlet created by storms, and will have a similar life span if other conditions remain approximately similar. It is probable, therefore, that it will be closed within the next 15 years.

The instability of an inlet should be reflected in its morphological and depositional pattern. Although Palmer and Alberton Inlets both appear to be sand trappers of

littoral drifts, the depositional patterns at the two inlets are quite different. At Palmer Inlet, sand is trapped either within the entrance as spit shoals, or in the rear compartment as the flood tidal delta. The ebb tidal delta is comparatively small. Field investigations and numerical simulations provide strong evidence that at present net flood-dominated transport prevails in most shoaling areas. Only in the deepest part of the channel is the flow able to clear the sand, and maintain a relatively open channel. Because of the flood-dominated nature of the inlet, the sand entrapment within and beyond the throat is expected to continue. Further siltation will mainly take place in the rear entrance of the inlet and the final closure of the inlet will be due to the clogging of the landward channels.

On the other hand, littoral sand at Alberton Inlet is trapped on the seaward side of the inlet. Alberton Inlet has a large ebb tidal delta, which extends 1500 m offshore. The spit platform is also substantial on both sides of the entrance. In contrast, the flood tidal delta is essentially absent. These facts strongly suggest that Alberton Inlet was and will still be very stable.

5.5 Summary

In this Chapter, the stability of Palmer-Alberton-Cascumpec Bay is considered through hydrodynamic calculations. The method used is a combination of three

earlier developed techniques:

(1) a calibrated form of Seelig's spatially integrated numeral inlet model (1976);

(2) van de Kreeke's stability model for multiple inlet-systems; and

(3) Jarrett's $A_c \alpha P$ equilibrium relationship (1976).

The results of the hydraulic calculation indicate that the Palmer-Alberton-Cascumpec Bay system as a whole is currently not in an equilibrium state. The system with its present tidal prism is only able to support a single inlet of the size of Alberton Inlet. To accommodate this, Palmer Inlet, which the analysis indicates is unstable, is going to be closed. This prediction is in line with geological evidence which indicates that Palmer Inlet is in its mature stage of siltation, and with the fact that flood currents currently prevail in most areas. Although the barrier island is being eroded during storm overwash, there appears to be no possibility of a new inlet being established permanently. Such breakthroughs will be closed by wave-induced littoral drifts as has happened to two ephemeral inlets in the past.

Summary of Part II

Part I described hydraulic data measured at Palmer Inlet, but left some basic questions unanswered. Why does a large flood tidal delta exist in a tidal system in which the ebb phase dominates? What is the reason that the bay tide at Palmer Inlet rises more quickly and falls more slowly than the gulf tide? To answer these questions, a series of numerical simulations were made in Part II using Seelig's spatially-integrated inlet model. The effects of various physical and hydraulic parameters on tide/current responses were examined using idealized cases. These include the flood tidal delta, the spit platform, the bay surface area and bay wall slope, the throat cross-section area and its slope, friction, effects of a second inlet, etc. The model, adjusted with measured data, was then applied to calculate inlet hydraulics at Palmer Inlet. It was then used to calculate the equilibrium curves in combination with van de Kreeke's stability model. As the model is configured after a class of tidal inlets typified by a restricted throat, a large flood delta and spit platform, the findings obtained in this study are applicable in general with respect to the microtidal inlets, and in particular with respect to Palmer Inlet. The main conclusions drawn from the model studies are:

(1) Seelig's spatially-integrated numerical inlet model is a useful tool for examination of inlet hydraulics without spending large amount of time and money. It can be used as a supplement to field-oriented program. The present study found that the model is well-behaved. The transient effect disappears within the first half cycle of the tide after the model is started. It can accurately predict the bay tide, and reasonably well predict tidal flow.

(2) Many factors affect inlet hydraulics. The observed hydraulics is the net result of the effects of these factors. Parametric studies provide an effective way to isolate the effect of each factor.

(3) Tidal asymmetries are related to the non-linearities in the dynamic equation, and also arise through the interactions between them. Geometries, such as bay surface area, inlet cross section and internal sand bodies, are other important sources of tidal asymmetry. Their interactions with other dynamic terms and with the rise and fall of tide can have large non-linear effect on the flood and the ebb flows.

(4) Small tidal inlets with water depths not much greater than the tidal range are friction-dominated. Friction exceeds inertial terms over most of the tidal cycle, except in a short period near slack when current speed is very low.

(5) The existence of the two large sand bodies, the

flood tidal delta and the spit platform, affects non-linearly both the resistance and the cross-sectional area of the system. The sand bodies have larger effects on inlet hydraulics than the values of manning's friction coefficient. Unlike the friction, their effects are not uniform across the inlet. They cause flood-dominance in the shoaling area, and ebb-dominance in the deep channel. This pattern is consistent with the measured flow data, and with sediment characteristics at Palmer Inlet. It explains how the main channel at Palmer Inlet is able to remain open even though the system is increasingly clogged with sand.

(6) In mesotidal inlets, the marshlands play an important role, and cause ebb-dominance. In microtidal inlets, the flood tidal delta and the spit platform play the most important role. The overall effect of these sand bodies is a flood-dominance with the bay tide rising more rapidly and falling more slowly than the tide outside the inlet. Therefore, despite the long ebb runouts, the sediment transport is more or less balanced. With the wave pushing sand inward, the net sediment transport is flood-directed. This answers the question why a large flood delta exists in a tide which is ebb-tide-dominated.

(7) The Palmer-Alberton-Cascumpec Bay system is currently not in an equilibrium state. The tidal prism in the system is able to support only a single inlet of the size of Alberton Inlet. Palmer Inlet is the one which is

unstable, and expected to close. This prediction is in line with geological evidence which indicates that Palmer Inlet is in its mature stage of siltation, and with the fact that flood currents currently prevail in most areas.

Part II References

Ackers, P., and White, W. R., 1973. Sediment transport: new approach and analysis. Journal of Hydraulic Division, Proceeding of American Society of Civil Engineering, HY11, 2041-2060.

American Society of Civil Engineers, 1975. Sedimentation Engineering. Manual No. 54, Task Committee on sediment transport, American Society of Civil Engineering, 145p.

Armon, J.W., McCann, S.B., 1979. Morphology and landward sediment transfer in a transgressive barrier island system, Southern Gulf of St. Lawrence, Canada. Marine Geology, 31, 333-344.

Armon, J.W., 1975. The dynamics of a barrier island chain, Prince Edward Island. Unpublished Ph.D, Thesis, Department of Geography, McMaster University, Hamilton, 546p.

Armon, J.W., 1980. Changeability in small flood tidal deltas and its effects, P.E.I. In S.B. McCann ed., The Coastline of Canada, Geological Survey of Canada Paper 80-10, 65-79.

Aubrey, D. G., and P.E. Speer, 1985. A Study of nonlinear tidal propagation in shallow inlet/estuarine system. Part I: Observations. Estuarine, Coastal and Shelf Science, 21, 185-205.

Bagnold, P. A., 1963. Mechanics of marine sedimentation. In: Hill, M.N., ed., The Sea, 3., Wiley-Interscience, New YorK, N,Y., 507-582.

Baijker, E.W., 1967. Some considerations about scales for coastal models with moveable beds. Deft Hydraulics Laboratory Report No. 50, 142p.

Black, K., 1987. A numerical sediment transport model for application to natural estuaries, harbors and rivers. In Noye, J., ed., Numerical Modelling: Applications to Marine system. Elsevier Science Publishers B.V. (North Holland).

Bayliss-Smith, T. P., Healey, R., Lailey, R., Spencer, T., and Stoddart, D. R., 1979. Tidal flows in salt marsh creeks. Estuarine, Coastal and Marine Science, 9, 235-255.

Black, K. P., and Healy, T. R., 1986. The sediment thresh old over tidally induced megarriples. Marine Geology, 69, 219-234.

Black, K. P., and Healy, T. R., 1982. Sediment transport investigations in a New Zealand tidal inlet. Proceedings of 18th Coastal Engineering Conference, American Society of Civil Engineering, Cape Town, South Africa, 3, 2436-2455.

Boon, J. D., 1975. Tidal discharge asymmetry in a salt marsh drainage system. Limnology and Oceanography, 20, 71-80.

Boon, J. D., and Byrne, R.J., 1981. On Basin Hypsometry and the Morphodynamic Response of Coastal Inlet Systems. Marine Geology, 40, 27-80.

Boothroyd, J. C., 1985. Tidal inlets and tidal delta. In Davis, R.A., Jr, ed., Coastal Sedimentary Environments, 2nd edition, Springer-Verlag, New York, 445-525.

Brown, E. I., 1928. Inlets on Sandy Coasts. Proceedings of American Society of Civil Engineering, 54, Part 1, 505-553.

Bruun, P., 1960. Stability of Coastal Inlets. North Holland Publishing Company, Amsterdam, 123p.

Bruun, P. Gerritsen, F., and Bhakta, N. P., 1974. Evaluation of overall entrance stability of tidal entrances. Proceedings of the 14th coastal engineering conference, American Society of Civil Engineering, Copenhagen, Denmark, chapter 41, 1567-1584.

Bruun, P., 1978. Stability of Tidal Inlets, theory and engineering. Elsevier Scientific publishing Company, 510p.

Chang, H. H., 1988. Fluvial Processes in River Engineering. John Wiley & Sons, 432p.

Chen, R. J., and Hembree, J. N., 1977. Numerical Simulation of Hydrodynamics (Tracer). Appendix 3, GITI Report 6, Comparison of numerical and physical models, Masonboro Inlet, North Carolina, U.S. Army Coastal Engineering Research Center, Fort Belvoir, Virginia.

Costa, S. L., and Isaacs, J. D., 1975. Anistropic sand transport in tidal inlets. Symposium on modeling technique, 1, Harbors and Coastal Engineering Division of American Society of Civil Engineering, 254-273.

Costa, S. L., 1978. Sediment Transport Dynamics in Tidal Inlets. Unpublished Ph.D Thesis, University of California, San Diego, 222p.

Dalrymple, R. W., 1977. Sediment Dynamics of Macrotidal Sand Bars, Bay of Fundy. Unpublished Ph.D Thesis, Department of Geology, McMaster University, Hamilton, Ontario, Canada, 635p.

Dean, R. G., 1983. Hydraulics of Port Entrances. UFL/COEL-83/004, Department of Coastal and Oceanographic Engineering, University of Florida, Gainesville.

DeLorenzo, J. L., 1986. The overtide and filtering response of deep inlet/bay systems. Unpublished Manuscript.

Dennis, W.A., Lanan, G.A. and Darlymple, R.A., 1978. Case studies of Delaware's tidal inlets: Roosevelt and Indian River inlets. Proceedings of the 16th coastal engineering conference, American Society of Civil Engineering, Chapter 41, 1282-1301.

Dyer, K. R., and Soulsby, R. L., 1988. Sand transport on the continental shelf. Annual Review of Fluid Mechanics, 20, 295-324.

Einstein, H. A., 1950. The Bedload Function for Sediment Transportation in Open Channel Flows. Soil Conserv. Serv. U.S. Dept. Agriculture Tech. Bull., No. 1026, 78p.

Einstein, H. A., and Barbarossa, N. L., 1952. River channel roughness. Transactions of American Society of Civil Engineering, 117, 1121-1146.

Engelund, F., and Hansen, E., 1967. A Monograph on Sediment Transport in Alluvial Streams. Technisk Vorlag, Copenhagen, 62p.

Environmental Canada, 1986. Station No. 01CA003, Carruthers Brook near St. Aathony. In Surface Water Data, Atlantic Provinces, 119p.

Escoffier, F. F., and Walton, T. L., 1979. Inlet stability solutions for tributary inflow. Journal of Waterways, Harbors and Coastal Engineer Division, American Society of Civil Engineering, WW4, 341-356.

Escoffier, F. F., 1977. Hydraulics and Stability of Tidal Inlets. GITI Report 13, U.S. Army, Corps of Engineers, Coastal Engineering Research Center, Fort Belvoir, Va., and the U.S. Army Engineer Waterways Experiment Station Vicksburg, Miss., 73p.

Escoffier, F. F., 1940. The stability of tidal inlets. Shore and Beach, 8(4), 114-115.

Fitzgerald, D. M., and Nummedal, D., 1983. Response characteristics of an ebb dominated tidal inlet channel. Journal of Sedimentary Petrology, 53, 833-854.

Gadd, P. E., Lavelle, J. W., and Swift, D. J., 1978. Estimates of sand transport on the New York Shelf using near bottom current meter observations. Journal of Sedimentary Petrology, 48, 239-252.

Gallagher, B., 1973. Model for nonlinear tides in small basins with openings of restricted depth. Journal of Geophysical Research, 78(27), 6359-6400.

Guy, H. P., Simons, D. B., and Richardson, E. V., 1966. Summary of alluvial channel data from flume experiments, 1955-1961. U.S. Geological Survey Professional Paper, 462-I, 92p.

Harris, D. L., and Bodine, B. R., 1977. Comparison of Numerical and Physical Hydraulic Models, Masonboro Inlet, North Carolina. GITI Report 6, U.S. Army Coastal Engineering Research Center, Fort Belvoir, Virginia and U.S. Army Engineer Waterways Experiment Station, Vicksburg, Miss.

Hayes, M. O., 1979. Barrier-island morphology as a function of tidal and wave regime. In Leatherman, S.P., ed., Barrier islands — from the Gulf of St. Lawrence to the Gulf of Mexico, New York, Academic Press, 1-28.

Hayter, E. J., 1979. Verification of the Hydrodynamic Regime of a Tidal Waterway Network. Unpublished M.S. Thesis presented to the University of Florida at Gainesville, Florida, 149p.

Healy, T. R., Black, K. P., and de Lange, W. P., 1987. Field investigations required for numerical model studies of port developments in large tidal inlet harbors. In Gardiner, V., ed., International Geomorphology 1986 part I, John Wiely & Sons Ltd., 1099-1112.

Heathershaw, A. D., 1981. Comparison of measured and predicted sediment transport rates in tidal currents. Marine Geology, 42, 75-104.

Huval, C. J., and Wintergerst, G. L., 1977. Simplified Numerical (Lumped Parameter) Simulation. Appendix 4, GITI Report No. 6, Comparison of Numerical and Physical Models, Masonboro Inlet, North Carolina, U.S. Army Coastal Engineering Research Center, Fort Belvoir, Virginia and U.S. Army Engineer Waterways Experiment Station, Vicksburg, Miss.

Isaji, T., and Spaulding, M., 1981. A simplified model for assessing the impact of breachway modifications on coastal pond circulation and flushing dynamics. Proceedings of Ocean 81, Boston, Massachusetts, 824-828.

Jarrett, J. T., 1974. Tidal Prism-Inlet Area Relationships. Draft report on GITI, U.S. Army Engineers, Waterways Experiment Station, Vicksburg, Miss.

Johnson, J. W., 1973. Characteristics and behaviors of Pacific coast tidal inlets. Journal of Waterways, Harbors and Coastal Engineer Division, American Society of Civil Engineering, 99(WW3), 325p.

Kachel, N. B., and Sternberg, R. W., 1971. Transport of bedload as ripples during an ebb current. Marine Geology, 10, 229-244.

keulegan, G. H., 1967. Tidal Flow in Entrances: Water-Level Fluctuations of Basins in Communication with Seas. Technical Report No. 14, Committee on Tidal Hydraulics, U.S. Army Corps of Engineers, Vicksburg, Miss., 83p.

Keulegan, G. H., and Hall, J. V., 1950. A formula for the calculation of tidal discharge through an inlet. U.S. Beach Erosion Board Bulletin, 4(1), 12-29.

Keulegan, G. H., 1951. Water Level Fluctuations of Basins in Communication with Seas. Third Progress Report on Tidal Flow in Entrance, Beach Erosion Board.

King, D. B., 1974. The Dynamics of Inlets and Bays. Technical Report No. 22, Oceanographical Engineering Laboratory, Gainesville, Florida.

Lambiase, J. J., 1977. Sediment Dynamics in the Macro tidal Avon River Estuary, Nova Scotia. Unpublished Ph.D Thesis, Department of Geology, McMaster University, Hamilton, Ontario, Canada, 415p.

Lee, B. J., 1983. The relationship of sediment transport rates and paths to sandbanks in a tidally dominated area off the coast of East Anglia, U.K. Sedimentology, 30, 461-483.

Ludwick, J. C., 1975. Variations in the boundary drag coefficient in the tidal entrance to Chesapeake Bay, Virginia. Marine Geology, 19, 19-28.

Masch, F. D., Brandes, R. L., and Reagan, J. D., 1977. Numerical Simulation of Hydrodynamics (WRE). Appendix 2, GITI Report 6, Comparison of numerical and physical models, Masonboro Inlet, North Carolina, U.S. Army Coastal Engineering Research Center, Fort Belvoir, Virginia.

Mason, C., 1981. Hydraulics and Stability of Five Texas inlets. Miscellaneous Report No. 81-1, U.S. Army Corps of Engineers, Coastal Research Center, Fort Belvoir, Virginia.

Mayor-Mora, R. E., 1973. Hydraulics of Tidal Inlets on Sandy Coasts. HEL-24-16, Hydraulic Engineering Laboratory, University of California, Berkeley, California, 241p.

McCann, S. B., Reinson, G. E., and Armon, J. W., 1977. Tidal inlets of the Southern Gulf of St. Lawrence, Canada. In Coastal Sediments 77. Fifth Symposium of the Waterway, Port, Coastal and Ocean Div. of the ASCE, 504-519, Charleton, S. C.

McCann, S.B., Reinson, G.E., and Armon, J.W., 1977. Tidal inlets of the Southern Gulf of St. Lawrence, Canada. In Coastal Sediments 77. Fifth symposium of the Waterway, Port, Coast and Ocean Division of ASCE, Charleston, S.C., 504-519.

Mehta, A.J. and Brooks, H.K., 1973. Mosquito lagoon barrier beach study. Shore and Beach, 4(2), 27-34.

Mehta, A. J., and Hou, H. S., 1974. Hydraulic constants of tidal entrances II: Stability of Long Island inlets. Technical Report, AD/A-004 992, Coastal and Oceanographic Engineering Laboratory, University of Florida, Gainesville, Florida, 88p.

Mehta, A. J., and Ozsoy, E., 1978. Inlet Hydraulics. In Bruun, P., ed., Stability of Tidal Inlets, Elsevier Scientific, Publishing Company, New York, 83-161.

Mehta, A. J., 1978. Bed friction characteristics of three tidal entrances. Coastal Engineering, 2, 69-83.

Middleton, G.V., and Southard, J.B., 1984. Mechanics of Sediment Movement. Society of Economic Paleontologists and Mineralogists, Short Course No.3, Providence, Ma.

Mota Oliveira, I. B., 1970. Natural flushing ability in tidal inlets. Proceedings of the 12th Coastal Engineering Conference, American Society of Civil Engineers, Washington, D.C, 1827-1845.

O'Brien, M. P., and Dean, R. G., 1972. Hydraulic and sedimentary stability of coastal inlets. Proceedings of the 13th coastal engineering conference, Vancouver, Canada, American Society of Civil Engineering, VII, 761-780.

O'Brien, M. P., 1969. Equilibrium flow areas of tidal inlets on sandy coasts. Journal of the Waterways and Harbors Division, American Society of Civil Engineering, 95(WW1), Proc. Paper 6405, 43-52.

O'Brien, M. P., and R.R. Clark, 1974. Hydraulic Constants of Tidal Entrances. Proceedings of the 14th Coastal Engineering Conference, 2, American Society of Civil Engineering, Copenhagen, Denmark, 1546-1565.

Pickrill, R. A., 1986. Sediment pathways and transport rates through a tide-dominated entrance, Rangaunu Harbour, New Zealand. Sedimentology, 33, 887-898.

Raju, V. S., Varma, P. U., and Pylee, A., 1979. Hydrographic characteristics and tidal prism at the Cochin Harbour mouth. Indian Journal of Marine Science, 8, 78-84.

Reinson, G.E., 1980. Variations in tidal inlet morphology and stability, northeast New Brunswick. In S.B. McCann, ed., The Coastline of Canada. Geological

Survey of Canada, Paper 80-10, 23-39.

Robinson, I.S., Warren, L. and Longebottom, J,F., 1983. Sea level fluctuations in the fleet, an English tidal lagoon. Estuarine, Coastal and Shelf Science, 16, 651-668.

Seagergh, W. C., and Sager, R. A., 1977. Supplementary Tests of Masonboro Inlet Fixed-Bed Model. GITI Report 18, U.S. Army Coastal Engineering Research Center, Fort Belvoir, Virginia.

Seelig, W. N., Harris, D. L., and B.E.Herchenroder, 1977. A Spatially Integrated Numerical Model of Inlet Hydraulics. GITI Report No.14, U.S. Army Coastal Engineering Research Center, Fort Belvoir, Virginia, 100p.

Seelig, W., and Sorensen, R. M., 1978. Numerical model investigation of selected tidal inlet-bay systems characteristics. Proceedings of the 16th Coastal Engineering Conference, American Society of Civil Engineering, 1302-1319.

Seeling, W., 1976. Computer Program Documentation. Unpublished Report, U.S. Army Coastal Engineering Research Center, Ft. Bolvoir, VA.

Semdin, O. H., and R.M. Forney, 1970. Tidal motions in bays. Proceedings of 12th Coastal Conference, 3, American Society of Civil Engineering, Washington, D.C, 2224-2242.

Sorensen, R. M., and Seelig, W., 1976. Hydraulics of Great Lake inlet-harbors systems. Proceedings of the 15th Coastal Engineering Conference, Honolulu, Hawaii, American Society of Civil Engineering, 1646-1665.

Stauble, D. K., Costa, S. L. Da, Monroe, K. L., Bhogal, V. K., and Vassal, G. de., 1987. Sediment dynamics of a sand bypass inlet. Coastal Sediments '87, Vol. II, Proceedings of a Specialty Conference on advances in Understanding of Coastal Sediment Processes, New Orleans, Louisiana, May, 12-14, 1987. p. 1625-1639

Sternberg, R. W., 1972. The bottom boundary layer of shelf seas. In: Swift, D. J. P., Duane, D. B., and Pikey, O. H. Jr., ed., Shelf Sediment Transport, Stroudsburg, Pennsyl vania: Dowden, Hutchinson and Ross, 61-82.

Sternberg, R. W., 1968. Friction factors in tidal channels with differing bed roughness. Marine Geology, 6, 243-260.

van de Kreeke, J., 1984. Stability of multiple inlets. Proceedings of 19th coastal engineering conference, American Society of Civil Engineering, 1360-1370.

van de Kreeke, J., 1985. Stability of tidal inlets; Pass Cavallo, Texas. Estuarine, Coastal and Shelf Science, 21, 33-43.

Van den Berg, J. H., 1987. Bedform migration and bed-load transport in some rivers and tidal environments. Sedimentology, 34(4), 681-698.

Van Rijn, L. C., 1984a. Sediment transport, Part I: bed-load transport. Journal of Hydraulic Engineering, American Society of Civil Engineering, 110, 1431-1456.

Van Rijn, L. C., 1984b. Sediment transport, Part II: suspension load transport. Journal of Hydraulic Engineering, American Society of Civil Engineering, 110(11), 1613-1639.

Van Rijn, L. C., 1984c. Sediment transport, Part III: bedforms and alluvial roughness. Journal of Hydraulic Engineering, American Society of Civil Engineering, 110, 1733-1754.

Vanoni, V. A., and Hwang, L. S., 1967. Relation between bed forms and friction in streams. Journal of Hydraulic Division, Proceeding of American Society of Civil Engineering, 93(HY3), 121-144.

Winton, T. C., 1979. Long and short term stability of small tidal inlets. M.S. Thesis, University of Florida, Gainesville, Florida, 135p.

Wright, L. D., 1977. Sediment transport and deposition at river mouths: A synthesis. Geological Society of America Bulletin, 88, 857-868.

Yalin, M. W., 1963. An expression for bedload transportation. Journal of Hydraulic Division, Proceeding of American Society of Civil Engineering, HY3, 89, 221-250.

Yang, C., 1986. On Bagnold's sediment transport equation in tidal marine environments and the practical

definition of bedload. Sedimentology, 33, 465-486.

Zarillo, G. A., and Park, M., 1987. Sediment transport prediction in a tidal inlet using a numerical model: Application to Stony Brook Harbour, Long Island, New York, USA. Journal of Coastal Research, 3(4), 429-444.

Conclusion and Summary of the Thesis

On the microtidal Gulf of St. Lawrence coast, there is a class of tidal inlets that typically have a restricted throat, a large flood delta, and a deeply intruding updrift spit. By combining a field study program with an in-house numerical simulation, this paper gives a complete assessment of sediment and hydraulic characteristics of one of such systems — Palmer Inlet on the north shore of Prince Edward Island. Although important findings were summarized in each chapter, they are drawn together here.

Historical evidence and areal mapping indicate that Palmer Inlet migrated downdriftward during the past 50 years (at an average rate of 11-15 m/yr). This results from an annual resultant wave energy flux to the south controlled by the regional wind pattern. The migration, however, is not uniform along the length of the main channel. Instead, the flood tidal delta remained positionally stable, indicating that the inlet was probably incised in the mud substrate as early as 1935.

Harmonic analyses indicate that tides at Palmer Inlet are mixed and diurnal-dominated. O_1 and K_1 tidal components are nearly equal in magnitude, while M_2 is about four times that of S_2. The beat between these components results in a fortnightly tide with small (synoptic) tides coinciding with semidiurnal periods, and large (tropic)

tides with those of diurnal periods. The diurnal inequality of the large tide is characterized by every second high tide being more elevated than its predecessor. The result is a daily tide characterized by strong ebb runouts.

The time-variation of the tidal currents follows the same pattern of tides in both strength and periodicity. Spatially, velocities reach 1 m/s at the throat, but decrease to below 0.2 m/s a short distance into the inlet. Tidal currents are invariably flood-dominated on the shoals, but are symmetrical to slightly ebb dominated in the throat. In the other parts of the channels, various shoals function as topographic shields. They create local flow dominance, with the flood and the ebb each dominating its discharging end.

The surface sediments of the inlet are divided into five depositional environments based on their lateral and vertical positions. The most prominent feature is the uniformity in texture and areal domination of small-scale features. Except in the throat where gravel/shell lags occur, the grain size distribution is characterized by fine sand (over 95% of the total sample) which constitutes a narrow-ranged, well-sorted intermittent suspension population. The traction and wash-load populations are either rare or completely missing. The rareness of mud is due to the lack of a source. Minor amounts of mud are present in the water but are unable to settle to the bed.

With this modification, the grain size distributions of suspended sediment were reasonably well predicted from the bed material using the method proposed by Middleton (1976).

Small ripples are by far the dominant surface feature on the spit platforms and the flood tidal delta, replaced only by loose sand or aeolian/adhesion ripples on the subaerial spit. While these surface features give rise to cross-laminations on the subtidal spit platform, they seldom do so in the other two environments. This indicates extremely weak flows and thus limited tractive transport in those two areas.

Strong tidal currents are restricted to subtidal channels, and their immediate intertidal vicinities. Of the two types of megaripples produced, Type II megaripples are concentrated around the throat. While active in large tides, megaripples remain dormant during small tides. The resultant internal structure is sets of medium-scale cross-bedding in direct contact. Reactivation surfaces are rare. Speed-depth and wavelength-height plots show a general fit of these megaripples with the stability fields known from experiments. The results, however, also indicate that use of observations other than those from large tides could lead to underestimate of the current speeds responsible for the formation of the megaripples. This is because megaripples in microtidal inlets are developed close to hydraulic equilibrium only during large tides.

A three-dimensional model of the stratigraphy was constructed using tube- and box-cores. The observations reveals a Holocene transgressive sequence, 2-4 m in thickness, with inlet sand resting upon shallow backbarrier mud deposits. Three depositional units can be distinguished within the system based on structure associations resulting from their movement relative to the transgression. The updrift unit is an inlet-fill sequence, resulting from the lateral migration of inlet into the main channel. It resembles the typical sequence of Kumar and Sanders (1974). The megaripple cross-bedded middle section, however, lacks the following elements: large-scale sandwave structures, reactivation surfaces and the shallow channel unit. This is due to: (1) the fine-grained texture of the sediment; (2) the lack of mud; (3) the small time-velocity asymmetry of tidal currents and small tidal ranges; (4) the shallow channel depth. On the seaward side, the megaripple bedding is replaced by large-scale tabular foresets, representing avalanching of bar-front deposits. The growth of both the downdrift unit and the landward unit is in the vertical direction. The former, however, represents in-place accretion of swash bar deposits along the barrier shoreline. The resultant sequence is dominated by clean sand and wave-dominated structures. The upward growth of the landward unit (2 m) took place in extremely quite water. The sequence is monotonously structureless. It also lacks the

intercalations of overwash or lagoon deposits commonly observed in many other locations.

A spatially-integrated numerical model was used to provide a better understanding of the hydraulic behaviour demonstrated by the field data. Various parameters that could generate asymmetry of the bay tide and associated inlet currents were investigated using idealized cases. They include the bay surface area, the bay wall slope, the cross-sectioned area of the inlet channel and its slope, the type of tides, time-inertia, friction, and topographic changes in the flood tidal delta and the spit platform. The results show that in a small tidal inlet, where water depths are not much greater than the tidal range, friction is the dominant factor in generating non-linearities. In particular, at Palmer Inlet, a large portion of the friction comes from the two large intertidal sand bodies. The existence of these sand bodies also creates non-linear variations of the cross-section as they emerge and submerge. This interacts with the other hydraulic terms, and has an additional effect on the flood and the ebb flow. The overall effect is a one that retards the ebb more than the flood, especially in the shoaling areas. This induced force explains the observed larger reduction in amplitude and the longer delay of the ebb tides. The resultant tidal hydraulic regime is nearly balanced even though the ebb is inherently stronger. With waves pushing bayward, the result

is that the sediment transport system is flood-directed. This explains the apparent contradiction of the large flood delta at Palmer Inlet where daily tides are characteristically ebb dominated.

Littoral sand once transported inside the inlet will stay there, causing the inlet to be choked with sand. The system is ultimately unstable. Stability analysis using a model calibrated with field data confirms the conclusion. It indicates that with the present framework of physical and geometric configuration, Palmer inlet will probably be closed by natural processes within the next one or two decades.

On the other hand, the model results indicate that deformation of the tide is small in magnitude at Palmer Inlet compared with other similar areas. This is consistent with two facts: (1) the long period of the tidal waves makes it easier to fill the bay here than in areas with a shorter tidal period; and (2) tidal inlets generally act as a low-pass filters which preferentially filter out short semidiurnal components.

Appendix A

Besides commercial software, a number of proprietary computer programs were used for data analysis. These programs were written by the authors listed below. I thank these authors for making these programs available.

Program	Author	Function
FFT.FOR	S. Zhang	Fast Fourier Transformation
FILTER.FOR	T. Isaji	Low or High Pass Digital Filter
INLET.FOR	Seelig, et al.	Numerical Simulation for Inlet hydraulics
HINDWAVE.FOR	S. Zhang	Wave Hindcast Using Wind Data
PROBPLOT.BAS	G. Middleton	Probability Plot of Grain Size Distribution
PSD.FOR	T. Isaji	Power Spectrum Density Estimation
RECTFOT.BAS	A. Roggeband	Vertical Tilt Correction for Oblique Air Photo
REFRACT.FOR	R. Dodson	Wave Refraction
ROSE.BAS	G. Middleton	Plotting Rose Diagram
SM.BAS	F. Futon	Driver for Summa-Sketch Digit Pad

Appendix A documents three programs, chosen for their potential usefulness to students or research workers at McMaster University. Other programs should be available at the source or can be obtained by writing to this author.

Appendix A-1

Documentation of HINDCAST.FOR

HINDWAVE.FOR is a computer program for predictions of wave heights and periods, given wind speed, duration, fetch and water depth. The program is based on Sverdrup-Munk-Bretschneider (SMB) method, outlined in SHORE PROTECTION MANUAL (Vol. I, 1973, p.3-33 — 3-52). Although written as a stand-alone program in WATCOM FORTRAN language, the program can be easily converted into a subroutine, and incorporated into a larger program, in which wave parameters are used as input parameters.

HINDWAVE.FOR consists of a main program, and 4 subroutines. Input data (wind speed, direction, fetch and duration) are stored in WINDDATA.INP one direction per file over a range of speeds. The subroutine call to WINDDATA.INP also performs conversions of units, and calculations of friction compensation for wind blowing over different (land or sea) surface. The subroutine SMBSHL and SMBDEP perform the actual calculations of wave heights and periods for shallow and deep water, respectively. Input and output are in metric units, while internal calculations are in imperial units. The necessary variables for the program are shown in the following table, followed by a sample of input data and a listing of the program.

List of variables in HINDWAVE.FOR

DEPTH — Water depth

DEPTH — Water depth

DIR — Wind direction

DURAT — Duration of wind

FETCH — Wind fetch

HSIG1 — Significant wave height in shallow water

HSIG2 — Significant wave height in deep water

THSIG1 — Array for significant wave height in shallow water

THSIG2 — Array for significant wave height in deep water

TSIG1 — Significant wave period in shallow water

TSIG2 — Significant wave period in deep water

TTSIG1 — Array for significant wave period in shallow water

TTSIG2 — Array for significant wave period in deep water

TWSPD — Temporary storage array for wind speed

WSPD — Wind speed

WINDDATA.INP
— A sample of input data for HINDWAVE.FOR

DIRECTION DEGREE	SPEED M/S	DURATION HOURS	FETCH KM	DEPTH M
45.0	3.0	10.0	637.50	10.5
45.0	6.0	10.0	637.50	10.5
45.0	9.0	10.0	637.50	10.5
45.0	12.0	10.0	637.50	10.5
45.0	15.0	10.0	637.50	10.5
45.0	18.0	10.0	637.50	10.5
45.0	21.0	10.0	637.50	10.5
45.0	24.0	10.0	637.50	10.5
45.0	27.0	10.0	637.50	10.5
45.0	30.0	10.0	637.50	10.5

PROGRAM LISTING OF HINDWAVE.FOR

```
      PROGRAM MAIN
C     PREDICTION OF SHALLOW WATER AND DEEP WATER WAVE CONDITIONS
C     FROM WIND DATA USING SVERDRUP-MUNK-BRETSCHNEIDER (SMB) METHOD
C     REFERENCE: SHORE PROTECTION MANUAL, Vol. I, 1973
C     PAGE: 3-33 — 3-52.
C
      DIMENSION THSIG1(10),TTSIG1(10),TWSPD(10),THSIG2(10),TTSIG2(10)
      CHARACTER*30, CHAR
      PARAMETER (G = 32.2)
      PARAMETER (CUNIT = 0.3048)
C
      OPEN(1,FILE = 'WINDDATA.INP',STATUS = 'OLD')
C
      N = 0
1     N = N + 1
      IF(XEND.EQ.9999.0)CALL OUTPUT (TWSPD,THSIG1,TTSIG1,THSIG2,TTSIG2)
      CALL INPUT(WSPD,FETCH,DEPTH,DURAT,CHAR,DIR,N,XEND)
      IF(DIR.GT.330.0.OR.DIR.LT.150.0)THEN
C
C     SAVE RESULTS IN .OUT FILES
C
      CALL SMBSHL(WSPD,FETCH,DEPTH,G,HSIG1,TSIG1)
      CALL SMBDEP(WSPD,FETCH,DURAT,G,HSIG2,TSIG2)
      ELSE
      CALL SMBSHL(WSPD,FETCH,DEPTH,G,HSIG1,TSIG1)
      ENDIF
C
C
      HSIG1 = HSIG1 * CUNIT
      HSIG2 = HSIG2 * CUNIT
      WSPD = WSPD * CUNIT
      DURAT = DURAT/3600.
      FETCH = FETCH * CUNIT/1000.0
      DEPTH = DEPTH * CUNIT
C
C     OUTPUT TO SCREEN
C
      WRITE(*,35)CHAR,DIR
35    FORMAT(10X,A30,'DIRECTION=',F5.1/)
      WRITE(*,2000)
2000  FORMAT(4X,'WIND SPEED M/S',6X,'FETCH M',6X
     .      ,'DEPTH M',6X,'DURATION HR')
      WRITE(*,1000)WSPD,FETCH,DEPTH,DURAT
1000  FORMAT(4F14.1,/)
      IF(DIR.GT.330.0.OR.DIR.LT.150.0)THEN
      WRITE(*,2002)
2002  FORMAT('SHALLOW WATER SIG.WAVE THSIG1HT',10X,'SIG.WAVE TTSIG1OD')
      WRITE(*,1008)HSIG1,TSIG1
1008  FORMAT(8X,F9.1,21X,F9.1,/)
      WRITE(*,1100)
1100  FORMAT('DEEP WATER SIG.WAVE THSIG1HT',10X,'SIG.WAVE TTSIG1OD')
      WRITE(*,1008)HSIG2,TSIG2
      ELSE
      WRITE(*,5002)
5002  FORMAT('SHALLOW WATER SIG.WAVE THSIG1HT',10X,'SIG.WAVE TTSIG1OD')
      WRITE(*,5008)HSIG1,TSIG1
5008  FORMAT(8X,F9.1,21X,F9.1,/)
      ENDIF
C
      THSIG1(N) = HSIG1
      THSIG2(N) = HSIG2
      TTSIG1(N) = TSIG1
      TTSIG2(N) = TSIG2
      TWSPD(N) = WSPD
C
      HSIG1 = 0.
      HSIG2 = 0.
      TSIG1 = 0.
```

```
      TSIG2 = 0.
      GOTO 1
777   END
C
C-----------------------------------------
C
      SUBROUTINE SMBSHL(WSPD,FETCH,DEPTH,G,HSIG,TSIG)
C
C     *** SHALLOW WATER SMB WAVE PREDICTION ***
C
      PARAMETER (PI2=3.141592 * 2.0)
C     PARAMETER (G=32.2)
C
      WSPD2 = WSPD ** 2
      A = G * FETCH/WSPD2
      B = G * DEPTH/WSPD2
C
      TANHB = TANH(0.530 * B ** 0.75)
      HSIG = 0.283 * TANHB * TANH(0.0125 * A ** 0.42/TANHB)
      HSIG = HSIG * WSPD2/G
C
      TANHB = TANH(0.833 * B ** 0.375)
      TSIG = 1.2 * TANHB * TANH(0.077 * A ** 0.25/TANHB)
      TSIG = TSIG * PI2 * WSPD/G
C
      HAVE = 0.6257 * HSIG
C     --- AVERAGE WAVE THSIG1HT
      TAVE = SQRT(HSIG/0.45)
C     --- AVERAGE WAVE TTSIG10D
C
      RETURN
      END
C
C-----------------------------------------
C
            SUBROUTINE SMBDEP(WSPD,FETCH,DURAT,G,HSIG,TSIG)
C
C    *** DEEP WAVE SMB PREDICTION ***
C
      PARAMETER (PI2=3.141592*2.0)
      PARAMETER (K=6.5882)
      PARAMETER (A=0.0161)
      PARAMETER (B=0.3692)
      PARAMETER (C=2.2024)
      PARAMETER (D=0.8798)
      PARAMETER (ERR=0.05)
C
      WSPD2 = WSPD ** 2
      F = G * FETCH/WSPD2
C     NON-DIMENSIONAL FETCH
      T = G * DURAT/WSPD
C     NON-DIMENSIONAL TTSIG10D
      FLOG = ALOG(F)
      SFLOG = SQRT(A * FLOG ** 2 - B * FLOG + C)
      T0 = K * EXP(SFLOG + D * FLOG)
      IF(T0.LT.T)GOTO 1
C
C     FETCH LIMITED
C
      F0 = F
      DF = F/100.0
C
2     F = F - DF
      FLOG = ALOG(F)
      SFLOG = SQRT(A * FLOG ** 2 - B * FLOG + C)
      T0 = K * EXP(SFLOG + D * FLOG)
      IF(T0.GT.T)GOTO 2
C
C
C     WRITE(*,1000)F0,F
```

```
1000    FORMAT('DURATION LIMITED',2F10.2)
C
C
1       HSIG = 0.283 * TANH(0.0125 * F ** 0.42)
        HSIG = HSIG * WSPD2/G
C
C
        TSIG = 1.2 * TANH(0.077 * F ** 0.25)
        TSIG = TSIG * WSPD * PI2/G
C
C
C       HAVE = 0.6257 * HSIG
C       TAVE = SQRT(HSIG/0.45) --- COULD BE WRRONG, CHECK!
C
C
        RETURN
        END
C
C-----------------------------------------
C
        SUBROUTINE INPUT(WSPEED,FETCH,DEPTH,DURAT,CHAR,DIR,N,XEND)
C
        CHARACTER*45,CHAR
        PARAMETER (CUNIT=0.3048)
C
        REWIND 1
C
        READ (1,101)CHAR
        READ (1,101)CHAR
        READ (1,101)CHAR
  101   FORMAT(A45)
C
        READ(1,1002,END=999)DIR,WSPEED,DURAT,FETCH,DEPTH
1002    FORMAT(5F10.1)
C
        IF(DIR.GT.150.AND.DIR.LT.250.0)THEN
        WSPEED = WSPEED/0.70
C
C       WIND BLOWING OFFSHORE
C
        ELSE
        WSPEED = WSPEED/0.80
C
C       WIND BLOWING ONSHORE
C
        ENDIF
C
C       ACCOUNT FOR LAND FRICTION FACTOR
C       - 'SHORE PROTECTION MANUAL,CERE,1976,P.3-29
C
        WSPEED = WSPEED/CUNIT
        DURAT = DURAT * 3600.0
        FETCH = FETCH/CUNIT * 1000.0
        DEPTH = DEPTH/CUNIT
C
C       CONVERT FROM METRIC TO IMPERIAL UNITS
C
        RETURN
999     XEND = 9999.0
        RETURN
        END
C
C-------------------------------------------------------
C
        SUBROUTINE OUTPUT (TWSPD,THSIG1,TTSIG1,THSIG2,TTSIG2,N)
C
        DIMENSION THSIG1(10),TTSIG1(10),TWSPD(10),THSIG2(10),TTSIG2(10)
C
        OPEN(2,FILE='SHALWAVE.OUT',STATUS='NEW')
        OPEN(3,FILE='DEEPWAVE.OUT',STATUS='NEW')
```

```
C
      N = N - 1
      DO 103 K = 1,N
      WRITE(2,201)TWSPD(K),THSIG1(K),TTSIG1(K)
      WRITE(3,201)TWSPD(K),THSIG2(K),TTSIG2(K)
 105  CONTINUE
 201  FORMAT(1X,3F10.2)
      RETURN
      END
C
C-------------------------------------------------------
```

Appendix A-2

RECTIFOT.BAS

RECTIFOT.BAS was written by Roggeband (1988) in MicroSoft QuickBasic for correction of tilt of air photos taken at oblique angles. The basic equations used for the correction are from Mapping from Aerial Photographs (Burnside, 1979). The equation assumes that the ground is flat without major changes in topography. The program is user-friendly, and within the validity of the assumption, is fully operational.

The variables and function calls are annotated within the text and self-explanatory. To use the program, three ground objects should be marked on the oblique photo, and their distance measured. Alternatively, it can be used if a vertical air photo is available with ground objects identifiable on the corresponding oblique photo. The program can be operated in either interactive or batch mode. The interactive mode allows the import of vertical air photo, over which the oblique photo is superimposed. The user then adjusts the vertical tilt interactively with the arrow keys and grey (+) and (-) keys. This is done until the corresponding objects are visually matched. The batch mode is for use when a series of photos to be processed are taken under similar conditions. The value of parameters used for the correction can then be pre-specified, and the correction proceeded without user interactions.

Listing of Program RECTIFOT.BAS

```
100 GOSUB 500 '****INITIALIZE ****
101 PRINT "*****************************************************************************************"
102 PRINT "*                                PROGRAM RECTIFOT                                       *"
103 PRINT "*                                                                                       *"
104 PRINT "* Written by:Adrian Roggeband, 2 Kitto Blvd., Grimsby, Ont., Tel.(416)-643-2821*"
105 PRINT "*                                                                                       *"
106 PRINT "*                                                                                       *"
107 PRINT "*****************************************************************************************":FOR T=1
TO 5000:NEXT T
110 CLS:PRINT "I)nteractive or B)atch mode ?";
120 RESP$=INKEY$:IF RESP$="" THEN 120
130 IF RESP$="I" OR RESP$="i" THEN PRINT RESP$: GOSUB 200 :GOTO 150
140 IF RESP$="B" OR RESP$="b" THEN PRINT RESP$: GOSUB 300 ELSE PRINT RESP$ CHR$(7):GOTO 110
150 GOSUB 7000 '****SAVE RESULTS****
155 CNTS="Repeat program":GOSUB 6000  '****REPEAT PROGRAM ON REQUEST****
160 IF QUIT=0 THEN 110
165 SYSTEM 'END
170 '
171 '
172 '
200 :'****INTERACTIVE MODE****
210 FILNUM=1:FTYPE$="INPUT":GOSUB 5000:IF QUIT=1 THEN 160 '****OPEN INPUT FILES****
215 FILNUM=2:FTYPE$="REFERENCE":GOSUB 5000:IF QUIT=1 THEN NOREF=1: QUIT=0 ELSE NOREF=0
220 GOSUB 1000:IF QUIT=1 THEN 250'****INPUT DATA****
230 GOSUB 2000 '****PERFORM CORRECTIONS****
235 GOSUB 2200 '****SAVE CORRECTION PARAMETERS****
240 '
250 RETURN
251 '
252 '
253 '
300 : '****BATCH MODE****
310 FILNUM=1:FTYPE$="INPUT":GOSUB 5000:IF QUIT=1 THEN 160 '****OPEN INPUT FILE****
320 NOREF=1
330 GOSUB 1000:IF QUIT=1 THEN 390 '****INPUT DATA****
340 GOSUB 2300 '****PROCESS DATA****
390 RETURN
391 '
392 '
393 '
500 :'****INITIALIZE SCREEN FUNCTIONS AND ARRAYS****
501 ' ****  Variables:                                                    ****
502 ' ****        POINTS(IMAX,)=array to hold coord's of points          ****
503 ' ****        Elements:1,2 hold x,y coord's of uncorrected data,     ****
504 ' ****                 3,4, coords after lateral tilt correction,    ****
505 ' ****                 5,6, coords after vertical correction,        ****
506 ' ****                 7,8, coords after final rotation and inflation ****
507 ' ****                 9,   index for line drawing purposes          ****
508 ' ****                 10,11,12, reference coordinates and index     ****
509 ' ****     Other variables described as encountered.                 ****
510 PI# = 3.1415926536#
515 OPTION BASE 1'****START ALL ARRAYS AT 1 ****
520 IMAX=1000:DIM POINTS(IMAX, 12), GSAVE%(8000)'****Dimension arrays (GSAVE%=array to hold graphics
screen)****
530 '****FUNCTION TO TRANSFORM (X,Y) COORDINATES TO GRAPHICS COORDINATES.****
540 DEF FNSCRX (X) = INT(-X * SCALE * XCORR + SXCTR)+XD
550 DEF FNSCRY (Y) = INT(Y * SCALE * YCORR + SYCTR)+YD
560 READ SXMIN,SXMAX,SYMIN,SYMAX
570 SXSPAN = SXMAX - SXMIN'****FIND GRAPHICS SCREEN WIDTH****
580 SXCTR = (SXMIN + SXMAX) / 2'****X-COORD. OF SCREEN CENTRE****
590 SYSPAN = SYMAX - SYMIN'****FIND GRAPHICS SCREEN HEIGHT****
600 SYCTR = (SYMAX + SYMIN) / 2'****Y-COORD. OF SCREEN CENTRE****
610 SASPECT = ABS(SXSPAN / SYSPAN) * 12 / 5
680 RETURN
690 '
691 '
```

```
692 '
900 LOCATE 1 '****CLEAR PROMPT LINES.****
910 PRINT SPC(79):PRINT:PRINT SPC(79):PRINT
920 LOCATE 1
930 RETURN
940 '
950 '
960 '
970 '
1000 :'****INPUT  DATA. CALCULATE DISPLAY PARAMETERS                    ****
1001 ' ****VARIABLES:POINTS(IMAX,12), DATA ARRAY                        ****
1002 ' **** XMIN,XMAX,YMIN,YMAX, primary data limits                    ****
1003 ' **** RXMIN,RXMAX,RYMIN,RYMAX, reference data limits              ****
1004 ' **** MINX,MINY,MAXX,MAXY, generic data limits                    ****
1005 ' **** Other variables described as encountered.                   ****
1006 '
1009 '*****DATA INPUT****
1010 FILNUM=1 '****SET FILE NUMBER**** ****OBLIQUE PHOTO****
1020 XPSN=1:IPSN=9 '****SET POSITION OF X AND INDEX IN ARRAY****
1030 GOSUB 1500:IF QUIT=1 THEN RETURN '****INPUT DATA****
1040 ILAST=LAST'****TRANSFER DATA LIMITS****
1045 '****SHRINK DATA TO PROPER FORMAT****
1050 XDIM = 35 / POINTS(1, 1)'****35 mm FILM****
1060 FOR I = 1 TO ILAST
1070      POINTS(I, 1) = POINTS(I, 1) * XDIM
1080      POINTS(I, 2) = POINTS(I, 2) * XDIM
1090 NEXT I
1100 '
1110 '****CENTRE PHOTO AXES****
1130 XMAX = POINTS(1, 1) / 2
1140 YMAX = POINTS(1, 2) / 2
1150 XMIN = -POINTS(1, 1) / 2
1160 YMIN = -POINTS(1, 2) / 2
1165 XSPAN= XMAX-XMIN '****WIDTH OF PHOTO****
1170 YSPAN=YMAX-YMIN '****HEIGHT OF PHOTO****
1174 '
1175 MINX=XMIN: MINY=YMIN: MAXX=XMAX: MAXY=YMAX '****SET PARAMETERS FOR SUBROUTINES****
1176 XPSN=1: LAST=ILAST
1180 GOSUB 1800 '****TRANSLATE X,Y COORDINATES****
1190 GOSUB 1400 '****SCALE SUBROUTINE ****
1195 INFL=1 '****NO INFLATION IF NO REFERENCE****
1200 IF NOREF=1 THEN 1340 '**CASE OF NO REFERENCE FILE ****
1210 FILNUM=2 '****SET FILE NUMBER**** ****REFERENCE PHOTO****
1220 XPSN=10:IPSN=12 '****SET POSITION OF X AND INDEX IN ARRAY****
1230 GOSUB 1500: IF QUIT=1 THEN RETURN '****INPUT DATA****
1240 RXMAX=MAXX: RYMAX=MAXY: RLAST=LAST'****TRANSFER DATA LIMITS****
1250 '
1260 RXSPAN= RXMAX '****WIDTH OF REFERENCE PHOTO****
1270 RYSPAN= RYMAX '****HEIGHT OF REFERENCE PHOTO****
1280 RXMAX= RXSPAN/2 '****NEW DATA LIMITS ****
1290 RYMAX= RYSPAN/2
1300 RXMIN= -RXSPAN/2
1310 RYMIN= -RYSPAN/2
1320 MINX=RXMIN:MINY=RYMIN:MAXX=RXMAX:MAXY=RYMAX '****SET PARAMETERS FOR SUBROUTINES ****
1325 XPSN=10:LAST=RLAST
1330 GOSUB 1800 '****TRANSLATE REFERENCE COORDINATES****
1335 GOSUB 1400 '****SCALE SUBROUTINE ****
1338 INFL=RXSPAN/XSPAN '****ADJUST OBLIQUE PHOTO TO SAME SCALE****
1340 CLS:INPUT"FOCAL LENGTH OF CAMERA LENS";FLENS
1348 RETURN
1350 '
1360 '
1370 '
1400 :'****SCALE CALCULATION****
1410 '
1420 SPANX=MAXX-MINX:SPANY=MAXY-MINY '****SET DATA RANGES ****
1430 ASPECT = SPANX / SPANY '****CALCULATE ASPECT RATIO OF REFERENCE PHOTO****
1440 XSCALE = SXSPAN / SPANX '****CALCULATE SCALE BASED ON X AXIS****
```

```
1450 YSCALE = SYSPAN / SPANY '****CALCULATE SCALE BASED ON Y AXIS****
1460 '****SELECT PROPER SCALE BASED ON ASPECT RATIOS****
1470 IF ASPECT < SASPECT THEN XCORR = 12 / 5: YCORR = 1: SCALE = YSCALE ELSE YCORR = 5 / 12: XCORR =
     1: SCALE = XSCALE
1480 '
1490 RETURN
1495 '
1496 '
1497 '
1500 :'**** LOAD DATA FROM FILE INTO ARRAY. FIND DATA LIMITS.        ****
1520 ' **** VARIABLES:POINTS(IMAX,12), I, MINX, MAXX, MINY, MAXY     ****
1530 ' ****           XPSN, IPSN, FILNUM, CNTS, X, Y                 ****
1535 MINX=9.999999E+37:MAXX=-9.999999E+37:MINY=MINX:MAXY=MAXX
1540 FOR I = 1 TO IMAX
1545      ON ERROR GOTO 1700
1550      IF EOF(FILNUM) THEN 1580                    '****CHECK FOR END OF FILE****
1560      INPUT #FILNUM, POINTS(I,XPSN), POINTS(I,XPSN+1), POINTS(I,IPSN)
1561      ON ERROR GOTO 0
1562      X = POINTS(I, XPSN): Y = POINTS(I, XPSN+1)
1564      IF X < MINX THEN MINX = X
1566      IF X > MAXX THEN MAXX = X
1568      IF Y < MINY THEN MINY = Y
1569      IF Y > MAXY THEN MAXY = Y
1570 NEXT I
1580 LAST = I - 1
1590 PRINT LAST; "records found in file "FILNUM
1600 IF LAST=0 THEN I=LOG(-1)   '****GOTO ERROR ROUTINE IF NO RECORDS FOUND****
1610 ON ERROR GOTO 0
1615 CLOSE(FILNUM)
1620 RETURN
1630 '
1631 '
1632 '
1700 :'****ERROR ROUTINE ****
1705 CLOSE(FILNUM)
1710 CNTS=CHRS(7)+"ERROR IN INFUT FILE. CONTINUE"
1720 IF QUIT=1 THEN RESUME 1610
1730 GOSUB 5000                 '****OPEN NEW FILE****
1740 IF QUIT=1 THEN RESUME 1610
1750 RESUME 1500
1760 '
1761 '
1762 '
1800 :'****SIMPLE TRANSLATION OF POINTS                              ****
1801 ' **** Variables: POINTS(IMAX,12), MINX, MINY, XPSN, LAST, I     ****
1805 '
1810 FOR I = 1 TO  LAST
1820      POINTS(I, XPSN) = MINX + POINTS(I, XPSN)
1830      POINTS(I, XPSN+1) = MINY + POINTS(I, XPSN+1)
1840 NEXT I
1850 RETURN
1860 '
1861 '
1862 '
2000 :'****TRANSFORMATION USING CURSOR CONTROLS****
2001 ' ****Variables:INC=Increment
2010 INC = 10: ROT = 0: TILT = 0: ROTF=0:XDISP=0:YDISP=0:INCINC=5:INFL0=INFL
2020 CLS : PRINT "1=1ST ROT. LEFT" : PRINT "3=1ST ROT RIGHT"
2022 PRINT "8=TILT UP" : PRINT "2=TILT DOWN"
2024  PRINT "4=LAST ROT. LEFT" : PRINT "6=LAST ROT RIGHT"
2026 PRINT "7=SHRINK" : PRINT "9=EXPAND"
2028 PRINT "'Q'TO QUIT,'+','-' TO VARY INCREMENT"
2030 PRINT "TYPE <SPACE> TO CONTINUE"
2035 RESP$ = INKEY$:IF RESP$="" THEN  2035 ELSE SCREEN 2:GOTO 2045
2040 RESP$ = INKEY$: IF (RESP$ = "") THEN 2040
2045 IF RESP$ = " " THEN GOSUB 3000: GOTO 2040
2050 IF (RESP$ = "Q") OR (RESP$ = "q") THEN GOTO 2138
2060 IF RESP$ = "1" THEN ROT = ROT - INC : GOSUB 3000: GOTO 2040
```

```
2070 IF RESP$ = "3" THEN ROT = ROT + INC : GOSUB 3000: GOTO 2040
2080 IF RESP$ = "4" THEN ROTF = ROTF - INC : GOSUB 3050 : GOTO 2040
2085 IF RESP$ = "6" THEN ROTF = ROTF + INC : GOSUB 3050 : GOTO 2040
2090 IF RESP$ = "7" THEN INFL = INFL - INFL*INC/100 : GOSUB 3050 : GOTO 2040
2095 IF RESP$ = "9" THEN INFL = INFL + INFL*INC/100 : GOSUB 3050 : GOTO 2040
2100 IF RESP$ = "8" THEN TILT = TILT + INC : GOSUB 3040 : GOTO 2040
2110 IF RESP$ = "2" THEN TILT = TILT - INC : GOSUB 3040 : GOTO 2040
2120 IF RESP$ = "+" THEN INC = INC + INCINC : IF INC > 50 THEN INC = 50
2125 IF RESP$ = "-" THEN INC = INC - INCINC : IF INC < .1 THEN INC = .1
2126 IF INT(INC)=1  AND RESP$="+" THEN INCINC=1
2127 IF INT(INC)=1  AND RESP$="-" THEN INCINC=.1
2128 IF INT(INC)=5  AND RESP$="+" THEN INCINC=5
2129 IF INT(INC)=5  AND RESP$="-" THEN INCINC=1
2130 IF INT(INC)=20 AND RESP$="+" THEN INCINC=10
2131 IF INT(INC)=20 AND RESP$="-" THEN INCINC=5
2134 GOSUB 3100
2135 GOTO 2040
2138 GET (SXMIN, SYMAX)-(SXMAX, SYMIN), GSAVE%'****Save graphics screen
2140 CLS:SCREEN 0'****Clear screen, switch to text mode****
2150 RETURN
2160 '
2161 '
2162 '
2200 :'****CREATES PARAMETER FILE****
2205 CNT$="SAVE TRANSFORMATION PARAMETERS"
2210 GOSUB 6000: IF QUIT=1 THEN 2280
2215 FTYPE$="PARAMETER":FILNUM=2
2220 GOSUB 5500:IF QUIT=1 THEN QUIT=0: GOTO 2280 '****OPEN FILE ****
2230 PRINT #FILNUM, ROT  '****SAVE PARAMETERS ****
2240 PRINT #FILNUM, TILT
2250 PRINT #FILNUM, ROTF
2260 PRINT #FILNUM, INFL
2265 PRINT #FILNUM, SCALE
2270 CLOSE(FILNUM) '****CLOSE FILE****
2280 RETURN
2290 '
2291 '
2292 '
2300 :'****TRANSFORMATION USING INPUT PARAMETERS****
2310 CNT$="ARE CORRECTIONS IN A PARAMETER FILE"
2320 GOSUB 6000: IF QUIT=1 THEN QUIT=0: GOTO 2355
2325 FTYPE$="PARAMETER":FILNUM=2:GOSUB 5000:IF QUIT=1 THEN 2390 '****OPRN FILE****
2330 INPUT #FILNUM, ROT    '****INPUT PARAMETERS FROM FILE ****
2335 INPUT #FILNUM, TILT
2340 INPUT #FILNUM, ROTF
2345 INPUT #FILNUM, INFL
2348 INPUT #FILNUM, SCALE
2350 CLOSE(FILNUM): GOTO 2378
2355 INPUT "1ST ROTATION "; ROT   '****INPUT PARAMETERS FROM KEYBOARD ****
2360 INPUT "TILT CORRECTION "; TILT
2365 INPUT "FINAL ROTATION "; ROTF
2370 INPUT "INFLATION "; INFL
2372 INPUT "SCALE "; SCALE
2375 SCALE = SCALE / INFL          '****CORRECT SCALE TO KEEP GRAPH ON SCREEN ****
2378 SCREEN 2                     '****ACTIVATE GRAPHICS****
2380 GOSUB 3000                   '****PERFORM TRANSFORMATIONS ****
2385 RESP$ = INKEY$: IF RESP$="" THEN 2385 '****HOLD SCREEN ****
2386 GET (SXMIN, SYMAX)-(SXMAX, SYMIN), GSAVE%'****Save graphics screen
2387 CLS:SCREEN 0'****Clear screen, switch to text mode****
2390 RETURN
2391 '
2392 '
2393 '
3000 :'****PERFORM ALL TRANSFORMATIONS****
3010 '
3020 COSR=COS(ROT/180*PI#):SINR=SIN(ROT/180*PI#):XPND=1
3030 XIN=1:XOUT=3:GOSUB 3200'****LATERAL TILT CORRECTION****
3035 '
```

```
3040 XIN=3:XOUT=5:GOSUB 3300'****VERTICAL TILT CORRECTION****2ND ENTRY POINT****
3045 '
3050 COSR=COS(ROTF/180*PI#):SINR=SIN(ROTF/180*PI#):XPND=INFL'****3RD ENTRY POINT****
3060 XIN=5:XOUT=7:GOSUB 3200'****FINAL ROTATION****
3065 '
3070 CLS'****CLEAR SCREEN ****4TH ENTRY POINT****
3080 XIN=7:XD=XDISP:YD=YDISP:GOSUB 3500'****DISPLAY PHOTO****
3090 IF NOREF=0 THEN XIN=10:XD=0:YD=0:GOSUB 3500'****DISPLAY REFERENCE****
3095 '
3100 GOSUB 3600 '**** PRINT HEADER **** 5TH ENTRY POINT ****
3110 '
3130 RETURN
3140 '
3141 '
3142 '
3200 :'****SUBROUTINE TO PERFORM ROTATIONS****
3210 '
3220 FOR I = 1 TO ILAST
3230      POINTS(I, XOUT) = XPND*(POINTS(I, XIN) * COSR + POINTS(I, XIN+1) * SINR)
3240      POINTS(I, XOUT+1) = XPND*(-POINTS(I, XIN) * SINR + POINTS(I, XIN+1) * COSR)
3250 NEXT I
3260 RETURN
3270 '
3271 '
3272 '
3300 :'****PERFORM VERTICAL TILT CORRECTION****
3310 '
3320 SINT = SIN(TILT / 180# * PI#)
3330 COST = COS(TILT / 180# * PI#): SECT = 1 / COST
3340 FCOST= COST*FLENS
3350 FOR I = 1 TO ILAST
3360      Y = POINTS(I, XIN+1)
3370      DENOM=(Y*SINT+FCOST)/FLENS*SECT
3380      POINTS(I, XOUT+1) = Y * SECT / DENOM
3390      X = POINTS(I, XIN)
3400      POINTS(I, XOUT) = X / DENOM
3410 NEXT I
3420 RETURN
3430 '
3431 '
3432 '
3500 :'****Draw MAP                          ****
3510 '****VARIABLES:POINTS(IMAX,12),XIN,I  ****
3520 '
3530                                        '****PLOT MAP****
3540 FOR I = 2 TO ILAST
3550      IF POINTS(I, XIN+2) > POINTS(I - 1, XIN+2) THEN LINE (FNSCRX(POINTS(I - 1, XIN)),
FNSCRY(POINTS(I - 1, XIN+1)))-(FNSCRX(POINTS(I, XIN)), FNSCRY(POINTS(I, XIN+1)))
3560 NEXT I
3570 RETURN
3580 '
3581 '
3582 '
3600 :'****SUBROUTINE TO PRINT HEADER****
3610 GOSUB 900'****CLEAR PROMPT ****
3620 PRINT  "1ST ROT=";: PRINT USING "###.#"; ROT;: PRINT "   TILT=";
3630 PRINT USING "###.#"; TILT;:PRINT "     2ND ROT=";:PRINT USING "###.#"; ROTF
3640 '
3650 PRINT "INFL=";: PRINT USING "###.###"; INFL;: PRINT "    SCALE=";
3660 PRINT USING "###.###"; SCALE;: PRINT "  INC=";: PRINT USING "##.#"; INC;
3670 PRINT "      (Q TO QUIT)"
3680 RETURN
3690 '
3691 '
3692 '
5000 :'****Get FILENAME and open INPUT file.****
5020 '****VARIABLES: FILENAMES, RESPS, QUIT
5030 '
```

```
5040 '
5050 '
5060 QUIT = 0
5070 GOSUB 900
5080 PRINT"NAME OF "+FTYPES+" FILE";
5090 INPUT FILENAMES
5120                            '****VERIFY EXISTENCE OF FILE****
5130 ON ERROR GOTO 5250         '****If file nonexistent GOTO error routine****
5140 OPEN "I", FILNUM, FILENAMES
5155 ON ERROR GOTO 0            '****DISABLE ERROR TRAPPING****
5230 FTYPES=""
5235 RETURN                     '****If file exists.****
5240 '
5250 :      '****ERROR ROUTINE****
5260 PRINT "File does not exist. ";
5270 GOSUB 6000
5280 IF QUIT = 1 THEN RESUME 5230 ELSE PRINT:PRINT:FILES:RESUME 5060
5290 RETURN
5300 '
5301 '
5302 '
5500 :'****Get FILENAME and open OUTPUT file.****
5510 '****VARIABLES:FILENAMES,RESPS,FTYPES,QUIT
5520 '
5530 '
5540 '
5550 QUIT = 0
5560 GOSUB 900
5565 PRINT "NAME OF "+FTYPES+" OUTPUT FILE";
5570 INPUT FILENAMES
5580                            '****VERIFY EXISTENCE OF FILE****
5590 ON ERROR GOTO 5670         '****GOTO 5670 IF NON EXISTENT
5600 OPEN "I",FILNUM , FILENAMES:CLOSE(FILNUM):ON ERROR GOTO 0
5610 GOSUB 5690:IF QUIT=0 THEN 5630  '****GOTO error routine If user insists****
5620 GOSUB 900:GOSUB 6000:IF QUIT=0 THEN 5560 ELSE GOTO  5650
5630 ON ERROR GOTO 0            '****DISABLE ERROR TRAPPING****
5640 OPEN "O",FILNUM , FILENAMES
5650 FTYPES="":RETURN
5660 '
5670 RESUME 5630 '****ERROR ROUTINE****
5680 '
5690 GOSUB 900:PRINT"File already exists.OVERWRITE (Y/N)?";
5700 RESPS=INKEYS:IF RESPS="" THEN 5700
5710 PRINT RESPS:IF RESPS="y" OR RESPS="Y" THEN QUIT=0:GOTO 5730
5720 IF RESPS="N" OR RESPS="N" THEN QUIT=1 ELSE PRINT CHRS(7):GOTO 5690
5730 GOTO 5650'****RETURN****
5740 '
5741 '
5742 '
6000 :'****GETS Y/N RESPONSE TO "CONTINUE?" ****
6010 IF CNTS="" THEN PRINT "Continue (Y,N)? ";ELSE PRINT CNTS" (Y,N)? ";
6020 RESPS = INKEYS: IF RESPS = "" THEN 6020
6030 PRINT RESPS
6050 IF RESPS = "Y" OR RESPS = "y" THEN QUIT = 0: RESPS = "": GOTO 6080
6060 IF RESPS = "N" OR RESPS = "n" THEN QUIT = 1: RESPS = "": GOTO 6080 ELSE PRINT CHRS(7); : GOTO
6010
6070 '
6080 CNTS=""
6090 RETURN
6100 '
6101 '
6102 '
7000 :'****PROCEDURE TO OUTPUT DATA****
7010 '
7020 GOSUB 900 '****CLEAR PROMPT LINES
7025 CNTS="OUTPUT DATA TO FILE ?" '****PROMPT
7030 GOSUB 6000:IF QUIT=1 THEN 7080 '****CHECK USER'S WILL TO CONTINUE
7040 GOSUB 900
```

```
7050 PRINT"TYPE OF OUTPUT, A) ASCII B)Binary or C)Both?"; '****PROMPT FOR OUTPUT TYPE****
7060 RESP$=INKEY$
7070 IF RESP$="A" OR RESP$="a" THEN PRINT RESP$: GOSUB 7100:GOTO 7090
7080 IF RESP$="B" OR RESP$="b" THEN PRINT RESP$: GOSUB 7300: GOTO 7090
7085 IF RESP$="C" OR RESP$="c" THEN PRINT RESP$: GOSUB 7100:GOSUB 7300 ELSE 7060
7090 RETURN
7091 '
7092 '
7100 :'****SAVE AS ASCII FILE****
7105 XPSN=7:IPSN=9:FTYPE$="ASCII"
7110 FILNUM=3:GOSUB 5500 '****GET FILENAME AND OPEN FILE
7120 IF QUIT=1 THEN 7195
7130 FOR I=1 TO ILAST
7140      ON ERROR GOTO 7200
7150      PRINT #FILNUM, POINTS(I,XPSN), POINTS(I,XPSN+1), POINTS(I,IPSN)
7160      ON ERROR GOTO 0
7180 NEXT I
7190 CLOSE(FILNUM)
7195 RETURN
7200 :'****ERROR ROUTINE ****
7205 CLOSE(FILNUM)
7210 CNT$=CHR$(7)+"ERROR WRITING FILE.":GOSUB 6000
7220 IF QUIT=1 THEN RESUME 7195 ELSE RESUME 7100
7230 '
7231 '
7232 '
7300 :'****SAVE AS BINARY FILE****
7305 FTYPE$="BINARY"
7310 FILNUM=3:GOSUB 5500 '****GET FILENAME AND OPEN AS ASCII FILE
7315 IF QUIT=1 THEN 7490 '****QUIT ON USER REQUEST****
7320 CLOSE(FILNUM):KILL FILENAME$ '****DELETE NEW ASCII FILE****
7330 OPEN "R", #FILNUM, FILENAME$, 2 '****RE-OPEN AS RANDOM ACCESS FILE
7340 FIELD #FILNUM, 2 AS GSPOINT$ '****FIELD IS ENTIRE RECORD LENGTH****
7350 FOR I=1 TO 8000 '          ****LOOP TO SAVE DATA****
7360 LSET GSPOINT$ = MKI$(GSAVE%(I)) '****LOAD BUFFER ****
7370 PUT #FILNUM, I '****SAVE RECORD****
7380 NEXT I
7390 CLOSE(FILNUM)
7490 RETURN
8000 DATA   50,  590,  190,   50
8001 '****XMIN, XMAX, YMIN, YMAX ;SCREEN LIMITS
```

Appendix A-3

Documentation for INLET.FOR

Seelig et al.'s (1977) inlet computer program was written for a CDC 6600 computer in standard FORTRAN. To use it on VAX and personal computers, the program was converted into WATCOM FORTRAN. Although the basic principle has not been altered, the routines for input and output accomplished by punched cards, tapes and plotter were removed, and some instructions for flow controls changed. The input and output are now accomplished through file calls. The results are later graphed using commercial software. The modified program was tested on a VAX 6400 machine using VMS operating system, and on a Zenith 286 personal computer using MS-DOS. It should be system independent.

The program consists of three main parts. A main program controls the overall flow of data. Subroutine SETEQ sets up the differential equations. Subroutine RKGS performs the integration using a fourth order Runge-Kutta-Gill method at time steps specified by DELTI. All variables are stored in a common file (INLET.CMN), and passed to the program and subroutines with the metacommand INCLUDE. The required geometric and hydraulic data are specified in INLET.INP file. The subroutine which invokes the file also performs the initialization of parameters. The tidal data can be input, at intervals specified by DEL, either as

measured or as sine waves specified by parameters AMP and PERIOD. Output of intermediate results and peak values can be set at any time interval by changing the value of TIOUT and IOUT, respectively. For detailed description of the program, please see Seelig et al.'s original paper (1977). Notations of variables are given below, followed by the listing of the program and a sample of INLET.INP with abbreviated tidal data.

Listing of Variables

AMP — Amplitude of input tides

BETA — Bay surface area variation ratio

C1, C2 — Coefficients for evaluating manning's n

CAREA — Instantaneous cross-section area of a cell

CDE, CDF — Keulegan's entrance and exit loss coefficients

CDEPTH — Instantaneous water depth of a cell

CFRICT — Instantaneous cross-section area of a cell

CLENGT — Instantaneous length of a cell

CWFACE — Grid cell water level

CWIDTH — Instantaneous width of a cell

DATA — Number of time series

DEL — Sample interval for sea tides or fresh water input

DELTI — Time step for integration

DQDHDT — Derivative of discharge or water level

HILO(K,1) — High water of bay water level

HILO(K,2) — Low water of bay water level

I — Subscript indicating section number

IC, NCHANN — Number of channels

IOUT — Time period for output of peak values

IS, NSECTI — Number of cross-sections

IWFLAG — Flag controlling the evaluation of the weighting function

ISFLAG — Flag controlling the interpolation of cell water levels

J — Subscript indicating channel number

K — Subscript indicating inlet number

MAXTEM — The largest of the dynamic terms

N1 — Number of water body where inlet begins

N2 — Number of water body where inlet ends

NBAY — Number of bays

NINLET — Number of inlets

NINLET — Number of inlets

NPNTS — Number of data points of measured time series of sea tides

NSEA — Number of seas

NSFLAG — Flag controlling the interpolation of water levels of input tides

NWL — Counter for water level data points

PERIOD — Period of input tides

Q — Instantaneous inlet discharge

QINFLO — Fresh water input into the bay

QSUMS — Ebb tidal prism (m^3/ebb cycle)

QSUMS — Flood tidal prism (m^3/flood cycle)

SBFACE — Sea and bay water level

TERM — Dynamic terms in the equation of motion

TERM2 — Convection term

TERM3 — Hydraulic head

TERM4 — Friction term

TIMEND — Total run time

TIOUT — Integer controlling the time interval for data output

TITLE — Title

VM — Instantaneous velocity

VMAXS(K,1) — Peak flood velocity

VMAXS(K,2) — Peak ebb velocity

WEIGHT — Friction weighting function

Y — Temporary storage for inlet discharge or bay water levels

YMAX(K,1) — Peak flood discharge

YMAX(K,2) — Peak ebb discharge

ZETA — Inlet channel side slope (in radian)

Listing of Program INLET.FOR

```
      PROGRAM MAIN
CSINCLUDE INLET.CMN
      CHARACTER*4 TITLE
C
      CALL INPUT
C
      OPEN(1,FILE='MAXMIN.OUT',STATUS='NEW')
      OPEN(2,FILE='ELEVTION.OUT',STATUS='NEW')
      OPEN(3,FILE='Q-VELO.OUT',STATUS='NEW')
      OPEN(4,FILE='DYNATERM.PRN',STATUS='NEW')
C
 335  CALL RKGS
C
      CLOSE (1)
      CLOSE (2)
      CLOSE (3)
      CLOSE (4)
      STOP
      END
C
C----------------------------------------
C
      SUBROUTINE RKGS
CSINCLUDE INLET.CMN
C
      CHARACTER*4 TITLE
      DIMENSION AUX(10,10),A(4),B(4),C(4)
C
C     RUNGE-KUTTA-Gill INTEGRATION WITH VARIABLE TIME STEP
C
      DATA A/0.5, 0.292893, 1.70711, 0.166667/
      DATA B/2., 1., 1., 2./
      DATA C/0.5, 0.292893, 1.70711, 0.5/
C
C-----------------------------------------INITIAL CONDITION
C
      DO 1122 JN = 1,NINLET
      Y(JN) = 0.001
 1122 DQDHDT(JN) = 0.001
C
      DO 1123 JN = 1,NBAY
      Y(JN + NINLET) = 0.
 1123 DQDHDT(JN + NINLET) = 1./FLOAT(NBAY) - FLOAT(NINLET) * 0.001
C
      DO 1 I = 1,NBYLET
    1 AUX(8,I) = 0.066666667 * DQDHDT(I)
      TIME = 0.0
C
      CALL SETEQ(1)
C
      DO 3 I = 1,NBYLET
      AUX(1,I) = Y(I)
      AUX(2,I) = DQDHDT(I)
      AUX(3,I) = 0.
    3 AUX(6,I) = 0.
C
      GOTO 5
C
    2 READ(7) Y,DQDHDT,AUX
C
    5 TIME  = 0.0
      DT    = DELTI * 2.
      IHLF  = -1
      ISTEP = 0
C------------------------------------------------ RETURN PT.
    4 ITEST = 0
```

```
      NWL = 0
      IF(TIME + DT .GT. TIMEND) DT = TIMEND-TIME
    9 ISTEP = ISTEP + 1
C
      DO 10 J = 1,4
      DO 11 I = 1,NBYLET
      R1 = DT * DQDHDT(I)
      R2 = A(J) * ( R1 - B(J) * AUX(6,I) )
      Y(I) = Y(I) + R2
      R2 = R2 * 3.
   11 AUX(6,I) = AUX(6,I) + R2 - C(J) * R1
C
      IF(J .EQ. 4) GOTO 10
      IF(J .LE. 2) TIME = TIME + 0.5 * DT
C
      CALL SETEQ(1)
   10 CONTINUE
C  ------------------------------------ TIME NOW, TIME + DT
      IF(ITEST .EQ. 1) GOTO 20
C
      DO 17 I = 1,NBYLET
   17 AUX(4,I) = Y(I)
C
      ITEST = 1
      ISTEP = ISTEP + ISTEP - 2
C
   18 IHLF = IHLF + 1
      TIME = TIME - DT
      DT = 0.5 * DT
C
      DO 19 I = 1,NBYLET
      Y(I) = AUX(1,I)
      DQDHDT(I) = AUX(2,I)
   19 AUX(6,I) = AUX(3,I)
C
      GOTO 9
C
   20 IF(MOD(ISTEP,2) .EQ. 0) GOTO 23
C
      CALL SETEQ(1)
C
      DO 22 I = 1,NBYLET
      AUX(5,I) = Y(I)
   22 AUX(7,I) = DQDHDT(I)
C
      GOTO 9
C
   23 DTST = 0.
      DO 24 I = 1,NBYLET
   24 DTST = DTST + AUX(8,I) * ABS(AUX(4,I) - Y(I))
C
      IF(DTST .LE. 0.1) GOTO 28
      IF(IHLF .GE. 10) GOTO 99
C
      DO 27 I = 1,NBYLET
   27 AUX(4,I) = AUX(5,I)
C
      ISTEP = ISTEP + ISTEP - 4
      TIME = TIME - DT
      GOTO 18
C
   28 CALL SETEQ(1)
C
      DO 29 I = 1,NBYLET
      AUX(1,I) = Y(I)
      AUX(2,I) = DQDHDT(I)
      AUX(3,I) = AUX(6,I)
      Y(I) = AUX(5,I)
```

```
   29 DQDHDT(I) = AUX(7,I)
C-------------------------------------------------------END OF
      CALL SETEQ(2)
C
      IF(TIME .GE. TIMEND) GOTO 39
      IHLF = IHLF - 1
      ISTEP = ISTEP/2
      DT = DT + DT
C
      IF(IHLF .LT. 0) GOTO 4
      IF(MOD(ISTEP,2) .NE. 0) GOTO 4
      IF(DTST .GT. 0.002) GOTO 4
C
      IHLF = IHLF - 1
      ISTEP = ISTEP/2
      DT = DT + DT
      GOTO 4
      RETURN
      END
C
C---------------------------------------
C
      SUBROUTINE SETEQ(NGO)
CSINCLUDE INLET.CMN
      REAL C(7),F(7),MAXTEM(4),TERM(4,4),TERM2(4),TERM3(4),TERM4(4)
      INTEGER*2 NP10(10)
      CHARACTER*4 TITLE
C
      PARAMETER (G = 9.81)
      DATA NP10/1,2,3,4,5,6,7,8,9,10/, PTIME/0./
      IF(NGO .EQ. 2) GOTO 12
C
C     FIND SEA LEVELS
C
      DO 1 I = 1,NSEA
      CALL WATERH(I,YY,TIME)
 1    SBFACE(I) = YY
C
      DO 2 I = 1,NBAY
      II  =  NSEA + I
      SBFACE(II) = Y(NINLET + I)
      IF(NPNTS(II).EQ.0) GOTO 2
C     CALL WATERH(II,YY,TIME)
      CALL WATERH(II,YY,TIME)
      QINFLO(I) = YY
 2    CONTINUE
C
C       SET UP EQUATION OF MOTION FOR EACH INLET
C-------------------------------------------------------INLET
      DO 100 K = 1,NINLET
C
      IFLAG(K) = 0
      AMIN(K) = 1.0E25
      Q = Y(K)
      IF(ABS(Q).LT.0.00038)Q = 0.00038
      CD = CDF(K)
      IF(Q.LT.0.) CD = CDE(K)
C
      IC = NCHANN(K)
      IS = NSECTI(K)
      LE = 0.
C
      DO 95 I = 1,IS
      DO 94 J = 1,IC
 94   LE = LE + CLENGT(I,J,K)/(FLOAT(IC))
 95   CONTINUE
      IF(IWFLAG.EQ.2) GOTO 595
C
```

```
      ISFLAG = 0
      SUMF = 0.
      DO 1001 I = 1,IS
      F(I) = 0.
      SUMC = 0.
C
      DO 50 J = 1,IC
      DEPTH = CDEPTH(I,J,K) + CWFACE(I,J,K)
      DEN = CFRICT(I,J,K) ** 2 * Q ** 2 * CWIDTH(I,J,K) * CLENGT(I,J,K)
      IF(DEN.LE.0.0001)DEN = 0.1
      C(J) = CAREA(I,J,K) ** 2 * DEPTH ** 0.33333/DEN
 50   SUMC = SUMC + C(J)
C
      DO 60 J = 1,IC
 60   WEIGHT(I,J) = C(J)/SUMC
C
      F(I) = 1./SUMC
 1001 SUMF = SUMF + F(I)
      GOTO 596
C
595   SUMF = 0.
      SUMC = 0.
      ISFLAG = 1
      O 6001 J = 1,IC
      C(J) = 0.
C
      DO 650 I = 1,IS
      DEPTH = CDEPTH(I,J,K) + CWFACE(I,J,K)
      DEN = CFRICT(I,J,K) ** 2 * Q ** 2 * CWIDTH(I,J,K) * CLENGT(I,J,K)
      IF(DEN.LE.0.0001)DEN = 0.1
 650  C(J) = C(J) + CAREA(I,J,K) ** 2 * DEPTH ** 0.33333/DEN
 6001 SUMC = SUMC + C(J)
C
      DO 660 I = 1,IS
      DO 660 J = 1,IC
660   WEIGHT(I,J) = C(J)/SUMC
C
 596  IF(ISFLAG.EQ.1)GOTO 9002
      I1 = N1(K)
      I2 = N2(K)
      FF = F(1)/2.
      DO 71 J = 1,IC
 71   CWFACE(1,J,K) = SBFACE(I1) - (SBFACE(I1) - SBFACE(I2))/SUMF * FF
C
      IF(IS.LE.1) GOTO 74
      DO 72 I = 2,IS
      FF = FF + (F(I-1) + F(I))/2.
      DO 73 J = 1,IC
      CWFACE(I,J,K) = SBFACE(I1) - (SBFACE(I1) - SBFACE(I2))/SUMF * FF
C
 73   IF(ABS(CWFACE(I,J,K)).GT.30.4) CWFACE(I,J,K) = 0.
 72   CONTINUE
 74   CONTINUE
      GOTO 9012
C
9002  DO 9003 J = 1,IC
      XL = 0.
      DO 9004 I = 1, IS
9004  XL = XL + CLENGT(I,J,K)
      XXL = CLENGT(1,J,K) / 2.
      CWFACE(1,J,K) = SBFACE(I1) + (SBFACE(I2) - SBFACE(I1))/XL * XXL
      DO 9007 I = 2, IS
      XXL = XXL + (CLENGT(I-1,J,K) + CLENGT(I,J,K))/2.
9007  CWFACE(I,J,K) = SBFACE(I1) + (SBFACE(I2) - SBFACE(I1))/XL * XXL
9003  CONTINUE
C
C     FIND CROSSECTIONAL AREAS OF INLET SECTION
C
```

```
9012  AE = 0.
      DO 97 I = 1,IS
      DL = 0.
      AA = 0.
C
      DO 96 J = 1,IC
      DL = DL + CLENGT(I,J,K)/(FLOAT(IC) * LE)
      CAREA(I,J,K) = CWIDTH (I,J,K) * (CWFACE(I,J,K) + CDEPTH(I,J,K))
      IF(J.GT.1.AND.J.LT.IC) GOTO 104
      CAREA(I,J,K) = CAREA(I,J,K) + 0.5/ZETA(K) * (CWFACE(I,J,K) *
                     ABS(CWFACE(I,J,K)) - CDEPTH(I,J,K) ** 2)
104   IF(CAREA(I,J,K).LT.0.001) CAREA(I,J,K) = 0.1
C
      U(I,J,K) = WEIGHT(I,J) * Q/CAREA(I,J,K)
      IF(CAREA(I,J,K).LT.0.001)U(I,J,K) = 0.0
 96   AA = AA + CAREA(I,J,K)
      IF(AA.LT.1.0)IFLAG(K) = 1
      IF(AA.LT.AMIN(K)) AMIN(K) = AA
 97   AE = AE + DL/AA
      AE = 1./AE
      VELO(K) = Q/AMIN(K)
      IF(IFLAG(K).EQ.1)VELO(K) = 0.0
C
C     EVALUATE CONVECTIVE ACCELERATION
C
      TERM2(K) = AE/(2. * LE) * CD * Q * ABS(Q)/(AMIN(K) ** 2)
C
C     EVALUATE HEAD
C
      TERM3(K) = G * AE/LE * (SBFACE(I2) - SBFACE(I1))
C
C     EVALUATE FRICTION (EQ.10)
C
      TERM4(K) = 0.
      DO 85 I = 1,IS
      AC = 0.
C
      DO 84 J = 1,IC
 84   AC = AC + CAREA(I,J,K)
      AGLEAC = G * AE /(LE * AC)
C
      DO 83 J = 1,IC
      CC = 0.0
      DEPTH = CWFACE(I,J,K) + CDEPTH(I,J,K)
      IF(DEPTH.LT.0.03)DEPTH = 0.03
      W8 = WEIGHT(I,J)
      CUP = AGLEAC * CFRICT(I,J,K) ** 2 * ABS(W8*Q) * W8 * Q
      CDN = (DEPTH ** 0.333 * CAREA(I,J,K) ** 2)/CLENGT(I,J,K)/CWIDTH(I,J,K)
      IF(CDN .LT. 1.0E-20) GOTO 83
      CC = CUP/CDN
 83   TERM4(K) = TERM4(K) + CC
 85   CONTINUE
C
C     PUT TERMS TOGATHER TO FORM EQ.12, 1977
C
      DQDHDT(K) = - TERM2(K) - TERM3(K) - TERM4(K)
 100  CONTINUE
C
C     SET UP CONTINUITY EQUATIONS
C
      DO 200 I = 1,NBAY
      QT = QINFLO(I)
      NN = I + NSEA
      DO 205 J = 1,NINLET
      IF(N1(J).EQ.NN) QT = QT - Y(J)
 205  IF(N2(J).EQ.NN) QT = QT + Y(J)
      ABAY = BYAREA(I) * (1. + BETA(I) * SBFACE(NN))
 200  DQDHDT(NINLET + I) = QT/ABAY
```

```
      RETURN
C
C     RETAIN MAXMIN OF BAY WATER LEVEL
C
   12 DO 106 I = 1,NBAY
      NN = NSEA + I
      IF(HILO(I,1).LT.SBFACE(NN)) HILO(I,1) = SBFACE(NN)
  106 IF(HILO(I,2).GT.SBFACE(NN)) HILO(I,2) = SBFACE(NN)
C
C     RETAIN MAXMIN OF INLET VELOCITY, AND
C     ACCUMULATE INLET FOLW
C
      DO 108 K = 1,NINLET
      IF(VMAXS(K,1).LT.VELO(K)) VMAXS(K,1, = VELO(K)
      IF(VMAXS(K,2).GT.VELO(K)) VMAXS(K,2) = VELO(K)
      IF(YMAX(K,1).LT.Y(K)) YMAX(K,1) = Y(K)
C     MAX. FLOOD DISCHARGE
      IF(YMAX(K,2).GT.Y(K)) YMAX(K,2) = Y(K)
C     MAX. EBB DISCHARGE
      IF(Y(K)) 103,108,102
  102 QSUMS(K,1) = QSUMS(K,1) + Y(K) * (TIME - PTIME)
C     FLOOD TIDAL PRISM
      GOTO 108
  103 QSUMS(K,2) = QSUMS(K,2) + Y(K) * (TIME - PTIME)
C     EBB TIDAL PRISM
C
  108 CONTINUE
C
      PTIME = TIME
      ITT = INT((TIME)/DELTI)
C
      IF(MOD(ITT,IOUT))733,734,733
  733 RETURN
C
C     CONTROL THE OUTPUT FREQUENCY FOR HYDRAULICS
C
  734 DO 7897 I = 1,NINLET
      MAXTEM(I) = 0.
      TERM(1,I) = TERM2(I)
      TERM(2,I) = TERM3(I)
      TERM(3,I) = TERM4(I)
      TERM(4,I) = DQDHDT(I)
 7897 CONTINUE
      DO 9090 I = 1,NINLET
      DO 9090 J = 1,4
      IF (MAXTEM(I).LT.ABS(TERM(J,I))) MAXTEM(I) = ABS( RM(J,I))
 9090 CONTINUE
      DO 4514 I = 1,NINLET
      DO 4514 J = 1,4
      TERM(J,I) = 100. * TERM(J,I)/MAXTEM(I)
C     NORMALIZATION WITH THE LARGEST TERM
 4514 CONTINUE
      PAUSE'SET EQUATIONS'
 3786 FORMAT(1X,'TIME, TIDE=',F10.1,3F8.3)
      HOUR = TIME/3600.
 3737 WRITE(2,3773)HOUR,(SBFACE(I),I=1,NSEBY)
      WRITE(3,3774)(Y(I),I=1,NINLET),(VELO(I),I=1,NINLET)
      WRITE(4,3775)((TERM(J,I),J=1,4),I=1,NINLET)
 3773 FORMAT(1X,F8.4,1X,2F8.2)
 3774 FORMAT(1X,'DISCHARGE, VELO.=',4F9.3)
 3775 FORMAT(1X,'TERM=',8F9.3)
C
C     *** SAVE PEAK VALUES ***
C
      IF(TIME .LT.TIOUT) RETURN
      TIOUT = TIOUT + PERIOD(I)
C
      WRITE(1,1002) HOUR
```

```
 1002 FORMAT(' TIME(HOURS)=',T30,F8.4)
      WRITE(1,1003)  (NP10(I),I=1,NINLET)
 1003 FORMAT(' INLET=',T30,10I10)
      WRITE(1,1019) (VMAXS(K,1),K=1,NINLET)
 1019 FORMAT(1H ,'PEAK FLD. VELOCITY(CM/S)',T30,10F10.5)
      WRITE(1,1022) (VMAXS(K,2),K=1,NINLET)
 1022 FORMAT(1H ,'PEAK EBB VELOCITY(CM/S)',T30,10F10.5)
      WRITE(1,737) (YMAX(K,1),K=1,NINLET)
  737 FORMAT(1H ,'PEAK FLD.DISCHARGE(M3/S)',T30,10F10.5)
      WRITE(1,767) (YMAX(K,2),K=1,NINLET)
  767 FORMAT(1H ,'PEAK EBB DISCHARGE(M3/S)',T30,10F10.5)
C
      WRITE(1,1004) (QSUMS(K,1),K=1,NINLET)
 1004 FORMAT(1H ,'FLOOD PRISM(M3)',T30,10F10.0)
      WRITE(1,1005) (QSUMS(K,2),K=1,NINLET)
 1005 FORMAT(1H ,'EBB PRISM(M3)',T30,10F10.0)
C
      DO 105 K = 1,NINLET
      QSUMS(K,1) =
     .(QSUMS(K,2) + QSUMS(K,1))/(ABS(QSUMS(K,1)) + ABS(QSUMS(K,2))) * 200.
  105 CONTINUE
C
      WRITE(1,1009) (QSUMS(K,1),K=1,NINLET)
 1009 FORMAT(1H ,'PERCENT DIFF',T30,10F10.3)
C
      WRITE(1,1012) (NP10(I),I=1,NBA..
 1012 FORMAT(1H0,5X,'BAY # = ',T30,10I10)
C
      WRITE(1,1016) (HILO(J,1),J=1,NBAY)
 1016 FORMAT(1H ,'HIGH WATER',T30,6F10.5)
      WRITE(1,1017) (HILO(J,2),J=1,NBAY)
 1017 FORMAT(1H ,'LOW WATER ',T30,6F10.5)
C
      DO 107 I = 1,NBAY
      SBFACE(I) = (HILO(I,1) + HILO(I,2))/2.
      RANGE(I) = HILO(I,1) - HILO(I,2)
  107 HILO(I,2) = BYAREA(I) * RANGE(I)
C
      WRITE(1,1018) (SBFACE(J),J=1,NBAY)
 1018 FORMAT(1H ,'SUPERELEVATION ',T30,6F10.5)
      WRITE(1,1010) (HILO(J,2),J=1,NBAY)
 1010 FORMAT(1H ,'BAY TIDAL PRISM',T30,6F10.0)
      WRITE(1,1011) (RANGE(J),J=1,NBAY)
 1011 FORMAT(1H ,'BAY TIDAL RANGE',T30,10F10.5)
C
      DO 208 J = 1,NBAY
      HILO(J,1) = -999.
  208 HILO(J,2) =  999.
C
      DO 209 J = 1,NINLET
      QSUMS(J,1) = 0.
      QSUMS(J,2) = 0.
C     YMAX(J,1)= -99999999.9
C     YMAX(J,2)= +99999999.9
      VMAXS(J,1) = -99999.9
  209 VMAXS(J,2) = +99999.9
C
      RETURN
      END
C---------------------------------------
      SUBROUTINE WATERH(I,YY,X)
C$INCLUDE INLET.CMN
C
      NWL = NWL + 1
      IF(NPNTS(I).EQ.1) GOTO 5
      IF(NPNTS(I).LT.1) GOTO 10
      IF(DEL(I).LE.0.) RETURN
      IF(NSFLAG.EQ.0) GOTO 345
```

```
      IT = X/(FLOAT(NPNTS(I)) * DEL(I))
C
C     CUBIC INTERPOLATION OF SEA LEVEL
C
      XT = X - IT * (FLOAT(NPNTS(I)) * DEL(I))
      JJ = XT/ DEL(I)
      J = JJ + 2
      T2 = DEL(I)/2.
      TT = (X - (FLOAT(JJ) * DEL(I) + T2))/T2
      AA = (-DATA(I,J-1) + 9. * DATA(I,J) + 9. * DATA(I,J+1) - DATA(I,J+2))/16.
      BB = (DATA(I,J-1) - 11. * DATA(I,J) + 11. * DATA(I,J+1) - DATA(I,J+2))/16.
      CC = (DATA(I,J-1) - DATA(I,J) - DATA(I,J+1) + DATA(I,J+2))/16.
      DD = (-DATA(I,J-1) + 3. * DATA(I,J) - 3. * DATA(I,J+1) + DATA(I,J+2))/16.
      YY = AA + TT * (BB + TT * (CC + TT * DD))
      RETURN
  345 IT = X / PERIOD(I)
C
      XT = X - IT * PERIOD(I)
      J = XT / DEL(I)
      J = J + 1
      YY = DATA(I,J) + ((DATA(I,J+1) - DATA(I,J)) * (XT - (J-1) * DEL(I))/DEL(I))
      RETURN
    5 YY = DATA(I,1)
      RETURN
   10 YY = AMP(I) * SIN(2. * 3.14158 * X/PERIOD(I))
      RETURN
      END
C
C--------------------------------------
C
      SUBROUTINE INPUT
CSINCLUDE INLET.CMN
      CHARACTER*4 TITLE
C
      OPEN(5,FILE='INLET.INP',STATUS='OLD')
C
      REWIND 5
      READ(5,1) (TITLE(I),I=1,20)
    1 FORMAT(20A4)
C
      READ(5,1020) TIMEND,DELTI,IOUT
 1020 FORMAT(2(10X,F10.0),10X,I10)
C
      IF(TIMEND.LE.0.) CALL EXIT
C
    2 FORMAT(8F10.2)
C
      READ(5,1013) NSEA
 1013 FORMAT(10X,I10)
      DO 4 I = 1,NSEA
      READ(5,1006) PERIOD(I),AMP(I),NPNTS(I),DEL(I)
 1006 FORMAT(2(10X,F10.0),10X,I10,10X,F10.0)
C
      NN = NPNTS(I)
      IF(NPNTS(I).GT.0)READ(5,1021) (DATA(I,II),II=1,NN)
 1021 FORMAT(1X,10F7.4)
 4    CONTINUE
      TIOUT = PERIOD(1)
C
      READ(5,1013) NBAY
C
C     NBAY = NUMBER OF BAY
C
      NSEBY = NSEA + NBAY
      DO 7 I = 1,NBAY
      NN = I + NSEA
      READ(5,1006) BYAREA(I),BETA(I),NPNTS(NN),DEL(NN)
      WRITE(6,1008) I,BYAREA(I),BETA(I),NPNTS(NN),DEL(NN)
```

```
 1008 FORMAT(1H0,'     BAY # =',I5/
     .'    BYAREA : AREA OF BAY (METER**2)',T55,F10.0/
     .'    BETA : BAY AREA RATIO OF HIGH OVER LOW',T55,F10.4/
     .'    NPNTS  : # OF POINTS OF TIME SERIES(0:NO-DATA)',T55,I5/
     .'    DEL    : SAMPLING INTERVAL (SEC)',T55,F10.0)
      HILO(I,1) = -999.
      HILO(I,2) =  999.
      RANGE(I) = -999.
C
      NM = NPNTS(NN)
      IF(NM.LT.1) GOTO 7
      READ(5,52)QINFLO(NN)
 52   FORMAT(10X,F10.2)
 7    CONTINUE
C
      READ(5,1013) NINLET
      DO 20 K = 1,NINLET
      READ(5,1014) N1(K),N2(K),NCHANN(K),NSECTI(K),C1,C2,CDE(K),
     .             CDF(K),ZETA(K)
 1014 FORMAT(10X,2I10/2(10X,I10/),2(10X,2F10.0/),10X,F10.0)
      IC = NCHANN(K)
      IS = NSECTI(K)
C
      DO 55 I = 1,IS
 55   READ(5,22) (CDEPTH(I,J,K),J=1,IC)
 22   FORMAT(10X,7F10.5)
C
      DO 66 I = 1,IS
 66   READ(5,22) (CWIDTH(I,J,K),J=1,IC)
C
      ICP1 = IC + 1
      IS = IS - 1
      NSECTI(K) = IS
C
      DO 77 I = 1,IS
 77   READ(5,22) (CLENGT(I,J,K),J=1,ICP1)
      WRITE(6,3678) K,N1(K),N2(K)
 3678 FORMAT(/,1X,'SUMMARY OF GRID CHARACTERISTICS  INLET',I2/
     .'     CONNECTS FROM',I5,' TO',I5)
      DO 10 I = 1,IS
      DO 11 J = 1,IC
C
C     CONVERT THE GEOMETRY PARAMETERS AT BOUNDARIES OF GRID CELLS
C     TO THE CENTERS OF THE CELLS
C
      CWFACE(I,J,K) = 0.0
C
      CWIDTH(I,J,K) = (CWIDTH(I,J,K) + CWIDTH(I+1,J,K))/2.
      CLENGT(I,J,K) = (CLENGT(I,J,K) + CLENGT(I,J+1,K))/2.
      CDEPTH(I,J,K) = (CDEPTH(I,J,K) + CDEPTH(I+1,J,K))/2.
      CAREA(I,J,K) = CWIDTH(I,J,K) * CDEPTH(I,J,K)
      CFRICT(I,J,K) = C1 - C2 * CDEPTH(I,J,K)
      IF(CDEPTH(I,J,K).LT.1.2) CFRICT(I,J,K) = .055 - 0.005
     . * CDEPTH(I,J,K)
 11   CONTINUE
C
      WRITE(6,1297) I
 1297 FORMAT(/,1X,'SECTION',I3)
      WRITE(6,1971) (CAREA(I,J,K),J=1,IC)
      WRITE(6,1972) (CWIDTH(I,J,K),J=1,IC)
      WRITE(6,1973) (CDEPTH(I,J,K),J=1,IC)
      WRITE(6,1974) (CLENGT(I,J,K),J=1,IC)
      WRITE(6,1975) (CFRICT(I,J,K),J=1,IC)
   10 CONTINUE
 1972 FORMAT(5X,'WIDTH(M)',10F10.1)
 1971 FORMAT(5X,'AREA(M2)',10F10.1)
 1973 FORMAT(5X,'DEPTH(M)',1X,10F10.2)
 1974 FORMAT(5X,'LEN(M)',2X,10F10.1)
```

```
 1975 FORMAT(5X,'N',10X,10F10.4)
      NBYLET = NBAY + NINLET
C
      READ(5,913)IWFLAG
      WRITE(6,917)IWFLAG
 913  FORMAT(10X,I10)
 917  FORMAT(2(5X,I10))
C
      QSUMS(K,1) = 0.0
      QSUMS(K,2) = 0.0
      YMAX(K,1) = -99999999.9
      YMAX(K,2) = +99999999.9
      VMAXS(K,1) = -99999999.9
      VMAXS(K,2) = +99999999.9
   20 CONTINUE
C
      RETURN
      END
C---------------------------------------
      SUBROUTINE EXIT
      RETURN
      END
```

INLET.INP

— A sample of input data for INLET.FOR

```
PALMER INLET TEST CASE --- 2-SEA,1-BAYS AND 2-INLETS.
  TIMEND =   153000.  DELTI =      150.   IOUT =        8 NSFLAG =         1
  NSEA   =        2
  PERIOD =    86400.  AMP   =        0.  NPNTS =       60  DEL   =      300.
 -0.2398-0.2359-0.2317-0.2271-0.2220-0.2166-0.2107-0.2044-0.1976-0.1903
 -0.1825-0.1743-0.1656-0.1564-0.1467-0.1366-0.1260-0.1151-0.1037-0.0920
 -0.0800-0.0676-0.0551-0.0423-0.0292-0.0161-0.0028 0.0106 0.0241 0.0377
  0.0513 0.0650 0.0786 0.0923 0.1060 0.1196 0.1332 0.1468 0.1604 0.1739
  0.1873 0.2007 0.2140 0.2271 0.2402 0.2531 0.2658 0.2784 0.2907 0.3028
  0.3146 0.3262 0.3374 0.3483 0.3588 0.3690 0.3788 0.3882 0.3971 0.4057
  PERIOD =    86400.  AMP   =        0.  NPNTS =       60  DEL   =      300.
 -0.2507-0.2462-0.2412-0.2358-0.2298-0.2236-0.2168-0.2095-0.2017-0.1934
 -0.1846-0.1753-0.1655-0.1552-0.1444-0.1331-0.1215-0.1094-0.0969-0.0840
 -0.0708-0.0574-0.0436-0.0296-0.0154-0.0010 0.0136 0.0284 0.0433 0.0583
  0.0735 0.0887 0.1041 0.1195 0.1349 0.1504 0.1660 0.1816 0.1972 0.2127
  0.2283 0.2437 0.2591 0.2744 0.2895 0.3045 0.3192 0.3337 0.3480 0.3618
  0.3755 0.3887 0.4015 0.4139 0.4259 0.4374 0.4484 0.4590 0.4691 0.4786
  NBAY   =        1
  BYAREA =      3E+7    BETA =      0.0  NPNTS =        1  DEL   =     3600.
 QINFLOW =       0.1
  NINLET =         2
 FROM-TO =         1         3     /* INLET 1
 NCHANN  =         4
 NSECTI  =         6
 FRICTION=     0.065       0.0
 ENTRANCE=       0.8       1.2
   ZETA  =       0.1
D1               3.16      4.00      4.00      0.92
D2               2.00      2.10      3.10      0.38
D3               2.38      2.88      3.78      0.32
D4               2.08      2.88      3.50      0.38
D5               1.90      2.00      2.80      0.67
D6               1.92      2.30      1.80      0.93
W1               65.0      50.0      50.0     150.0
W2               35.0      25.0      25.0      95.0
W3               21.5      11.5      11.5      51.5
W4               11.5      11.5      11.5      31.5
W5               31.5      25.0      25.0      31.5
W6               65.0      50.0      50.0      65.0
L1               65.0      65.0      65.0      65.0     65.0
```

L2	45.	50.	50.	50.	45.
L3	55.	55.	55.	55.	55.
L4	25.	30.	30.	30.	25.
L5	65.	65.	65.	65.	65.
FROM-TO =	2	3	/* INLET 2		
NCHANN =	3				
NSECTI =	6				
FRICTION=	0.065	0.0			
ENTRANCE=	0.8	1.2			
ZETA =	0.1				
D1	3.05	6.00	3.05		
D2	3.45	5.88	3.65		
D3	3.05	5.05	3.05		
D4	3.05	4.05	3.05		
D5	3.05	4.65	3.05		
D6	3.00	3.96	3.00		
W1	250.0	250.0	250.0		
W2	225.0	200.0	250.0		
W3	200.0	150.0	200.0		
W4	225.0	200.0	200.0		
W5	250.0	250.0	250.0		
W6	250.0	240.0	250.0		
L1	120.	165.	165.	120.	
L2	65.	60.	60.	65.	
L3	120.	120.	120.	120.	
L4	120.	120.	120.	120.	
L5	60.	65.	65.	60.	
IWFLAG	1				

Appendix B

Grain Size Data

This section lists raw grain size data of 109 sediment samples. The bed samples are listed in B-1 by environments; their locations are shown in Figure 4-2. Suspended sediments are list in B-2 by time with the depth at which the sample was collected shown at the left of the page. Their locations are given in Figure 2-17. The figures are cumulative weight percentages at intervals of 0.2 ϕ. The first two figures of each sample are starting and ending grain size in phi (ϕ).

Grain size analyses were made in the Atlantic Geoscience Center sedimentological laboratory at Bedford Institute of Oceanography. All samples were carefully mixed, split into subsamples, and transferred to a 2 mm sieve to separate gravels. The resultant samples were washed repeatedly to remove soluble salts. Organic materials were removed using hydrogen peroxide following the normal procedure. Analyses of >4 ϕ sand fractions was made in the settling tube. An Apple II computer, interfaced to an electronic balance, recorded the weight accumulated in the pan at the bottom of the tube at 0.2 sec intervals. The <4 mud fractions of suspended sediment were analyzed with the SediGraph 5000D by lab technician Clattenburg. The results are re-calculated to 0.2 ϕ intervals on the Cyber mainframe, and plotted as frequency diagrams.

Appendix B-1

Cumulative Weight Percentages of Bed Materials

Flood Tidal Delta

GZ-1
0, 4.8, 0, 0, 0, 0, 0, 0, 0, .74, 3.43, 10.94, 28.33, 55.07, 78.5, 89.7, 94.53, 96.89, 97.98, 98.76, 99.37, 99.85, 100, 100, 100, 100, 100

GZ-2
0, 4.8, 0, .09, .11, .11, .25, .44, .82, 2.17, 6.47, 16.57, 36.42, 56.59, 72.94, 83.32, 89.06, 92.52, 94.97, 96.95, 98.47, 99.68, 100, 100, 100, 100, 100

GZ-3
0, 4.8, 0, 0, 0, 0, 0, 0, 0, .97, 3.46, 9.66, 26.15, 47.62, 67.28, 81.38, 88.43, 92.72, 95.09, 96.87, 98.25, 99.58, 100, 100, 100, 100, 100

GZ-4
0, 4.8, 0, 0, 0, 0, 0, 0, .31, 2.04, 10.24, 29.82, 61.64, 81.3, 90.86, 95.5, 97.47, 98.37, 98.8, 99.16, 99.52, 99.92, 100, 100, 100, 100, 100

GZ-5
0, 4.8, 0, 0, 0, 0, 0, 0, .13, 1.31, 8.11, 24.89, 51.88, 68.49, 82.09, 90.65, 94.8, 97.01, 98.05, 98.71, 99.26, 99.82, 100, 100, 100, 100, 100

GZ-6
0, 4.8, 0, 0, 0, 0, 0, 0, 0, 0, 0, 2.27, 9.65, 25.58, 47.15, 65.88, 77.66, 85.21, 90.06, 93.83, 96.96, 99.4, 100, 100, 100, 100, 100

GZ-7
0, 4.8, 0, 0, 0, 0, 0, 0, .35, 1.69, 6.97, 19.17, 43.19, 65.5, 83.43, 91.81, 95.41, 97.39, 98.28, 98.92, 99.53, 99.89, 100, 100, 100, 100, 100

GZ-8
0, 4.8, 0, 0, 0, 0, 0, 0, 0, .26, 1.87, 7.8, 23.02, 45.1, 67.45, 81.54, 88.98, 93.29, 95.54, 97.27, 98.66, 99.72, 100, 100, 100, 100, 100

GZ-9
0, 4.8, 0, 0, 0, 0, 0, 0, 0, .16, 1.85, 8.45, 30, 58.64, 80.32, 91.52, 95.83, 97.75, 98.42, 99, 99.49, 99.87, 100, 100, 100, 100, 100

Inlet Channel

GZ-10
0, 4.8, 0, 0, 0, 0, 0, .41, .78, 2.68, 10.13, 30.48, 68.3, 91.76, 98.62, 99.83, 100, 100, 100, 100, 100, 100, 100, 100, 100, 100, 100

GZ-11
0, 4.8, .46, .64, .79, .89, 1.24, 2.48, 6.41, 17.24, 35.65, 53.62, 75.26, 91.57, 97.49, 98.86, 99.39, 99.5, 99.51, 99.54, 99.8, 100, 100, 100, 100, 100, 100

GZ-12
0, 4.8, 0, 0, 0, 0, .66, .84, 1.69, 5.66, 18.5, 46.29, 80.05, 93.82, 97.78, 99.1, 99.44, 99.69, 99.79, 99.85, 99.98, 99.98, 100, 100, 100, 100, 100

GZ-13
0, 4.8, 3.5, 3.84, 4.06, 4.46, 5.1, 6.17, 8.68, 16.26, 34.02, 63.9, 88.05, 96.1, 98.35, 99.16, 99.48, 99.69, 99.75, 99.75, 99.79, 99.93, 100, 100, 100, 100, 100

GZ-14
0, 4.8, 0, 0, 0, 0, 0, 0, 0, .62, 2.7, 8.14, 22.86, 52.22, 79.28, 92.3, 96.68, 98.37, 98.99, 99.46, 99.67, 99.89, 100, 100, 100, 100, 100

GZ-15
0, 4.8, 0, 0, .42, .42, .53, .94, 2.75, 11.06, 38.26, 76.35, 94.1, 98.47, 99.39, 99.86, 100, 100, 100, 100, 100, 100, 100, 100, 100, 100, 100

GZ-16
0, 4.8, 0, 0, 0, 0, .15, .44, 1.74, 6.57, 20.52, 42.18, 67.21, 86.02, 94.38, 97.5, 98.7, 99.02, 99.25, 99.57, 99.73, 99.94, 100, 100, 100, 100, 100

GZ-17
0, 4.8, .53, .59, .81, .88, 1.21, 1.58, 2.87, 7.33, 20.46, 44.11, 76.72, 92.32, 97.0, 98.74, 99.17, 99.46, 99.58, 99.79, 99.9, 99.95, 100, 100, 100, 100, 100

GZ-25
0, 4.8, 0, .18, .2, .2, .25, .6, 1.88, 5.77, 16.91, 38.01, 65.83, 84.03, 94.25, 97.89, 98.96, 99.16, 99.16, 99.28, 99.43, 99.65, 99.73, 99.75, 99.97, 100, 100

GZ-26
0, 4.8, 0, 0, 0, 0, 0, 0, .03, 1.3, 6.51, 22.82, 55.17, 81.67, 94.57, 98.6, 99.33, 99.42, 99.47, 99.54, 99.68, 99.85, 99.89, 99.89, 100, 100, 100

GZ-39
0, 4.8, 0, 1.47, 1.58, 1.99, 2.37, 3.1, 5.05, 9.7, 19.57, 33.33, 55.24, 77.95, 90.97, 96.45, 98.08, 98.39, 98.89, 99.3, 99.6, 99.84, 100, 100, 100, 100, 100

GZ-40
0, 4.8, 0, 0, 0, 0, 0, 0, .18, 2.65, 14.92, 43.4, 74.9, 88.81, 95.38, 97.7, 98.65, 98.99, 99.18, 99.47, 99.71, 99.97, 100, 100, 100, 100, 100

Spit Platform (Channel Margin Linear Bar)
GZ-18
0, 4.8, 0, 0, 0, 0, 0, 0, 0, 1.14, 6.75, 24.3, 60.85, 83.86, 94.47, 97.54, 98.67, 99.07, 99.26, 99.55, 99.79, 99.93, 100, 100, 100, 100, 100

GZ-19
0, 4.8, 0, 0, 0, .84, 1.11, 1.80, 4.03, 10.43, 25.66, 49.22, 77.02, 89.93, 95.66, 97.73, 98.77, 99.11, 99.37, 99.56, 99.74, 99.94, 100, 100, 100, 100, 100

GZ-20
0, 4.8, 2.73, 3.14, 3.43, 4.11, 5.13, 7.21, 11.16, 20.14, 38.4, 61.78, 82.51, 92.27, 95.9, 97.88, 98.63, 99.04, 99.23, 99.37, 99.66, 99.9, 100, 100, 100, 100, 100

GZ-21
0, 4.8, 0, 0, 0, .21, .52, 1.48, 3.64, 9.28, 21.6, 41, 72.47, 93.24, 98.32, 99.5, 99.75, 99.87, 99.87, 99.87, 99.87, 99.9, 100, 100, 100, 100, 100

GZ-22
0, 4.8, 2.59, 3.39, 3.57, 3.8, 3.96, 4.38, 4.85, 5.42, 7.05, 9.93, 14.3, 20.28, 31.3, 54.34, 68.23, 78.61, 86.16, 92.34, 95.95, 98.04, 99.04, 99.53, 99.98, 100, 100

GZ-23
0, 4.8, 0, 0, 0, 0, 0, 0, 0.22, 2.37, 10.21, 30.25, 63.96, 85.05, 94.24, 97.76, 99.03, 99.20, 99.22, 99.41, 99.57, 99.75, 99.87, 99.92, 99.97, 100, 100

GZ-24
0, 4.8, .45, 1.02, 1.35, 1.35, 1.38, 1.86, 3.36, 7.44, 20.55, 51.22, 83.92, 95.57, 98.67, 99.32, 99.6, 99.65, 99.65, 99.82, 99.92, 100, 100, 100, 100, 100, 100

Spit (Beach, Dune, Overwash)
GZ-33
0, 4.8, 0, 0, 0, 0, 0, 0, 0, 2.21, 10.53, 29.17, 54.92, 76.6, 89.53, 95.33, 97.75, 98.76, 99.11, 99.42, 99.69, 99.86, 100, 100, 100, 100, 100

GZ-34
0, 4.8, 0, 0, 0, 0, .05, .47, 2.25, 7.59, 21.53, 41.46, 66.05, 84.42, 93.82, 97.26, 98.69, 99.1, 99.39, 99.73, 99.89, 100, 100, 100, 100, 100, 100

GZ-35
0, 4.8, 0, 0, 0, 0, 0, 0, .59, 3.34, 13.04, 32.87, 60.74, 82.55, 93.86, 97.4, 98.67, 98.89, 99.34, 99.66, 99.9, 100, 100, 100, 100, 100, 100

GZ-36
0, 4.8, 0, 0, 0, 0, 0, 0, 0, 2, 7.8, 19.15, 45.01, 75.05, 91.33, 96.58, 98.47, 99.11, 99.37, 99.55,

99.77, 99.95, 100, 100, 100, 100, 100

GZ-37
0, 4.8, 0, 0, 0, 0, 0, 0, 0, .7, 8.29, 35.58, 74.54, 92.47, 97.72, 99.13, 99.62, 99.68, 99.76, 99.77, 99.83, 99.88, 100, 100, 100, 100, 100

GZ-38
0, 4.8, .11, .15, .21, .29, .55, 1.13, 2.48, 5.92, 13.06, 26.23, 49.51, 75.49, 90.58, 95.72, 98.04, 98.87, 99.31, 99.56, 99.74, 99.95, 100, 100, 100, 100, 100

Nearshore
GZ-27
0, 4.8, 0, 0, 0, 0, 0, 0, .9, 1.27, 5.74, 21.07, 66.46, 91.06, 97.93, 99.31, 99.8, 99.81, 99.81, 99.81, 99.81, 99.89, 99.92, 99.94, 100, 100, 100

GZ-28
0, 4.8, 0, 0, 0, 0, 0, 0, 0, 0, .33, .69, 1.44, 3.58, 9.93, 25.34, 47.54, 67.91, 79.31, 87.75, 93.58, 96.9, 98.56, 99.43, 99.89, 100, 100

GZ-29
0, 4.8, 0, 0, 0, 0, 0, 0, .83, 1.13, 2.27, 5.03, 11.44, 22.56, 40.25, 62.44, 78.19, 88.23, 92.89, 95.58, 97.2, 98.29, 99.02, 99.49, 99.95, 100, 100

GZ-30
0, 4.8, 0, 0, 0, 0, 0, .16, .69, 1.62, 2.81, 4.96, 8.05, 12.54, 21.09, 37.11, 52.38, 65.50, 75.0381.77, 88.14, 93.49, 97.20, 98.98, 99.92, 100, 100

GZ-31
0, 4.8, 0, 0, 0, 0, 0, 0, 0, .2, 2.6, 9.33, 24.72, 47.22, 71.26, 84.01, 90.48, 94.38, 96.43, 97.53, 98.46, 99.16, 99.5, , 99.72, 99.97, 100, 100

GZ-32
0, 4.8, 0, 0, 0, 0, 0, 0, 0, .11, 1.67, 4.8, 11.71, 24.2, 43.2, 63.44, 77.06, 85.56, 91.16, 94.83, 97.63, 99.59, 100, 100, 100, 100, 100

Bay
GZ-41
-.8, 11.8, .55, .57, .79, 1.32, 1.89, 2.07, 2.08, 2.23, 2.25, 2.49, 3.12, 4.18, 5.6, 8.14, 13.14, 20.88, 28.37, 35.36, 41, 69, 48.61, 55.16, 60.3, 63.97, 67.07, 69.37, 71.34, 73.06, 74.62, 76.08, 77.64, 78.19, 80.62, 81.8, 82.86, 83.8, 84.59, 85.27, 85.82, 86.32, 86.79, 87.18, 87.64, 88.13, 88.66, 89.24, 89.77, 90.27, 90.75, 91.21, 91.68, 92.18, 92.7, 93.3, 93.92, 94.5, 95.09, 95.59, 95.88, 96.19, 100

GZ-42
0.8, 11.8, .74, .74, .78, .86, 1.29, 2.24, 4.52, 9.53, 18.01, 32.35, 46.04, 54.95, 60.98, 64.76, 67.83, 70.53, 73.04, 75.59, 77.79, 79.75, 81.43, 83.28, 85.06, 86.68, 87.85, 88.73, 89.14, 89.95, 90.37, 90.60, 90.73, 90.85, 91.0, 91.21, 91.46, 91.74, 92.07, 92.40, 92.72, 93.06, 93.38, 93.62, 93.84, 94.05, 94.26, 94.52, 94.78, 95.02, 95.25, 95, 53, 95.78, 100

Appendix B-2

Cumulative Weight Percentages of Suspended Sediments

August 6, 1986

Depth	6:21 - 7:20
0.06	1.6, 5, .36, 4.49, 20.72, 50.9, 75.71, 88.03, 93.73, 96.58, 97.8, 98.39, 98.78, 99.07, 99.29, 99.44, 99.58, 99.78, 99.95, 100
0.30	1.8, 5.0, 1.53, 8.53, 27.61, 56.73, 78.01, 87.68, 92.22, 94.4, 95.63, 96.66, 97.46, 98.1, 98.66, 99.16, 99.57, 99.91, 100
0.70	1.8, 4.6, .56, 3.9, 13.08, 31.14, 57.66, 75.64, 84.34, 88.8, 91.65, 93.63, 95.48, 97.15, 98.43, 99.86, 100
1.00	1, 5, .83, .83, .83, .83, 1.24, 4.12, 10.52, 21.65, 38.35, 53.2, 64.12, 68.9, 76.29, 80.41, 82.27, 87.01, 89.07, 92.78, 95.67, 99.59, 100

Depth	7:30 - 8:30
0.06	0, 4.6, 0, 0, 0, 0, 0, 0, 0, .53, 2.58, 9.56, 27.13, 56.29, 82.01, 93.18, 96.43, 97.82, 98.4, 98.82, 99.07, 99.3, 99.51, 99.75, 99.98, 100
0.30	0, 5.0, 0, 0, 0, 0, 0, 0, 0, 0, .26, 1.9, 8.24, 27.01, 58.89, 80.64, 88.67, 92.54, 94.1, 95.39, 96.39, 97.15, 97.77, 98.31, 98.85, 99.36, 99.89, 100
0.70	0., 5., 0., 0., 0., 0., 0., 0., 0., 0.01, 0.12, 0.28, 4.22, 19.76, 42.76, 69.38, 86.39, 92.31, 94.32, 95.94, 96.04, 96.92, 97.61, 98.23, 98.81, 99.36, 99.88, 100
1.00	0, 5.0, 0, 0, 0, 0, 0, 0, 0, .09, .4, 1.72, 6.25, 17.22, 39.1, 65.86, 81.42, 89.04, 92.16, 94.1, 95.16, 96.12, 97.09, 97.93, 98.55, 99.25, 99.87, 100

Depth	8:48 - 9:48
0.06	0, 4.6, 0, 0, 0, 0, 0, 0, 0, .27, 3.43, 13.71, 39.86, 73.48, 89.9, 94.78, 96.95, 98.1, 98.7, 99.06, 99.29, 99.53, 99.72, 99.95, 99.98, 100
0.30	0, 5.0, 0, 0, 0, 0, 0, 0, 0, 0, 0, 0, 2.58, 12.98, 39.11, 70.72, 88.34, 94.19, 96.58, 97.56, 98.14, 98.49, 98.73, 99.0, 99.23, 99.43, 99.67, 99.95, 100
0.70	0, 5.0, 0, 0, 0, 0, 0, 0, 0, 0, 0, .97, 6.45, 21.43, 48.81, 73.97, 85.52, 91.29, 93.74, 95.37, 96.45, 97.09, 97.75, 98.21, 98.72, 99.28, 99.91, 100
1.00	0, 5.0, 0, 0, 0, 0, 0, 0, .03, .11, .29, .94, 4.95, 15.6, 36.83, 62.2, 78.51, 86.95, 90.14, 92.48, 94.13, 95.39, 96.57, 97.59, 98.4, 99.11, 99.87, 100

Depth	10:58 - 12:00
0.06	0, 4.0, 0, 0, 0, 0, 0, 0, .55, 2.95, 9.95, 24.65, 55.68, 82.35, 94.39, 98.06, 98.86, 99.22, 99.33, 99.51, 99.7, 100
0.30	0, 5.0, 0, 0, 0, 0, 0, 0, 0, 0, 0, 1.57, 7.29, 23.66, 53.04, 79.71, 91.76, 95.74, 97.42, 97.97, 98.4, 98.69, 98.92, 99.12, 99.33, 99.5, 99.68, 99.97, 100
0.70	0, 5.0, 0, 0, 0, 0, 0, 0, 0, 0, 0, .94, 5.12, 21.08, 53.23, 80.1, 91.67, 95.12, 96.86, 97.35, 97.8, 98.19, 98.48, 98.76, 99.03, 99.31, 99.61, 99.95, 100
1.00	0, 5.2, 0, 0, 0, 0, 0, 0, 0, 0, 0, 2.2, 13.54, 39.91, 73.2, 88.69, 93.32, 95.08, 96.22, 96.8, 97.17, 97.49, 97.89, 98.21, 98.53, 98.91, 99.28, 99.63, 100

Depth	12:10 - 13:10
0.06	0, 4.0, 0.12, 0.17, 0.17, 0.17, 0.17, 0.17, 0.17, 0.17, 1.59, 7.53, 26.83, 63.3, 87.68, 95.7, 97.81, 98.66, 99.04, 99.23, 99.49, 99.8, 100
0.30	0, 5.0, 0, 0, 0, 0, 0, 0, 0, .12, 1.5, 6.8, 23.64, 56.35, 83.24, 93.35, 96.43, 97.69, 98.2, 98.45, 98.68, 98.9, 99.13, 99.3, 99.49, 99.71, 99.96, 100
0.70	0, 5.0, 0, 0, 0, 0, 0, 0, 0, 0, 0, 2.54, 14.03, 44.37, 76.43, 90.26, 94.9, 96.74, 97.41, 97.77, 98.12, 98.43, 98.74, 99.03, 99.35, 99.68, 99.94, 100
1.00	0, 5.0, 0, 0, 0, 0, 0, 0, 0, 0, .05, 1.71, 10.71, 35.2, 67.85, 85.21, 90.55, 92.99, 93.93, 94.61, 95.23, 95.97, 96.72, 97.54, 98.32, 99.14, 99.91, 100

Depth	13:20 - 14:20
0.06	-1, 4.6, 0, .01, .03, .04, .04, .06, .06, .06, .06, .06, .06, .06, .7, 3.58, 11.15, 35.3, 70.69, 90.7, 96.64, 97.96, 98.58, 98.92, 99.08, 99.25, 99.41, 99.6, 99.75, 99.97, 100
0.30	0, 5.2, 0, 0, 0, 0, 0, 0, 0, 0, 0, .81, 4.59, 18.39, 50.98, 79.3, 91.27, 94.5, 95.95, 96.47, 96.91, 97.28, 97.65, 98.13, 98.59, 99.02, 99.5, 99.94, 100
0.70	0, 5.2, 0, 0, 0, 0, 0, 0, 0, 0, 0, 1.56, 10.02, 30.5, 62.49, 79.74, 85.7, 87.98, 89.09, 90.04, 90.99, 91.82, 93.21, 94.94, 96.55, 98.16, 99.67, 100
1.00	0, 5.2, 0, 0, 0, 0, 0, 0, 0, 0, .95, 1.5, 2.05, 6.82, 20.87, 44.61, 59.89, 64.8, 69.03, 72.31, 74.76, 76.67, 80.63, 83.77, 87.59, 91.13, 95.23, 98.18, 100

August 7, 1986

Depth	10:00 - 11:00
0.06	-1, 4.6, .05, .09, 0.09, 0.09, 0.09, .09, .09, .09, .09, .09, .09, .41, 2.76, 10.54, 29.15, 62.76, 85.18, 94.83, 97.85, 98.68, 99.09, 99.2, 99.35, 99.47, 99.58, 99.7, 99.8, 99.99, 100
0.30	1.8, 5.0, 1.53, 8.53, 27.61, 56.73, 78.01, 87.68, 92.22, 94.4, 95.63, 96.66, 97.46, 98.1, 98.66, 99.16, 99.57, 99.81, 100
0.70	1.8, 4.6, .56, 3.9, 13.08, 31.14, 57.66, 75.64, 84.34, 88.8, 91.65, 93.63, 95.48, 97.15, 98.43, 99.86, 100
1.00	1, 5, .83, .83, .83, .83, 1.24, 4.12, 10.52, 21.65, 38.35, 53.2, 64.12, 69.9, 76.29, 80.41, 82.27, 87.01, 89.07, 92.78, 95.67, 99.59, 100

Depth	11:10 - 12:10
0.06	-1, 4.6, .02, .02, .02, .02, .02, .02, .02, .02, .02, .02, .02, .02, .35, 3.08, 12.18, 37.94, 67.9, 87.04, 94.83, 97.33, 98.37, 98.84, 99.05, 99.3, 99.47, 99.65, 99.8, 99.97, 100
0.30	1.6, 5, .89, 5.23, 22.5, 51.93, 78.08, 90.39, 94.92, 96.99, 97.83, 98.41, 98.66, 98.9, 99.16, 99.33, 99.51, 99.7, 99.93, 100
0.70	1.6, 5, .16, 2.48, 12.14, 34.04, 63.65, 83.24, 91.61, 95.24, 96.55, 97.4, 98.06, 98.54, 98.89, 99.2, 99.44, 99.68, 99.94, 100
1.00	1.8, 5, 1.25, 9.54, 29.9, 57.22, 78.72, 88.29, 93.26, 95.39, 96.56, 97.36, 97.87, 98.45, 98.87, 99.23, 99.59, 99.92, 100

Depth	12:20 - 13:20
0.06	1.2, 4.4, .1, .78, 3.97, 13.25, 38.77, 71.55, 90.87, 97.12, 98.58, 99.15, 99.23, 99.3, 99.42, 99.62, 99.72, 99.85, 100
0.30	1.4, 4.6, .35, 2.59, 10.28, 35.58, 68.45, 88.82, 95.97, 98.04, 98.7, 98.93, 99.1, 99.25, 99.37, 99.56, 99.77, 99.95, 100
0.70	1.6, 5.0, .42, 4.54, 19.64, 50.71, 78.74, 90.85, 95.15, 97.15, 97.95, 98.37, 98.74, 99.01, 99.24, 99.43, 99.6, 99.76, 99.94, 100
1.00	1.6, 5, .11, 2.82, 14.91, 45.63, 76.01, 90.16, 94.77, 96.66, 97.5, 97.95, 98.25, 98.49, 98.76, 98.99, 99.26, 99.6, 99.94, 100

Depth	13:35 - 14:35
0.06	-.8, 4.6, .03, .03, .03, .03, .03, .03, .03, .03, .03, .03, .27, 1.61, 5.76, 18.26, 50.69, 81.02, 94.92, 98.26, 98.89, 99.2, 99.33, 99.33, 99.43, 99.61, 99.72, 99.83, 99.98, 100
0.30	1.6, 5, .36, 4.49, 20.72, 50.9, 75.71, 88.03, 93.73, 96.58, 97.8, 98.39, 98.78, 99.07, 99.29, 99.44, 99.58, 99.78, 99.95, 100
0.70	-.6, 5, .05, .05, 0.25, .93, .93, .93, .96, .96, .96, .96, .66, .96, .96, 5.94, 28.27, 70.82, 92.47, 97.20, 98.36,98.67,98.87, 98.98, 99.16, 99.33, 99.42, 99.57, 99.73, 99.85,100
1.00	1.6, 5, .36, 3.75, 19.49, 55.45, 85.18, 94.35, 96.56, 97.54, 97.93, 98.12, 98.3, 98.51, 98.69, 98.9, 99.19, 99.5, 99.84, 100

Depth	14:45 - 15:45
0.06	-1, 4.4, .02, .02, .02, .02, .02, .02, .02, .02, .02, .02, .02, .11, 1.29, 6.15, 20.02, 56.8, 85.38, 96.35, 98.69, 99.15, 99.36, 99.40, 99.49, 99.54, 99.67, 99.79, 99.89, 100
0.30	1.6, 5, .75, 5.18, 21.34, 53.31, 79.84, 91.18, 95.07, 96.85, 97.57, 98.02, 98.43, 98.78, 99.03, 99.2, 99.43, 99.64, 99.88, 100
0.70	1.6, 5.0, .38, 3.80, 18.00, 53.31, 84.28, 94.50, 97.14, 98.01, 98.28, 98.48, 98.72, 98.94, 99.11, 99.27, 99.46, 99.68, 99.94, 100
1.00	1.6, 5.2, .25, 3.33, 20.14, 53.09, 80.75, 91.66, 94.93, 96.21, 96.77, 97.14, 97.41, 97.75, 98.15, 98.58, 98.98, 99.38, 99.67, 99.87, 100

Depth	16:00 - 17:00
0.06	1.2, 4.6, .27, 1.84, 6.65, 19.24, 51.29, 81.22, 94.23, 97.57, 98.48, 98.79, 98.94, 99.05, 99.23, 99.38, 99.58, 99.81, 99.99, 100
0.30	-.8, 5, .04, .09, .21, .26, .3, .39, .47, .51, .51, .51, 1.11, 2.74, 8.77, 22.84, 50.34, 74.85, 87.94, 92.05, 92.86, 93.54, 93.71, 94.23, 95, 95.81, 96.54, 97.26, 97.99, 98.85, 99.79, 100
1.00	-.8, 5, .25, 1.01, 1.01, 1.01, 2.52, 2.77, 2.77, 3.02, 3.02, 3.02, 3.27, 3.78, 5.04, 6.8, 12.34, 22.67, 36.78, 47.61, 52.14, 54.66, 57.93, 60.45, 63.98, 67.51, 74.06, 78.85, 85.89, 92.95, 99.24, 100

August 8, 1986

Depth	8:30 - 9:30
0.06	1.4, 4.0, .97, 5.53, 18.23, 51.1, 78.29, 92.29, 97, 98.29, 98.89, 99.11, 99.36, 99.53, 99.78, 100
0.30	1.6, 5.0, .23, 2.3, 11.42, 32.05, 61.73, 81.45, 89.95, 93.89, 95.38, 96.47, 97.34, 98.02, 98.56, 98.95, 99.34, 99.66, 99.95, 100

0.70	1.6, 5, 1.13, 2.46, 9.03, 23.39, 46.77, 69.85, 81.33, 87.08, 89.95, 92, 93.13, 94.15, 95.08, 95.8, 96.62, 97.95, 99.59, 100
1.00	1.6, 5, 1.13, 2.46, 9.03, 23.39, 46.77, 69.85, 81.33, 87.08, 89.95, 92, 93.13, 94.15, 95.08, 95.8, 96.62, 97.95, 99.59, 100

Depth	9:45 - 10:45
0.06	-1, 4.4, .02, .02, .02, .1, .1, .1, .1, .1, .1, .1, .16, .62, 3.17, 11.19, 30.89, 67.37, 88.48, 96.51, 98.58, 99.04, 99.29, 99.4, 99.59, 99.59, 99.64, 99.68, 99.84, 100
0.30	1.8, 4.4, 1.74, 12.91, 37.72, 65.56, 84.12, 91.7, 95.27, 97.13, 98.07, 98.69, 99.1, 99.44, 99.71, 100
0.70	1.8, 5, 1.44, 7.78, 23.58, 51.28, 74.91, 86.47, 91.54, 93.53, 94.9, 95.9, 96.74, 97.44, 98.06, 98.71, 99.28, 99.9, 100
1.00	1.4, 5, .27, .63, 2.78, 9.68, 24.02, 47.67, 69.18, 81.18, 86.83, 89.16, 91.04, 92.92, 94.54, 95.79, 96.6, 97.49, 98.48, 99.82, 100

Depth	10:55 - 11:55
0.06	1.4, 4.6, .22, 2.81, 10.99, 37.4, 72.16, 91.24, 97.02, 98.5, 99.1, 99.31, 99.64, 99.68, 99.74, 99.81, 99.86, 99.99, 100
0.30	1.6, 4.4, .28, 3.91, 18.53, 45.9, 73.37, 88.12, 94.3, 96.3, 98.03, 98.69, 99.16, 99.51, 99.72, 99.92, 100
0.70	1.8, 5, 3.08, 15.32, 45.88, 74.35, 87.2, 92.66, 95.39, 96.52, 97.26, 97.91, 98.38, 98.8, 99.09, 99.38, 99.66, 99.94, 100
1.00	1.8, 5, 2.5, 13.4, 39.72, 70.45, 86.24, 92.84, 95.51, 96.66, 97.32, 97.87, 98.21, 98.57, 98.93, 99.23, 99.61, 99.85, 100

Depth	12:10 - 13:10
0.06	1.4, 3.8, 1.15, 6.06, 19.9, 54.26, 82.78, 95.6, 98.74, 99.37, 99.59, 99.61, 99.73, 99.97, 100
0.30	1.4, 4.6, .24, 2.34, 9.42, 28.25, 58.14, 81.74, 91.94, 95.66, 97.38, 98.22, 98.8, 99.08, 99.37, 99.59, 99.76, 99.95, 100
0.70	1.6, 4.6, .44, 4.09, 17.83, 46.43, 71.81, 85.75, 91.65, 94.73, 96.43, 97.55, 98.28, 98.88, 99.34, 99.68, 99.98, 100
1.00	1.8, 4.6, 1.38, 6.97, 22.94, 51.08, 74.65, 85.81, 91.14, 94.24, 96.41, 97.82, 98.78, 99.4, 99.75, 99.98, 100

Depth	13:26 - 14:26
0.06	1.4, 4, .77, 5.06, 17.94, 53.54, 82.84, 95.43, 98.46, 99.09, 99.34, 99.4, 99.51, 99.65, 99.84, 100
0.30	1.6, 5, .8, 6.47, 29.52, 68.33, 89.93, 95.27, 96.61, 97.18, 97.46, 97.61, 97.78, 98.01, 98.3, 98.6, 98.95, 99.4, 99.92, 100
0.70	1.6, 5.2, .34, 3.14, 18.1, 49.14, 72.39, 81.39, 83.94, 84.93, 85.51, 85.95, 86.46, 87.08, 88.07, 89.43, 91.38, 93.53, 95.86, 98.03, 100
1.00	1.6, 5, .37, 1.25, 7.05, 21.68, 41.29, 52.02, 55.03, 56.65, 57.82, 59.15, 61.06, 63.78, 68.85, 75.09, 82.81, 90.74, 98.75, 100

Appendix C

Bedform Data

This section lists the data of bedform measurements using tapes and rulers. Wave lengths of megaripples are the average of the distance between the crests of two bedforms. The height is the average of vertical distances between the trough and the crest involved. For small ripples, the corresponding figures are the averages of six forms instead of two.

Type II Megaripples

Subtidal Channels				Intertidal Flats			
South Channel		Main channel		North CMLB		South CMLB	
Length (m)	Height (m)	Length (m)	Height (m)	Length (m)	Height (m)	Length (m)	Height (m)
7/30/1987		7/30/1987		6/22/1986		7/23/1986	
3.48	0.09	5.00	0.24	1.60	0.12	1.70	0.07
5.85	0.12	2.20	0.27	2.65	0.17	2.10	0.08
3.07	0.13	5.29	0.22	3.20	0.28	2.30	0.11
4.24	0.15	5.90	0.28	2.70	0.20	1.30	0.05
3.49	0.12	4.20	0.22	1.80	0.10	1.90	0.07
2.81	0.15	8/9/1987		2.10	0.18		
8/9/1987		6.00	0.60	2.80	0.21		
6.33	0.23	4.90	0.30	2.50	0.20		
8.03	0.30	4.70	0.29	8/9/1987			
7.05	0.31	5.50	0.45	2.10	0.27		
5.10	0.29	3.60	0.30	1.80	0.09		

3.52	0.19	4.00	0.28	2.30	0.12
5.88	0.44	7/30/1987(Throat)		1.10	0.14
8/4/1986(spit)		3.30	0.30	2.50	0.15
4.95	0.32	2.70	0.28	7/2/1984	
6.40	0.26	4.20	0.09	1.5	0.45
4.70	0.20	3.60	0.15	2.7	0.30
6.50	0.27	2.80	0.20	4.0	.55
5.00	0.28	8/17/1986(Throat)		2.4	0.35
4.00	0.18	5.60	0.39	3.1	0.35
2.90	0.26	4.70	0.28	3.5	0.45
8/6/1986		3.90	0.31		
5.60	0.28	5.20	0.29		
4.60	0.30	7/9/1986			
4.10	0.12	4.80	0.33		
7.15	0.28	3.81	0.23		
6.23	0.24	4.50	0.25		
		8/9/1987(Throat)			
		4.30	0.27		
		3.21	0.21		
		3.86	0.21		

Type I Megaripple

Subtidal Channels				Intertidal Flats			
South Channel		Marginal channel		Flood ramp		North CMLB	
Length (m)	Height (m)	Length (m)	Height (m)	Length (m)	Height (m)	Length (m)	Height (m)
6/23/86		7/4/1986		8/10/1987		8/10/1987	
7.54	0.17	8.35	0.22	3.45	0.24	11.60	0.21
10.45	0.14	4.54	0.21	7.77	0.27	7.80	0.14

6.91	0.21	6.50	0.27	6.21	0.33	10.60	0.11
9.38	0.20			8/4/1986		9.20	0.24
11.60	0.31			2.20	0.15	6/22/1988	
5.99	0.24			1.85	0.20	9.30	0.08
7/30/1987						12.70	0.08
8.28	0.21					8.50	0.06
9.33	0.27					10.10	0.09
7.99	0.21					(Middle section)	
8/10/1987						2.20	0.13
6.88	0.25					1.60	0.12
11.0	.44					3.10	0.22
9.66	0.37					2.70	0.20
8.45	0.36						

Small Ripples

0.15	0.014
0.18	0.016
0.16	0.012
0.17	0.008
0.12	0.011
0.11	0.012
0.07	0.010
0.09	0.010
0.32	0.028
0.42	0.035
0.29	0.019

Appendix D

Current Data

Three types of current meters were used in recording current speeds at various stages of the study. The following table lists the specifications of the current meters.

Specifications of Current Meters Used in the Study

Type	Aanderaa	Endeco	Marsh-Mcbirney
Model	RCM4	110	201
Range	0.025-2.5	0 - 2.57	0 - 3.1
Accuracy	±1 cm/s	±2 cm/s	±3% of full scale
Speed Sensor	Rotor with magnetic coupling	Impeller & reed switch	Transducer prober
Recording Method	Magnetic tape	Panel reading	Panel reading

Data produced by the current meters are too lengthy to list here all. They are stored either on 5 1/4 inch floppy disks or tapes, and are available upon request. This appendix selects two examples of data obtained using the Marsh-McBirney current meter. Appendix D-1 lists results of velocity profile measurements during suspended sediment measurements, followed by hydraulic parameters calculated from these measurements. Appendix D-2 lists current speeds and other hydraulic data corresponding to bedform data in Appendix C.

Appendix D-1

Velocity Profile Measurements Using Marsh-McBirney 201

August 6, 1986

Time (hours)	Tide (m)	Depth (m)	Sample number	Times Depth	Sample elevation	Speed (m/s)
6.6	0.51	2.41	1	0.15	0.36	0.07
			2	0.24	0.57	0.07
			3	0.37	0.89	0.10
			4	0.58	1.39	0.11
			5	0.90	2.16	0.13
6.7	0.51	2.41	1	0.15	0.36	0.14
			2	0.24	0.57	0.17
			3	0.37	0.89	0.18
			4	0.58	1.39	0.22
			5	0.90	2.16	0.25
7.0	0.50	2.40	1	0.15	0.36	0.23
			2	0.24	0.57	0.26
			3	0.37	0.88	0.28
			4	0.58	1.39	0.32
			5	0.90	2.16	0.35
7.2	0.49	2.39	1	0.15	0.35	0.32
			2	0.24	0.57	0.33
			3	0.37	0.88	0.39
			4	0.58	1.38	0.43
			5	0.90	2.15	0.45
7.5	0.49	2.39	1	0.15	0.35	0.39
			2	0.24	0.57	0.47
			3	0.37	0.88	0.49
			4	0.58	1.38	0.52
			5	0.90	2.15	0.59
7.7	0.48	2.38	1	0.15	0.35	0.54
			2	0.24	0.57	0.55
			3	0.37	0.88	0.57
			4	0.58	1.38	0.64
			5	0.90	2.14	0.70
8.0	0.46	2.36	1	0.15	0.35	0.55
			2	0.24	0.56	0.58
			3	0.37	0.87	0.64
			4	0.58	1.36	0.68
			5	0.90	2.12	0.77
8.2	0.44	2.34	1	0.15	0.35	0.58
			2	0.24	0.56	0.66
			3	0.37	0.86	0.69
			4	0.58	1.35	0.73
			5	0.90	2.10	0.85
9.0	0.35	2.25	1	0.15	0.33	0.67

			2	0.24	0.54	0.76
			3	0.37	0.83	0.82
			4	0.58	1.30	0.85
			5	0.90	2.02	0.97
9.2	0.32	2.22	1	0.15	0.33	0.64
			2	0.24	0.53	0.72
			3	0.37	0.82	0.77
			4	0.58	1.28	0.87
			5	0.90	1.99	0.88
9.5	0.29	2.19	1	0.15	0.32	0.62
			2	0.24	0.52	0.66
			3	0.37	0.81	0.75
			4	0.58	1.27	0.78
			5	0.90	1.97	0.89
9.7	0.25	2.15	1	0.15	0.32	0.60
			2	0.24	0.51	0.62
			3	0.37	0.79	0.71
			4	0.58	1.24	0.77
			5	0.90	1.93	0.80
11.1	0.1	2	1	0.15	0.30	0.49
			2	0.24	0.48	0.56
			3	0.37	0.74	0.58
			4	0.58	1.16	0.63
			5	0.90	1.80	0.72
11.3	0.07	1.97	1	0.15	0.29	0.46
			2	0.24	0.47	0.47
			3	0.37	0.72	0.58
			4	0.58	1.14	0.59
			5	0.90	1.77	0.67
11.6	0.04	1.94	1	0.15	0.29	0.42
			2	0.24	0.46	0.46
			3	0.37	0.71	0.53
			4	0.58	1.12	0.59
			5	0.90	1.74	0.71
11.8	0.01	1.91	1	0.15	0.28	0.42
			2	0.24	0.45	0.46
			3	0.37	0.70	0.53
			4	0.58	1.10	0.60
			5	0.90	1.71	0.67
12.2	-0.04	1.86	1	0.15	0.27	0.37
			2	0.24	0.44	0.42
			3	0.37	0.68	0.47
			4	0.58	1.07	0.51
			5	0.90	1.67	0.62
12.5	-0.06	1.84	1	0.15	0.27	0.33
			2	0.24	0.44	0.37
			3	0.37	0.68	0.38
			4	0.58	1.06	0.43
			5	0.90	1.65	0.44
12.7	-0.09	1.81	1	0.15	0.27	0.32
			2	0.24	0.43	0.35

			3	0.37	0.66	0.38
			4	0.58	1.04	0.39
			5	0.90	1.62	0.49
13.0	-0.11	1.79	1	0.15	0.26	0.30
			2	0.24	0.42	0.34
			3	0.37	0.66	0.35
			4	0.58	1.03	0.39
			5	0.90	1.61	0.47
13.4	-0.14	1.76	1	0.15	0.26	0.28
			2	0.24	0.42	0.29
			3	0.37	0.65	0.32
			4	0.58	1.02	0.36
			5	0.90	1.58	0.43
13.7	-0.16	1.74	1	0.15	0.26	0.26
			2	0.24	0.41	0.28
			3	0.37	0.64	0.29
			4	0.58	1.00	0.32
			5	0.90	1.56	0.34
13.9	-0.17	1.73	1	0.15	0.25	0.15
			2	0.24	0.41	0.16
			3	0.37	0.64	0.17
			4	0.58	1.00	0.22
			5	0.90	1.55	0.27
14.2	-0.19	1.71	1	0.15	0.25	0.15
			2	0.24	0.41	0.16
			3	0.37	0.63	0.18
			4	0.58	0.99	0.21
			5	0.90	1.53	0.23

August 8, 1986

Time (hours)	Tide (m)	Depth (m)	Sample number	Times Depth	Sample elevation	Speed (m/s)
8.7	0.35	2.35	1	0.15	0.35	0.30
			2	0.24	0.56	0.37
			3	0.37	0.86	0.38
			4	0.58	1.36	0.39
			5	0.90	2.11	0.47
8.9	0.34	2.34	1	0.15	0.35	0.30
			2	0.24	0.56	0.38
			3	0.37	0.86	0.40
			4	0.58	1.35	0.41
			5	0.90	2.10	0.49
9.2	0.32	2.32	1	0.15	0.34	0.41
			2	0.24	0.55	0.43
			3	0.37	0.85	0.44
			4	0.58	1.34	0.50
			5	0.90	2.08	0.57
9.4	0.3	2.3	1	0.15	0.34	0.43

			2	0.24	0.55	0.47
			3	0.37	0.85	0.52
			4	0.58	1.33	0.54
			5	0.90	2.07	0.66
9.9	0.24	2.24	1	0.15	0.33	0.44
			2	0.24	0.53	0.46
			3	0.37	0.82	0.52
			4	0.58	1.29	0.56
			5	0.90	2.01	0.64
10.2	0.21	2.21	1	0.15	0.33	0.46
			2	0.24	0.53	0.53
			3	0.37	0.81	0.55
			4	0.58	1.28	0.56
			5	0.90	1.98	0.63
10.4	0.19	2.19	1	0.15	0.32	0.51
			2	0.24	0.52	0.54
			3	0.37	0.81	0.62
			4	0.58	1.27	0.66
			5	0.90	1.97	0.65
10.7	0.17	2.17	1	0.15	0.32	0.52
			2	0.24	0.52	0.62
			3	0.37	0.80	0.67
			4	0.58	1.25	0.74
			5	0.90	1.95	0.77
11.1	0.12	2.12	1	0.15	0.31	0.54
			2	0.24	0.50	0.63
			3	0.37	0.78	0.66
			4	0.58	1.22	0.73
			5	0.90	1.90	0.73
11.3	0.1	2.1	1	0.15	0.31	0.50
			2	0.24	0.50	0.54
			3	0.37	0.77	0.60
			4	0.58	1.21	0.67
			5	0.90	1.89	0.68
11.6	0.07	2.07	1	0.15	0.31	0.44
			2	0.24	0.49	0.48
			3	0.37	0.76	0.54
			4	0.58	1.20	0.57
			5	0.90	1.86	0.71
11.8	0.04	2.04	1	0.15	0.30	0.43
			2	0.24	0.48	0.48
			3	0.37	0.75	0.54
			4	0.58	1.18	0.56
			5	0.90	1.83	0.67
12.3	-0.01	1.99	1	0.15	0.29	0.38
			2	0.24	0.47	0.42
			3	0.37	0.73	0.46
			4	0.58	1.15	0.51
			5	0.90	1.79	0.54
12.6	-0.03	1.97	1	0.15	0.29	0.33
			2	0.24	0.47	0.36

			3	0.37	0.72	0.43
			4	0.58	1.14	0.49
			5	0.90	1.77	0.51
12.8	-0.05	1.95	1	0.15	0.29	0.32
			2	0.24	0.46	0.35
			3	0.37	0.72	0.40
			4	0.58	1.13	0.43
			5	0.90	1.75	0.47
13.1	-0.08	1.92	1	0.15	0.28	0.30
			2	0.24	0.46	0.33
			3	0.37	0.71	0.38
			4	0.58	1.11	0.40
			5	0.90	1.72	0.43
13.6	-0.12	1.88	1	0.15	0.28	0.16
			2	0.24	0.45	0.21
			3	0.37	0.69	0.27
			4	0.58	1.09	0.28
			5	0.90	1.69	0.31
13.8	-0.14	1.86	1	0.15	0.27	0.13
			2	0.24	0.44	0.14
			3	0.37	0.68	0.17
			4	0.58	1.07	0.17
			5	0.90	1.67	0.19
14.1	-0.17	1.83	1	0.15	0.27	0.11
			2	0.24	0.43	0.13
			3	0.37	0.67	0.14
			4	0.58	1.06	0.16
			5	0.90	1.64	0.15
14.3	-0.19	1.81	1	0.15	0.27	0.10
			2	0.24	0.43	0.11
			3	0.37	0.66	0.11
			4	0.58	1.04	0.13
			5	0.90	1.62	0.13

Hydraulic Parameters Calculated From August 6 Current Data

U	U_*	δU_*	Z_o	δZ_o	Chezy	τ	$\delta\tau$	R	Student t
0.09	1.53	0.71	7.96	9.61	18.87	0.24	0.22	0.969	6.845
0.18	2.53	0.71	4.52	4.01	23.30	0.64	0.36	0.988	11.292
0.28	2.72	0.46	1.32	0.97	32.88	0.74	0.25	0.996	18.822
0.38	3.24	1.28	0.79	1.53	36.88	1.06	0.84	0.977	8.018
0.49	4.07	1.63	0.71	1.41	37.73	1.66	1.33	0.977	7.938
0.59	3.66	2.24	0.12	0.52	51.15	1.35	1.65	0.949	5.190
0.64	4.85	1.69	0.43	0.83	41.45	2.36	1.64	0.982	9.120
0.70	5.50	2.48	0.52	1.26	39.86	3.03	2.73	0.971	7.047
0.81	6.21	2.14	0.44	0.83	40.91	3.87	2.67	0.983	9.202
0.77	5.67	2.04	0.34	0.71	42.74	3.22	2.33	0.981	8.807
0.73	5.94	2.07	0.56	1.02	38.86	3.54	2.47	0.982	9.123
0.69	4.93	1.83	0.27	0.60	44.32	2.44	1.81	0.980	8.542
0.59	4.78	1.81	0.51	1.03	38.90	2.29	1.74	0.979	8.382
0.55	4.87	2.52	0.78	1.99	35.42	2.38	2.46	0.963	6.147
0.53	6.59	2.33	2.78	3.59	25.40	4.34	3.08	0.982	8.965
0.53	5.88	1.07	1.89	1.38	28.28	3.46	1.26	0.995	17.441

Continued --

U	U_*	δU_*	Z_o	δZ_o	Chezy	τ	$\delta\tau$	R	Student t
0.47	5.44	2.05	2.11	3.13	27.21	2.96	2.23	0.980	8.428
0.38	2.51	0.85	0.13	0.34	48.45	0.63	0.48	0.979	8.388
0.38	3.44	2.41	0.76	2.64	34.89	1.18	1.66	0.934	4.526
0.36	3.55	1.96	1.04	2.66	32.46	1.26	1.40	0.957	5.744
0.33	3.37	1.88	1.23	3.07	30.88	1.14	1.27	0.957	5.697
0.29	1.79	0.46	0.08	0.15	51.97	0.32	0.17	0.990	12.261
0.18	2.85	1.80	4.52	9.07	20.69	0.82	1.03	0.946	5.038
0.18	1.91	0.57	1.34	1.74	30.12	0.37	0.22	0.987	10.680

Hydraulic Parameters Calculated from August 8 Current Data

U	U_*	δU_*	Z_o	δZ_o	Chezy	τ	$\delta\tau$	R	Student t
0.38	3.26	2.15	0.81	2.59	36.55	1.06	1.40	0.94	4.82
0.39	3.73	2.14	1.26	3.21	33.04	1.39	1.60	0.95	5.52
0.46	3.50	2.23	0.40	1.43	41.90	1.23	1.57	0.94	4.98
0.52	4.80	2.62	1.10	2.74	33.99	2.31	2.53	0.95	5.81
0.52	4.51	1.66	0.80	1.44	36.20	2.04	1.50	0.98	8.63
0.54	3.32	1.79	0.11	0.42	51.38	1.11	1.19	0.95	5.89
0.59	3.58	2.39	0.10	0.48	51.97	1.29	1.72	0.94	4.75
0.66	5.61	1.78	0.71	1.13	36.91	3.15	2.01	0.98	9.98
0.55	4.31	2.28	0.17	0.58	47.64	1.87	1.97	0.96	6.02
0.59	4.40	1.54	0.34	0.68	42.39	1.94	1.36	0.98	9.07
0.54	5.76	3.12	1.75	3.89	29.52	3.33	3.60	0.95	5.87
0.53	5.09	2.11	1.13	2.13	32.80	2.59	2.15	0.97	7.66
0.46	3.69	0.43	0.50	0.31	39.01	1.37	0.32	0.99	27.12
0.42	4.48	1.45	1.70	2.28	29.35	2.01	1.31	0.98	9.78
0.39	3.43	0.52	0.74	0.56	35.75	1.18	0.36	0.99	20.86
0.36	2.97	0.73	0.50	0.67	38.62	0.89	0.44	0.99	12.84
0.24	3.49	1.63	4.42	6.59	21.52	1.22	1.14	0.96	6.80
0.15	1.35	0.65	0.61	1.53	36.87	0.18	0.18	0.96	6.56
0.13	0.99	0.84	0.26	1.33	43.47	0.10	0.17	0.90	3.73
0.11	0.71	0.46	0.10	0.46	50.48	0.05	0.07	0.94	4.96

Appendix D-2

Date		U_{max} m/s	T.R.* m	h_{max}	M_z phi	M_z mm	$\frac{U_{max}}{\sqrt{(gh_{max})}}$	$\frac{h_{max}}{M_z}$
				Type II Megaripples (Subtidal)				
8/4/86	Ebb spit	-0.73	0.76	1.3	2.09	0.235	0.204416	0.005531
8/6/86	South channel	-0.64	0.74	1.7	2.09	0.235	0.156718	0.007234
8/17/86	Main channel	-0.85	0.92	2.5	2.025	0.246	0.171638	0.010162
7/9/86	Main Channel	-0.69	0.74	2.1	2.015	0.247	0.152021	0.008502
7/30/87	South Channel	-0.43	0.40	1.6	2.09	0.235	0.108536	0.006808
8/9/87	South Channel	-0.79	0.97	1.7	2.09	0.235	0.193449	0.007234
7/30/87	Main Channel	-0.57	0.4	2.5	2.025	0.246	0.115098	0.010162
8/9/87	Main Channel	-0.88	0.97	2.7	2.025	0.246	0.170988	0.010975
7/30/87	Main Channel	-0.48	0.40	2.0	2.015	0.247	0.108365	0.008097
8/9/87	Main channel	-0.85	0.87	2.3	2.015	0.247	0.178945	0.009311
				Type II Megaripples (Intertidal)				
6/22/86	North CMLB	-0.75	1.05	0.35	2.01	0.248	0.404755	0.001411
8/9/87	North CMLB	-0.67	0.97	0.32	2.01	0.248	0.378151	0.001290
7/23/86	South CMLB	-0.71	0.82	0.41	2.14	0.227	0.354023	0.001806
				Type I Megaripples (Subtidal)				
7/4/86	Marginal Ch.	-0.36	0.73	1.73	2.06	0.24	0.087386	0.007208
6/23/86	South Ch.	-0.66	1.08	2	.14	0.227	0.149002	0.008810
7/30/87	South Ch	0.41	0.40	1.9	2.14	0.227	0.092650	0.008370
8/10/87	South Ch.	-0.68	0.88	2	.14	0.227	0.153518	0.008810
8/10/87	Flood Ramp	-0.57	0.88	1.6	2.245	0.211	0.143873	0.007582
				Type I Megaripples (Intertidal)				
8/10/87	North CMLB	0.45	0.88	0.4	2.01	0.248	0.227168	0.001612
6/22/86	North CMLB	0.49	1.05	0.4	2.01	0.248	0.247361	0.001612
6/22/86	North CMLB	0.60	1.05	0.4	2.01	0.248	0.367236	0.001209

* T.R. = Tidal Range

Appendix E

Vertical Aerial Photographs Used in the Study

Date	Run number	Altitude (metre)	Focal pt. (cm)	Scale
March 3,1958	A16096-197	2,500	15.24	
June 23,1964	A18452-197	5,486	15.24	
May 8, 1968	A20380-140	1,890	15.24	
Oct. 10,1971	A22600-48	3,115	15.24	
July 24,1981	81400-73			1,000
July 24,1981	81400-74			1,000